



The
University
Of
Sheffield.

PhD Thesis Elisabeth Kugler, BSc MSc

3D Quantification and Description of the Developing Zebrafish Cranial Vasculature

Department of Infection, Immunity and Cardiovascular Disease
Faculty of Medicine, University of Sheffield, United Kingdom

First Supervisor: Dr. Paul Armitage

Second Supervisor: Prof. Dr. Timothy Chico MBChB MRCP MD

Sheffield, April 2020

Contents

1	Introduction	6
1.1	Relevance of vascular quantification	6
1.2	Zebrafish are a suitable pre-clinical model to study the cardiovascular system . .	7
1.2.1	Embryonic development of the vascular system in zebrafish	8
1.2.2	Limitations of zebrafish as pre-clinical model	10
1.2.3	Visualization of the vascular system in zebrafish	10
1.3	Descriptive modelling of the cardiovascular system in zebrafish	12
1.3.1	Current approaches to vascular quantification	14
1.3.2	Machine Learning	24
1.3.3	3D vasculature quantification in embryonic zebrafish	24
1.3.4	Discussion of vasculature quantification	27
1.4	Endothelial cell membrane behaviours	28
1.5	Thesis aims and objectives	29
2	Segmentation of the Vasculature	33
2.1	Introduction	33
2.2	Material and methods	38
2.2.1	Zebrafish strains, handling, and husbandry	38
2.2.2	Image acquisition	39
2.2.3	Manual Signal-to-Noise and Contrast-to-Noise measurement	40
2.2.4	Motion artefact quantification and correction	41
2.2.5	Signal noise, filtering, and segmentation	42
2.2.6	Total cerebrovascular volume measurement	44
2.2.7	Evaluation of segmentation robustness and sensitivity	45
2.2.8	Biological application datasets	45
2.2.9	Developed image analysis macros	46
2.2.10	Statistics and data display	46
2.3	Results and discussion	46
2.3.1	Vascular Contrast-to-Noise ratio (CNR) differs in transgenic lines, but not over time or vessels of different size	46
2.3.2	Motion artefacts can be corrected using SIFT	48
2.3.3	Enhancement of the cerebral vasculature to improve image quality	52
2.3.4	Segmentation of the cerebral vasculature	64
2.3.5	Assessment of segmentation sensitivity and robustness	71
2.4	Conclusion	80
3	Vascular Intra-Sample Symmetry and Inter-sample Similarity	85
3.1	Introduction	85
3.2	Material and methods	87
3.2.1	Zebrafish strains, handling, and husbandry	87
3.2.2	Morpholino antisense gene knockdown	87
3.2.3	Imaging methodology	87
3.2.4	Intra-sample symmetry	87
3.2.5	Manual measurements of growth rates	89
3.2.6	Manual landmark-based inter-sample registration	90
3.2.7	Establishment of a vascular template at different developmental stages .	94
3.2.8	Vascular surface and density	94
3.2.9	Statistics and data display	96

3.3	Results and discussion	96
3.3.1	Intra-sample symmetry	96
3.3.2	Inter-object registration enables examination of vascular similarity	100
3.3.3	Establishment of vascular templates allows the study regions of similarity and variability	107
3.3.4	Inter-sample image registration to examine the impact of <i>dll4</i> knockdown	113
3.4	Conclusion	117
4	Extraction of Vascular Geometry	120
4.1	Introduction	120
4.2	Material and methods	125
4.2.1	Zebrafish strains, handling, and husbandry	125
4.2.2	Biological application datasets	125
4.2.3	Imaging methodology	126
4.2.4	2D ridge detection and analysis	126
4.2.5	Centreline extraction based on 3D thinning	126
4.2.6	2D/3D centreline analysis, branching point processing, and vessel segment identification	126
4.2.7	Vessel diameter analysis	126
4.2.8	Simple Neurite Tracer (SNT) for vessel tracing	127
4.2.9	Vascular network complexity assessment using Sholl analysis	127
4.2.10	Graphical User Interface (GUI)	128
4.2.11	Statistics and data display	128
4.3	Results and discussion	128
4.3.1	Centreline extraction based on ridge detection	128
4.3.2	Centreline extraction based on 3D thinning	128
4.3.3	Network analysis in 2D MIPs	131
4.3.4	Network analysis in 3D	135
4.3.5	Branching point detection and voxel identities	137
4.3.6	Vessel diameters sampling rate	138
4.3.7	Vessel diameter quantification	138
4.3.8	Extraction and analysis of individual vessel segments	140
4.3.9	Vascular network complexity assessment using Scholl analysis	147
4.3.10	Example biological application - Quantification of the effect of inhibiting actin polymerization	148
4.4	Conclusion	150
5	Characterisation of novel cystic endothelial membrane structures	153
5.1	Introduction	153
5.2	Material and methods	156
5.2.1	Zebrafish strains, handling, and husbandry	156
5.2.2	Generation of zebrafish with transient expression of <i>Tg(fli1a:myr-mCherry)</i>	156
5.2.3	Microangiography	157
5.2.4	Imaging methodology	157
5.2.5	Multiview image reconstruction	157
5.2.6	Morpholino injections	158
5.2.7	Dextran injection into brain ventricles	158
5.2.8	Reduction of blood flow and exsanguination	159
5.2.9	Chemical treatments	159
5.2.10	Live dyes	160
5.2.11	Image and data analysis	160

5.3	Results and discussion	160
5.3.1	Morphological description and physiological occurrence	160
5.3.2	<i>Kugel</i> cellular and sub-cellular context	169
5.3.3	Blood flow is not the driving factor of <i>kugel</i> formation	175
5.3.4	VEGF signalling inhibits <i>kugeln</i> , while NO is needed for their formation	176
5.3.5	Notch signalling is required for <i>kugel</i> formation	185
5.3.6	Wnt signalling has a balancing role in <i>kugel</i> formation	188
5.3.7	Neither lymphatic nor macrophages interact with <i>kugeln</i>	191
5.3.8	Neither osmotic pressure nor membrane rigidity impact <i>kugeln</i>	193
5.3.9	<i>Kugeln</i> show no similarity to previously described structures.	196
5.4	Conclusion	197
5.5	Future work	198
6	Overall Conclusion and Future Work	202
6.1	Summary of the conducted research and the contribution to knowledge	202
6.1.1	Image understanding, pre-processing, and segmentation	202
6.1.2	Intra-sample symmetry and inter-sample similarity	204
6.1.3	Quantification of vascular topology	204
6.1.4	Characterisation of a novel endothelial cell membrane behaviour	205
6.1.5	Publications in preparation	206
6.2	Study limitations and future work	207
6.3	Overall conclusion	209

List of Figures

0.1	Copyright clearance.	4
1.1	Zebrafish are a suitable model organism to study fundamental biology.	7
1.2	Principle and sample embedding in LSFM.	11
1.3	Visualization of the vasculature with fluorescence microscopy in transgenic zebrafish.	12
1.4	Parameters to describe the vascular architecture.	13
1.5	Methodological approaches for vasculature quantification.	27
1.6	Representation of vasculature quantification workflow.	30
1.7	Detailed steps of vasculature quantification workflow.	30
2.1	Theory of vessel enhancement filtering, based on the Hessian Matrix.	37
2.2	ROIs for vascular SNR and CNR quantification.	41
2.3	Anatomical region for cranial vascular volume measurement.	44
2.4	CNR differs depending on the transgenic line.	48
2.5	CNR is similar from 2-5dpf and in vessels of different size.	49
2.6	SIFT-based motion correction is applicable to data in (x,y,t).	51
2.7	SIFT-based motion correction is applicable to data in (x,y,z).	52
2.8	Examination of parameter sizes for pre-processing steps.	53
2.9	Application of Median filter and Rolling Ball increases vascular CNR.	54
2.10	Initial assessment of vessel enhancement filters implemented in Fiji.	55
2.11	Object-to-background colour filter response in selected vessels.	57
2.12	Filter response - 2D application.	58
2.13	Filter response - 3D application.	59
2.14	Filter response - distinctive model outset.	61
2.15	CNR is increased by TF.	61
2.16	FWHM is applicable to estimate vessel width.	63
2.17	Assessment of cross-sectional intensity distribution and FWHM after enhancement.	65
2.18	Comparison of different thresholding methods shows Otsu thresholding to be the most applicable to our data.	66
2.19	Comparing different segmentation approaches shows Otsu thresholding to be the most applicable to our data.	67
2.20	Intensity-based segmentation outcomes after GF and TF.	68
2.21	Cross-sectional intensity and vessel width after enhancement at increasing scales and segmentation.	70
2.22	Segmentation is robust against noise.	73
2.23	Segmentation in a double-transgenic line shows TF to deliver better segmentation outcomes.	75
2.24	Segmentation after exsanguination shows TF to deliver better segmentation outcomes.	76
2.25	Quantification of cranial vascular volume during early embryonic development.	78
2.26	Comparing segmentation outcomes from 2-5dpf.	79
2.27	Notch inhibition does not lead to a change in cerebrovascular volume.	81
2.28	VEGF inhibition leads to a decrease in cerebrovascular volume.	82
3.1	Workflow for intra-sample symmetry measurement.	88
3.2	Anatomical positions for manual measurements of growth rates.	90
3.3	Eleven landmarks were identified for manual landmark-based registration.	91

3.4	Registration methods and assessment of similarity.	91
3.5	Schematics of the examined 3D registration approaches.	93
3.6	Voxel-based overlap was used to generate averaged templates.	94
3.7	Producing vascular templates.	95
3.8	Visual assessment of intra-sample symmetry.	97
3.9	Vascular volume and length are symmetric from 2-5dpf.	97
3.10	Vascular topology is symmetric from 2-5dpf.	98
3.11	Manual measurements show that <i>dll4</i> is required for early embryonic vascular growth.	100
3.12	Automatic measurements show that <i>dll4</i> is required for early embryonic vascular growth.	101
3.13	Manual measurements of PMBC, MMctA, and PMCtA.	103
3.14	Manual measurements of brain width, BA, and DA diameter.	104
3.15	Validation of the suggested inter-sample registration approaches show automatic registration to be more robust than manual landmark-based registration.	106
3.16	Quantification of vascular similarity from 2-5dpf.	108
3.17	MIPs of vascular similarity at 2-5dpf.	109
3.18	3D vascular similarity between samples after landmark-based registration.	110
3.19	3D vascular similarity between samples after automatic registration.	111
3.20	Overlap of average templates established using 3D manual landmark-based and automatic registration.	112
3.21	Comparison of inter-sample registration methods.	114
3.22	Schematic vascular templates 2-5dpf.	115
3.23	Registration to single sample target to study impact of <i>dll4</i> MO.	115
3.24	Quantification of registration to single sample target to study impact of <i>dll4</i> MO.	116
3.25	Comparison of average templates of uninjected control, control MO, and <i>dll4</i> MO.	117
4.1	Parameters to describe the vascular architecture.	120
4.2	Classification of voxel identity.	122
4.3	Voxel identity assignment.	123
4.4	Ridge detection in distance maps.	128
4.5	Centreline extraction in Fiji after GF and TF.	129
4.6	Visual assessment of centreline extraction Fiji after TF.	130
4.7	3D vascular network length after 3D-thinning.	131
4.8	Visual output of the "Analyse Skeleton" Fiji Plugin.	132
4.9	2D network analysis of vascular development from 2-5dpf.	133
4.10	2D network analysis in <i>tnnt2a</i> morphants.	134
4.11	3D network analysis of vascular development from 2-5dpf.	135
4.12	3D network analysis in <i>tnnt2a</i> morphants.	136
4.13	Issues in branching point (BP) detection.	137
4.14	Vascular distance maps from 2-5dpf.	138
4.15	Impact of diameter sampling frequency.	139
4.16	Vascular quantification workflow.	141
4.17	Quantification of <i>tnnt2a</i> MO vascular properties.	142
4.18	2D local diameter quantification.	143
4.19	Schematic of 3D vessel segment analysis approaches and issues.	144
4.20	Application of SNT to annotate vessels.	145
4.21	Assessing vascular skeleton similarity.	146
4.22	Automated measurement of individual vessel diameters.	147
4.23	Sholl analysis of zebrafish with and without blood flow (<i>tnnt2a</i> MO).	148
4.24	Sholl analysis from 2-5dpf.	149
4.25	Example biological application - impact of actin polymerization inhibition.	151

5.1	Suggested workflow of <i>kugel</i> analysis.	154
5.2	Morphological description and physiological occurrence of <i>kugel</i> n.	162
5.3	3D <i>kugel</i> structure after multiview reconstruction.	163
5.4	<i>Kugeln</i> protrude from dorsal cerebral vessels and show no left-right pattern.	164
5.5	<i>Kugeln</i> are transient dynamic structures.	165
5.6	Some <i>kugel</i> n show oscillatory shape changes.	166
5.7	<i>Kugeln</i> show variable persistence.	166
5.8	<i>Kugeln</i> are not observed in non-membrane specific reporter lines.	167
5.9	Investigation of <i>kugel</i> n in <i>Tg(fli1ep:EGFP-CAAX)</i>	168
5.10	Investigation of <i>kugel</i> n in <i>Tg(fli1a:myr-mCherry)</i>	169
5.11	Cellular context of <i>kugel</i> n.	170
5.12	Impact of inhibition of F-Actin polymerization on <i>kugel</i> n.	172
5.13	Impact of inhibition of myosin II on <i>kugel</i> n.	173
5.14	Inverse membrane blebbing of the trunk vasculature is different to cranial <i>kugel</i> n.	174
5.15	<i>Kugeln</i> are not found in <i>tnnt2a</i> morphants.	175
5.16	Blood flow is not the driving factor of <i>kugel</i> formation.	177
5.17	<i>Kugeln</i> still form upon stopping cardiac contraction using Tricaine.	178
5.18	Parent vessel tortuosity at <i>kugel</i> locations.	178
5.19	VEGF signalling inhibits <i>kugel</i> n.	179
5.20	A subset of <i>kugel</i> n was positively stained for NO.	181
5.21	Cotreatment of VEGF and NOS inhibition does not alter effects of VEGF inhibition.	182
5.22	NO supply reduces the <i>kugel</i> numbers.	183
5.23	A subset of <i>kugel</i> n was acidic.	184
5.24	Quantification of <i>kugel</i> n filled with DAF-FM and LysoTracker.	185
5.25	Notch signalling is needed for <i>kugel</i> formation.	186
5.26	Studying Notch signalling in transgenic reporter lines.	187
5.27	Studying the role of <i>dll4</i> and <i>notch1b</i> in <i>kugel</i> formation.	188
5.28	Studying the role of <i>jagged-1a</i> and <i>jagged-1b</i> in <i>kugel</i> formation.	189
5.29	The impact of Wnt signalling on <i>kugel</i> number and diameter.	190
5.30	<i>Kugeln</i> do not interact with BLECs.	192
5.31	<i>Kugeln</i> do not serve a scavenger function.	193
5.32	<i>Kugeln</i> do not interact with local immune cells.	194
5.33	Osmotic pressure does not impact <i>kugel</i> n.	195
5.34	Membrane rigidity does not impact <i>kugel</i> n.	195
5.35	Summary of <i>kugel</i> cellular context, examined regulators, potential function, and working model of regulation.	199
6.1	Graphical User Interface (GUI).	212
6.2	Thesis Workflow Summary.	213

Acknowledgements

*“The first principle is that you must not fool yourself
and you are the easiest person to fool.”*
— Richard Feynman

Firstly, I need to thank my supervisors Paul Armitage and Tim Chico, who have supported both my scientific and personal development throughout this project. I am more than grateful for all the advice, support, and feedback they provided to widen my horizon on so many different aspects of life. I could have never imagined to have better *“Doktorväter”*.

Paul - I am so grateful for every single Monday morning meeting, I learned for life! You always had my back and I can not put into words how much breathing space this provided me. Thank you so much.

Tim - your talent, discipline, and energy to juggle so many different aspects of life was a pure inspiration. I really do not know how you manage to find the time and energy to always listen to our sorrows and worries.

My family, *Mum and Dad* - without you I would not be the person who I am. I am so endlessly grateful and proud to be your daughter. Breathing, loving, living. Danke! *Anna* - you are the very best sister. I am endlessly proud of you. *Michael* - for being my best friend, partner in crime, and so much more. There are no words to express how grateful I am for being with you. You have been an exceptional listener, sounding board, and contributor to this work in ways you will never know. *Matthias and Tabea* - you will always be a piece of home.

Thanks to all the members in Bateson C06/C10/C23 and Polaris, especially Karen for listening to every talk a hundred times, reading through so many rough drafts, and still having the energy to listen to my life stories.

A special thanks goes to Stephan Daetwyler, Jan Huisken, Max van Lessen, and Stefan Schulte-Merker for independent data verification of *kugeln*.

As Co-Chair of the IICD Student Society and member of the Faculty Forum, I had the chance to collaborate, discuss, and interact with so many people - I have learned so much from every single person.

I want to thank the reviewers and colleagues who had input along the way. The feedback provided helped to shape this work significantly.

Also, I want to thank the Department of Infection, Immunity and Cardiovascular Disease for the node studentship which made this work possible; the British Heart Foundation for the funding awarded to Tim for the light sheet microscope; the Bateson Centre aquarium staff for zebrafish husbandry, support, and guidance when needed.

Lastly, I need to thank everyone who is not mentioned by name but who shared knowledge, experiences, opportunities, help, hugs, and life along the way.

Abbreviations

ACeV	anterior cerebral vein	LSFM	light-sheet fluorescence microscopy
AJ	adherens junction	LPM	lateral plate mesoderm
AL	Artificial Life	LUT	lookup table
BA	basilary artery	MAT	medial axis transform
BAP	brightness area product	MO	morpholino
BBB	brain-blood-barrier	MOs	morpholinos
BLECs	Brain Lymphatic Endothelial Cells	MOC	midbrain organizing centre
BP	branching point	MRA	Magnetic Resonance Angiography
BPs	branching points	MRI	Magnetic Resonance Imaging
ccbe1	collagen and calcium-binding EGF-like domain 1	mRNA	messenger ribonucleic acid
CLAHE	Contrast Limited Adaptive Histogram Equalization	MSE	Mean Square Error
CNR	contrast-to-noise ratio	MIP	maximum intensity projection
CoV	coefficient of variation	MIPs	maximum intensity projections
CT	Computed Tomography	MMcTA	middle mesencephalic central artery
CTA	Computed Tomography Angiography	NICD	Notch intracellular domain
CtA	central artery	nNOS	neuronal nitric oxide synthase
CtAs	central arteries	NO	nitric oxide
DA	dorsal aorta	NOS	nitric oxide synthase
DAPT	N-[N-(3,5-Difluorophenylacetyl-L-alanyl)]-S-phenylglycine tButyl Ester	PCeV	posterior cerebral vein
DAF-FM-DA	4-amino-5-methylamino-2,7-difluorofluorescein diacetate	PCS	posterior communicating segment
DCV	dorsal ciliary vein	PCV	posterior cardinal vein
DLAV	dorsal longitudinal anastomotic vessel	PDE	partial differential equations
dll4	delta-like ligand 4	PHBC	primordial hindbrain channel
DLV	dorsal longitudinal vein	PICA	primitive internal carotid artery
DMSO	dimethylsulfoxide	PMBC	primordial midbrain channel
DoG	Difference of Gaussian	PMcTA	posterior mesencephalic central artery
dpf	days post fertilization	PrA	prosencephalic artery
EC	endothelial cell	PSF	point spread function
ECs	endothelial cells	RANSAC	Random Sample Consensus
EDMs	Euclidean Distance Maps	RBCs	red blood cells
eNOS	endothelial nitric oxide synthase	ROC	rostral organizing centre
EPs	end points	ROI	region of interest
F-actin	filamentous actin	ROIs	regions of interest
FEP	fluorinated ethylene propylene	SIFT	Scale Invariant Feature Transform
flk1	fetal liver kinase 1	SNP	sodium nitroprusside
FOV	field-of-view	SRG	Seeded Region Growing
FWHM	full width half maximum	SSD	Sum of Squared Differences
FWTM	full width 10% maximum	TF	Tubeness Filter
GF	General Filter	tnnt2a	cardiac troponin T2a
hpf	hours post fertilization	VEGF	vascular endothelial growth factor
iNOS	inducible nitric oxide synthase	vegfr2	vascular endothelial growth factor receptor 2
IOC	inner optic circle	VMTK	Vascular Modelling ToolKit
ISVs	Intersegmental vessels	VOI	volume of interest
KV	Kupffer's vesicle	vSMC	vascular smooth muscle cell
L-NAME	N-nitro-L-arginine hydrochloride	WSS	wall shear stress

Output and Impact

Parts of this work were published and reproduced herein with permission from the journals. Additionally, this work was presented in the form of talks and posters at scientific meetings and public outreach events.

* *Corresponding Author*

Publications - Journal Paper

- [1] **Kugler***, van Lessen, Daetwyler, Chhabria, Savage, Silva, Plant, MacDonald, Huisken, Wilkinson, Schulte-Merker, Armitage and Chico* (2019) *Cerebrovascular endothelial cells form transient Notch-dependent cystic structures in zebrafish*, EMBO Reports, Volume 20, Issue 8, 20: e47047.
- [2] **Kugler***, Plant, Chico and Armitage (2019), *Enhancement and Segmentation Workflow for the Developing Zebrafish Vasculature*, Journal of Imaging, MDPI, Vol. 5, Issue 1.
- [3] Chhabria, Plant, Bandmann, Wilkinson, Martin, **Kugler**, Armitage, Santoscoy, Cunliffe, Huisken, McGown, Ramesh, Chico*, and Howarth* (2018), *The effect of hyperglycemia on neurovascular coupling and cerebrovascular patterning in zebrafish*, Journal of Cerebral Blood Flow and Metabolism.

Publications - Conference Proceedings Paper

- [4] **Kugler***, Chico, and Armitage (2020), *Validating Segmentation of the Zebrafish Vasculature*. In: Y. Zheng et al. (eds) Medical Image Understanding and Analysis. MIUA 2019. Volume Communications in Computer and Information Science, Vol. 1065. Springer, Cham (2020) pp. 1-13.
- [5] **Kugler***, Chico, and Armitage (2018), *Image Analysis in Light Sheet Fluorescence Microscopy Images of Transgenic Zebrafish Vascular Development*. In: Nixon M., Mahmoodi S., Zwiggelaar R. (eds) Medical Image Understanding and Analysis. MIUA 2018. Volume Communications in Computer and Information Science, Vol. 894. Springer, Cham (2018) pp. 343–353.

Talks

- 2020: Departmental Research in Progress (virtual meeting)
- 2019: Invited visit to the Moorfield Eye Institute (London, United Kingdom)
- 2019: Medical Image Understanding and Analysis 2019 Conference (Liverpool, United Kingdom)
- 2019: MDHRSA Biomedical Imaging Research Forum 2019 (Sheffield, United Kingdom)
- 2019: Medical School Research Day 2019 (Sheffield, United Kingdom)
- 2019: Departmental Research in Progress (Sheffield, United Kingdom)
- 2019: Flashtalk - Insigneo Showcase Day 2019 (Sheffield, United Kingdom)
- 2018: Departmental Research in Progress (Sheffield, United Kingdom)
- 2018: Flashtalk- NC3Rs summer school (Manchester, United Kingdom)
- 2018: Medical Image Understanding and Analysis 2018 Conference (Southampton, United Kingdom)
- 2018: Flashtalk - Bateson Center Away Day (Sheffield, United Kingdom)
- 2018: Flashtalk - Krebs Institute Symposium (Sheffield, United Kingdom)
- 2017: Departmental Research in Progress (Sheffield, United Kingdom)

Posters

- 2019: Insigneo Showcase Day 2019 (Sheffield, United Kingdom)

- 2018: Autumn British Society for Cardiovascular Research meeting (Sheffield, United Kingdom)
- 2018: Bateson Center Away Day (Sheffield, United Kingdom)
- 2018: Medical School Research Day (Sheffield, United Kingdom)
- 2018: Insigneo Showcase Event (Sheffield, United Kingdom)
- 2017: Northern Vascular Biology Forum (NVBF; Liverpool, United Kingdom)
- 2017: BMS and MBB Retreat (Ashbourne, United Kingdom)

Order Date	Article Title	Publication	Type Of Use	Price	Order Status	Expiration Date	Order Number
9-Feb-2020	Validating Segmentation of the Zebrafish Vasculature	Springer eBook	Thesis/Dissertation	0.00 £	Completed		4764790544144
20-Jun-2019	Cerebrovascular endothelial cells form transient Notch-dependent cystic structures in zebrafish	EMBO Reports	Dissertation/Thesis	0.00 £	Completed		4613080722025
12-Dec-2018	Retinal vasculature development in health and disease	Progress in Retinal and Eye Research	reuse in a thesis/dissertation	0.00 £	Completed		4486470703632
10-Dec-2018	Retinal vasculature development in health and disease	Progress in Retinal and Eye Research	reuse in a thesis/dissertation	0.00 £	Completed		4485241081215
12-Nov-2018	Image Analysis in Light Sheet Fluorescence Microscopy Images of Transgenic Zebrafish Vascular Development	Springer eBook	Journal/Magazine	0.00 £	Completed		4466480468142
25-Aug-2018	Image Analysis in Light Sheet Fluorescence Microscopy Images of Transgenic Zebrafish Vascular Development	Springer eBook	Thesis/Dissertation	0.00 £	Completed		4415821037994
16-May-2018	A review of 3D vessel lumen segmentation techniques: Models, features and extraction schemes	Medical Image Analysis	reuse in a thesis/dissertation	0.00 £	Completed		4350760698941
10-Jan-2018	The Vascular Anatomy of the Developing Zebrafish: An Atlas of Embryonic and Early Larval Development	Developmental Biology	reuse in a thesis/dissertation	0.00 £	Completed		4265431331406
10-Jan-2018	Shape description using weighted symmetric axis features	Pattern Recognition	reuse in a thesis/dissertation	0.00 £	Completed		4265431209738
13-Dec-2017	Computer location of medial axes	Computers and Biomedical Research	reuse in a thesis/dissertation	0.00 £	Completed		4247030408389
6-Oct-2017	Fundamentals of Biomedical Image Processing	Springer eBook	Thesis/Dissertation	0.00 £	Completed		4202971067512
6-Oct-2017	Multiscale vessel enhancement filtering	Springer eBook	Thesis/Dissertation	0.00 £	Completed		4202960891300

Figure 0.1: Copyright clearance details of images reproduced in this thesis.

Summary

Background: Zebrafish are an excellent model to study cardiovascular development and disease. Transgenic reporter lines and state-of-the-art microscopy allow 3D visualization of the vasculature *in vivo*. Previous studies relied on subjective visual interpretation of vascular topology without objective quantification. Thus, there is the need to develop analysis approaches that model and quantify the zebrafish vasculature to understand the effect of development, genetic manipulation or drug treatment.

Aim: To establish an image analysis pipeline to extract quantitative 3D parameters describing the shape and topology of the zebrafish vasculature, and examine how these are impacted during development, disease, and by chemicals.

Methods: Experiments were performed in zebrafish embryos, conforming with UK Home Office regulations. Image acquisition of transgenic zebrafish was performed using a Z.1 Zeiss light-sheet fluorescence microscope. Pre-processing, enhancement, registration, segmentation, and quantification methods were developed and optimised using open-source software, Fiji (Fiji 1.51p; National Institutes of Health, Bethesda, USA).

Results: Motion correction was successfully applied using Scale Invariant Feature Transform (SIFT), and vascular enhancement based on vessel tubularity (Sato filter) exceeded general filter outcomes. Following evaluation and optimisation of a variety of segmentation methods, intensity-based segmentation (Otsu thresholding) was found to deliver the most reliable segmentation, allowing 3D vascular volume measurement. Following successful segmentation of the cerebral vasculature, a workflow to quantify left-right intra-sample symmetry was developed, finding no difference from 2-to-5dpf. Next, the first vascular inter-sample registration using a manual landmark-based approach was developed and it was found that conjugate direction search allowed automatic inter-sample registration. This enabled extraction of age-specific regions of similarity and variability between different individual embryos from 2-to-5dpf. A workflow was developed to quantify vascular network length, branching points, diameter, and complexity, showing reductions in zebrafish without blood flow. Also, I discovered and characterised a previously undescribed endothelial cell membrane behaviour termed *kugeln*.

Conclusion: A workflow that successfully extracts the zebrafish vasculature and enables detailed quantification of a wide variety of vascular parameters was developed.

1 Introduction

1.1 Relevance of vascular quantification

The vasculature is pivotal throughout an organism's lifespan, ensuring balanced supply of life-essential compounds. In the physiological context, the vasculature is needed for wound healing, regeneration, immune response, menstrual cycle, and pregnancy [6, 7, 8]. In the pathological context, it plays a role in chronic inflammatory disease, stroke, and vasculopathies [9], as well as cancer growth, progression, and metastasis [10].

The geometric and structural appearance of the vasculature can be used as a readout of physiology and pathology and is often clinically relevant [9, 11]. Examples are hyper-vascularization in cancer, hypo-vascularization in diabetes, or structural changes in hypoxia [10, 12, 13], which can be quantified as changes in vascular network volume, length, branching points, or patterning. Similarly, in vascular diseases such as stenosis, local vessel diameter changes are quantified to describe the disease status and support surgical planning. Reliable interpretation of the vascular status as indicator of vascular health requires objective quantification which is unbiased and reliably extracts even subtle changes. This is of particular interest when wanting to examine patient disease progression or response to treatment over time.

Besides this relevance in the clinical setting, vascular geometry can be used to describe morphogenic changes during development, as gradual vascularization occurs in parallel to body plan establishment to supply organisms with oxygen, nutrients, and signalling cues [14].

The geometric vascular framework can be used to model blood flow, which is increasingly applied to study the local impact of blood flow on vascular biomechanics and genetics [15, 16].

Together, it becomes clear that objective quantification of vascular anatomy and architecture is needed to reliably investigate vascular development, disease status, disease progression, as well as treatment responses. To achieve this, the medical field has made a concerted effort in the last decade to produce image analysis pipelines which allow for these quantifications to be conducted and thus vascular architecture to become quantifiable.

This is exemplified by major scientific projects, such as the AI-driven research on diabetic retinopathy, which aims to use artificial intelligence to assess the retinal microvascular architecture to assess disease status prevent diabetes induced vision loss [17, 18].

However, the availability of myriads of data acquisition techniques, clinical questions, and analysis approaches limit the applicability of specifically designed approaches to particular

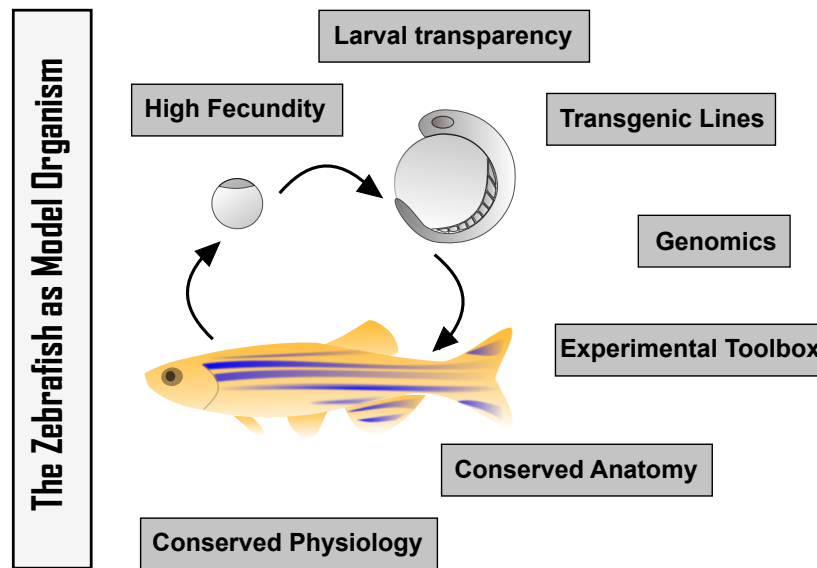


Figure 1.1: **Zebrafish are a suitable model organism to study fundamental biology.** Intrinsic biological characteristics and effective experimental design make zebrafish a suitable model to study cardiovascular development and disease (modified from [14]).

medical questions. Similarly, quantification approaches for the vascular architecture in pre-clinical models is still lacking.

1.2 Zebrafish are a suitable pre-clinical model to study the cardiovascular system

The zebrafish, *Danio rerio*, is a widely used vertebrate model organism to study development and disease [19, 20, 21, 22]. Characteristics such as high fecundity, larval transparency, sexual maturity after three months, and *ex utero* development allow cost-effective and high-throughput experimental design (Fig. 1.1) [14].

Zebrafish have become an established model to study vascular development, homeostasis, and pathology [23, 24, 25]. The availability of gene specific fluorescent transgenic markers and well-established experimental techniques allows cutting-edge non-invasive *in vivo* image acquisition over prolonged periods of time [14, 26]. Moreover, small embryonic size during the first days of development enables passive diffusion to supply the embryo with oxygen in the absence of blood flow, allowing the study of the impact of absent flow on vascular development [27, 28].

In zebrafish the first functioning organ is the heart [29], blood development starts at 12 hours post fertilization (hpf) [25], and at 17hpf arterio-venous markers are expressed [30]. At 22hpf

the newly formed vasculature becomes lumenized, and at 24hpf the two main axial vessels, the dorsal aorta (DA) and posterior cardinal vein (PCV), are formed by vasculogenesis [30, 31]. At 24-26hpf heart contraction starts, which induces vascular perfusion with blood to ensure the systemic supply of gas, nutrients, metabolites, hormones and components of the immune-system [32, 33]. A description of the early developing zebrafish vascular architecture, including the vessel nomenclature used in this thesis, was published by Isogai *et al.* for the cranial and trunk vasculature [31, 34].

1.2.1 Embryonic development of the vascular system in zebrafish

Establishing a functional vascular network requires a fine-tuned orchestration on multiple levels [35, 36]. Morphogenic processes such as cell differentiation, migration, lumenization, and cell-cell interactions are governed by the integration of several key signalling pathways such as vascular endothelial growth factor (VEGF) or Notch [37]. Importantly, many of the basic underlying vasculogenic and angiogenic mechanisms are highly conserved in vertebrates, allowing clinical translation from zebrafish to human.

The formation of the vascular network can be classified into vasculogenesis and angiogenesis [38]. *Vasculogenesis*, is *de novo* vessel formation by migration and coalescence of precursor cells, called haemangioblasts, from the lateral plate mesoderm (LPM) during embryonic development [39, 40]. *Angiogenesis* remodels and refines pre-existing vessels by sprouting, anastomosis, and pruning [9, 40, 41].

For more detailed reviews about vasculogenesis and angiogenesis in zebrafish the reader is referred to the following: cranial vasculature formation in [31], trunk vasculature formation in [34], molecular pathway review [42], vascular heterogeneity review [43].

Trunk vasculature.

In zebrafish the trunk vasculature is a highly studied vascular bed due to its stereotypic and reproducible growth pattern.

Cell lineage-restriction of angioblasts is considered to start during mid-gastrula at about 7 hpf by *cloche* [44, 45]. Angioblast migration towards the embryonic midline is guided by *elabela* from the notochord, which is sensed by angioblasts (receptors *aplnr1a* and *aplnr1b*) [46]. These angioblasts coalesce and form primordia for the two main axial vessels, DA and PCV [45, 47].

Cellular assembly, for vessel formation, is accompanied by progressing cell-fate specification by arterio-venous differentiation [24, 43, 48].

How vascular lumenization is achieved in each vascular bed remains to be elucidated [37], but it is known that cell polarity establishment is required prior to functional lumen formation

[49, 50, 51, 52, 53, 54].

Intersegmental vessels (ISVs) start to sprout dorsally as the first angiogenic vessels from the DA and migrate in parallel to vertical somite boundaries. Tip cells sense the guidance cue VEGF, which is provided by somites, for migration by *vascular endothelial growth factor receptor 2 (vegfr2)* (or *kdrl*) and *vegfr3*, leading to increased expression of the cell-membrane-bound Notch ligand *delta-like ligand 4 (dll4)* in the tip cell. This in turn leads to induction of stalk-cell fate in neighbouring cells by lateral inhibition. In stalk cells, Notch signalling and *vegfr1* expression are increased, while *vegfr2* and *vegfr3* are downregulated [55, 56].

Besides this molecular distinction (VEGF vs. Notch signalling), tip and stalk cells can be morphologically and functionally distinguished. Tip cells extend protruding lamellipodia and filopodia to sense migrational guidance cues, and are highly motile [57, 58], while stalk cells are proliferative lumenized trailing cells which serve a mechanically stabilizing function [57, 59].

After reaching the dorsal surface of the neural tube, ISVs grow antero-posteriorly, anastomose with neighbouring ISVs, and fuse to form the dorsal longitudinal anastomotic vessel (DLAV) [60].

Cranial vasculature.

The primitive cranial architecture is established during early vasculogenesis [61].

The origin of vascular precursors from the LPM was shown to be based on the relative anatomical position of cells. Cells for future cranial vessels and the myeloid lineage (monocytes) are derived from the anterior LPM, while cells for axial vessels and the erythroid lineage derive from the posterior LPM [62]. This leads to the establishment of two organizing centres, namely the rostral organizing centre (ROC) and midbrain organizing centre (MOC), which are joined by posterior migration from the ROC and anterior migration from MOC to form the primordial midbrain channel (PMBC) and primitive internal carotid artery (PICA) at about 24hpf [63].

After the initially separate formation of the cranial and spinal vasculature the two vascular beds are joined via a connection of the DA (trunk) and primordial hindbrain channel (PHBC) (cranial) via the first pair of ISVs at around 2days post fertilization (dpf) [64].

The cranial and trunk vasculature show conservation of basic signalling pathways, but the molecular interpretation of signals is highly complex and context-dependent [65, 66, 67]. Moreover, recent findings suggest that there are substantial differences between the cranial and trunk vasculature [1, 68], making it particularly interesting to study these two vascular beds in the same organism.

1.2.2 Limitations of zebrafish as pre-clinical model

Whole genome studies showed that zebrafish and humans share about 70% genomic similarity [69]. However, zebrafish have undergone a partial genome duplication [70], which can complicate the investigation of certain genes by functional redundancy of paralogous genes.

Anatomically, there are obvious differences between zebrafish and human, such as the difference in the respiratory system. Vascular-specific this is exemplified by the following: Firstly, zebrafish do not have an anatomical homologue to the human Circle of Willis, which is the central vascular bed for cranial blood supply in humans [31]. Secondly, blood flow modelling in embryonic zebrafish embryos has so far not received much attention, but it is becoming increasingly clear that differences exist with regard to hematocrit, vascular scale, and flow regimes [71, 72].

Lastly, some experimental limitations of zebrafish still exist. For example, the development and availability of antibodies for immunohistochemistry is still less well adapted than in other pre-clinical models, such as mice [14].

Thus, it has to be acknowledged that one model organism can never fulfil all needs in pre-clinical research, but that complementary integration across model organisms and disciplines is required to understand cardiovascular development and disease.

1.2.3 Visualization of the vascular system in zebrafish

The vasculature can be visualized using microangiography in which contrast medium is injected to visualize the blood, and therefore perfused vessels [73]. However, this is labour-intensive as well as prone to signal-loss due to clearance of injected contrast. Hence, different transgenic reporter lines, which express fluorescent proteins in vascular-specific cell types, have become the gold standard for vessel visualization (Fig. 1.3A) [74].

Vascular reporter lines visualize endothelial cells (ECs) which outline the vascular lumen, leading to a cross-sectional double-peak intensity distribution in perfused vessels, while small or unperfused vessels show a single-peak distribution. In microangiography and Magnetic Resonance Imaging (MRI), the cross-sectional intensity distribution is typically a Gaussian single-peak (Fig. 1.3B) [5]. Therefore, when working with transgenic lines, both double- and single-peak intensity distributions have to be considered equally.

In the last decades, fluorescence microscopy techniques have developed towards higher resolution, increased tissue penetration depth, and a reduction of image acquisition artefacts (Fig. 1.3C). This is typified by light-sheet fluorescence microscopy (LSFM) in which the

illumination (excitation) and detection (emission) paths are uncoupled. A sheet of light is detected orthogonally (Fig. 1.2B) [75] so that only a thin specimen section is illuminated, while the whole plane is detected. Thus, allowing rapid acquisition with high tissue penetration, minimal photobleaching, and phototoxicity [76, 77]. LSFM also has the advantage that sample embedding in an agarose block enables free rotation during acquisition (Fig. 1.2C), while the sample chamber setup allows maintenance of physiological conditions and application of drugs/anaesthetic. Together, LSFM allows image acquisition at a greater anatomical depth, and imaging duration of hours-to-days [76, 78, 79].

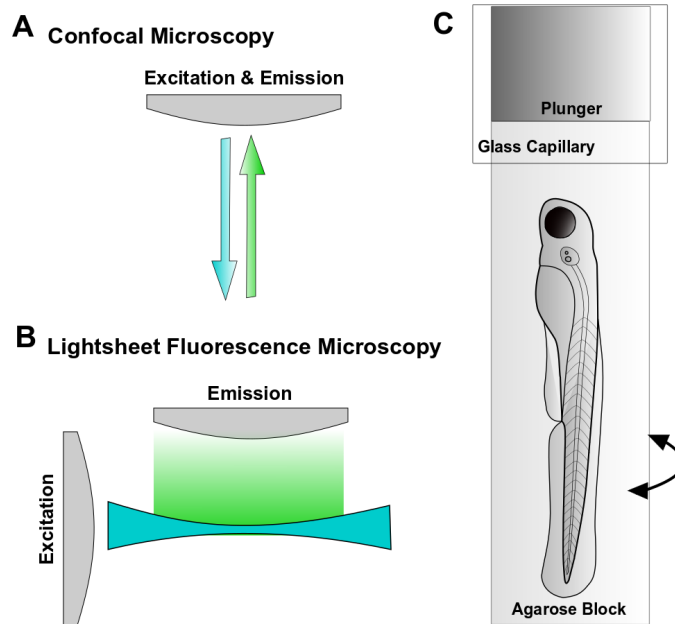


Figure 1.2: **Principle and sample embedding in LSFM.** (A) In confocal microscopy excitation (illumination) and emission (detection) share the same lightpath. (B) Lightpaths are uncoupled in LSFM, allowing for optical sectioning with higher penetration depth and reduced photobleaching. (C) LSFM sample embedding in an agarose block allows free 360° sample rotation for image acquisition.

While quantitative image analysis is widely applied in the medical field, it has received less attention in zebrafish vascular studies. If image analysis approaches applied in the medical field are to be adapted for LSFM in zebrafish, two major aspects have to be considered. First, zebrafish embryonic vessels are at the scale of about 10-20 μm [80, 81], whereas the diameter of human vessels range from 2.5cm arteries, 2-9mm veins, to a few μm for capillaries [82].

Secondly, voxel size in LSFM is around 0.33x0.33x0.5 μm with a field-of-view (FOV) of about 1920x1920x500 voxels, which allows the detection of about 30 voxels across a vessel and the detection of small scale details. In standard clinical MRI, the voxel size is about 1x1x1mm, resulting in a lower data load, but also the likelihood of missing smaller vessels during image

acquisition due to resolution limitations.

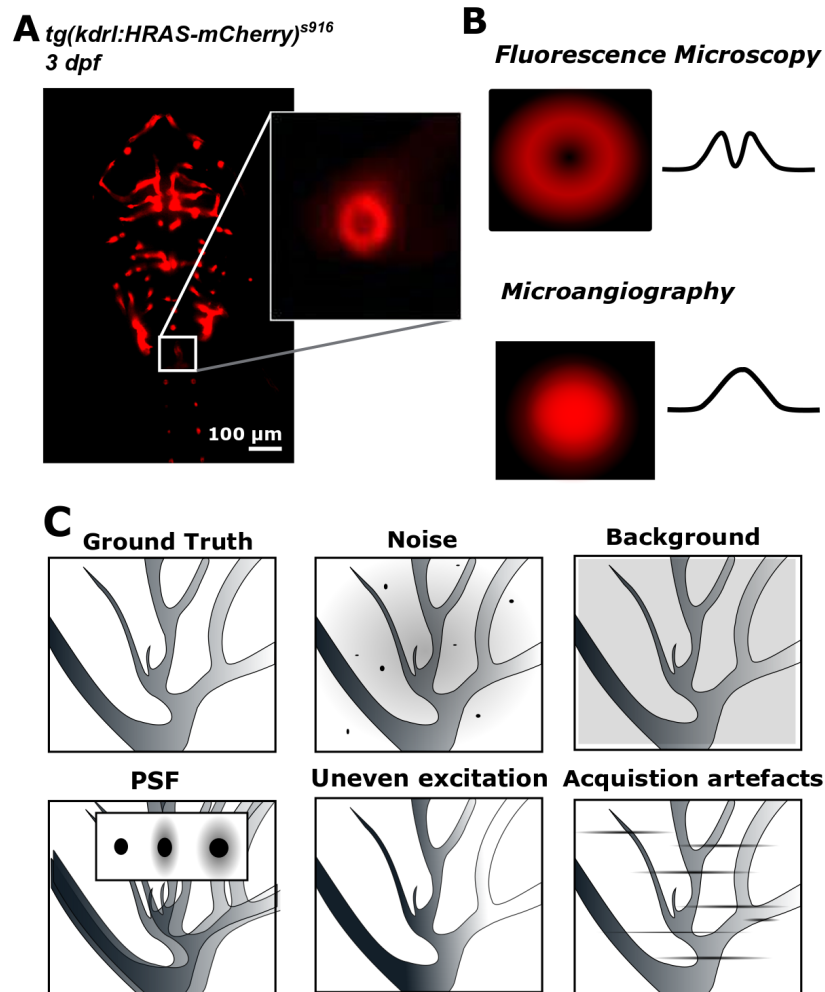


Figure 1.3: **(A)** Vascular fluorescent transgenic reporter lines visualize endothelial cells which outline the vascular lumen. **(B)** Cross-sectional intensity distribution in perfused vessels in transgenic reporter lines show a double-peak. In small/unperfused vessels and microangiography, intensity distribution is typically single-peak Gaussian. **(C)** Image quality in fluorescence microscopy can be influenced by artefacts such as noise, background/autofluorescence, point spread function (PSF), uneven excitation, or acquisition artefacts (i.e. shadowing or stripe artefacts; *A and B reproduced with permission from [5] under licence 4415821037994*).

1.3 Descriptive modelling of the cardiovascular system in zebrafish

To produce a model of the zebrafish cardiovascular system, an interdisciplinary approach is needed to combine experimental and computational findings. One challenge of interdisciplinary work is a lack of common semantics between disciplines (for example the word "model" means something different in biology, cardiology, mathematics, or to the public) [83].

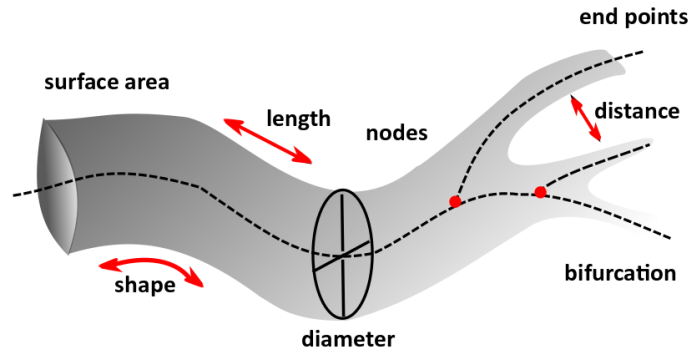


Figure 1.4: Common mathematical shape descriptors can be applied to describe the local and global vascular architecture.

Here, the term modelling is used to describe a set of parameters that characterise the vascular architecture and its changes during development, disease, and after application of drugs. This phenotypic outread is usually considered to allow the understanding of the underlying biological processes. Hence, describing the vascular architecture helps to understand, define, and visualize biological processes in zebrafish as a pre-clinical model in cardiovascular research.

Parameters that describe the vascular anatomy To describe the vascular topology (global features) and geometry (local features), common mathematical descriptors can be utilized (Fig. 1.4).

Volume: Enclosed vascular space, which can be computationally derived following voxel-classification as vascular and non-vascular, called segmentation. *Density*: Ratio of local vascular coverage to total volume of interest. *Segment length*: Length of individual vessels. Computationally defined as the length between branching points or between one branching point and a vascular end point. *Diameter*: Vascular local thickness given by the distance from local centreline (or vessel radius midpoint) to corresponding vessel walls. *Surface area*: Vascular edges or walls, being the interface between the vessel and surrounding tissue. *Branching points*: Point where vessel splits up into two (bifurcation) or more daughter branches. The relationship between individual network components can be described using branching angles or hierarchical classification. *End points*: Anatomical local vascular termination. *Curvature*: Measure of local vascular bending, or deviation from straight line.

1.3.1 Current approaches to vascular quantification

With the advent of new experimental techniques and image acquisition methods, image analysis became beyond the scope of commercially available software. Thus, a variety of analytical approaches have been developed to address the needs of image processing in the research fields of development, toxicology, or phenotype assessment via the application of recognition, tracking, or behavioural analysis [84].

Publications which address vascular quantification *in vivo* in a 3D context are discussed here (further reviews [85, 86, 87]). Papers discussed here use a variety of different imaging modalities, model organisms, analytical methodologies and quantitative approaches; see Fig. 1.1. Studies which solely describe image acquisition, pre-processing, segmentation, vascular reconstruction, or redundant methodological application were excluded from in-depth discussion.

First, methodologies that enhance images prior to analysis which can be applied to increase image quality by suppressing non-vascular and enhancing vascular information will be briefly listed. Subsequently, publications are discussed which derive object centrelines by object thinning as a foundation for quantitative vessel measurements. Iterative thinning to derive centrelines of objects was the first approach to be described (grassfire transform, [88, 89]) and only requires limited *a priori* knowledge. Thus, myriads of approaches and algorithms based on object thinning have been described previously [90, 91, 92, 93, 94].

Next, approaches based on mathematical modelling to obtain quantitative parameters are discussed. In this section, methods are classified into those based on the following: **(i)** techniques based on the Hessian matrix, **(ii)** energy regularization and evolution, and **(iii)** mathematical shapes. These methods are computationally more demanding and require optimized parameter settings with *a priori* knowledge. Thus, their application is usually limited to specific biological applications and refinement is more in-depth.

In recent years machine learning for automated image classification and quantification came into scientific focus, but will only briefly be discussed.

Lastly, current approaches for zebrafish vascular quantification will be discussed.

Vessel enhancement

Vessel enhancement, prior to vessel extraction, can be applied as a pre-processing step to attempt to increase vascular information, while reducing non-informative image noise or background. Approaches for vascular enhancement can be classified based on their objective, imaging modality, and mathematical foundation, including the use of: **(i)** image filtering [95],

Table 1.1: This table summarises the characteristics of each study discussed here, according to imaging modality, investigated species, and vascular bed. Also, it indicates whether image pre-processing, segmentation, visualization or quantification were performed (grey - applicable/performed; white - not performed). “Growth metric” indicates whether developmental vascular changes were studied, while “biological comparison” depicts if normal and abnormal (eg. stenosis, ischemia, or mutation) vasculature phenotypes were investigated. *Abbreviations: AC: artificial chamber, CM: Confocal Microscopy, CT: Computer Tomography, H: human, M: mouse, MA: microangiography, MO: monkey, MRA: Magnetic Resonance Angiography, R: rat, P: phantom, SC: stem cells, U: unspecified, V: vasculature, Z: zebrafish;*

Publication	Imaging	Species	Vascular bed	Pre-Processing	Segmentation	Visualization	Quantification	Growth Metric	Biological comparison	in vivo
Iterative Thinning										
Marks et al., 2013	MRA	M	hindlimb							
Kelch et al., 2015	CM	M	lymph node							
Peeters et al., 2017	CT	R	liver							
Milde et al., 2013	CM	M	retina							
Tan et al., 2016	X-ray	M	liver							
Mathematical Modelling										
Frangi et al., 2001	MRI	H	carotid aorta							
Energy Regularization and Evolution										
Rytlewski et al., 2012	CM	H; R	SC; aortic ring							
Hernandez-Hoyos et al., 2017	MRA	H	diff. vessels							
Kurugol et al., 2015	CT	H	aorta							
Manniesing et al., 2005	CT	H	Circle of Willis							
McIntosh & Hamareneh, 2006	MRA; CT	P; H	unspecified							
Mathematical Geometry										
Shingrani et al., 2010	CT	R	lungs							
Lugo-Hernandez et al., 2017	LSFM	M	brain							
Barber et al., 2003	CM	R; M	AC							
Risser et al., 2009	X-ray	Mo	brain							
Zebrafish Vasculature										
Feng et al., 2004	MA	Z	entire V							
Feng et al., 2005	MA	Z	caudal V							
Feng and Ip, 2009	MA	Z	entire V							
Tam et al., 2012	CT; CM	M; Z	brain							
Chen et al., 2012	CM	Z	brain							

(ii) derivatives [96], (iii) Hessian matrix [97, 98, 99, 100, 101], (iv) point-spread-function deconvolution [102], (v) mathematical morphology [103, 104], (vi) frequency [105, 106], (vii) anisotropic diffusion [107, 108], (viii) flux [109], and (ix) structure tensor [110, 111] (reviewed in [86]).

Segmentation

Subsequent to vessel enhancement, image segmentation is applied to distinguish vascular from non-vascular information. Detailed coverage of the myriad of segmentation approaches is beyond the scope of this thesis and has been extensively described [85, 112, 113, 114].

Quantitative characterisation based on iterative thinning to extract vascular centrelines

Centrelines are an abstraction and simplification to describe the geometry of objects (vs. implicit volume representation of shape) [115]. They can be used, together with vascular wall information, to quantify vessel properties such as diameter, length, curvature and branching points.

Iterative thinning was the first approach to be described to extract vascular centrelines (grassfire transform, [88, 89]). Hence, many centreline approaches and algorithms have been developed based on thinning of binarized objects to extract centrelines after object segmentation [90, 91, 92, 93, 94].

Generally, iterative thinning is based on the removal of so called *simple points* at the object border [116, 117, 118, 119, 120] (object border voxel definition: [115]), similar to peeling off layer after layer (Fig. 1.5A). According to the centreline requirements proposed in [121], the removal of simple points shall not interfere with the overall object geometry or topology. Thinness is achieved by the stopping criterium of one-voxel-thickness.

It has been shown previously that thinning of 3D tubular objects (which a vessel can be locally considered to be) is applicable [92, 122], whereas special conditions have to be met for the extraction, representation, and quantification of true object cavities (such as vascular loops) [123, 124].

Application of object thinning for vascular centreline extraction prior to vascular quantification has been applied in the following studies: To globally quantify the influence of ischemia in the rodent hindlimb vasculature from *in vivo* Magnetic Resonance Angiography (MRA) and micro-Computed Tomography (CT) images Marks *et al.* [125] extended existing Fiji Plugins for object skeletonization and analysis [91, 126, 127]. Additionally, a semi-automatic Plugin was established to measure the total vascular volume.

This method is applicable to measure substantial differences between samples, but manual annotation is needed to investigate individual vessels, making it unsuitable for in-depth analysis - especially in complex vascular beds. Also, as MRA and micro-CT were used as image acquisition modalities, pre-processing and segmentation would need to be altered for other modalities and vascular beds to allow application of this method.

Kelch *et al.* [128] investigated the vasculature in murine lymph nodes after visualization with immunohistochemistry and the use of 'Extended Volume Imaging System' (EVIS) [129], which employs automatic tissue sectioning during fluorescence microscopy image acquisition. After pre-processing, including the suppression of background and noise as well as 3D reconstruction, image binarization was achieved by local thresholding, followed by a custom-made hole-filling step to overcome structural artefacts. Centrelines were extracted, based on tubular vessel modelling, with subsequent post-processing steps to remove spurious branches by length-to-diameter-thresholding. Delivered quantification encompassed individual vessel diameter, number, branching points, and distance information, as well as overall network length, volume and density. Although this proposed workflow delivered an in-depth quantification of the lymph node vasculature in mice, the use of three commercial and two creative-commons software tools is a major drawback of this analysis pipeline. Nevertheless, the implementation of local adaptive thresholding to overcome local uneven vessel illumination as well as the proposed hole-filling approach prior to volume measurements seem to be a reasonable approach and generalizable to zebrafish vascular quantification. Also, the suggested length-to-diameter thresholding for pruning of spurious branches may well be useful in the zebrafish cranial vasculature, although it would need testing and optimization.

In Peeters *et al.* [130], a quantification approach for the rat liver vasculature was presented. CT (after corrosion casting) and confocal microscopy images (immunohistochemistry) were analysed. Image pre-processing of confocal microscopy data was performed with Fiji [127], including depth-intensity correction, bleaching correction, denoising, PSF deconvolution [131], and local contrast enhancement [132]. Quantification was conducted with the custom-made software DeLiver which utilized graph theory [133, 134] after thinning of binarized objects, to obtain segment radius, curvature, porosity and length. The use of graph theory to hierarchically describe and analyse the vasculature provided an elegant way to describing the vascular network. However, due to the use of LSM, the need for depth-intensity correction and bleaching seemed dispensable. Unfortunately, as the DeLiver code for quantification is not readily available, the exact steps of this analysis are not reproducible.

Milde *et al.* [135] studied developmental remodelling and maturation in embryonic and adult

murine retinas. Visualization of vascular endothelium was by multiphoton image acquisition after isolectin staining. After image pre-processing, including background and noise removal, local adaptive thresholding was used for segmentation. Based on manual vessel annotation a custom-made Matlab program was used to quantify vascular area, density, circumference, and intersprout distance. Topology measurements, such as vessel length or diameter, were not conducted, but this study contributed to the understanding of vasculature remodelling and maturation processes, presenting an intuitive visualization and representation approach using area, perimeter and intervascular spaces [136]. Such representations are of particular interest for the investigation and visualization of individual vessels during development or disease.

To increase the geometry and topology conservation during iterative 3D thinning, Tan *et al.* [137] presented an advanced method of object thinning. Data were obtained from the mouse liver via synchrotron-radiation-based micro-tomography (SR- μ CT) [138]. After 3D binarization, vessel root and endpoints were detected and fixed by automatic voxel coding. Thus, object thinning [91] was solely applied to vascular segments, leading to increased topology preservation. This study is of particular interest due to its 3D implementation, as most thinning approaches are based on 2D mathematical constraints due to implementation and definition constraints. However, the zebrafish vasculature is considered to be an enclosed vascular circulatory system. Therefore, it is unclear whether vessel root and endpoint detection would be needed to overcome artificial vascular pruning, which can be introduced by thinning.

Summary and discussion The majority of centreline extraction approaches, based on iterative thinning, are reliant on 2D mathematical constraints, whilst 3D constraints are generally considered to be more suitable to preserve the original object geometry and structure [139].

Moreover, iterative thinning to obtain vascular centrelines was previously shown to be sensitive to small surface heterogeneities [140]. Thus, spurious branches may be produced, which can lead to false quantification of branching points, number of segments, length, or diameter.

Therefore, post-processing techniques may need to be implemented, such as pruning, to derive accurate centrelines after thinning. Pruning can be achieved, for example by length-thresholding (as suggested in [128]), angle-constraints, length-surface-ratios [141, 142, 143, 144], or surface smoothing prior to iterative thinning may decrease the amount of spurious branches [145].

In conclusion, object thinning can be applied to a variety of objects without *a priori* knowledge and should be suitable for use on the zebrafish cranial vasculature, but detailed

visual inspection is likely to be necessary to evaluate applicability and accuracy as vessel segment shortening or spurious branch production may occur. If required, an appropriate method of spurious branch removal would need to be developed.

Quantitative characterisation based on mathematical modelling

Methods for quantifying the vascular architecture described in this section use mathematical constraints with the aim of delivering comprehensive and robust results. Mathematical modelling is often very sophisticated with regard to model development, initialization, and refinement, but *a priori* knowledge is needed for accurate parameter selection. Moreover, modelling approaches tend to be computationally more demanding and require customization as well as optimization for specific applications.

Techniques based on the Hessian matrix The local structure of images can be described by first- and second-order partial derivatives of image intensities [146]. The 3D composition of these can be arranged in matrix structures such as the Jacobian and Hessian respectively. Within these matrices the local orientation of image gradients can be described via eigenvectors (\mathbf{e}_1 , \mathbf{e}_2 , \mathbf{e}_3); and their respective size (magnitude) via eigenvalues (λ_1 , λ_2 , λ_3). Utilizing this vectorial information allows the vasculature to be described (Fig. 1.5B) and enhanced locally by utilization of geometric descriptors, such as blobs, tubes, lines, or plates [99, 101, 147]. Integration of vessels of different size is generally achieved by inclusion of the maximum response of multiscale filtering, based on scale space theory [148, 149, 150].

Using eigenvectors and eigenvalues, a model for the human carotid aorta in 3D, visualized by MRA, was established by Frangi *et al.* [151, 152]. After manual initialization of vessel walls, centrelines were derived from spline-fitting using all three eigenvectors and eigenvalues of the Hessian matrix [153, 154]. Vessel walls were fitted based on the derived centreline; while vessel diameters were estimated via local full width 10% maximum (FWTM) measurements of intensity-distributions of vessel cross-sections. The vascular enhancement filter, based on [99], was optimized for MRI images. Hence, a Gaussian intensity distribution across vessels is assumed. As described in section 1.2.3., the cross-vessel intensity distribution in zebrafish vascular transgenic reporter lines often resembles a double-peak [5], so it is unclear whether the proposed enhancement method will enhance vascular edges or the whole vessel over background. The use of three eigenvectors and three parameters suggest that this approach would need in-depth assessment and parameter optimization to be applicable to zebrafish data. Furthermore, the use of spline fitting for the vascular centreline and walls can lead to

over- or under-fitting, especially in high-curvature regions and at branching points.

Techniques based on energy regularization and evolution To extract features or objects of interest, energy regularization of deformable curves can be used. This was originally proposed by the use of *snakes* as deformable contours, which would be deformed based on two energy components, namely an internal and external component, leading to an energy minimization problem solved by an iterative fitting approach [154, 155, 156, 157] (Fig. 1.5C). The *internal force* is considered to be an inflating balloon force which expands more strongly in homogeneous regions to ensure continuity and smoothness. The *external energy* is mainly driven by image intrinsic properties, such as gradients and intensity, to steer the deformable contour towards regions of interest by counterbalancing the internal energy of continuous inflation.

Rytlewski *et al.* [158] published an analysis pipeline to quantify vessels in two different *in vitro* angiogenesis assays, visualized with confocal fluorescent microscopy. After pre-processing and vessel enhancement, based on the maximum response of eigenvectors and eigenvalues [99, 159], segmentation was performed via fast marching level set evolution starting from manually placed seeds [160, 161, 162]. Vascular centreline endpoints were, again, chosen manually and 3D Voronoi diagram implementation was used to derive centrelines (Delaunay's tessellation) [160, 161, 163]. Quantification of vessel volume, length, and branching degree were performed using Matlab. Despite extensive documentation it is not clear whether this approach would be applicable to other data types. Three different software kits (Fiji, VTK, and Matlab) were used, hindering the dissemination of the approach to biologists not fluent with these analysis programmes. It should also be noted that the authors mentioned the occurrence of a global pruning error, but gave no further details. Thus, it can not be excluded that global underestimations occurred.

Hernandez-Hoyos *et al.* [164, 165] used a hybrid approach of energy regularization and geometric features in self-developed software, Magnetic Resonance Angiography Computer Assisted Analysis (MARACAS), for stenosis quantification. Centrelines were extracted based on manual seeding and local ray casting from vessel surfaces. Based on this, vessel walls were initialized via local tubular geometry and refined by deformable active contours (Fig. 1.5C) [164, 166]. Quantitative parameters measured included vessel diameter, perimeter and area, with a special focus on stenosis. As this method was developed for MRA data, centreline extraction relied on the cross-section intensity peak being in the centre of vessels. For the reasons described previously, this would not always be true for zebrafish data. Similarly, ray casting would need to be optimized to fit the double-peak intensity distribution with an inverse

intensity in comparison to MRA. Moreover, the study reported issues with noise and bifurcation sensitivity.

The Seeded Region Growing (SRG) [167] method starts from seed points (manually or automatically placed) and relies on an iterative voxel-inclusion to distinguish between vascular and non-vascular voxels (Fig. 1.5D). The algorithms can be categorized as greedy, and mainly rely on inclusion criteria based on voxel-connectedness and intensity value similarity. To avoid leakage or false-positive voxel inclusion, more stringent inclusion criteria to separate fore- and background can be applied [86]. Also, the actual seeding, voxel-labelling, and voxel-wise growing procedure can be refined to yield higher accuracy [168].

The level set approach [169, 170] is based on the principle of region growing, but utilizes partial differential equations (PDE) for the propagation of a wave front or boundary, rather than single-voxel decisions. Hence, locally more homogeneous results can be achieved.

Kurugol *et al.* [171] performed vascular and calcification quantification in human aorta CT images. Vessel walls were extracted after manual anatomical landmark selection and template application ('aorta tubular candy cane shape') via circularity similarity measures (Hough transform; [172]). Following, fast marching level set evolution was applied for vessel wall refinement [169, 170, 173]. Vascular centrelines were derived via parametrized iterative thinning, and subsequent spline fitting, as well as interpolation at high curvature regions [154, 174, 175]. Calcification plaques were extracted via intensity-based thresholding and returned together with vessel radius, curvature and length measurements. This method was specifically tailored for the analysis of the human carotid aorta, thus template fitting and refinement are not easily applicable to other vascular beds; but the concept of similarity measures to extract vascular walls, as well as the parametrized thinning with subsequent spline fitting could probably be generalized. It must be mentioned that the presented method was applied to an individual vessel segment lumen, meaning application to more complex/bigger vascular beds is likely to be more challenging.

Manniesing *et al.* [108] studied the human Circle of Willis, visualized by Computed Tomography Angiography (CTA). First, bone masking was performed by subtraction of a rigidly registered additional low-dose image. Level set evolution in a user defined volume of interest (VOI), optimized via previous training of parameters, was used to segment the vasculature based on image intensity. Local vessel diameters were extracted via 2D iterative thinning [93]. The authors stated that the acquisition of low-dose images, to perform bone masking, came with the downside of additional patient radiation as well as the possibility of inaccuracies occurring during rigid registration for bone masking. Also, the local diameter

measurement was performed based on 2D constraints, which does not consider requirements needed for 3D centreline extraction. Lastly, no further details were given about the handling of vessel diameter measurement in vessels at an oblique angle in images. As each step (bone masking, speed function, and level set) was optimized for CTA images, it is unlikely that this method could be directly translated to fluorescence microscopy images of the zebrafish vasculature.

An advanced approach, namely via Artificial Life (AL), in the form of unguided 3D deformable bodies, was developed by McIntosh *et al.* [176] for the analysis of MRA images of the human Circle of Willis and phantom CTA data of nylon tubes in silicon gel. After manual initialization, front propagation was based on local tubular geometry extracted by eigenvalues [99, 149].

Front propagation was driven on AL layers, including cognition, behaviour, locomotion and geometry, which are fed by input of sensory modules. Quantification included vessel radius, branching points, volume, branch hierarchy, and branching angles. Considering the complexity of the method, it can be assumed that extensive *a priori* knowledge is needed to transfer this AL approach to images from fluorescent transgenic reporter lines. Moreover, the method was applied to vascular trees, which implies that an additional sensory layer for the detection of loops or vascular plexi would be required. As the method was optimized for vessels with Gaussian intensity distribution, the double-peak distribution found in transgenic lines would require additional pre-processing to achieve a single-peak intensity.

Techniques utilizing mathematical geometry The methods described in this section all section utilized mathematical geometry descriptors to model and/or quantify the vasculature. Most commonly vessels are assumed to be locally tube-, cylinder-, line-, or circle-like; meaning the vessel diameter can be quantified by a local radius measurement.

Shingrani *et al.* [177] studied vessel diameter changes upon hypoxia in images of rat lungs acquired with CT. Image segmentation, based on intensity-based binarization, was followed by 3D hole filling and 3D object thinning to obtain vascular centrelines [139]. Centreline connectivity was tested prior to analysis to remove unconnected components. This was followed by hierarchical ordering and indexing of branches. Diameter quantification was done after calibration using a tube with known diameter filled with contrast medium by a combination of the full width half maximum (FWHM) and the brightness area product (BAP) [178]. Fitting was performed using a modified Gaussian function with non-linear least squares fitting [179]. Oblique vessels were excluded from diameter measurements by inclusion of a circularity threshold, which also ensured also that diameters were not estimated at branching point regions, which displayed an elliptical circumference. This paper delivered excellent

documentation, validation against an operator-guided technique, and future plans for image registration. As this method was optimized for CT images, again optimization for our data would be required, but the general theoretical principle (such as circularity threshold or branch indexing) seem reasonable and generalizable.

Lugo-Hernandez *et al.* [180] investigated the vasculature in locally ischemic mouse brains after tissue clearing [181] in images acquired with LSM [75]. Pre-processing of images, to reduce noise and background, was performed using ImageJ software (National Institutes of Health, Bethesda, MD, USA). Vessel enhancement, based on eigenvector and eigenvalues [99] was done using Vascular Modelling ToolKit (VMTK) software [160]. Quantification of vessel diameter, network length and volume were conducted using the commercial software Imaris (Imaris, Bitplane AG, Zurich; module 3D filament tracer). No specifications about analysis steps towards segmentation or vessel quantification were given, thus comprehensibility and reproducibility is fairly limited.

Barber *et al.* [182] published the Trace3D software, which was used to quantify the vasculature in rat and mice back skin fold vessels, visualized via multiphoton acquisition after tracer injection [183]. After manual vessel selection in the XY-direction, the software performed semi-automatic tracking in the Z-direction. Based on vascular wall extraction via Sobel edge detection [184], vessel centrelines were determined as the centre of mass of a fitted circularity measure (Hough transform; [172]). Further specifications of additional software features, such as PSF deconvolution, or software support were not provided. Generally, manual vessel tracking in XY provides a very laborious approach and similarity measurements, based on circularity, may be falsified in oblique vessels. Additionally, the extraction of centre of mass in XY may lead to unsmooth or unconnected centrelines.

Risser *et al.* [185] quantified the vasculature from subregions of primate brains, visualized in biopsies of neonatal and adult monkey specimens. After image segmentation (unspecified method), vessel centrelines were obtained via 3D iterative thinning [92]. Vessel diameters were approximated via spheres (sphere centre located at centreline candidates, Fig. 1.5E) extending 10% over the vascular edge. Here, the authors stated that the 10% threshold was empirically determined, but did not give any further specifications. The vascular surface was derived by surface summation of fitted cylinders. No specification about branching point criteria or vessel length quantification was given. Moreover, shrinkage artefacts, due to tissue fixation, were generally corrected by a factor of 1.4, which may lead to global data falsifications.

Summary and discussion Methods for initialization, refinement, training, as well as the iterations needed for sufficient quantification and modelling were found to be highly variable in

the published literature. Moreover, most vascular structures analysed displayed a simpler architecture in comparison to the zebrafish vasculature, which shows a high degree of complexity due to regions of high curvature and branching point density.

Vessel segment centreline smoothing via spline fitting is a commonly used approach within the literature and may be more accurate than purely voxel-based approaches, as voxel-based approaches could be affected by pixelation or staircasing artefacts [154, 186].

The majority of vascular modelling approaches performed to-date have focused on vascular subregions and were customized to specific applications based on the respective imaging modality, vessel architecture, and analytical requirements. Thus, a direct translation of published approaches to the quantification of the embryonic zebrafish vasculature seems unlikely. Nevertheless, the described principles could form the basis for an image analysis pipeline optimized for the requirements of images from the zebrafish vasculature obtained from transgenic reporter lines with LSM.

1.3.2 Machine Learning

Although machine learning has become a widely applied approach to segment and quantify images [187, 188, 189, 190], few publications consider generalizability of the proposed approach (eg. acquisition with machines from different manufacturers; imaging modalities; application to other diseases). Similarly, often output validation and in-depth quantification are lacking. Machine learning approaches for vascular segmentation are especially challenging due to complex vascular topology and the establishment of training data being very labour-intensive.

In 2019, a machine learning approach for data of the cranial vasculature in mice was described [191]. Although data were acquired after immunohistochemistry rather than *in vivo*, data were acquired with LSM. Machine learning was used for vascular segmentation and the vascular topology subsequently quantified.

1.3.3 3D vasculature quantification in embryonic zebrafish

3D quantification and modelling of the embryonic zebrafish trunk vasculature in microangiography images was addressed by Feng *et al.* [192, 193, 194, 195]. In the relational-tubular deformable model (*ReTu*) [192] and the statistical assembled model for tubular structureness (*Samtus*) [194], energy deformations based on active contours were used to model a subregion of the trunk vasculature in embryonic zebrafish [156]. Whilst both models relied on the assumption of tubular structures for model initialization, *Samtus* included

model-training to reach higher accuracy. Additionally, Feng *et al.* developed Zebvars software [193] to analyse images from the embryonic trunk vasculature via edge tracking and graph representations [196, 197]. As all of these proposed models were applied on microangiography data, it is unclear whether these would be applicable to data from transgenic reporter lines. Also, the trunk vasculature consists of fewer and less complex vessels than the cranial vasculature, and regions of high curvature may be prone to errors during active contour fitting.

In Tam *et al.* [198], the role of two death receptors (DR6/TNFRSF21 and TROY/TNFRSF19) in dorsal brain vasculature development and brain-blood-barrier (BBB) formation was studied in mice with micro-CT, as well as in zebrafish with fluorescence confocal microscopy (transgenic reporter line, microangiography, and antibody stainings). Quantification in 3dpf zebrafish focused on the left dorsal cranial vasculature innervating the hindbrain (central arteries (CtAs)). Measurements of vascular density and diameter were performed after deconvolution using Imaris software. As no further specification was given about pre-processing steps or parameter settings, replication of this quantification method is not possible. Moreover, reported density measurements were normalized to an approximated local brain volume (assumption of cubic volume, rather than actual brain volume), suggesting biased measurement outcomes. Regarding 3D rendering and volume measurements, the authors mentioned the need for manual refinement, but, again, did not specify further details. Lastly, it is not clear whether all quantification was performed in the left anatomical half of the vasculature only, and which anatomical position was chosen to be the left-right discriminator.

3D *in vivo* quantification of the embryonic zebrafish cerebral vasculature development in images acquired with confocal microscopy in transgenic lines was demonstrated by Chen *et al.* [80]. Vessel length, branching hierarchy [133], existence of loops, and vascular pruning events were quantified in the cranial vasculature by the use of commercial software NeuroLucida. As no further description about image pre-processing, extraction of vascular centrelines, branching point definition, or diameter estimation (expansion of spheres) was given, an in-depth assessment of this method is not possible. Also, testing of the suggested workflow by Chen *et al.* [80] was not possible due to NeuroLucida licencing requirements and dataset differences. Methodologically, segment length was measured as minimum Euclidean distance between endpoints, rather than actual length, which may lead to an underestimation of actual vascular segment length in vessels with high curvature. Lastly, the analysis presented in Chen *et al.* [80] focused only on two vessel segments in the anterior cranial vascular bed (middle mesencephalic central artery (MMCtA) and posterior mesencephalic

central artery (PMcTA)). This limitation to two segments is likely to be caused by limitations in tissue penetration depth using confocal microscopy, which can be overcome in LSM (section 1.2.3).

In 2019 two new methods to segment the zebrafish vasculature were suggested. Zhang *et al.* [199] presented a machine learning based approach to segment the trunk vasculature (dual ResUNet), but poor writing and documentation made it unclear whether the segmentation was performed in 3D or in maximum intensity projections (MIPs) in 3D.

Daetwyler *et al.* [200] presented cerebral vascular segmentation using voxel feature maps and thresholding using the triangle algorithm. To establish voxel feature maps in the transgenic *Tg(kdrl:eGFP)* a second transgenic line was used to visualize luminal signal, namely *Tg(gata1:dsRed)* labeling RBCs. As the authors themselves state, not all vessels are perfused at the examined time-points and *Tg(gata1:dsRed)* only labels RBCs, not the whole blood volume. Thus, using a double-transgenic for segmentation was not very intuitive. Additionally, documentation of the analysis workflow is incomplete.

Unfortunately, neither method included any validation of the proposed segmentation or further quantification of vascular features, so it is difficult to determine how robust or reliable the segmentations were. Interestingly, Daetwyler *et al.* was the first publication to suggest using vascular segmentation to examine vascular left-right symmetry.

Summary and discussion The above presented methods all addressed 3D quantification of the zebrafish vasculature, but details of approaches and validation are scarce.

This lack of a previously developed and readily available analysis approach to quantify the zebrafish cerebral vasculature is likely to be caused by the following:

(i) state-of-the-art microscopy such as LSM is a relatively new technique, and became commercially available only in recent years [201, 202], and (ii) while zebrafish are now an established pre-clinical model in cardiovascular development [14, 21], they were first proposed as model organism for haematopoiesis [33] and angiogenesis [203] less than 20 years ago.

Together, it becomes clear that none of the current studies addressed an in-depth assessment of data properties or investigated the quality and robustness of the proposed approach. Generalization to bigger vascular beds or other transgenic lines was never studied; limiting applicability and dissemination of the suggested methods. The overall lack of documentation makes it impossible to reproduce most of these methods and it is unclear what the computational limitations/requirements of these methods are.

In conclusion, no segmentation and quantification method applicable to experimental data for the zebrafish vasculature exists. Objective quantification of vascular topology and its changes

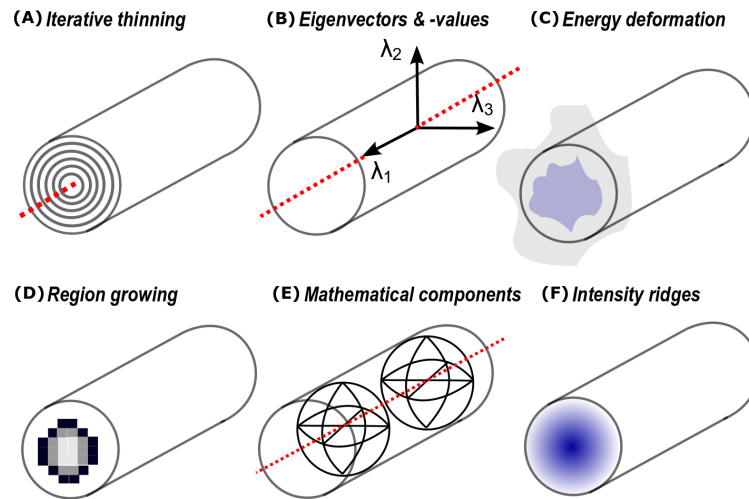


Figure 1.5: Methods to derive vascular centrelines vary widely in their underlying objectives. **(A)** Iterative thinning needs no *a priori* knowledge, but can be sensitive to surface inhomogeneities [88, 91, 140]. **(B)** Eigenvectors and eigenvalues are widely applied in applications of vascular enhancement as well as modelling [99, 151, 152]. **(C,D)** Modelling based on energy deformation or region growing require *a priori* knowledge and parametrization in order to deliver accurate results. **(E)** Mathematical components, such as spheres or tubes can be used to locally describe vascular topology as well as diameter measurements or centreline predictions. **(F)** Intensity ridges or valleys in vessels can be used to extract the vascular centreline and wall candidates.

in development and disease are needed. Especially examinations of inter-sample similarity and variability by registration and intra-sample left-right symmetry have lacked attention so far.

1.3.4 Discussion of vasculature quantification

With the emergence of full 3D data sets and the goal of establishing 3D image analysis, not just data load, but also the complexity in computational requirements, changed dramatically [204].

While some sophisticated vascular quantification methodologies have been implemented, most papers lack sufficient documentation about the steps taken to assess data properties, segmentation, and centreline connectedness/characteristics. Also, quantification robustness and inter-sample comparisons were incompletely addressed. This is likely to be caused by the fact that analysis gold-standards are lacking for pre-clinical models, and most validation is still reliant on observer-based assessments.

Developed image analysis approaches use either data sets from *post-mortem* or *in vivo* acquisitions. The first often requires tissue preservation and clearance techniques, which may lead to tissue distortion [205, 206, 207], while the latter can be subject to sample-induced motion artefacts [208, 209].

Most analytical approaches have been developed for specific applications. Thus, it is not clear whether these would be transferable to other vascular beds, distinct imaging modalities, or model organisms. Similarly, most quantitative approaches focused on data acquired from a single time-point and did not consider or evaluate vascular pattern changes over time or biological inter-sample heterogeneity [210, 211].

Based on the knowledge gained from the literature, the 3D quantification of zebrafish vasculature in images obtained from transgenic reporter lines with LSM has to take the following into account:

(i) Transgenic vascular endothelial reporter lines display a distinctive cross-sectional intensity profile in comparison to imaging modalities such as microangiography (Fig. 1.3A) [5]. Additionally, investigations of vessels at various scales and data from different transgenic reporter line constructs have received less attention so far.

(ii) Visualization with fluorescence microscopy can cause image acquisition artefacts such as point-spread-function, noise, autofluorescence, scattering, bleaching, etc. (Fig. 1.3B) [212, 213, 214].

(iii) The cerebral vascular architecture in zebrafish displays a high complexity, due to vascular loops, pruning, and remodelling, as well as potential scale variations within and between organisms [215, 216, 217].

(iv) The rapid development of the embryonic vascular system in zebrafish is likely to require a fine-meshed temporal image acquisition sampling rate to fully describe remodelling processes.

Therefore, it is likely that a bespoke and novel image analysis workflow will need to be implemented to provide reliable and reproducible quantitative insights into the zebrafish cranial vasculature.

1.4 Endothelial cell membrane behaviours

ECs and other cells are known to form a variety of membrane protrusions [218], including lamellipodia, filopodia [219, 220], as well as spherical protrusions such as apoptotic bodies (1-4 μm diameter), microvesicles (0.15-1 μm diameter), and exosomes (40-150nm diameter) [221, 222].

Of special interest are membrane blebs and the cell volume changes induced by blebbing, which play a role in cell migration, polarization, as well as apoptosis [223, 224, 225]. Cell blebs are typically formed by individual cells and are driven by cytosolic pressure [226]. There is increasing evidence that these cellular protrusions also play important roles in intracellular signalling [227], vascular development [57], and in vascular diseases such as atherosclerosis

[228]. Due to their biological relevance, a lot is known about cell blebs in particular.

Blebs form outwards from cells and usually have a constriction at their base, called neck. These necks can be either formed by localized membrane growth or global cortex contraction [229, 230, 231]. Their life-cycle is staged into the following: nucleation/seeding, protrusion, maintenance, and retraction, with dynamic shape changes of oscillation around the main cell body called "circus movement" being observed in some blebs [232].

Blebs are formed following actin cortex breaks and cytosolic pressure leading to the outward movement of the membrane, while their retraction highly depends on Myosin II which allows actin cortex re-assembly and its re-attachment to the cell membrane [233, 234].

The membrane required for protrusion formation can be provided by either membrane storage via folding [235, 236] or alternatively by localized recruitment of exo- and endocytosis [231].

EC-specifically, atypical membrane blebbing was shown during mitosis and lumenization in zebrafish trunk angiogenesis [224, 225].

Also, blood vessel protrusion are found on a larger scale (centimetres) as aneurysms, which are blood-filled, formed by multiple cells, and occur at regions of vascular wall thinning [237, 238, 239].

In the scope of this project a so far undescribed endothelial cell (EC) membrane behaviour, termed *kugeln*, was discovered. Due to the versatile roles of membrane protrusions in general, understanding *kugeln* was of both biological and clinical significance.

1.5 Thesis aims and objectives

Previous literature has demonstrated that the extraction of meaningful parameters to describe the geometry and topology of the vascular architecture is feasible and can be used to understand vascular development and disease.

I hypothesise that it will be possible to establish an image analysis pipeline to quantify the zebrafish cerebrovascular architecture in 3D which provides new insights into cardiovascular development and disease.

Thus, the aim of this project is to establish an image analysis pipeline to quantify the 3D *in vivo* vascular architecture in zebrafish (Fig. 1.6; 1.7) which will enhance the potential of zebrafish as a pre-clinical model for vascular development and disease.

Firstly, intrinsic image features, such as vascular signal, noise patterns, cross-sectional vessel edge responses, and vessel scale should be assessed to gather insights into the analytical requirement of images acquired with LSM in different transgenic vascular reporter

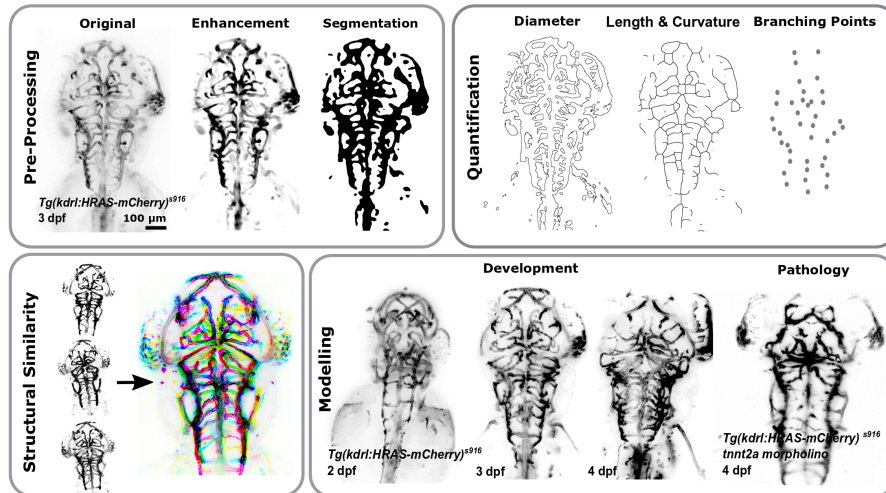


Figure 1.6: After image pre-processing and segmentation, quantification of vessel diameter, length, curvature and branching points will be extracted. Patterns of structural similarity will be investigated via image registration and establishment of a vascular development template. Subsequently, data can be integrated into a descriptive vascular model to investigate alterations during development, in pathologies, or after experimental manipulation of the vasculature in zebrafish.

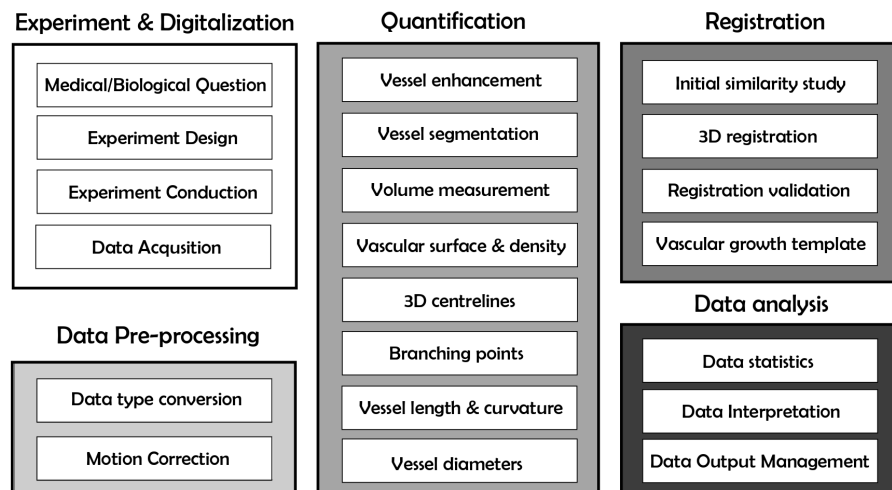


Figure 1.7: Detailed steps of vasculature quantification workflow.

lines. Based on this, a pre-processing pipeline will be established to enhance vascular information and reduce background. This will be the foundation for subsequent image segmentation to distinguish vascular from non-vascular voxels in images. Based on successful image segmentation, the total vascular volume should be derived as the first meaningful quantitative vasculature measure.

Secondly, automatic 3D inter-sample registration will deliver information about regions of structural similarity and variability of the vasculature, allowing the comparison between embryonic zebrafish. To achieve this, an initial assessment of similarity (based on growth metric measurements and manual landmark-based registration) will inform later automatic registration. Successful inter-sample registration will be used to establish age-specific vasculature templates to investigate regions of anatomical homology and/or heterogeneity between samples as well as changes during early embryonic development. Using experimental data, it should be examined how these patterns may be influenced by selected drugs or genetic alterations.

Thirdly, based on successful vasculature segmentation, the aim will be to extract quantitative shape descriptors such as vasculature branching points, segment length, and diameter. This will be addressed by the extraction of vascular centrelines from the segmented vasculature as a foundation for individual vessel identification. Following this, measurements of diameter and length of individual vessels will be performed. Global vascular information will be extracted based on summation and averaging of individual vessel information.

Fourthly, in the scope of this project a so far undescribed EC membrane behaviour was discovered and will be characterised. As these novel structures are spherical in shape they were termed *kugeln* (German for sphere; singular *kugel*). Studies will include the characterisation of their morphology, dynamics, and role in vascular development, as well as understanding their vascular bed, anatomical location, dynamic behaviour, and cellular components. Experiments addressing the role of blood flow and parent vessel specification will be performed to understand the biology of *kugel*-formation in-depth. Furthermore, the role of osmotic pressure, membrane rigidity, as well as selected key signalling pathways (VEGF and Notch) in *kugel*-formation will be studied.

This thesis contains four results chapters with separate sections for "Material and Methods".

Together, the integration of image understanding, pre-processing, inter-sample registration, and vascular quantification will fuel our understanding of vascular development and disease in zebrafish to support their use as a pre-clinical model for translational biology. The established image analysis pipeline will allow novel insights into the 3D vascular architecture and inter-

sample biological variability. Implementing the image analysis pipeline in Fiji [127], which is the most widely used open-source image analysis software in the biology community, will allow dissemination and further development.

2 Segmentation of the Vasculature

Parts of this work were published in: [5], [2], and [4] and figures reproduced with permission under licences 4415821037994, CC, and 4764790544144, respectively.

2.1 Introduction

Image segmentation can be used to distinguish vascular from non-vascular tissue (reviews see [85, 112, 240]).

Successfully segmented images are the foundation of meaningful image quantification. This allows total vascular volume measurements from binarized images, and many aspects of subsequent geometric quantifications (such as vessel length or diameter) are reliant on clear object-to-background distinction. Thus, image segmentation is often considered as the foundation of successful geometric measurements in 3D image analysis.

Prior to segmentation, image enhancement can be used to reduce image acquisition artefacts (such as noise or signal non-uniformity) and increase data quality, which can raise the accuracy of subsequent object segmentation [241]. In fluorescence microscopy images, the most commonly applied pre-processing methods include the removal of small-scale noise artefacts and speckles [95], as well as the suppression of large-scale artefacts, such as autofluorescence.

During image pre-processing, motion artefacts also have to be considered. These artefacts can be introduced by the sample itself (eg. cardiac pulsation or muscle tone), by gravity (eg. sample embedding), image acquisition system instabilities, or motion-like artefacts such as focus drift [242]. As these motions may distort the representation of the actual biological architecture, and therefore are prone to falsify subsequent analysis, motion correction is used to restore vascular integrity.

Segmentation methods can be classified into two major groups, intensity-based or model-based. Whilst intensity-based segmentation can be applied to a broad variety of vascular phenotypes and imaging modalities with limited *a priori* knowledge, model-based segmentation relies on mathematical modelling and tends to be more comprehensive and robust. However, the models used can be specific to a particular mode of acquisition or vascular bed and, thus, are often not directly transferable to other biological/medical questions.

Using transgenic lines it is possible to visualize expression patterns of specific genes with

different fluorophores. In this Chapter, the focus is on three specific transgenic lines. Firstly, *Tg(kdr1:HRAS-mCherry)^{sg16}* [243, 244] expresses a membrane-tagged mCherry fluorophore under the endothelial-specific promoter *kdr1* (synonyms: *vegfr2* or fetal liver kinase 1 (*flk1*)). Secondly, *Tg(fli1a:eGFP)^{y1}* [74] expresses cytosolic eGFP under the pan-neural promoter *fli1a*, resulting in endothelial specific and non-specific gene expression. These two transgenic lines were chosen as they are the most widely used transgenic reporter lines in zebrafish cardiovascular research. Thirdly, *Tg(fli1a:LifeAct-mClover)^{sh467}* [245] visualizes endothelial filamentous actin (F-actin), again using the pan-endothelial *fli1a* promoter but with an mClover fluorophore. No systematic analysis of image properties in these transgenic lines has been previously conducted. Therefore, prior to this study, only differences regarding biological expression (fluorophore subcellular localization and promoter-based tissue specificity of expression) were known and not whether different computational approaches would be required for their analysis.

As discussed in the introduction (section 1.3.3), previously suggested vascular quantification approaches in zebrafish were mostly performed after microangiography, focused on the trunk vasculature, or only quantified small sub-regions of vessels in the cranial vasculature. No study existed which addresses data properties, enhancement, or segmentation in different transgenic lines or during vascular development. Also, no study addressed motion artefact assessment and correction in the zebrafish vasculature, which is especially important considering that *in vivo* image acquisition is usually performed. Lastly, no study addressed the lack of a segmentation gold-standard for the zebrafish vasculature, making data output interpretation perceptible to human bias.

This gap of knowledge in data understanding is addressed in this Chapter as follows:

- (i) Image properties are studied and quantified in different transgenic lines, in a range of vessels, as well as during early embryonic development to assess whether different approaches for analysis might be required.
- (ii) The extent of motion artefacts is assessed in time-lapse (x,y,t) as well as 3D single-time-point acquisitions (x,y,z) and intra-stack motion correction is evaluated for applicability as well as its performance in different transgenic lines.
- (iii) We examine image noise, as one step to successful vasculature segmentation is to suppress local noise peaks/valleys [95, 213, 246] as well as large-scale signal fluctuations such as scattering, shadowing, or autofluorescence [214, 247].

Subsequent to this data understanding, image enhancement methods are tested to suppress image noise and enhance vascular signal as a step towards improved image segmentation in

section 2.3.3. General filters (such as Wiener or Median) as well as geometry-based filters are tested (based on "Vessel Enhancement Filtering" as proposed by Sato *et al.* and Frangi *et al.* [98, 99]).

Sato and Frangi filters mathematical background

Eigenvectors and eigenvalues

Local image gradients (Fig. 2.1A) can be described as a local intensity function (Fig. 2.1B). The sensitivity to change of this intensity function can be described by the first derivative (*image gradient*; stored in a Jacobian matrix; Fig. 2.1C) and the second derivative (*change of gradient*; stored in a Hessian matrix; Fig. 2.1D,E).

The change of gradient in the image $I(x,y,z)$ can be derived after Gaussian convolution and stored in the Hessian matrix (H ; Fig. 2.1E), which describes the local neighbourhood. To describe the local curvature in the Hessian matrix *eigenvectors* ($\lambda_1, \lambda_2, \lambda_3$) and their respective *eigenvalues* (e_1, e_2, e_3) can be used. For more detailed explanations the interested reader is referred to the following references: [97, 98, 99, 100, 101].

Line/tube and ellipsoidal model

Eigenvectors and eigenvalues can be used to describe local structures, such as sheets/plates, tubes/lines, or blobs/spheres (Fig. 2.1F).

Two fundamental approaches to enhance vessels, based on the use of Hessian matrix information, were examined here:

- (a) the line/tube model proposed by Sato *et al.* [98];
- (b) the ellipsoidal model proposed by Frangi *et al.* [99].

Both methods use local eigenvectors and eigenvalues to describe local image structures. Sato *et al.* [98] only used 2 out of 3 eigenvectors for calculations with eigenvalues sorted as $\lambda_3 \leq \lambda_2 \leq \lambda_1$. Frangi *et al.* [99] utilize the absolute values of $|\lambda_1| \leq |\lambda_2| \leq |\lambda_3|$. Due to the use of absolute values, the Frangi filter is functions when bright vessels are found on dark background and *vice versa* when dark vessel are found on bright background.

As seen in Fig. 2.1F, an ideal tubular structure in 3D could be described with:

- $|\lambda_1| \approx 0$, pointing along the vessel
- $|\lambda_1| \leq |\lambda_2|$
- $|\lambda_2| \approx |\lambda_3|$, spanning the vessel cross section perpendicular

In the Frangi filter sheets/plates and tubes/ lines (Eq. 2.1, R_a) and blobs/ spheres (Eq. 2.2, R_b) are defined as follows [99]:

$$R_a = \frac{|\lambda_2|}{|\lambda_3|} = \frac{(largest\ cross - sectional\ area/\pi)}{(largest\ axis)^2} \quad (2.1)$$

$$R_b = \frac{|\lambda_1|}{\sqrt{|\lambda_2\lambda_3|}} = \frac{volume/(4\pi/3)}{(largest\ cross - sectional\ area/\pi)^{3/2}} \quad (2.2)$$

Additionally, the Frangi filter takes so called "structureness" of the image into account, describing grey level variations (Eq. 2.3):

$$S = \|H\|_F = \sqrt{\sum_{j \leq D} \lambda_j^2} \quad (2.3)$$

Together, the filter defines so called "vesselness" with the following function:

$$\mathcal{V}_o(s) = \begin{cases} 0 & \text{if } \lambda_2 > 0 \text{ or } \lambda_3 > 0, \\ (1 - \exp(-\frac{\mathcal{R}_A^2}{2\alpha^2})) \exp(-\frac{\mathcal{R}_B^2}{2\beta^2}) (1 - \exp(-\frac{S^2}{2c^2})) & \end{cases}$$

With α , β , and γ controlling filter sensitivity, with α and β being set to 0.5, and γ depending on image grey-scale.

The Sato filter [98] relies on two eigenvectors:

$$f(\lambda_1, \lambda_c) = \begin{cases} e^{\frac{-\lambda_1^2}{2(\alpha_1\lambda_c)^2}} \cdot \lambda_c & \lambda_1 \leq 0, \lambda_c \neq 0 \\ e^{\frac{-\lambda_1^2}{2(\alpha_2\lambda_c)^2}} \cdot \lambda_c & \lambda_1 > 0, \lambda_c \neq 0 \\ 0 & \lambda_c = 0 \end{cases}$$

and uses two parameters $\alpha_1 = 0.5$ and $\alpha_2 = 2.0$ to enable cross-sectional filter asymmetry.

Shape extraction and enhancement

While the filter of Sato *et al.* [98] is based on line-structure enhancement, Frangi *et al.* [99] include three components for structure distinctions, namely blob, line vs. plates, and so called "structureness".

Parameterization

The Sato filter uses two parameters (α_1 and α_2 control cross-sectional filter asymmetry), while Frangi filter uses three parameters (α , β , γ control sensitivity of filter components).

Maximum scale response

Both approaches consider multi-scale responses with parametrization (scale space theory [149, 150, 248]). Multi-scale response is achieved by convolution with various

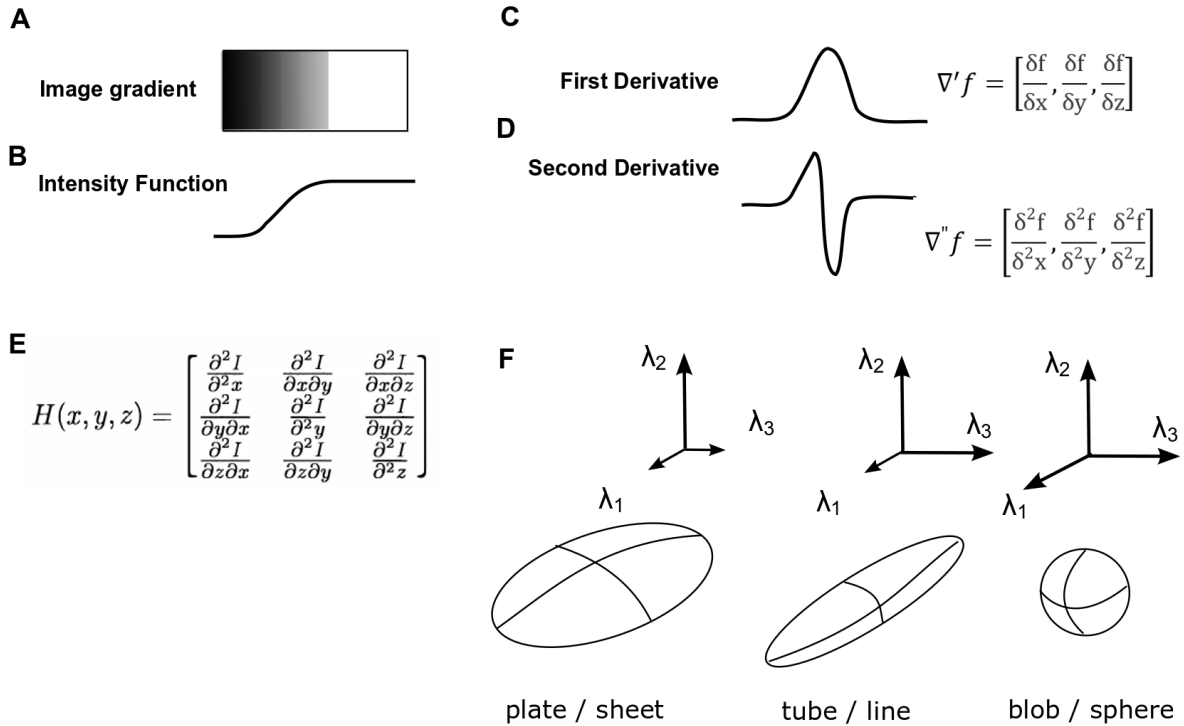


Figure 2.1: **Theory of vessel enhancement filtering, based on the Hessian Matrix.** (A) The local image gradient can be described as a local intensity function (B). (C) The sensitivity to change of the intensity function can be described via the first derivative (image gradient; Jacobian matrix) or (D) the second derivative (change of gradient; Hessian matrix (E)). (F) Structures can be described by the composition, directionality and magnitude of eigenvectors, which can be approximated via second order image derivatives.

Gaussian kernel sizes (*sigma*) and extraction of maximum response at the respective scale (Eq. 2.4).

$$R(x, y, z) = \max R(x, y, z; \sigma) \quad (2.4)$$

Filter implementations

Additional complexity is added by the fact that filters can be computationally implemented in different ways to solve the above mathematical questions. This is exemplified by two implementations of the Frangi filter in the image analysis software Fiji as "Frangi Filter" (<https://imagej.net/Tubeness>) and "FrangiExp" (<https://imagej.net/Frangi>).

A paper comparing the Sato and Frangi filter was written by Drechsler and Laura [249].

As these methods were successfully applied in the medical field, there was the rationale to test their suitability and efficacy in images of the zebrafish vasculature. As these vessel enhancement filters were originally implemented for MRI data, the following had to be considered:

- MRI data showed a different intensity distribution across vessels in comparison to transgenic lines (Fig. 1.3B). Therefore, vessel enhancement filters were generally optimized for signal peaks to be located at the vessel centre.
- Data acquired with LSFM delivered a higher image resolution and data load, which could especially impact the extraction of 3D second derivatives.

(iv) Different segmentation methods are tested subsequent to image enhancement for image binarization and the extraction of the vasculature.

(v) While in the medical field gold standards for object segmentation are sometimes available (although with varying quality), these are completely lacking for the zebrafish vasculature. Generally, such gold standards can be derived by the use of phantom models, manual segmentation, or the comparison of existing methods. Here, enhancement and segmentation robustness are studied in images with controlled decrease of vascular contrast-to-noise ratio (CNR), double-transgenic reporter lines, and scenarios of pre- vs. post-exsanguination (blood letting).

Using the above image enhancement and segmentation pipeline, the following two biological applications were examined in greater detail:

(a) Cerebral vascular volume during embryonic development.

(b) The effect of Notch and VEGF signalling inhibition on the cranial vascular volume.

These signalling pathways were chosen to be investigated as they are known to be key signalling pathways, inhibiting and promoting vasculogenesis, respectively [55, 56, 58, 250]. Thus, were ideal candidates to examine the applicability of our analysis pipeline to biologically relevant datasets, *i.e.* zebrafish treated with VEGF inhibitors are expected to show reduced vascular volume and length.

2.2 Material and methods

2.2.1 Zebrafish strains, handling, and husbandry

Studies were performed under the Home Office Project Licence 70/8588 held by Prof. Chico. Maintenance of adult zebrafish (*Danio rerio*) in the Bateson Centre Zebrafish Facility of the University of Sheffield was conducted according to previously described husbandry standard protocols at 28 °C with a 14:10 hours light:dark cycle [251]. Fertilized eggs, obtained from controlled pair-mating or controlled group-mating, were retained in E3 buffer (5mM NaCl, 0.17mM KCl, 0.33mM CaCl and 0.33mM MgSO₄ diluted to 1X E3 with distilled H₂O) with

methylene blue at 26-30 °C and staged according to Kimmel et al. [44]. Embryo dechoriation prior to 3dpf was performed manually. Anaesthesia for sample mounting and imaging was done with E3 holding 0.01% tricaine (MS-222, Sigma-Aldrich).

Transgenic lines used were: *Tg(kdrl:HRAS-mCherry)^{s916}* [244], *Tg(fli1a:eGFP)^{y1}* [74], and *Tg(fli1a:LifeAct-mClover)^{sh467}* [245].

2.2.2 Image acquisition

Microscope settings

Images were obtained with Zeiss Z.1 LSM with a scientific complementary metal-oxide semiconductor (sCMOS) detection unit. During image acquisition pivot scan, dual-side illumination, and online fusion were activated. 16-bit image depth, 1920x1920 pixel (px) image size and minimum z-stack interval were chosen for data acquisition (voxel dimensions were in the range of 0.33x0.33x0.5 μ m to 0.5x0.5x1.5 μ m in x,y,z, respectively). Multi-colour images were acquired in sequential mode. Calibration of light-sheet positioning was performed using the Zeiss Software default implementation [252]. The Zeiss Z.1 medium-filled image acquisition chamber was fitted with a water-dipping detection-objective (Plan-Apochromat 20x/1.0 Corr nd=1.38). System incubation during image acquisition was done at 28 °C, if not otherwise stated in text. Sample embedding was performed using 2%-low melting point (LMP) agarose (Sigma-Aldrich) in E3 with 0.01 % tricaine for short-time image stack acquisition, or 1% LMP-agarose with 0.01 % tricaine (MS-222, Sigma-Aldrich) for long-time image acquisition (agarose refractive index 1.33 [253]).

Optimised data acquisition

The following steps were performed to ensure data quality and inter-sample comparability to be as high as possible:

- **time-points:** Embryos were collected at the same times for all experimental repeats (*ie.* 0830-0900. Staging was conducted at approximately 5hpf and 24hpf. Imaging was conducted at the same timepoints for all experimental repeats with a 1.5h cut-off.
- **sample embedding:** Samples were embedded as straight as possible into agarose with 2-4 samples per capillary. The top-most sample was imaged first to expose all fish to the surrounding medium, the agarose block was then moved upwards to image the next fish.
- **imaging angle:** Coarse sample positioning was achieved with "locate capillary" setting. Following, "locate sample" was used to align sample dorsally (left and right eye mirrored

to each other and brain ventricles orthogonal to lens) or laterally (midbrain-hindbrain boundary to be orthogonal to lens) in the brightfield. Lastly, using fluorescent signal, fine alignment was achieved by assuring left and right PMBC being mirrored to each other.

- **imaging depth:** The dorsal longitudinal vein (DLV) was used as dorsal cut-off, while the basilar artery (BA) was used as ventral cut-off.
- **lightsheet position:** Both lightsheets were used to visualize vessels and calibration with "autocorrection" performed to assure accurate beam waste positioning.
- **data settings:** Optimum z-stack intervals and 1920x1920px (x and y) were used. Although this produced rather large data, data could be reduced during image processing (eg. downsampling in x, y, or z).

Data handling

As LSFM produces large datasets, data handling is an important consideration to store and process data effectively.

The used commercial Zeiss Z.1 setup has an internal 40Tb data storage, which was used for temporary raw data storage during data acquisition. For data processing, data were stored on 8Tb Seagate external hard drives which were used to store converted .tiff raw and processed datafiles (permanent storage). Long-term storage was conducted by storage on GDrive TeamDrives (storage until 10 years after research ends) provided by the University of Sheffield and lab-internal Synology Servers.

Data naming and processing was conducted as follows:

- **dataset naming:**
DD-MM-YYYY_Xdpf_Treatment/MO/gene_Transgenic_additionalComments
- **data folder convention:** raw>tiff(3D and MIPs)>TF>TH>Reg>512x512>analysed
- **analysis files naming:** DD-MM-YYYY_Experiment (colour coding for experimental repeats in respective files)
- **code naming:** version control by date
- **lab book:** progress control and cross-referencing by date

2.2.3 Manual Signal-to-Noise and Contrast-to-Noise measurement

Manual measurements of embryo growth, vessel diameters, and vessel length were conducted using the line region of interest (ROI) tool in Fiji [127]. Signal-to-Noise ratio (SNR, Eq. 2.5) [254] was measured using the mean vascular intensity (μ_v) divided by the intensity standard-deviation of the image background (σ ; Fig. 2.2). Contrast-to-Noise ratio (CNR, Eq. 2.6) was

calculated via the difference of mean vascular (μ_v) and non-vascular signal (μ_{nv}), divided by background signal standard-deviation (σ). Mean intensity was measured in a ROI placed inside vessels, spanning the vascular cross-section along a $5\mu\text{m}$ length from anterior-to-posterior. Non-vascular mean intensity was measured in a similarly sized non-vascularized brain region at the same anatomical depth as the vessel of interest, while background standard-deviation of intensity was estimated outside of fish (see also Appendix A).

$$SNR = \frac{\mu_v}{\sigma} = \frac{\text{mean vascular signal}}{\text{standard deviation of background}} \quad (2.5)$$

$$CNR = \frac{\mu_v - \mu_{nv}}{\sigma} = \frac{\text{mean vascular signal} - \text{mean non-vascular signal}}{\text{standard deviation of background}} \quad (2.6)$$

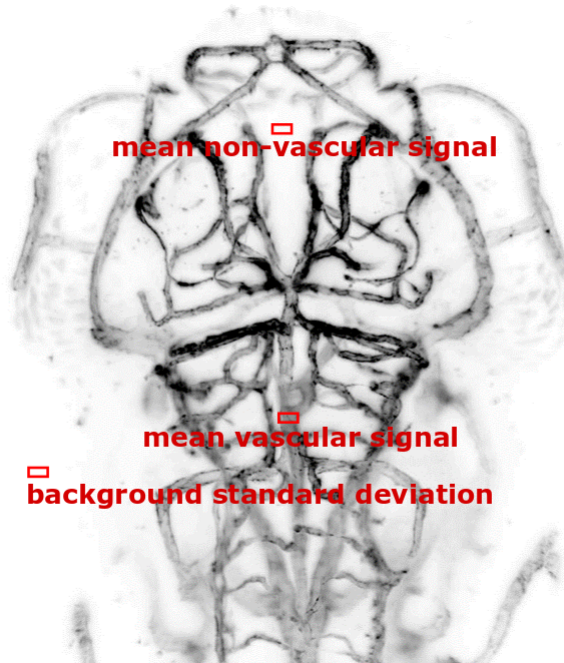


Figure 2.2: **ROIs for vascular SNR and CNR quantification.** SNR was measured using the vascular mean intensity divided by the intensity standard-deviation of the image background. CNR was calculated via the difference of mean vascular and non-vascular signal, divided by background signal standard-deviation.

2.2.4 Motion artefact quantification and correction

Estimation of motion artefacts was performed in 80 second (sec) and 10 minute (min) time-lapses acquired with 3 second intervals, resulting in 27 and 200 frames, respectively. Correlation analysis was performed using Pearson's correlation coefficient (ρ) and Mean Square Error (MSE) (MSE) between the first (A) and last frame (B) of the image series (Eq.

2.7; Eq. 3.5). *Cov* describes covariance and σ the respective standard-deviation.

$$\rho_{A,B} = \frac{\text{cov}(A,B)}{\sigma_A \sigma_B} \quad (2.7)$$

$$MSE_{A,B} = \sum_{i=1}^n |A - B| \quad (2.8)$$

Motion artefact correction was performed with intra-stack registration using the Fiji [127] Plugin "Linear Stack Alignment with SIFT" based on [255]. Parameters were set as follows, after optimization: 1.6px Gaussian blur, 5 steps per scale octave, 30px minimum image size, 1920px maximum image size, 8 feature descriptors, 0.98 closest/next ratio, 3/10 px maximum alignment error, 0.05 inlier ratio, rigid transform and without interpolation.

2.2.5 Signal noise, filtering, and segmentation

Noise assessment and reduction

Occurrence of periodic stationary noise artefacts (stripe noise) was evaluated by intensity measurement outside of samples (in 2% LM-agarose (Sigma) of sample embedding) using a 700 μm line ROI in Fiji [127].

Removal of spike and shot noise was evaluated using Gaussian, Wiener, and Median filter, which reduce local high frequency signal domains (noise and speckles) by spatial filtering while considered to leave edges intact [256]. Closer examinations were performed for the Median filter with different radii [95, 246, 257, 258]. Local contrast enhancement to increase background-foreground contrast for subsequent segmentation was evaluated using Contrast Limited Adaptive Histogram Equalization (CLAHE) [132]. To examine the impact of image background (eg. autofluorescence, uneven excitation, etc.) the rolling ball algorithm was studied for large-scale artefact removal [247]. To examine signal distributions across vessels, cross-sectional intensity profiles were produced with 15 μm line regions of interest (ROIs) [127].

Object-based enhancement

Enhancement of vessels based on their tube-like structure (see [98, 99]; discussed below) was examined using the following available Fiji implementations [127]:

- "Tubeness Filter" Plugin implemented by Jean-Yves Tinevez, Mark Longair, Stephan Preibisch and Johannes Schindelin based on [98] (<https://imagej.net/Tubeness>)
- "Frangi Filter" (Process>Filters>Frangi Vesselness) based on [99]

- "FrangiExp" implemented by Curtis Rueden, Mark Longair, Johannes Schindelin, and Mark Hiner based on [99] (<https://imagej.net/Frangi>)

Assessment of intensity response in Difference of Gaussian (DoG) with different sigma size was performed by application of Gaussian filter with user-specified sigma and subsequent image subtraction.

Intensity-based segmentation

Intensity-based vasculature binarization of 16-bit images was evaluated using the Auto Threshold Plugin implemented in Fiji [127] (https://imagej.net/Auto_Threshold).

Advanced segmentation methods

Segmentation using k-means clustering [127, 259], based on pixel proximity, was done using 16-bit images after pre-processing with Median filter (radius 6) and application of rolling ball algorithm (size 200). As by default, 48 randomized seeds were automatically placed by the k-means++ algorithm [260, 261]. Additional parameters were set as follows: 0.0001 cluster center tolerance, interpretation as 3D stack, and detection of four clusters (this was found to deliver reliable results, especially after tubular filtering (TF; one background cluster and three vessel clusters with varying brightness)).

Statistical region merging segmentation [262, 263], which computes objects based on statistical property homogeneity, was done in 8-bit images due to input requirements. It was performed with pre-processing as above, detection of two regions (fore- and background) and delivery of absolute values (calculation of absolute pixel value differences, independent of sign [264]).

Level set segmentation [170], based on gradually evolving active contours to find object boundaries based on intensity differences found on object edges, was done in 8-bit images (to achieve more sufficient processing times) with 50 user-specified vasculature seeds, using the "Fast Marching" option with a distance threshold of zero and user-selected image-specific grey value thresholds.

Segmented images classified vasculature as black voxels (intensity 255) on white background (intensity 0).

Modelled Tubes. Modelled tubes (hollow, filled and Gaussian blurred) were produced manually with uniform signal intensity of 255 against zero background intensity circular ROI selection using Fiji [127]. Tubes were produced to resemble the following biological settings: **(i) hollow tubes** - 20 μm outer diameter (1.13 μm wall thickness), 8.3 μm outer diameter (0.8 μm wall thickness), 5 μm outer diameter (0.6 μm wall thickness); resembling lumenized vessels; **(ii) filled tubes** - resembling unlumenized vessels (with the same outer diameter as

above); **(iii) Gaussian blurred tubes** - Gaussian filter with sigma 5vx; resembling a more realistic intensity distribution of fluorescence; **(iv) increasing noise** - Gaussian white noise with standard deviation 25, 50 or 100 (zero background intensity); resembling autofluorescence and background noise.

2.2.6 Total cerebrovascular volume measurement

The total vascular volume (Vol , Eq. 2.9) was quantified in a region of interest which was determined dorsal-ventral during image acquisition using the dorsal aorta (DA) as the most ventral boundary, while the dorsal longitudinal vein (DLV) constituted the most dorsal. Lateral exclusion of unspecified regions, such as the eye was done via manual ROI selection (user-defined free-hand selection in original maximum intensity projection (MIP), Fig. 2.3). Anterior and posterior inclusion were based on prosencephalic artery (PrA) and posterior cerebral vein (PCeV), respectively.

The vascular volume (Eq. 2.9) within this region of interest was derived from the histogram black voxel count (V_{black}) and the respective voxel volume ($V_{x,y,z}$).

$$Vol = V_{black} * V_{x,y,z} \quad (2.9)$$

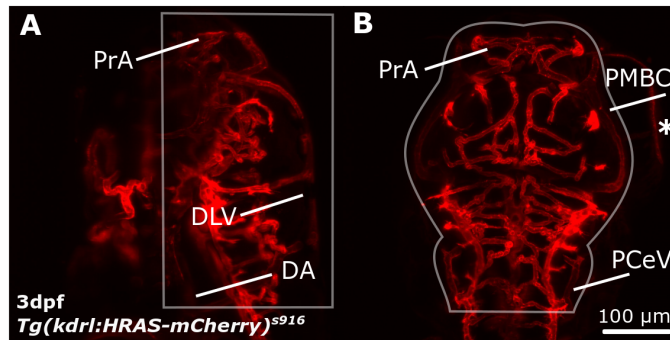


Figure 2.3: **Anatomical region for cranial vascular volume measurement.** Dorsal cranial volume was measured in the region indicated by white boxes. **(A)** During image acquisition the dorsal aorta (DA) was chosen as the most ventral boundary, while the dorsal longitudinal vein (DLV) constituted the most dorsal. **(B)** Exclusion of unspecified regions, such as the eye (indicated with asterisk) was done via manual ROI selection. Anterior and posterior inclusion were based on prosencephalic artery (PrA) and posterior cerebral vein (PCeV), respectively (figure reproduced with permission from [5] under licence 4415821037994).

2.2.7 Evaluation of segmentation robustness and sensitivity

Vessel diameter and FWHM measurements

Manual diameter measurements of a variety of vessels were performed in original images. Intensity profiles were plotted using line ROI in original, enhanced, and segmented images. FWHM was quantified from extracted cross-sectional intensity distributions using Matlab.

Controlled CNR changes

Segmentation robustness was studied by measuring the total cranial vascular volume (as described above; Eq. 2.9) in images with varying CNR levels. Decreasing CNR levels were induced by consecutive image acquisition of 4dpf *Tg(kdrl:HRAS-mCherry)^{s916}* [244] embryos with a laser power of 1.2%, 0.8%, and 0.4%. CNR was measured in BA as described above (Eq. 2.6; n=10).

Segmentation in double-transgenic line

Data acquisition was performed in 4dpf double-transgenic *Tg(fli1a:eGFP)^{y1}, Tg(kdrl:HRAS-mCherry)^{s916}* [74, 244] (n=21 embryos; 2 experimental repeats) with separate colour tracks. Image enhancement and segmentation was performed independently for the two colour channels, with selection of ROI in original MIP of red (*kdrl*) channel.

Segmentation in pre- and post-exsanguinated samples

Data acquisition was performed in 4dpf *Tg(kdrl:HRAS-mCherry)^{s916}* [244] (n=16 larvae; 2 experimental repeats). Cessation of blood flow was achieved by mechanical opening of the heart cavity with forceps. Control of blood cessation was performed by visual assessment of lack of heart contraction and blood flow. The ROI for volume measurement was separately determined for pre- and post-cessation images using the procedure described in Section 2.2.6.

2.2.8 Biological application datasets

Vascular development *Tg(kdrl:HRAS-mCherry)^{s916}* [244] samples were imaged from 2-5dpf (n=17 from 2 experimental repeats).

Inhibition of Notch signalling Inhibition of γ -secretase in the Notch signalling cascade was achieved by application of 50 μ M N-[N-(3,5-Difluorophenyl)-L-alanyl]-L-S-phenylglycine tButyl Ester (DAPT) for 12h between 84-98hpf (Sigma-Aldrich; D4952) [265] (4dpf; control n=21, DAPT n= 22; 3 experimental repeats).

Inhibition of VEGF signalling Inhibition of VEGF signalling was conducted by application of the VEGF-receptor inhibitor AV951 at a concentration of 250nM for 2-4h between 96-98hpf or 96-100hpf (Selleckchem; S1207; Tivozanib - AVEO pharmaceuticals) [266] (4dpf; control n=21,

AV951 n= 23; 3 experimental repeats).

2.2.9 Developed image analysis macros

See Appendix B for workflow overview, Appendix C for individual macros, and Appendix D for GUI.

2.2.10 Statistics and data display

Gaussian distribution conformity of data was tested using the D'Agostino-Pearson omnibus test [267]. Statistical analysis of normally distributed data was performed using a One-Way ANOVA to compare multiple groups, or Students t-test to compare two groups. Non-gaussian distributed data were analysed with a Kruskal-Wallis test to compare multiple groups or Mann-Whitney tests to compare two groups. Analysis was performed in GraphPad Prism Version 7 (GraphPad Software, La Jolla California USA; <https://www.graphpad.com>). P values in the text are displayed as follows: $p < 0.05$ *, $p < 0.01$ **, $p < 0.001$ ***, $p < 0.0001$ ****. Data representations use mean values and standard deviation, if not otherwise stated in text. Correlation analysis was performed with the Pearson's correlation coefficient.

Image representation was done with GNU Image Manipulation Program Version 2.8 (GIMP; <https://www.gimp.org>) or Inkscape Version 0.48 (<https://www.inkscape.org>). Visualized data are MIPs, displaying either grey (single channel) or red/green (multi-channel) colour representations (using Fiji [127]). Intensity inversion was applied, as appropriate, to give clearest rendering of relevant structures. Similarly, time-lapse visualization was done using MIPs and intensity inversions.

In the subsequent sections, experimental repeats refer to multiple measurements during the same image acquisition session, while experimental replicates are measurements from different image acquisition sessions.

2.3 Results and discussion

2.3.1 Vascular Contrast-to-Noise ratio (CNR) differs in transgenic lines, but not over time or vessels of different size

As it was not known whether different transgenic reporter lines (different promotor, fluorophore, and cellular localization of fluorophore) have different image properties, CNR levels and vascular cross-sectional intensity distribution were assessed in the following three

transgenic lines: *Tg(kdrl:HRAS-mCherry)^{s916}* [244], *Tg(fli1a:eGFP)^{y1}* [74], and *Tg(fli1a:LifeAct-mClover)^{sh467}* [245].

Tg(kdrl:HRAS-mCherry)^{s916} had the highest CNR level (48.26 ± 19.35 ; Fig. 2.4A), being higher than *Tg(fli1a:eGFP)^{y1}* (26.92 ± 9.91) or *Tg(fli1a:LifeAct-mClover)^{sh467}* (18.74 ± 14.20), with $p < 0.0001$ for each ($n=20$ 4dpf larvae; 3 experimental repeats; One-Way ANOVA).

Assessment of the vascular cross-sectional intensity distribution of the MMCTA showed a double-peak for all three transgenic lines (Fig. 2.4B). This was in accordance with the fact that endothelial cells, which express the fluorophore of interest, outline the vascular lumen, reinforcing the assumption that lumenized vessels would resemble hollow tubes. Studying edge response strength visually, it was found to be the highest for *Tg(kdrl:HRAS-mCherry)^{s916}* and lower for *Tg(fli1a:eGFP)^{y1}* as well as *Tg(fli1a:LifeAct-mClover)^{sh467}*; in agreement with *Tg(kdrl:HRAS-mCherry)^{s916}* having the highest CNR.

Visual assessment furthermore confirmed that vascular structures were clearly observed in *Tg(kdrl:HRAS-mCherry)^{s916}*, while less specific structures such as skin were visualized in *Tg(fli1a:eGFP)^{y1}* and *Tg(fli1a:LifeAct-mClover)^{sh467}* (Fig. 2.4; white arrowheads). This was assumed to be due to the lower CNR in *Tg(fli1a:eGFP)^{y1}* and *Tg(fli1a:LifeAct-mClover)^{sh467}* requiring a higher laser power for image acquisition, which ultimately resulted in increased image scattering, autofluorescence, and reflection of non-vascular tissues as well as pan-endothelial expression under the *fli1a* promoter.

The observed variability within the examined transgenics was likely to be caused by differences in allele insertion numbers for which the samples were not controlled. For the following experiments animals were selected based on the brightest fluorescence at 24hpf.

Together, these data indicated that *Tg(kdrl:HRAS-mCherry)^{s916}* had the highest CNR, the clearest edge response, and the most specific expression pattern, suggesting that segmentation would be computationally less demanding in this transgenic, compared to the other transgenic reporter lines tested.

To assess whether image quality changes during early vascular development, CNR was quantified in the BA from 2-5dpf in *Tg(kdrl:HRAS-mCherry)^{s916}*. A trend towards decrease was found from 2-5dpf (Fig. 2.5A; $p = 0.1032$; $n=15-17$; 3dpf; 2 experimental repeats; Kruskal-Wallis test), suggesting that vascular segmentation should be equally successful during this developmental time-frame as image quality did not change dramatically. CNR was most variable at 2dpf with a coefficient of variation (CoV) of 105.11% ($n=15$; $\text{CoV } 3\text{dpf}=56.87\%$ $n=16$, $4\text{dpf}=60.86\%$ $n=17$, $5\text{dpf}=76.33\%$ $n=17$; 2 experimental repeats).

Following this, vessels of different size were examined to analyse whether CNR patterns

would be similar and thus be detected with a similar likelihood. As shown in Fig. 2.5B,C vascular CNR was not different in vessels of different diameter (p 0.3007; $n=16$ 3dpf larvae; 2 experimental repeats; Kruskal-Wallis test). This suggested that successful segmentation of vessels of different diameter should be equally feasible.

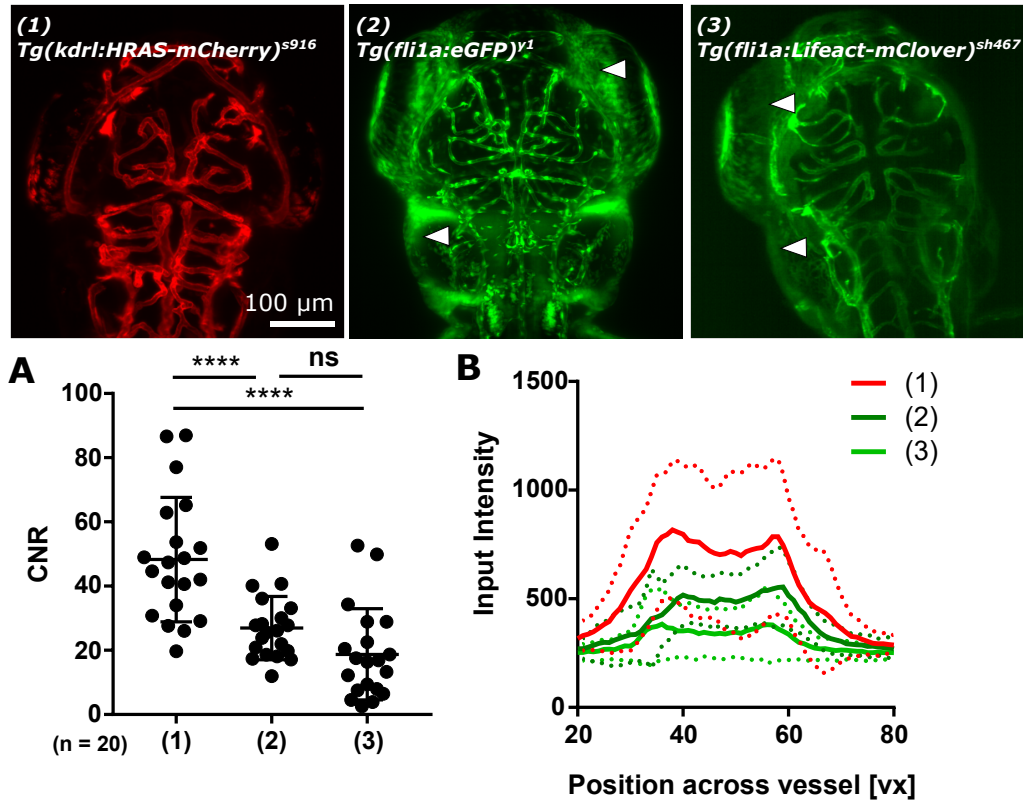


Figure 2.4: **CNR differs depending on the transgenic line.** (A) Comparing the CNR in the BA of different transgenic lines (1,2,3; reproduced with permission from [5] under licence 4415821037994) showed varying CNR levels depending on the transgenic construct. A difference was found between (1) and (2), as well as between (1) and (3), with $p < 0.0001$ for both. No difference was found between (2) and (3) with p 0.0898 ($n=20$ 4dpf larvae; 3 experimental repeats; One-Way ANOVA). Moreover, more unspecific signal was visualized in (2) and (3), indicated with white arrowhead. (B) Intensity distribution across vessels showed a double-peak for all three studied transgenic lines at vascular edges. The highest intensity and edge-response was found in (1), while edge-responses were lower in (2) and (3). (average is solid line; standard deviation is dotted line)

2.3.2 Motion artefacts can be corrected using SIFT

As motion artefacts could interfere with subsequent vascular quantification the extent of motion occurring in our image acquisition setup was assessed, and it was tested whether the occurring motions could be sufficiently corrected.

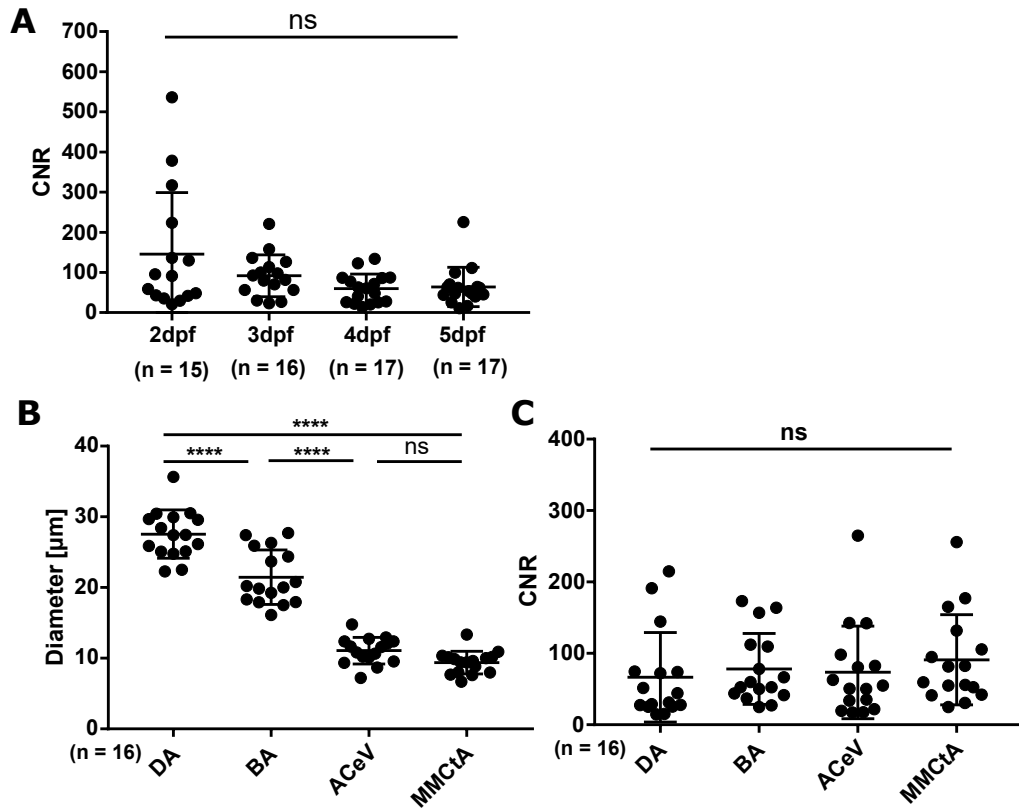


Figure 2.5: **CNR is similar in vessels of different size.** (A) Measurement of the CNR in the BA during early vascular development in *Tg(kdrl:HRAS-mCherry)^{s916}*, showed no difference between 2-5dpf (p 0.1032; 2dpf n=15, 3dpf n=16, 4dpf n=17, and 5dpf n=17 larvae; Kruskal Wallis test), indicating that vascular segmentation should be equally successful for all timepoints of the investigated timeframe. CNR measurement in candidate vessels of different diameter (B) showed no difference (C), suggesting that vessels of different size should be segmented with the same likelihood (B and C: n=16 3dpf larvae from 2 experimental repeats; B - One-Way ANOVA; C - Kruskal Wallis; graphs reproduced under CC licence from [2]). *Abbr.:* ACeV - anterior cerebral vein, BA - basal aorta, DA - dorsal aorta, MMCTA - middle mesencephalic central artery;

Linear Stack Alignment with SIFT in (x,y,t)

Depending on the image acquisition setup an average 3D single-time point acquisition takes about 80sec. Thus, it was measured whether motion artefacts would occur within 80sec using single plane acquisition (x,y,t). The correlation between the first and last slice was 0.971 ± 0.01839 , suggesting that motion does happen and possibly could interfere with later quantification. After application of "Linear Stack Alignment with SIFT", correlation between first and last slice was increased to 0.993 ± 0.001341 . Similarly, the MSE was decreased from 13.35 ± 10.24 to 2.692 ± 0.7006 (n=5 3dpf larvae; 1 experimental repeat). Together, these data suggested that motion could occur in this short time-frame, but can be corrected with the suggested motion correction approach, based on scale invariant features.

To evaluate if more extensive motion artefacts could be equally corrected and whether SIFT-based stack alignment would be applicable to transgenic lines with different CNR levels (Fig. 2.4A), alignment was applied to 10min time-lapse acquisitions in *Tg(kdrl:HRAS-mCherry)^{S916}* [244] and *Tg(fli1a:eGFP)^{Y1}* [74] (Fig. 2.6 A,B). Correlation between the first and last slice was increased by linear stack alignment based on SIFT from 0.503 ± 0.275 to 0.879 ± 0.904 ($p < 0.0001$; n=15; 3dpf; 2 experimental repeats) in *Tg(kdrl:HRAS-mCherry)^{S916}* [244] (Fig. 2.6C). Similarly, correlation was increased in *Tg(fli1a:eGFP)^{Y1}* [74] from 0.722 ± 0.202 to 0.927 ± 0.046 (Fig. 2.6D; p 0.0008; n=15; 3dpf; 2 experimental repeats).

Higher correlation after motion correction was achieved in *Tg(fli1a:eGFP)^{Y1}* [74]. We suggest that this was due to higher signal abundance based on the pan-endothelial expression under the *fli1a* promoter.

Together, these data suggest that motion correction, based on scale invariant features, can correct for larger-scale motion artefacts. Additionally, this was applicable to transgenics with different CNR levels, indicating applicability to a variety of transgenic lines. Future work might examine whether iterative application of linear stack alignment results in further improvement of motion correction.

Linear Stack Alignment with SIFT in (x,y,z)

Next, motion correction was applied to image stacks (x,y,z) to assess whether the proposed approach would be applicable in the 3D context. Motion artefacts were corrected to a high degree, upon visual inspection, and structures appeared less blurred in MIP images (Fig. 2.7). Quantification of stack motion correction was performed, but data not included here, correlation analysis was inconclusive in terms of what differences between slices were biological or motion.

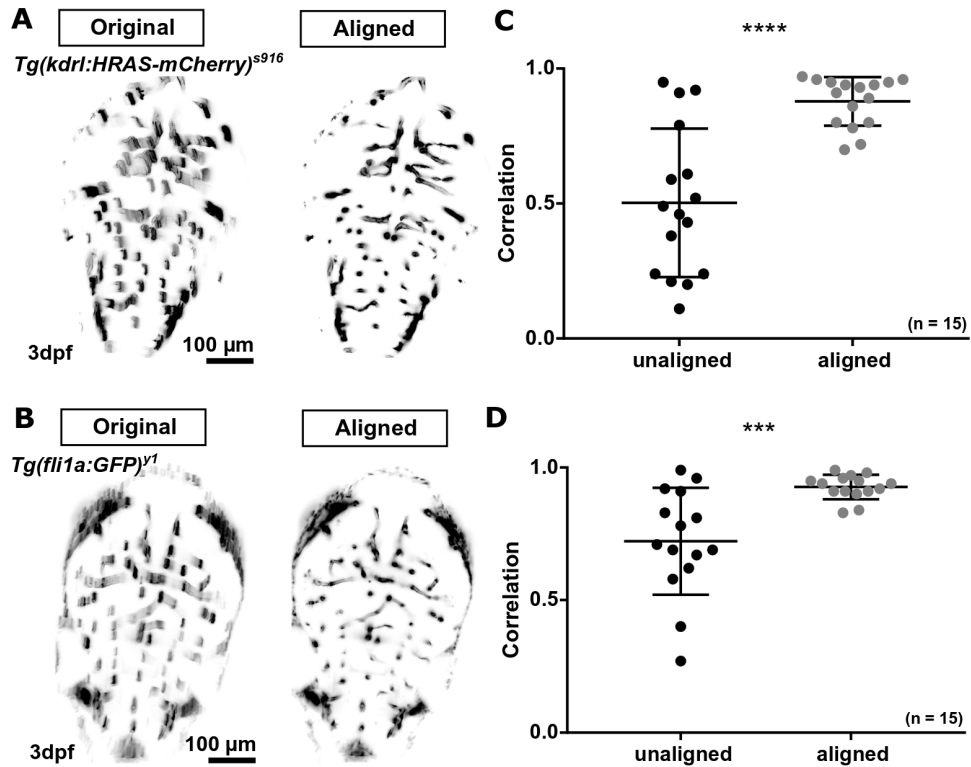


Figure 2.6: **SIFT-based motion correction is applicable to data in (x,y,t).** (A) Motion artefacts were evaluated in 10min time-lapse acquisitions in *Tg(kdrl:HRAS-mCherry)^{s916}* [244] and (B) *Tg(fli1a:eGFP)^{y1}* [74]. (C,D) Quantification of correlation between the first and last slices of time-lapses showed an increase after the application of linear-stack alignment, based on scale-invariant feature transformation (SIFT), in both *Tg(kdrl:HRAS-mCherry)^{s916}* [244] and *Tg(fli1a:eGFP)^{y1}* [74] (A,B inverted MIP; paired Students t-test; n=15 3dpf larvae; 2 experimental repeats; C p<0.0001; D p 0.0008; graph C reproduced with permission from [5] under licence 4415821037994; graph D reproduced under CC licence from [2]).

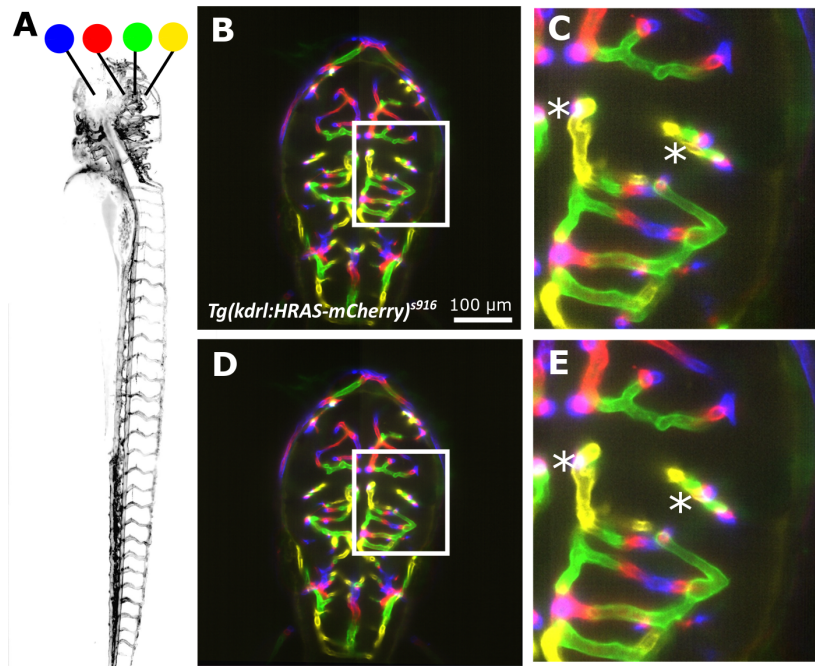


Figure 2.7: **SIFT-based motion correction is applicable to data in (x,y,z).** Motion correction in 3D stacks showed overall enhancement of vascular structures. Colours in (B)-(E) correspond to the height of indicated sagittal plane in (A). (B) Sample data of stack before alignment. (D) Sample data after intra-stack alignment with SIFT for motion correction. (C,E) Close-up of (B) pre- and (D) post-alignment, respectively. Asterisk indicates increased structure correspondence due to linear stack alignment.

As no gold-standard was available, no threshold could be set between biological or motion-induced differences in correlation.

2.3.3 Enhancement of the cerebral vasculature to improve image quality

Testing image filtering for image enhancement

The structure of background noise was assessed to understand whether structured/patterned noise would be found in our images, and whether this would require specific correction during image pre-processing. Assessment of image background noise showed that noise was random rather than structured, suggesting that there was no need to correct for patterned noise (Fig. 2.8A).

As the reduction of local high frequency signal domains (noise and speckles) is commonly approached by image filtering or local smoothing [95] using filters such as Gaussian, Wiener or Median [256], these different filtering methods were tested.

Median filtering with a radius of 6 (13-by-13 neighbourhood) showed the best results regarding high frequency smoothing efficiency, while preserving the intensity-distribution and

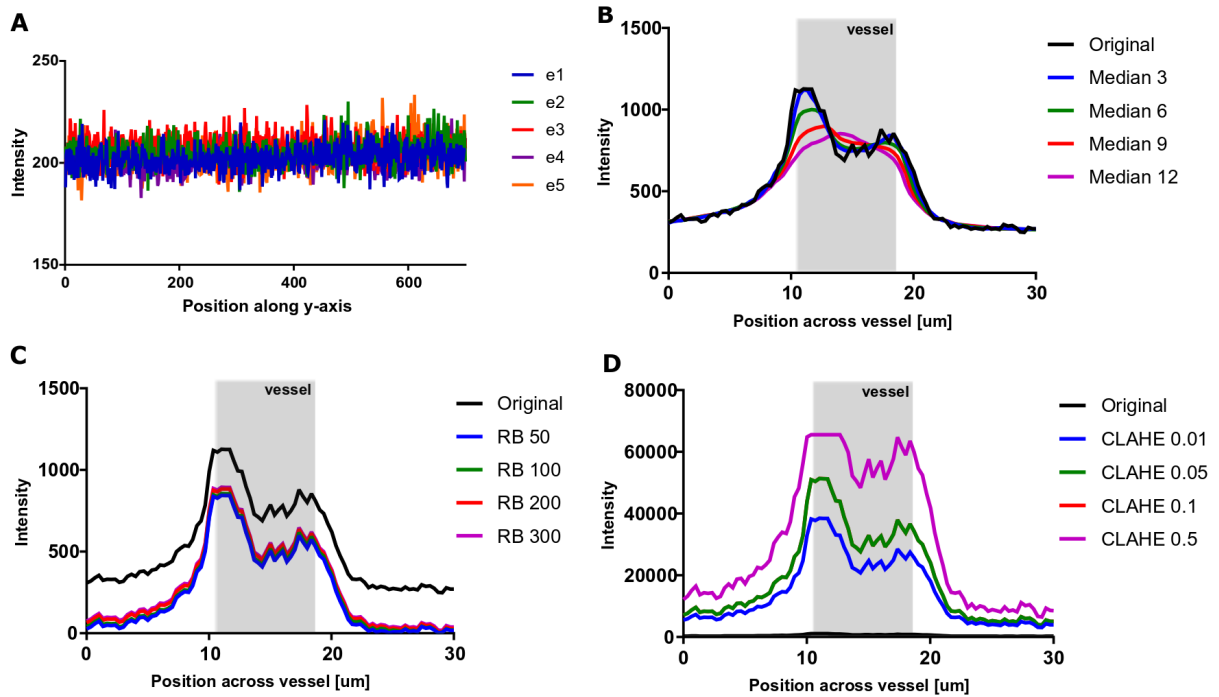


Figure 2.8: **Examination of parameter sizes for pre-processing steps.** (A) Periodic noise was not found to occur in images ($n=5$ 3dpf larvae). (B) Median filtering was assessed for its potential reduce spike and shot noise. Application of Median filter with a radius of 6 delivered smoothed, but preserved, cross-vessel intensity distribution. (C) The rolling ball algorithm (RB) efficiently suppressed non-vascular background signal, whilst not interfering with vascular signal. (D) Local intensity enhancement with Contrast Limited Adaptive Histogram Equalization (CLAHE) produced equally increased vascular and non-vascular signal.

edge-response of vessels (Fig. 2.8B). The subtraction of background noise was attempted using a rolling ball algorithm [247], which sufficiently suppressed larger-scale non-vascular signal (Fig. 2.8C). Setting the parameter size to 200 was most applicable to images from different samples and acquisition settings. Testing local contrast enhancement with CLAHE [132] showed an overall enhancement of intensities without obvious improvement of vascular structures and, therefore, was excluded from further investigation (Fig. 2.8D).

Based on the above, 13-by-13 Median filtering with subsequent application of the rolling ball algorithm (size 200) was applied to images and the CNR pre- and post-enhancement measured in the BA. This filtering sequence increased CNR (Fig. 2.9; $p<0.0001$; $n=20$; 3dpf; 3 experimental repeats; paired Student's t-test).

Testing tubular filtering for image enhancement

In the framework of the bioimage analysis software Fiji [127] three already implemented "Vessel Enhancement Filters" were available and were tested for their applicability to images of the

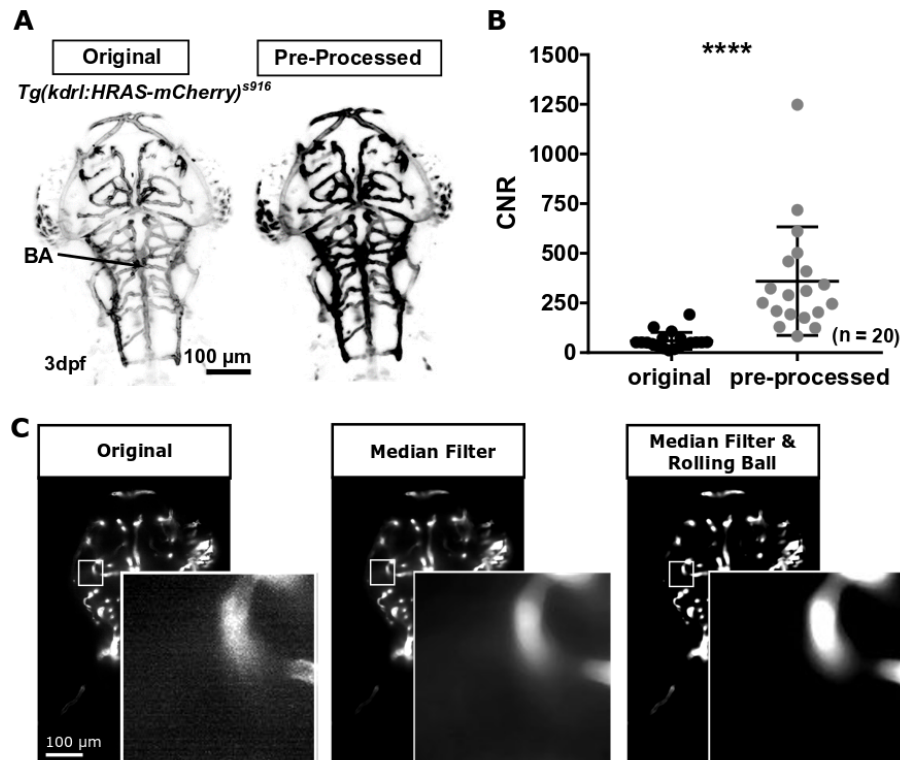


Figure 2.9: **Application of Median filter and Rolling Ball increases vascular CNR.** (A) Application of image pre-processing, by median filtering and rolling ball algorithm, increased the vascular CNR in the BA (B). Pre-processing based on Median Filter and Rolling Ball increased vascular signals (C). (A inverted MIP; B n=20 3dpf larvae from 3 experimental repeats; paired Student's t-test; $p < 0.0001$; figure B reproduced with permission from [5] under licence 4415821037994)

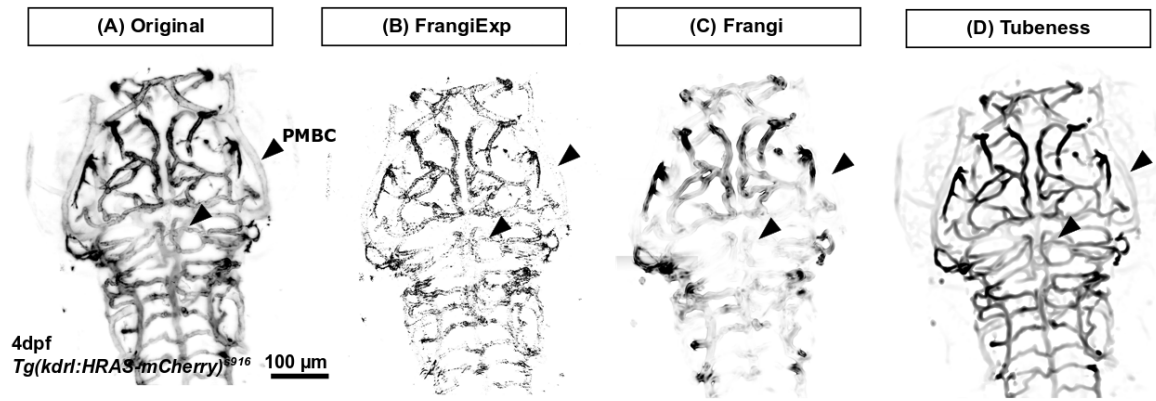


Figure 2.10: **Initial assessment of vessel enhancement filters implemented in Fiji.** (A) Enhancement of vascular structure was tested by application of filters to original data of 4dpf *Tg(kdr:HRAS-mCherry)^{S916}*. (B) Application of "FrangiExp" resulted in suppression of dimmer vessels (black arrowheads) and globally grainier structures. (C) "Frangi Filter" also delivered an unsatisfactory outcome with, again, dim vessels being suppressed and vessels overall appearing blurred. (D) Application of "Tubeness Filter" returned enhanced vessel without the loss of dimmer structures.

zebrafish vasculature acquired with LSMF.

For an initial assessment, the filters were applied at scale sizes similar to the average vessel size to images of 4dpf *Tg(kdr:HRAS-mCherry)^{S916}* with the assumption that a maximum scale response should occur at the scale of the examined vessels (Fig. 2.10A; scale $10\mu\text{m}$). Upon visual inspection, "FrangiExp" and "Frangi Filter" returned insufficiently enhanced vessels (Fig. 2.10B,C). Mainly, dimmer structures, such as the PMBC, were suppressed and the returned images were low in detail. In comparison, "Tubeness Filter" application resulted in sufficiently enhanced vasculature, without interference of original structures (Fig. 2.10D).

(a) Filter response - Vessel-to-background intensity

As the unsatisfactory outputs from "FrangiExp" and "Frangi Filter" were surprising as Frangi filters are commonly used in the medical field, these filter responses were studied more in-depth to understand what may have caused the observed issues. The examination of three different vessels, namely PMBC, PMcTA and MMcTA, is presented here.

First, all filters were applied to bright vessels on a dark background as was the case in our original data (Fig. 2.11A).

"FrangiExp" and "Frangi Filter" enhanced local fluorophore speckles as blobs (white arrowheads). We anticipated that this was caused by the Frangi "blob"-detection term (Eq. 2.10; R_b), which enhanced fluorescent speckles due to their rounded structure (Fig. 2.11A;

white arrowheads) [99].

$$R_b = \frac{|\lambda_1|}{\sqrt{|\lambda_2\lambda_3|}} \quad (2.10)$$

Additionally, a suppression of vascular signal was observed after both Frangi filter implementations (Fig. 2.11A; black arrowheads), which was likely to be caused by the illumination-dependent "structureness term" of the filter (Eq. 2.11; S).

$$S = \|H\|_F = \sqrt{\sum_{j \leq D} \lambda_j^2} \quad (2.11)$$

Where R_b corresponds to local measure of sphericity (blob), λ_j denotes eigenvectors, S denotes structureness term, and H denotes Hessian matrix. Again, enhancement via "Tubeness Filter" (TF) delivered satisfactory enhancement, without information loss as encountered by the other filters.

Following, filter response in the same images but with inverted intensity (dark vessels on bright background) was examined. This was conducted because the Sato filter is not designed to enhance under this intensity configuration [98], whereas Frangi filters are configured to be independent of the dark-to-bright status of the vessel and background [99]. Thus, any deviation from the theoretical framework may highlight any issue with the computational implementation of the filters.

While the FrangiExp filter delivered more speckled data, the Frangi filter was comparable to the bright-on-dark situation. As expected from the theory, TF was unable to enhance vessels in this dark-on-bright state.

Together, our data suggested that the under-performance of the FrangiExp and Frangi Filters was not due to the intensity status of images, while TF indeed required bright-on-dark vascular information to enhance vessels.

(b) Filter response - 2D application

To further understand the different outcomes for the tested filters in 2D, filters were applied to 2D hollow circles of different size (4.95, 8.25 and $20\mu\text{m}$) at the filter scale of $10\mu\text{m}$. Hollow tubes were chosen because lumenized vessels are visualized as hollow tubes in transgenic zebrafish reporter lines (Fig. 1.3B). Only one scale size was assessed to gather initial insights into the filter responses regardless of enhancement scale.

While no changes to the images were observed after FrangiExp and Frangi Filter (Fig. 2.12), TF enhanced the circular structures, broadening the simulated vessel wall to the point where, for the smaller circles (4.95 and $8.25\mu\text{m}$), it returned a single-peak intensity distribution.

To further challenge this "ideal scenario", Gaussian noise was added in increasing

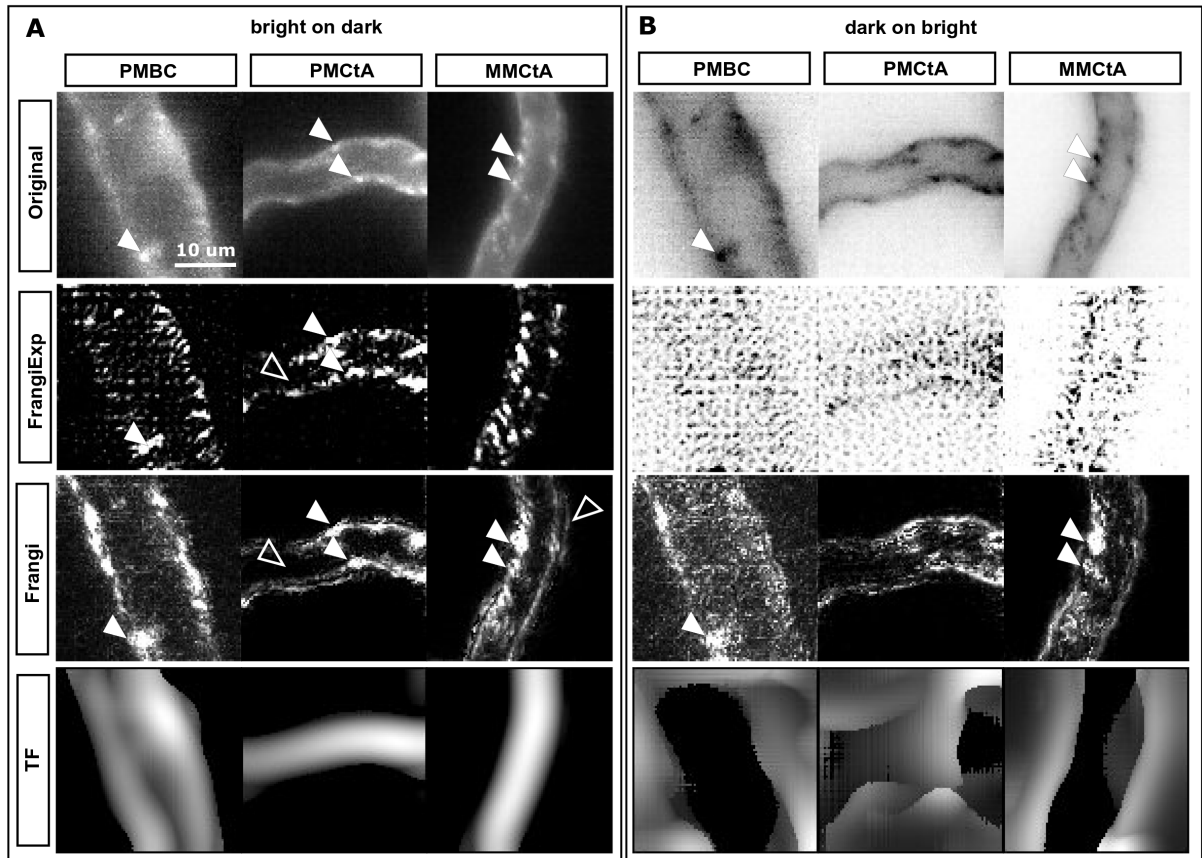


Figure 2.11: **Object-to-background colour filter response in selected vessels.** (A) In images with bright vessels on dark background, TF delivered the best enhancement of vessels, while FrangiExp and Frangi Filter enhanced fluorophore speckles and suppressed true vascular signal. (B) Application of filters to images with dark vessel on bright background showed that TF was not delivering enhanced vessels, as was assumed from the filter theory. Interestingly, FrangiExp seemed even slightly worse, while Frangi Filter delivered similar results.

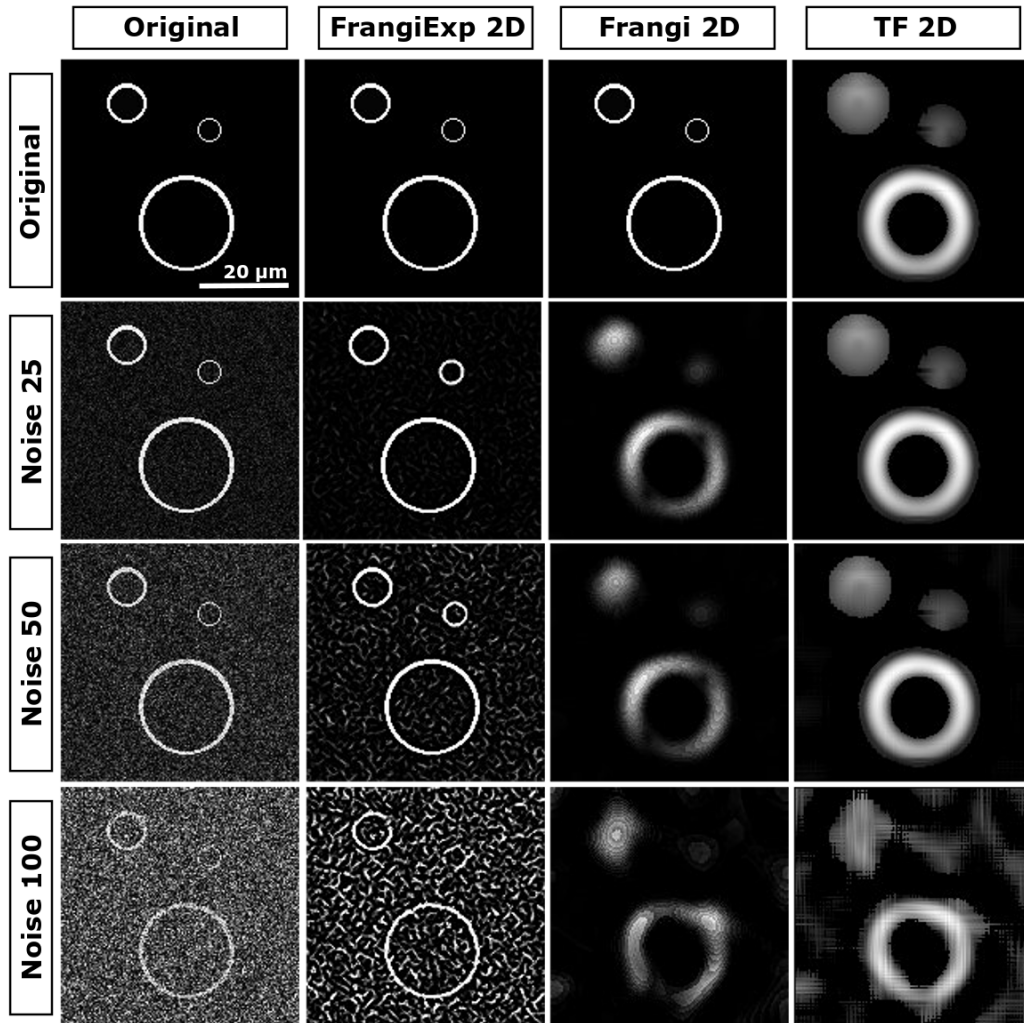


Figure 2.12: **Filter response - 2D application.** TF delivered a single-peak intensity distribution in smaller vessels and showed a low sensitivity to noise. FrangiExp was less noise sensitive than the Frangi Filter.

increments. FrangiExp and TF were less sensitive to noise than the Frangi Filter, which already delivered less satisfying results after the lowest addition of noise.

(c) Filter response - 3D application

Filters were applied to 3D hollow cylinders (same parameters as above) to understand differences in the 2D and 3D filter responses. It was found that the 3D application of TF delivered similar results to the 2D scenario (Fig. 2.13). On the other hand, the FrangiExp and Frangi Filters both perturbed the original tube structure upon 3D filter application. It was thought that this was due to λ_1 , which is the eigenvector corresponding to the vessel direction, and was the highest along the vessel wall (z-axis) and, thus, the filters enhanced the walls/edges. Interestingly, both filters were highly sensitive to pixelation, as enhancement of the pole regions of circles was observed (Fig. 2.13, white arrowheads). Again, noise

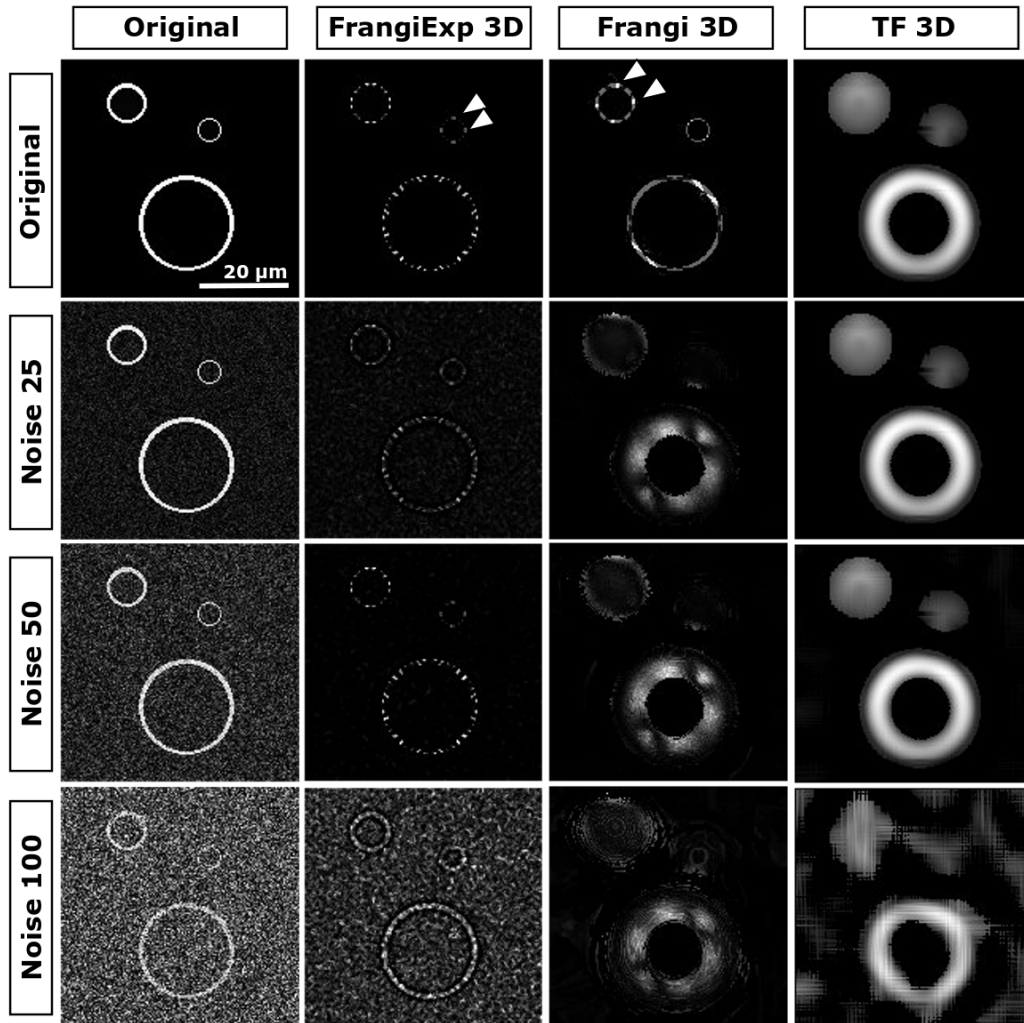


Figure 2.13: **Filter response - 3D application.** Frangi-based filters showed unsatisfactory enhancement of 3D cylinders, suggesting that 3D application was not suitable. Again, TF showed double-to-single peak conversion in smaller vessels and sensitivity against noise was low.

sensitivity was most pronounced for the Frangi Filter, while FrangiExp and TF were less influenced by the addition of simulated Gaussian noise.

(d) Filter response - variable model configurations

Based on the above findings and the fact that vessel enhancement filters were designed for MRI images, which show a single-peak intensity distribution, there was the rationale to examine whether the original hollow circle and tube models (ie. shape/intensity distribution) would impact the filter outcome. Thus, the filter responses from 3D hollow cylinders were further compared to filled cylinders and cylinders with Gaussian blurred edges. The latter was assumed to be the most comparable to actual MRI data.

Enhancement via TF was similarly effective for the three different model configurations (Fig. 2.14A).

In the case of filled cylinders, both Frangi enhancement methods seemed to enhance vascular edges (Fig. 2.14B,C). FrangiExp did not enhance central "vascular" information at all, whilst the Frangi filter enhanced edges, but the originally filled tube was returned with a diagonal signal-dampening and fuzzy edges.

Studying the filter outcome after Gaussian blurring of filled tubes, FrangiExp now enhanced the "lumen", but the overall shape was skewed towards an ellipsoidal rather than the original shape. Again, the Frangi filter returned diagonal signal reduction, but fuzzy edges were observed to be improved. This is of particular interest as the Frangi filter was developed for MRI images, which actually do show this type of cross-sectional intensity profile. These findings suggest that both of the Frangi filter are not working correctly, as the Frangi filter has been used widely to enhance MRI images with a Gaussian vessel cross section. Due to time constraints, this lack of expected performance was not further examined, but should be examined in future research work.

Interestingly, all three filters delivered a signal dip in middle for the filled cylinder scenario in the bigger tubes, which was counter-intuitive to the theoretical framework and further examination is needed.

Despite the disappointing performance of the Frangi filters, TF delivered promising results and will be explored further, while Frangi filters were excluded from further examination in the scope of this project.

(e) CNR changes upon Tubular Filtering (TF)

To understand the impact of TF on CNR in our zebrafish vasculature data, CNR was quantified before and after enhancement. An increase of CNR was found upon enhancement (Fig. 2.15; p 0.0051; $n=12$; 3dpf; 2 experimental repeats; paired Student's t-test; scale $10\mu\text{m}$), with maximum CNR fold-changes of 106.

This suggested that TF was applicable to enhance vascular signal in our data.

(f) Tubular filter response - enhancement in vessels of different diameter

While human cranial vessels include diameters of μm -cm most cranial vessels of the developing zebrafish vasculature during the investigated time-frame are of a similar size (approx. $7\text{-}10\mu\text{m}$; maximum $20\mu\text{m}$; Fig. 2.5B). Here, we wanted to examine how cross-sectional intensity distribution would be influenced, in vessels of different size, when enhancement is performed at different scales (sigma μm).

To take a quantitative approach, it was first examined whether FWHM (Fig. 2.16A) from cross-sectional intensity profiles of vessels would provide a reasonable estimate of vessel diameters. Thus, vessel diameters of the selected vessels were quantified manually using line

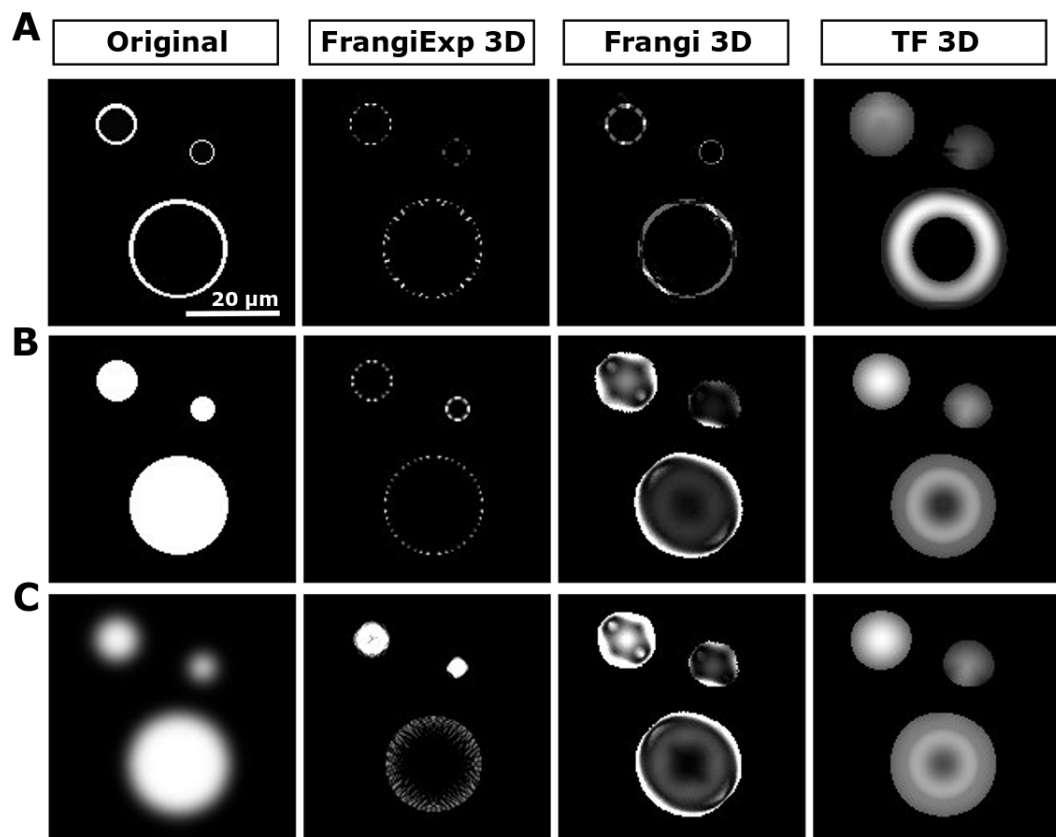


Figure 2.14: **Filter response - distinctive model outset.** Examining filter responses for 3D hollow cylinders, filled cylinders, and cylinders with blurred edges.

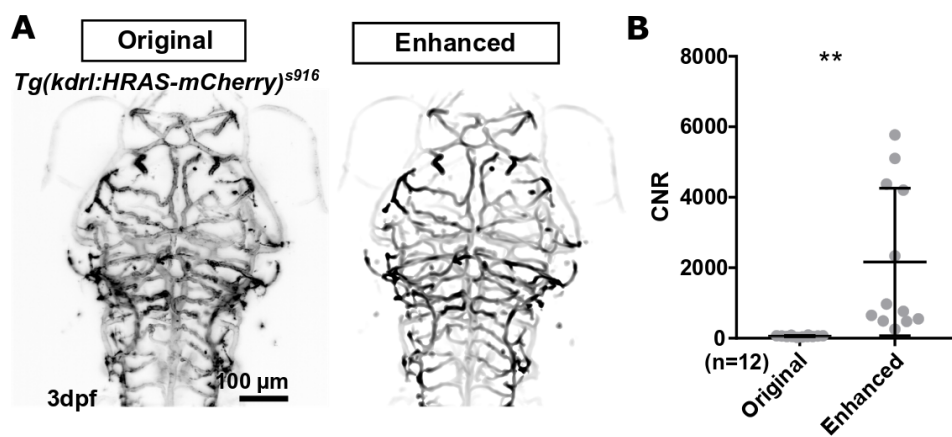


Figure 2.15: **CNR is increased by TF.** CNR quantification in original and enhanced images (A) showed an increase (B; p 0.0051; $n=12$ 3dpf embryos; 2 experimental repeats; paired Student's t-test).

ROIs spanning from edge-edge across the vessel cross-section (referred to as *manual*) and the FWHM from intensity profiles of the same vessels quantified (referred to as *FWHM*; Fig. 2.16B). If successful, this would enable FWHM to be used as a proxy for vessel diameter, meaning that laborious manual measurements could be avoided.

The studied vessels were the central artery (CtA) with a diameter of $8.154 \pm 1.274 \mu\text{m}$, MMCTA with a diameter of $9.779 \pm 2.097 \mu\text{m}$, PMBC with a diameter of $11.14 \pm 1.682 \mu\text{m}$, and the BA with a diameter of $22.28 \pm 3.886 \mu\text{m}$ (Fig. 2.16B; n=12 3dpf larvae).

No difference between manual and FWHM measurements were found (Fig. 2.16B; CtA $p > 0.9999$, MMCTA $p > 0.9999$, PMBC $p > 0.9999$, BA $p = 0.9879$; n=12; 3dpf; 2 experimental repeats). The Pearson Correlation between manual and FWHM measurements was low with CtA R 0.630, MMCTA R 0.806, PMBC R 0.675 and BA R 0.238; while the mean absolute voxel error was: CtA 4.38, MMCTA 2.75, PMBC 4.09, and BA 11.60 (voxel; Fig. 2.16C). We anticipate that the encountered differences were mainly due to human error during manual measurements as well as outliers in the FWHM measurements (black arrowheads). These outliers were caused by a left/right skewed intensity distribution, where one side of a double peak distribution was excessively large. We believe that these outliers could be minimised by averaging multiple diameter measurements at different orientations to the vessel. Together, this suggested that the FWHM can be used as a measure of vascular diameter, provided that the effect of outliers has been considered.

Cross-sectional intensity distributions of vessels were measured before and after application of the Sato filter (tubeness filter; TF) at scales from $5.3424 \mu\text{m}$ (16 voxels) to $30.718 \mu\text{m}$ (92 voxels). Plotting the original intensity distribution, a double-peak intensity distribution was observed in all four investigated vessels to a varying degree (Fig. 2.17A,C,E,G: black line; n=12 embryos).

In vessels with a smaller diameter (CtA, MMCTA, and PMBC), filter application started to change double- to single-peak intensity distributions at a scale size of 8.0232 (24 pixels; Fig. 2.17A,C,E). This was particularly of interest as most vessels in the cranial zebrafish vasculature were expected to have a double-peak intensity distribution when lumenized, while smaller/unperfused vessels would have a single-peak distribution. Thus, conversion of double-to-single-peaks, or at least sufficient enhancement of the luminal signal, should allow for a subsequent segmentation approach which can address both types of vessels with equal effectiveness.

Visually, the scale sizes 10.6848 and 15.359 returned the most accurate appearing enhancement results with vessels being returned as tubes (rather than vessel walls

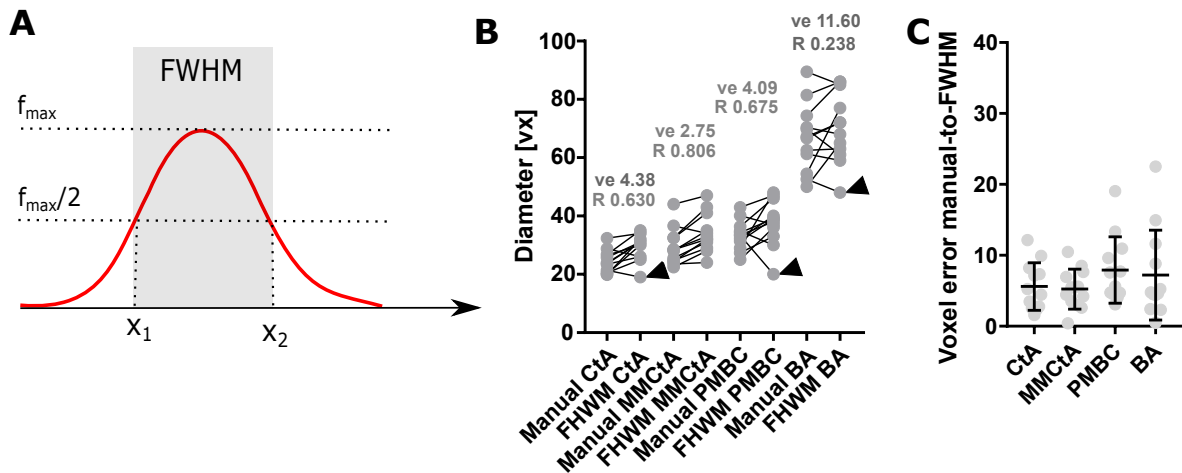


Figure 2.16: **FWHM is applicable to estimate vessel width.** (A) FWHM was used to measure vascular diameter. (B) Comparing manual diameter measurements with the FWHM obtained from the cross-sectional intensity profiles showed no difference (CtA $p > 0.9999$, MMcTA $p > 0.9999$, PMBC $p > 0.9999$, and BA $p = 0.9879$), but Pearson Correlation was rather low (CtA $R = 0.630$, MMcTA $R = 0.806$, PMBC $R = 0.675$, and BA $R = 0.238$; $n = 12$; 3dpf; 2 experimental repeats). This was assumed to be caused by error in manual measurements and outliers in the FWHM data. (C) Absolute values of voxel error between manual and FWHM measurements ($n = 12$; 3dpf; 2 experimental repeats). (B reproduced with permission from [4] under licence 4764790544144) Abbreviations: f - function, FWHM - full width half maximum, R - Pearson correlation, ve - voxel error;

individually being enhanced) and vessel thickness being comparable to the original (rather than artificially reduced or increased). To examine this further, the scale parameter that gives rise to the highest correlation between manual measurement and FWHM post enhancement, double-to-single peak conversion, and voxel error were visually and quantitatively examined (Fig. 2.17B,D,F,H; table 2.1; table 2.2). This showed that enhancement with the scale parameter smaller than the vessels diameter lead to an underestimation of the vessel diameter, while scale parameters bigger than the vessel of interest would lead to an artificial overestimation. As $10.6848\mu\text{m}$ (32 voxels) was sufficient to obtain a single-peak distribution in the majority of standard-sized cranial vessels without artificially broadening of smaller vessels, this was the focus in the rest of this thesis.

Further examination of the BA intensity profiles showed that larger scales (e.g. 23.718) would be required to convert the double- to a single-peak distribution (Fig. 2.17G) and deliver the most accurate vessel diameter measurements (Fig. 2.17H); but for the BA no artificial underestimation of vessel diameter was encountered when enhanced at smaller scales, so luminal enhancement must've been sufficient at the smaller scale. Again, this would be in the size range of the vessel of interest, but far larger than most vessels of interest. As the BA is the

Table 2.1: This table shows the Sato enhancement scale with the highest correlation of manual measurements to vessel diameters after enhancement (top row) and the enhancement scale when double-to-single peak conversions happened (bottom row) for the CtA, MMcTA and PMBC.

	CtA	MMcTA	PMBC	BA
Scale of Highest Correlation Manual-to-FWHM	9.3604	15.369	10.6848	9.3604
Double-to-Single Peak Conversion	8.0232	9.3604	10.6848	23.718

Table 2.2: Absolute voxel error after TF (lowest values highlighted in bold).

	CtA	MMcTA	PMBC	BA
Manual-FWHM	4.39 ± 3.92	2.7 ± 2.4	4.10 ± 4.53	11.60 ± 12.66
Manual-5.3424	5.81 ± 4.49	6.3 ± 7.0	10.19 ± 10.40	8.86 ± 7.32
Manual-8.0232	3.84 ± 1.96	4.9 ± 4.6	5.48 ± 6.30	5.98 ± 6.39
Manual-9.3604	3.07 ± 2.03	3.8 ± 3.2	5.49 ± 4.23	5.90 ± 6.25
Manual-10.6848	3.37 ± 2.19	2.7 ± 2.2	4.50 ± 4.17	7.23 ± 6.33
Manual-15.359	5.25 ± 2.89	3.8 ± 1.6	9.07 ± 15.91	7.98 ± 7.23
Manual-23.0385	25.83 ± 27.80	13.5 ± 8.0	19.63 ± 16.43	9.08 ± 6.37
Manual-30.718	36.68 ± 27.52	15.7 ± 11.8	27.30 ± 14.40	8.70 ± 4.67

largest cranial vessel at this time-point and also one of the most anatomically similar vessels between samples (see Chapter 3) one could argue that the vessels bifurcating from the BA (posterior communicating segment (PCS)) could be used as a starting point rather than the BA itself to examine the dorsal cerebral vasculature.

2.3.4 Segmentation of the cerebral vasculature

Comparison of segmentation method outcomes

Based on the above proposed image pre-processing steps, the following image segmentation methods (already implemented in Fiji [127]) were studied for their efficiency to discriminate vascular from non-vascular tissue.

First, different intensity-based thresholding methods were tested [127]. Comparing the original image to segmentation outcomes, Otsu thresholding [268] delivered the most accurate segmentation result (Fig. 2.18, only subset of thresholding methods shown).

Next, more advanced segmentation methods after application of the General Filter (GF) (Median and Rolling Ball) and Tubeness Filter (TF) were compared. Again, intensity-based thresholding based on Otsu to deliver the most accurate segmentation results (Fig. 2.19A,B).

K-means clustering delivered locally variable segmentation results, with some regions being well segmented, while others were not segmented at all (Fig. 2.19A,B red asterisk) [127, 259]. Thus, k-means clustering was not investigated further to avoid underestimation bias.

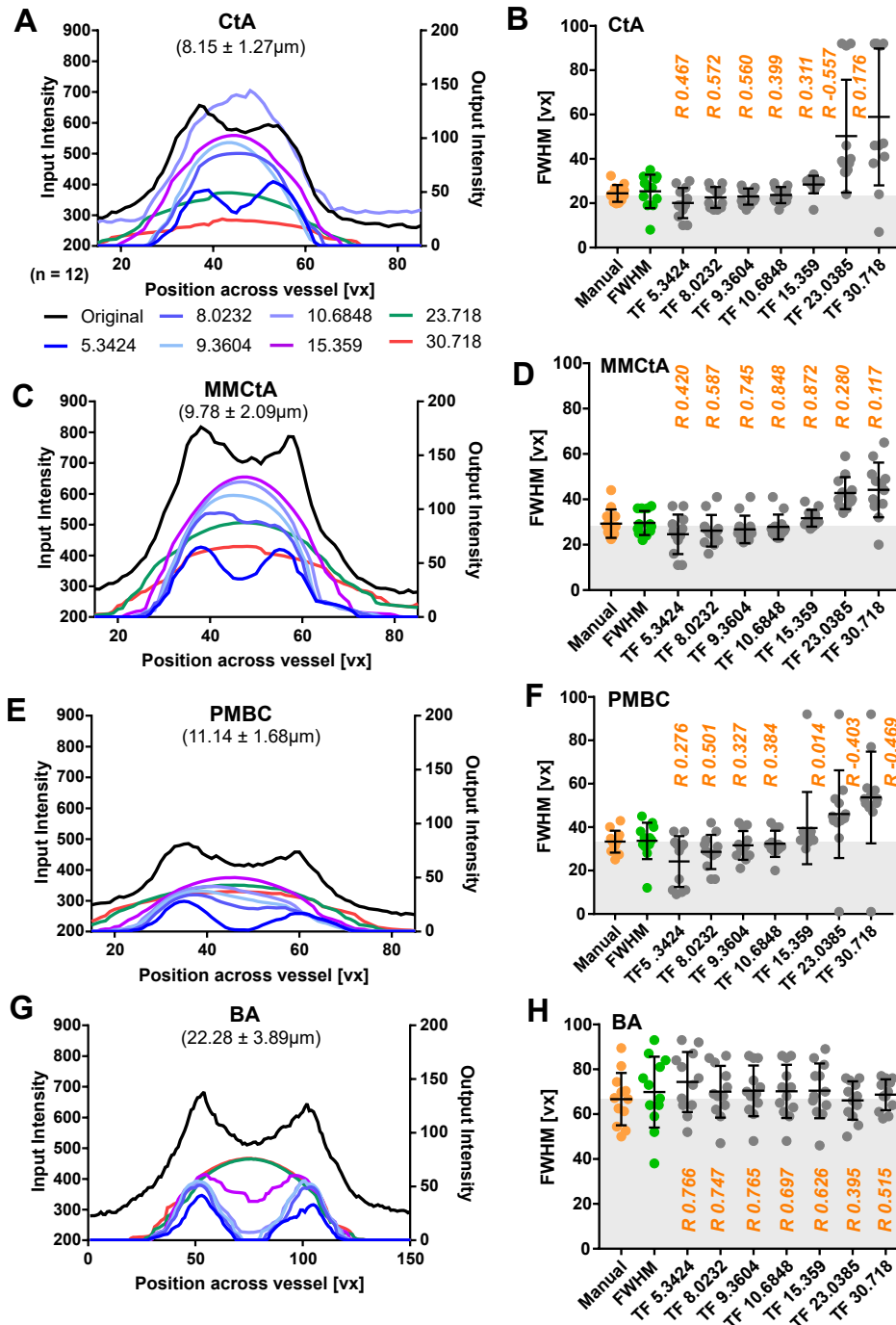


Figure 2.17: **Assessment of cross-sectional intensity distribution and FWHM after enhancement.** The impact of filtering size on the intensity distribution of vessel cross-sections was measured in four dorsal cranial vessels of different diameters, namely the CtA (A; $8.154 \pm 1.274 \mu\text{m}$), MMcTA (C; $9.779 \pm 2.097 \mu\text{m}$), PMBC (E; $11.14 \pm 1.682 \mu\text{m}$) and BA (G; $22.28 \pm 3.886 \mu\text{m}$; lines represent the average value of $n=12$ 3dpf *Tg(kdrl:HRAS-mCherry)^{S916}* larvae; 2 experimental repeats; graph C reproduced under CC licence from [2]). Double-peak intensity distributions were converted to single-peaks when the enhancement filter scale was approximately at the size of the vessel of interest. Measuring the FWHM of the respective vessels (B,D,F,H) also showed that enhancement at the scale of the vessels of interest delivered the most accurate results, while too small scale parameters resulted in underestimations and too big led to artificial overestimations.

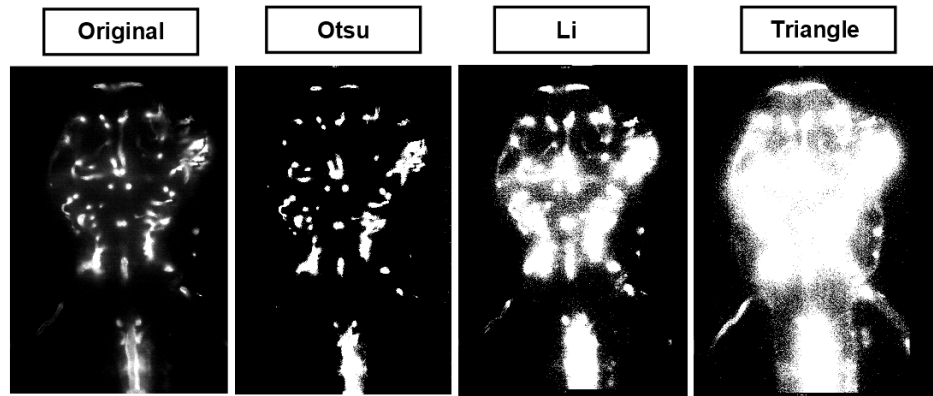


Figure 2.18: **Comparison of different thresholding methods shows Otsu thresholding to be the most applicable to our data.** Testing different thresholding approaches, Otsu thresholding delivered the most robust and reliable results in comparison to other thresholding methods, all of which are readily implemented in the Auto Threshold Plugin in Fiji [127] (only subset shown; Otsu based on [268]; Li based on [269, 270]; Triangle based on [271]).

The default implementations of level set (fast marching implementation in Fiji software [127]) [170] and statistical region merging [262, 263] did not perform well with our data. Thus, these methods need further investigation in future to examine implementation specificities, applicability, parameter settings, and constraints (Fig. 2.19).

Having found that intensity-based segmentation using Otsu-thresholding [268] is globally the most applicable to our data, it was investigated how the proposed pre-processing methods (GF and TF) would impact segmentation.

Visual inspection of delivered segmentation results (Fig. 2.20C,F) showed that segmentation subsequent to TF delivered consistently more reliable results than after GF. This judgement was based on the following criteria:

- individual vessel distinction (especially at vascular loops; Fig. 2.20 magenta arrowhead)
- enhancement of dimmer vessels (eg. PMBC and dorsal ciliary vein (DCV), Fig. 2.20 green arrowhead)
- handling of vascular single- and double-peak intensity (Fig. 2.20 blue arrowhead)

While a variety of sophisticated segmentation methods have been successfully applied in the medical field (such as level set), readily available implementations of these did not translate well when applied to segmentation of the zebrafish cranial vasculature. We believe this was due to the following reasons:

- Most vessel segmentation methods applied in the medical field are optimized for central peak/valley intensities; but most vessels in transgenic zebrafish showed cross-sectional

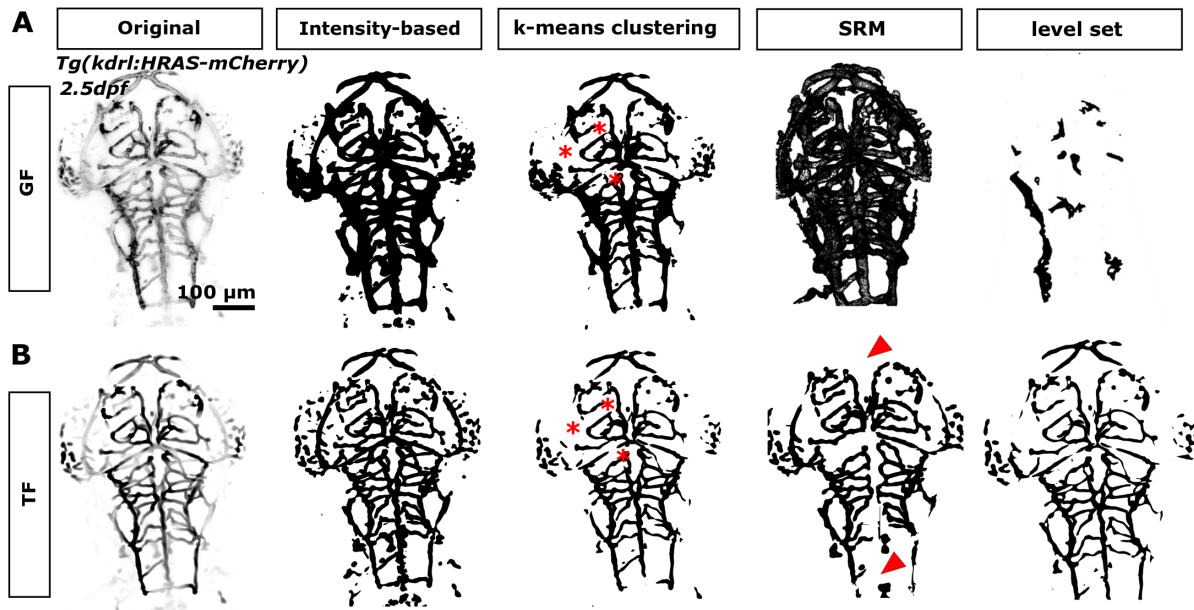


Figure 2.19: **Comparing different segmentation approaches shows Otsu thresholding to be the most applicable to our data.** Comparing different segmentation methods after GF (**A**, Median and Rolling Ball) and TF (**B**) showed that most approaches applicable in the medical field are not directly transferable to fluorescence microscopy images (representative images). Intensity-based thresholding delivered the best segmentation upon visual inspection. K-means clustering delivered reasonable segmentation outputs locally, but low-intensity vessels were often underestimated (red asterisks). Statistical Region Merging (SRM) consistently delivered under- or over-segmentation after either filtering method. Similarly, level set segmentation (Fast Marching implementation) was found to be not directly applicable without further parameter fine-tuning to fluorescence microscopy images (inverted MIPs; representative images; reproduced under CC licence from [2]).

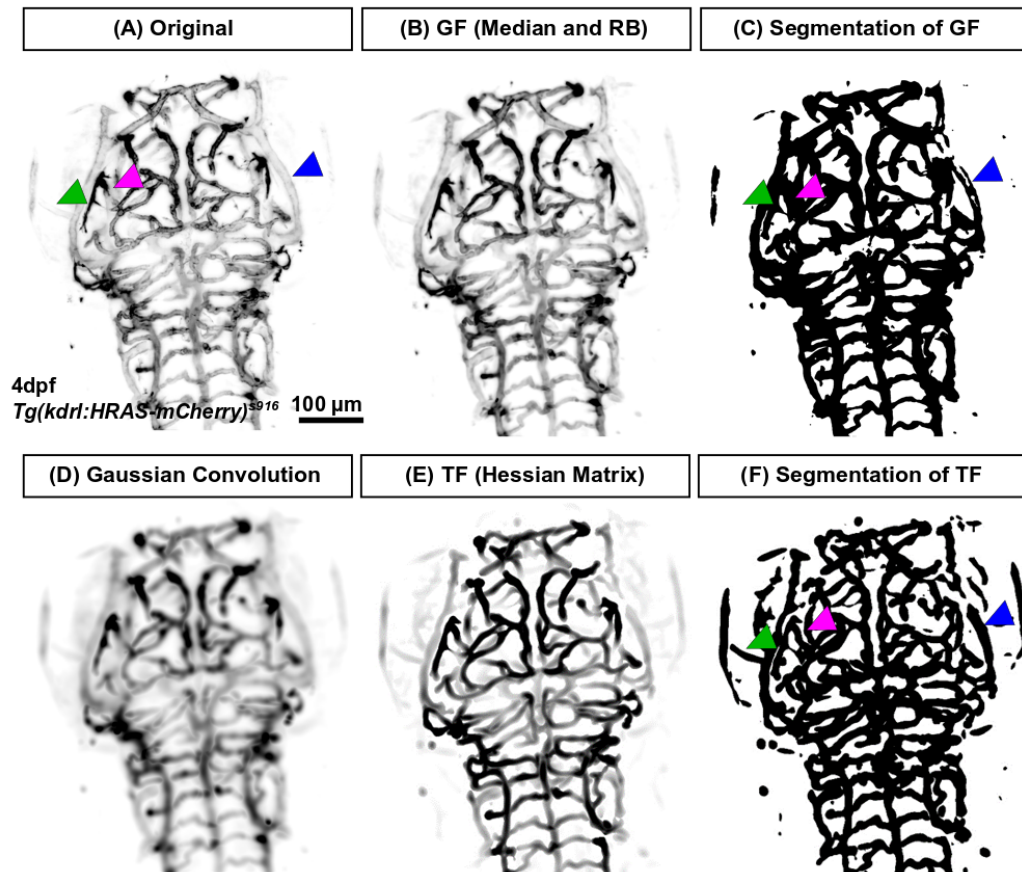


Figure 2.20: **Intensity-based segmentation outcomes after GF and TF.** Vascular segmentation of original images (A) was compared after pre-processing with GF (B) and TF (E) (relying on Gaussian Convolution (D) with user-specified scale size), delivering binarized images (C) and (F), respectively. Segmentation after TF enhanced dim vessels (green arrowhead), resolve complex structures (magenta arrowhead) and overcome double-peak intensity distributions (blue arrowhead) more reliably than GF (representative images; 4dpf *Tg(kdrl:HRAS-mCherry)^{s916}*; inverted MIPs).

double-peak intensity distributions due to visualization of ECs in reporter lines. These cross-sectional intensity distributions may differ in images acquired with other microscopy setups (eg. confocal microscope); but it was decided against further comparisons due to two reasons **(i)** LSFM is a state-of-the art microscopy method, which is becoming more widely adapted due to commercially available setups, **(ii)** LSFM allows for a deeper tissue penetration depth, which allowed the analysis of the total cranial vasculature, rather than superficial vascular segments.

- Data properties differ between LSFM and MRI or CT. This is important, not just in terms of resolution (voxel size of $0.3 \times 0.3 \times 0.5 \mu\text{m}$ vs. $1 \times 1 \times 1 \text{mm}$, respectively), but also regarding to input requirements and computational cost. Additionally, some analysis methods assume voxel isotropy, which is not fulfilled in our datasets.
- The actual size of vessels is different in data obtained from human and zebrafish. Also, the human vasculature is a vascular tree with vessel sizes over a broad scale (μm -cm), while the zebrafish vasculature is an enclosed system with lower size variation (μm). Thus, local vascular density may differ and vascular loops are special challenges distinct from conventional medical applications.
- Intensity variability in MRI images is considered to be lower, as a homogeneous distribution of contrast medium in perfused vessels is assumed.
- Data from different transgenic reporter lines are often not directly comparable, as not just the transgenic reporter line characteristics, but also image acquisition settings can influence data properties directly. Herein, the focus was mainly on the globally most widely used transgenic reporter lines *Tg(kdrl:HRAS-mCherry)^{S916}* [243, 244] and *Tg(fli1a:eGFP)^{y1}* [74]. Application to other transgenic lines may, therefore, require further optimization or investigation.

Comparing Sato vessel (TF) enhancement vessel width to segmented (TH) vessel width

As vascular enhancement influenced vessel width measurements based on filter scale (Fig. 2.17), it was next examined how this would translate into vessel width measurements after segmentation (TH).

Very similar results were found in the data before segmentation (Fig. 2.21), which was confirmed by high correlations between enhancement and segmentation data (Table 2.3), while minimal voxel error assessment showed other scale parameters to be optimal (Table 2.4). Together, this suggested that a combination of diameter measurements and visual assessment are the most appropriate for scale parameter selection.

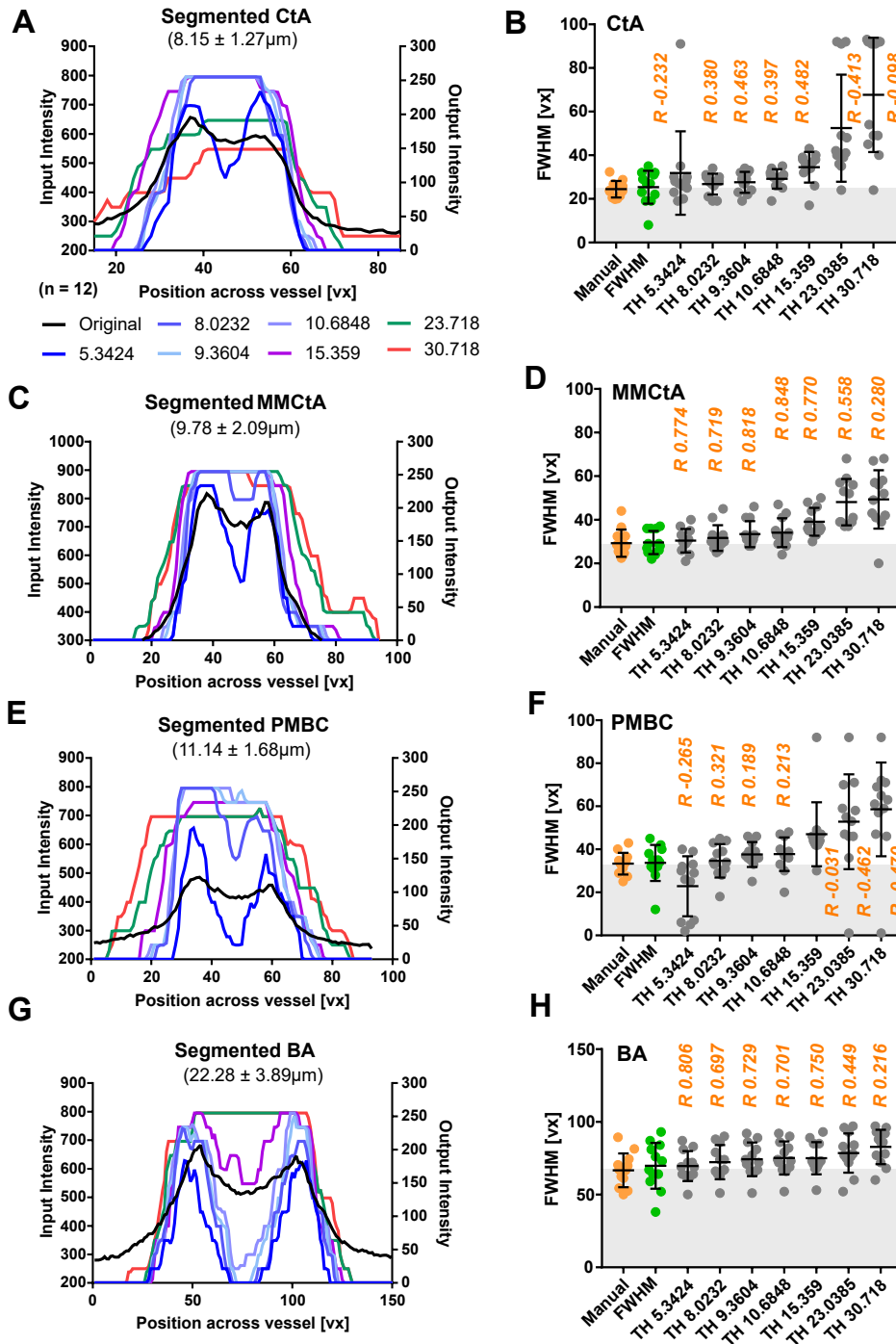


Figure 2.21: **Cross-sectional intensity and vessel width after enhancement at increasing scales and segmentation.** Impact of enhancement scale prior to segmentation in the CtA (A), MMcTA (C), PMBC (E) and BA (G) (lines represent the average value of $n=12$ 3dpf *Tg(kdr1:HRAS-mCherry)^{S916}* larvae; 2 experimental repeats). Measuring vessel width after TF and TH showed highest correlation of vessel width with manual measurements when filter scale was in the range of vessel size (B,D,F) - except for the BA (H).

Table 2.3: This table shows the enhancement scale parameter that results in the highest correlation between manual measurements and vessel diameters after segmentation (top row) and the scale when the highest correlation of diameters between TF and segmented was observed (bottom row) for the CtA, MMCTA and PMBC.

	CtA	MMCTA	PMBC	BA
Scale of Highest Correlation Manual-to-vessel width	9.3604	10.6848	10.6848	15.359
Correlation vessel width of TF to TH at 10.6848	0.878	0.894	0.940	0.973

Table 2.4: Absolute voxel error after TF and TH (lowest values highlighted in bold).

	CtA	MMCTA	PMBC	BA
Manual-FWHM	4.39 ± 3.92	2.75 ± 2.40	4.10 ± 4.53	11.60 ± 12.66
Manual-5.3424	9.74 ± 19.28	3.66 ± 1.69	13.74 ± 13.10	5.12 ± 5.40
Manual-8.0232	4.33 ± 3.00	4.41 ± 2.44	6.07 ± 4.72	8.00 ± 6.88
Manual-9.3604	4.22 ± 3.48	5.07 ± 2.08	6.59 ± 4.46	8.39 ± 7.66
Manual-10.6848	5.60 ± 3.35	5.24 ± 2.81	7.92 ± 4.68	9.14 ± 8.14
Manual-15.359	10.81 ± 4.63	9.80 ± 4.30	14.43 ± 15.10	9.03 ± 7.14
Manual-23.0385	28.00 ± 6.32	18.80 ± 8.82	26.46 ± 16.17	15.01 ± 9.24
Manual-30.718	43.25 ± 26.89	20.85 ± 11.68	32.21 ± 12.90	19.08 ± 9.93

2.3.5 Assessment of segmentation sensitivity and robustness

As no phantom models are available for the zebrafish vasculature, and manual segmentation was too laborious (due to vessel number and image size), segmentation after GF and TF using Otsu thresholding was compared using visual assessment, the CoV within sample groups, and segmentation robustness on different data sets as readouts.

Segmentation is robust against changing CNR levels

Image acquisition with decreasing laser power (1.2%, 0.8%, and 0.4%) lead to a controlled CNR decrease in the BA from 47.59 ± 21.04 at 1.2%, 17.73 ± 7.73 at 0.8% to 7.99 ± 3.30 at 0.4%.

The extraction of the total cranial vascular volume (Fig. 2.3), subsequent to pre-processing and segmentation, suggested a high segmentation robustness with both pre-processing methods over a broad range of noise-levels (CoV of GF 7.68% and TF 6.43%, between laser power (LP) 1.2% and 0.4%, respectively). This implied the applicability of the segmentation pipeline to a wide range of image qualities (Fig. 2.22A).

Segmentation after GF delivered increasing vascular volume measurements with decreasing CNR (LP 1.2% $0.002600 \pm 0.000488 \text{ mm}^3$; LP 0.4% $0.002915 \pm 0.000512 \text{ mm}^3$), whilst extraction of volume with TF prior to segmentation returned a reduction in volume with CNR decrease (LP 1.2% $0.002580 \pm 0.000201 \text{ mm}^3$; LP 0.4% $0.002482 \pm 0.0002269 \text{ mm}^3$)

(GF p 0.3248; TF p 0.9981; n=10; 4dpf; 2 experimental repeats; One-Way ANOVA).

To investigate the reason for vascular volume differences upon decreasing CNR levels (Fig. 2.22B) in segmented images pre-processed with either GF or TF, images were visually compared. Decreasing laser power, therefore CNR, enabled the segmentation of anatomically deeper vessels after GF (eg. MMCTa and BA; Fig. 2.22B red arrowheads), which may be explained by overall equalization of intensity. While signal loss resulted in loss of segmented vessels with TF (eg. prosencephalic artery (PrA) or DCV; Fig. 2.22C red arrowheads).

Segmentation in a double-transgenic line shows that TF delivers better segmentation outcomes than GF

Due to the different CNR levels and transgenic reporter expression in different transgenic lines (Fig. 2.4), we examined whether our suggested segmentation approach was applicable to a double-transgenic such as *Tg(kdrl:HRAS-mCherry)^{s916}*, *Tg(fli1a:eGFP)^{y1}* [74, 244].

The transgenic *Tg(kdrl:HRAS-mCherry)^{s916}* has higher CNR levels and is more specific to the vasculature than *Tg(fli1a:eGFP)^{y1}* (Fig. 2.23A, eye and otic vesicle (OV) are pan-endothelial expression and were excluded via ROI selection). Thus, it is more challenging to extract vascular signal in *Tg(fli1a:eGFP)^{y1}* and the assumption would be that more vasculature would be extracted due to the pan-endothelial expression of fluorophores driven by the *fli1a* promoter.

Segmentation was performed individually for each transgenic reporters, vascular volumes quantified, and images merged for representation following GF and TF (Fig. 2.23B,C).

The cranial vascular volume was extracted as the primary quantitative segmentation readout. The extraction of vascular volume in *Tg(kdrl:HRAS-mCherry)^{s916}* (*kdrl*) was not different after GF or TF and subsequent segmentation via Otsu thresholding (p>0.9999; Fig. 2.23D; n=21; 4dpf; 2 experimental repeats; Kruskal-Wallis test).

The vascular volume in *Tg(fli1a:eGFP)^{y1}* (*fli1a*) was highly variable after GF with a CoV of 35.97%; while the CoV after TF was 17.28%.

The vascular volume was different between "*GF kdrl*" and "*GF fli1a*" (p<0.0001), while the difference was less pronounced comparing "*TF kdrl*" to "*TF fli1a*" (p 0.0088).

Based on the high CoV in "*GF fli1a*" and the fact that the average total cranial vascular volume in "*GF fli1a*" was 2.14 times the volume of "*GF kdrl*" ("*TF fli1a*" was 1.3 times the volume of "*TF kdrl*"), it was anticipated that TF delivered a more robust and biologically relevant output.

Together, these data showed that TF and Otsu thresholding are suitable to extract the zebrafish cerebral vasculature in both transgenic lines, and that TF-based enhancement

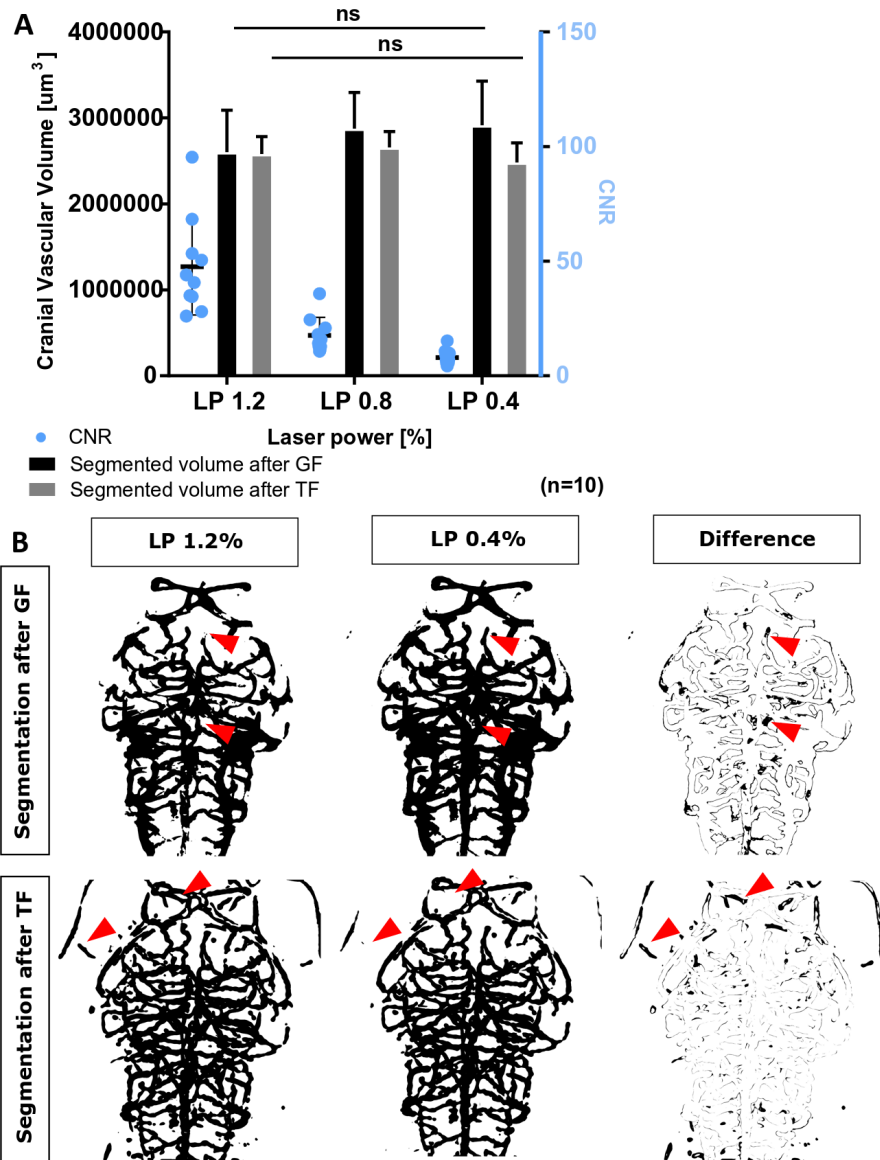


Figure 2.22: **Segmentation is robust against noise.** (A) Segmentation robustness was evaluated by total cranial vascular volume measurements (left Y-axis) in images with decreasing CNR levels (blue; right Y-axis), which was achieved via decrease of laser power (LP) from 1.2% over 0.8% to 0.4% (X-axis) during image acquisition. This implied that segmentation post GF (black bars) or TF (grey bar) would be applicable to a range of image qualities ($n=10$; 4dpf; 2 experimental repeats; One-Way ANOVA). (B) Visual assessment of differences in vascular segmentation after GF seemed to enhance deeper structures at lower CNR levels (eg. MMcTA or BA, red arrows). (C) Segmentation after TF seemed to be more directly reliant on CNR levels, leading to loss of dimmer vessels in images with decreased CNR (eg. PrA or DCV; red arrowhead; representative images; inverted MIPs; (A) reproduced with permission from [4] under licence 4764790544144).

delivered better segmentation than GF.

Segmentation in pre- and post-exsanguinated samples shows that TF delivers better segmentation outcomes than GF

Exsanguination of embryos by mechanical opening of the heart resulted in a decrease of the total cranial vascular volume upon visual inspection (Fig. 2.24A).

This dataset was therefore examined to evaluate whether the proposed segmentation workflow (GF or TF with following Otsu thresholding) would detect changes of total vascular volume pre- and post-exsanguination.

After GF and segmentation, high CoVs were found in the total vascular volume in control (38.26%) and exsanguinated (26.28%) samples. This variation was lower after TF in control (10.22%) and exsanguinated (9.65%) samples. Volume comparison pre- and post-exsanguination after GF was not different ($p = 0.2596$; Fig. 2.24B; average control: 0.00227 mm^3 , average exsanguinated: 0.002093 mm^3 ; $n=16$; 4dpf; 2 experimental repeats; paired Student's t-test), while volume obtained after TF was decreased ($p < 0.0001$; Fig. 2.24C; average control: 0.002107 mm^3 , average exsanguinated: 0.00184 mm^3 ; $n=16$; 4dpf; 2 experimental repeats; paired Student's t-test).

As embryos were removed from the LSM acquisition setup for the exsanguination procedure, vessel CNR and stack intensity were quantified to test whether the procedure had an effect on the signal intensity. CNR in the BA (Fig. 2.24D) and the overall stack mean intensity (Fig. 2.24E), showed no difference between acquisitions ($p = 0.0876$ and $p = 0.2728$, respectively). This suggested that the detected volume differences were due to a true biological vascular volume reduction, rather than signal intensity differences caused by sample damage.

Together, these data suggested that TF with subsequent segmentation was able to detect true biological differences.

Vascular volume increases from 2-5dpf

Based on the above findings, a robust and sensitive extraction of the cranial vascular volume was demonstrated. Thus, image pre-processing and segmentation was applied to *Tg(kdrl:HRAS-mCherry^{S916})* embryos from 2-5dpf to measure changes of the vascular volume during early development.

Application of segmentation after GF showed an increase of the average vascular volume between 3-5dpf (Fig. 2.25A), with vascular volume at 2dpf higher than 3dpf ($p = 0.0065$; $n=10$ -

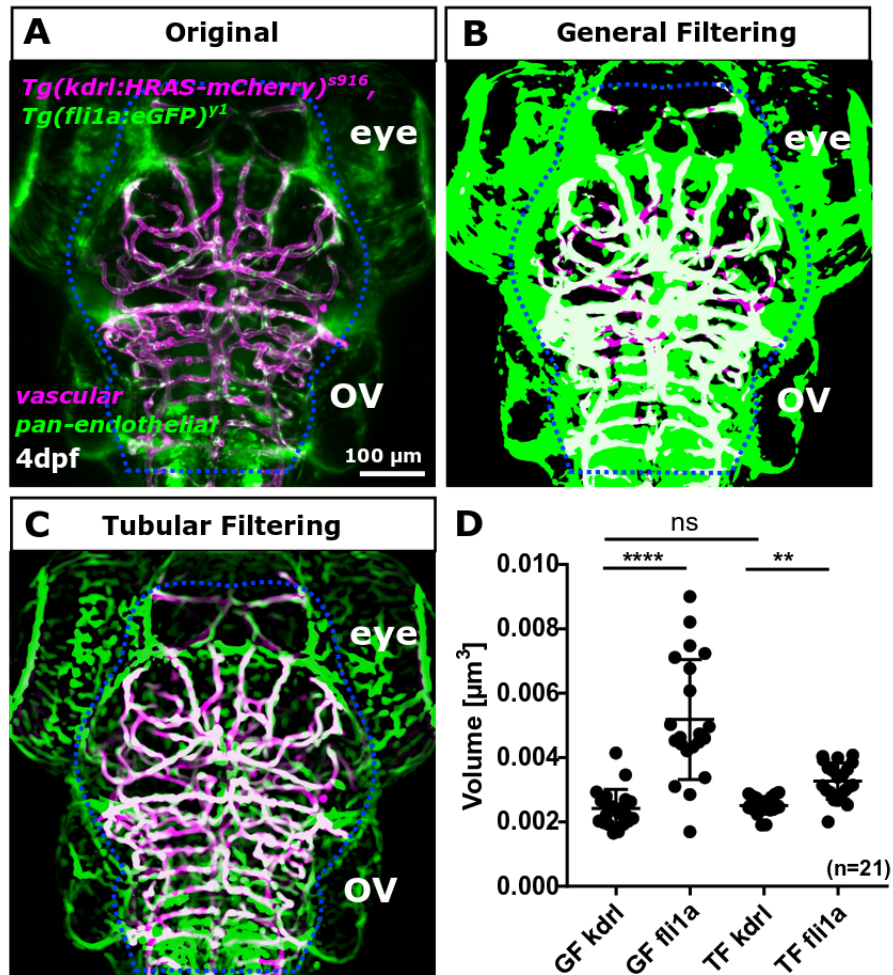


Figure 2.23: **Segmentation in a double-transgenic line shows TF to deliver better segmentation outcomes.** (A) To compare the segmentation sensitivity in transgenic lines with different CNR levels and expression patterns, the cranial vascular volume in a double-transgenic line after pre-processing, using general filtering (GF, (B)) or tubular filtering (TF, (C)) prior to intensity-based segmentation was extracted. (D) The vascular volume was extracted similarly well with both methods in the *Tg(kdrl:HRAS-mCherry)^{S916}* (*kdrl*; $p > 0.9999$). In *Tg(fli1a:eGFP)^{Y1}* the CoV was 35.97% after GF and 17.28% after TF. Both methods showed a difference when comparing the vascular volume in the *kdrl* and *fli1a* transgenics (GF $p < 0.0001$; TF $p = 0.0088$; $n = 21$; 4dpf; 2 experimental repeats; Kruskal-Wallis test; Quantification reproduced with permission from [4] under licence 4764790544144).

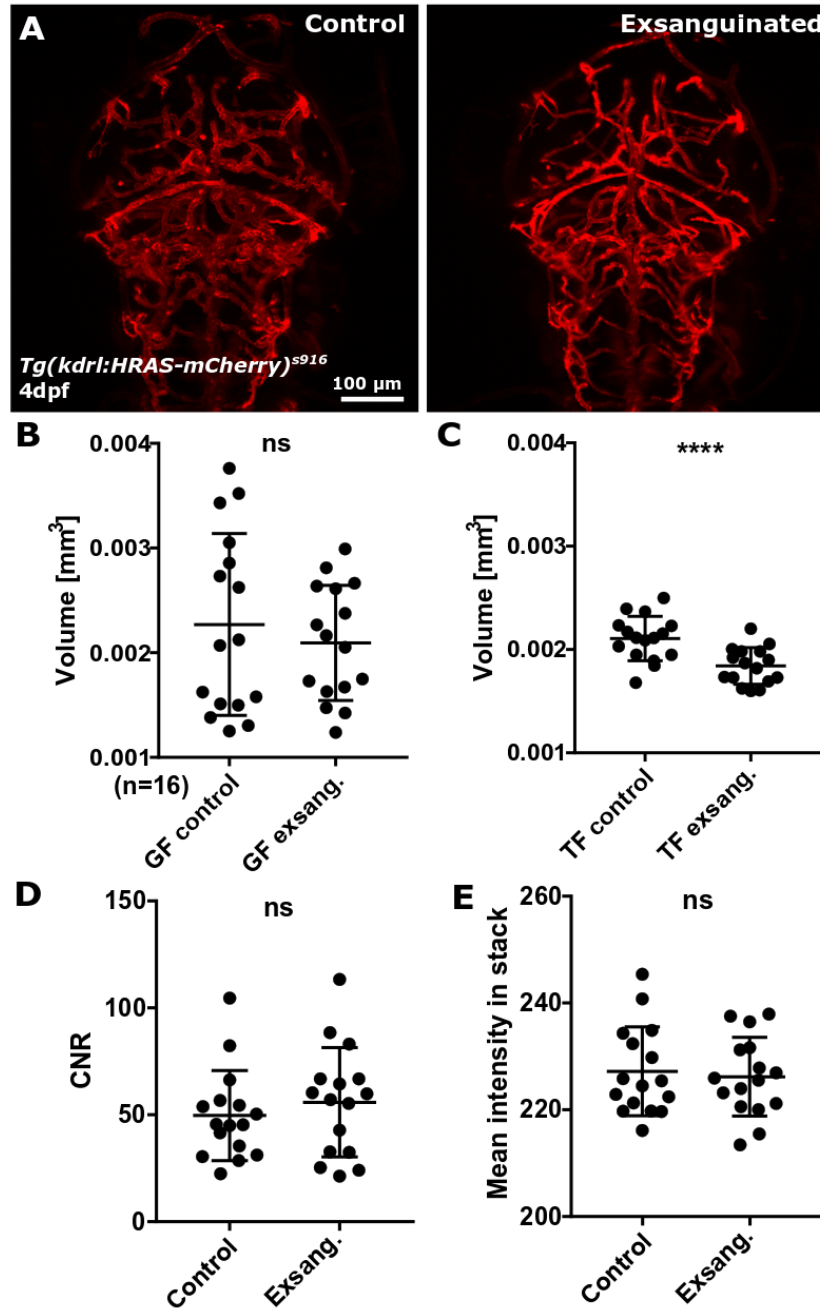


Figure 2.24: **Segmentation after exsanguination shows TF to deliver better segmentation outcomes.** (A) Pre-processing and segmentation were applied to embryos pre- and post-exsanguination to test whether the differences in the cranial vascular volume would be detected by our proposed analysis method. (B) The vascular volume showed no difference between control and exsanguinated embryos after GF and segmentation (p 0.2596; n= 16; 4dpf; 2 experimental repeats; paired Student's t-tests). (C) A vascular volume reduction was found after TF and segmentation (p<0.0001). (D,E) Neither CNR of the BA, nor the stack mean intensity were changed after the exsanguination procedure, which had required the disassembly of the image acquisition setup (n= 16; 4dpf; 2 experimental repeats; paired Student's t-tests). *Abbr.:* exsang. - exsanguinated; (B-C) reproduced with permission from [4] under licence 4764790544144.

15; 2 experimental repeats; One-Way ANOVA). An increase in the average vascular volume between 2-5dpf was also found after segmentation following TF (Fig. 2.25B).

Interestingly, both pre-processing methods resulted in a high CoV at 2dpf (GF 21.86% and TF 26.44%). Visual assessment suggested that this variation was likely to be caused by two main reasons. First, during embryonic development the head-to-trunk angle is lower in younger embryos [44]; resulting in the need to acquire a larger stack (z-axis) to allow imaging of the most anterior vessels. As the head-to-trunk angle and embedding of younger fish can be variable, this might lead to higher variability during image acquisition. Second, at earlier stages of development vessels are less defined and resemble more the structure of a vascular plexus rather than vessels with clearly distinguishable edges (Fig. 2.26 red arrowhead). Thus it is unclear whether the 2dpf vascular plexi are truly larger in vascular volume, or whether image acquisition and/or image processing led to an artificial volume increase.

Therefore, until this has been explored in more detail, 2dpf data from vascular volume difference calculations were excluded and applied One-Way ANOVA again to the acquired data (Fig. 2.25C,D). This showed that both, GF and TF, were able to detect the vascular volume increase from 3-5dpf with statistical significance (GF p 0.0009, Fig. 2.25C; TF p <0.0001, Fig. 2.25D). This suggests, both methods are sensitive enough to extract meaningful data during this developmental time-frame.

From 3-5dpf the CoV within age-groups was smaller after TF than GF (3dpf: GF 18.18% and TF 12.94%; 4dpf: GF 17.96% and TF 14.59%; 5dpf: GF 27.14% and TF 13.20%).

Examining the differences of pre-processing on segmentation (Fig. 2.26B-D) showed that dimmer vessels were consistently less likely to be detected after GF, whilst they were successfully extracted after TF (Fig. 2.26; blue arrowhead: inner optic circle (IOC); purple arrowhead: PMBC). Furthermore, while some vascular structures were not detected after GF, which would intuitively indicate a lower vascular volume than after TF, vessels also appeared to be less clearly discriminated and some vessels seemed to be thicker (Fig. 2.26D). Calculating the ratio of volume after GF to TF showed a higher vascular volume after GF (ratio GF to TF 2dpf: 1.73, 3dpf: 1.21, 4dpf: 1.19, 5dpf: 1.26).

Vascular volume is unchanged upon inhibition of Notch signalling

Notch inhibition was achieved by application of the γ -secretase inhibitor DAPT (12h 50 μ M; Fig. 2.27A). Measuring the distance between the left and right PMBC showed an decrease in growth upon DAPT treatment (p 0.0357; Fig. 2.27B; control $415.02 \pm 12.02 \mu\text{m}$, DAPT $406.9 \pm 13.37 \mu\text{m}$; $n=24$; 4dpf; 3 experimental repeats; unpaired Student's t-test). The mean

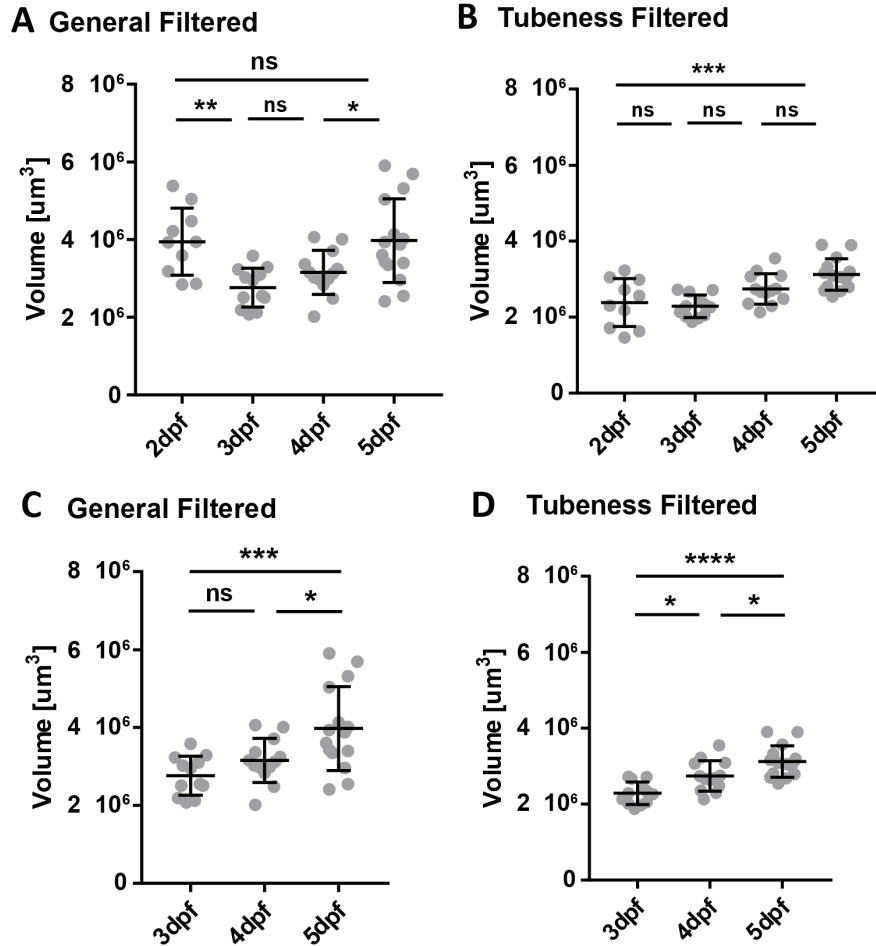


Figure 2.25: **Quantification of cranial vascular volume during early embryonic development.** (A) The total cranial vascular volume after GF was not changed from 2-5dpf (p 0.9998; 2-3dpf p 0.0065, 3-4dpf 0.6181, 4-5dpf p 0.0465). (B) An increase in the total cranial vascular volume was observed after TF (p 0.0008; 2-3dpf p 0.9577, 3-4dpf p 0.0596, 4-5dpf p 0.1150). (C) Comparing GF data from 3-5dpf showed an increase for the examined time-frame (p 0.0009; 3-4dpf p 0.436, 4-5dpf p 0.0243). (D) Comparing TF data from 3-5dpf showed an increase for the examined time-frame (p<0.0001; 3-4dpf p 0.436, 4-5dpf p 0.0243; all graphs: larvae 2dpf n=10; 3dpf n=12; 4dpf n=13; 5dpf n=15; 2 experimental repeats; One-Way ANOVA).

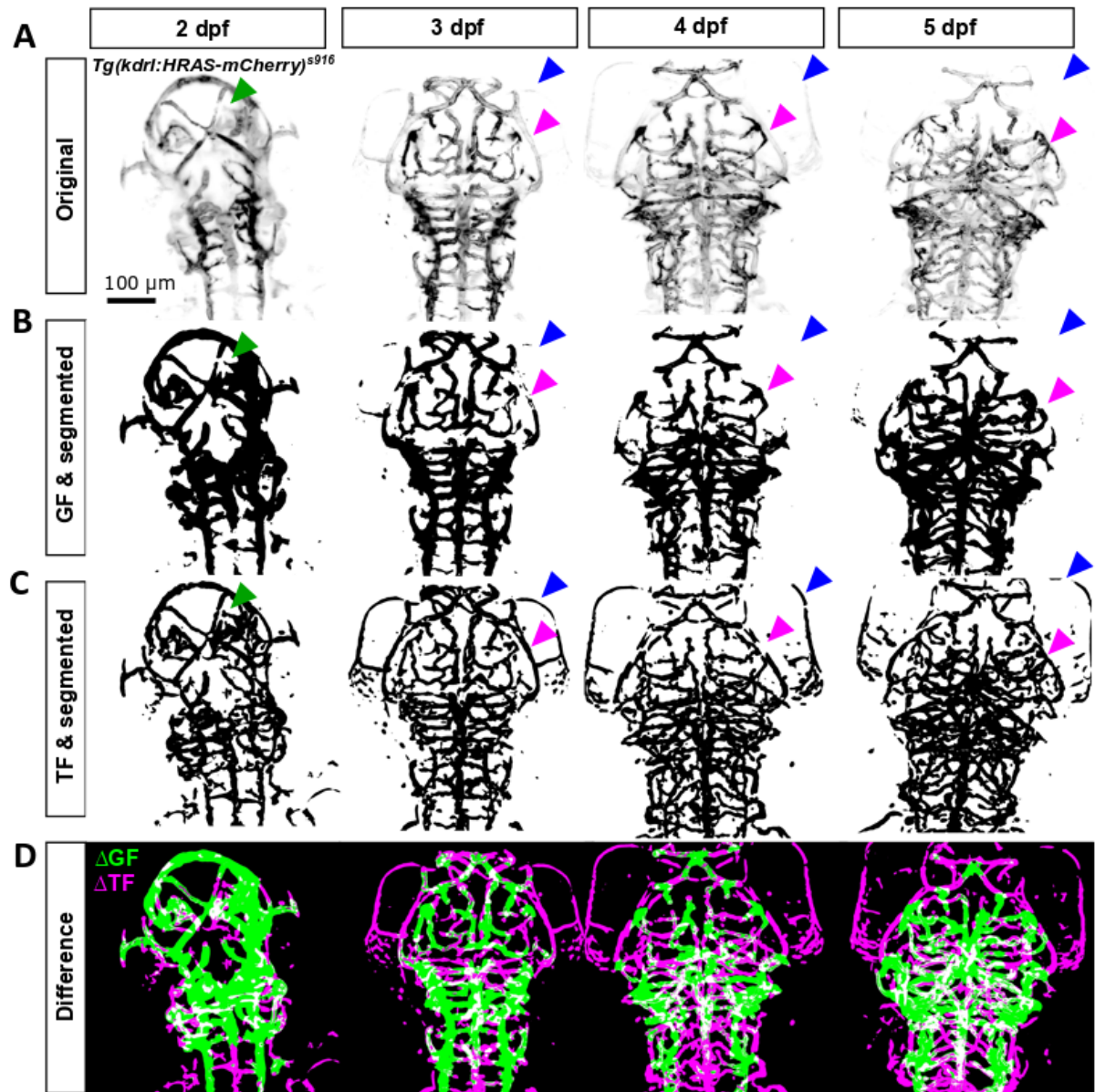


Figure 2.26: **Comparing segmentation outcomes from 2-5dpf.** (A) Original images for analysis. (B) Segmented vasculature after GF. (C) Segmented vasculature after TF. *Green arrowhead* indicates MMcTA at 2dpf. *Magenta arrowhead* indicates PMBC. *Blue arrowhead* indicates IOC (inverted MIPs). (D) Direct comparison of segmented images after GF and TF, based on differences in detection. *Green* represents vasculature detected by GF, but not TF. *Magenta* is vice versa (representative images; false colour MIPs).

stack intensity showed no difference between untreated and treated larvae (p 0.1238; Fig. 2.27C; control 230.6 ± 12.65 , DAPT 225.4 ± 9.068 ; unpaired Student's t-test). The cranial vascular volume showed no difference (p 0.1385; Fig. 2.27D; control $2181668 \pm 210038 \mu\text{m}^3$, DAPT $2302225 \pm 302607 \mu\text{m}^3$; unpaired Student's t-test). These data suggested that while the lateral growth was impacted by Notch signalling inhibition, this did not translate into changes of the cranial vascular volume.

Vascular volume is decreased following inhibition of VEGF signalling

VEGF inhibition was achieved by application of the VEGFR inhibitor AV951 (2h 250nM; Fig. 2.28A). The distance between left-right PMBC was not changed (p 0.7087; Fig. 2.28B; control $412.00 \pm 10.74 \mu\text{m}$, AV951 $413.41 \pm 15.47 \mu\text{m}$; $n=30-31$; 4dpf; 3 experimental repeats; unpaired Student's t-test). The mean stack intensity was similar between untreated and treated larvae (p 0.4187; Fig. 2.28C; control 229.2 ± 13.66 , AV951 232.2 ± 15.03 ; $n=30-31$; 4dpf; 3 experimental repeats; unpaired Student's t-test). Interestingly, the cranial vascular volume was decreased after treatment with AV951 (p 0.0039; Fig. 2.28D; control $2224310 \pm 205487 \mu\text{m}^3$, AV951 $2014663 \pm 245664 \mu\text{m}^3$; $n=30-31$; 4dpf; 3 experimental repeats; unpaired Student's t-test). This data suggested that VEGF signalling is required to establish and/or maintain the cranial vascular volume, in agreement with the literature [272, 273].

2.4 Conclusion

Vascular data properties were assessed using CNR measurements. Measuring the vascular CNR in the BA showed differences of signal intensity between transgenic reporter lines, which is likely to be caused by differences in local transgene expression (promotor or fluorophore levels) as well as image acquisition artefacts (Fig. 2.4). CNR was independent of vessel size and anatomical location, which suggested that the examined vessels should be detected with equal likelihood.

Encountered motion artefacts, caused by muscle contraction, cardiac pulsation, or gravity, interfered with structural vascular integrity, especially in time-lapse acquisitions (Fig. 2.6), and to a lesser extent in single-time-point 3D stack acquisition (Fig. 2.7). Correction of motion artefacts, using linear stack alignment based on SIFT [274], successfully restored data integrity.

While motion extent may differ with other methods of sample embedding (eg. fluorinated ethylene propylene (FEP) tubing [253]), or different percentages of agarose, we consider the presented assessment and correction of motion as proof of principle for the necessity of motion

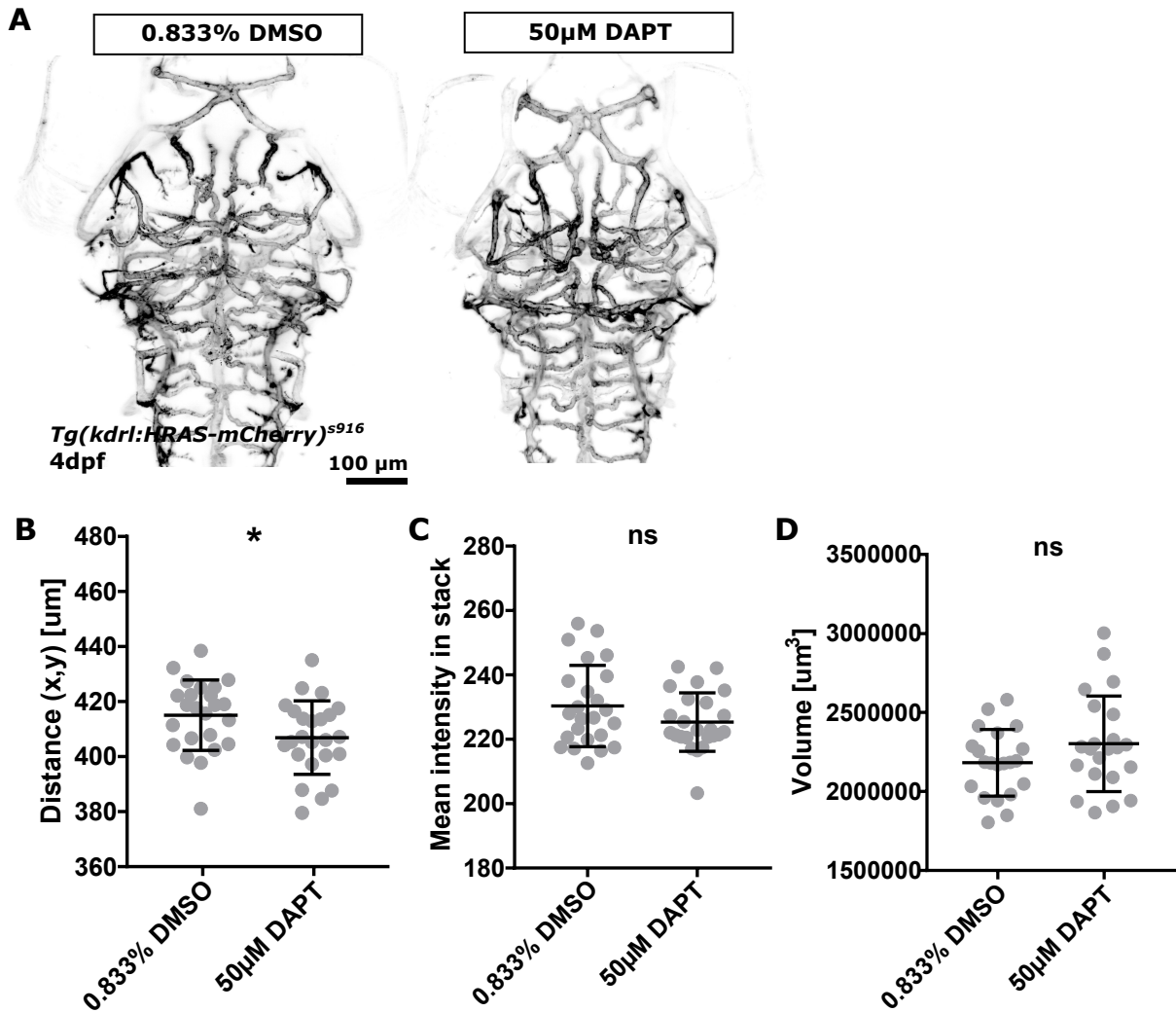


Figure 2.27: **Notch inhibition does not lead to a change in cerebrovascular volume.** (A) Inhibition of Notch signalling was achieved by application of the pharmaceutical γ -secretase inhibitor DAPT (12h 50µM). (B) Measurement of distance between left and right PMBC showed a decrease upon Notch inhibition (p 0.0357; n=24; 4dpf; unpaired Student's t-test; 3 experimental repeats). (C) Mean stack intensity measurement showed no difference upon treatment (p 0.1238; n=24; 4dpf; unpaired Student's t-test; 3 experimental repeats). (D) Cranial vascular volume measurement showed no difference (p 0.1385; control n=21, DAPT n=22; 4dpf; unpaired Student's t-test; 3 experimental repeats).

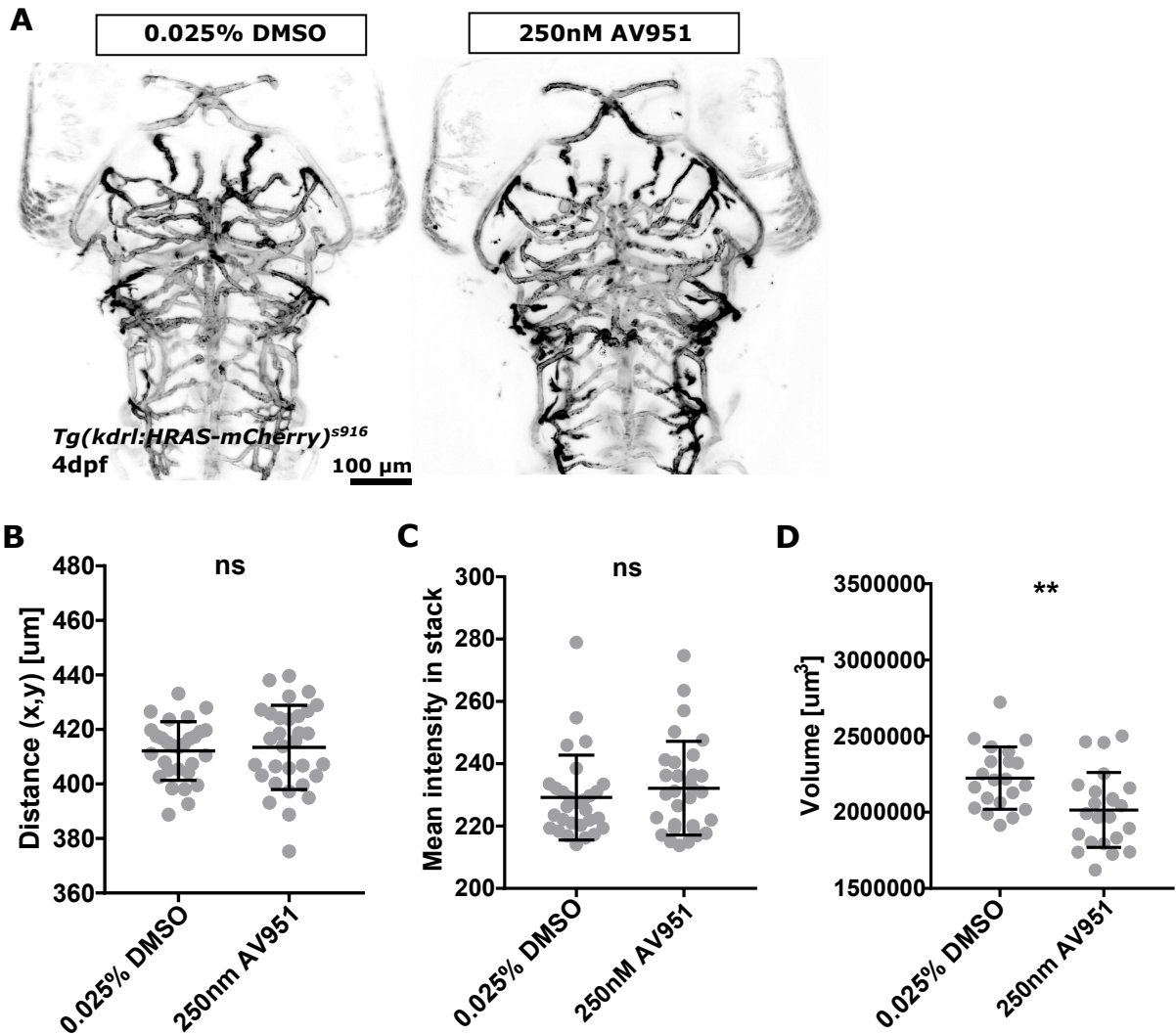


Figure 2.28: **VEGF inhibition leads to a decrease in cerebrovascular volume.** (A) Inhibition of VEGF signalling was achieved by application of the pharmaceutical VEGFR inhibitor AV951 (2h 250nM). (B) Measurement of distance between left and right PMBC showed no difference in growth (p 0.7087; control $n=30$, AV951 $n=31$; 4dpf; unpaired Student's t-test; 3 experimental repeats). (C) Mean stack intensity measurement showed no difference upon treatment (p 0.4187; control $n=30$, AV951 $n=31$; 4dpf; unpaired Student's t-test; 3 experimental repeats). (D) Cranial vascular volume measurement showed a reduction upon VEGF signalling inhibition (p 0.0039; control $n=21$, AV951 $n=23$; 4dpf; unpaired Student's t-test; 3 experimental repeats).

correction to restore data integrity, as well as the usability of Scale Invariant Feature Transform (SIFT) to correct for motion artefacts.

In the scope of image-enhancement, prior to segmentation, the application of a general filter-set (Median filter radius 6 and Rolling Ball algorithm of size 200) was sufficient to significantly increase the vascular CNR in the BA (Fig. 2.9).

Evaluating image-enhancement using "Vessel Enhancement Filters" implemented in Fiji [127], the "Frangi" Plugin was not applicable to fluorescence microscopy images of the dorsal cranial vasculature in zebrafish; while the "Tubeness Filter" Plugin delivered satisfactory enhancement of tubular, and suppression of non-tubular, structures (Fig. 2.10 2.17, 2.19, 2.20; filters based on [98, 99], respectively).

Comparison of different segmentation methods showed that intensity-based thresholding, using Otsu thresholding, sufficiently distinguished vascular from non-vascular tissue for all evaluated datasets (Fig. 2.18, 2.19), while disappointing results were obtained with initial implementations of k-means clustering, SRM, and level set segmentation. However, it was beyond the scope of this work to fully evaluate and optimise all of the parameters involved in these methods and so future work may be able to develop bespoke solutions using these approaches.

Due to the lack of a "gold-standard" vascular model of zebrafish, segmentation sensitivity and robustness were assessed in datasets with varying CNR, double-transgenic embryos, and pre- vs. post-exsanguination. Using the total cranial vascular volume as readout, GF and TF pre-processing delivered good results in data with decreased CNR (Fig. 2.22). Additional quantification in the double-transgenic line *Tg(kdrl:HRAS-mCherry)^{s916},Tg(fli1a:eGFP)^{y1}* [74, 243, 244] showed that TF-based pre-processing combined with Otsu segmentation delivered results with lower variation in the total cranial vascular volume at 4dpf, especially for the *Tg(fli1a:eGFP)^{y1}* data (Fig. 2.23). Both pre-processing methods showed a higher vascular volume in *Tg(fli1a:eGFP)^{y1}* than *Tg(kdrl:HRAS-mCherry)^{s916}* (GF 2.14 and TF 1.3, respectively). Our data show that TF and Otsu-based thresholding are suitable to segment the vasculature in different transgenic lines, even though the approach was originally optimized for *Tg(kdrl:HRAS-mCherry)^{s916}*.

Total vascular volume measurements in embryos pre- and post- exsanguination showed that segmentation subsequent to TF was sufficient to detect the vascular differences, while this was not the case for pre-processing with GF. Also, a lower variation in the total vascular volume between samples after TF was found (Fig. 2.24). Lastly, we established that the differences in the total vascular volume between control and exsanguinated samples were not introduced by

changes of vascular CNR or whole-image intensity. Thus, our proposed segmentation method is able to detect changes in the total cranial vasculature sufficiently.

Analysis of the total cranial vascular volume during early embryonic development showed a steady increase of vascular volume between 3-5dpf after pre-processing with either GF or TF (Fig. 2.25). Regardless of pre-processing approach, the CoV of the total vascular volume was highest at 2dpf. Also, segmentation with GF resulted in a larger cranial vascular volume, with less defined vascular structures and thicker vessels than after TF. Lastly, it was observed that dimmer vessels that are successfully enhanced and extracted after TF, were lost upon pre-processing with GF (Fig. 2.26). Thus, our data suggest that application of TF prior to intensity-based thresholding is the more reliant and accurate method for the segmentation of the zebrafish cranial vasculature in images acquired with LSM.

In summary, we presented an analysis and understanding of our data, which enabled us to develop suitable enhancement and segmentation methods using freely available image analysis software framework Fiji. We performed extensive assessments to establish the robustness of the methods for segmenting the zebrafish cranial vasculature and demonstrated their suitability for providing biologically relevant insights. The validated image segmentation workflow described in this Chapter will provide the foundation for the analysis presented in the remainder of this thesis.

3 Vascular Intra-Sample Symmetry and Inter-sample Similarity

3.1 Introduction

Most animals (99%) show overall bilateral symmetry [275], although the positioning of internal organs is often lateralized (eg. heart is located in the left thoracic cavity). The processes that break axis symmetry, to enable the lateralized positioning of organs, are highly conserved between vertebrates [276, 277] and are of clinical relevance due to clinical manifestations such as *situs inversus* or congenital heart diseases such as heterotaxy [278, 279].

The brain is structurally and functionally lateralized, and zebrafish have helped to understand the mechanisms of brain lateralization [280, 281, 282]. Key factors are Nodal [277, 283, 284, 285] and Notch signalling [286, 287], where Nodal is a key for overall body a-/symmetry, and Notch is required more specifically for brain/neuron lateralization in human and zebrafish. Increasing evidence suggests that the direction of brain lateralization is independent of age, but strength of lateralization does depend on age [288, 289, 290], with left-right asymmetries developing early.

Although the overall topology of the cranial vasculature is symmetric [291], lateralization of cerebral blood flow is associated with behavioural lateralization, and cognitive stimulation in humans. Dysfunctions of blood flow lateralization are associated with conditions such as depression or schizophrenia [292, 293, 294].

In zebrafish, vascular symmetry and lateralization are of increasing interest to help understand vascular patterning and remodelling [200]. There is currently no method available to compare vascular symmetry, which would allow us to understand **(i)** vascular (a)symmetry in general, **(ii)** whether symmetry changes during early embryonic development, **(iii)** if Notch signalling components are required to establish symmetry or lateralization, similar to their role in brain/neuron lateralization.

In addition to intra-sample left-right symmetry/variability, similarity/heterogeneity between individuals is of increasing interest to understand inter-sample variability which plays a role in the planning of surgical intervention, as well as predisposition to diseases such as atherosclerosis [295, 296, 297].

To compare vascular geometry between samples, image registration can be applied to bring objects into spatial correspondence [298]. Generally, a *moving image* $I_M(x)$ is registered by transformation to a *target/fixed image* $I_T(x)$. Transformation methods for image registration

can be classified, depending on the registration methodologies and constraints, into translation, rigid, affine, or non-linear methods, often based on B-spline or kernel spline transforms [298, 299, 300].

The extraction of features that drive the transformation estimation are typically based on intensity distributions, image-intrinsic features, or object landmarks [301]. Subsequent to the extraction of features, images/objects are brought into spatial correspondence by reduction of distances (or increase of similarity) between corresponding image features.

Inter-sample 3D registration of zebrafish larvae has previously been used to derive structural templates of the brain [302, 303, 304], but 3D registration of the zebrafish vasculature has only been applied to caudal vascular beds and did not include comparative measures or the construction of vascular templates or "idealised" fish at certain ages [193]. An inter-sample registration approach for the 3D cranial vasculature of transgenic zebrafish has never been established. Thus, there is a need to establish such an approach to allow the study of inter-sample similarity and variability, and how these change in development or disease.

When comparing vascular topology between samples the following must be considered: **(i)** the sparse nature of the vasculature in images challenges the extraction of features for automatic registration; **(ii)** due to the nature of fluorescent transgenic reporter lines intensity fluctuations may hamper intensity-based registration; **(iii)** intrinsic biological variability of the vascular architecture impacts the registration outcome; **(iv)** image acquisition angles can vary along all common axes, suggesting the necessity for a comprehensive registration method which takes all directions into consideration; **(v)** interpolation of data during registration could falsify true biological data and the subsequent quantification.

In this chapter, we develop and apply image analysis workflows to answer the following questions:

- (1)** Is the cerebral vasculature of zebrafish symmetric during early embryonic development?
- (2)** Does the Notch signalling component *dll4* play a role in cerebrovascular symmetry?
- (3)** Do fish of the same age share enough overall similarity to allow for inter-sample registration?
- (4)** Can anatomical landmarks be identified for inter-sample registration?
- (5)** Can automatic inter-sample registration be applied to bring samples into spatial correspondence without *a priori* knowledge?
- (6)** Can age-specific templates of vascular similarity be established?
- (7)** Does registration to an individual template perform better than registration to an averaged template?

(8) Does loss of *dll4* impact cerebrovascular topology similarity?

3.2 Material and methods

3.2.1 Zebrafish strains, handling, and husbandry

Zebrafish handling and husbandry were performed as described in 2.2.1. *Tg(kdrl:HRAS-mCherry)^{s916}* [244] line was used for vasculature visualization in 2-5dpf embryos.

3.2.2 Morpholino antisense gene knockdown

Inhibition of Notch signalling was investigated by injection of an ATG blocking morpholino (MO) against delta-like ligand 4 (*dll4*; 3ng; Genetools, LLC; sequence 5' - GAGAAAGGTGAGCCAAGCTGCCATG - 3') [305] and *notch 1b* (0.25ng; Genetools, LLC; sequence 5' - GTTCCTCCGGTTACCTGGCATAACAG - 3') [306]. This MO prevented *dll4* RNA transcription, thus, *dll4* protein production (more information on morpholinos (MOs): [307]). Control MO injection was performed, according to the same protocol, with final concentrations as above (5'-CCTCTTACCTCAGTTATTTATA-3'; Genetools, LLC). All MO injections were conducted at one-cell-stage using phenol red as injection tracer.

3.2.3 Imaging methodology

Image acquisition was performed as in section 2.2.2.

3.2.4 Intra-sample symmetry

Processing for intra-sample symmetry quantification

Intra-sample symmetry was assessed using the segmented vasculature to allow topological (rather than intensity-based) similarity assessment (Fig. 3.1A). Image rotation was performed to align the anterior-posterior axis of samples with the image y-axis to allow for subsequent mirroring of the right vasculature by horizontal transformation (Fig. 3.1B). ROI selection was performed on the MIP as described previously in section 2.2.6 [2] and the area outside of the ROI was set to 0 (Fig. 3.1C; Edit > clear outside). The mirroring axis was chosen centrally along the BA, between L-R PCS, between L-R MMcTA and the bifurcation point of L-R anterior cerebral vein (ACeV) (Fig. 3.1D). The right vascular volume was mirrored by horizontal image

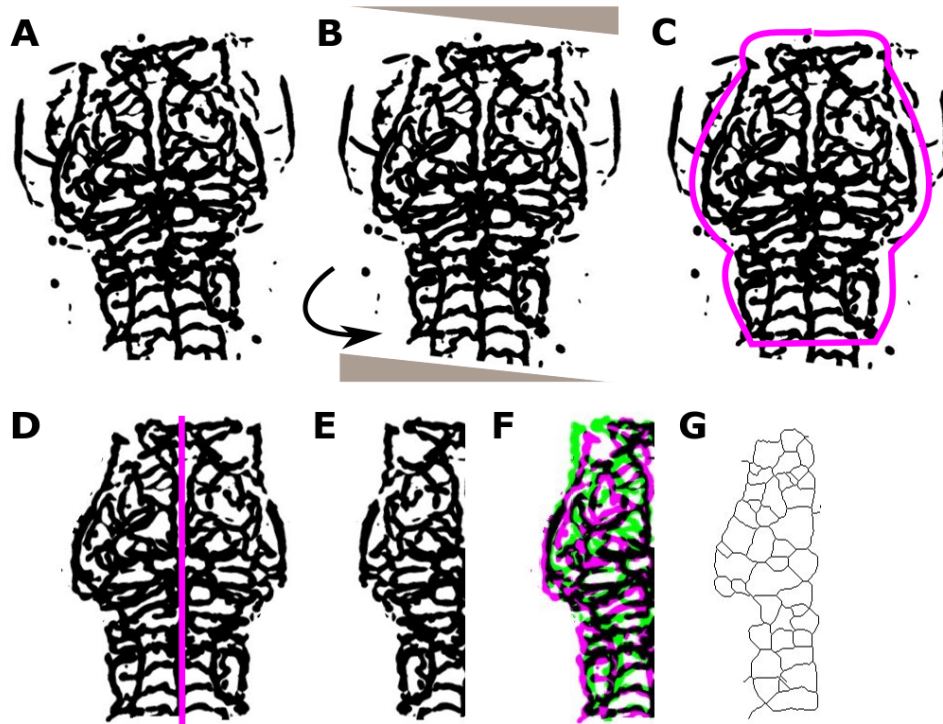


Figure 3.1: **Workflow for intra-sample symmetry measurement.** **A** Image pre-processing included motion correction, enhancement using Sato enhancement filtering and segmentation using Otsu thresholding, as described in section 2.3.4. **B** Image rotation was performed to align sample anterior-posterior axis with image y-axis. **C** ROI was selected from 2D MIP and transferred to 3D stack to remove signal outside the ROI. **D** Cerebral vascular volume was quantified and the mirroring axis determined along BA, between L-R PCS, between L-R MMCTA, and the bifurcation point of L-R ACeV. **E** Right vascular volume was mirrored by horizontal transformation. **F** Vascular volume was quantified for the left (green) and right (magenta) vasculature. Similarity measures were extracted to compare left and mirrored right vasculature (Jaccard Index, Dice Coefficient, Total Overlap, MI, MSE, and SSD). **G** Left and right vascular network length were quantified after skeletonization to extract vascular centrelines (representative images).

transformation (Fig. 3.1E). Similarity was compared as described below (Fig. 3.1F). 3D skeletonization was performed using the Fiji Plugin "Skeletonize 2D/3D". Following skeletonization, network length was quantified as the number of skeleton voxels (Fig. 3.1G).

Measurement of image similarities

To compare mathematical morphology between two images (eg. left and right vasculature or moving and target image; M and T, respectively) the Fiji Plugin MorphoLibJ [308] was used to compute the Jaccard Coefficient (Eq. 3.1), Dice Coefficient (Eq. 3.2) and Total Overlap (Eq. 3.3) [309].

$$JC(M, T) = \frac{\sum |M \cap T|}{\sum |M \cup T|} \quad (3.1)$$

$$DC(M, T) = 2 \frac{\sum |M \cap T|}{\sum (|M| + |T|)} \quad (3.2)$$

$$TO(M, T) = \frac{\sum |M \cap T|}{\sum |T|} \quad (3.3)$$

Quantification of the mutual information (Eq. 3.4), MSE (Eq. 3.5) and Sum of Squared Differences (SSD) (Eq. 3.6) was performed using Matlab.

$$MI(M, T) = \sum_{M, T} p(M, T) \log \frac{p(M, T)}{p(M)p(T)} \quad (3.4)$$

$$MSE(M, T) = \frac{1}{N} \sum |M - T|^2 \quad (3.5)$$

$$SSD(M, T) = \sum |M - T|^2 \quad (3.6)$$

Visual representation of structural similarity was achieved by visualization of vascular voxels present in both images of interest using "Image Calculator > AND" in Fiji to show voxels which are present in both images.

3.2.5 Manual measurements of growth rates

Measurements were performed manually using the line ROI tool in Fiji [127] at the positions indicated in Fig. 3.2. Distance [x,y; μm] between left and right MMCtA was measured at the most anterior points, PMBC distance was measured at the height of posterior edges of the eyes, BA diameter was measured before branching into PCS' and PCS", DA diameter was measured at the height of posterior cerebral vein (PCeV) branching into PHBC.

Brain growth [x,y; μm] (Fig. 3.2B) measurement positions were selected as follows: forebrain at the height of PrA, midbrain at the height of posterior edges of the eyes, hindbrain at the height of PCeV branching into PHBC (see also Appendix A).

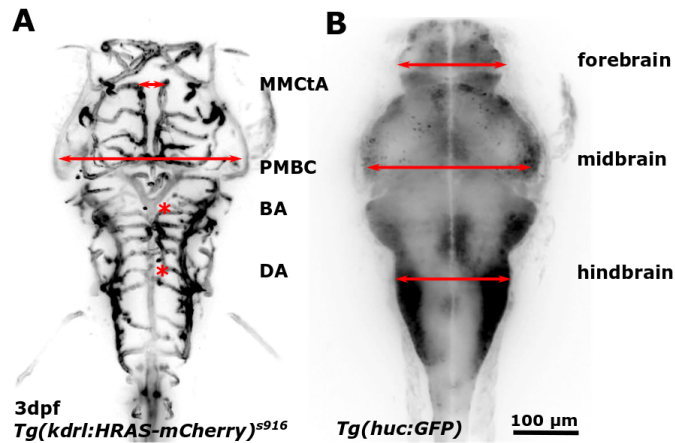


Figure 3.2: **Anatomical positions for manual measurements of growth rates.** Growth rate was measured as distance between left and right MMCTa as well as PMBC. Vessel diameters were measured in BA and DA (**A**). Brain growth rates were measured as distance of forebrain, midbrain, and hindbrain (**B**).

3.2.6 Manual landmark-based inter-sample registration

Selection of anatomical landmarks

To understand regions of similarity between different samples, their vasculatures were visually compared. An intensity-based lookup table (LUT) was used to allow for simultaneous assessment of fluorescence-level similarities and variabilities to find regions of high similarity, distributed along the common body axis (Fig. 3.3), to identify anatomical landmarks.

Registration using anatomical landmarks

Inter-object registration from 2-5dpf was conducted with the "landmark registration" Plugin in Fiji using a rigid, affine and thin-plate spline transformation [127] to test the impact of different degrees of transformation freedom on the registration outcome (Fig. 3.4A).

The plugin calculates a transformation between two corresponding landmark clouds (manually placed, Fig. 3.3) and renders a transformed image using Moving Least Squares (Fig. 3.5A). Landmarks were placed manually in segmented images with the *caveat* to distribute them along the common body axis (Fig. 3.3). Target fish were selected based on **(a)** sample orientation along common image axis (anterior-posterior along image y-axis, coronal plane along image z-axis and x-axis), **(b)** all common vessels visualized in image, **(c)** no obvious abnormalities. Similarity between samples before and after registration was quantified as described in section 3.2.4 and shown in Fig. 3.4B,C (M and T, refer to moving and target image, respectively).

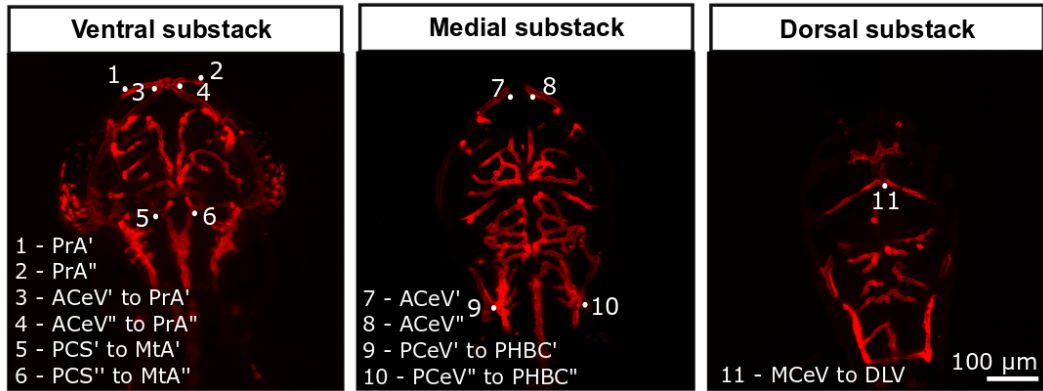


Figure 3.3: **Eleven landmarks were identified for manual landmark-based registration.** Anatomical locations of eleven manually selected landmarks were considered to cover principal body-axis along anterior-posterior, left-right as well as ventral-dorsal. (Abbr.: PrA - prosencephalic artery, ACeV - anterior cerebral vein, PCS - posterior communicating segment, MtA - mesencephalic artery, PHBC - primordial hindbrain channel, DLV - dorsal longitudinal vein;)

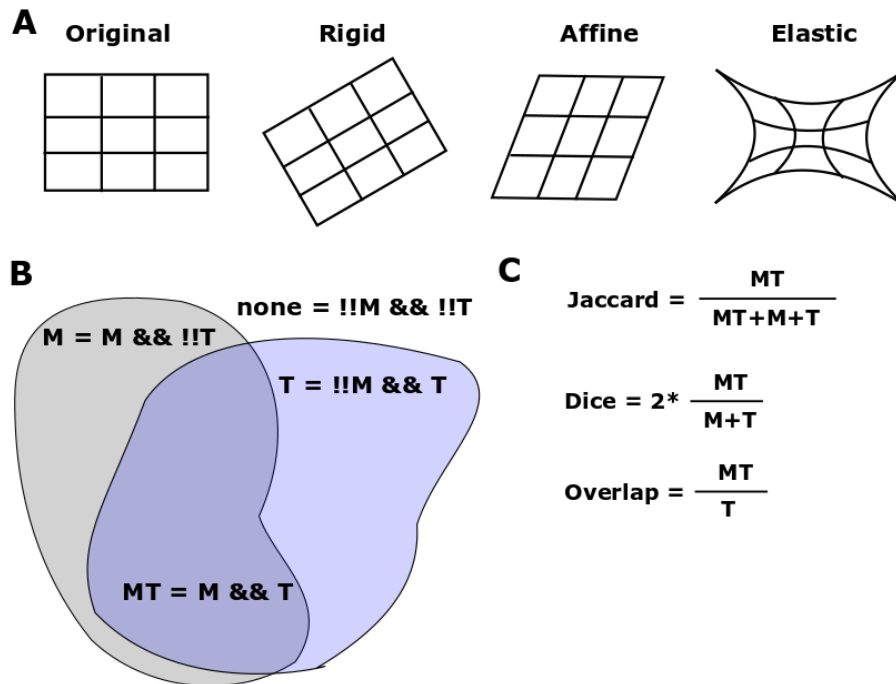


Figure 3.4: **Registration methods and assessment of similarity.** (A) Registration methods with different degrees of freedom were tested. (B) Similarity of images (M and T) was compared before and after registration (&& meaning *and*; !! meaning *not*). (C) Jaccard Index, Dice Coefficient and Total Overlap were used to quantify object overlap before and after registration.

Automatic inter-sample registration

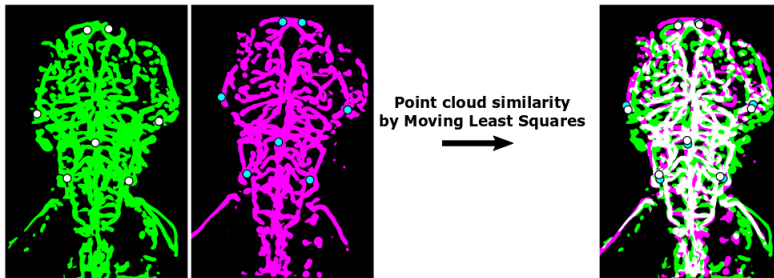
The "2D/3D descriptor-based registration" Fiji plugin, implemented by Stephan Preibisch [310], was tested on segmented images. This registration approach relies on the extraction of 2D/3D descriptors, which uses a DoG to extract descriptors and fits their maximum intensity to sub-pixel/sub-scale accuracy to voxels using a 3D quadratic fit (Fig. 3.5B) [311]. Following detection, the translation and rotation invariant local geometric descriptor is established by the local descriptor constellation (of the central descriptor to its neighbours). The following settings were used: interactive brightness detection (user sets the threshold for detecting descriptors), 3D quadratic fit for sub-pixel localization (to locate the intensity maxima to sub-pixel or sub-scale accuracy by fitting a 3D quadratic fit; as described in [311]), rigid (3D) transformation model, not pre-aligned images, 6 neighbours for descriptors (descriptor is described by the geometric constellation of 6 neighbours), redundancy of 3 neighbours, and a Random Sample Consensus (RANSAC) error of 30 voxels (for outlier removal) [312]. Sigma was tested from 6-10 with one-step intervals (sigma being the standard deviation of the DoG to extract descriptors; see *interest point detection in scale-space* [148, 149, 150]).

The automatic rigid inter-sample registration method, implemented by Johannes Schindelin, Benjamin Schmid, and Mark Longair, is based on the Virtual Insect Brain Protocol (VIB) protocol (Fig. 3.5C) [313, 314]. Briefly, the centre of gravity of segmented objects is used to calculate a global rigid transformation. This global rigid registration is then used to initialise local rigid alignments which are achieved by an iterative optimization algorithm (conjugate direction search [315]) which uses scale space down-sampling to align stacks rigidly [314]. A diffusion-like iterative algorithm is then used to interpolate between local rigid transformations (vector field with the displacements is interpolated). The parameters used were as follows: transformation without initial transform, 5 best matching orientations for further optimization, tolerance of 10-50, downsampling 2-6 times (scale space), no ROI reduction (ie. bounding box selection) for optimisation, using Euclidean measure of difference, and showing transformed image.

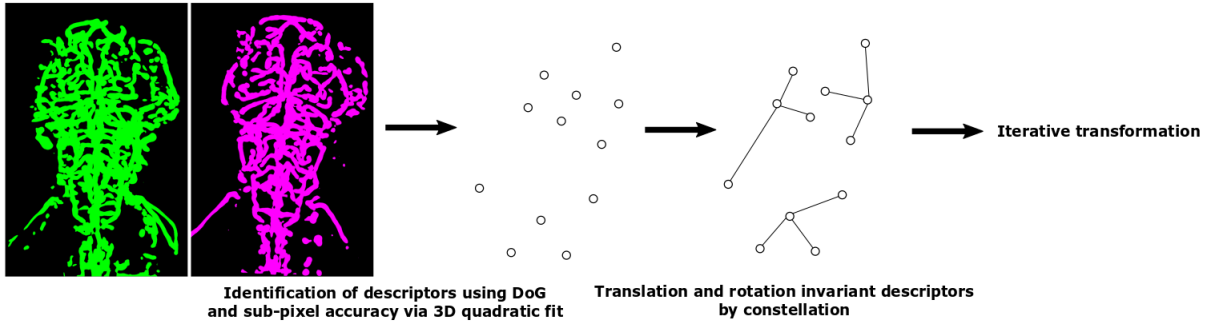
Dataset to validate inter-sample registration

A first round of image acquisition was performed as described in section 2.2.2. Following, the embedding agarose around the sample was removed, the sample embedded in fresh agarose, and imaged again to acquire images from the same sample. The second approach acquired an initial image as above, then the plunger manually moved (side-ways, up-down, and rotation; see Fig. 1.2), and an image was acquired of the same fish after this movement. In total

(A) Landmark-based Registration



(B) 2D/3D Descriptor-based Registration



(C) Automatic Rigid Registration

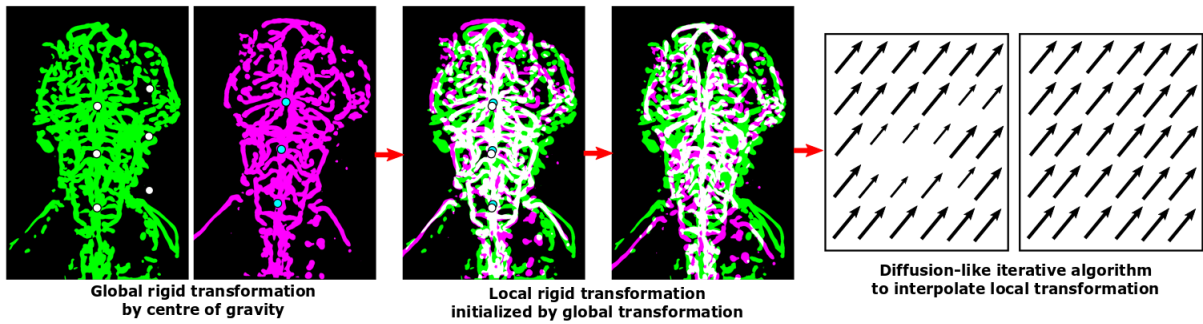


Figure 3.5: **Schematics of the examined 3D registration approaches. (A)** Landmark-based registration. **(B)** 2D/3D descriptor-based registration. **(C)** Automatic 3D rigid registration (based on VIB).

four acquisitions of the same sample were performed, with one serving as a target for the registration of the other three acquisitions.

3.2.7 Establishment of a vascular template at different developmental stages

To examine regions of vascular similarity and variability, vascular templates were established which allow for the identification of vessels consistently appearing at certain ages. This would allow the establishment of an "ideal" template fish at different ages to examine vascular similarity individual between fish, as well as vascular growth. After the initial inter-sample registration, three samples were overlaid in one image and LUT blue, green and red were assigned to individual embryos. MIPs from stacks, as well as resliced stacks, were produced to compare 2D similarity.

To further examine true 3D topological similarity between samples, six embryos were registered to a target and vascular voxels which were found in at least two fish extracted (Fig. 3.6; Fig. 3.7). This allowed the construction of vascular templates based on voxel-based similarities to produce shape-based averages (versus intensity-based similarity).

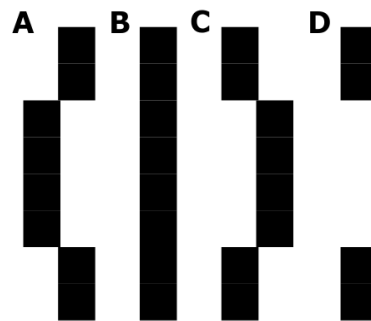


Figure 3.6: **Voxel-based overlap was used to generate averaged templates. (A-C)** Segmented data. **(D)** Voxel-based majority decision to create shape-based average template.

3D rendering was performed using Arivis Software, and used for visual examination to produce vascular template schematics. Schematics, based on 3D vascular similarity, were produced using Inkscape software.

3.2.8 Vascular surface and density

The total vascular surface was calculated in images after edge-detection with the Sobel edge detection in segmented images [316, 317]. As it is not clear how much of the voxel contributes to the surface (one or multiple faces, edges, or sides), the number of voxel was quantified as

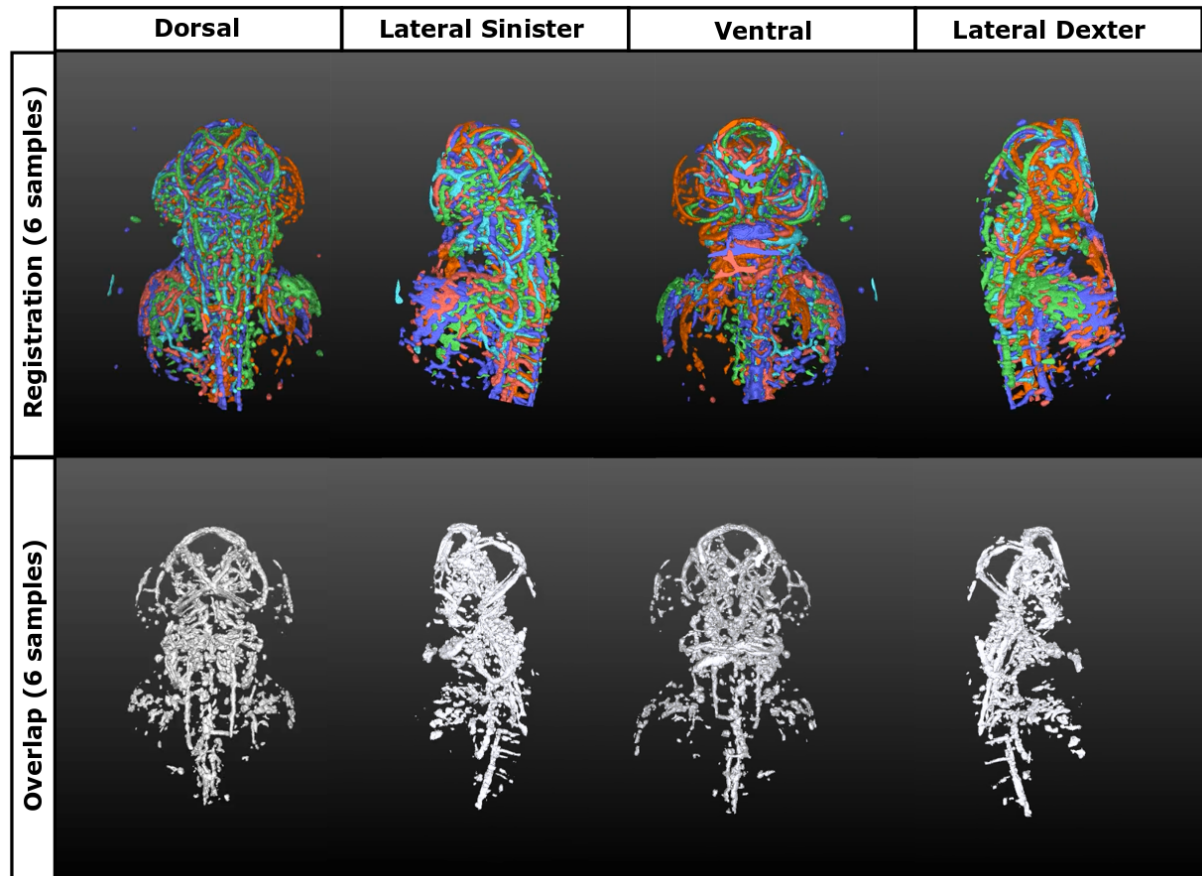


Figure 3.7: **Producing vascular templates.** Samples were registered to a target (top panel) and vascular voxels occurring in at least two samples extracted to establish vascular templates (bottom panel).

in section 2.2.6 within the the user-defined vascular region of interest (Fig. 2.3) rather than the surface.

The vascular cranial density (D) was derived by measurement of the total volume within the user-defined vascular region of interest (V_{total}) divided by the vascular volume within this region ($V_{vascular}$; Eq. 3.7).

$$D = V_{total}/V_{vascular} \quad (3.7)$$

3.2.9 Statistics and data display

As described in section 2.2.10.

3.3 Results and discussion

3.3.1 Intra-sample symmetry

The cerebral vasculature is symmetric from 2-5dpf

To investigate whether embryonic vascular growth in zebrafish was symmetric, left-right vascular topology was examined from 2-5dpf (Fig. 3.8A-D) and similarity studied initially by visually assessing vascular overlap (Fig. 3.8E-H). A high degree of left-right symmetry was observed and mapping of left-right symmetric vessels (Fig. 3.8I-L) suggested that vessels formed by vasculogenesis (such as BA, PHBC, and PMBC) were more left-right symmetric than vessels formed by angiogenesis (such as CtA and MMCTA).

Quantifying the cranial vascular volume from 2-5dpf showed an increase over time ($p < 0.0001$), with no differences between the left and right vasculature (Fig. 3.9A; 2dpf L-R $p > 0.9999$, 3dpf L-R $p > 0.9999$, 4dpf L-R $p > 0.9999$, 5dpf L-R $p = 0.9946$; 2dpf $n = 9$, 3dpf $n = 9$, 4dpf $n = 10$, 5dpf $n = 10$; 2 experimental repeats; One-Way ANOVA). Similarly, the total cranial vascular length increase from 2-5dpf ($p = 0.0194$), with no left-right differences (Fig. 3.9B; 2dpf L-R $p > 0.9999$, 3dpf L-R $p > 0.9999$, 4dpf L-R $p > 0.9999$, 5dpf L-R $p > 0.9999$; Kruskal Wallis test).

To compare left-right vascular topology after segmentation, the left-right Jaccard Index (Fig. 3.10A), Dice Coefficient (Fig. 3.10B), and Total Overlap (Fig. 3.10C) were quantified. No difference was found between the left and right vascular topology in embryos from 2-5dpf (Jaccard $p = 0.8642$; Dice $p = 0.8058$; Total Overlap $p = 0.5364$). Surprisingly, generally low levels of similarity were observed, but as this was the first comparison of this kind in the zebrafish cerebral vasculature there is no reference as to what "high" or "low" similarity is.

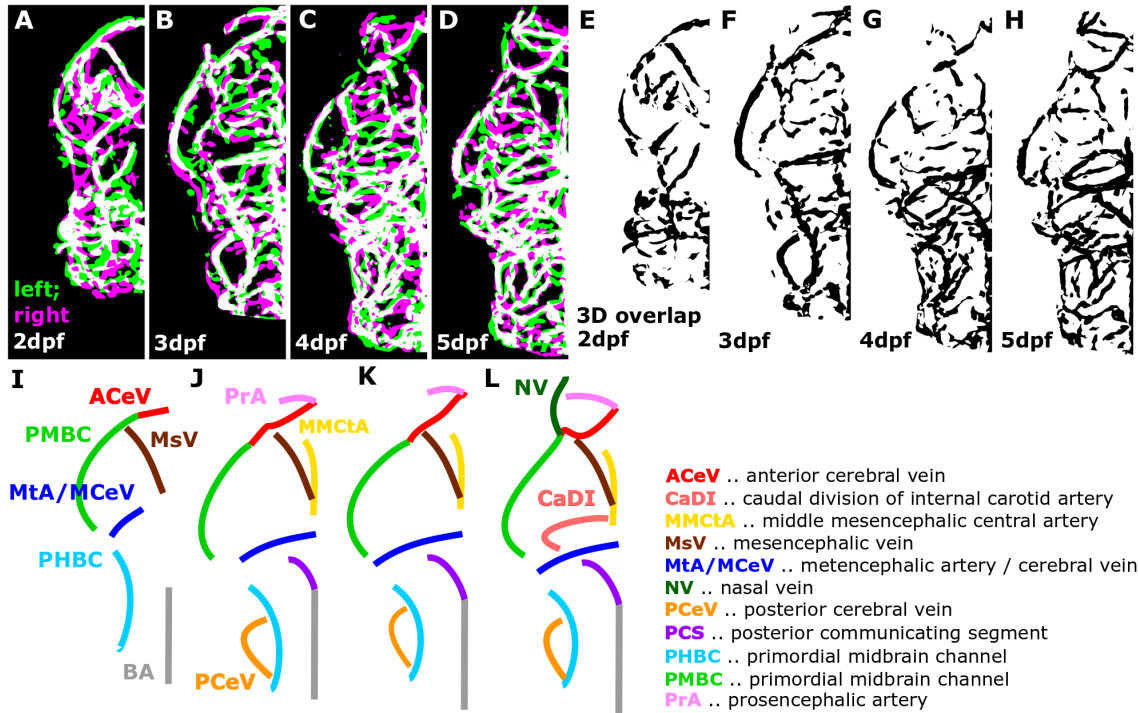


Figure 3.8: **Visual assessment of intra-sample symmetry.** (A-D) MIPs of left (green) and right (magenta) vasculature, showing regions of similarity (white). (E-H) Regions of left-right vascular overlap, suggesting vessels formed by vasculogenesis were more symmetric than vessels formed by angiogenesis. (I-L) Schematics highlighting left-right symmetric vessels from 2-5dpf.

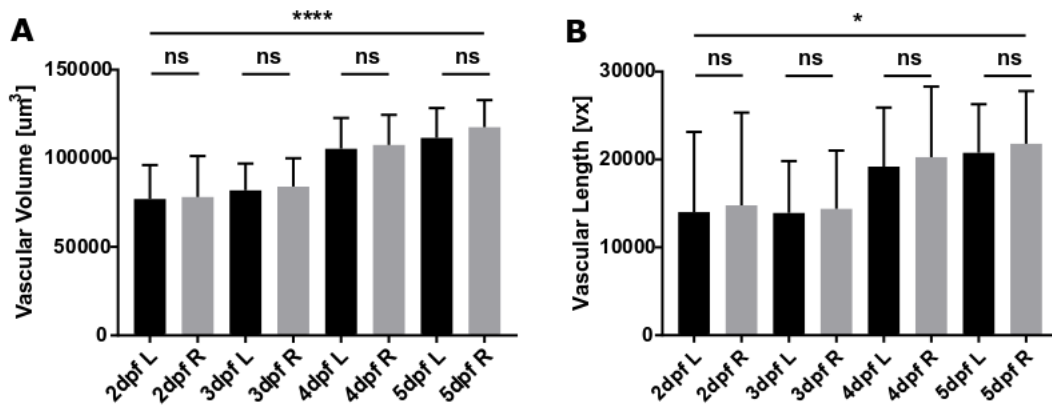


Figure 3.9: **Vascular volume and length are symmetric from 2-5dpf.** (A) Vascular volume was not different between left (L) and right (R) side, but an overall increase was encountered from 2-5dpf ($p < 0.0001$; 2dpf L-R $p > 0.9999$, 3dpf L-R $p > 0.9999$, 4dpf L-R $p > 0.9999$, 5dpf L-R $p = 0.9946$; 2dpf $n = 9$, 3dpf $n = 9$, 4dpf $n = 10$, 5dpf $n = 10$; 2 experimental repeats; One-Way ANOVA). (B) Vascular network length was not different between left (L) and right (R) side, but an overall increase was encountered from 2-5dpf ($p = 0.0194$; 2dpf L-R $p > 0.9999$, 3dpf L-R $p > 0.9999$, 4dpf L-R $p > 0.9999$, 5dpf L-R $p > 0.9999$; Kruskal Wallis test).

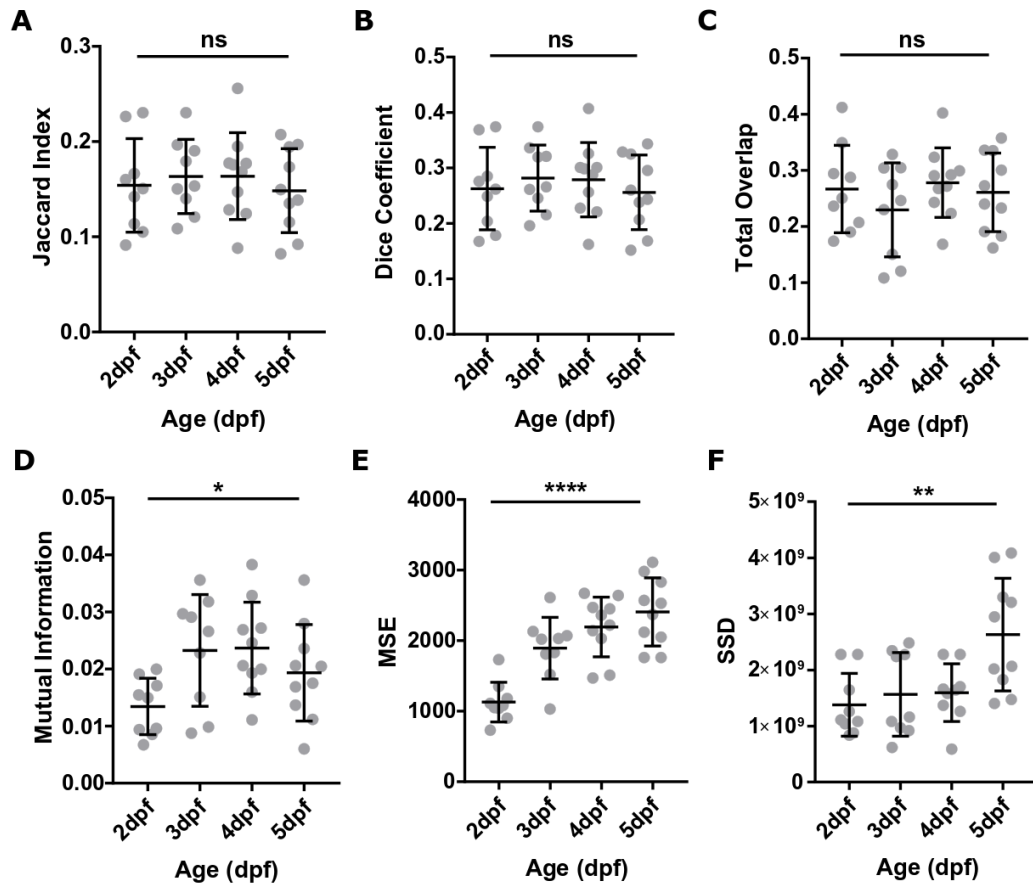


Figure 3.10: **Vascular topology is symmetric from 2-5dpf.** **A** Jaccard Index was not changed from 2-5dpf (p 0.8462; 2dpf $n=9$, 3dpf $n=9$, 4dpf $n=10$, 5dpf $n=10$; 2 experimental repeats; One-Way ANOVA). **B** Dice Coefficient was not changed from 2-5dpf (p 0.8058; data as B; One-Way ANOVA). **C** Total Overlap was not changed from 2-5dpf (p 0.5364; data as B; One-Way ANOVA). **D** MI was changed from 2-5dpf, where lowest MI was observed at 2dpf (p 0.0346; data as B; One-Way ANOVA). **E** MSE was increased from 2-5dpf with the error increasing with age ($p < 0.0001$; data as B; One-Way ANOVA). **F** SSD was increased from 2-5dpf with the error increasing with age (p 0.0029; data as B; One-Way ANOVA).

I further quantified MI (Fig. 3.10D; $p < 0.0346$) which was lowest at 2dpf, peaked at 3dpf-4dpf and dropped again at 5dpf. Furthermore, quantification of MSE (Fig. 3.10E; $p < 0.0001$) and SSD (Fig. 3.10F; p 0.0029) showed an increase from 2-5dpf. Together, these data suggest that mutual information, MSE, and SSD were the lowest at 2dpf, and increased during development. It was anticipated that this increase of error was potentially impacted by an increase of vascular volume over time rather than true biological differences.

Together these data suggest that vascular volume, and length are globally left-right symmetric during the examined timeframe, but vascular topology changes over time and symmetry is mainly observed in vessels formed by vasculogenesis.

In future, voxel-wise statistical comparisons, or more detailed vessel specific parametric

modelling, would be interesting to explore to gain further insights into regional similarity and variability.

Loss of *dll4* impacts vascular growth, but not symmetry

To investigate the impact of loss of *dll4* on vascular growth and left-right-symmetry *dll4* knockdown was performed using an antisense morpholino (MO; Fig. 3.11A). Measurement of PMBC width showed a reduction in *dll4* morphants at 3dpf (Fig. 3.11B; control-*dll4* MO $p < 0.0001$, control MO-*dll4* MO $p = 0.0007$), while distance of MMCtA anterior ends showed no difference (Fig. 3.11C; control-*dll4* MO $p = 0.1997$, control MO-*dll4* MO $p = 0.1520$). Quantification of MMCtA angle showed a lower angle in *dll4* morphants (Fig. 3.11D; control-*dll4* MO $p = 0.0079$, control MO-*dll4* MO $p = 0.0029$), while PMcTA angle was higher in *dll4* morphants than in control groups (Fig. 3.11E; control-*dll4* MO $p = 0.0125$, control MO-*dll4* MO $p = 0.0158$). Together, the observed MMCtA and PMcTA angles recapitulated the vascular patterning at 2dpf rather than 3dpf (see Fig. 3.13).

The cranial vascular volume was decreased after *dll4* knockdown (Fig. 3.12A; control-*dll4* MO $p = 0.0436$, control MO-*dll4* MO $p = 0.0315$), while no alteration of left-right volume (Fig. 3.12B; $p = 0.0055$; control L-R $p > 0.9999$, control MO L-R $p = 0.9996$) or vascular network length (Fig. 3.12C; $p = 0.8557$; control L-R $p = 0.9979$, control MO L-R $p = 0.9473$, *dll4* MO L-R $p > 0.9999$) was encountered. Comparison of left-right vascular topology showed a decrease of MSE after *dll4* knockdown (Fig. 3.12D; control MO -*dll4* MO $p = 0.0060$), while SSD (Fig. 3.12E; control-*dll4* MO $p = 0.0750$, control MO-*dll4* MO $p = 0.2009$) or MI (Fig. 3.12F; control-*dll4* MO $p = 0.9584$, control MO-*dll4* MO $p = 0.3993$) were not different. This difference in MSE was thought to be due to volumetric differences encountered in the *dll4* MO group.

In summary, our data suggested that *dll4* is required for early embryonic vascular growth (vascular volume) and maturation (vessel rearrangements), but that a loss of *dll4* would not impact vascular left-right symmetry at the investigated time point.

Future work, could examine how data normalization of *dll4* MO vascular parameters translates into the findings of reduced vascular growth. We here abstained from normalization procedures as in-depth analysis is needed to understand the appropriate type of normalization, such as

(a) rescaling factors to reduce variability (fold-changes, consideration of minimum or maximum), which requires appropriate parameters establishment,

(b) normalization to a set parameter of control samples, which might result in not being able to detect subtle biological differences,

(c) normalization to intrinsic parameters such as brain volume, which could be achieved by data acquisition in double-transgenic lines but therefore would result in doubled data sizes.

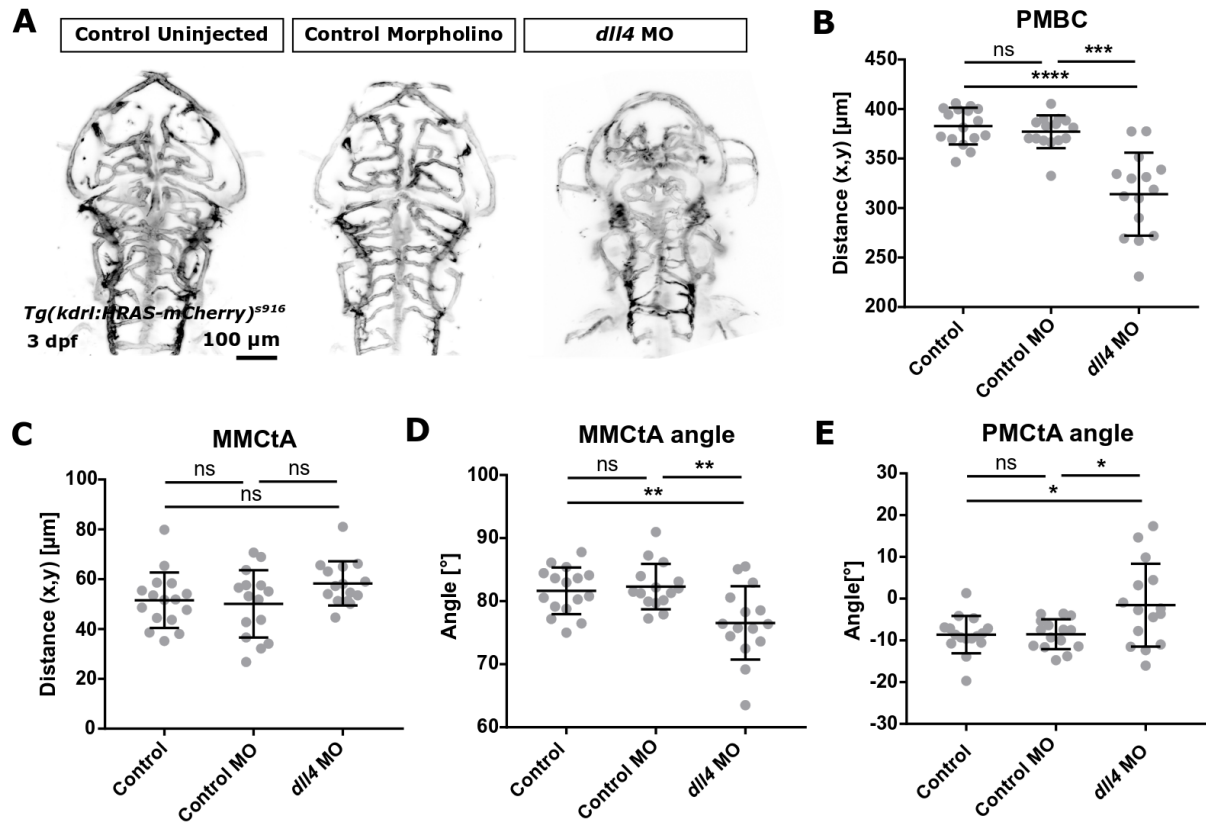


Figure 3.11: **Manual measurements show that *dlla* is required for early embryonic vascular growth.** **A** The impact of *dlla* knockdown on vascular growth was examined in 3dpf uninjected controls (control), control morpholino (control MO) injected samples and *dlla* MO injected samples. **B** Expansion of the PMBC was decreased upon *dlla* MO injection (control-*dlla* MO $p < 0.0001$, control MO-*dlla* MO $p = 0.0007$; 3dpf; control $n = 16$, control MO $n = 15$, *dlla* MO $n = 15$; 2 experimental repeats; Kruskal-Wallis test). **C** Distance between anterior ends of MMCTA was not changed upon *dlla* knockdown (control-*dlla* MO $p = 0.1997$, control MO-*dlla* MO $p = 0.1520$; data as in B; One-Way ANOVA). **D** MMCTA angle was decreased upon *dlla* knockdown (control-*dlla* MO $p = 0.0079$, control MO-*dlla* MO $p = 0.0029$; data as in B; One-Way ANOVA). **E** PMCTA angle increased upon *dlla* knockdown (control-*dlla* MO $p = 0.0125$, control MO-*dlla* MO $p = 0.0158$; data as in B; One-Way ANOVA).

3.3.2 Inter-object registration enables examination of vascular similarity

Manual measurements to obtain initial insights into structural similarity

To understand vascular growth and its reproducibility, manual measurements of selected vessels were performed (Fig. 3.13A). Lateral growth measurement of the primordial midbrain channel (PMBC) showed an increase from 2-4dpf (Fig. 3.13B; $p < 0.0001$; One-Way ANOVA).

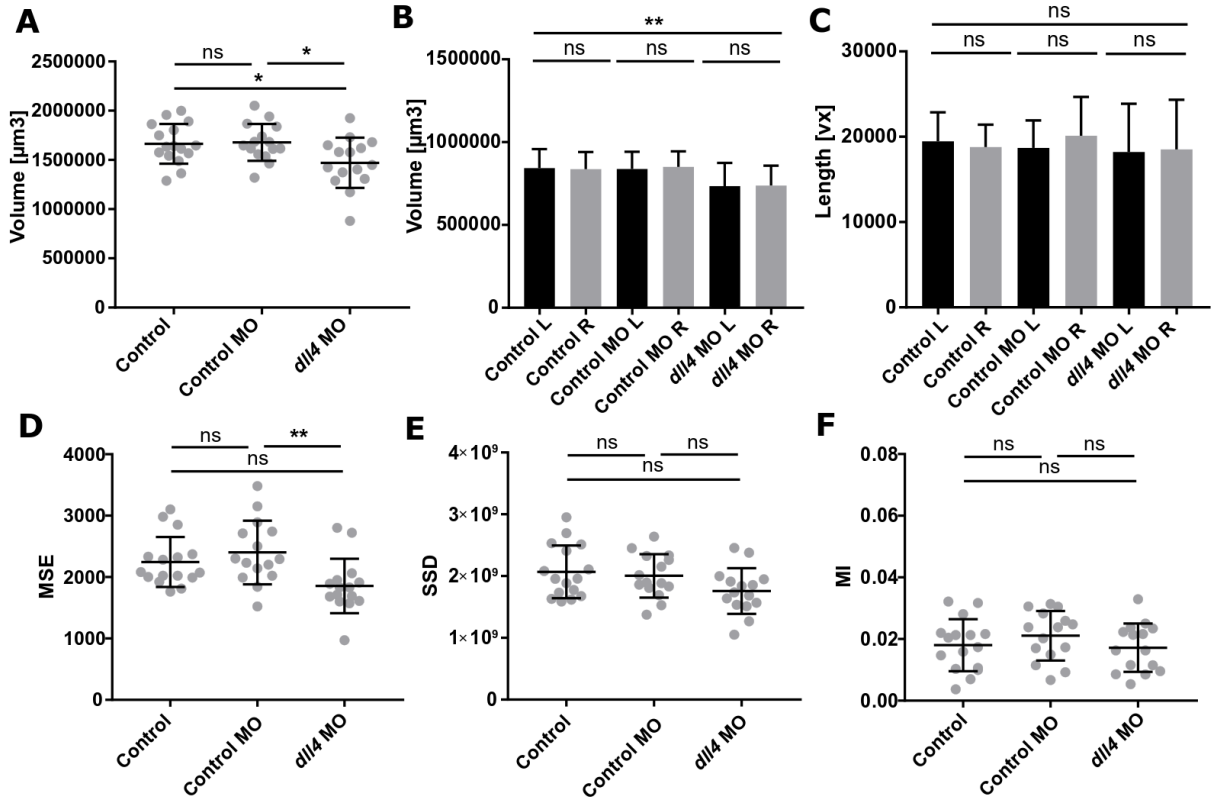


Figure 3.12: **Automatic measurements show that *dll4* is required for early embryonic vascular growth.** **A** Total cranial vascular volume was decreased upon *dll4* knockdown (control-*dll4* MO p 0.0436, control MO-*dll4* MO p 0.0315; 3dpf; control n=16, control MO n=15, *dll4* MO n=15; 2 experimental repeats; One-Way ANOVA). **B** Left-right vascular volume was decreased in *dll4* MO, but not different within groups (p 0.0055; control L-R p>0.9999, control MO L-R p 0.9996, *dll4* MO L-R p>0.9999; data as in A; One-Way ANOVA). **C** Left-right vascular network length was not different between or within groups (p 0.8557; control L-R p 0.9979, control MO L-R p 0.9473, *dll4* MO L-R p>0.9999; data as in A; One-Way ANOVA). **D** MSE of L-R vasculature was not different between uninjected controls and *dll4* MO (p 0.0574), but different between control MO and *dll4* MO (p 0.0060; data as in A; One-Way ANOVA). **E** SSD of L-R vasculature was not different between groups (control-*dll4* MO p 0.0750, control MO-*dll4* MO p 0.2009; data as in A; One-Way ANOVA). **F** MI of L-R vasculature was not different between groups (control-*dll4* MO p 0.9584, control MO-*dll4* MO p 0.3993; data as in A; One-Way ANOVA).

Interestingly, the growth was highly similar between samples at the investigated time points, with coefficients of variation of: 2dpf 5.21%, 3dpf 5.78%, 4dpf 6.08% and 5dpf 5.24%. Quantification of width between anterior ends of middle metencephalic central artery (MMCtA) showed a decrease over time (Fig. 3.13C; $p < 0.0001$; One-Way ANOVA), while MMCtA length increased (Fig. 3.13D; $p < 0.0001$; One-Way ANOVA; coefficients of variation as follows: MMCtA width 2dpf 11.90%, 3dpf 25.11%, 4dpf 22.55% and 5dpf 28.77%; MMCtA length 2dpf 11.50%, 3dpf 12.55%, 4dpf 8.38% and 5dpf 4.98%). To examine whether the observed MMCtA anterior width changes were caused by overall vessel rearrangements or changes in the vessel angle respective to the main anterior-posterior body axis, MMCtA angle was quantified. The MMCtA angle increased from 2-3dpf (Fig. 3.13E; $p < 0.0001$; Kruskal-Wallis test). Similarly, the angle of the posterior metencephalic central artery (PMCtA) decreased from 2-3dpf (Fig. 3.13F; $p < 0.0001$; One-Way ANOVA). Together these data showed that the base of the MMCtA and PMCtA did not rearrange, but that their angle, respective to the main body axis, changed over time (Fig. 3.13G).

Brain growth, like vascular growth, was highly consistent during early embryonic development (CoV: 3dpf: 6.98%, 4dpf: 5.37%, 5dpf: 2.86%). Assessed lateral brain growth in the forebrain did not change significantly during the first days of development (Fig. 3.14A; $p < 0.0001$; One-Way ANOVA), while the midbrain significantly expanded laterally (Fig. 3.14B; $p < 0.0001$; One-Way ANOVA).

Diameter measurements of the BA showed no significant changes over time (Fig. 3.14C; 2dpf: $20.3 \pm 3.5 \mu\text{m}$, 3dpf: $21.3 \pm 3.6 \mu\text{m}$, 4dpf: $23.1 \pm 3.3 \mu\text{m}$, 5dpf: $23.0 \pm 3.2 \mu\text{m}$; $p = 0.0809$; One-Way ANOVA), whilst the diameter of the DA was found to decrease (Fig. 3.14D,E; $p < 0.0001$; One-Way ANOVA; 2dpf: $33.0 \pm 2.3 \mu\text{m}$, 3dpf: $27.4 \pm 4.3 \mu\text{m}$, 4dpf: $22.7 \pm 2.7 \mu\text{m}$, 5dpf: $23.8 \pm 3.0 \mu\text{m}$), as was also recently shown in a more caudal region of the DA [81].

Testing inter-sample registration approaches by intra-sample registration

The dataset to study segmentation, acquired by consecutive de- and re-mounting, was not usable to test the proposed inter-sample registration approaches due to high rates of sample death. Thus, a second dataset, which did not use de- and re-mounting but manual sample displacement, was used to examine and validate registration (Fig. 3.15A).

To allow registration based on vascular topology, registration methods were applied to segmented images as the intensity fluctuations in transgenic lines as well as the cross-sectional intensity distribution were likely to interfere with registration outcomes.

Testing anatomical landmark-based registration, visual assessment showed that the selected

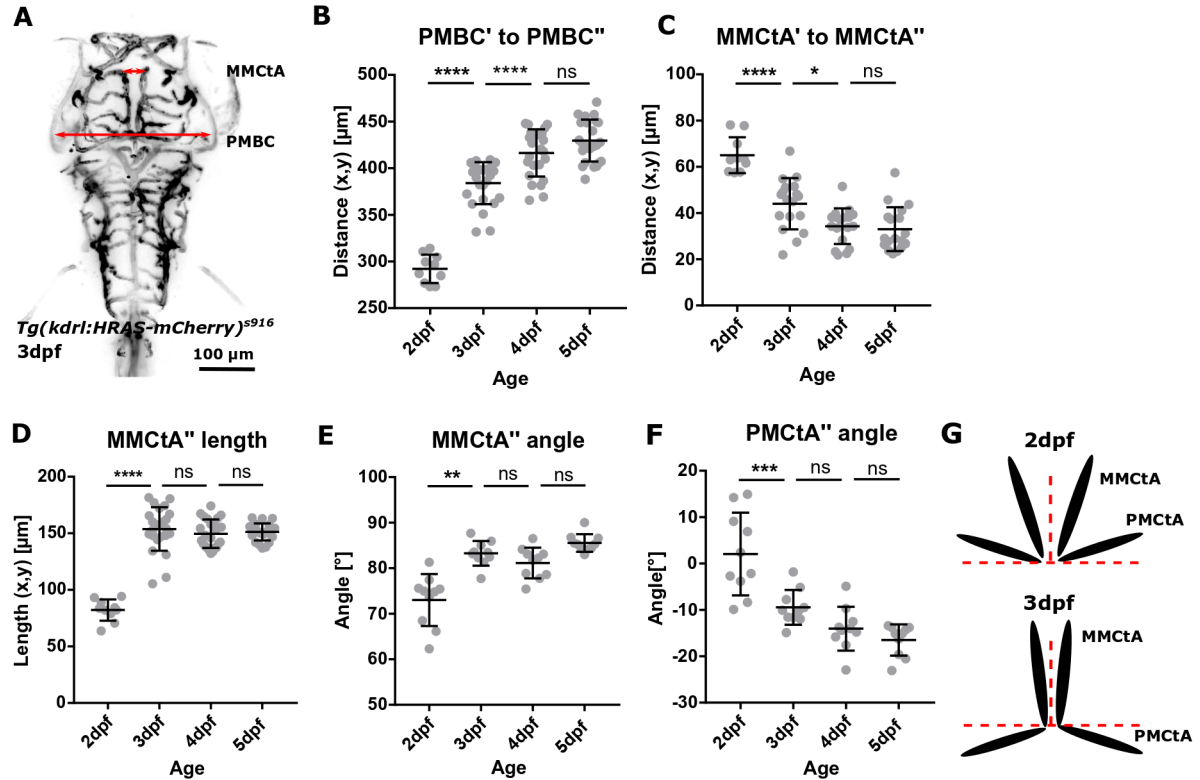


Figure 3.13: **Manual measurements of PMBC, MMcTA, and PMcTA show that samples of a certain age are comparable.** (A) Manual measurements of cranial vascular parameters were performed with focus on the PMBC and MMcTA. (B) Distance between PMBC' and PMBC'' significantly increased during early embryonic development ($p < 0.0001$; 2-3dpf $p < 0.0001$; 3-4dpf $p < 0.0001$, 4-5dpf $p = 0.1786$; 2dpf $n = 10$ (1 repeat), 3dpf $n = 25$, 4dpf $n = 25$, 5dpf $n = 25$; 3 experimental repeats; One-Way ANOVA). (C) Distance between anterior ends of MMcTA' and MMcTA'' decreased ($p < 0.0001$; 2-3dpf $p < 0.0001$; 3-4dpf $p = 0.0137$, 4-5dpf $p = 0.9739$; 2dpf $n = 10$ (1 repeat), 3dpf $n = 18$, 4dpf $n = 18$, 5dpf $n = 18$; 3 experimental repeats; One-Way ANOVA). (D) Length of MMcTA increased from 2-3dpf ($p < 0.0001$; 2-3dpf $p < 0.0001$; 3-4dpf $p = 0.7138$, 4-5dpf $p = 0.9773$; 2dpf $n = 10$ (1 repeat), 3dpf $n = 25$, 4dpf $n = 25$, 5dpf $n = 25$; 3 experimental repeats; One-Way ANOVA). (E) The MMcTA angle move towards the midline ($p < 0.0001$; 2-3dpf $p = 0.0028$; 3-4dpf $p > 0.9999$, 4-5dpf $p = 0.0657$; 2dpf $n = 10$, 3dpf $n = 10$, 4dpf $n = 10$, 5dpf $n = 10$; 2 experimental repeats; Kruskal-Wallis test). (F) Similarly, the PMcTA folded downwards ($p < 0.0001$; 2-3dpf $p = 0.0003$; 3-4dpf $p = 0.2790$, 4-5dpf $p = 0.7652$; 2dpf $n = 10$, 3dpf $n = 10$, 4dpf $n = 10$, 5dpf $n = 10$; 2 experimental repeats; One-Way ANOVA). (G) Angle of MMcTA and PMcTA were drastically changed from 2-3dpf.

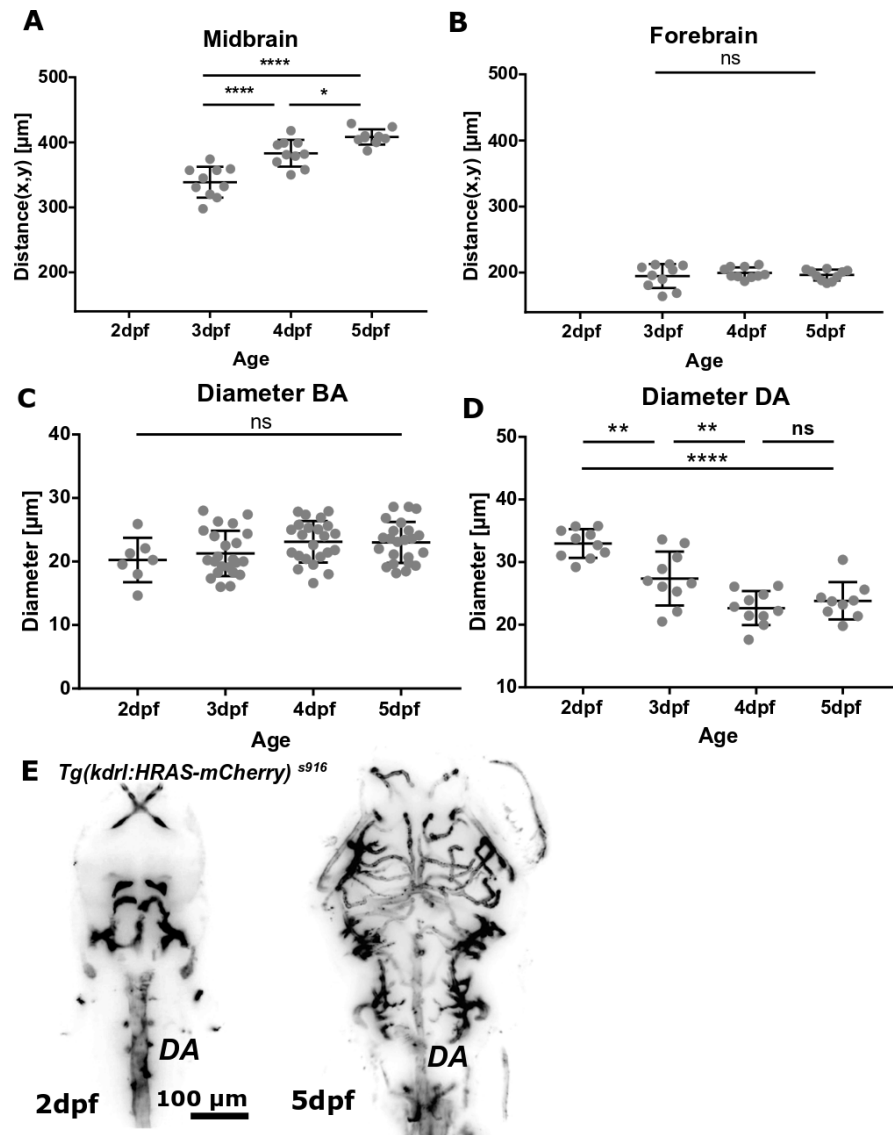


Figure 3.14: **Manual measurements of brain width, BA, and DA diameter.** (A) Manual measurement of midbrain width showed an increase from 3-5dpf ($p < 0.0001$; 3-4dpf $p < 0.0001$, 4-5dpf $p = 0.0187$; 3dpf $n = 10$, 4dpf $n = 10$, 5dpf $n = 10$; 2 experimental repeats; One-Way ANOVA). (B) No change was found in forebrain width from 3-5dpf ($p = 0.9560$; 3-4dpf $p = 0.6706$, 4-5dpf $p = 0.8360$; 3dpf $n = 10$, 4dpf $n = 10$, 5dpf $n = 10$; 2 experimental repeats; One-Way ANOVA). (C) Diameter of BA showed no difference from 2-5dpf ($p = 0.0809$; 2-3dpf $p = 0.8880$, 3-4dpf $p = 0.2688$, 4-5dpf $p = 0.9997$; 2dpf $n = 10$ (2 experimental repeats), 3dpf $n = 23$, 4dpf $n = 23$, 5dpf $n = 23$; 3 experimental repeats; One-Way ANOVA). (D) Diameter of DA decreased from 2-5dpf ($p < 0.0001$; 2-3dpf $p = 0.0021$, 3-4dpf $p = 0.0103$, 4-5dpf $p = 0.8496$; 2dpf $n = 10$, 3dpf $n = 10$, 4dpf $n = 10$, 5dpf $n = 10$; 2 experimental repeats; One-Way ANOVA). (E) Visual comparison of DA at 2dpf and 5dpf showed diameter constriction over time (substacks of representative images shown).

anatomical landmarks (Fig. 3.3) were suitable for registration when using rigid constraints (Fig. 3.15B). Importantly, this was the first ever inter-sample registration of the 3D zebrafish cerebral vasculature and no reference for registration performance was available.

Testing "2D/3D descriptor-based registration" with a variety of parameters did not result in enough inliers to allow for automatic registration. This was not surprising as the plugin was originally developed for registration of fiducial markers (beads and nuclei). We further examined this plugin in the scope of multiview reconstruction in chapter 5 section 5.2.5.

Visual assessment of registration outputs after automatic rigid registration, based on iterative optimization using scale space, suggested this method to be applicable to our data (Fig. 3.15C).

Applying anatomical landmark-based affine registration and thin-plate spline transformation both were unsatisfactory and were therefore not further investigated (Fig. 3.15D,E). Future studies might examine other implementations or registration approaches to examine how the degree of registration freedom impacts registration outcomes.

To quantitatively compare the registration outcome after rigid landmark-based and automatic registration, image similarity was quantified using the Dice Coefficient before and after registration.

This showed an improvement of sample overlap after registration (Fig. 3.15F; original-landmark-based registration $p = 0.0017$; original-automatic registration $p = 0.0003$; One-Way ANOVA), with a lower CoV after automatic registration (Table 3.1).

Although one could argue that a Dice Coefficient of about 0.5-0.6 is not very high, the presented registration methods were the first of their kind and no reference value for a "satisfactory" zebrafish cerebral vasculature registration existed. Also, the registration outcome was potentially impacted by the independent image acquisition, processing, and segmentation. Future work might address this by including examination with data augmentation. Still, we were confident that landmark-based and automatic rigid registration perform well enough to enable development and evaluation of methods that require alignment of embryos into one spatial coordinate system.

Table 3.1: Rigid landmark-based and automatic registration both increased sample overlap, but automatic registration delivered slightly higher mean values and lower coefficients of variation.

	Original	Landmark-based	Automatic
Mean	0.0586	0.4876	0.5845
Standard Deviation	0.01522	0.2379	0.09485
CoV	25.98%	48.79%	16.23%

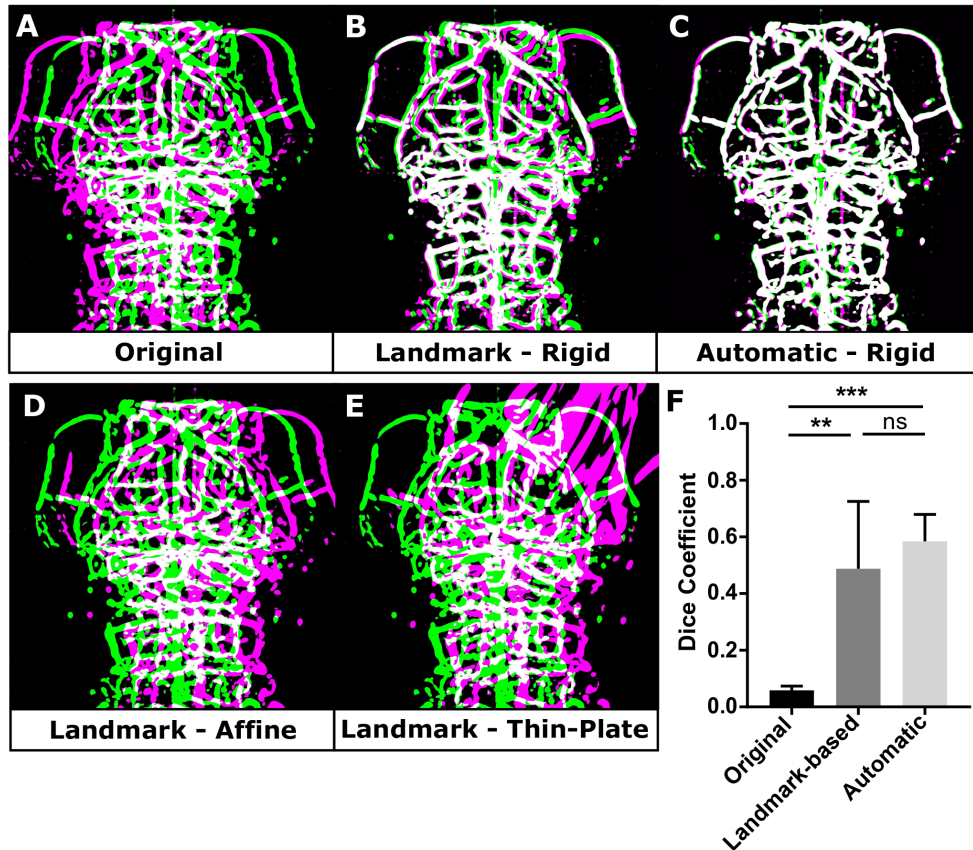


Figure 3.15: **Validation of the suggested inter-sample registration approaches show automatic registration to be more robust than manual landmark-based registration.** (A) Same sample from two acquisitions overlaid (green - target; magenta - moving image; white - overlap). (B) Samples after rigid anatomical landmark-based registration. (C) Samples after rigid automatic registration. (D) Samples after anatomical landmark-based affine registration. (E) Samples after anatomical landmark-based thin-plate spline transformation registration. (F) The Dice Coefficient was increased after landmark-based (p 0.0017) and automatic registration (p 0.0003; $n=5$; 3dpf; 3 experimental repeats; One-Way ANOVA).

Inter-sample registration can be performed from 2-5dpf and shows regions of vascular similarity

Having found that landmark-based and automatic rigid registration were both suitable to register samples, both methods were applied to bring samples from 2-5dpf into a common spatial coordinate system (Fig. 3.16A-C).

The Dice Coefficient was increased after inter-sample registration, with automatic registration delivering higher similarity than landmark-based registration (Fig. 3.16). The Dice Coefficient was only different after automatic registration at 3dpf (Fig. 3.16D; 2dpf $p = 0.2154$, 3dpf $p < 0.0001$, 4dpf $p = 0.3334$, 5dpf $p > 0.9999$) and no difference was found by landmark-based registration (2dpf $p > 0.9999$, 3dpf $p > 0.9999$, 4dpf $p > 0.9999$, 5dpf $p > 0.9999$).

Together, both methods were suitable to bring samples into one spatial coordinate system, but automatic registration showed an overall better performance. The overall low similarity suggested that even though regions of similarity were found between samples, overall vascular similarity was low.

While automatic registration delivered a quantitatively higher inter-sample overlap and required no observer-interaction, registration outcomes needed to be visually validated. In the 2-5dpf dataset only one sample was incorrectly registered (anterior-posterior axis along dorsal-ventral; 1 out of 37 samples). In future, this visual assessment of registration accuracy could be replaced by automatically flagging up registration errors, ie. sub-threshold Dice scores. Together, the advantage of automatization and higher registration accuracy of the automatic registration method outweighed the initial approach of manual landmark-based registration.

3.3.3 Establishment of vascular templates allows the study regions of similarity and variability

To further examine the local similarity and variability between samples, vascular templates were established initially in 2D showing various regions of similarity from 2-5dpf (Fig. 3.17).

To visualize vascular similarity in 3D, sample overlap was examined after manual landmark-based (Fig. 3.18) and automatic (Fig. 3.19) registration to an individual template embryo and regions of similarity were extracted based on voxel similarity (Fig. 3.6). This showed high similarity of vessels formed by vasculogenesis between samples.

Once the vascular templates were produced with landmark-based and automatic rigid registration, these templates were compared to each other from 2-5dpf (Fig. 3.20A). Comparison of the overlapping regions (Fig. 3.20B,C) showed again that it was the main

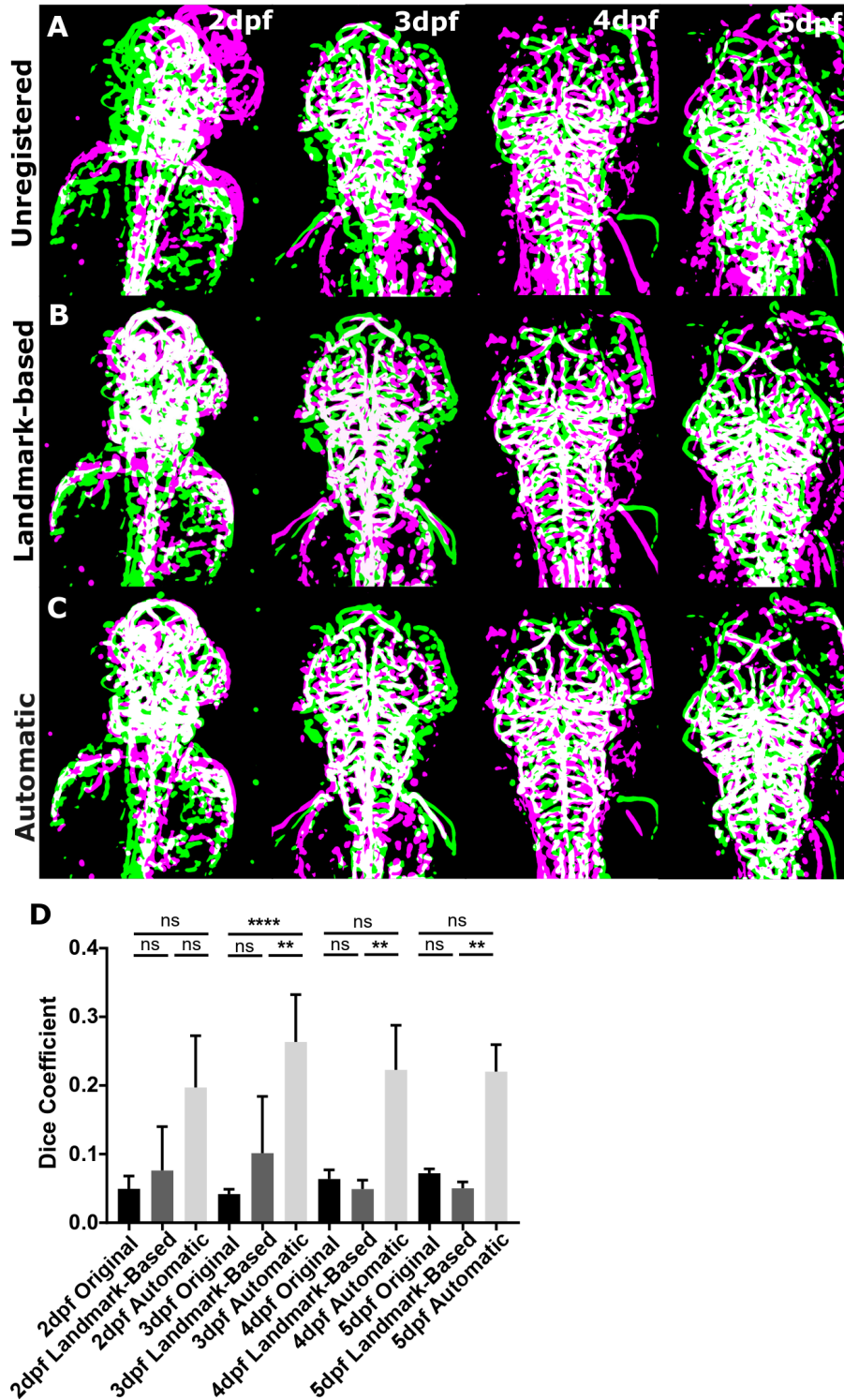


Figure 3.16: **Quantification of vascular similarity from 2-5dpf.** (A) MIP of unregistered samples (green - target, magenta - moving image, white - overlap). (B) MIP of samples after landmark-based rigid registration. (C) MIP of samples after automatic rigid registration. (D) The Dice Coefficient between target and moving image was increased after application of rigid registration using anatomical landmark-based and automatic rigid registration (2dpf $n=7$, 3dpf $n=10$, 4dpf $n=10$, 5dpf $n=10$; 2 experimental repeats; Kruskal-Wallis test).

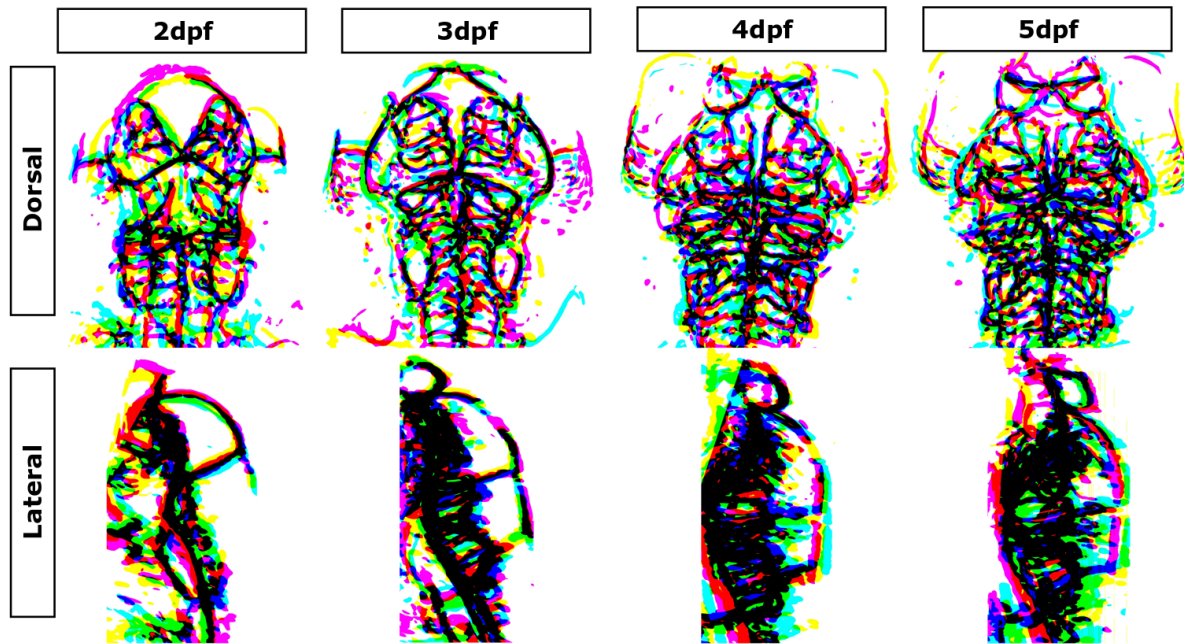


Figure 3.17: **MIPs of vascular similarity at 2-5dpf.** 2D MIP of three registered samples (magenta, cyan, yellow), showing regions of similarity between samples (black).

vessels which were overlapping between the two templates and that similarity decreased over time (table 3.2).

Table 3.2: Measurement of similarity between landmark-based and automatic registration shows overall low values of percentage of vascular voxels in images (*Abbrev.: vv- Vascular voxels in % of whole image*) and a decrease of similarity with age, with lowest values at 5dpf.

	vv landmark-based template	vv automatic template	vv both	Dice
2dpf	0.77	1.17	0.22	0.227
3dpf	1.30	1.21	0.43	0.257
4dpf	2.13	1.92	0.59	0.289
5dpf	1.83	2.52	0.30	0.137

This suggested that there were vascular regions which were similar enough between fish to establish vascular templates of similarity from 2-5dpf with either registration method, but that it is only the main vessels showing similarity between samples.

Importantly both inter-sample registration methods (landmark-based and automatic) were so far only performed using one target fish (target selected based on (a) sample orientation along common image axis (see section 3.2.6), (b) all common vessels visualized in image, (c) no obvious abnormalities), which could potentially introduce target bias. Thus, after this initial registration using a single target, averaging was performed based on voxel-similarity (Fig. 3.6) and samples re-registered to this averaged target.

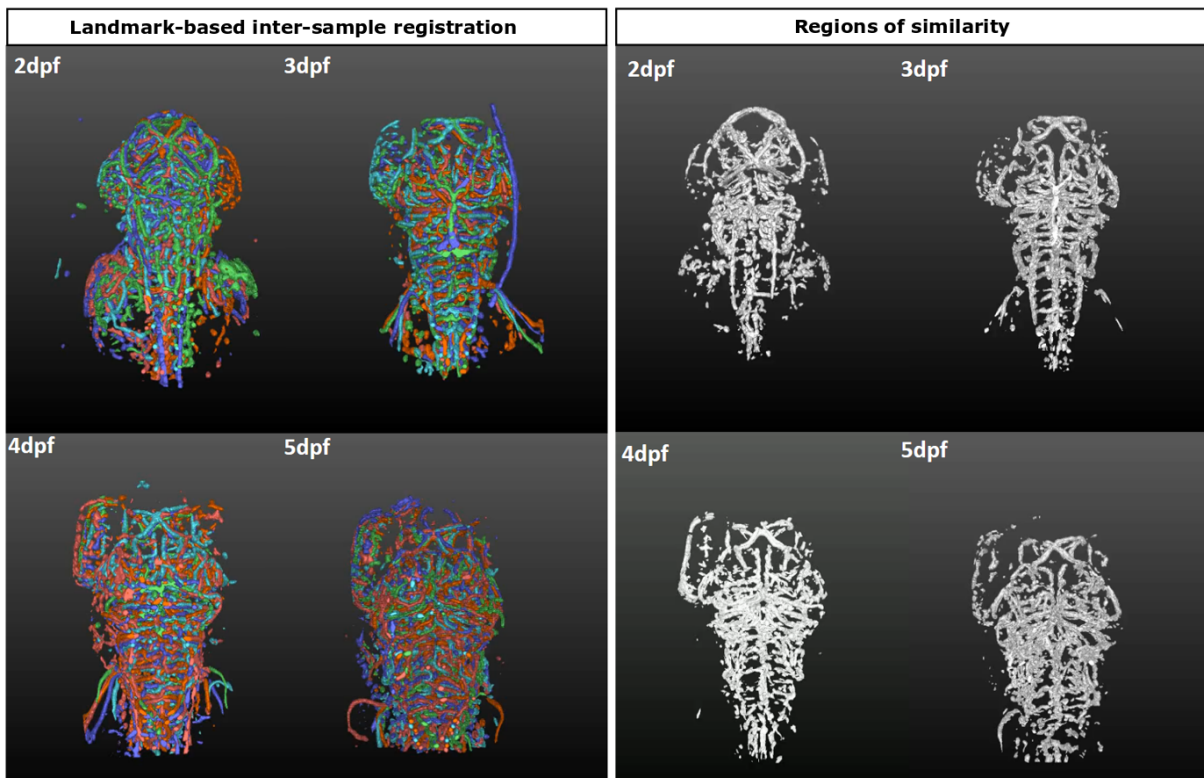


Figure 3.18: **3D vascular similarity between samples after landmark-based registration.** Samples were registered using landmark-based rigid registration ($n=6$ for each time point; colours represent different embryos) and regions of similarity in 3D extracted by voxel overlap (white).

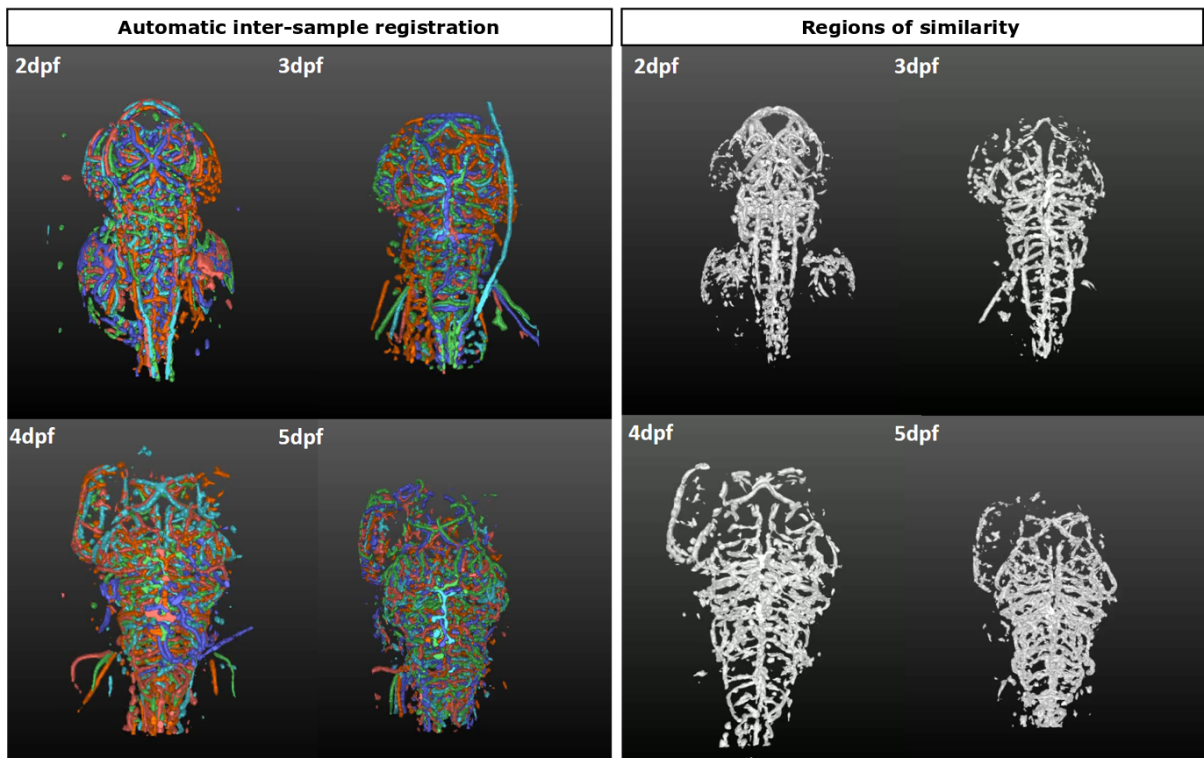


Figure 3.19: **3D vascular similarity between samples after automatic registration.** Samples were registered using automatic rigid registration (n=6 for each time point; colours represent different embryos) and regions of similarity in 3D extracted by voxel overlap (white).



Figure 3.20: **Overlap of average templates established using 3D manual landmark-based and automatic registration.** (A) Average templates established using 3D manual landmark-based (green) and automatic (magenta) registration from 2-5 dpf. (B) MIP of 3D overlapping voxels. (C) Depth-coded overlapping voxels shows anatomical location of vascular similarity (purple - ventral, white - dorsal).

Comparing image overlap between unregistered (Fig. 3.21A-D), landmark-based registration to one target (Fig. 3.21E-H), automatic registration to one target (Fig. 3.21I-L), and automatic registration to averaged target (Fig. 3.21M-P), suggested that all three registration methods were suitable for inter-sample registration at 2dpf and 3dpf. At 4dpf and 5dpf (Fig. 3.21), automatic registration to the averaged target delivered less satisfying results in comparison to landmark-based registration and automatic registration to one target. This may have been due to image features that drive the registration being blurred during the template averaging process, which would be expected to have greater influence as the developing vasculature becomes more intricate.

In summary, this suggested that automatic registration delivers better registration outcomes than landmark-based registration (Fig. 3.16) and that registration to an individual target delivers consistently better registration outcomes than registration to an averaged target (Fig. 3.21).

Based on the above results and visual comparison of 3D registered samples, schematic templates of vascular similarity were established from 2-5dpf (Fig. 3.22A-D).

3.3.4 Inter-sample image registration to examine the impact of *dll4* knockdown

Having established a successful registration approach, it was used to examine the impact of *dll4* loss on inter-sample vascular similarity.

First, overall vascular properties were compared, finding clear differences when comparing controls (Fig. 3.23A, white) to *dll4* morphants (red). In *dll4* morphants, a reduction of vascular volume (p 0.0017; Fig. 3.23B), surface (p 0.0006; Fig. 3.23C), and density (p 0.0028; Fig. 3.23D) was found in comparison to control morpholino injected samples.

Next, samples were registered to an uninjected control target. Quantification of Jaccard Index (Fig. 3.24A), Dice Coefficient (Fig. 3.24B), and Total Overlap (Fig. 3.24C) showed an increase of similarity when comparing unregistered and registered uninjected controls (p 0.0001 for all). Comparing uninjected controls to *dll4* MO showed no difference in Jaccard Index (p 0.9573), Dice Coefficient (p 0.3888) or Total Overlap (p 0.5563). While a difference was found when comparing control MO to *dll4* MO in Jaccard Index (p 0.0439) and Total Overlap (p 0.0189), but not in Dice Coefficient (p 0.3888). The bimodal distribution observed in the *dll4* MO data was thought to be due to overall dataset variability (eg. morpholino injection variability).

Following, sample groups were compared to each other. To achieve this, sample averages of uninjected controls (Fig. 3.25A), control MO (Fig. 3.25B), and *dll4* MO (Fig. 3.25C) were established (again using voxel similarity between samples; Fig. 3.6; $n=6$). As expected, comparing the average template of uninjected controls to control MO showed a higher

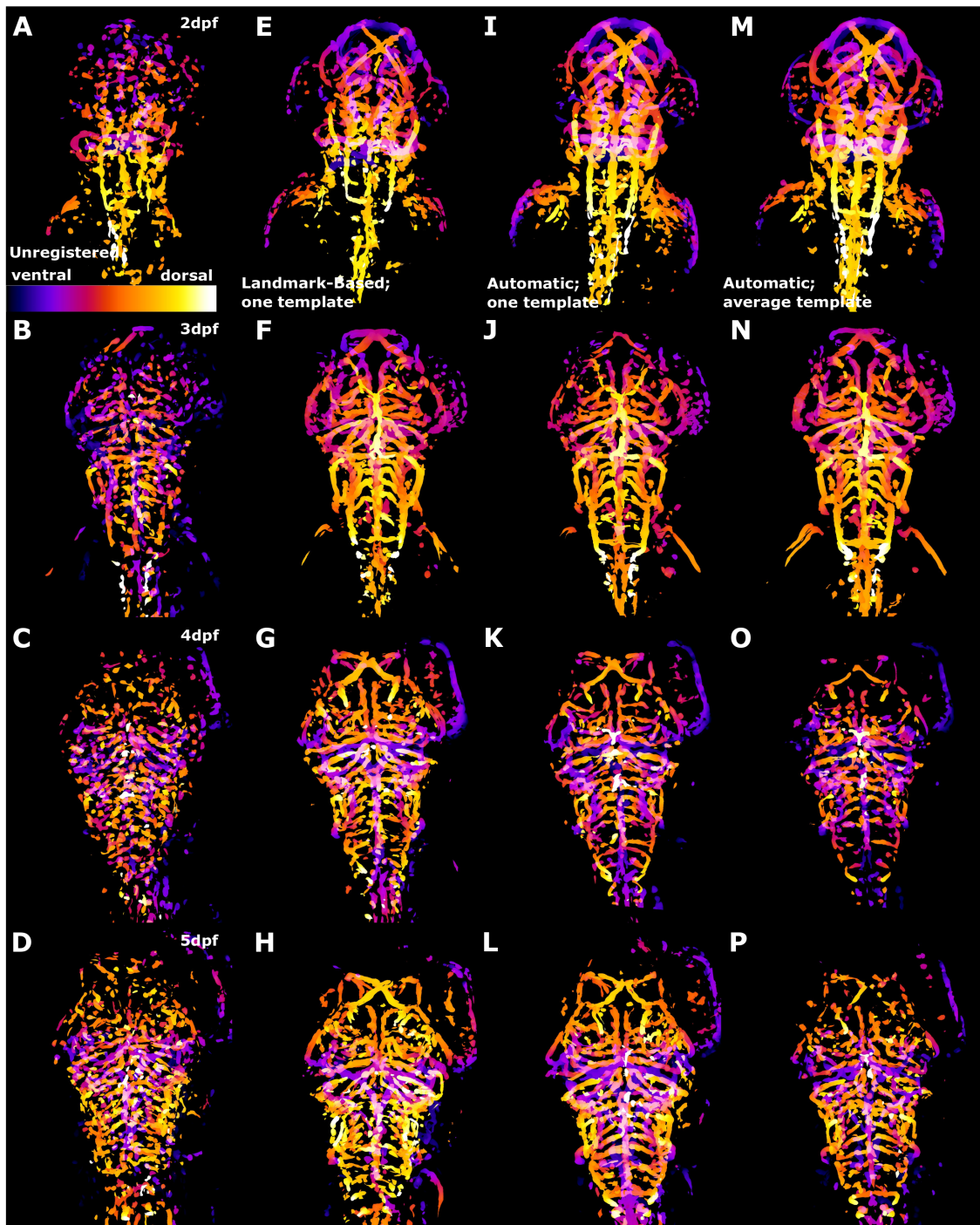


Figure 3.21: **Comparison of inter-sample registration methods.** Depth-coded MIP showing regions of overlap (purple - ventral, white - dorsal). **(A-D)** Overlap of unregistered samples from 2-5dpf. **(E-H)** Overlap of samples after landmark-based registration to individual registration target from 2-5dpf. **(I-L)** Overlap of samples after automatic registration to individual registration target from 2-5dpf. **(M-P)** Overlap of samples after automatic registration to averaged registration target from 2-5dpf (n=6 larvae each; depth-coded: ventral - purple, dorsal - white).

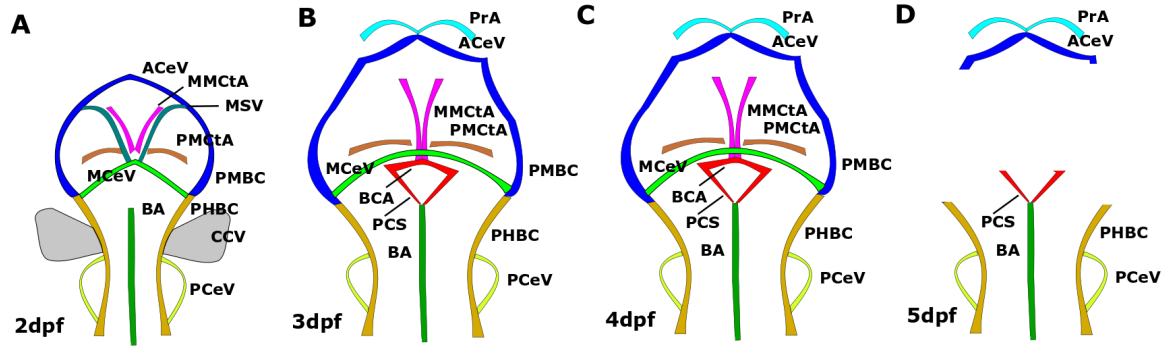


Figure 3.22: **Schematic vascular templates 2-5dpf.** (A-D) Schematic showing regions of high similarity between samples from 2-5dpf.

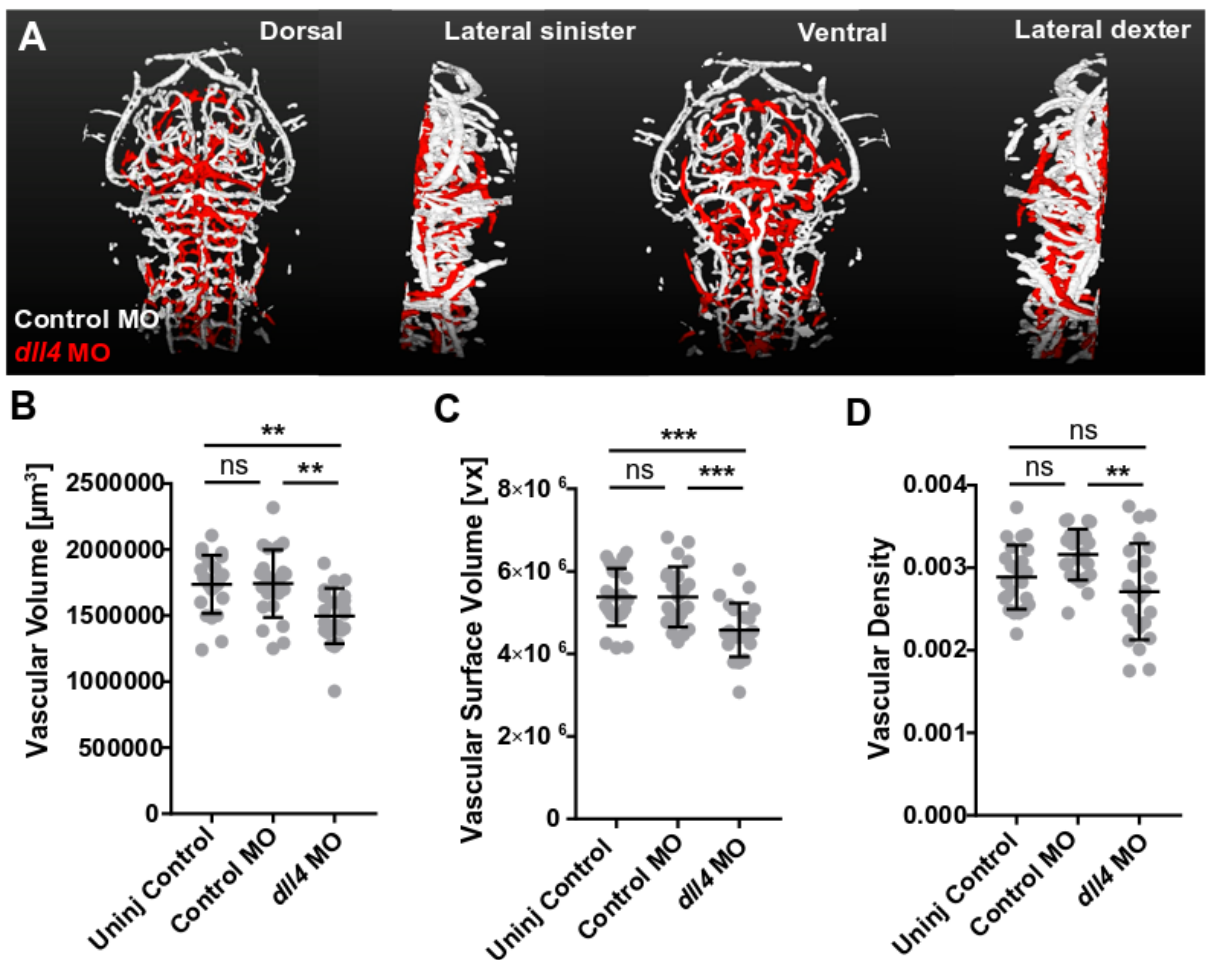


Figure 3.23: (A) Images show 3D structure of control morphants (white) and *dll4* morphant (red), showing clear structural differences. (B) Vascular volume was decreased in *dll4* morphants in comparison to uninjected controls (p 0.0023) as well as control morphants (p 0.0017; n=23; 3dpf; 3 experimental repeats; One-Way ANOVA). (C) Vascular surface was decreased in *dll4* morphants in comparison to uninjected controls (p 0.0007) as well as control morphants (p 0.0006; One-Way ANOVA). (D) Vascular density was not changed comparing uninjected controls to *dll4* morphants (p 0.3718), but was decreased in comparison to control morphants (p 0.0028; One-Way ANOVA).

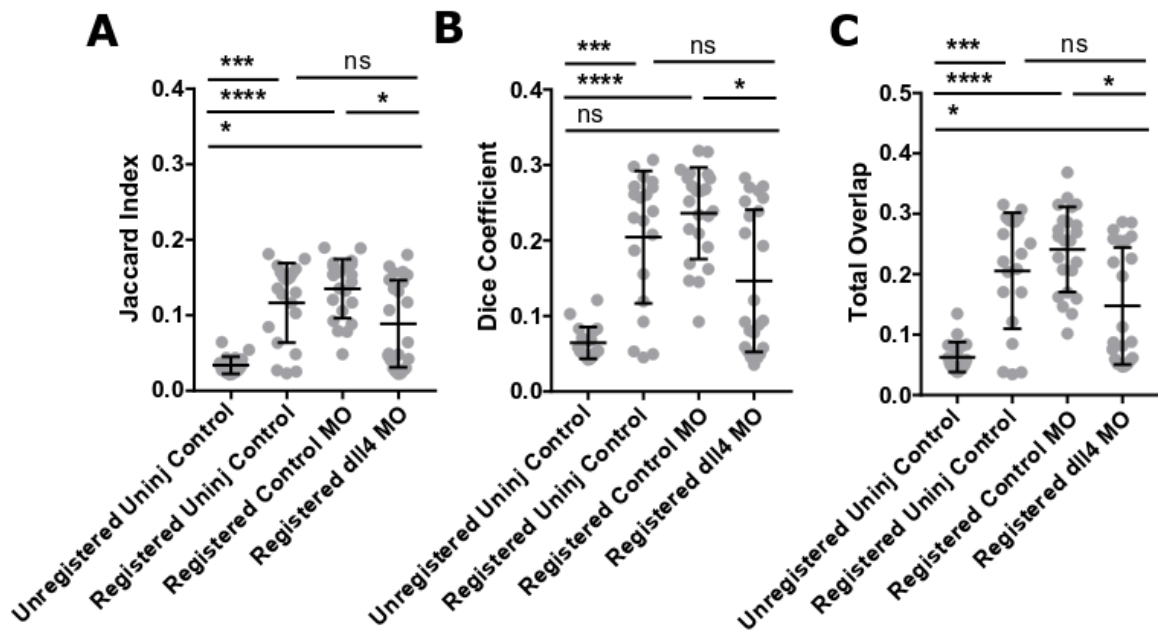


Figure 3.24: **Quantification of registration to single sample target to study impact of *dlla* MO.** (A) Jaccard index showed a difference between control MO and *dlla* MO (p 0.0439), but not uninjected controls (p 0.9573; $n=23$; 3dpf; 3 experimental repeats; Kruskal-Wallis test). (B) Dice coefficient showed a difference between control MO and *dlla* MO (p 0.0103), but not uninjected controls (p 0.3888; Kruskal-Wallis test). (C) Total Overlap showed a difference between control MO and *dlla* MO (p 0.0189), but not uninjected controls (p 0.5563; Kruskal-Wallis test).

similarity (Dice 0.684; Fig. 3.25D) than comparing uninjected controls to *dll4* MO (Dice 0.259; Fig. 3.25E). When comparing average templates of uninjected controls to *dll4* MO (Fig. 3.25F) it was found that AMcTA, PCeV, PHBC, and BA were developed structurally normal in *dll4* MO at 3dpf.

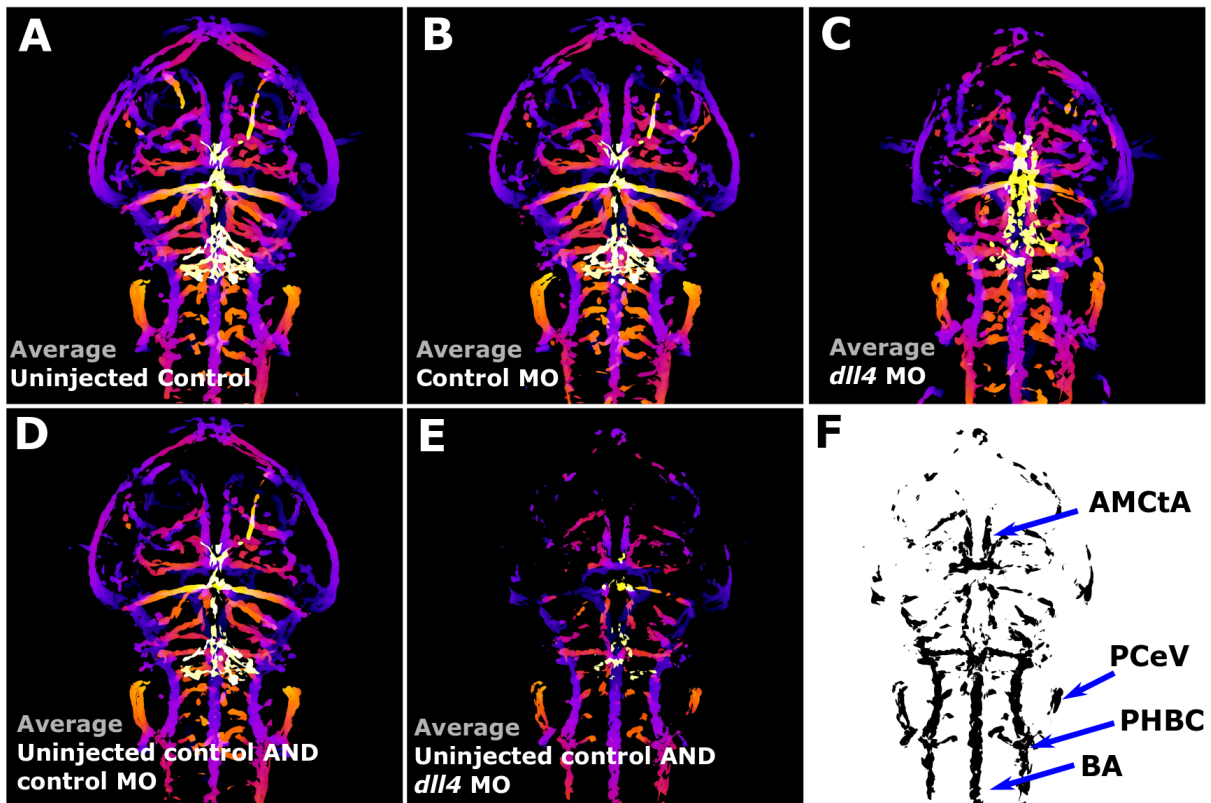


Figure 3.25: **Comparison of average templates of uninjected control, control MO, and *dll4* MO.** (A) Average template of uninjected controls. (B) Average template of control MO. (C) Average template of *dll4* MO. (D) Overlap of average template of uninjected control and control MO. (E) Overlap of average template of uninjected control and *dll4* MO. (F) Overlap of average template of uninjected control and *dll4* MO shows that AMcTA, PCeV, PHBC, and BA are developed normally in *dll4* MO at 3dpf (A-E depth-coded MIP ventral - purple and dorsal - white; n=6).

3.4 Conclusion

Based on the establishment of an image analysis workflow to assess intra-sample symmetry we showed that the cranial vascular topology in embryonic zebrafish does not display a dominant/adominant side at the investigated time points. Furthermore, the BA, PHBC, and PMBC are more symmetric than the CtAs and MMcTAs.

Knock-down of *dll4* resulted in decreased embryonic and vascular growth, but no changes in vascular symmetry were observed, suggesting that *dll4* is required for embryonic and/or

vascular growth and maturation, but is dispensable for symmetry establishment at the investigated time-point.

Using visual assessment and manual measurements of vascular similarity between samples allowed the identification of anatomical landmarks for landmark-based inter-sample registration. We showed that anatomical landmark-based inter-sample registration is applicable to bring embryos into one spatial coordinate system, using both original or segmented data. Testing readily available registration methods in Fiji, we found that rigid, but not affine, nor thin-plate spline registration was applicable to our data. Future work might examine other implementations of registration methods with higher degrees of freedom.

Our data showed that automatic rigid inter-sample registration allows registration of samples, but requires images to be segmented to deliver meaningful results, while descriptor-based registration did not result in a meaningful registration of our data using either original or segmented data.

After validation of the proposed registration approaches using consecutive acquisition of the same sample with altered positioning, we investigated inter-sample similarity and variability from 2-5dpf. Both, rigid landmark-based and automatic registration, were applicable to bring embryos at these ages into one spatial coordinate system, with automatic registration delivering higher values of similarity between samples. Data from both registration methods suggest that vascular similarity is highest at 2-3dpf and that similarity decreases with age. Overall similarity between samples was low (as quantified using the Dice Coefficient), suggesting that only a subset of vessels are highly similar between samples, namely the main vessels such as BA, PHBC, and PMBC. Future work could examine regional similarity and variability, by combining the presented registration approach with quantification methods described in Chapter 4 to extract individual vascular segments.

Examining the impact of target averaging, it was found that registration to individual samples actually delivered better results and future work might examine alternative sample averaging procedures.

Identifying inter-sample similar vessels showed a similarity to intra-sample left-right vascular symmetry, suggesting that vessels which are left-right symmetric are also highly similar between samples.

Future work could identify which factors influence vessels to be stereotypic or stochastic in topology. Future studies could also examine whether vascular topological asymmetry can be observed in older zebrafish and whether this is related to (a)symmetric blood flow. We anticipate that our approach to examine vascular asymmetry will be applicable to examine the

role of compounds and genes in the development of cerebrovascular (a)symmetry.

4 Extraction of Vascular Geometry

4.1 Introduction

The 3D vascular anatomy can be described by geometric shape descriptors such as branching pattern, length, diameter, and curvature (Fig. 4.1).

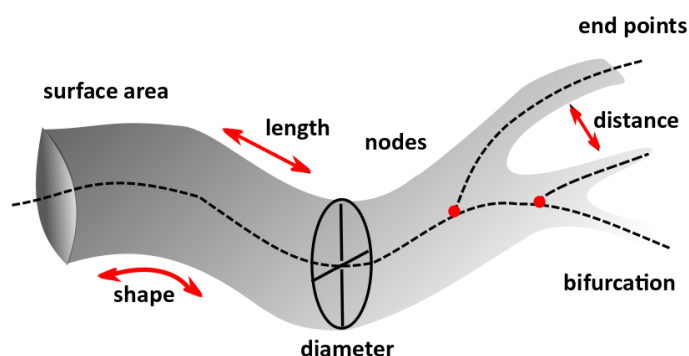


Figure 4.1: **Parameters to describe the vascular architecture.** Common mathematical shape descriptors can be applied to describe the local and global vascular architecture.

Following enhancement and segmentation, a variety of approaches can be used to extract these geometric shape descriptors (reviews [85, 86, 87]). Centreline extraction approaches can be broadly grouped as follows: **(i)** iterative thinning via layer-by-layer removal [88, 89], **(ii)** centre of maximally inscribed discs (2D) or spheres (3D) [318], **(iii)** eigenvalues and eigenvectors [101, 151, 152, 319], **(iv)** intensity ridge detection [320], **(v)** Voronoi diagram based [163] as applied in [321, 322], **(vi)** Dijkstra's shortest path [323, 324, 325], **(vii)** fluid dynamics [326], or **(viii)** distance transform from border [327].

While 2D object centrelines are called medial axis transform (MAT) [88], 3D skeletons are called medial surface [91, 94], surface skeleton [328], curve skeleton [121, 186] or centrelines [320, 329]. In the following, vascular centrelines will be referred to as centreline or skeleton.

In 2007, Cornea et al. [121] proposed the following requirements should be fulfilled by object skeletons. **(i) Homotopy:** Centrelines shall preserve and represent the topology and geometry of the original object, i.e. no shrinking or left-right-bias [115, 318, 330]. **(ii) Isometric transformation invariance:** Skeleton shape descriptors shall be invariant to object transformation and orientation, especially if centrelines are used for inter-sample registration, as for example proposed by [331, 332, 333, 334]. **(iii) Reconstructability:** 3D volume reconstruction from centrelines can be a useful application for volumetric animation, but is not

always a requirement if deriving 3D skeletons [174, 335, 336, 337]. **(iv) Thinness:** Centrelines shall be one-voxel-thick representations of the original objects. Whereas vessel segment voxels have two neighbours, endpoints have one and branching points (BPs) may have three or more (Fig. 4.2) [89]. As loops in the vasculature represent a special case of true object cavities, special definitions are required, as described in [123, 124]. **(v) Centredness:** Skeletons shall be positioned on the object medial axis, but may be spatially relaxed if centredness can not be achieved, as in the case of surface medial axis, which may be disturbed by surface inhomogeneity [140]. **(vi) Reliability:** All boundaries shall be used to produce a skeleton, which will in turn see all the respective boundary points. This ensures all-voxel inclusion and "insideness" (centreline does not cross object boundary and vice versa) [338]. **(vii) Component differentiation:** Based on centreline extraction, junction points can be used to extract object components, here vessel segments. These may be distinguished later based on hierarchical structuring, such as graph theory or Strahler order numbers [115, 133, 339], which represent the object intrinsic hierarchy [186]. **(viii) Smoothness:** Object centrelines shall be smooth (avoidance of pixelation or staircasing), whilst preserving object homotopy. **(ix) Robustness:** Extracted skeletons should be independent of noise levels (see homotopy of geometry). **(x) Connectedness:** One-voxel-thick skeletons should preserve object continuity.

One of the most commonly used methods to analyse object topology is the extraction of vascular centrelines by iterative thinning [88, 89], which, together with vascular wall information, allows quantification of vessel diameter, length, curvature and BPs. In the Fiji image analysis framework a 3D thinning approach was already implemented (2D/3D skeletonize).

As images are based on voxels in x,y,z-dimensions, centrelines derived by iterative thinning of segmented objects are constituted by individual centreline voxels which share connectivity, thus a relationship to each other. This relationship (R) between voxel a and voxel b can be described as path $\pi(a,b,R)$ given by voxel sequences $(a_1, a_2, .. a_n)$ [340].

A voxel itself has a volume, faces, edges, and vertices (Fig. 4.2A). Following, the relationship of a voxel to its neighbours can be used to determine its identity (Fig. 4.2B) [115, 341]: **(i)** centreline endpoints have one 26-neighbour (Fig. 4.2C), **(ii)** vessel segments having two 26-neighbours, **(iii)** bifurcation or BPs having more than two 26-neighbours, **(iv)** loops will be constituted by two bifurcation/BPs being connected by vessel segment voxels.

To assign these centreline voxel identities and detect BPs commonly two approaches are used:

(1) *Object based:* User identifies skeleton starting point and algorithm subsequently identifies

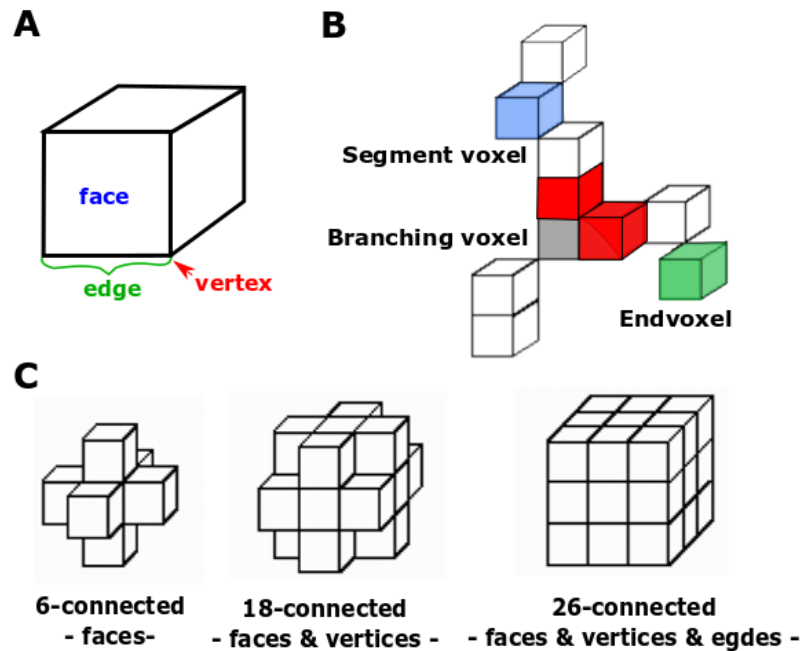


Figure 4.2: **Classification of voxel identity.** (A) A voxel itself has a volume, faces, edges, and vertices. (B) Relationships between voxels determine their individual identity. (C) Voxel-neighbourhoods are used to determine voxel relationships such as segment (blue), branching (grey), or end (green). Images B and C adapted with permission from [341].

connected skeleton voxels by iterative neighbourhood assessment and assigns voxel identity by 26-neighbourhood status (Fig. 4.3A). As not all image voxels are visited this approach is less computationally demanding, but requires user interaction to assign starting voxel. To overcome this user input, automated starting point detection could be implemented by initial detection of a skeleton voxel of a vessel which always shows the same location/anatomy. In embryonic zebrafish this could for example be the BA if the fish is aligned anterior-posteriorly along the Y-axis, the left-right aligned along X-axis, and dorso-ventral aligned along Z-axis. The starting point would be the voxel which has the highest Y value and is most central in X and Z. As images are not perfectly aligned the orientation of BA may be skewed and therefore the implementation of an automated starting detection would either require ideal image acquisition or sample registration prior to skeleton analysis. The advantage of this object based approach is the possibility to assign vascular hierarchy simultaneously by increasing the branch order number after each nodes/BP (Fig. 4.3B) [133]. The downside of this object based approach is that it requires complete skeleton connectivity to be able to iterate through the skeleton as any breaks would halt the algorithm.

(2) *Raster based*: Each voxel is visited in a raster based approach (eg $X_0..X_n$, $Y_0..Y_n$, $Z_0..Z_n$; Fig. 4.3C) and voxel identity assigned by 26-neighbourhood status. Although this approach

is slower and a hierarchy assignment less straightforward, the lack of connectivity requirement makes this approach often favourable.

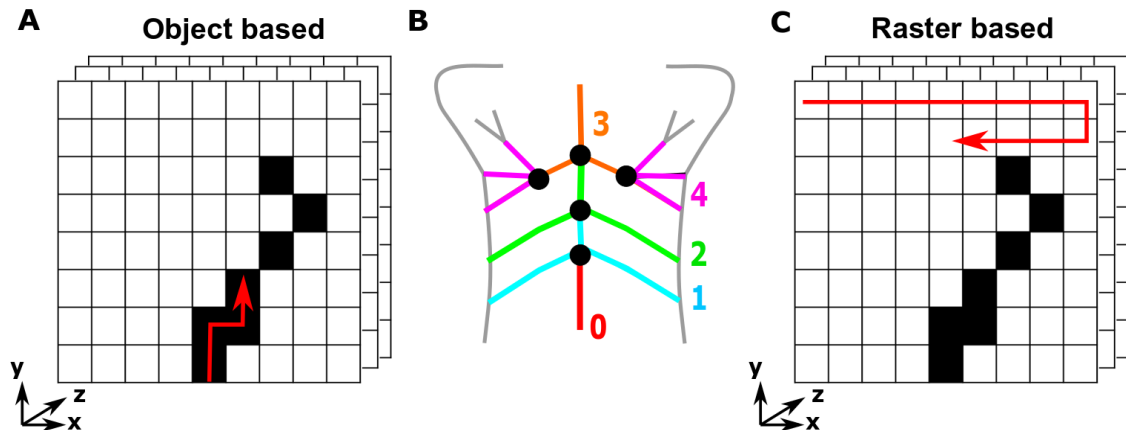


Figure 4.3: **Voxel identity assignment.** (A) Object based approaches require a start point. The algorithm subsequently identifies connected skeleton voxels by iterative neighbourhood assessment and assigns voxel identity by 26-neighbourhood status. (B) Vascular hierarchy can be assigned using graph theory (nodes - black - BPs; leaves - colour - vessel segments). (C) Raster based approaches do not require a start point, but iterate through the whole image visiting all voxels to assign identity based on 26-neighbourhood status.

For the analysis of centrelines a ridge detection based approach (Ridge Detection [342]) and a 3D thinning based approach with raster-based analysis (AnalyseSkeleton 2D/3D Plugin [126]) were already implemented in Fiji.

Additional parameters to describe vascular geometry are vascular hierarchy and complexity. **Vascular hierarchy** can be used to describe vascular geometry by the number of branch orders after nodes/BP and was originally used in hydrology to indicate the level of branching in a river system called "Strahler analysis" (Fig. 4.3B) [133].

Vascular complexity can be described in various ways but is often assessed by the number of branches distally from a selected centre. One commonly applied method is "Sholl analysis", which was originally used to describe neuronal branching, quantifies the number of intersections along concentric spherical shells with increasing diameter [343].

In this chapter the following key questions are examined:

(i) **Is the Fiji ridge detection plugin applicable to extract and analyse the 2D and/or 3D vasculature?** Here it will be examined whether ridges are detected correctly, whether analysis extracts branching points and vessels, and whether the method is sensitive enough to extract biologically meaningful insights.

(ii) **Is 3D thinning applicable to extract and analyse the 2D and/or 3D vascular skeletons?** Applying the "2D/3D Skeletonize" plugin the outcomes of 3D thinning in respect to

the requirements postulated by Cornea et al. [121] will be studied, and the "AnalyseSkeleton 2D/3D" Plugin branching point detection examined.

(iii) How can vascular diameters be described on a voxel, local, and global level? Euclidean Distance Maps (EDMs) [344], which compute 3D discrete distance transforms from the boundary to centre of the segmented vasculature, returning greylevel intensities of foreground (vascular) regions based on distance to the closest boundary, will be examined.

(iv) Is a combination of a 2D and 3D approach applicable to extract information about individual vascular segments? So far, no method exists to examine vascular information on the level of individual segments in 3D for the zebrafish cerebral vasculature, but as lightsheet data are very large in size, it will be examined whether a combination of a 2D and 3D computational approach will allow the extraction of information of individual vascular segments.

(v) Can 2D branching analysis be applied to describe vascular network complexity? Sholl dendritic arbor analysis [343] is a method using a series of concentric shells (circles or spheres), counting the number of branch intersections per sampling shell. The number of shells and distance from centre can be used to examine branching complexity (shell intersection numbers) and overall vascular size (shell distance from centre).

Following the initial examination of the above analysis approaches, cases for validation and biological application will be presented. These include:

(i) Zebrafish with and without blood flow, which is achieved by inhibition of the development of a protein required for cardiac contraction via morpholinos, namely *tnnt2a* [345]. The lack of blood flow results in visibly impacted vascular growth. Thus, this dataset is used to test whether the suggested methods are able to extract and quantify vascular differences between samples.

(ii) Vascular development from 2-5dpf. It is thought that vascular complexity, length, and volume will increase during development, but no quantification has so far ever been conducted and the extent of vascular changes over time are not known.

Following the development and testing of the individual image analysis steps, the developed workflow will be integrated into one workflow as Fiji Macro, a graphical User Interface (GUI) established, and appropriate workflow documentation produced to allow usability, distribution, and application by other researchers.

4.2 Material and methods

4.2.1 Zebrafish strains, handling, and husbandry

Zebrafish handling and husbandry were performed as described in 2.2.1. *Tg(kdrl:HRAS-mCherry)^{s916}* [244] line was used for vasculature visualization.

4.2.2 Biological application datasets

Examining vascular development from 2-5dpf

To study vascular development data were acquired from 2-5dpf in *Tg(kdrl:HRAS-mCherry)^{s916}* [244].

Inhibition of VEGF and Notch signalling

To examine the impact of inhibiting VEGF and Notch signalling drug treatments were performed. VEGF signalling was inhibited using VEGF receptor inhibitor AV951 [266] at 250nM for 2h from 96-98hpf (Selleckchem; S1207; Tivozanib - AVEO pharmaceuticals). Notch signalling was inhibited using 50 μ M DAPT (Sigma-Aldrich; D4952) for 12h from 84-96hpf [265]. Controls for both experiments were performed using the same concentration and duration of DMSO during active treatments.

F-actin polymerization inhibition

F-actin polymerization inhibition was achieved by application of 100nM Latrunculin B for 1h between 96-97hpf (Sigma-Aldrich; L5288-1MG; kindly provided by Rob Wilkinson) [346]. DMSO control at the same concentration and duration.

Lack of blood flow by *tnnt2a* MO

Development of functional heart contraction was inhibited via injection of cardiac troponin T2a (*tnnt2a*) ATG morpholino (1.56 ng final concentration), as described in [345] (sequence 5'-CATGTTTGCTCTGATCTGACACGCA-3').

Control morpholino injections (5'-CCTCTTACCTCAGTTATTTATA-3'; no target sequence and little/no biological activity; Genetools, LLC) were performed with the above final concentration to study off-target effects of injections. Injections were conducted at one-cell-stage using phenol red as injection tracer.

4.2.3 Imaging methodology

Image acquisition was performed as described in section 2.2.2.

4.2.4 2D ridge detection and analysis

Following image pre-processing and segmentation, EDMs were produced from binary segmented images using the Fiji plugin "Distance Map 3D" (Process > Binary > Distance Map in 3D; https://imagej.net/Distance_Transform_3D, implemented by Jens Bache-Wiig and Christian Henden [344]) and ridges were extracted in 2D MIPs and 3D stacks using the Fiji "Ridge Detection" Plugin implemented by Thorsten Wagner and Mark Hiner based on [342] (Plugins > Ridge Detection).

4.2.5 Centreline extraction based on 3D thinning

Centreline extraction was performed after image pre-processing and segmentation using the Fiji "Skeletonize 2D/3D" Plugin (by Ignacio Arganda-Carreras), based on 3D thinning proposed by [91], using a layer-by-layer removal as shown in (Fig. 1.5). Total network length was quantified as centreline voxels (0 value) in the selected ROI (as described in section 2.2.6).

4.2.6 2D/3D centreline analysis, branching point processing, and vessel segment identification

The "Analyse Skeleton" Plugin in Fiji (Analyse > Skeleton > Analyse Skeleton 2D/3D; by Ignacio Arganda-Carreras) [126] was used. It relies on a raster-based analysis approach to identify and assign voxel identities based on a 8-voxel-neighbourhood in 2D MIPs and 26-voxel-neighbourhood in 3D stacks. It delivers assignment of BPs and end points (EPs), BP position, branch length, Euclidean distance, and mean intensity of centreline voxels.

4.2.7 Vessel diameter analysis

To assess required vessel diameter sampling rates manual measurements were performed in three cerebral vessels (MMcTA, ACeV, and CtA) and one trunk vessel (first ISV). Using linear ROIs diameters were measured along three and ten points along the vessel (first and last measurement location were placed 10 μ m from respective bifurcations, remaining measurement points were placed equally along vessel depending on length).

EDMs were produced from binary segmented images using the Fiji plugin "Distance Map 3D" (Process > Binary > Distance Map in 3D; https://imagej.net/Distance_Transform_3D, implemented by Jens Bache-Wiig and Christian Henden [344]).

For automatic quantifications of average diameter in MIPs, EDMs were produced in 2D. To derive 1-voxel-thick EDMs, the produced EDM was merged with the extracted skeleton (Process> imageCalculator > "AND create") and LUT "Fire" was applied for visualization purposes. For visual representation, 3D skeletons were again skeletonized after creation of MIPs to ensure 1-voxel-thickness of the centreline.

The resulting 1-voxel-thick EDM allowed the quantification of diameters based on voxel greyscale intensity. In 2D, this was used to quantify the global average diameter, assignment of diameters to individual voxels in the 2D stored MIP, raster-based average diameter analysis, and analysis of average diameters in user selected ROIs.

4.2.8 Simple Neurite Tracer (SNT) for vessel tracing

Simple Neurite Tracer (SNT) is a Fiji Plugin by Mark Longair [347] which allows semi-automatic tracing of other tube-like structures through 3D image stacks, allowing the tracing (spatial assignment) and annotation of topologies. To allow detection of the same vessel(s) in other fish (which were segmented, registered, and skeletonized), the SNT traces were extracted as vessel-specific ROIs (x,y,z) (eg. for an individual vessel multiple ROIs were produced by SNT to describe the vessel (x,y,z) position). These vessel-specific ROIs were then used to produce rectangular ROIs (x,y; 30 x 130 vx) on specific z-planes to allow the detection of centrelines in other fish which might be not at the exactly same position. The ROIs were then used to detect and quantify vessel intensities (from EDM and skeleton) to quantify vessel-specific diameters.

4.2.9 Vascular network complexity assessment using Sholl analysis

To analyse vascular complexity by assessment of branching, Sholl dendritic arbor analysis [343] was applied using the Fiji Sholl Analysis plugin [348] (https://imagej.net/Sholl_Analysis; developed and maintained by Tom Maddock, Mark Hiner, Curtis Rueden, Johannes Schindelin, and Tiago Ferreira). Application was performed on 2D Skeleton due to it being more time-efficient. Default parameters were used except for distance from centre (700 voxel) and step size (5 voxel), bounding boxes were placed to position the centre of shells in the midbrain at the BA-PCS junctions.

4.2.10 Graphical User Interface (GUI)

The image analysis steps presented in this thesis were included into one analysis workflow and a GUI was produced using Fiji Macro language. Individual macros, complete workflow, and analysis documentation are freely available (see Appendix).

4.2.11 Statistics and data display

As described in section 2.2.10.

4.3 Results and discussion

4.3.1 Centreline extraction based on ridge detection

Testing whether ridge detection would be suitable to extract vascular centrelines and quantify their properties in our data, it was found that application was meaningful in 2D (Fig. 4.4A) but not 3D (Fig. 4.4B), as the Plugin operates on a slice-by-slice basis.

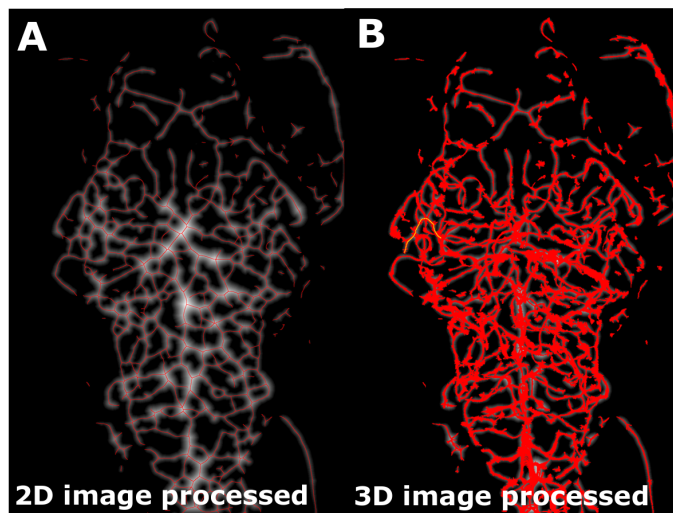


Figure 4.4: **Ridge detection in distance maps.** (A) Ridge detection output in 2D after distance map extraction. (B) Ridge detection plugin applied in 3D stack after distance map extraction.

4.3.2 Centreline extraction based on 3D thinning

After 2D/3D Skeletonization with Fiji, extracted centrelines after GF and TF were compared, showing that centreline extraction after GF produced more spurious branches (Fig. 4.5A,B) than TF (Fig. 4.5C,D).

The large amount of spurious branches after GF was maybe due to object surface inhomogeneities after segmentation, which were less pronounced after TF due to the morphology-based processing considering local neighbourhood.

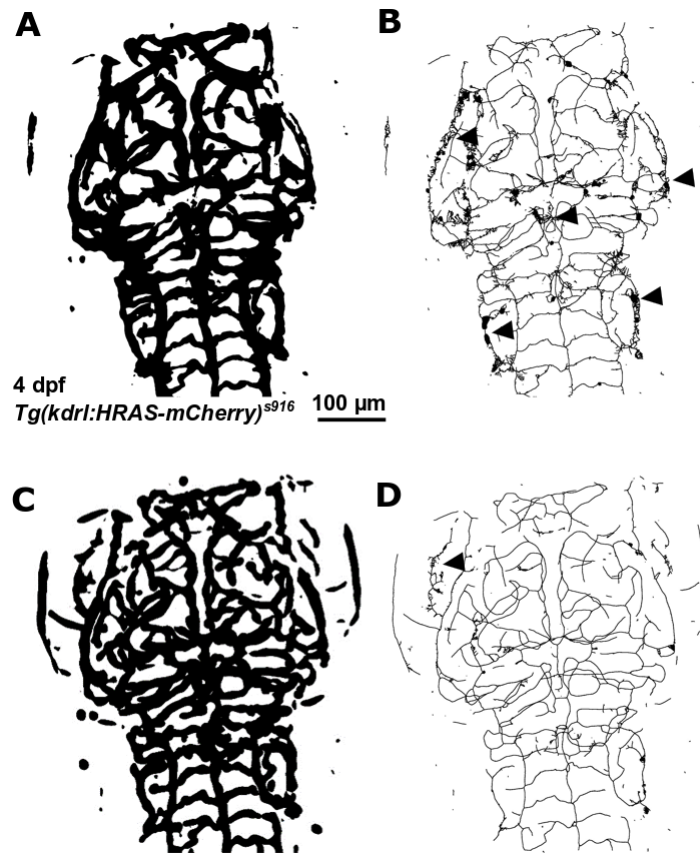


Figure 4.5: **Centreline extraction in Fiji after GF and TF.** (A) Segmentation after GF. (B) Skeletonization using Fiji 2D/3D Skeletonization after segmentation with GF produced several spurious branches (black arrowheads). (C) Segmentation after TF. (D) Skeletonization using Fiji 2D/3D Skeletonization after segmentation with TF produced less spurious branches than GF (black arrowhead).

To assess accuracy of centreline extraction after TF, original data were visually compared to data after TF (Fig. 4.6A), segmentation (Fig. 4.6B) and centreline extraction (Fig. 4.6C). Obtained centrelines were one voxel thick (except in regions with spurious branches) and even in oblique vessels were positioned in the vessel centre. This suggested that this skeletonization approach successfully generates centrelines.

To assess whether this skeletonization approach allows quantification of vascular network length, this was measured as number of voxels in the cerebral ROI during embryonic development. From 3-5dpf an increase was found (p 0.0112; Fig. 4.7A; Kruskal-Wallis test), while there was no difference from 3-4dpf (p 0.0545) or 4-5dpf (p >0.9999).

To further examine the sensitivity of the proposed centreline extraction approach, network

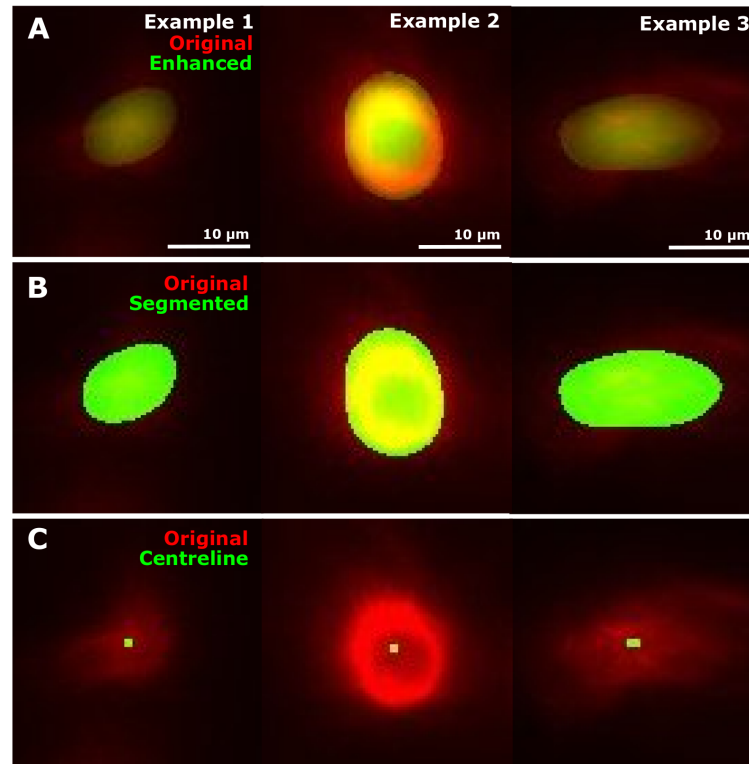


Figure 4.6: **Visual assessment of centreline extraction Fiji after TF.** (A) Visual comparison of original (red) vessel cross-sections to data after TF (green) in three examples showing successful enhancement. (B) Visual comparison of original (red) vessel cross-sections to data after segmentation (green) showing a meaningful segmentation (as validated in Chapter 2). (C) Visual comparison of original (red) vessel cross-sections to data after skeletonization (green) showing centrelines to be one voxel thick and positioned centrally.

length was quantified in samples after Notch inhibition which showed no difference in vascular volume (Chapter 2.3.5; Fig. 2.27) and after VEGF inhibition which showed a reduction in vascular volume, probably due to a reduction in vascular growth and, therefore, network length (Chapter 2.3.5; Fig. 2.28). Thus, the assumption was that extracted centrelines after Notch inhibition would be similar to controls, while they would be potentially reduced after VEGF inhibition (based on reduced vascular growth). Network length was not changed after Notch inhibition ($p = 0.5566$, Fig. 4.7B; Mann-Whitney U test) but reduced after VEGF inhibition ($p = 0.0031$, Fig. 4.7C; unpaired Student's t-test).

These data suggested that this skeletonization approach shows promise to allow network length quantification when there are true biological differences.

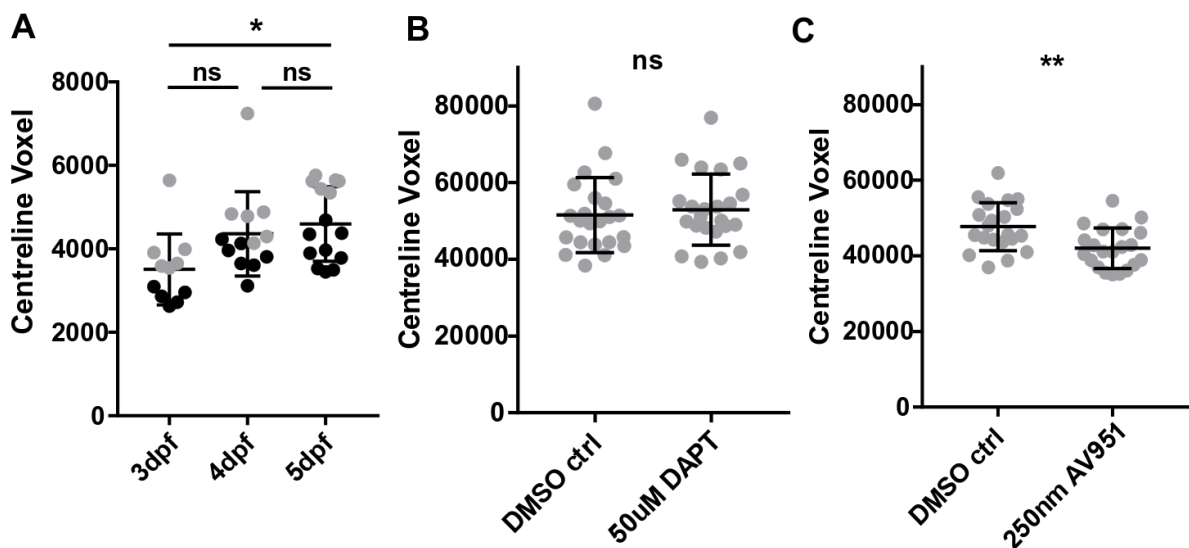


Figure 4.7: **3D vascular network length after 3D-thinning.** (A) Vascular network length increased between 3-5dpf ($p = 0.0112$). Difference was not different between 3-4dpf or 4-5dpf, which was likely due to variability between experimental repeats (3dpf $n=11$, 4dpf $n=13$, 5dpf $n=15$; 2 experimental repeats indicated with grey and black data points; Kruskal-Wallis test; *post hoc* statistical power was 1). (B) Total network length was not changed upon treatment with the Notch inhibitor DAPT ($p = 0.5566$; control $n=23$, DAPT-treated larvae $n=23$; 4dpf; 3 experimental repeats; Mann-Whitney U test; *post hoc* statistical power was 0.1192518). (C) Total network length was decreased upon treatment with the VEGF inhibitor AV951 ($p = 0.0031$; control $n=21$, AV951-treated $n=21$; 4dpf; 3 experimental repeats; unpaired Student's t-test; *post hoc* statistical power was 0.9904608).

4.3.3 Network analysis in 2D MIPs

Application of the "Analyse Skeleton" Fiji Plugin showed that skeleton breaks resulted in several sub-skeletons (Fig. 4.8). For quantitative analysis sub-skeletons were added together if having

10 or more branches as sub-skeletons with less branches were artefacts (visual inspection and length).



Figure 4.8: **Visual output of the "Analyse Skeleton" Fiji Plugin.** Visual output of applying the "Analyse Skeleton" Fiji Plugin to the cranial vasculature of a 2dpf fish, showing skeleton breaks to result in several sub-skeletons (different colours).

Wanting to compare the "Analyse Skeleton" and "Ridge Detection" plugins in 2D, both were applied to data from 2-5dpf (Fig. 4.9A,B). Quantifying the number of branches showed an increase over time for both methods (Fig. 4.9C; ridges $p < 0.001$; skeletonization $p < 0.019$), but a lower CoVs for ridge-based detection (2dpf 15.70%, 3dpf 18.35%, 4dpf 14.85%, 5dpf 10.43%) in comparison to centreline-based detection (2dpf 35.84%, 3dpf 31.12%, 4dpf 25.83%, 5dpf 10.03%). Extracted average branch length was similar with both methods, but an increase over time was only observed with ridge detection (Fig. 4.9D; ridges $p < 0.0019$; skeletonization p

0.1116).

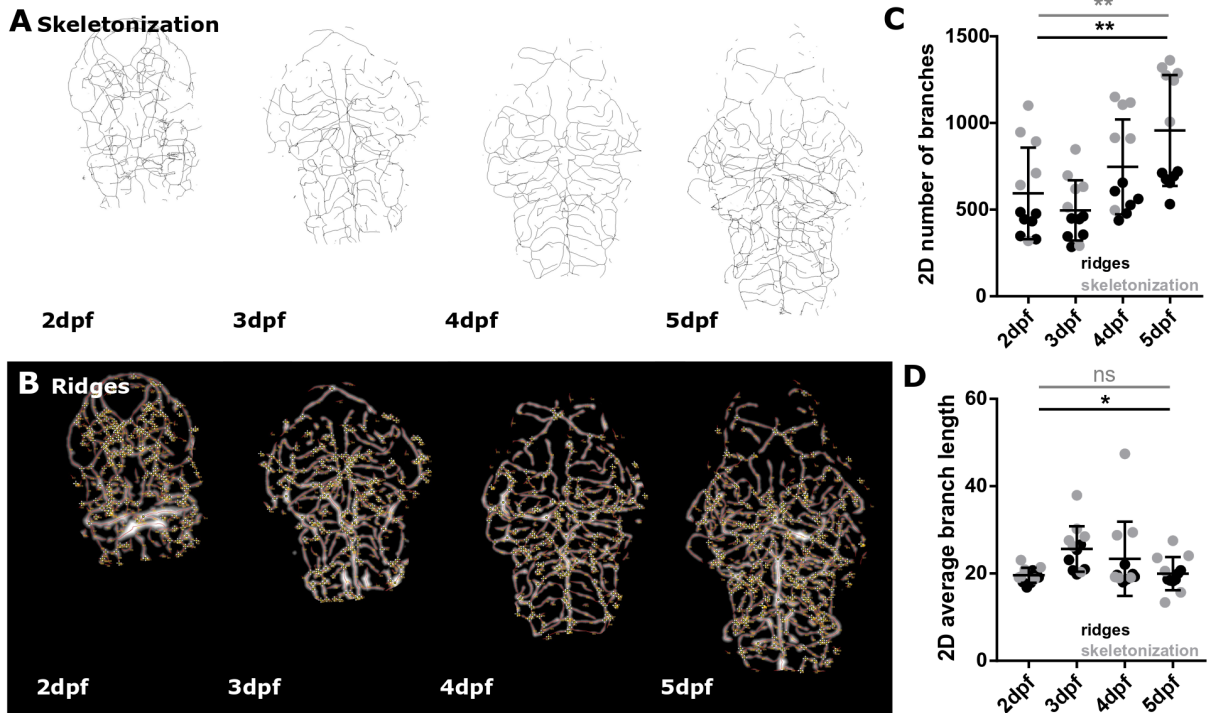


Figure 4.9: **(A)** Vascular centrelines were analysed after skeletonization using the "Analyse Skeleton" plugin. **(B)** Vascular ridges were analysed after creation of distance maps using the "Ridge Detection" plugin. **(C)** For both extraction methods, ridges (black) and skeletonization (grey), an increase of branches was detected over time, with ridge detection delivering lower CoVs (ridges p 0.001; skeletonization p 0.019; 2-5dpf n=6; 2 experimental repeats; Kruskal-Wallis test). **(D)** Average branch lengths extracted were comparable for both methods (ridges p 0.0019; skeletonization p 0.1116; 2-5dpf n=6; 2 experimental repeats; Kruskal-Wallis test).

Next, sensitivity of both methods was studied in data where morphological differences are visually obvious. Namely, fish which did not experience blood flow for 48 hours by injection of *tnnt2a* morpholino (Fig. 4.10A,B). Quantification using the "Analyse Skeleton" plugin showed no difference of branch number (Fig. 4.10C; control-*tnnt2a* MO p 0.1296, control MO-*tnnt2a* MO p 0.0524; One-Way ANOVA) or average branch lengths (Fig. 4.10D; control-*tnnt2a* MO p 0.7024, control MO-*tnnt2a* MO p 0.9641; One-Way ANOVA), while ridge-based quantification showed a reduction of branch number (Fig. 4.10E; control-*tnnt2a* MO p 0.0107, control MO-*tnnt2a* MO p 0.0132; One-Way ANOVA) but not average branch length (Fig. 4.10F; control-*tnnt2a* MO p 0.4829, control MO-*tnnt2a* MO p 0.9983; One-Way ANOVA).

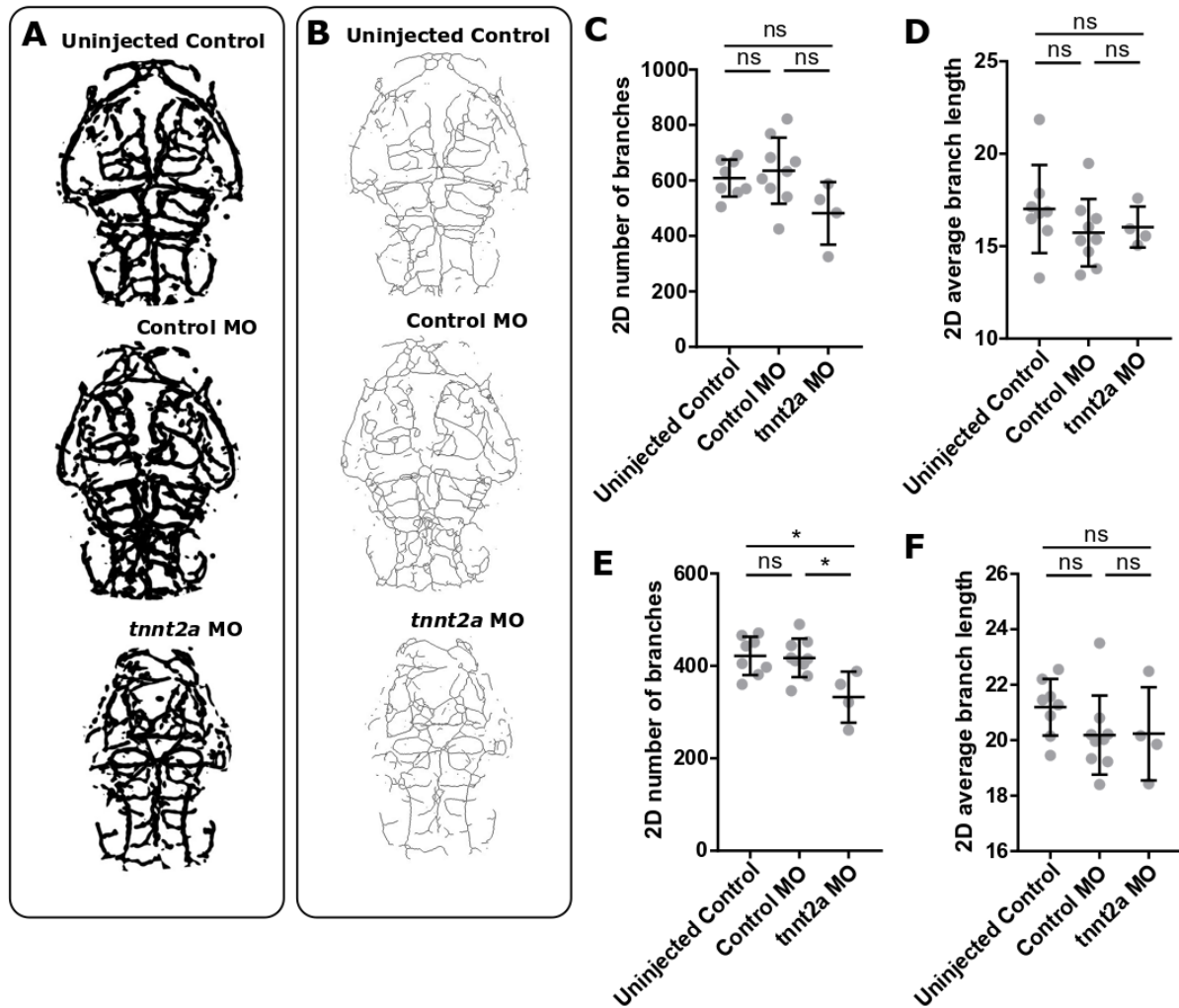


Figure 4.10: **2D network analysis in *tnnt2a* morphants.** (A) Segmented cerebral vasculature. (B) Extracted vascular centrelines. (C) Number of branches extracted using the "Analyse Skeleton" plugin in 2D showed no difference between uninjected controls (p 0.1296) and control MO (p 0.0524) in comparison to *tnnt2a* MO (uninjected control n=8, control MO n=9, *tnnt2a* MO n=4; 3dpf; One-Way ANOVA; *post hoc* statistical power was 1). (D) Average branch length extracted using the "Analyse Skeleton" showed no difference between uninjected controls (p 0.7024) and control MO (p 0.9641) in comparison to *tnnt2a* MO (One-Way ANOVA; *post hoc* statistical power was 0.5911638). (E) Number of branches extracted using "Ridge Detection" showed a difference between uninjected controls (p 0.0107) and control MO (p 0.0132) in comparison to *tnnt2a* MO (One-Way ANOVA; *post hoc* statistical power was 1). (F) Average branch length extracted using "Ridge Detection" showed no difference between uninjected controls (p 0.4829) and control MO (p 0.9983) in comparison to *tnnt2a* MO (One-Way ANOVA; *post hoc* statistical power was 0.4237113).

4.3.4 Network analysis in 3D

The "Analyse Skeleton" Plugin was applied to analyse vascular networks from 2-5dpf in 3D (Fig. 4.11A-D), resulting in multiple sub-skeleton branches (Fig. 4.11E) as shown above (Fig. 4.8). Sub-skeletons were added together if having 10 or more branches, resulting in clearer results showing branch numbers to increase over time (Fig. 4.11F). No clear trend of average branch lengths were observed (Fig. 4.11G), while number of junctions increased from 2-5dpf (Fig. 4.11H).

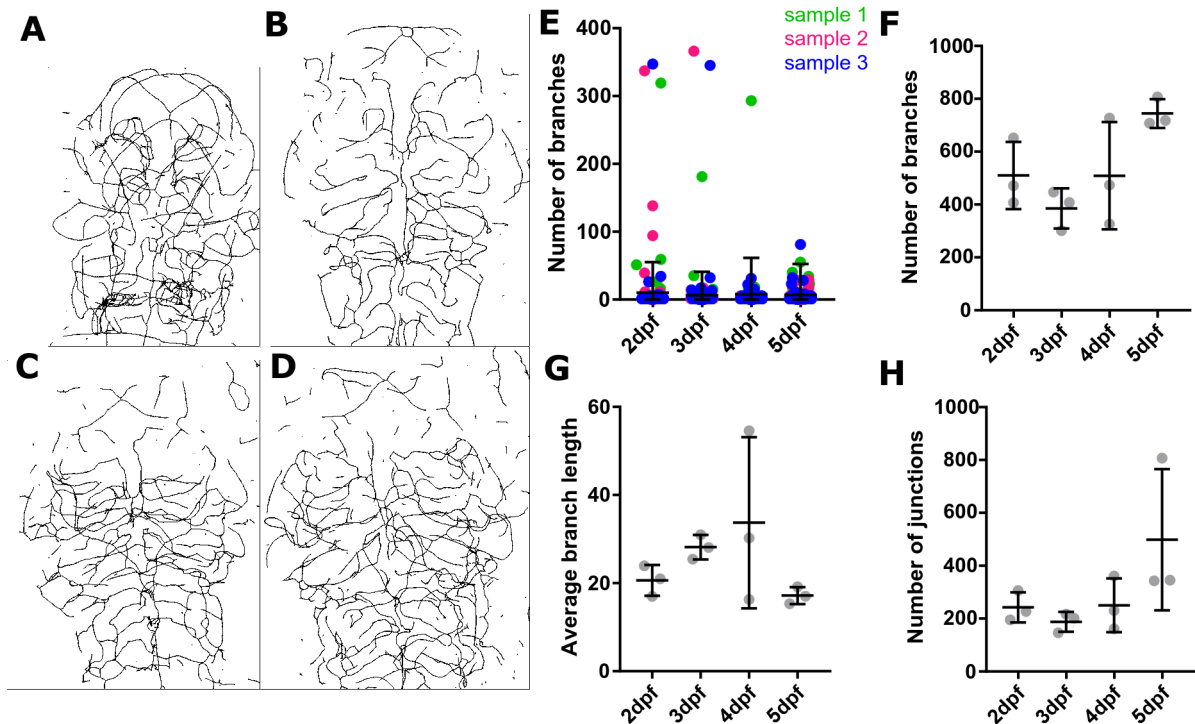


Figure 4.11: **3D network analysis of vascular development from 2-5dpf.** (A-D) The "Analyse Skeleton" Fiji Plugin was applied to vascular skeletons from 2-5dpf. (E) Number of branches extracted from sub-skeletons from 2-5dpf in three samples (colours show data from 3 samples/fish, dots represent sub-skeletons). (F) Summed up number of branches extracted (minimum 10 branches per sub-skeleton), showed an increase of branches from 2-5dpf. (G) Average branch length from 2-5dpf showed no trend over time, but a surprisingly high variability at 4dpf. (H) Number of junctions increased in the examined time-frame.

Quantification of *tnnt2a* data in 3D showed a reduction of vascular volume (Fig. 4.12A; control-*tnnt2a* MO $p < 0.0001$, control MO-*tnnt2a* MO $p < 0.0001$; One-Way ANOVA), network length (Fig. 4.12B; control-*tnnt2a* MO $p = 0.0330$, control MO-*tnnt2a* MO $p = 0.0461$; One-Way ANOVA), and number of junctions (Fig. 4.12C; control-*tnnt2a* MO $p = 0.0125$, control MO-*tnnt2a* MO $p = 0.0255$; One-Way ANOVA).

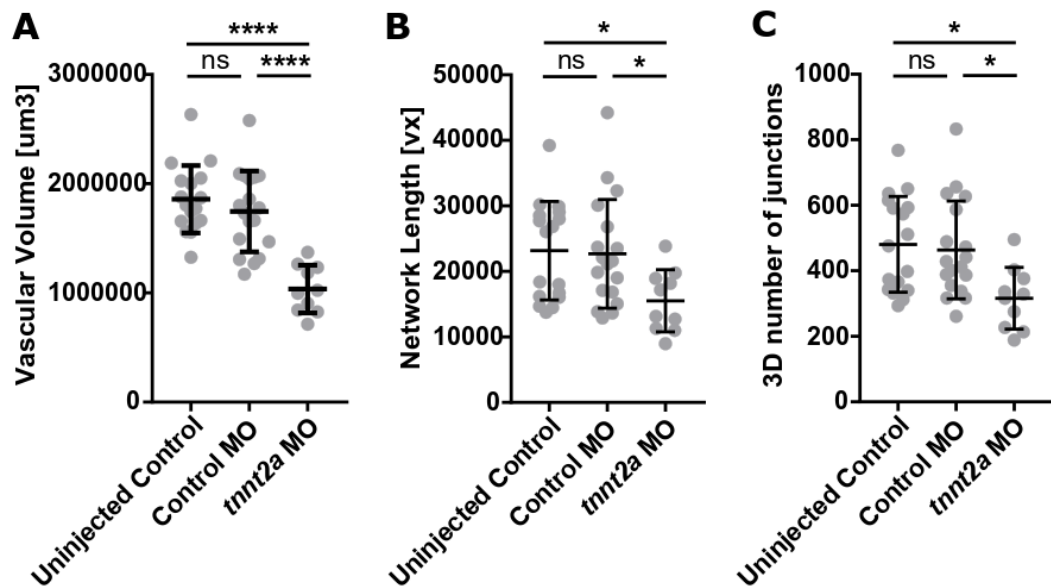


Figure 4.12: **3D network analysis in *tnt2a* morphants.** (A) Vascular volume was reduced comparing *tnt2a* MO to uninjected controls ($p < 0.0001$) and control MO ($p < 0.0001$; One-Way ANOVA; *post hoc* statistical power was 1). (B) 3D vascular network was reduced comparing *tnt2a* MO to uninjected controls ($p = 0.0330$) and control MO ($p = 0.0461$; One-Way ANOVA; *post hoc* statistical power was 1). (C) The number of junction points were reduced comparing *tnt2a* MO to uninjected controls ($p = 0.0125$) and control MO ($p = 0.0255$; One-Way ANOVA; uninjected control $n = 17$, control MO $n = 18$, *tnt2a* MO $n = 10$; 2 experimental repeats; *post hoc* statistical power was 1).

4.3.5 Branching point detection and voxel identities

As mentioned above, the common approaches are to either use a raster-based or object-based approach. Despite images had typically a large number of voxels (typically about 1920 x 1920 x 500 in x,y,z) a raster based approach was more intuitive due to the skeleton breaks which would stop an object based approach.

The "AnalyseSkeleton" Plugin had implemented such a raster based approach and extracted branching points and endpoints based on voxel 26-connectivity (Fig. 4.2). In some cases, false-positive BPs were detected (Fig. 4.13A, white arrowheads). To be able to extract true BPs, BPs extracted in 3D were compared to BPs in 2D and only the BPs found in both were considered as true BPs (Fig. 4.13B). The rationale for this was that in 2D MIPs true-positive BPs as well as BPs at overlapping vessels (false-positive) would be detected, while in 3D stacks true-positive BPs as well as false-positive BPs would be detected. Thus, by identifying the BPs extracted by *both* methods, the result was a reduction of false-positive BPs.

An additional *caveat* with the raster based approach was to consider that voxels with more than two neighbours were classified as BPs (Fig. 4.13C), but analysis of junctions might result in multiple voxels extracted as potential BPs. This was especially in 2D the case, and comparing 3D to 2D BPs helped addressing this issue, but future work is needed to examine this in further detail.

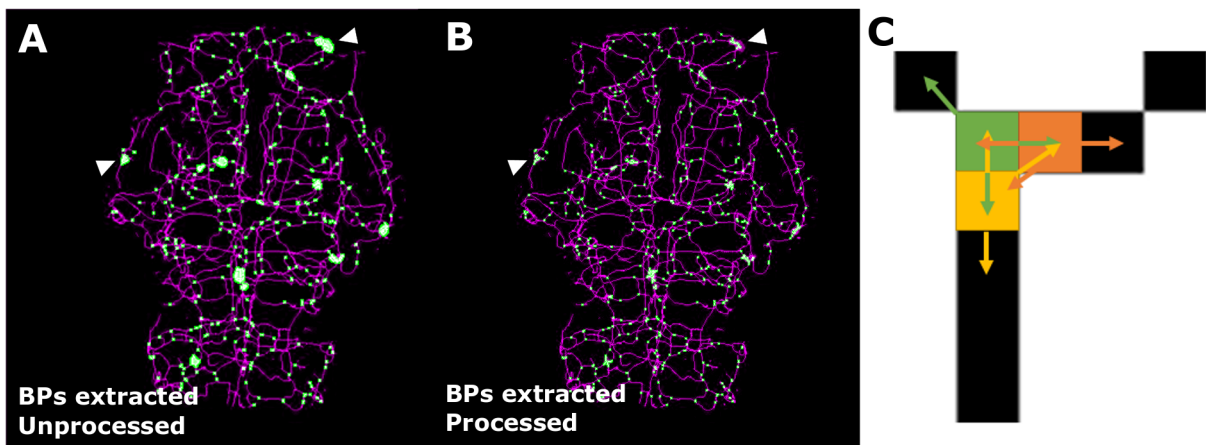


Figure 4.13: **Issues in BP detection.** (A) When skeletonization did not result in 1-voxel thick centerlines, BP detection delivered false-positive BPs (vascular skeleton - magenta; BPs - green, skeleton and BPs for visualization diluted). (B) Extraction on BPs found when analysing the 2D and 3D skeleton, allowed reduction of false-positive BPs (vascular skeleton - magenta; BPs - green, for visualization diluted). (C) The green, orange and yellow voxel were detected as BPs (arrows indicate neighbourhood relations), but only the green voxel is a true BP.

4.3.6 Vessel diameters sampling rate

To obtain initial insights into the range of vessel diameters Euclidean distance maps (EDM) of the segmented 3D vasculature were produced, showing a low range of vessel widths (Fig. 4.14) and changes to be subtle from 2-5dpf. This was important to gain an indication of vessels width ranges and that individual vessels stayed rather consistent in size, thus suggesting that lower sampling rates along individual vessels would be sufficient to examine vessel diameters.

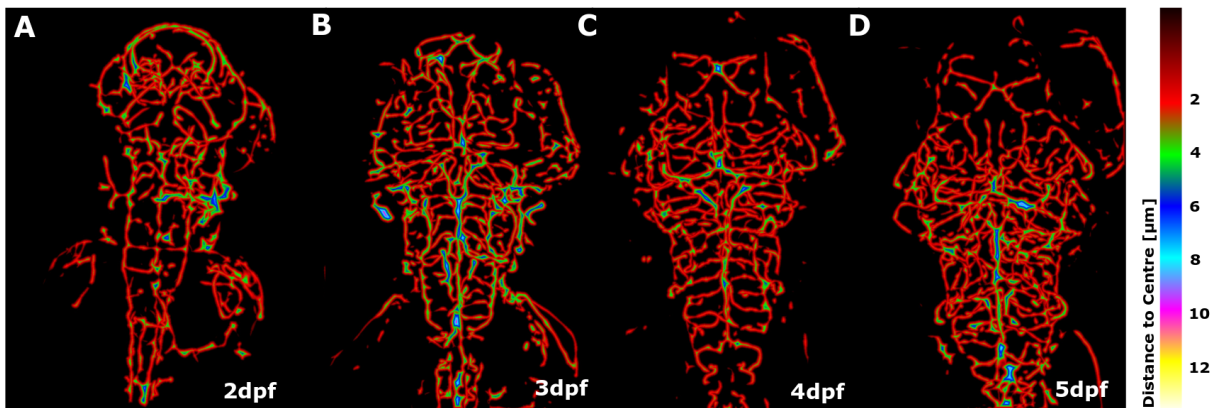


Figure 4.14: **Vascular distance maps from 2-5dpf.** (A-D) Distance maps of the cerebral vasculature from 2-5dpf showing local thickness, showing that most vessels display similar thickness (red).

To assess the impact of sampling rate on vessel diameters further, measurements of diameters of four different vessels (Fig. 4.15A,B) were performed, showing that diameter sampling rates of three or ten diameters per vessel did not impact the obtained average vascular segment diameter (Fig. 4.15C; MMCtA p 0.9609, ACeV p 0.8143, CtA p 0.9260, ISV p 0.4727). Further examination of standard deviations showed that only for the CtA a lower standard deviation was obtained when sampling the diameter at higher frequency (Fig. 4.15D; MMCtA p 0.2971, ACeV p 0.1729, CtA p 0.0346, ISV p 0.9688). This, again, suggested that the diameter of individual vessels could be extracted without high sampling numbers.

4.3.7 Vessel diameter quantification

Before preliminary examination of vessel diameters, we used a combination of 2D and 3D analysis to assess vessel properties. EDMs of processed images (Fig. A-D) were utilized to quantify vessel diameters by combining these with the extracted vascular skeleton. This allowed to have 1-voxel-thick representation of the local vessel diameter, represented by grey scale intensity.

To achieve this, EDMs were extracted in 2D (Fig. 4.16E), the 3D skeleton extracted (Fig.

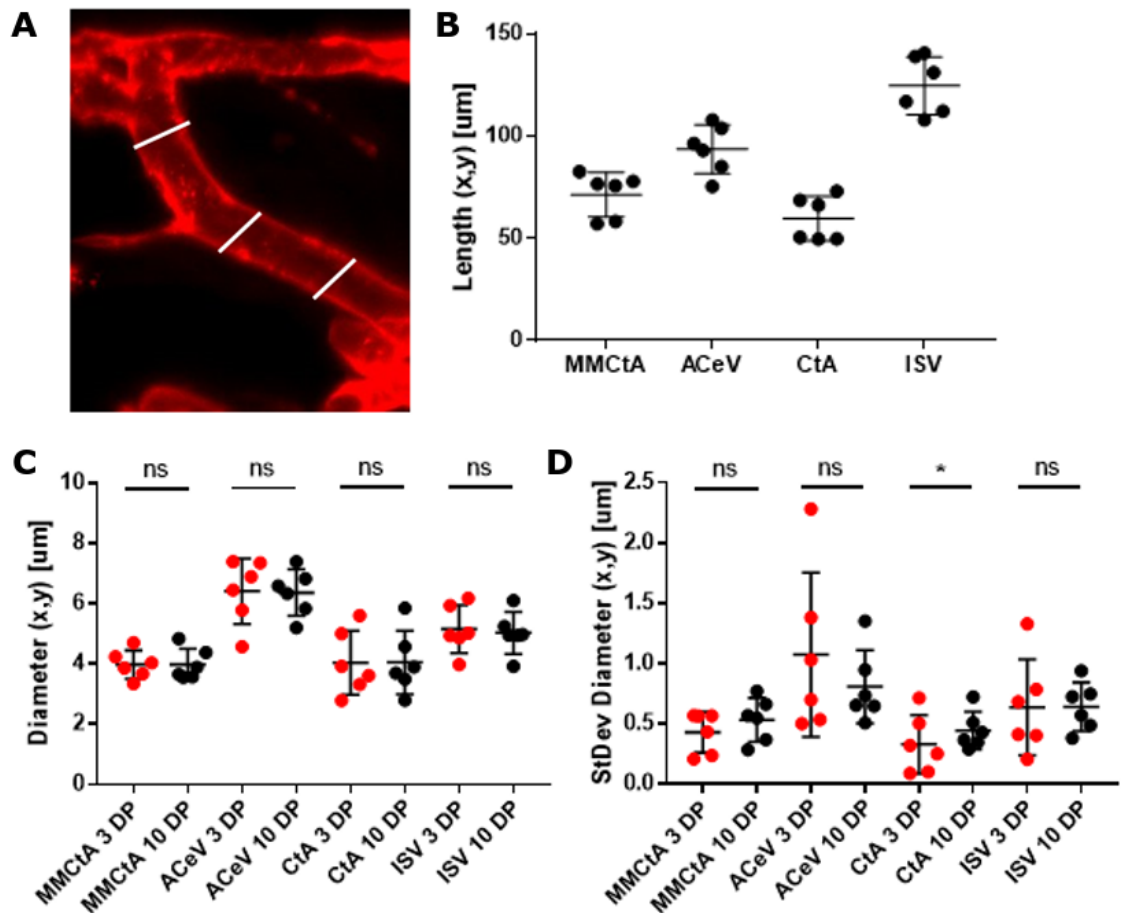


Figure 4.15: **Impact of diameter sampling frequency.** (A,B) Vessel diameters were measured from four different vessels. (C) Average diameters were not changed by sampling frequency of three (red dots) or ten (black dots; MMcTA p 0.9609, ACeV p 0.8143, CtA p 0.9260, ISV p 0.4727; n=6; 3dpf; 1 experimental repeat; paired Student's t-test for individual vessels). (D) Standard deviation of average vessel diameters was only impacted by increased sampling frequency in the CtA (MMcTA p 0.2971, ACeV p 0.1729, CtA p 0.0346, ISV p 0.9688; n=6 3dpf larvae; 1 experimental repeat; paired Student's t-test for individual vessels).

4.16E), EDM and skeleton merged (Fig. 4.16G), EPs extracted (Fig. 4.16H), and BPs extracted (Fig. 4.16I). The resulting workflow delivered 3D network length, 3D branch length, 3D EPs, 3D BPs, and 2D vessel diameters, with produced images storing vessel diameters on a voxel basis allowing for closer examination later as well as visualization of thickness by colour (Fig. G).

To test the diameter analysis workflow, it was applied to datasets of animals with and without blood flow (*tnnt2a* MO), as fish without blood flow had visually decreased vessel diameters. Application to uninjected controls, control MO, and *tnnt2a* MO (Fig. A-C) confirmed this reduction of vessel diameter without blood flow. Quantification of network length (Fig. 4.17D), BPs (Fig. 4.17E), endpoints (Fig. 4.17F), and average diameter (Fig. 4.17G) showed a reduction of all parameters in animals without blood flow.

Encouraged by these results, additional automatic analysis approaches of diameters in 2D images (EDM and skeleton combination) were implemented to assess vascular diameters more locally in addition to the above global and voxel wise diameter (Fig. 4.18A). Firstly, a raster based analysis was implemented, allowing regional direct comparison of samples after registration (Fig. 4.18B). Secondly, measurements in manual ROI selections were implemented to allow additional examination of regions of particular interest (Fig. 4.18C).

4.3.8 Extraction and analysis of individual vessel segments

Although the extracted data allowed examination of vessel diameters to a satisfactory degree, we further examined 3D vessel segments. In theory, a vessel or vascular segment can be described as the voxels connecting a starting point $(x,y,z)_1$ and endpoint $(x,y,z)_2$, and can be described as the shortest vessel path between these points (Fig. 4.19A).

As the "2D/3D AnalyseSkeleton" Plugin is based on a raster-based analysis based approach, false-positive branching points (as discussed above; Fig. 4.19B, green) result in artificial segment breaks and delivery of more than the true vessel segment (Fig. 4.19B; grey, dark grey, blue).

To address this issue of artificial segment breaks, post-processing is required to extract true vessel segments. To achieve, two steps of post-processing are required: **(a) processing of BPs to reject false-positive** (for example as suggested above, by manual refinement (which is laborious), or applying alternative methods to extract BPs), and **(b) extraction of vessel segments**.

Vessel extraction can theoretically be addressed in various ways, such as the following:

(i) Shortest vessel path tracking between extracted BPs could be conducted automatically.

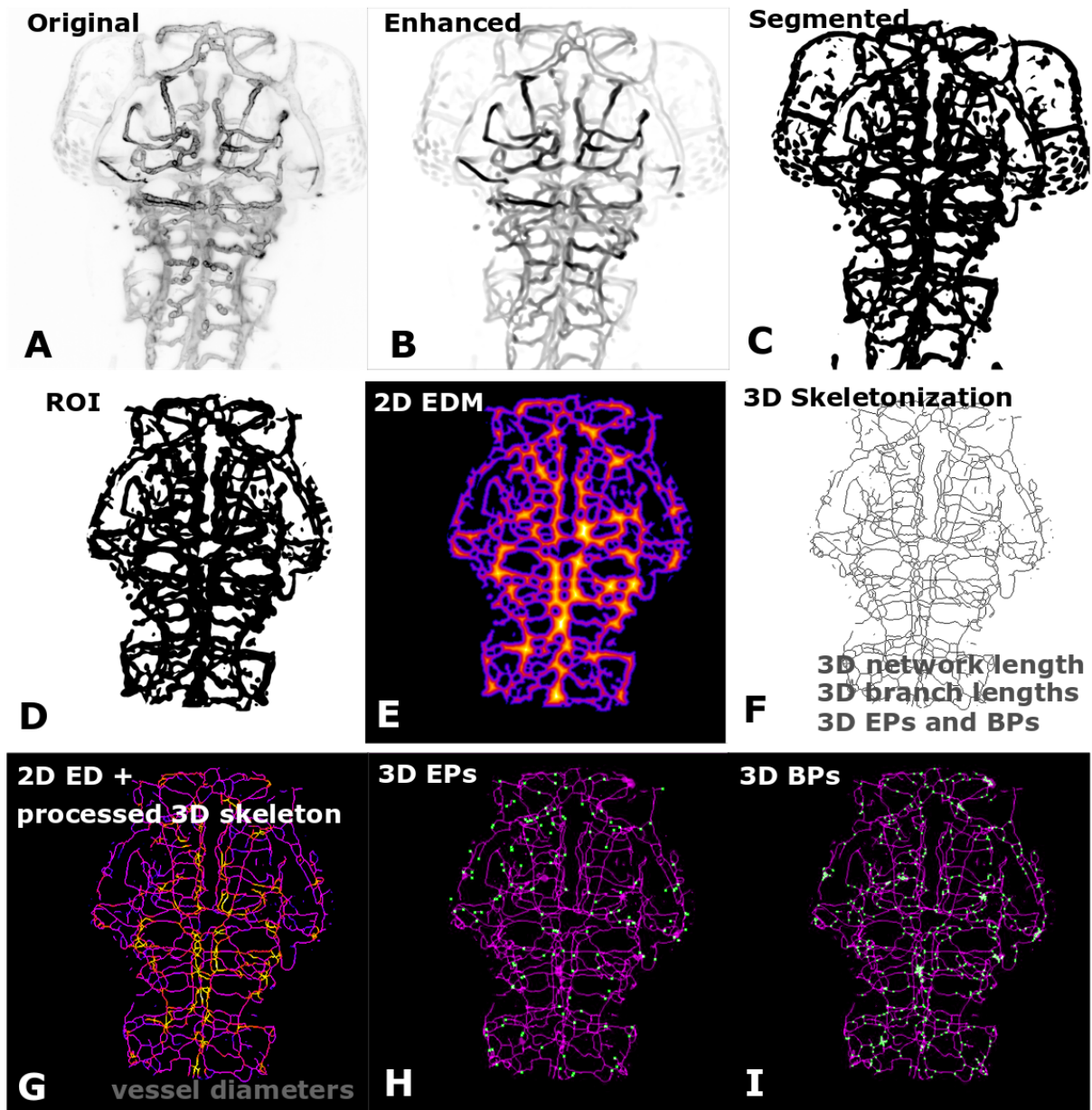


Figure 4.16: **Vascular quantification workflow.** (A) MIP of original image. (B) MIP of enhanced image. (C) MIP of segmented image. (D) MIP of selected vascular region. (E) 2D EDM of MIP of 3D segmented image. (F) MIP of 3D skeleton - used for 3D network length and branch length measurement as well as extraction of EPs and BPs. (G) Merged 2D EDM and MIP of 3D skeleton (post-processed) - colour range indicating vascular thickness / diameter. (H) MIP of 3D EPs (green). (I) MIP of 3D BPs (green).

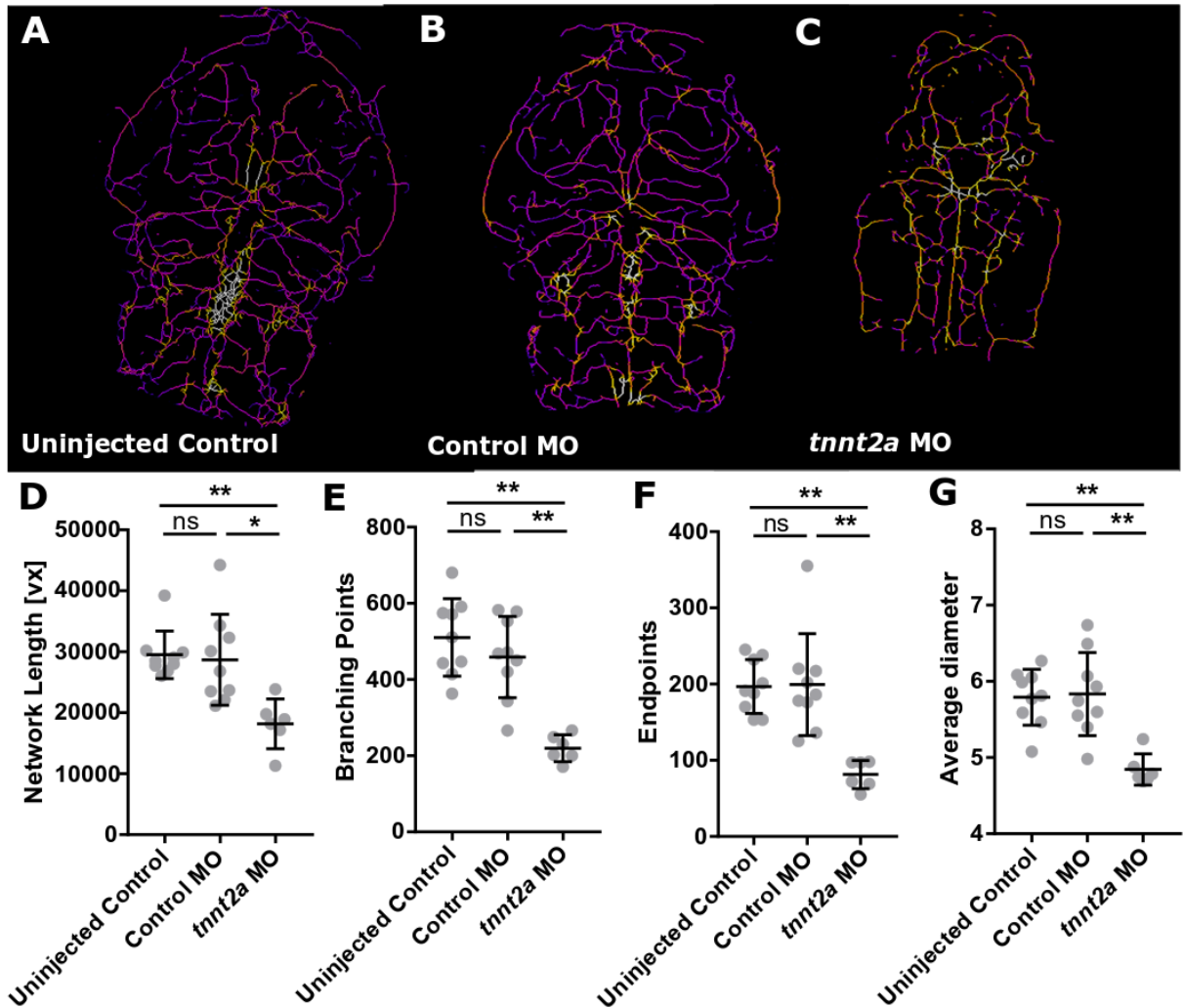


Figure 4.17: **Quantification of *tnnt2a* MO vascular properties.** (A-C) Vascular properties were quantified in uninjected controls, control MO, and *tnnt2a* MO (3dpf). (D) Vascular network length was decreased comparing uninjected controls (p 0.0033) and control MO (p 0.0209) to *tnnt2a* MO (uninjected control n=9, control MO n=6, *tnnt2a* MO n=6; Kruskal-Wallis test; *post hoc* statistical power was 1). (E) Branching point number was decreased comparing uninjected controls (p 0.0019) and control MO (p 0.0092) to *tnnt2a* MO (Kruskal-Wallis test; *post hoc* statistical power was 1). (F) Endpoint number was decreased comparing uninjected controls (p 0.0024) and control MO (p 0.0061) to *tnnt2a* MO (Kruskal-Wallis test; *post hoc* statistical power was). (G) Average diameter was decreased comparing uninjected controls (p 0.0050) and control MO (p 0.0067) to *tnnt2a* MO (Kruskal-Wallis test; *post hoc* statistical power was 0.5007516).

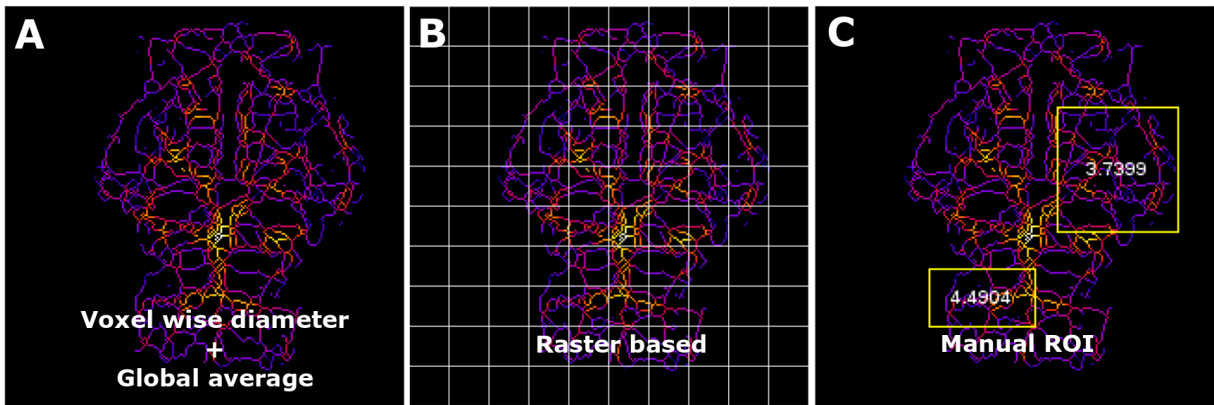


Figure 4.18: **2D local diameter quantification.** (A) The combination of EDM and skeleton based diameter analysis allowed diameter assessment voxel wise and globally. (B) Raster based analysis of average diameters enabled direct regional comparison of samples after registration. (C) Manual ROI selection allowed diameter examination in particular regions of interest.

(ii) Euclidean distance could be calculated between BPs, but this is an approximation rather than true examination of vessel segments (Fig. 4.19C). (iii) 3D cubic ROIs could be produced using BPs as start and endpoint, but this was likely to be not sufficient for vessels with high curvature and include voxels which are not part of the true vascular segment (Fig. 4.19D). (iv) ROI templates could be produced from target fish and applied to moving samples (Fig. 4.19E). (v) Vascular segments could be traced manually, but tracing of vessels in individual fish is laborious and time consuming.

Semi-automatic tracking using SNT

Based on the different options to extract and examine individual vessels, there was the rationale to examine whether it is possible to perform vascular extraction and annotation automatically in registered fish (chapter 3) based on manual tracing of one template fish.

To achieve this the SNT Plugin in Fiji was used, which was designed to allow semi-automatic tracking for tube-like structures [347].

Thus, manual tracking of an example fish in segmented image data was performed and it was found that SNT was suitable to allow tracking of our data (Fig. 4.20). As it required about 8h to do this correctly for the whole cerebral vasculature, including manual annotation, this highlights the need for automating such extraction and annotation.

Next, tracking was performed on the segmented image of a 3dpf registration template (see section 3.2.6), and ROIs for individual vessels (line ROI with x,y position, z plane information) extracted from this tracking (Fig. 4.20C).

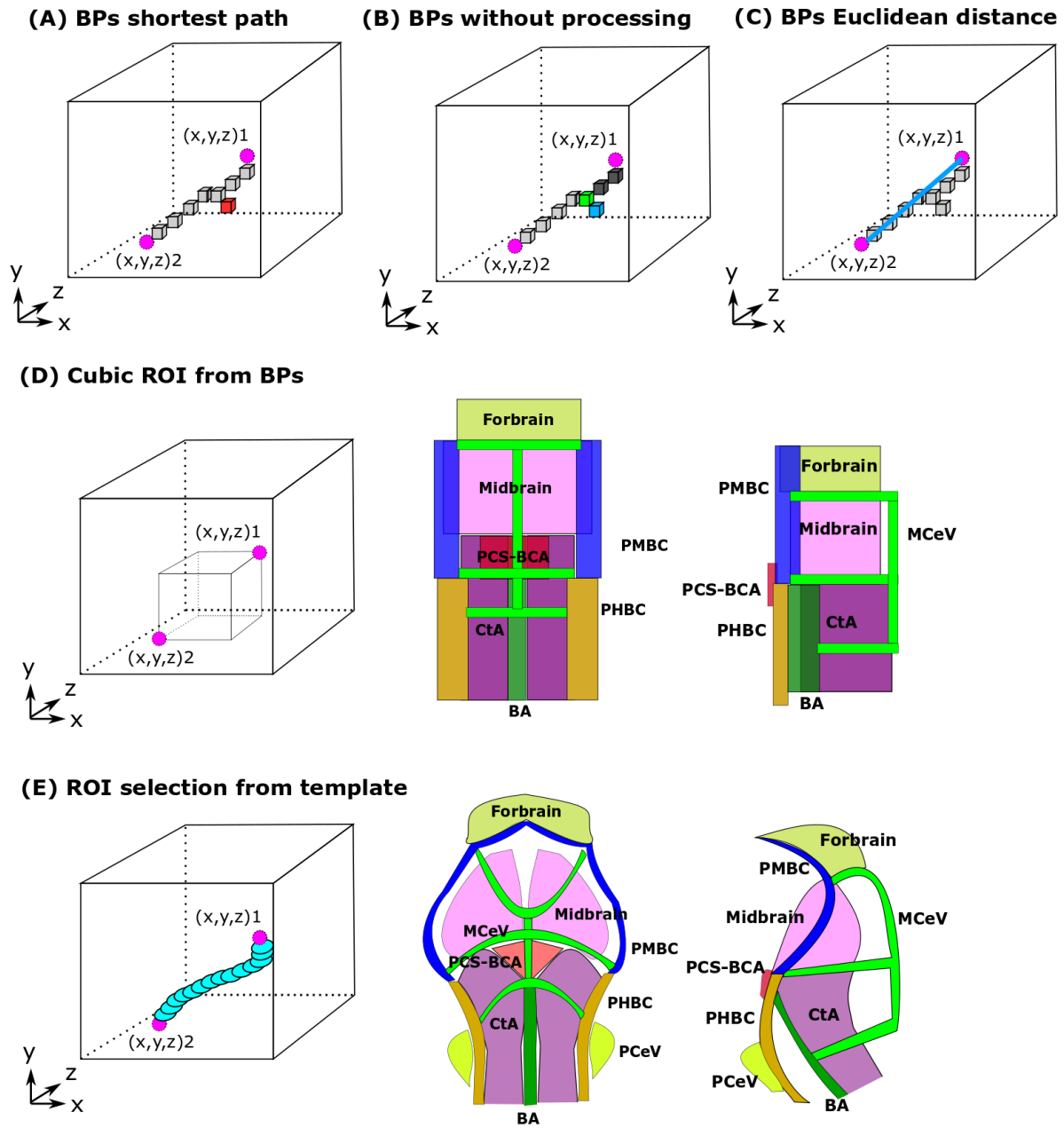


Figure 4.19: **Schematic of 3D vessel segment analysis approaches and issues.** Schematic of 3D vessel segment analysis approaches and issues (magenta circles indicate true vessel starting $(x,y,z)_1$ and endpoint $(x,y,z)_2$). **(A)** Shortest path analysis between start and endpoint (magenta circles) delivers true vascular segments (grey), excluding false positive voxel and vessels (red). **(B)** Vascular analysis with the "2D/3D AnalyseSkeleton" Plugin delivered true-positive BPs (magenta) and false-positive BPs (green), resulting in the extraction of vascular subsegments (light grey, dark grey, blue). **(C)** Euclidean distance between start and end point would deliver spatial not vascular connection. **(D)** Cubic ROIs would only approximate true vessels. **(E)** ROI selection from vascular templates would allow refinement of "2D/3D AnalyseSkeleton" Plugin data based on their location within these ROIs.

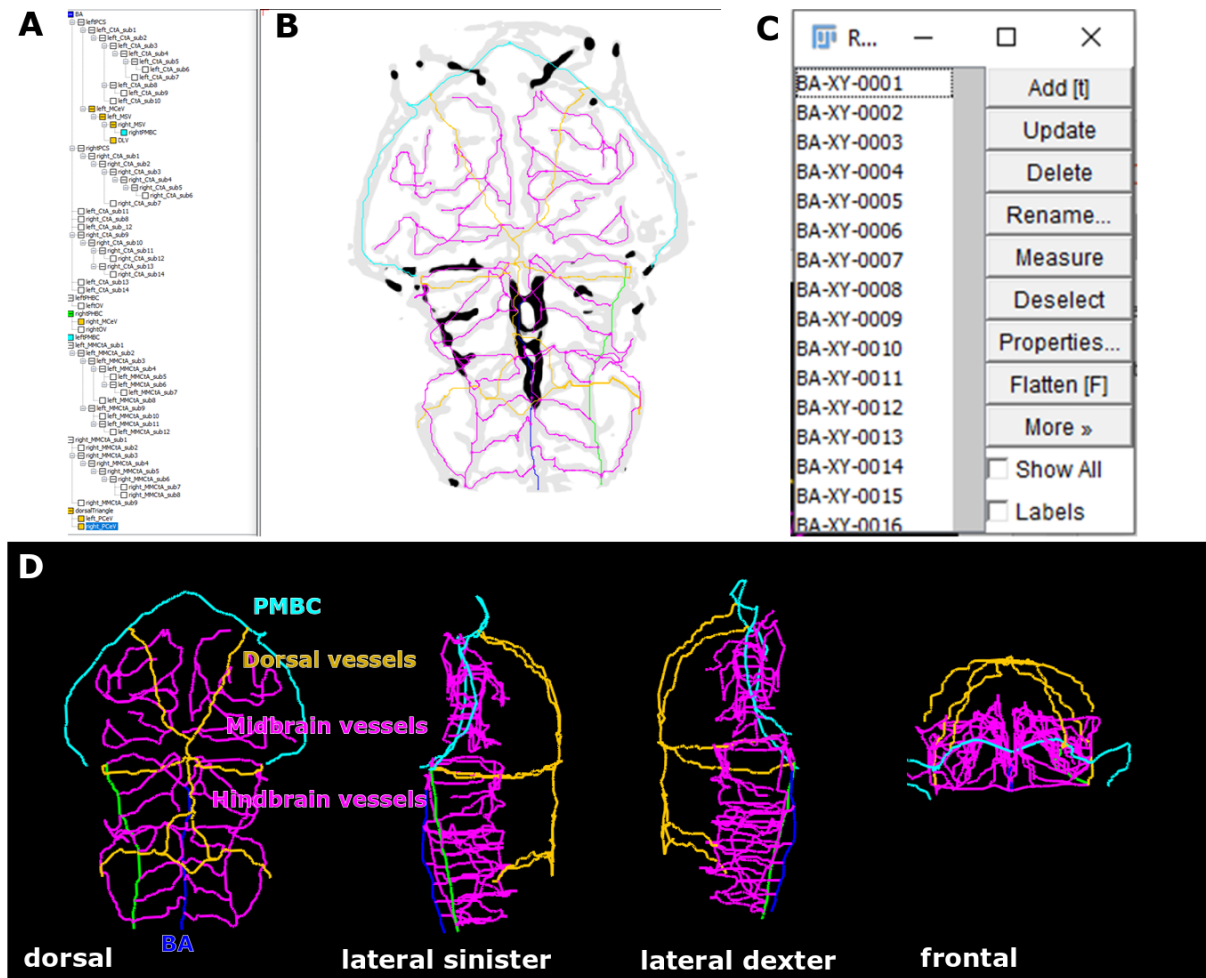


Figure 4.20: **Application of SNT to annotate vessels.** (A,B) SNT allows semi-automatic tracking and annotation of 3D vessels. (C) SNT allows extraction of ROIs of individual vessels. (D) Visual representation of semi-automatically annotated vessels.

To assess whether skeletons of different fish would be similar enough to use the trackings produced from the registration target to the moving image to identify and extract individual vessels, vascular skeletons of target and moving fish were compared visually finding a high degree of similarity (Fig. 4.21).

As the target and moving samples were not perfectly overlapping, we extended the initial trackings as ROIs (x,y,z) and extended these to larger rectangular ROIs (30 x 130vx; Fig. 4.19E) to allow measuring the grey value which represents diameter.

Once it was found that this was suitable to measure vessel-specific information in moving images, a macro was produced to iterate through the vessel-specific ROIs and automatically save the data.

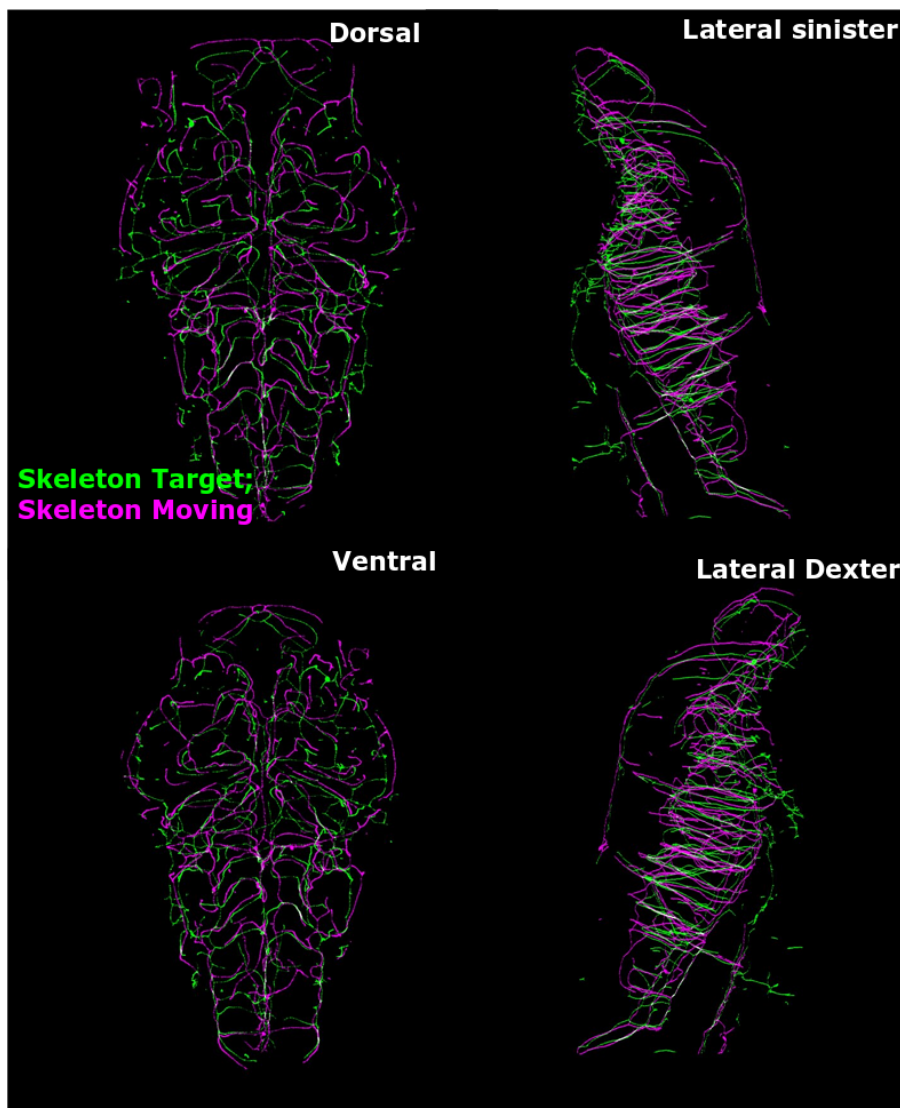


Figure 4.21: **Assessing vascular skeleton similarity.** To assess whether it was possible to use the skeleton from the target image (green) to quantify vessel diameters in moving (magenta) images, skeletons were overlapped and visually compared, showing a high degree of similarity.

Subsequently, this was applied to some registered fish to assess whether this approach would be applicable to other data. To compare measurement outcomes, I manually measured vessel diameters of CtA, MMcTA, PHBC, and BA in the target and three moving samples in the original data (Fig. 4.22, black dots) as well as segmented data (green dots) and compared these to the automatic measurements (magenta dots).

This showed that the automatic measurement in the target image delivered promising results (CoV: CtA 11.66%, MMcTA 7.90%, PHBC 20.92%, and BA 13.56%), but varying accuracy in the returned results for some of the vessels in the moving fish. Some measurements were highly accurate (ie. PHBC M3 CoV 9.41%), while other were not (ie. PHBC M2 CoV 40.14%).

We suggest that this method needs further refinement, but is theoretically applicable to allow the analysis of key vessels, such as CtA, MMcTA, PHBC, or BA.

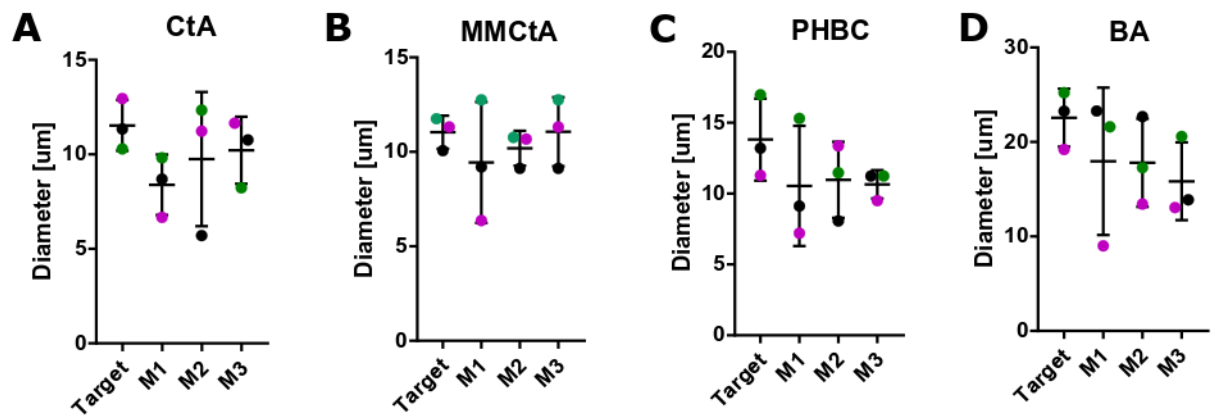


Figure 4.22: **Automated measurement of individual vessel diameters.** Diameter measurements of individual vessels based on SNT tracking in (A) CtA, (B) MMcTA, (C) PHBC and (D) BA (black - manual measurement in original image, green - manual measurement in segmented image, magenta - automatic measurement).

To enable wider application, this method could be used to assign a data set with annotated vessel identities, building the foundation for a vascular atlas which could be used to train machine learning methods to perform annotation and extraction automatically.

Still, we show here the first approach to extract vessels of interest, including annotation and diameter measurements.

4.3.9 Vascular network complexity assessment using Scholl analysis

Vascular complexity was analysed using Scholl analysis in zebrafish with and without blood flow at 3dpf (Fig. 4.23A-C), showing that zebrafish without blood flow (*tnnt2a* MO) have less vascular branches than controls and branches extend less far (Fig. 4.23D,E; number of branches -

uninjected control 20.5 ± 1.82 , control MO 19.25 ± 1.88 *tnnt2a* MO 11.56 ± 1.25 (mean \pm SEM)).

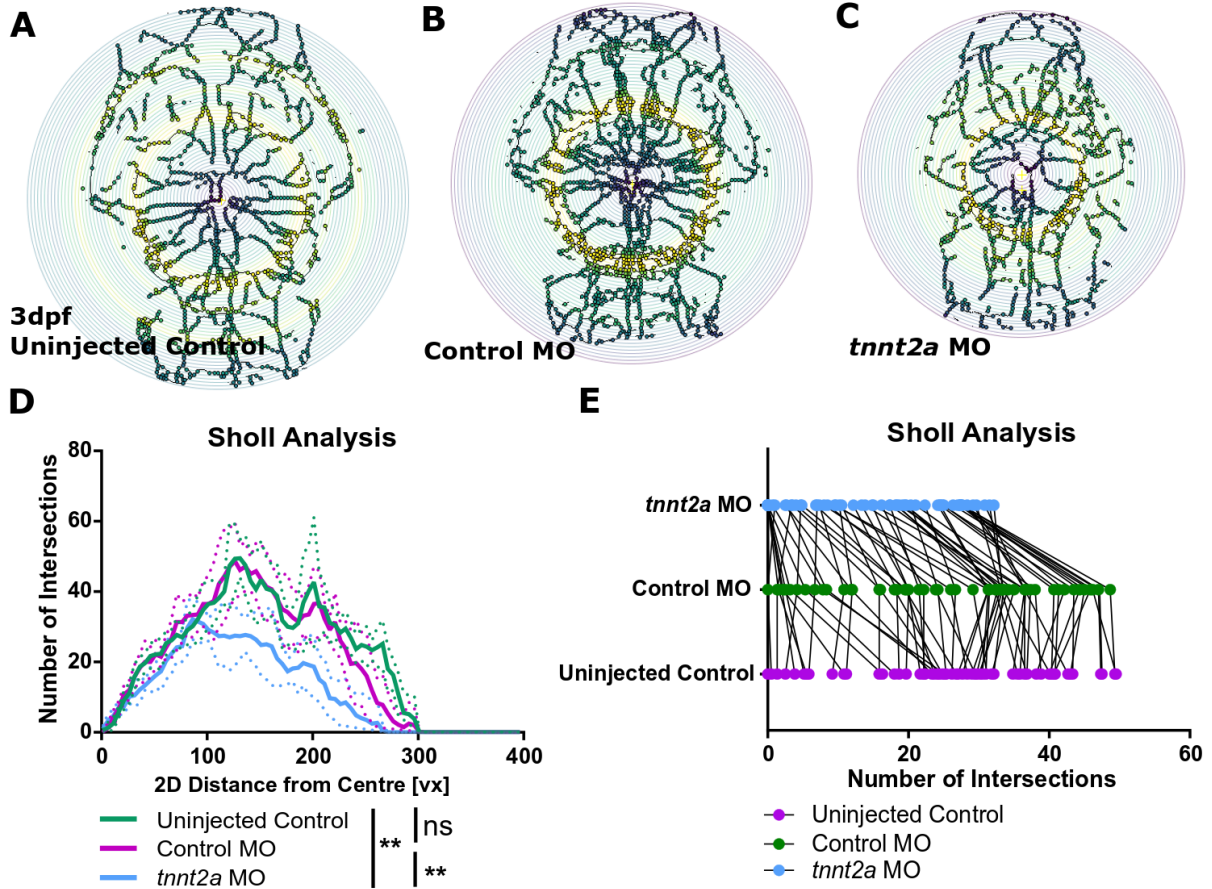


Figure 4.23: **Sholl analysis of zebrafish with and without blood flow (*tnnt2a* MO).** (A-C) Sholl analysis of uninjected controls, control MO, and *tnnt2a* MO. (D) Line graph of Sholl analysis of number of intersection of 2D distance from centre shows less branching and a reduced distance in *tnnt2a* MO. (E) Plot shows reduced number of intersections in *tnnt2a* MO in comparison to controls (3dpf, n=6, One-Way ANOVA).

To quantify vascular branching during embryonic development, Sholl analysis was applied from 2-5dpf, showing an increase of branches over time (Fig. 4.24; number of branches - 2dpf 19.37 ± 1.32 , 3dpf 15.08 ± 1.10 , 4dpf 18.33 ± 1.31 , 5dpf 22.49 ± 1.31 (mean \pm SEM)).

4.3.10 Example biological application - Quantification of the effect of inhibiting actin polymerization

Following the implementation and testing of workflows to analyse the cerebral vasculature in zebrafish, we wanted to examine the entire workflow applicability to biologically relevant experimental data. One such experiment was to examine the impact of actin polymerization

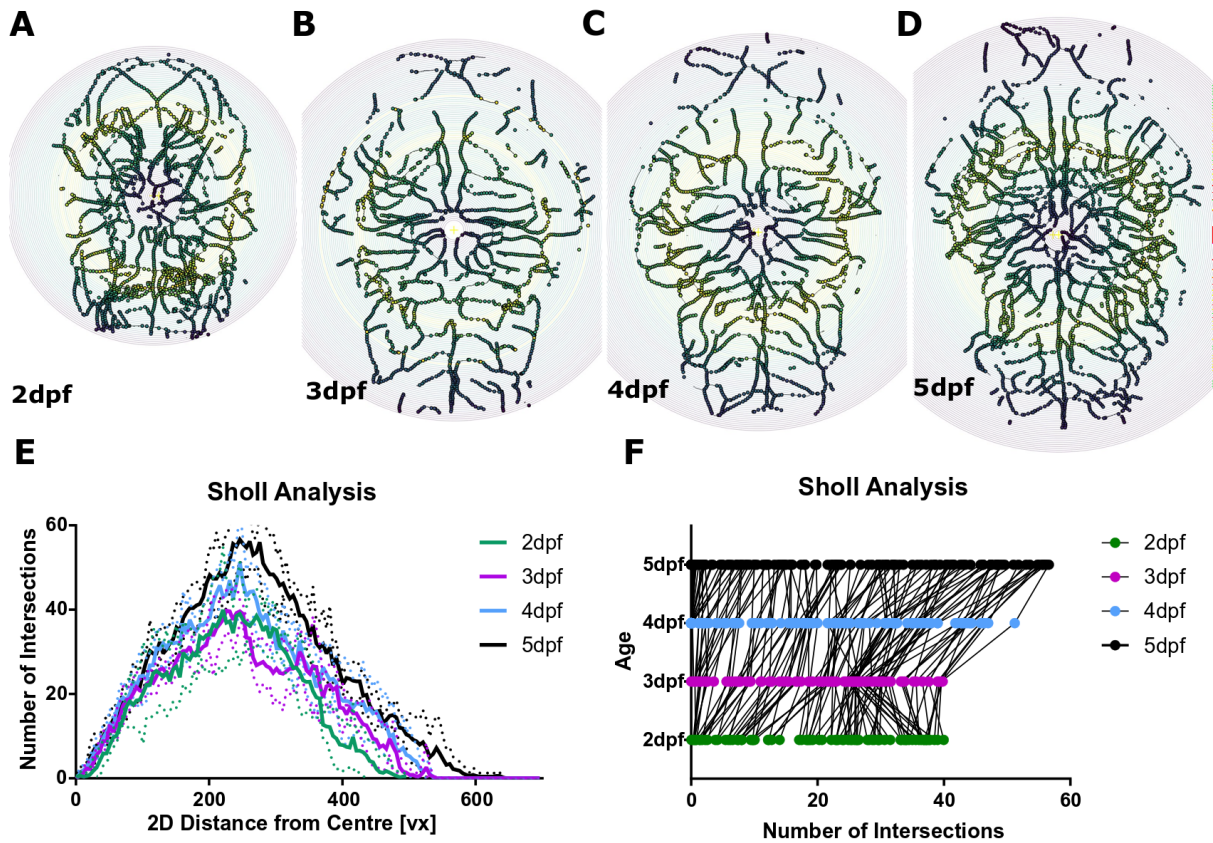


Figure 4.24: **Sholl analysis from 2-5dpf.** (A-D) Sholl analysis of zebrafish from 2-5dpf. (E) Line graph of Sholl analysis of number of intersection of 2D distance from centre shows increased branching and extending 2D distance from centre with age. (F) Plot shows increased number of intersections with development (n=5, One-Way ANOVA).

inhibition with the drug Latrunculin B which impacts the EC cytoskeleton (Fig. 5.12A). Data were pre-processed, enhanced, segmented as suggested in Chapter 2 (Fig. 5.12B), allowing for inter-sample registration as suggested in Chapter 3. This showed a difference in similarity metric between untreated and treated fish ($p < 0.0001$; Fig. 5.12C). Application of the complete analysis workflow showed that actin polymerization inhibition leads to a decrease in vascular volume ($p = 0.0008$; Fig. 5.12D), network length ($p < 0.0001$; Fig. 5.12E), branching points ($p < 0.0001$; Fig. 5.12F), and average vessel diameters ($p = 0.0002$; Fig. 5.12G,H). Analysis of vascular complexity using Sholl analysis showed a slight but non-significant reduction of number of intersections ($p = 0.1829$; Fig. 5.12I,J).

Together, this showed that the proposed analysis approach was able to extract a wide range of biologically meaningful parameters that characterise the cranial vasculature in great detail. It is our belief that these will allow new quantitative insights into vascular development and disease that would not be possible by more conventional approaches.

4.4 Conclusion

Here vascular centreline extraction using ridge detection and 3D thinning were examined and their applicability in both 2D and 3D tested. It was found that 2D ridge detection and 3D thinning-based skeleton analysis is applicable to extract and describe the zebrafish cerebral vasculature. Following this, 3D BP detection was studied using the "AnalyseSkeleton" Plugin, finding that post-processing is needed to reduce the number of false-positive BPs. When examining vessel diameter sampling rates, vessel diameters in the zebrafish head vasculature span a short range and increasing sampling frequency does not impact the extracted vessel diameter significantly. Combining EDMs and 3D thinning-based skeletons allowed the extraction of meaningful parameters such as network length, branching points, endpoints, and vessel diameters. Also, work to identify, extract, and annotate individual vessel segments was examined. We here show that 2D Scholl analysis, applied to skeleton MIPs, is applicable to quantify vascular complexity.

The suggested workflow steps were merged and a GUI provided. The tested datasets include examples of fish with and without blood flow (uninjected controls, control MO, and *tnnt2a* MO), early vascular development examples (3-5dpf), and fish with actin polymerization inhibition (DMSO controls and Latrunculin B treated).

Our data show that meaningful quantification of the zebrafish cerebral vasculature is possible, allowing to quantitatively assess vascular topology.

Future work, could examine additional approaches to post-process vascular skeletons to **(a)**

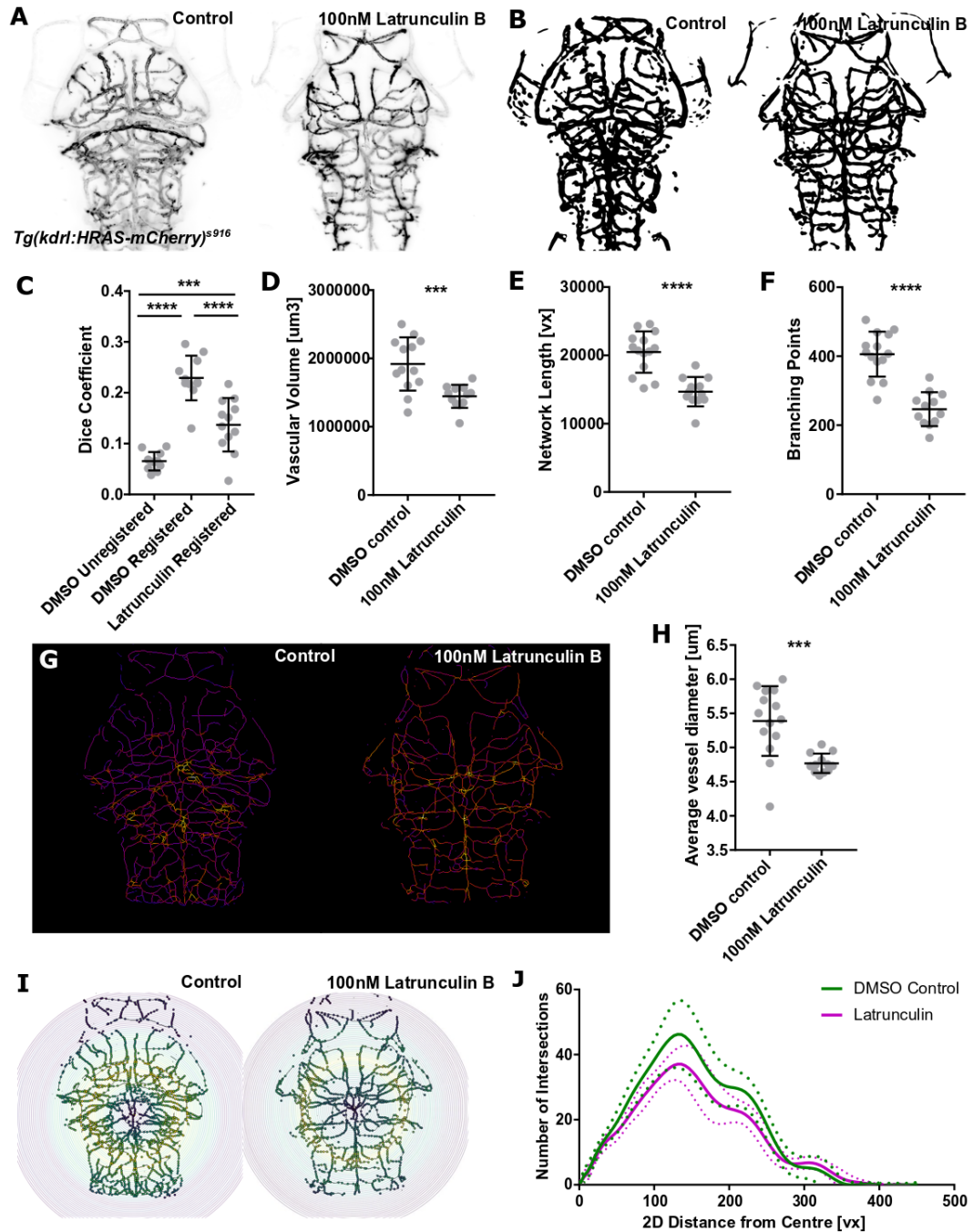


Figure 4.25: **Example biological application - impact of actin polymerization inhibition.** (A) Original data. (B) Segmented data. (C) A reduction of Dice was found when comparing registered controls to F-actin inhibitor treated samples ($p < 0.0001$; control=11, Latrunculin B=12; One-Way ANOVA; *post hoc* statistical power was 0.0602451). (D) Cerebrovascular volume was reduced ($p = 0.0008$; control=13, Latrunculin B=12; unpaired Student's t-test; *post hoc* statistical power was 0.9851150). (E) Network length was reduced ($p < 0.0001$; control=14, Latrunculin B=12; Mann-Whitney U test; *post hoc* statistical power was 0.9998935). (F) Branching points were reduced ($p < 0.0001$; control=14, Latrunculin B=12; Mann-Whitney U test; *post hoc* statistical power was 0.9999998). (G) Diameter representation. (H) Vessel diameter was reduced ($p = 0.0002$; control=14, Latrunculin B=12; Mann-Whitney U test; *post hoc* statistical power was 0.9911708). (I,J) Scholl analysis showed a non-significant reduction in complexity ($p = 0.1829$; control=14, Latrunculin B=12; Mann-Whitney U test).

decrease the number of spurious branches (this could be achieved either by surface smoothing before skeletonization, or by implementation of a length-to-diameter-thresholding after skeletonization [128]), **(b)** increase the accuracy of extracted BPs (this could be achieved by allowing only one BP in a certain 3D region, or including another approach to detect BPs such as spheres [349, 350] or deformable bodies [176]), and **(c)** decrease the number of unconnected components (this could either be achieved by performing connected component analysis before or after skeletonization [177, 351]).

More thorough evaluations are needed to ensure that the extracted vascular properties are robust. While this is obviously challenging, one approach may be to create and use a simulated zebrafish vasculature model, where the underlying parameters are known and can be varied / controlled, but this is currently beyond the scope of this thesis.

Although this work delivered the extraction of meaningful parameters, we appreciate that future work might want to focus on extracting information of individual vessels more in-depth. We here presented a theoretical of how this could be achieved, but more work needs to be done to provide a fully annotated atlas of the zebrafish cerebral vasculature. Such vascular annotation could be automated using machine learning.

If further examined, this would allow the establishment of a vascular growth atlas including a range of ages, which could then be combined with other data such as brain activity or colocalization analysis, as performed for zebrafish brain atlases [302, 303].

5 Characterisation of novel cystic endothelial membrane structures

Parts of this work were published in [1]; figures reproduced under the licence 4613080722025.

5.1 Introduction

While studying images of the embryonic cranial vasculature in *Tg(kdr:HRAS-mCherry)*^{S916} [244] previously undescribed structures were observed (Fig. 5.1A).

As these appeared to be spherical in shape, they were given the German name *kugel* (plural *kugeln*), which translates to sphere.

Initially, it was not clear whether *kugeln* were an image-acquisition artefact, or a real biological phenomenon. Further, the question arose whether *kugeln* should be included, or excluded in further vasculature quantification analysis; or if *kugeln per se* would have an impact on vascular architecture and development. Thus, experiments were designed and performed to examine the reproducibility, importance and role of *kugeln*. The key questions investigated in this Chapter are grouped into eight key categories and summarised below and in Figure 5.1B: One key question was whether *kugeln* were reproducible, what their morphology was (size, number, 3D structure, etc.), and whether they occurred in all vascular territories or just the cerebral vessels.

To elucidate the cellular and subcellular context of *kugeln*, vascular membrane, cytosol, and nuclei were examined and it was studied whether *kugeln* played a role in angiogenic sprouting and EC mitosis/apoptosis.

Following, the actin cytoskeleton was studied as the actin cytoskeleton plays a pivotal role for mechanical aspects of cells (such as adhesion or protrusion [219, 220]) as well as cellular transport processes (such as endocytosis or cell division [352]); but it was also shown that weaknesses in the cell actin cortex would lead to an outward movement of the cell membrane due to cytosolic pressure, resulting in blebbing [233, 234]. Thus, there was the rationale to examine whether loss of F-actin would impact *kugel* number or size. Similarly, the impact of Myosin II loss was studied, as it was shown for cell blebs that myosin II plays a role in actin cortex re-assembly, its re-attachment to the cell membrane, and subsequent bleb retraction [233, 234]. It was examined whether *kugeln* resembled bleb-like structures, which have been suggested to occur in the trunk vasculature in the context of mitosis [353] or lumenization [68]. Lastly, EC cytosol and surrounding neuronal tissue were studied.

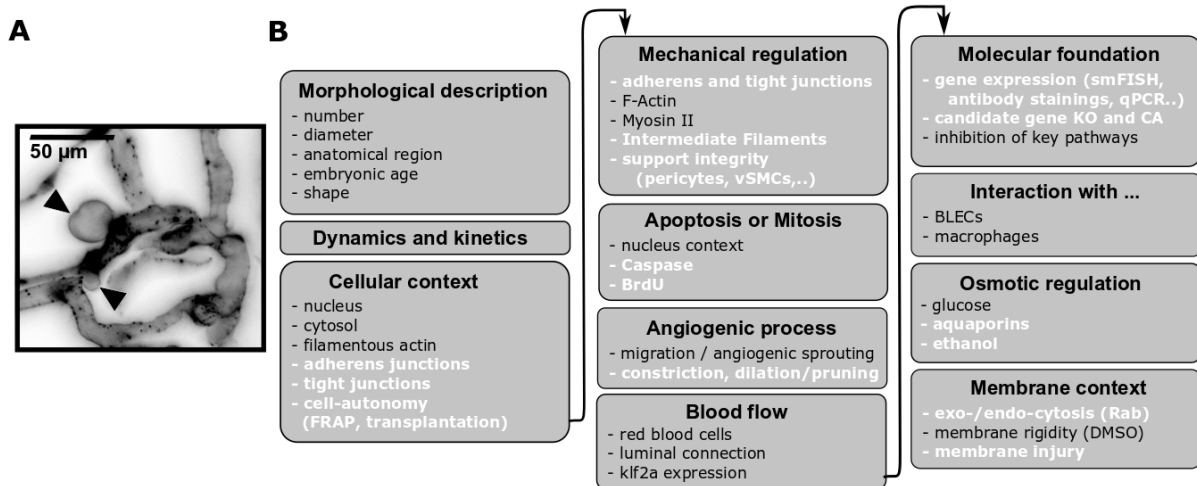


Figure 5.1: **Suggested workflow of *kugel* analysis.** (A) Previously undescribed endothelial structures, so-called *kugel*n (black arrowhead), were found during early experimental work in the scope of this project. (B) Suggested workflow towards characterisation and investigation of *kugel*n. The conducted experiments addressed description of morphology, dynamics, and cellular context of *kugel*n. Also, the involvement of *kugel*n in apoptosis, mitosis or angiogenesis was studied. Additionally, data were obtained to investigate the role of blood flow, major signalling pathways, the possible interaction with lymphatic cells and macrophages, as well as osmotic pressure, and membrane rigidity. (*black*: data or preliminary data acquired; *white*: suggested routes of investigation)

As *kugel*n structurally resembled aneurysms, there was the rationale to study whether blood flow was the driving force of *kugel* formation as it is the case for aneurysms.

Vascular Endothelial Growth Factor (VEGF) signalling is pivotal for physiological vasculogenesis and angiogenesis [56, 58, 354]. VEGF signalling plays a crucial role in different aspects of vessel formation as secreted VEGF ligand acts as a guidance cue for angiogenic sprouts during the *de novo* formation of vascular beds [56, 58, 355]. VEGF decreases paracellular junction complexes (adherens junction (AJ) by phosphorylation of VE-Cadherin) [356, 357] in cell lines [358], mice [356], as well as zebrafish [359]. This is of special relevance in the context of development, cancer, or ischaemia [360]. Due to these impacts of VEGF on ECs, there was the rationale to examine the impact of VEGF inhibition on *kugel*n.

Nitric oxide (NO) is a downstream signalling factor of VEGF and, as a gaseous signalling molecule, nitric oxide (NO) is thought to passively diffuse through membranes but was also reported to be transported via gap junctions [361]. NO plays also a role in inflammation, neurotransmission, and neurovascular coupling [362, 363, 364]. NO impacts the vasculature in a paracrine manner via vascular smooth muscle cell (vSMC)-mediated vasodilation [365],

as well as by playing a role in vascular oxidative stress [366]. In mammalia NO is either produced by enzymatic synthesis (endothelial nitric oxide synthase (eNOS), neuronal nitric oxide synthase (nNOS), or inducible nitric oxide synthase (iNOS) [366]), enzymatic reduction (xanthine oxidoreductase [367] or deoxygenated hemoglobin [368]), or chemically by acidic reduction [369]. The existence of eNOS in zebrafish remains controversial in the literature, as Syeda et al. [370] postulated the non-existence of messenger ribonucleic acid (mRNA) or protein in fish, while Fritsche et al. [371] reported eNOS occurrence in the dorsal vein. Still, NO itself was previously studied in zebrafish and shown to influence cranial neuronal development [372].

Together, there was the rationale to examine whether NO would be found to associate with *kugel*n or whether NO-level alteration could impact *kugel* formation.

The Notch signalling pathway counterbalances VEGF signalling, restricts angiogenesis, and is critical for arterial differentiation [55, 373, 374, 375]. Its role in cell-cell lateral inhibition is pivotal for development. Studies in vascular tip-stalk-cell formation showed that the VEGF-A ligand acts as a cytokine sensed by tip-cells via VEGFR2/kdr1. Following, *dll4* is increased in tip-cells, which leads to induction of Notch signalling in neighbouring stalk cells by lateral inhibition [42].

Thus, we investigated whether *kugel*n are affected upon inhibition of Notch signalling.

Recent studies highlighted the importance of Wnt signalling in angiogenesis. This is exemplified by the fact that canonical Wnt signalling is required for the formation of dorsal cerebral vessels and the formation of the BBB. A lack of canonical Wnt signalling via the Reck/Gpr124 receptor complex results in a lack of BBB-forming cerebral vessels [376, 377, 378, 379]. For example, Wnt signalling is required for tip-cell-fate specification during angiogenesis, but dispensable for sprout migration [377]. Also, Wnt signalling was shown to regulate cell-cell junctions via VE-Cadherin and Esama [379]. In mice, Wnt signalling was shown to regulate cerebral angiogenesis, but not angiogenesis in other vascular beds [378, 380]. To examine whether Wnt signalling had an impact on *kugel*n the impact of Wnt by inhibition and overactivation was studied using chemical compounds.

Brain Lymphatic Endothelial Cells (BLECs) were previously shown to constitute the cranial lymphatic system, deriving from veins, and closely interacting with certain cranial vessels [381]. Thus, it was investigated whether BLECs would possibly interact with *kugel*n, and whether *kugel*n maybe fulfilled a scavenging function within the cranium. Next, it was studied if *kugel*n would interact with macrophages, as it was previously shown that macrophages interact with vessels undergoing angiogenesis and repair and it was possible that *kugel*n were a vascular

response to angiogenesis or injury [382, 383]. We here use the term macrophages for the microglia examined, as microglia are a sub-type of macrophages.

Osmotic regulation was previously shown to induce changes of cellular morphology [223, 224]. Thus, preliminary experiments to investigate the role of osmotic pressure on *kugel*-formation were conducted. Moreover, the role of membrane rigidity on *kugel* appearance was studied by chemical increase of membrane fluidity with dimethylsulfoxide (DMSO).

5.2 Material and methods

5.2.1 Zebrafish strains, handling, and husbandry

Zebrafish handling and husbandry were performed as described in 2.2.1. Embryos were studied using fish lines described before as well as the following:

- *Tg(kdr1:HRAS-mCherry)^{s916}* [243] in a Casper background [384] for independent data validation were housed at the Max Planck Institute of Molecular Cell Biology and Genetics in Dresden according to institutional and international guidelines.
- Embryonic *Tg(fli1ep:EGFP-CAAX)*, to label EC membrane, were kindly provided by the Gerhardt lab [68] to be raised and housed at the University of Sheffield.
- *Tg(gata1:dsRed)* labels red blood cells (RBCs) [385];
- *Tg(fli1a:AC-tagRFP)^{sh511}* (unpubl., Aaron Savage) labels EC cytosol;
- *Tg(flk1:nls-eGFP)^{zf109}* [386] labels EC nuclei;
- *Tg(nbt:GCaMP3)* [387] labels developing neurons;
- *Tg(dll4in3:GFP)* labels the Notch delta-like ligand 4 (*dll4*; kindly provided by the De Val lab) [374];
- *Tg(TP1glob:venusPest)^{s940}* (kindly provided by Ryan McDonald) [388];
- *Tg(fms:GAL4.VP16)ⁱ¹⁸⁶*, *Tg(UAS-E1b:nfsB.mCherry)ⁱ¹⁴⁹*, *Tg(fli1a:eGFP)^{y1}*, *Tg(kdr1:HRAS-mCherry)^{s916}* [389] labels macrophages, EC cytosol, and EC membrane.

5.2.2 Generation of zebrafish with transient expression of

Tg(fli1a:myr-mCherry)

The plasmid pTol2-fli1a-myr-mCherry (8975bp) to label EC membrane under the *fli1a* promoter using myristoylated (myr) mCherry was kindly provided by Naoki Mochizuki [390, 391]. Plasmid was transformed using E.Coli (Sigma-Aldrich), followed by LB culturing

with Ampicillin resistance for amplification, and purification using Midi-prep (Macherey-Nagel). Concentration was quantified using Nanodrop.

Injection was performed at one-cell state with a final injection concentration of 50pg plasmid and 75pg Tol2.

5.2.3 Microangiography

Microangiography was performed to study whether a *kugel*-lumen connection existed. Visualization of perfused vessels was conducted as described in [73, 392], using 20 μ g dextran tetramethylrhodamine (2,000,000 molecular weight, ThermoFisher) at a concentration of 10mg/ μ L (2nl injection volume), kindly supplied by Rob Wilkinson.

5.2.4 Imaging methodology

Image acquisition was performed as described in section 2.2.2. 3D time-lapses were performed as follows: 10 minutes, total 200 images (every 3 seconds); 15 minutes, total 30 stacks (every 30 seconds); and overnight 12 hours, 36 stacks (every 10 or 20 minutes).

Independent data acquisition by Stephan Daetwyler at the Max Planck Institute of Molecular Cell Biology and Genetics in Dresden was conducted with a custom-built multidirectional SPIM (mSPIM) setup [393]. The whole head was imaged every 2-3 min over 2 days with dual-side illumination. The mSPIM setup was equipped with a Coherent Sapphire 561 nm laser, two Zeiss 10x/0.2 illumination objectives, an UMPlanFL N Olympus 20x/0.5 NA detection objective, and an Andor iXon 885 EM-CCD camera. To cover the whole head, several regions were imaged and later stitched using custom image processing plugins in Fiji [127] based on the stitching tool from Stefan Preibisch [394]. Sample embedding was performed in FEP tubes coated with 3% methyl cellulose and filled with 0.1% low-melting agarose containing 200 mg/l Tricaine to immobilize the zebrafish embryos during time-lapse imaging as described in [253].

Inter-sample registration for investigation of anatomical location of *kugel* occurrence was performed with a manual anatomical landmark-based approach as described in Chapter *Inter-sample Image Registration*.

5.2.5 Multiview image reconstruction

Multiview image acquisition was performed as described in [395]. Briefly, acquisition settings were as follows: minimum laser power and exposure time, activated pivot scan, automatic light-sheet alignment, dual side illumination with online fusion and separate colour-tracks for GFP and RFP.

Selection of four multiview acquisition angles (90° intervals) was performed via the built-in Zeiss multiview-acquisition wizard, while z-stack depth was defined manually. Acquisition of consecutive angles was performed with a delay of 2 seconds to avoid mechanical rotation bias.

Yellow-green 1 μ m fluorescent beads (Sigma; kindly supplied by Nick van Hateren) were used as fiduciary markers and stored at 4°C as 1:100 stock. A 1:20 dilution of stock was used as final working concentration in 2%-LM agarose (Sigma) with 0.01% Tricaine in E3. Image registration was performed using the "Multiview Reconstruction Application" Fiji Plugin [127, 310, 396] as described in [395]. 3D rendering for visualization was performed using Arivis Software.

5.2.6 Morpholino injections

Development of functional heart contraction was inhibited via injection of *tnnt2a* ATG morpholino (1.56 ng final concentration), as described in [345] (sequence 5'-CATGTTTGCTCT GATCTGACACGCA-3').

The role of the following Notch signalling ligands was studied using MO:

- *dll4* ATG MO at 3ng (5'-GAGAAAGGTGAGCCAAGCTGCCATG-3'; Genetools, LLC) [305]
- *notch1b* ATG MO at 0.25ng (5'-GTTCTCCGGTTACCTGGCATACAG-3'; Genetools, LLC) [305]
- *Jagged-1a* ATG MO at 0.1ng (5'-GTCTGTCTGTGTGTCTGTGCGCTGTG-3'; Genetools, LLC) [397]
- *Jagged-1b* ATG MO at 1.8ng (5'-CTGAACTCCGTCGCAGAATCATGCC-3'; Genetools, LLC) [397]

Development of lymphatic cells was inhibited by injection of collagen and calcium-binding EGF-like domain 1 (*ccbe1*) ATG MO (5ng final concentration; Genetools, LLC), as described in [398] (sequence 5'-CGGGTAGATCATTTTCAGACACTCTG-3'; kindly provided by Stefan Schulte-Merker).

Control morpholino injections (5'-CCTCTTACCTCAGTTATTTATA-3'; no target sequence and little/no biological activity; Genetools, LLC) were performed with the above final concentration to study off-target effects of injections. Injections were conducted at one-cell-stage using phenol red as injection tracer.

5.2.7 Dextran injection into brain ventricles

Scavenging activity of *kugeln* and BLECs was studied by injection of IgG-conjugated 150 kDa Alexa Fluor 674 (0.2mg/ml, ThermoFischer, A31573, RRID:AB_2536183; kindly provided by

Stefan Schulte-Merker) into the brain ventricle at 3dpf, as previously described [381].

5.2.8 Reduction of blood flow and exsanguination

Reduction of blood flow was achieved by temperature reduction of the image acquisition chamber to 10°C for 60min [399].

Exsanguination was performed by mechanical heart opening with forceps after control image acquisition.

Transient heart contraction stop was performed using 2.5mM Tricaine in E3 for 20min. Following image acquisition, samples were placed into E3 without Tricaine until full heart recovery was established to assess non-lethality of Tricaine exposure.

5.2.9 Chemical treatments

Inhibition of VEGF signalling was induced by the VEGF-receptor inhibitor AV951 at 250nM for 2-4h between 96-98hpf or 96-100hpf (Selleckchem; S1207; Tivozanib - AVEO pharmaceuticals) [266].

F-actin depolymerization was achieved by 100nM Latrunculin B for 1h between 96-97hpf (Sigma-Aldrich; L5288-1MG; kindly provided by Rob Wilkinson) [346].

Inhibition of Myosin II was achieved by 25 μ M Blebbistatin in E3 with 1% DMSO for 1h between 75-76hpf (Sigma; kindly provided by Emily Noel).

Inhibition of γ -secretase in the Notch signalling cascade was achieved by 50 μ M DAPT for 12h between 84-98hpf (Sigma-Aldrich; D4952) [265].

Inhibition of Wnt signalling was by 10 μ M XAV-939 for 4h from 72-76hpf (Sigma; kindly provided by the Perak lab).

Activation of Wnt signalling was by 10 μ M GSK-3 inhibitor XV for 4h from 72-76hpf (Merck; kindly provided by Henry Roehl).

DMSO control at the same concentration and duration was used for Latrunculin B, AV951, DAPT, GSK-3 inhibitor, and XAV-939 treatments.

Inhibition of nitric oxide synthase (NOS) was achieved by application of 0.5mM N-nitro-L-arginine methyl ester hydrochloride (L-NAME) (Sigma-Aldrich; 50912-92-0) for 18h from 3-4dpf. Controls were incubated in E3.

Nitric oxide was supplied by application of 0.1mM sodium nitroprusside (SNP) 25h in E3 for 25h from 2-3dpf.

Osmotic pressure was increased via treatment with 40mM glucose (Sigma) in E3 for 24h

(72-96hpf). Membrane rigidity was increased via 2.5% (v/v) DMSO (Sigma) in E3 for 24h (72-96hpf). Controls for osmotic pressure and membrane rigidity were incubated in E3.

5.2.10 Live dyes

Visualization of NO *in vivo* was performed via application of 2.5 μ M 4-amino-5-methylamino-2,7-

difluorofluorescein diacetate (DAF-FM-DA) (Molecular Probes; D23844) [400, 401] for 6h in 4-5dpf embryos. DMSO control was performed with the same concentration and duration.

Visualization of acidic components was performed using LysoTracker Green (Molecular Probes; L7526 DND-26) 1mM stock diluted to 8.33 μ M in E3 [402]. Incubation was done for 5h between 96-101hpf. Controls were incubated in E3.

5.2.11 Image and data analysis

Kugel diameter. Quantification of *kugel* diameters was performed manually using the line ROI tool in Fiji [127]. Dynamic changes of *kugel* diameter over time were visualized with kymographs. (Fiji "image > stacks > reslicing").

Vessel tortuosity. Vessel tortuosity (T) was measured by division of minimum Euclidean distance ($L_{shortest}$) by total length between measurement endpoints (L_{total} ; Eq. 5.1).

$$T = L_{shortest}/L_{total} \quad (5.1)$$

Statistics. As described in section 2.2.10.

5.3 Results and discussion

5.3.1 Morphological description and physiological occurrence

5.3.1.1. *Kugel* number and diameter is consistent during early vascular development

Observation of multiple embryos showed that the majority displayed at least one *kugel* from 3-5dpf: 3dpf 33/39, 4dpf 26/37 and 5dpf 29/37 (5 replicates). Measuring *kugel* number and diameter from 3-5dpf showed no difference over time (number p 0.8571 Fig. 5.2B; diameter p 0.3258; Fig. 5.2C). Together, these data suggested that neither *kugel* number nor diameter are age-dependent during the investigated time-frame and that *kugeln* are reproducible and highly prevalent.

Having found a high CoV in *kugel* diameters per sample (eg. 3dpf 46.28%) and in order to avoid over-sampling, average *kugel* diameter per sample will be shown in the remainder of this chapter.

Also, data from older samples were examined and *kugeln* in samples at 8dpf (Fig. 5.2D) as well as samples at 28dpf were observed (Fig. 5.2E; 28dpf data provided by Max van Lessen from the Stefan Schulte-Merker laboratory). As image quality in older fish was reduced due to increased sample size and, thus, decreased penetration depth during image acquisition, robust quantification of *kugel* number or diameter were not possible in these older fish.

As datasets were acquired in other laboratories (data from Stephan Daetwyler from the Jan Huiskens laboratory and Max van Lessen from the Stefan Schulte-Merker laboratory) showed *kugeln*, it was assumed that *kugeln* were not caused by an in-house transgenic line artefact or mutation. Additionally, observation of *kugeln* in older fish suggested that *kugeln* were not only a phenomenon of very early angiogenesis, but may persist in even older animals than those examined.

5.3.1.2. *Kugeln* are spherical in 3D

To gain insight into the 3D structure and tissue context of *kugeln*, 3D multiview reconstruction was performed as 3D multiview reconstruction was previously shown to increase structural resolution [310, 396]. This confirmed that *kugeln* were 3D spheres, rather than membranous sheets, extending abluminally from parent vessels (Fig. 5.3).

5.3.1.3. *Kugel* are restricted to the head vasculature

To understand on what vascular bed *kugeln* occurred, inter-sample registration using manually placed anatomical landmarks was performed as in Chapter 3. Bringing samples into a common spatial coordinate system enabled us to localize *kugeln* to the central dorsal cranial vasculature (Fig. 5.4A). As this restriction to the central cranial vasculature seemed striking, the type of vascular segments with *kugeln* were characterised more specifically. This showed that the majority of *kugeln* occurred on the MMcTA (57.01%) and CtA (16.82%; Fig. 5.4B), while very few were located on more peripheral vessels such as the PMBC (0.93%). No *kugeln* were observed in other vascular beds, such as the trunk vasculature. Interestingly, *kugeln* were never observed to protrude from the BA or DA. Assessing *kugel* localization regarding left-right distribution in the cranial vessels showed no difference ($p = 0.0605$; Fig. 5.4C).

5.3.1.4. *Kugel* are dynamic and transient

Time-lapse movies were acquired to elucidate *kugel* morphology over time. *Kugeln* were dynamic structures, inflating from, and retracting into parent vessels (Fig. 5.5A). Observed behaviours included shape changes, retraction, inflation, or more static behaviour (Fig. 5.5B).

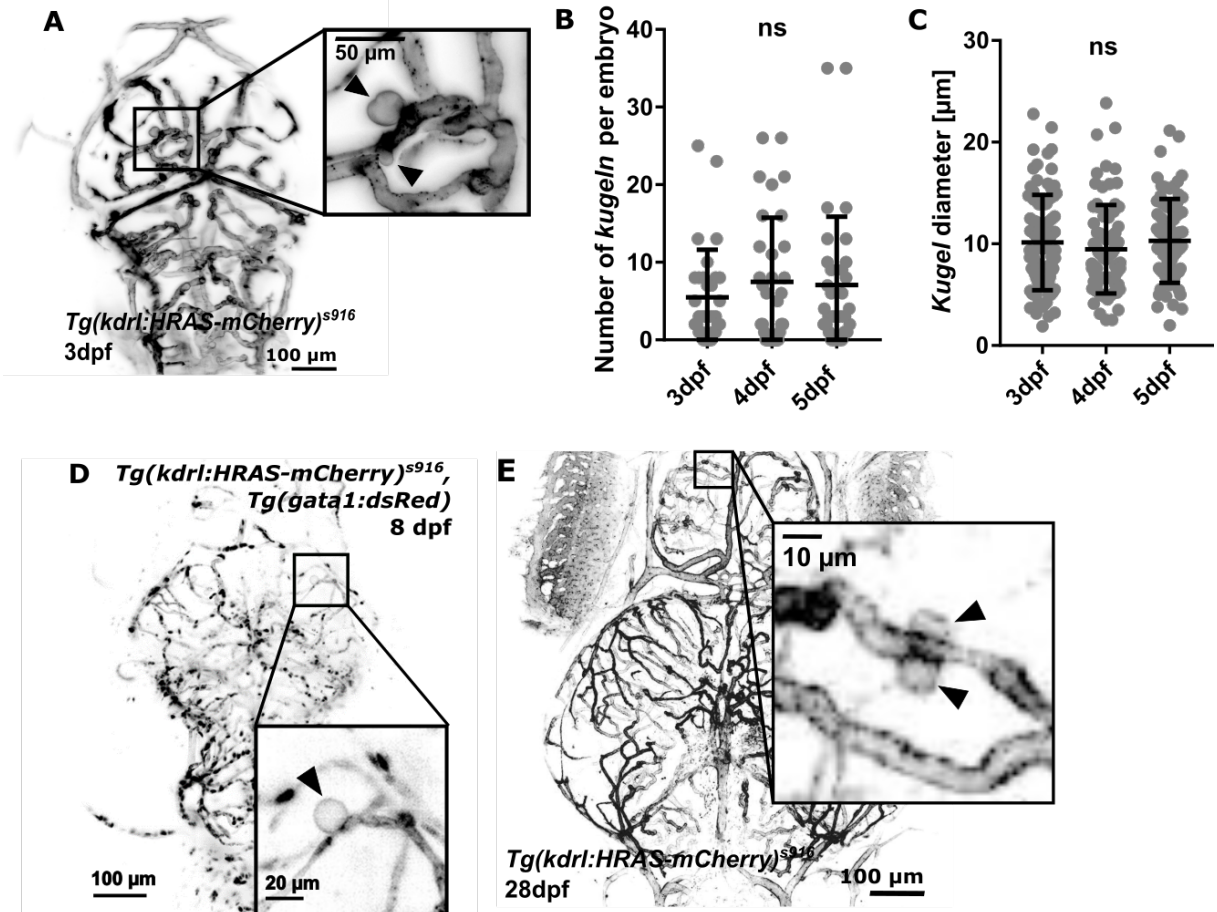


Figure 5.2: **Morphological description and physiological occurrence of *kugeln*.** (A) *Kugeln* displayed themselves as outward facing membrane bulges (black arrowhead; inverted MIP). (B) *Kugel* number showed no difference between 3-5dpf (p 0.8571; $n=32$ each; 4 experimental repeats; Kruskal Wallis test). (C) *Kugel* diameter showed no difference between 3-5dpf (p 0.3258; *kugeln* 3dpf $n=93$, 4dpf $n=81$, 5dpf $n=73$; 3 experimental repeats, Kruskal Wallis test). (D) *Kugeln* were observed at 8dpf in data acquired at the University of Sheffield (black arrowhead). (E) Embryos at 28dpf showed *kugeln* (black arrowhead; data kindly provided by Max van Lessen; University of Münster).

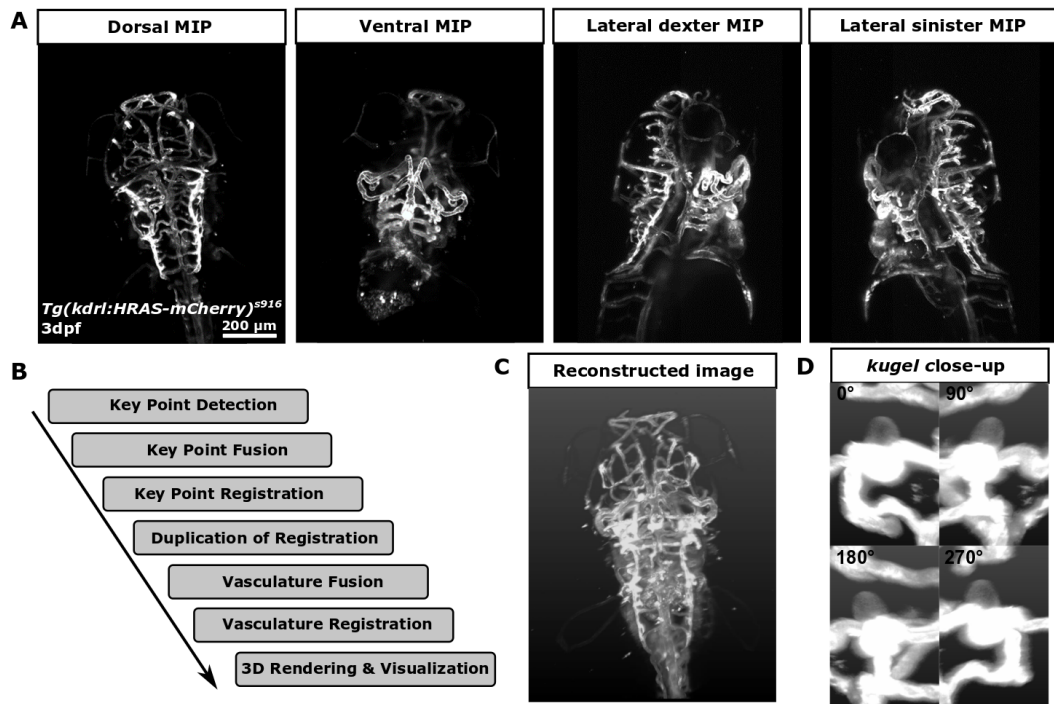


Figure 5.3: **3D *kugel* structure after multiview reconstruction.** (A) Data acquired from multiple views of the cardiovascular system were registered according to the workflow (B). (C) 3D rendering of multiview reconstruction of 3dpf *Tg(kdrl:HRAS-mCherry)^{s916}* showed that *kugeln* were 3D spheres extending abuminally from parent vessel segments (D; MMCtA).

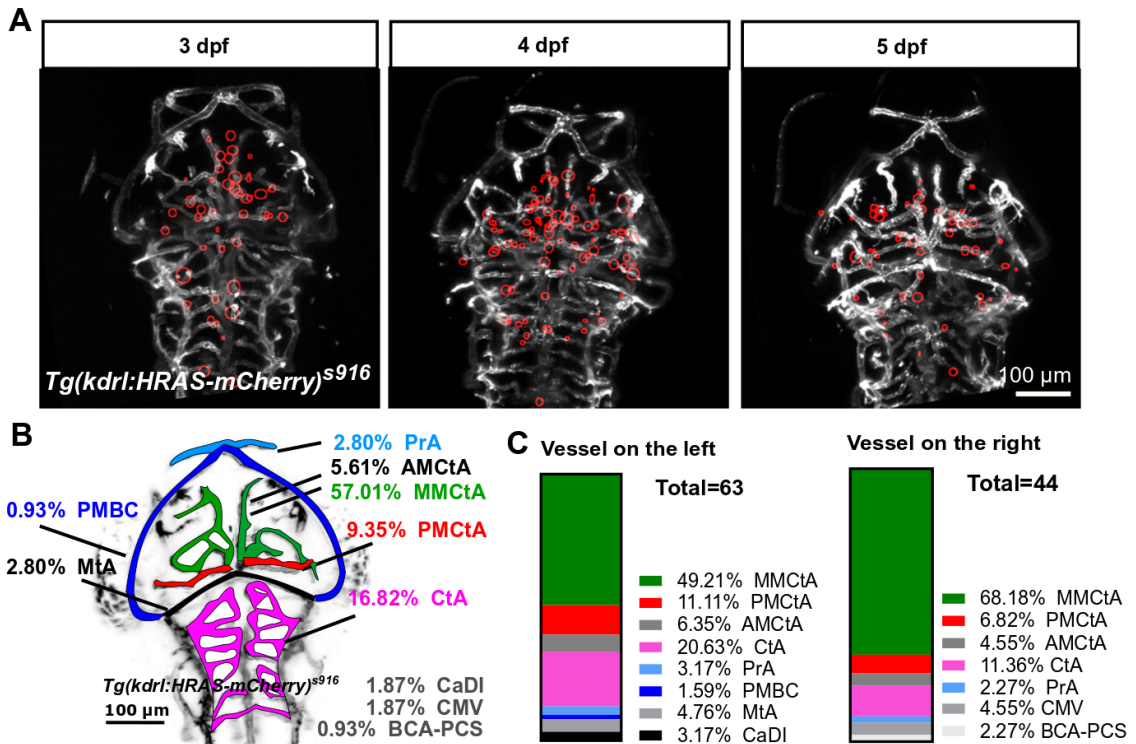


Figure 5.4: ***Kugel* protrude from dorsal cerebral vessels and show no left-right pattern.** (A) Overlay of *kugel* localization of six registered embryos showed that *kugel* predominantly protruded from central dorsal cranial vessels (n=6 embryos; representative vasculature image for anatomical context). (B) Quantification of *kugel*-parent-vessel identity showed that the majority of *kugel* protruded from the MMcTA (57.01%), CtA (16.82%) and PMcTA (9.35%). (C) Comparing *kugel* left-to-right distribution showed no difference (p 0.0605, 34 4dpf embryos, n=107 *kugel*; Wilcoxon test; 4 experimental repeats). Abbr.: AMcTA - anterior mesencephalic central artery, BCA - basal communicating artery, CaDI - caudal division of internal carotid artery, CMV - communicating vessel, CtA - central artery, MMcTA - middle mesencephalic central artery, MtA - metencephalic artery, PCS - posterior communicating segment, PMBC - posterior midbrain channel, PMcTA - posterior mesencephalic central artery, PrA - prosencephalic artery;

Importantly, *kugel*n were never observed to separate, burst or anastomose.

Further analysis of *kugel* shape and diameter in time-lapse movies showed that some *kugel*n displayed oscillatory changes in morphology (diameter and shape) over minutes (Fig. 5.6A), which is a very different timescale to heartbeat frequency (milliseconds; Fig. 5.6B).

Quantification of persistence showed that some *kugel*n protruded only for a few minutes, whilst others for hours (Fig. 5.7A). These data indicated that *kugel*n were dynamic rather than stable protrusions, showing variability in shape as well as duration of persistence. Also, embryos could display *kugel*n at a certain time-point (Fig. 5.7B, 55:20:00, red arrowhead) but later not (Fig. 5.7B 56:20:00).

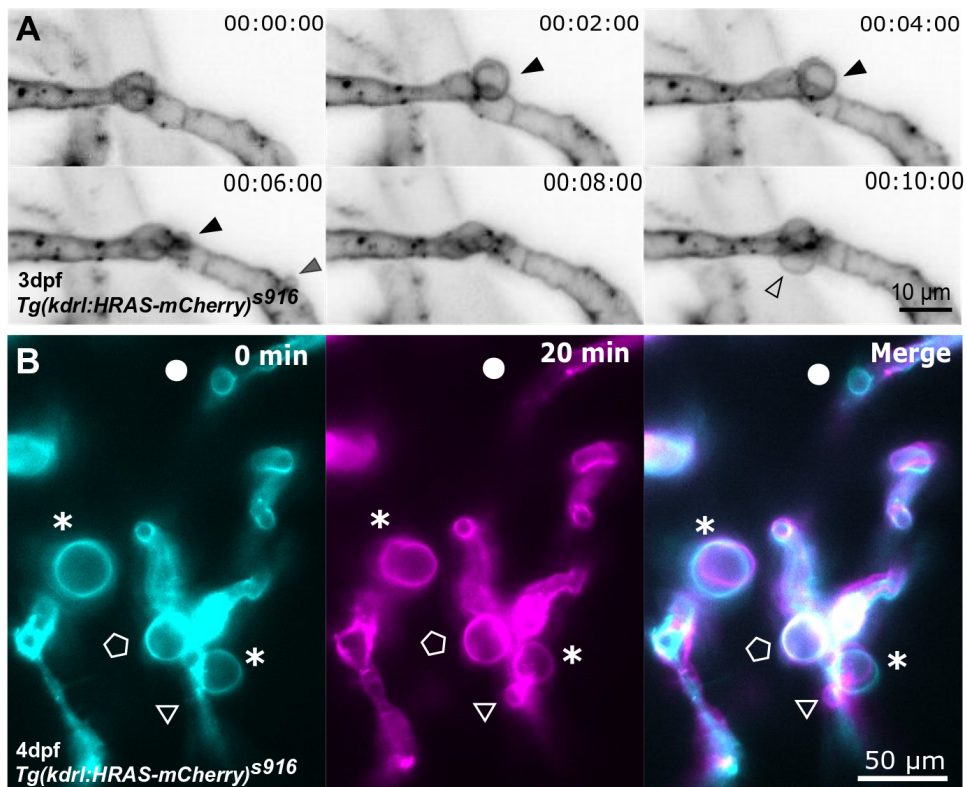


Figure 5.5: ***Kugel* are transient dynamic structures.** (A) *Kugel*n inflate and retract back into parent vessels, rather than bursting, shedding, or undergoing anastomosis (arrowheads; hh:mm:ss). (B) Comparing *kugel* morphology at 0min with their shape at 20min showed that *kugel*n were dynamic; included shape changes (asterisk), retraction (circle), inflation (triangle), and stationary (pentagon).

5.3.1.5. *Kugel*n are only found in membrane-tagged transgenic reporter lines

To investigate whether *kugel*n would be observed in transgenic lines other than the endothelial membrane-specific *Tg(kdrl:HRAS-mCherry)^{s916}*, we examined endothelial reporter lines which visualize F-actin (*Tg(fli1a:AC-tagRFP)^{sh511}*; Fig. 5.8A and *Tg(fli1a:Lifeact-mClover)^{sh467}*; Fig. 5.8B) and cytosol (*Tg(fli1a:eGFP)^{y1}*; Fig. 5.8C) under the pan-endothelial *fli1a* promotor. In

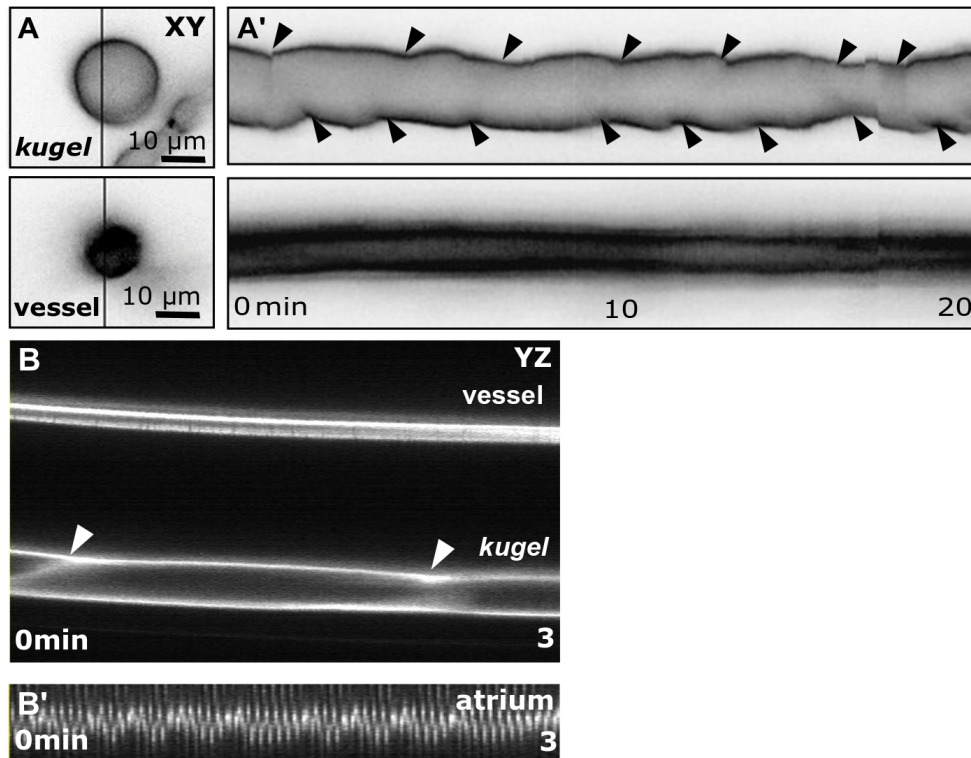


Figure 5.6: **Some *kugel*n show oscillatory shape changes.** (A) Timelapse acquisitions showed that some *kugel*n changed shape in an oscillatory fashion, as visualized by diameter kymographs (A'). (B,B') Such oscillations were not observed in vessels and were on a larger scale than the heartbeat frequency.

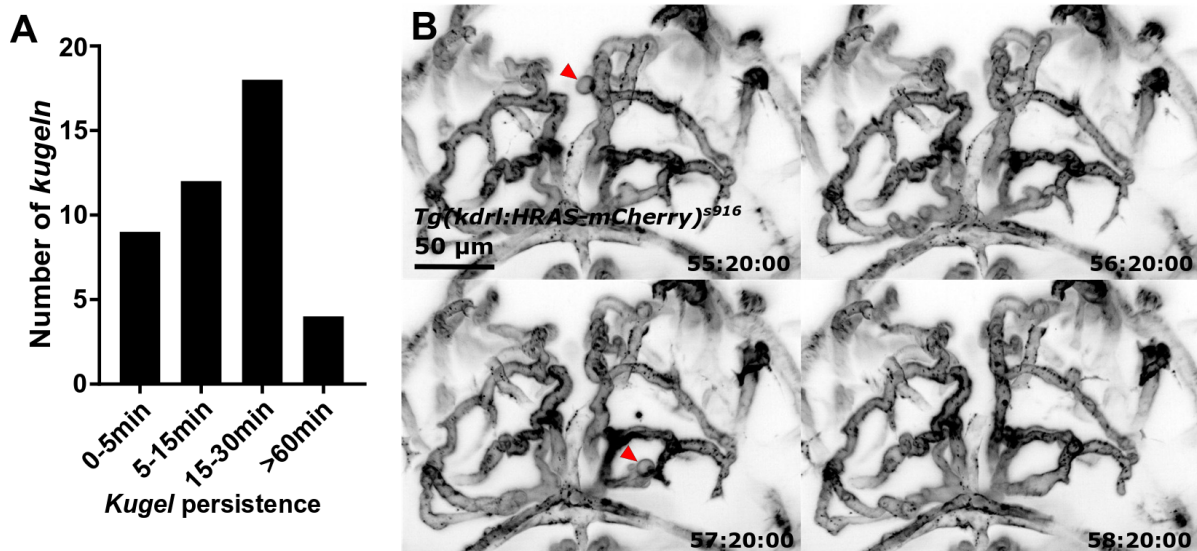


Figure 5.7: ***Kugel*n show variable persistence.** (A) Duration of *kugel* appearance was variable, ranging from a few minutes to hours (4dpf 9 embryos; n=43 *kugel*n). (B) *Kugel*n are dynamic structures, which were not persistently found in samples. Here, at 55:20:00hpf and 57:20:00hpf a *kugel* was observed (red arrowhead), while non were seen at 56:20:00hpf and 58:20:00hpf.

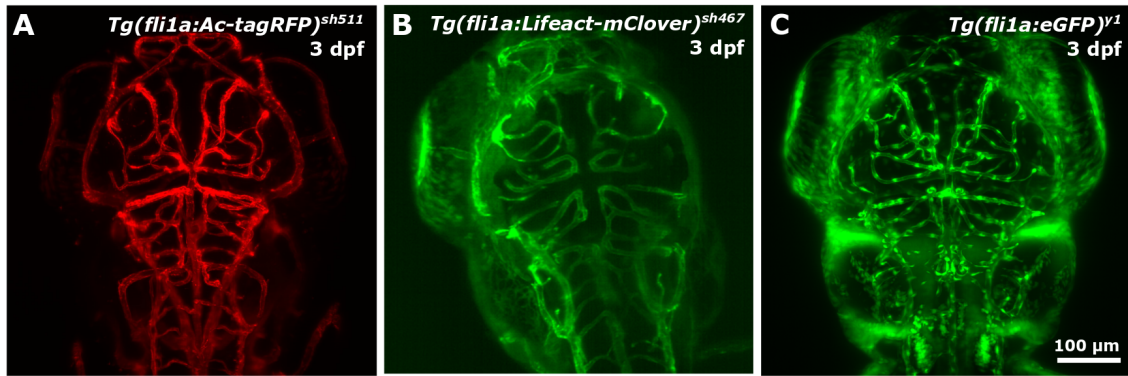


Figure 5.8: ***Kugeln* are not observed in non-membrane specific reporter lines.** *Kugeln* were not observed in transgenic reporter lines which do not specifically visualize the endothelial vascular membrane; such F-actin reporters (A) *Tg(fli1a:Ac-tagRFP)^{sh511}* or (B) *Tg(fli1a:Lifeact-mClover)^{sh467}*, or the cytosolic reporter line (C) *Tg(fli1a:eGFP)^{y1}*.

neither of them *kugeln* were detected.

Tg(fli1ep:EGFP-CAAX)

Next, the membrane-specific transgenic line *Tg(fli1ep:EGFP-CAAX)* was examined (Fig. 5.9A). This line uses *fli1a* (rather than *kdrl* as it is the case in *Tg(kdrl:HRAS-mCherry)^{s916}*) as a promoter and a shorter CAAX sequence to target eGFP to the membrane. *Kugeln* were indeed found in this transgenic and showed the same dynamic behaviour (Fig. 5.9B). This further suggested that *kugeln* were not a transgenic line artefact specific to *Tg(kdrl:HRAS-mCherry)^{s916}*.

Quantification of *kugel* number per embryo in *Tg(fli1ep:EGFP-CAAX)* at 4dpf showed an average of 1.67 ± 0.39 per embryo (Fig. 5.9C). The average diameter was $3.59 \pm 0.26 \mu\text{m}$ (Fig. 5.9D).

Finding a lower average number and diameter of *kugeln* in the *Tg(fli1ep:EGFP-CAAX)* in comparison to *kdrl:HRAS-mCherry)^{s916}* was likely to be due to the highly fluctuating signal levels in individual ECs in *Tg(fli1ep:EGFP-CAAX)* (Fig. 5.9E).

The lower CNR levels in *Tg(fli1ep:EGFP-CAAX)* in comparison to *kdrl:HRAS-mCherry)^{s916}* (p 0.0157; Fig. 5.9F) suggested that some *kugeln* may not be visualized in *Tg(fli1ep:EGFP-CAAX)*.

Tg(fli1a:myrCherry)

To further investigate whether *kugeln* were an artefact introduced by the prenylation of the CAAX-sequence in *Tg(kdrl:HRAS-mCherry)^{s916}* and *Tg(fli1ep:EGFP-CAAX)* lines, it was tested whether *kugeln* would be observed when the fluorophore was located to the membrane by myrosilation. The plasmid pTol2-fli1a:myr-mCherry was injected, together with Tol2 RNA,

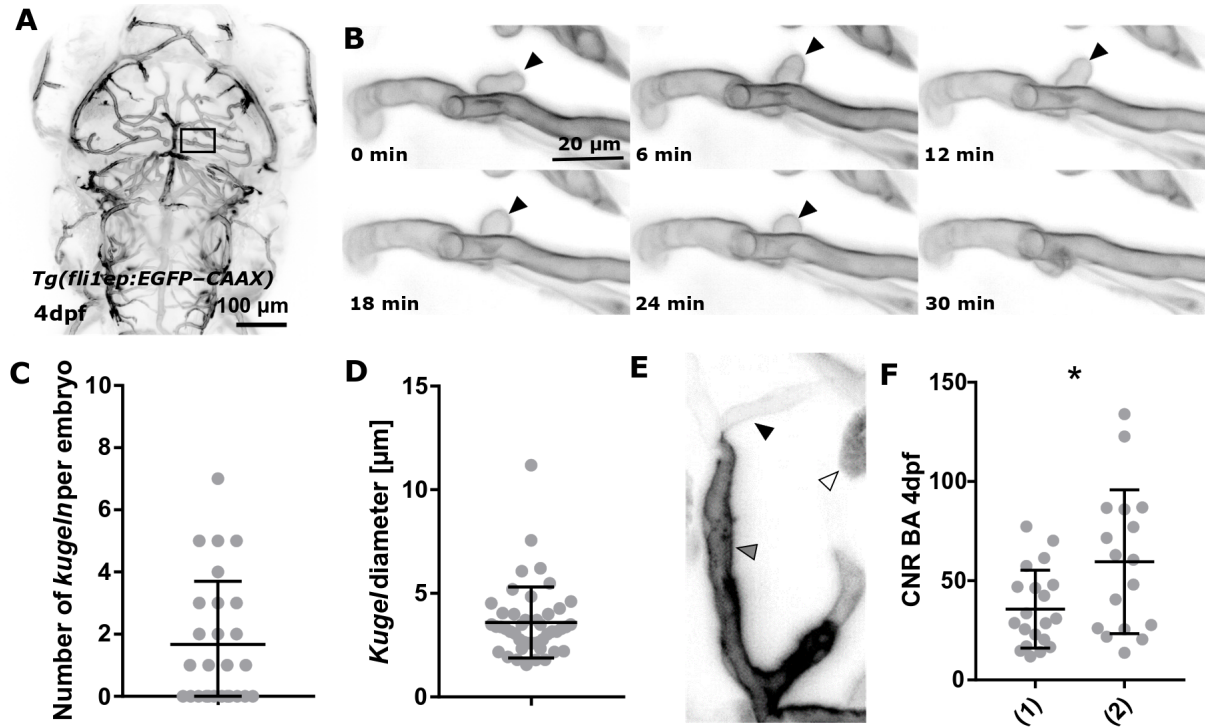


Figure 5.9: **Investigation of *kugeln* in *Tg(fli1ep:EGFP-CAAX)*.** **(A)** *Kugeln* were observed in the endothelial membrane-specific *Tg(fli1ep:EGFP-CAAX)*. **(B)** Time-lapse acquisitions showed that *kugeln* were equally dynamic as in *kdrl:HRAS-mCherry^{S916}*. **(C)** The average number of *kugeln* in *Tg(fli1ep:EGFP-CAAX)* was 1.67 ± 0.39 (s.e.m.; $n=27$; 4dpf; 3 experimental repeats). **(D)** The average diameter of *kugeln* was $3.59 \pm 0.26 \mu\text{m}$ (s.e.m.; $n=45$ *kugeln* from 27 embryos; 3 experimental repeats). **(E)** eGFP signal levels in ECs was highly variable, with some ECs being clearly visualized (grey arrowhead), while others barely visible (black arrowhead). Also, pigmentation and skin autofluorescence were visualized during image acquisition due to high laser power during image acquisition (white arrowhead). **(F)** Assessment of CNR levels showed that (1) *Tg(fli1ep:EGFP-CAAX)* had a lower fluorescence level than (2) *kdrl:HRAS-mCherry^{S916}* ($p=0.0157$; embryos *Tg(fli1ep:EGFP-CAAX)* $n=20$, *kdrl:HRAS-mCherry^{S916}* $n=17$; 2 experimental repeats; paired Student's t-test).

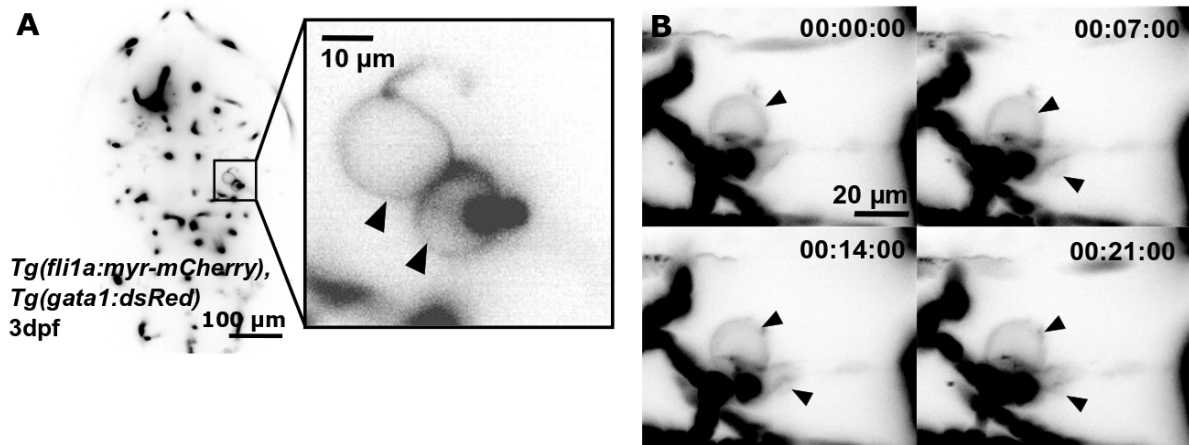


Figure 5.10: **Investigation of *kugeln* in *Tg(fli1a:myr-mCherry)*.** (A) *Kugeln* were observed in *Tg(gata1:dsRed)* injected with the plasmid pTol2-*fli1a:myr-mCherry* for EC membrane visualization (single-Z-plane representation). (B) Time-lapse acquisitions showed that *kugeln* were equally dynamic (hh:mm:ss).

into *Tg(gata1:dsRed)*. Injection into *Tg(gata1:dsRed)* was performed to allow vessel localization even in regions with no *fli1a:myr-mCherry* expression.

Image acquisition in 3dpf samples injected with the plasmid and Tol2 showed *kugeln* (Fig. 5.10A), which, again, showed similarly dynamic behaviours as in the other transgenic lines (Fig. 5.10B). Due to the mosaic nature of the construct insertion, no *kugel* quantification was performed.

This data further suggested that *kugeln* were not an artefact caused by the protein modification that induced for fluorophore localization to the EC membrane.

5.3.2 *Kugel* cellular and sub-cellular context

To study the cellular and sub-cellular context of *kugeln*, double-transgenic embryos were used to visualize the endothelial vascular membrane in parallel to cellular components of interest.

5.3.2.1. *Kugeln* are not associated with angiogenic sprouting

Parallel visualization of endothelial nuclei and membrane showed that *kugeln* did not harbour individual cell nuclei. This indicated that *kugeln* were not pathseeking angiogenic cells, but membrane protrusions from individual cells (Fig. 5.11A).

5.3.2.2. *Kugeln* are not associated with EC mitosis and/or apoptosis

Using the same double-transgenic line as above, time-lapse acquisitions were examined which showed neither mitosis nor nuclear defragmentation occurring that correlated to *kugel* formation, suggesting that *kugeln* were not a form of cell proliferation, apoptosis or necrosis.

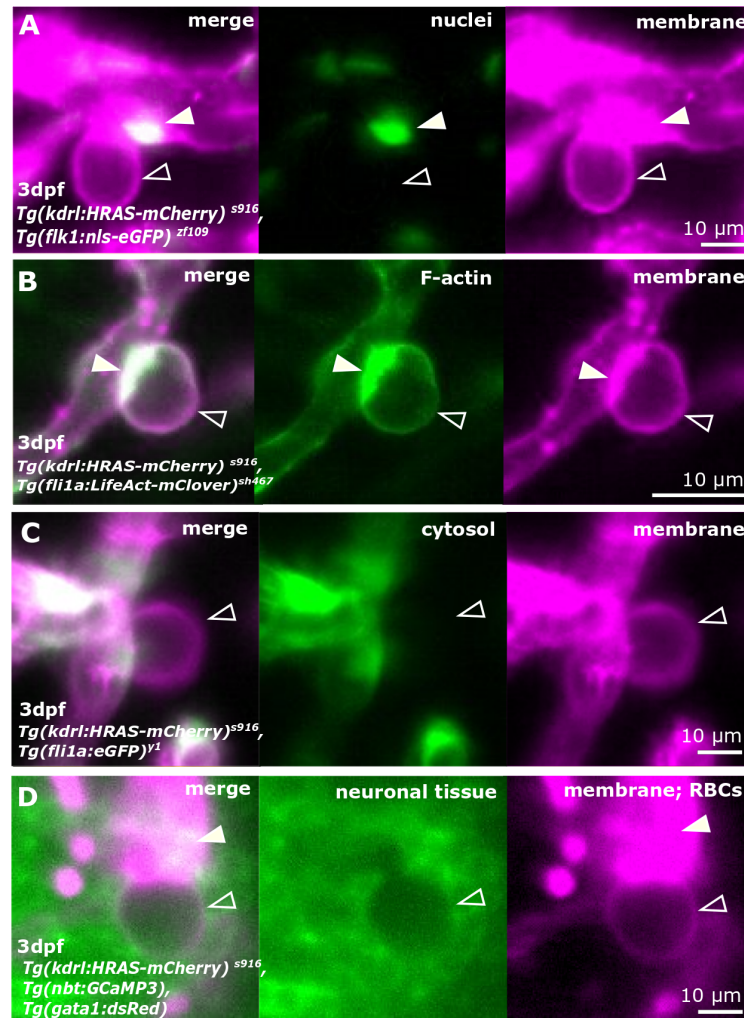


Figure 5.11: **Cellular context of *kugeln*.** (A) *Kugeln* (white unfilled arrowhead) had no individual cell nuclei (white arrowhead), which suggested that *kugeln* were abluminal membrane protrusions, rather than angiogenic sprouting cells. (B) Endothelial F-actin (white arrowhead) was localized clearly at *kugel* necks and, to a lesser extent, at *kugel* domes (white unfilled arrowhead). (C) Vascular cytosol was visualized to a very low extent or not at all in *kugeln* (white unfilled arrowhead). (D) Neuronal tissue was dislocated at *kugel* locations (white unfilled arrowhead). Also, RBCs were not inside *kugeln* (white arrowhead).

5.3.2.3. Filamentous actin (F-actin) plays a role in *kugel* formation

As it was not clear whether *kugeln* were a form of cell blebbing, the role of F-actin in *kugel* formation was investigated. Using the double-transgenic *Tg(kdrl:HRAS-mCherry)^{s916}*, *Tg(fli1a:Lifeact-mClover)^{sh467}* which visualizes EC membrane and F-actin in parallel. Endothelial F-actin was clearly co-localized at *kugel* necks and, to a lesser extent, at *kugel* domes/top (Fig. 5.11B). This co-localization suggested that F-actin may play a role in *kugel* formation or maintenance, which was further investigated.

Having seen a clear localization of vascular F-actin at *kugel* necks, the impact of actin polymerization inhibition on *kugel* formation was investigated next. To achieve this, the pharmacological actin polymerization inhibitor Latrunculin B was used (Fig. 5.12A,B) [346, 403].

Quantification of *kugel* number showed an increase in Latrunculin B treated embryos ($p = 0.0041$; Fig. 5.12C), while *kugel* diameter was decreased ($p = 0.0164$; Fig. 5.12D). The vascular lumen collapsed upon inhibition of actin polymerization; and the head vasculature was more affected than the trunk (based on visual assessment, without quantification). Moreover, *kugeln* were observed in the trunk vasculature of 2/14 embryos after Latrunculin B treatment (Fig. 5.12E, black arrowheads), suggesting that the interruption of actin cortex integrity could induce *kugeln* at ectopic anatomical locations. Further examinations are needed to examine whether these ectopically induced *kugeln* are the same as *kugeln* characterised here.

5.3.2.4. Myosin II is needed for *kugel* formation

To study whether myosin II was required for *kugel* formation or retraction, the effect of myosin II inhibition was examined by Blebbistatin application (Fig. 5.13A,B). A significant reduction in *kugel* number was found after myosin II inhibition ($p < 0.0001$; Fig. 5.13C), while no change of the average diameter was encountered ($p = 0.3731$; Fig. 5.13D).

The finding of a reduced number of *kugeln* upon Blebbistatin treatment was in coherence with the reduction of cell blebs after Blebbistatin application [225, 234]. Whether the underlying mechanisms are the same (ie. increased cellular stiffness) need to be investigated in future studies.

5.3.2.5. *Kugeln* differ from trunk inverse membrane blebbing

Previous studies suggested that bleb-like structures played a role in zebrafish trunk vascular mitosis [353] or lumenization [68]. Here, time-lapse acquisitions of the trunk vasculature were studied to compare these processes to *kugeln*. This showed that *kugeln* did not recapitulate trunk membrane blebbing which was found as membrane bulges inside the vascular lumen in order to allow lumenization (Fig. 5.14).

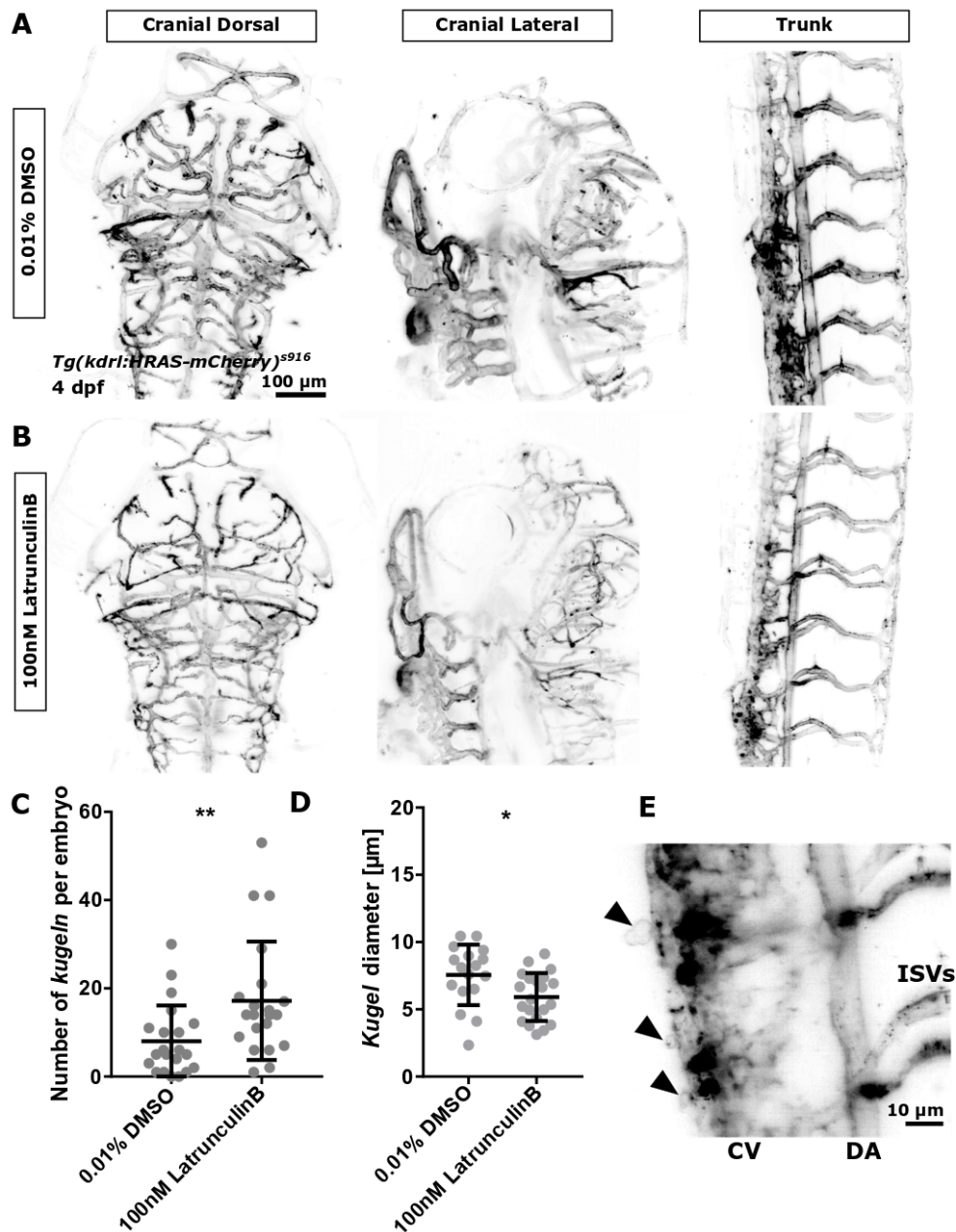


Figure 5.12: **Impact of inhibition of F-Actin polymerization on *kugeln*.** (A) Control embryos treated with 0.01% DMSO (1 hour); 4dpf *Tg(kdrl:HRAS-mCherry)^{s916}* embryos. (B) Inhibition of actin polymerization was conducted by application of Latrunculin B (100nM 1 hour). (C) Number of *kugeln* per embryo was increased (p 0.0041; n=21; 4dpf; 3 experimental repeats; Mann Whitney U test). (D) *Kugel* diameter was decreased (p 0.0164; control n=169 *kugeln* from 21 embryos; Latrunculin n=361 *kugeln* from 21 embryos; 3 experimental repeats; unpaired Student's t-test). (E) Upon treatment with Latrunculin B *kugeln* were found ectopically in the trunk vasculature in 2/14 embryos (black arrowheads; 4dpf; 2 experimental repeats). Abbreviations: CV - caudal vein, DA - dorsal aorta, ISVs - intersomitic vessels

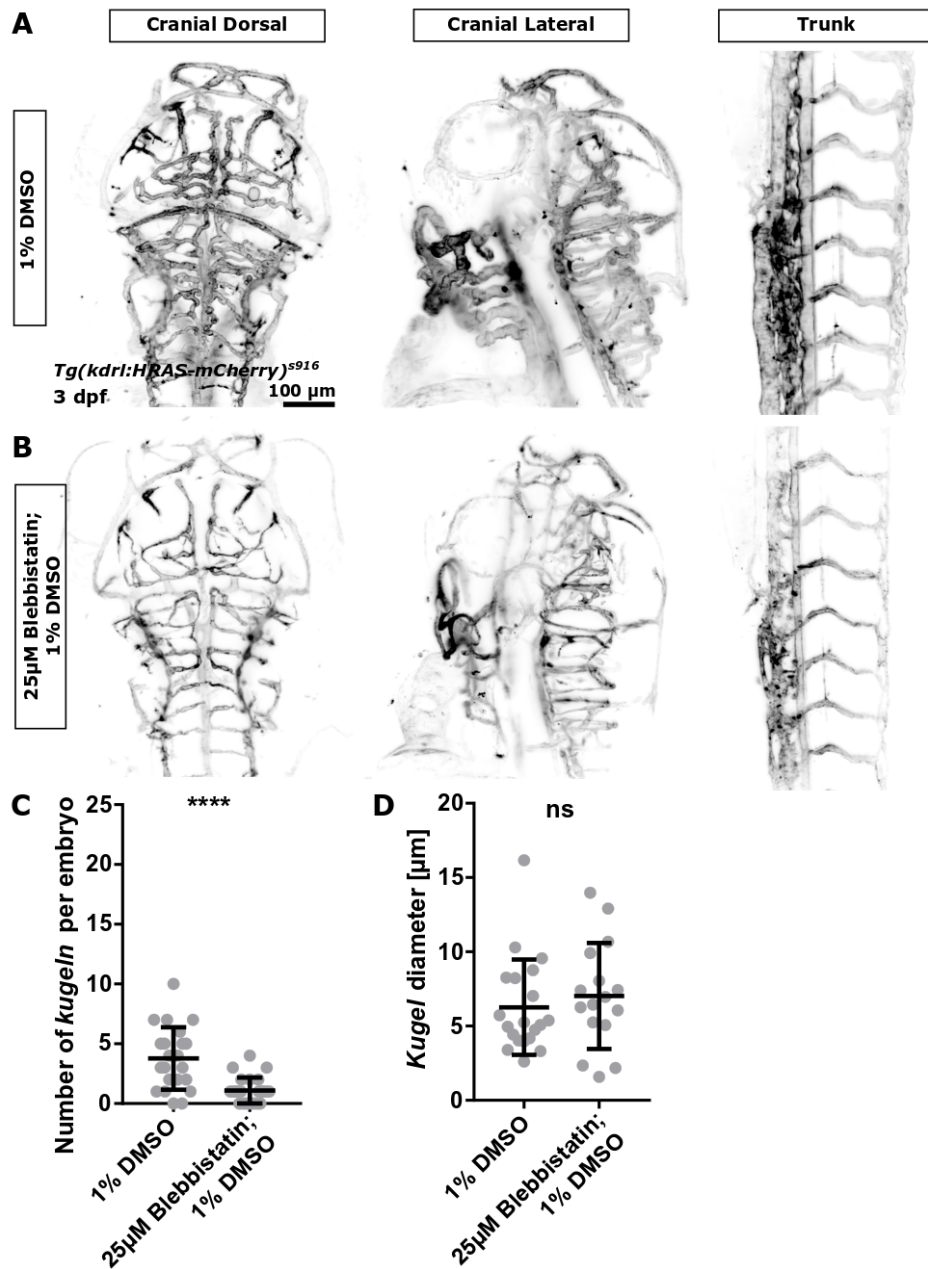


Figure 5.13: **Impact of inhibition of myosin II on *kugeln*.** (A) Control embryos were treated with 1% DMSO for 1h. (B) Myosin II was inhibited by application of 25 μM Blebbistatin and 1% DMSO for 1h. (C) The number of *kugeln* was decreased upon Myosin II inhibition ($p < 0.0001$; 3dpf control $n = 22$ embryos; Blebbistatin $n = 24$ embryos; 3 experimental repeats; Mann-Whitney U test). (D) The average diameter of *kugeln* was not changed upon Blebbistatin application ($p = 0.3731$; control = 83 *kugeln* from 22 embryos, Blebbistatin = 26 *kugeln* from 24 embryos; 3 experimental repeats; Mann-Whitney U test).

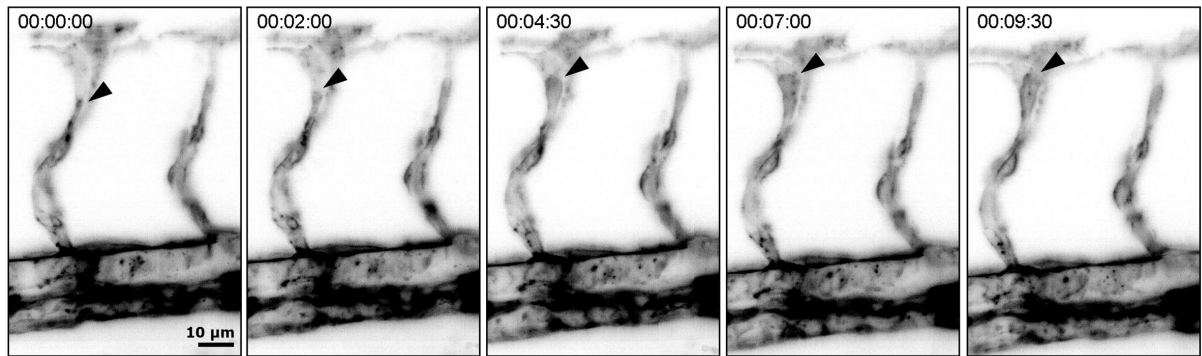


Figure 5.14: **Inverse membrane blebbing of the trunk vasculature is different to cranial *kugel*n**. Inverse membrane blebbing was previously shown to occur during trunk vasculature formation due to lumenization following blood flow onset [68]. Trunk time-lapse acquisitions showed that inverse membrane blebbing (black arrowheads) indeed occur in ISVs as described previously [68]; but did not recapitulate the outward protruding phenomenon seen in cranial *kugel*n (inverted MIPs).

5.3.2.6. EC cytosol is not driving *kugel* formation

Visualization of EC cytosol and membrane was performed in the double-transgenic *Tg(fli1a:eGFP)^{y1}*, *Tg(kdrl:HRAS-mCherry)^{s916}*. Vascular cytosol was found to be present at a very low level or completely absent within *kugel*n. This suggests that *kugel*n were membranous protrusions, constituted of the abluminal and luminal endothelial membranes in parallel and that this extensive thinning of the cytosolic compartments between the abluminal and luminal membrane may lead to reduced visibility of cytosol (Fig. 5.11C). Thinning of the cytosol between these membranes was also thought to explain why *kugel*n were not encountered in transgenic reporter lines which solely visualized the vascular cytosol or F-actin (Fig. 5.8).

5.3.2.7. Neuronal tissue surrounding *kugel*n is displaced

Visualizing neuronal tissue and EC membrane in parallel, using *Tg(kdrl:HRAS-mCherry)^{s916}*, *Tg(nbt:GCamp3)*, *Tg(gata1:dsRed)*, showed a displacement of neuronal tissue surrounding *kugel*n (Fig. 5.11D). This dislocation was thought to lead to a compression of the surrounding cerebral tissue, as previously suggested for cerebral aneurysms [237].

This transgenic line also allowed visualization of RBCs which were not observed to localize within *kugel*n, as would be assumed for aneurysms. This finding was the first suggestion that *kugel*n may not be driven by blood flow, which was further investigated in section 5.3.3.

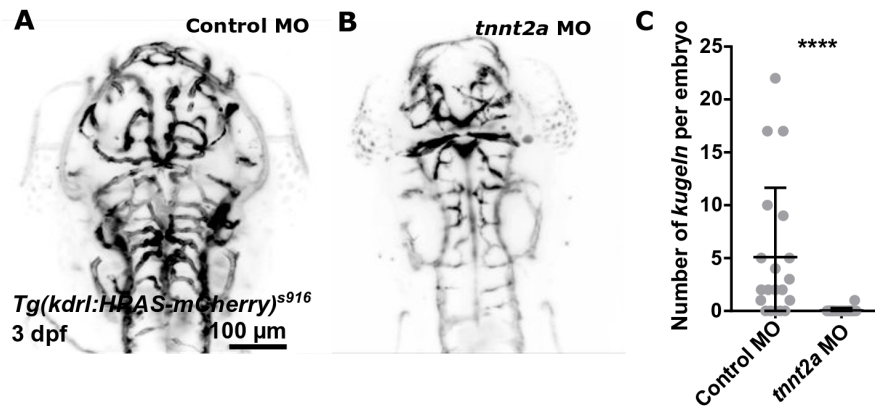


Figure 5.15: ***Kugeln* are not found in *tnnt2a* morphants.** (A,B) *Kugeln* were studied in control MO injected samples and compared to *tnnt2a* morphants, which lacked development of heart contraction. (C) Quantification of *kugel* number showed a decrease in *kugel* number upon *tnnt2a* MO injection ($p < 0.0001$; control MO $n = 20$, *tnnt2a* MO $n = 18$; 3 experimental repeats; Mann-Whitney U test).

5.3.3 Blood flow is not the driving factor of *kugel* formation

5.3.3.1. The impact of blood flow on *kugel*-formation

To study the role of blood flow in *kugel* formation, development of cardiac contraction was inhibited via MO injection against the cardiac specific thin-filament contractile protein *tnnt2a* [345, 404, 405, 406]. To account for injection-based side-effects, injection control was performed using a standard control-MO (Fig. 5.15A,B). Quantification of *kugel* number showed a decrease upon *tnnt2a* MO injection ($p < 0.0001$; Fig. 5.15C). Having found only one *kugel* in *tnnt2a* morphants, diameter quantification was not possible.

The significant reduction of *kugel* number suggested that blood flow, thus normal vascular development, was needed for *kugel* formation. In future, it has to be studied whether this is due to mechanical, genetic, or differentiation differences arising due to the lack of blood flow [15, 16, 36, 407, 408].

5.3.3.2. The impact of acute blood flow loss on *kugeln*

It is known that morpholino-based knockdowns can introduce unknown off-target effects [409, 410] and that blood flow is needed for an array of functions during angiogenesis (such as lumenization, pruning, or heart trabeculation [80, 407, 411, 412, 413]). Thus, we aimed to investigate the effects caused by more short-term alterations of flow.

Temporary reduction of blood flow was induced by temperature decrease (28°C to 10°C), while the influence of complete blood flow loss was studied via exsanguination (Fig. 5.16A). *Kugeln* were maintained upon both reduction and loss of flow (Fig. 5.16B1,2), while vascular diameters were decreased (Fig. 5.16B3). This suggested that a vessel lumen-to-*kugel*

connection was not required for *kugel* maintenance. This was validated by injection of rhodamine-tagged dextran, which showed no diffusion of dextran into *kugel*n (Fig. 5.16C).

As exsanguination lead to a rapid decrease in vascular fluorescence (approximately 20min), it was not possible to study robustly the role of blood flow in *kugel* formation in time-lapse acquisitions.

Thus, heart contraction was temporarily stopped by high-dose Tricaine incubation. Studying time-lapses, *kugel*n were found to form, retract, change shape as well as oscillate, all as observed during normal flow conditions (Fig. 5.17A-C).

Together, these data suggested that *kugel*n were not dependent on blood flow.

5.3.3.3. Local wall-shear-stress does not directly impact *kugel*n

Tortuosity of *kugel* parent vessels was quantified to evaluate whether locally altered wall shear stress (WSS) [414] could have an impact on *kugel* appearance. Parent vessels showed a high degree of tortuosity variability (CoV 17.80%), but were rather straight on average (Fig. 5.18A; mean 0.8228 ± 0.1465).

Additional quantification of *kugel* location, respectively to parent vessel curvature, showed that 60.71% of *kugel*n were facing outwards (Fig. 5.18B).

5.3.4 VEGF signalling inhibits *kugel*n, while NO is needed for their formation

5.3.4.1. VEGF signalling inhibits *kugel*n

To study whether inhibition of VEGF signalling has an impact on *kugel* number or diameter, embryos were exposed to the VEGFR inhibitor AV951 (Fig. 5.19A). The number of *kugel*n was increased by inhibition of VEGF signalling ($p < 0.0001$; Fig. 5.19B), while *kugel* diameter was not altered ($p = 0.7890$; Fig. 5.19C).

5.3.4.2. A subset of *kugel*n are filled with NO

In vivo NO visualization was achieved by application of the fluorescein-derivative DAF-FM-DA, which is hydrolyzed intracellularly by esterases (DAF-FM) and reacts with NO to a fluorescent benzotriazole (DAF-T) [400, 401]. DAF-FM-DA was used as a live dye to investigate whether NO, which is downstream of VEGF, would show any association with *kugel*n. Some *kugel*n displayed DAF-FM fluorescence inside them, while others did not (Fig. 5.20A; white arrowhead).

The number of *kugel*n filled with DAF-FM was 57.76% (118/323 being filled; Fig. 5.24A), but the level of fluorescence was variable.

Time-lapse image acquisition showed that some *kugel*n showed high levels of DAF-FM from initial inflation until retraction (5.20B), while others contained no nitric oxide during their life

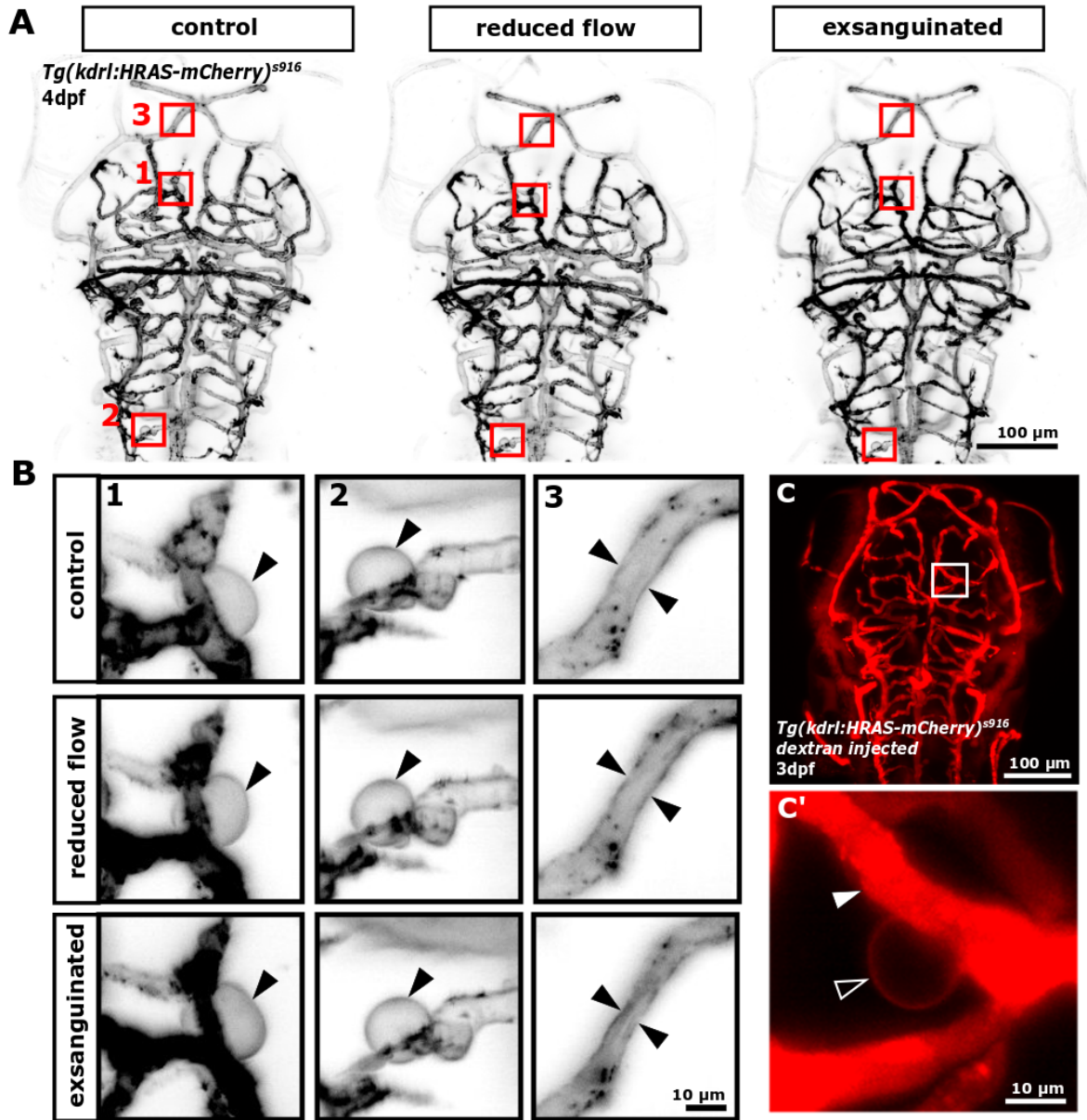


Figure 5.16: **Blood flow is not the driving factor of *kugel* formation.** (A) Role of blood flow in *kugel* initiation and maintenance was studied by reduction of blood flow via temperature decrease and removal of flow via exsanguination (inverted MIPs). (B) *Kugeln* did not retract upon reduction or loss of flow (1,2), while vascular diameter decreased (3; black arrowheads). This suggested that a *kugel*-lumen connection is not required for *kugel* maintenance. (C) Injection of rhodamine-tagged dextran into the circulatory system (filled white arrowhead), confirmed that a lumen-*kugel*-connection was not needed for *kugel* maintenance as no dextran diffused into *kugeln* (unfilled white arrowhead).

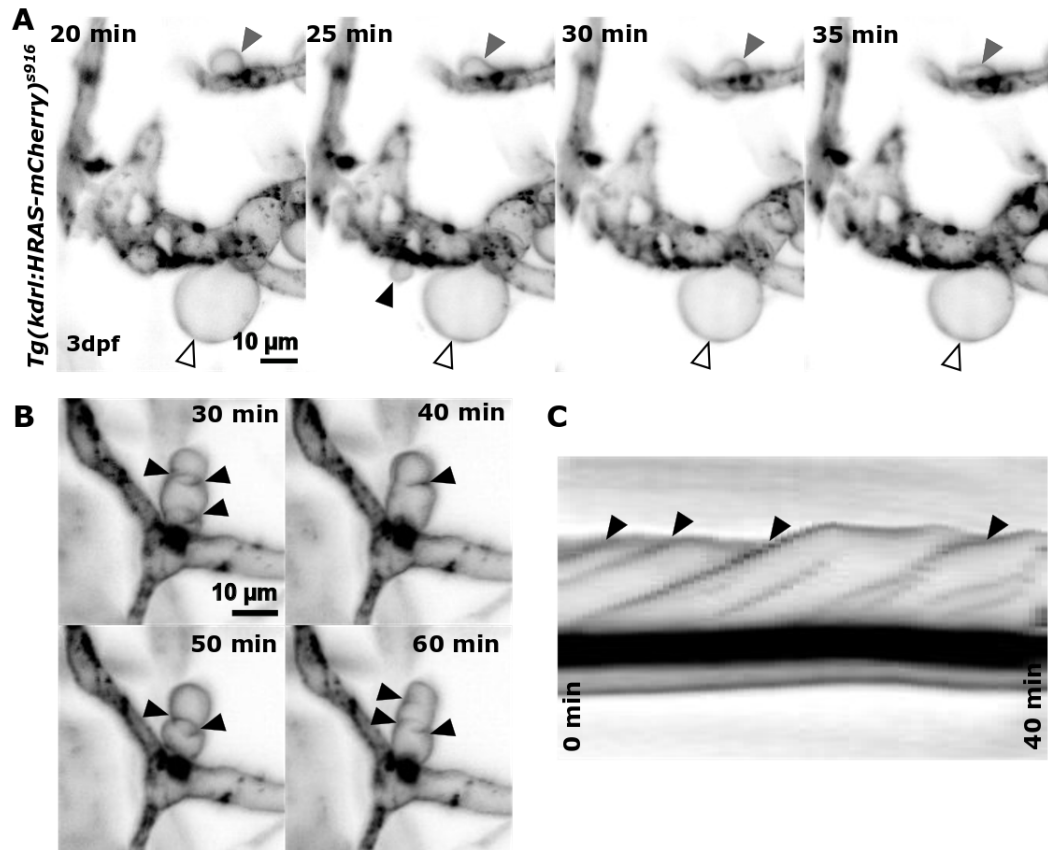


Figure 5.17: ***Kugeln* still form upon stopping cardiac contraction using Tricaine.** (A) Heart contraction was temporarily stopped by high-dose Tricaine. Time-lapse acquisitions showed that *kugeln* were still forming and retracting (black arrowhead) and changing their shape (grey arrowhead), while some retained shape (white arrowhead). (B,C) Some *kugeln* were found to oscillate without flow (time indicated post cessation).

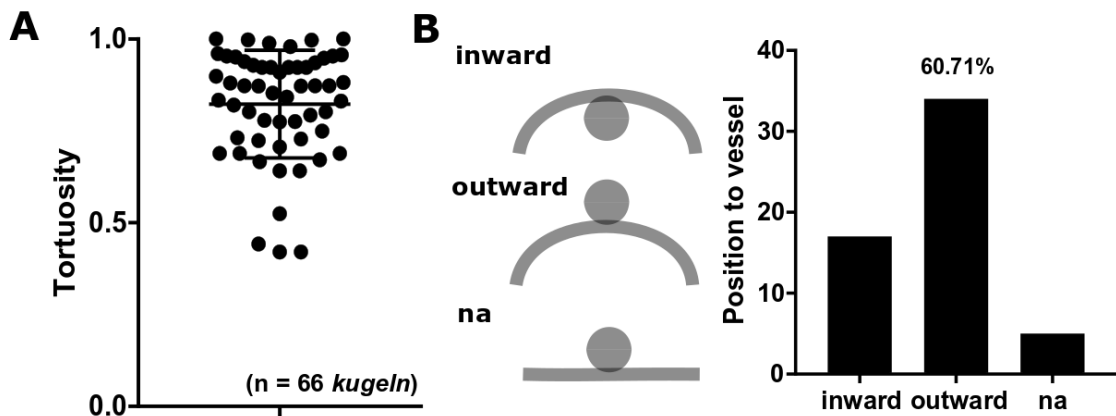


Figure 5.18: **Parent vessel tortuosity at *kugel* locations.** (A) Parent vessel tortuosity was low (0.8228 ± 0.1465). (B) The majority of *kugeln* (34/56) were facing outwards with respect to parent vessel bending direction.

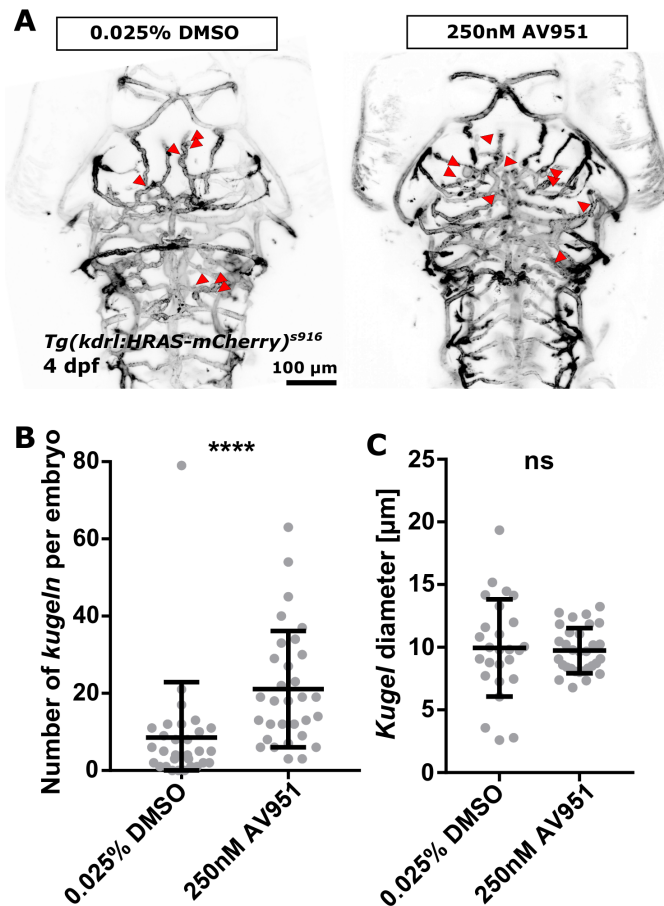


Figure 5.19: **VEGF signalling inhibits *kugel*n.** (A) Inhibition of VEGF signalling was achieved via treatment with the receptor tyrosine kinase inhibitor AV951 (250nM 2h), while controls were treated with 0.025% DMSO (2h). (B) VEGF inhibition showed an increase in *kugel* number ($p < 0.0001$; control $n = 30$ embryos; AV951 $n = 31$ embryos; 4 dpf; 4 experimental repeats; Mann-Whitney U test). (C) The average *kugel* diameter was not different after AV951 exposure ($p = 0.7890$; control $n = 243$ *kugel*n from 30 embryos; AV951 $n = 652$ *kugel*n from 31 embryos; unpaired Student's t-test).

cycle (5.20C).

As the visualization of DAF-FM in *kugeln* suggested an accumulation of NO in some *kugeln*, it was examined whether pharmacological inhibition of NOS via L-NAME would influence the number of *kugeln* (5.21). Also, having previously seen that the inhibition of VEGF signalling, via application of AV951 (chemical VEGFR inhibitor; 2h AV951), led to an increase in *kugel* number (Fig. 5.19B), it was studied whether application of L-NAME would either enhance or reduce the effect of AV951 (Fig. 5.21E; 4h AV951).

However, no difference between control, L-NAME treated or DMSO controls was found ($p > 0.999$; Fig. 5.21F). As above (Fig. 5.19), an increase of *kugel* number was found after pharmacological inhibition of the VEGFR with AV951 (250nM for 4h; $p < 0.0001$; mean number per embryo 37.82 ± 24.84) in comparison to DMSO control (mean number per embryo 7.44 ± 6.219). Parallel incubation of embryos with AV951 and L-NAME lead to a non-significant decrease of *kugel* number (mean number per embryo 25.21 ± 23.78), in comparison to AV951-only treated embryos (mean number per embryo 37.82 ± 24.84 ; $p = 0.6878$).

Despite *kugel* number quantification being obtained from 3 independent experimental repeats, the observed CoV within repeats was very high, leading to overall CoV as follows: control 110.04%, 0.5mM L-NAME 105.50%, 250nM DMSO 83.59%, 250nM AV951 65.68%, and 250nM AV951; 0.5mM L-NAME 94.33%.

Next, the effect of NO increase on *kugeln* was studied by provision of NO with the chemical SNP (Fig. 5.22A,B). Quantification of *kugel* number showed a decrease (Fig. 5.22C; $p = 0.0092$) while *kugel* diameter was unchanged (Fig. 5.22D; $p = 0.2381$). This suggests that NO either inhibits *kugel* formation, or that *kugeln* serve as a NO storage which becomes dispensable upon NO supply. Future studies are needed to elucidate the role of NO and why NOS inhibition with L-NAME does not in alterations of *kugel* formation.

5.3.4.3. A subset of *kugeln* are acidic

To study whether *kugeln* were acidic cellular compartments LysoTracker live staining was performed. LysoTracker probes are diffusive and have weakly basic amines, leading to an accumulation of probe in cellular regions of low pH. The linked fluorophore is partially protonated at neutral pH, thus allowing visualization of acidic cell compartments by de-protonation [415, 416].

Similarly to DAF-FM staining for NO, a proportion of *kugeln* were filled with LysoTracker staining (Fig. 5.23 k1), whilst others were not (Fig. 5.23 k2). Again, quantification of filled versus unfilled *kugeln* was performed. About a quarter of all *kugeln* showed LysoTracker staining (Fig. 5.24B; 62/301 *kugeln* from 31 embryos; 4dpf; 3 experimental repeats).

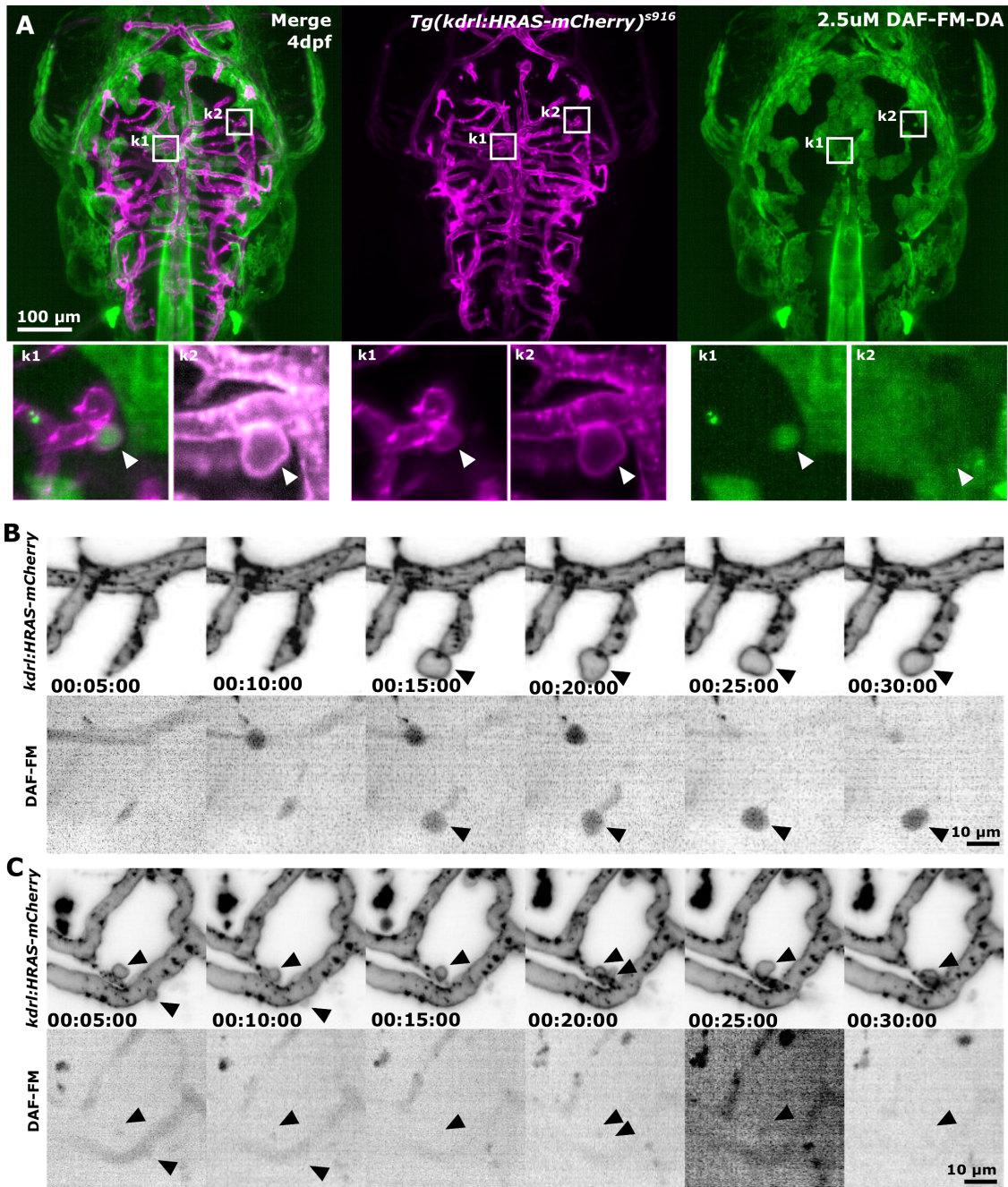


Figure 5.20: **A subset of *kugel*n was positively stained for NO.** (A) The NO live dye DAF-FM accumulated in some *kugel*n (**k1**), whilst other *kugel*n showed no green fluorescence (**k2**). (B) Time-lapse acquisition showed that some *kugel*n were filled with DAF-FM instantly (00:15:00; black arrowhead) and remained filled over the course of image acquisition (00:30:00). (C) Another *kugel*, from the same image acquisition (hh:mm:ss; inverted MIPs), showed no DAF-FM staining.

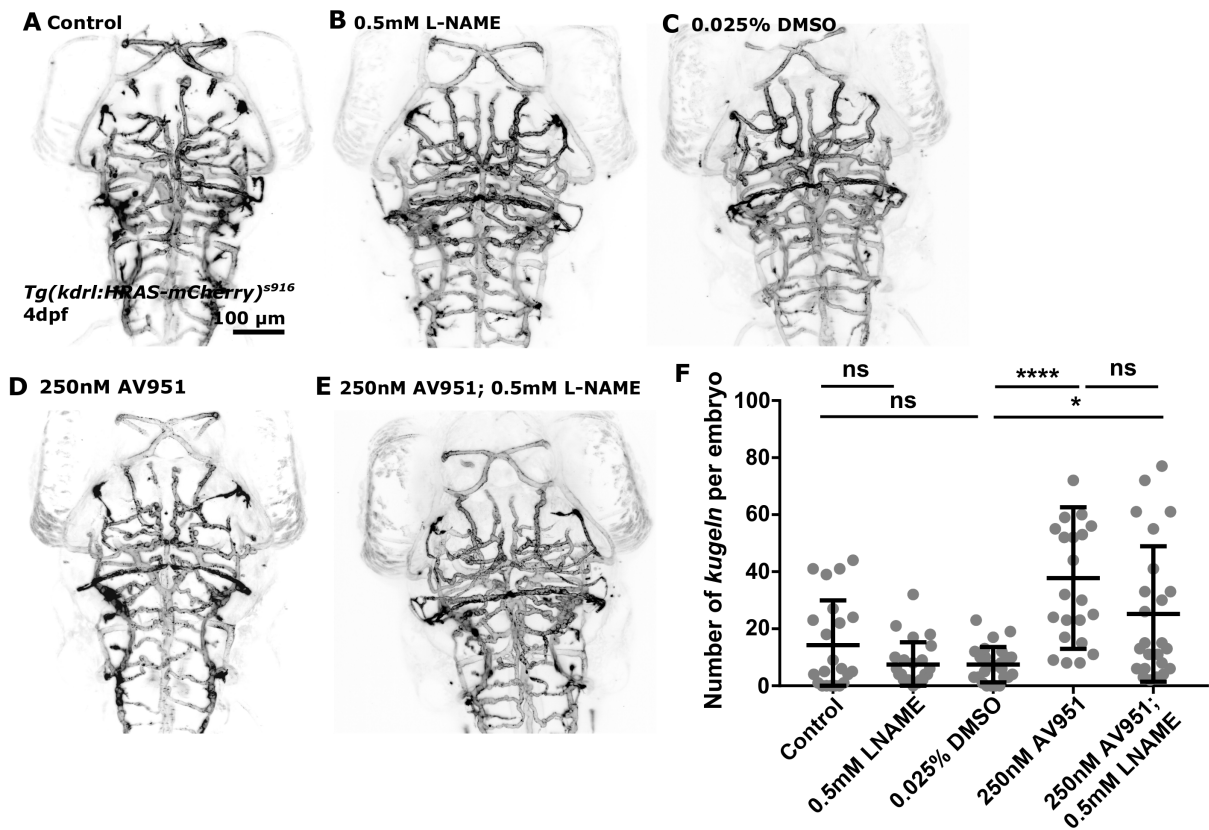


Figure 5.21: **Cotreatment of VEGF and NOS inhibition does not alter effects of VEGF inhibition.** (A) Control without treatment. (B) Application of pharmacological NOS inhibitor L-NAME (0.5mM LNAME 17h). (C) DMSO control (0.025% DMSO for 4h). (D) 250nM AV951 for 4h. (E) Cotreatment of 250nM AV951 for 4h and 0.5mM LNAME for 17h. (F) No difference between untreated control or LNAME treated embryos was found ($p > 0.9999$). Similarly, no significant difference between LNAME and DMSO control was found ($p > 0.999$). Again, an increase between DMSO control and AV951 was found ($p < 0.0001$), while the difference was less pronounced by simultaneous treatment with AV951 and LNAME ($p = 0.0270$). Interestingly, despite a decrease in the mean *kugel* number between sole AV951 treatment (37.82 ± 24.84) and additional LNAME application (25.21 ± 23.78), this was not different ($p = 0.6878$; embryos - control $n=22$, LNAME $n=24$, DMSO $n=25$, AV951 $n=22$, AV951 & LNAME $n=24$; non-parametric Kruskal Wallis; *post-hoc* statistical power of 1; 4dpf; 3 experimental repeats).

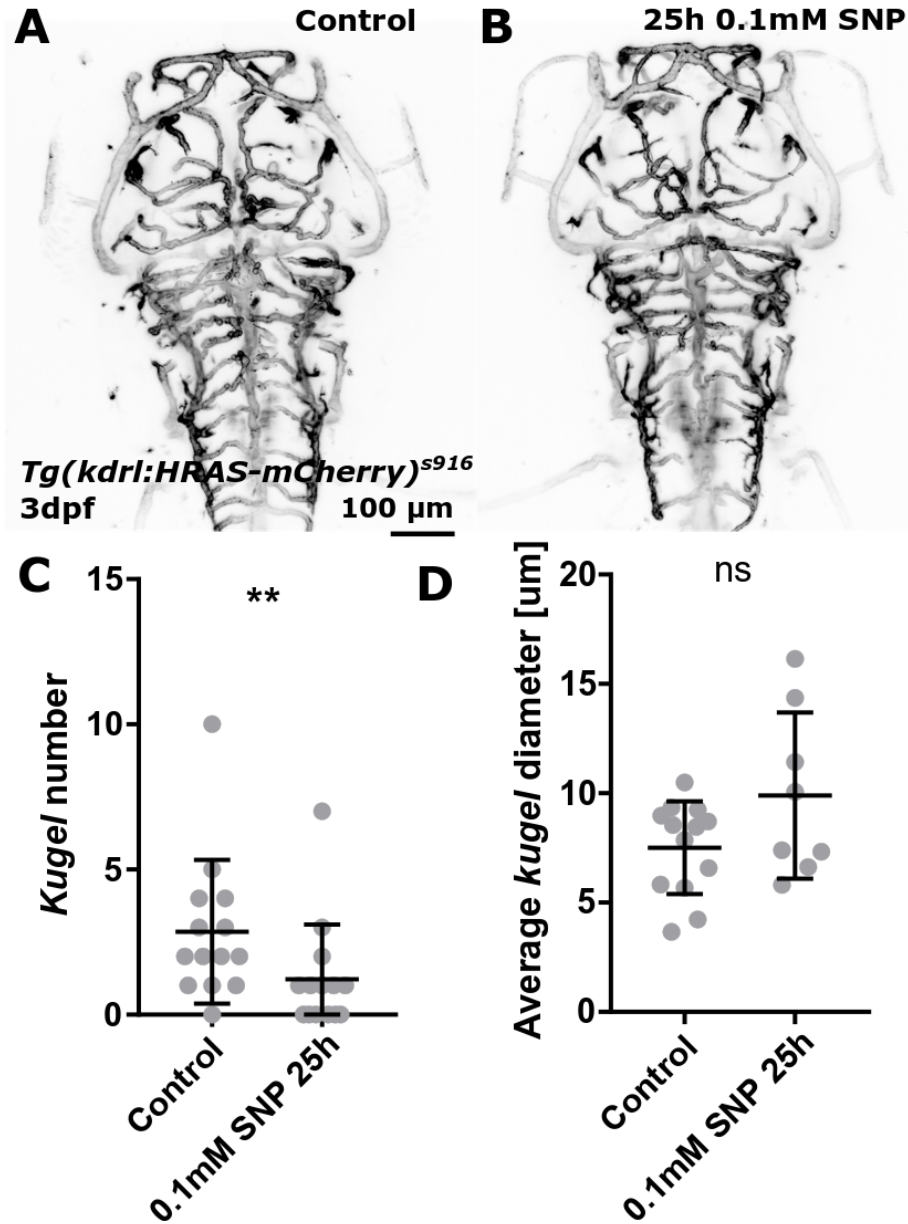


Figure 5.22: **NO supply reduces the *kugel* numbers.** (A) Control without treatment. (B) Application of pharmacological NO supply with SNP (0.1mM SNP 25h). (C) *Kugel* number was reduced upon application of SNP (p 0.0092; embryos control n=14, SNP n=14; Mann-Whitney U test; 2 experimental repeats). (D) *Kugel* diameter was not altered upon SNP application (p 0.2381; Mann-Whitney U test).

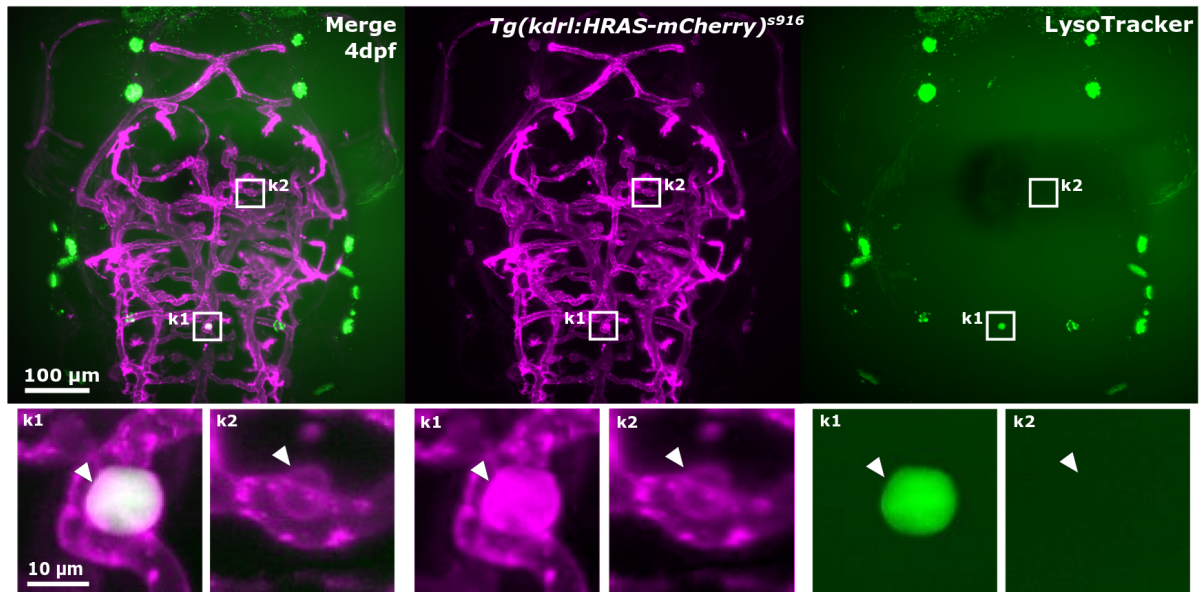


Figure 5.23: **A subset of *kugeln* was acidic.** LysoTracker staining was used to study whether *kugeln* are acidic cellular compartments. Similar to nitric oxide staining, some *kugeln* were filled with Lysotracker, whilst others were empty. But, quantification (Fig. 5.24C) showed nitric oxide staining in proportionally more *kugeln*.

Comparing the proportion of "filled" versus "unfilled" *kugeln* from DAF-FM (4dpf 118/323 *kugeln* filled) and LysoTracker (4dpf 62/301 *kugeln* filled) staining indicated that less *kugeln* were acidic than contained NO (Fig. 5.24). Due to time constraints, it was not further investigated whether acidic *kugeln* are also NO-containing or vice versa.

DAF-FM is generally thought to be stable at higher pH values (>5.8), but NO can also be produced by acidic chemical reduction [369]. Thus, it can not be fully understood whether DAF-FM and LysoTracker staining visualize different or the same *kugeln*.

But, the fact that just a proportion of *kugeln* was filled with LysoTracker suggested that not all *kugeln* were acidic, which would be the case if *kugeln* were a form of apoptotic bodies of cells [417, 418]. This would also agree with the "gap junction theory" of NO transport, which would collapse upon apoptosis, due to gap junction closure with reduction of pH [419, 420].

It remains to be investigated which mechanisms lead to the acidification or NO accumulation in *kugeln*. Especially, to understand the mechanisms which lead to the fact that some *kugeln* were filled, whilst others never were. Lastly, it has to be examined whether the actual acidification or NO-accumulation serve a biological function, such as NO cellular compartmentalization, to establish a signalling hub, or for waste storage.

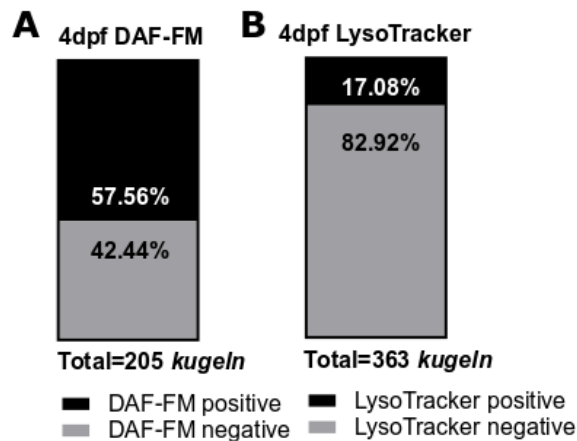


Figure 5.24: **Quantification of *kugeln* filled with DAF-FM and LysoTracker.** (A) 57.76% of *kugeln* were green fluorescent after application of the NO live dye DAF-FM (DAF-FM n=29 4dpf embryos 118/323 *kugeln* filled). (B) 17.08% of *kugeln* were green fluorescent after application of LysoTracker live dye, which visualizes acidic organelles (n=31; 4dpf; 62/301 *kugeln* filled). All data from 3 independent experimental repeats.

5.3.5 Notch signalling is required for *kugel* formation

5.3.5.1. Notch signalling is required for *kugel* formation

To study whether Notch signalling would have an impact on *kugel* formation, embryos were exposed to the pharmacological γ -secretase inhibitor DAPT (Fig. 5.25A), which inhibits the intracellular proteolytic cleavage of the Notch intracellular domain (NICD) [421]. *Kugel* number was decreased upon inhibition of Notch signalling ($p < 0.0001$; Fig. 5.25B), while *kugel* diameter was not changed upon DAPT exposure ($p = 0.0832$; Fig. 5.25C). This suggested that Notch signalling is essential for *kugel* formation.

5.3.5.2. Studying Notch signalling in *dll4* and *TP1* transgenic reporter lines

Due to the finding that Notch signalling was required for *kugel* formation, the following transgenic reporter lines were examined to see whether local changes in expression adjacent to *kugeln* would be detected. First, the transgenic *Tg(kdrl:HRAS-mCherry)^{s916}*, *Tg(dll4in3:GFP)*, which labelled the *dll4* Notch ligand in green and vessels in red/magenta was used (Fig. 5.26A) [374]. No pattern of *dll4* expression was observed nearby *kugeln* or in *kugel*-parent vessels.

I next examined the transgenic *Tg(kdrl:HRAS-mCherry)^{s916}*, *Tg(TP1glob:venusPest)^{s940}*, which visualized levels of Notch signalling (Fig. 5.26B) [388]. Again, no expression pattern could be identified in *kugel* proximity. As transgenic reporter lines rely on fluorescent proteins which usually require hours to fold and mature, while *kugeln* develop and regress on the

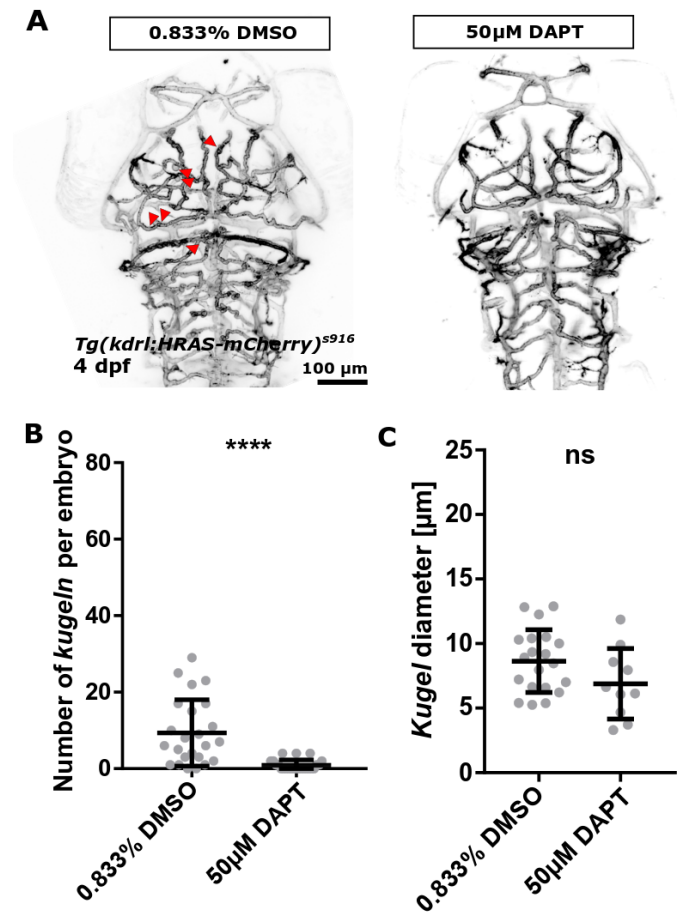


Figure 5.25: **Notch signalling is needed for *kugel* formation.** (A) Inhibition of Notch signalling was achieved via treatment with the γ -secretase inhibitor DAPT, while controls were treated with 0.833% DMSO for the same duration. (B) *Kugel* number was decreased upon inhibition of Notch signalling ($p < 0.0001$; $n = 24$ 4dpf embryos each; 3 experimental repeats; Mann-Whitney U test). (C) *Kugel* diameter was not changed ($p = 0.0832$; control $n = 225$ *kugel*n from 24 embryos; DAPT $n = 22$ from 24 embryos; unpaired Student's t-test).

timescale of minutes, the lack of an expression pattern might be due to these different timescales.

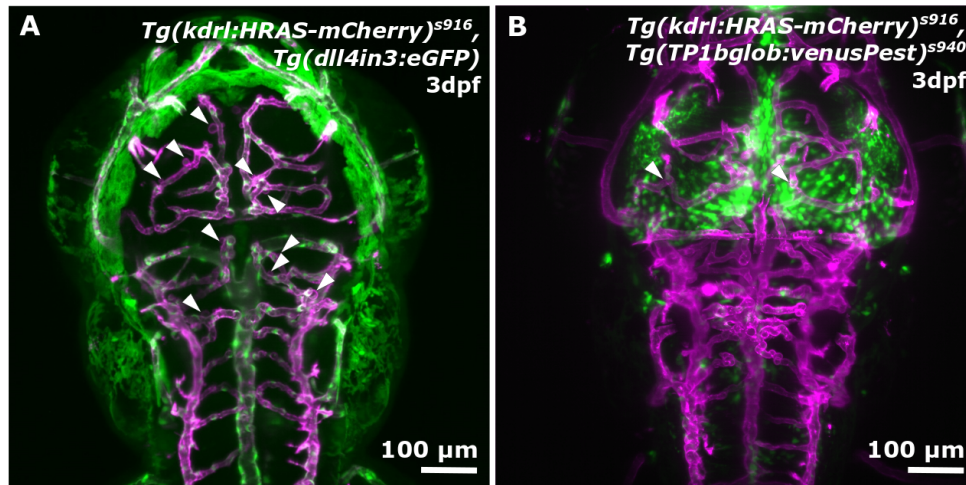


Figure 5.26: **Studying Notch signalling in transgenic reporter lines.** (A) The transgenic *Tg(kdrl:Hsa.HRAS-mCherry)^{s916}, Tg(dll4in3:eGFP)* was used to visualize the Notch ligand *dll4*. (B) The transgenic *Tg(kdrl:Hsa.HRAS-mCherry)^{s916}, Tg(TP1bglob:venusPest)^{s940}* was used to visualize levels of Notch signalling. Neither of the above showed a pattern nearby *kugel*n or in *kugel*-parent vessels.

5.3.5.3. The effect of Notch pathway component knockdown on *kugel*n formation

To further investigate the role of Notch signalling on *kugel* formation, genetic knockdown via morpholino injection against *dll4*, *notch1b*, *jagged-1a*, and *jagged-1b* was performed.

Quantification of *kugel*n after *dll4* MO injection showed neither a change in *kugel* number ($p = 0.9639$; Fig. 5.27A) nor diameter ($p = 0.0843$; Fig. 5.27B), suggesting that the *dll4*-ligand was not essential for *kugel* formation.

Quantification of *kugel* number after *notch1b* MO injection showed a decrease ($p = 0.0008$; Fig. 5.27C), while *kugel* diameter was not changed ($p = 0.3198$; Fig. 5.27D). This suggested that the Notch ligand *notch1b* was required to establish *kugel*n.

Quantification of *kugel* number after *jagged-1a* MO injection showed no change ($p = 0.9563$; Fig. 5.28A), while *kugel* diameter was increased ($p = 0.0097$; Fig. 5.28B), suggesting that *jagged-1a* was possibly involved in a negative feedback-loop to counteract the role of Notch signalling in *kugel* formation.

Quantification of *kugel*n after *jagged-1b* MO injection showed neither a change in *kugel* number ($p = 0.3042$; Fig. 5.28C) nor diameter ($p = 0.7060$; Fig. 5.28D). This suggested that the *jagged-1b*-ligand was dispensable for *kugel* formation.

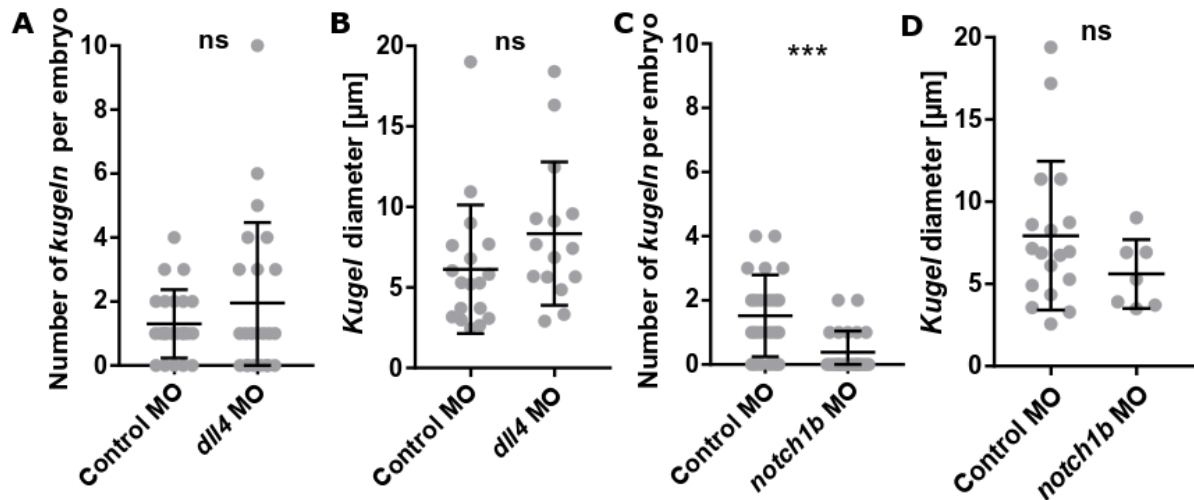


Figure 5.27: **Studying the role of *dll4* and *notch1b* in *kugel* formation.** **A** Number of *kugel* per embryo was not changed upon *dll4* MO injection (p 0.9639; 3dpf embryos control $n=23$, *dll4* MO $n=23$; Mann-Whitney U test). **B** *Kugel* diameter was not changed upon *dll4* MO injection (p 0.0843; *kugel* control $n=30$ from 23 embryos, *dll4* MO $n=45$ *kugel* from 23 embryos; Mann-Whitney U test). **C** Number of *kugel* was reduced after *notch1b* MO injection (p 0.0008; 3dpf embryos control $n=23$, *notch1b* MO $n=23$; Mann-Whitney U test). **D** *Kugel* diameter was not changed upon *notch1b* MO injection (p 0.3198; *kugel* control $n=37$ from 23 embryos, *notch1b* MO $n=9$ *kugel* from 23 embryos; Mann-Whitney U test).

5.3.6 Wnt signalling has a balancing role in *kugel* formation

To investigate the role of Wnt signalling on *kugel* formation, Wnt signalling was both chemically inhibited and activated.

5.3.6.1. Wnt inhibition leads to an increase in *kugel* number

Quantifying the number of *kugel*, an increase was found after Wnt inhibition via treatment with XAV-939 which increased β -catenin degradation by Axin stabilization [422] (p 0.0003; Fig. 5.29A), while diameter of *kugel* was unchanged (p 0.4098; Fig. 5.29B).

5.3.6.2. Wnt activation leads to an increase in *kugel* number

Wnt signalling activation was studied by application of the GSK3 inhibitor XV, which prevented β -catenin phosphorylation and thus degradation via GSK3 [423]. Again, an increase in *kugel* number was found ($p < 0.0001$; Fig. 5.29C), while *kugel* diameter was unchanged (p 0.5555; Fig. 5.29D).

Together these data suggested that both the inhibition and activation of Wnt signalling led to an increase in *kugel* number, suggesting that Wnt signalling potentially has a role in establishing an equilibrium of *kugel* formation. The exact mechanisms for this remain to be studied in the future.

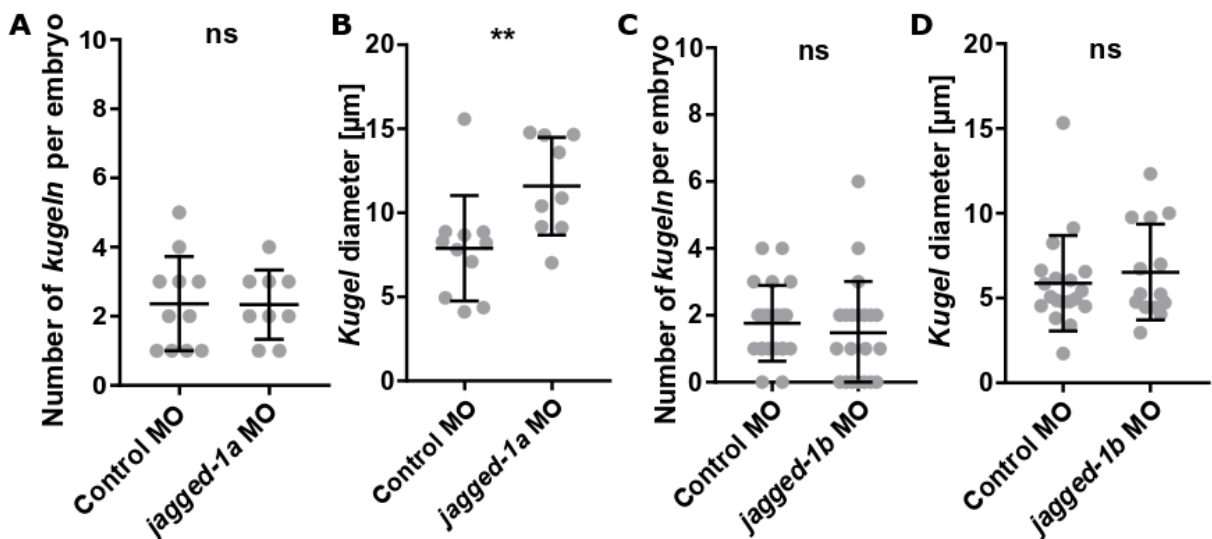


Figure 5.28: **Studying the role of *jagged-1a* and *jagged-1b* in *kugel* formation.** (A) Number of *kugeln* per embryo was not changed upon injection of *jagged-1a* morpholino (p 0.9563; 3dpf embryos control n=11, *jagged-1a* MO n=9; unpaired Student's t-test; 2 experimental repeats). (B) *Kugel* diameter was increased after injection of *jagged-1a* MO (p 0.0097; *kugeln* control n=23 from 11 embryos, *jagged-1a* MO n=20 *kugeln* from 9 embryos; Mann-Whitney U test). (C) Number of *kugeln* was not altered upon *jagged-1b* MO injection (p 0.3042; 3dpf embryos control n=21, *jagged-1b* MO n=21; Mann-Whitney U test; 3 experimental repeats). (D) *Kugel* diameter was not altered upon *jagged-1b* MO injection (p 0.7060; *kugeln* control n=19 from 21 embryos, *jagged-1b* MO n=14 *kugeln* from 21 embryos; Mann-Whitney U test).

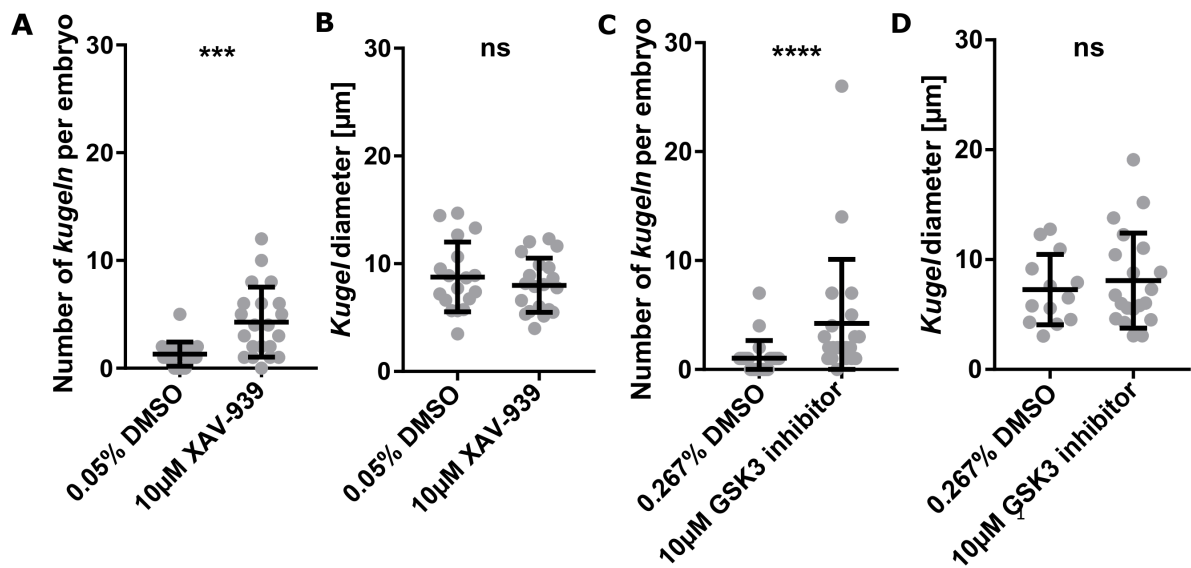


Figure 5.29: **The impact of Wnt signalling on *kugel* number and diameter.** **A** *Kugel* number was increased upon inhibition of Wnt signalling via XAV-939 application (p 0.0003; control n=22 embryos; XAV-939 n=21; 3 experimental repeats; Mann-Whitney U test). **B** The diameter of *kugel* was not changed upon XAV-939 application (p 0.4098; control n=29 *kugeln*; XAV-939 n=90; 3 experimental repeats; unpaired Student's t-test). **C** *Kugel* number was increased upon activation of Wnt signalling by the GSK3 inhibitor (p 0.0359; control n=22 embryos; GSK3 inhibitor n=21; 3 experimental repeats; Mann-Whitney U test). **D** The diameter of *kugel* was not changed upon GSK3 inhibitor application (p 0.5555; control n=23 *kugeln*; GSK3 inhibitor n=89; 3 experimental repeats; unpaired Student's t-test).

5.3.7 Neither lymphatic nor macrophages interact with *kugeln*

5.3.7.1. Lymphatics do not interact with *kugeln*

To investigate whether BLECs would interact with *kugeln*, the double-transgenic *Tg(kdrl:HRAS-mCherry)^{s916}, Tg(fli1a:Lifeact-mClover)^{sh467}* (Fig. 5.30A) was utilized to visualize BLECs as mClover-positive, mCherry-negative structures (Fig. 5.30B,C; black arrowhead). Visual assessment of *kugel*-BLECs co-localization showed that BLECs were not associated with *kugeln* (n=21 4dpf embryos; 3 experimental repeats), and BLECs were consistently encountered at distinct anatomical depths different to those of *kugeln* (Fig. 5.30D).

5.3.7.2. Loss of lymphatics does not impact *kugeln*

To study whether the loss of BLECs would impact *kugeln*, MO injection against the lymph-specifying *ccbe1* was performed [244]. Penetrance of *ccbe1* knockdown was validated by the loss of trunk lymphatics (Fig. 5.30E).

Quantification of *kugel* number and diameter showed no difference after *ccbe1* MO injection (p 0.3496 and p 0.8783, respectively; Fig. 5.30F,G), suggesting that lymphatics do not impact *kugel* formation.

5.3.7.3. *Kugeln* do not fulfil a scavenger function

To examine whether *kugeln* serve a scavenging function similar to BLECs in the cranium, IgG-conjugated Alexa was injected into the tectum. Uptake of IgG-conjugated Alexa by BLECs was observed as previously described [381], but no Alexa uptake by *kugeln* was observed (Fig. 5.31). This suggested that *kugeln* did not serve a scavenging function similar to BLECs in the cranium.

5.3.7.4. *Kugeln* do not interact with macrophages

To understand whether *kugeln* recruited or interacted with macrophages, timelapses were acquired in the transgenic reporter line *Tg(kdrl:HRAS-mCherry)^{s916}, Tg(fms:GAL4.VP16)ⁱ¹⁸⁶, Tg(UAS-E1b:nfsB.mCherry)ⁱ¹⁴⁹* [389], which visualized EC membranes and macrophages / microglia (Fig. 5.32A). As both, EC membranes and macrophages, were visualized with an mCherry fluorophore, depth-coding along the z-axis was applied to allow for better distinction (Fig. 5.32B).

Examining timelapses (2min intervals) no direct interaction was observed between *kugeln* and macrophages (Fig. 5.32C; 10min intervals shown), showing that *kugeln* were not interacting with macrophages.

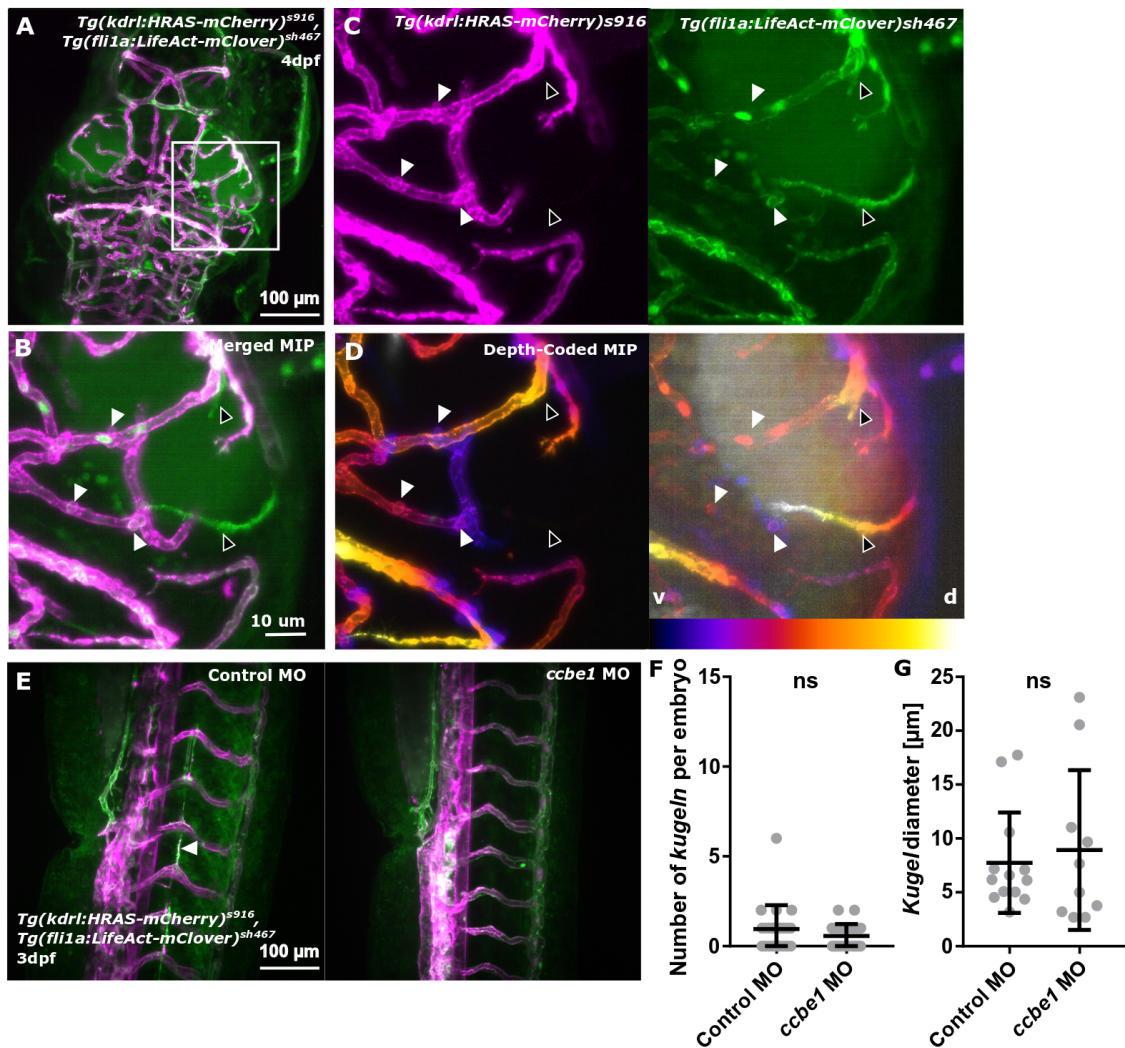


Figure 5.30: ***Kugeln* do not interact with BLECs.** (A) BLECs were studied in the double-transgenic *Tg(kdrl:HRAS-mCherry)^{s916}*, *Tg(fli1a:Lifeact-mClover)^{sh467}*. (B) BLECs were mClover-positive and mCherry-negative (black arrowhead). (C) No direct interaction between *kugeln* (white arrowhead) and BLECs was observed. (D) Depth-coded projections showed that BLECs and *kugeln* were not occurring on the same anatomical plane (white dorsal (d), purple ventral (v)). (E) Morpholino injection against *ccbe1* led to a loss of lymphatics, as validated by the loss of lymphatics in the trunk. (F) Quantification of *kugel* number showed no difference between *ccbe1* morphants and control MO injected samples (p 0.1472; 4dpf embryos control n=17, *ccbe1* MO n=17; 2 experimental repeats; Mann-Whitney U test). (G) *Kugel* diameter was also not different (p 0.0962; *kugeln* control n=27, *ccbe1* MO n=81; 2 experimental repeats; unpaired Student's t-test).

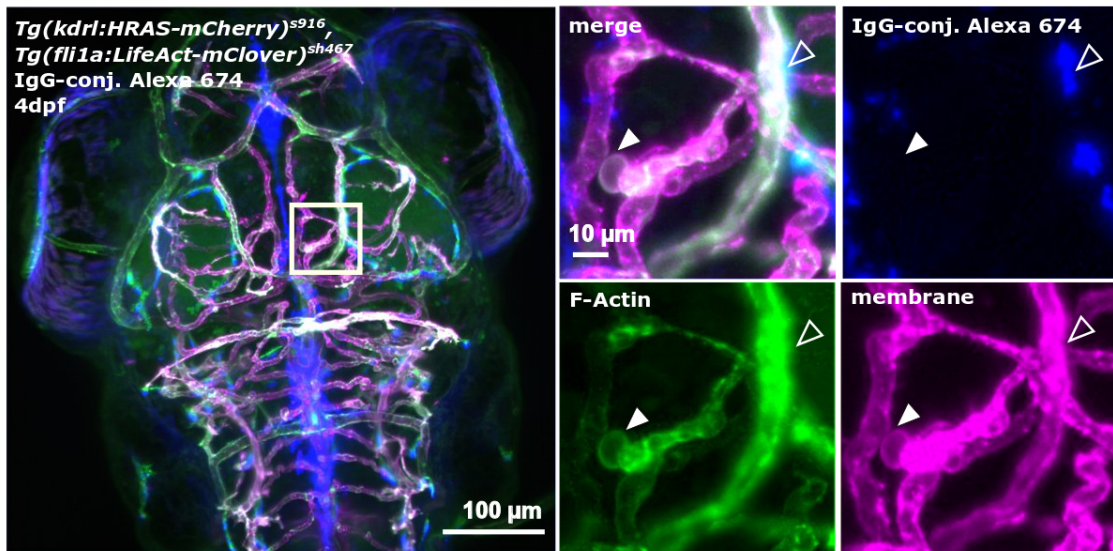


Figure 5.31: ***Kugeln* do not serve a scavenger function.** IgG-conjugated Alexa 674 was injected into the tectum to investigate whether *kugeln* would fulfil a scavenging function similar to BLECs. While BLECs were taking up the IgG-conjugated Alexa 674 (white unfilled arrowhead), no uptake was observed in *kugeln* (white arrowhead; 140 *kugeln* from 17 4dpf embryos; 2 experimental repeats).

5.3.8 Neither osmotic pressure nor membrane rigidity impact *kugeln*

5.3.8.1. Changes of osmotic pressure with glucose does not impact *kugeln*

To test whether *kugeln* were a phenomenon induced by volume changes as a result of cellular osmotic regulation, as it was suggested in the context of cell polarization and migration [223], osmotic pressure was increased via exposure of embryos to a 40mM glucose solution. No difference was found in control *kugel* number (2.455 ± 1.683) in comparison to glucose-exposed samples (3.238 ± 2.998 ; p 0.5746; Fig. 5.33A). Similarly, *kugel* diameter was not changed when comparing control to glucose-exposed samples (p 0.7060; Fig. 5.33B), showing that osmosis was not the driving force of *kugeln*.

5.3.8.2. Membrane rigidity changes with DMSO do not impact *kugeln*

To test if *kugel* number or diameter would be dependent on membrane rigidity, membrane rigidity was artificially increased by 24h exposure to 2.5% DMSO, as this was previously shown to increase membrane permeability and fluidity [424]. The average number of *kugeln* was slightly decreased from 4.00 ± 3.27 in controls to 3.00 ± 3.11 in DMSO-exposed embryos (p 0.1596; Fig. 5.34A). *Kugel* diameter was not significantly changed, comparing control to DMSO-exposed embryos (p 0.3665; Fig. 5.34B).

This suggested that *kugeln* were not a result of local membrane weakness due to rigidity fluctuations.

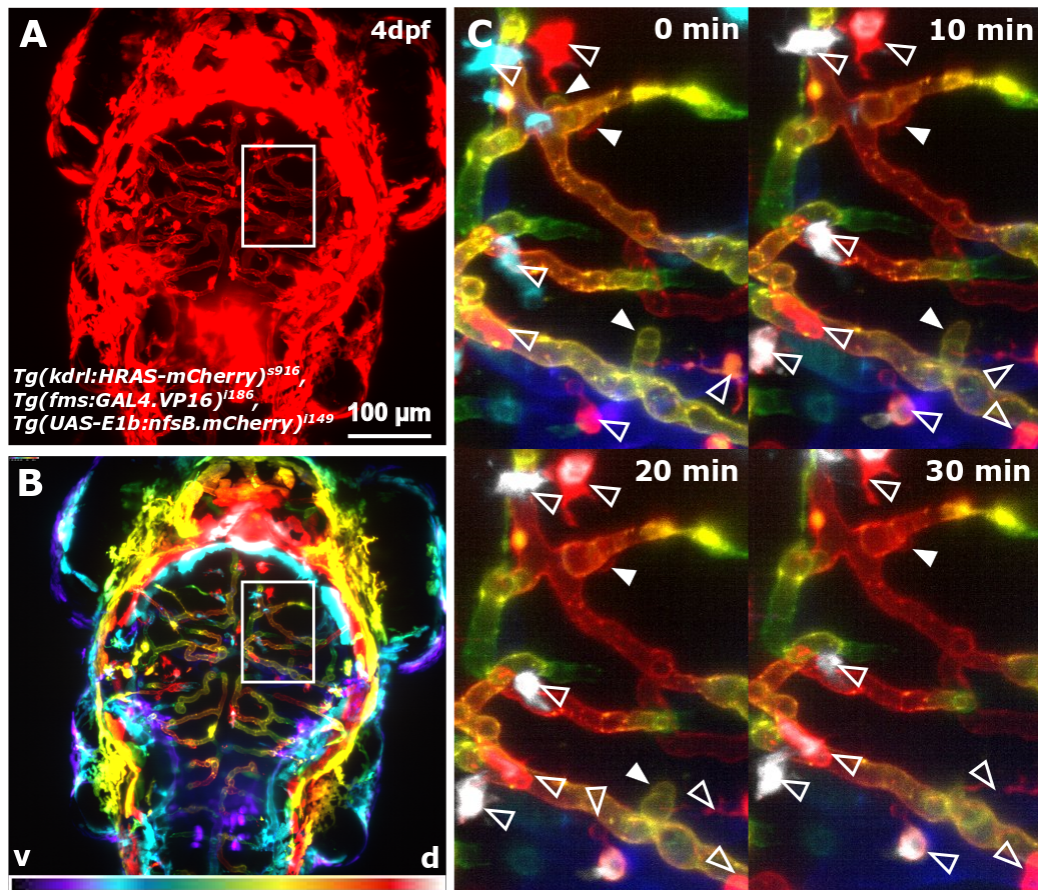


Figure 5.32: ***Kugeln* do not interact with local immune cells.** (A) The possible interaction of immune cells with *kugeln* was studied in the transgenic $Tg(fms:GAL4.VP16)^{i186}$, $Tg(UAS-E1b:nfsB.mCherry)^{i149}$, $Tg(kdrl:HRAS-mCherry)^{s916}$ [389]. (B) Depth-coded MIP projections were used to enable investigation of *kugeln* respective to macrophages. (C) Macrophages (white unfilled arrowhead) were not found to directly interact with *kugeln* (white arrowhead) in the examined samples (n=21 *kugeln* from 8 3dpf embryos).

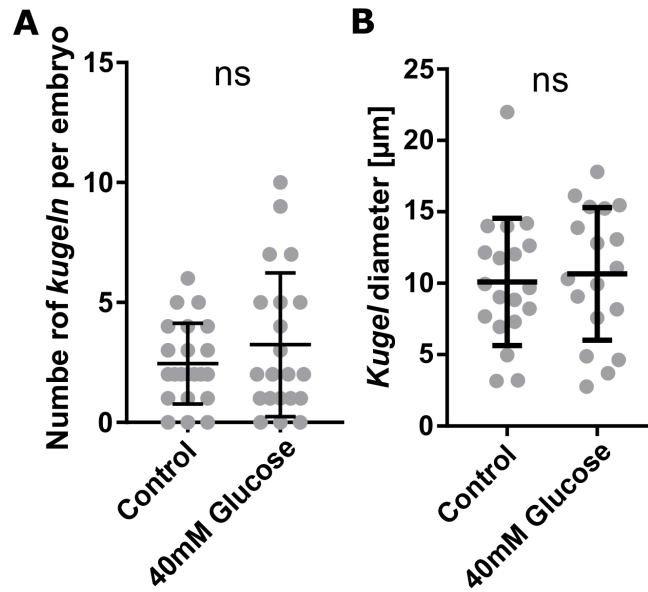


Figure 5.33: **Osmotic pressure does not impact *kugelIn*.** Incubation with 40mM glucose for 24h was performed to investigate the role of osmotic pressure in *kugel* formation. **(A)** Quantification of *kugel* number showed no difference between control and glucose-exposed samples (p 0.5746; control embryos $n=31$, glucose $n=29$; 2 experimental repeats; unpaired Student's t-test). **(B)** Quantification of *kugel* diameter showed no difference between control and glucose-exposed samples (p 0.7060; control $n=54$, glucose $n=67$; 2 experimental repeats; unpaired Student's t-test).

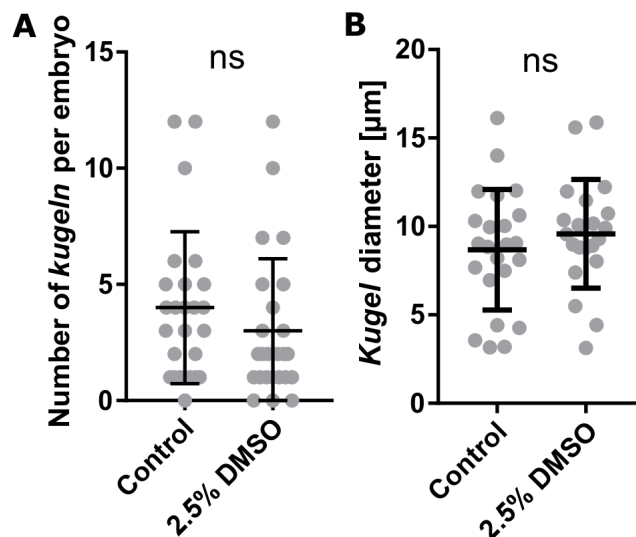


Figure 5.34: **Membrane rigidity does not impact *kugelIn*.** Incubation with 2.5% DMSO for 24h was performed to investigate the role of membrane rigidity in *kugel* formation. **(A)** Quantification of *kugel* number showed no difference between control and DMSO-exposed samples (p 0.1596; embryos $n=25$ per group; 3 experimental repeats; unpaired Student's t-test). **(B)** Quantification of *kugel* diameter showed no difference between control and DMSO-exposed samples (p 0.3665; control $n=97$, DMSO $n=75$; 3 experimental repeats; unpaired Student's t-test).

5.3.9 *Kugeln* show no similarity to previously described structures.

Cellular blebbing and volume changes. Mechanisms of membrane blebbing and cell volume changes were previously suggested in the context of cell migration, polarization, as well as apoptosis [223, 224, 225]. To understand whether *kugeln* recapitulated previously described forms of cell blebbing *kugel* structure and dynamics in double-transgenic reporter lines (eg. *Tg(kdr1:HRAS-mCherry)^{s916}*, *Tg(flk1:nls-eGFP)^{zf109}* or *Tg(kdr1:HRAS-mCherry)^{s916}*, *Tg(fli1a:eGFP)^{y1}*) were examined.

While *kugeln* have clear neck, while blebs are more blister-like with less pronounced necks [234]. The described "circus movement" [232] of blebs was not observed in *kugeln*, but further investigation is needed to understand whether the encountered oscillatory behaviour in *kugeln* is driven by similar mechanisms as the bleb "circus movement". Inhibition of F-actin polymerization lead to more, but smaller, *kugeln*; while bleb numbers decrease and size increases [234, 425]. Lastly, increasing osmotic pressure made no difference in *kugel* number or diameter, but was previously shown to reduce bleb size [426].

Zebrafish vessel blebbing. Atypical membrane blebbing during mitosis and lumenization was previously observed in zebrafish trunk angiogenesis [224, 225], but structurally *kugeln* were distinct to the previously described mechanism (*kugeln* facing outwards and extending described bleb size by far).

Lymphatic cells. Zebrafish lymphatic cells were previously shown to transdifferentiate from veins [427], but *kugeln* were never observed to specifically protrude from veins, which contraindicated *kugeln* to be lymphatic precursors.

Vesicles, Exosomes, and Microdomains. Endothelial vesicles or apoptotic bodies, which would also protrude outwards from membranes, were far smaller than *kugeln* with diameters <1000nm and <5000nm [222], respectively. Moreover, neither shedding or bursting of *kugeln* were observed. Also, nuclear defragmentation - which would be an apoptosis indicator - was not observed during timelapse imaging in the double-transgenic *Tg(kdr1:HRAS-mCherry)^{s916}*, *Tg(flk1:nls-eGFP)^{zf109}*, which visualized EC nuclei and membrane in parallel.

Exosomes, which play a pivotal role in inter-cellular communication, are far smaller with <120nm diameter and fuse with membranes, rather than maintain distinctive neck regions over long periods of time.

Caveolae are membrane invaginations, playing a role in cellular communication and signal transduction, and are usually <100 nm [428].

Thus, having quantified *kugel* diameters to be $10.13 \pm 4.686 \mu\text{m}$ (3dpf, 32 embryos, 93 *kugeln*) and observed *kugel* behaviour of inflation and retraction, but never shedding or

bursting, it was unlikely that *kugeln* were any of the above suggested mechanisms. Simultaneously, it can currently not be excluded that *kugel* subtypes exist. Further investigation is clearly needed to comprehend the molecular *kugel* composition and draw comparisons to any of the above.

Platelet ballooning. Previous work in human platelets suggested that cell membrane ballooning occurred to increase platelet surface for coagulation [429, 430]. I proposed that *kugeln* are not recapitulating the processes of platelet ballooning due to the following reasons: Platelet balloons ..

1. .. do not display a clear structural distinction between neck and dome as is observed in *kugeln*.
2. .. were never observed to retract (Alastair Poole, pers. communication).
3. .. did not display oscillatory behaviour as is observed in some *kugeln* (Fig. 5.5).
4. .. diameter is reduced upon increased osmotic pressure (sucrose), which was not observed upon glucose treatment (Fig. 5.33).
5. .. were shown to be associated with cell apoptosis. Based on our data, this is not the case for *kugeln* as nuclear defragmentation was not observed and not all *kugeln* were filled with Lyotracker, which would be an indication that *kugeln* are apoptotic bodies (Fig. 5.23).

Aneurysms. Observing *kugeln* one could argue that their shape as well as anatomical region of occurrence resembles human cranial aneurysms, but our data showed that *kugeln* are not driven by blood flow.

5.4 Conclusion

Kugeln appear variable in number and size (Fig. 5.2), but exclusively in the dorsal cranial zebrafish vasculature (Fig. 5.4). Morphologically, *kugeln* are 3D spheres protruding abuminally from parent vessels, and shape changes can occur in the range of minutes or hours. *Kugeln* were observed to collapse into parent vessels, but were never found to shed, burst, or anastomose. These morphological observations suggested that *kugeln* are a novel dynamic membrane phenomenon.

The cellular context of *kugeln* suggested that they are spherical membranous abluminal protrusions, which do not have individual cell nuclei, but show a clear co-localization of

F-actin, and to a lesser extent of cytosol. These cellular characteristics do not, to our knowledge, recapitulate any published bleb-like behaviour regarding to mitosis, apoptosis, migration, and/or lumenization [68, 225, 353].

The inhibition of F-actin polymerization led to a decrease in *kugel* size, but an increase in mean *kugel* number (Fig. 5.12). Additionally, inhibition of actin polymerization resulted in an ectopic *kugel*-occurrence in the trunk vasculature. This suggested that cell-cortex stability played a role in *kugel*-formation, and its loss would be able to induce *kugeln* in ectopic vascular beds.

Investigations of the role of blood flow in *kugel* dynamics showed blood flow was not the driving force for *kugel* formation (Fig. 5.16).

Studying the role of VEGF and Notch signalling, it was found that Notch had a positive regulatory effect on *kugeln*, while VEGF inhibited *kugel* formation (Fig. 5.25 and Fig. 5.19).

Studying NO localization showed that a portion of *kugeln* were filled with the live NO dye DAF-FM (Fig. 5.20), while a lower number of *kugeln* were filled with LysoTracker (Fig. 5.23 and Fig. 5.24) suggesting that *kugeln* were truly positive for NO.

Lastly, studying the role of osmosis (Fig. 5.33) and membrane rigidity (Fig. 5.34) in *kugel* formation, neither of them had a direct influence on *kugel* number or diameter.

Together, we performed an initial characterisation of a previously undescribed EC membrane behaviour and provided insights into *kugel* cellular context, upstream regulators, and their potential function, allowing to establish a working model of genetic regulation for *kugel* formation (Fig. 5.35).

5.5 Future work

I anticipate that the presented work is only the foundation for more in-depth investigations covering different aspects of *kugeln*. Therefore, suggested future work is based on the initially proposed workflow of investigation as shown in Fig. 5.1 and refined by the knowledge gathered so far.

Morphological Description. Data presented here focused on investigations in the early embryonic vasculature. It is not clear if *kugeln* are solely an embryonic phenomenon or whether these occur also in juvenile or adult zebrafish. Similarly, it remains to be elucidated if *kugeln* are specific to zebrafish, or would be found in other organisms as well.

Other aspects to be studied relate to parent vessel specification. Here, differences between trunk and cranial vessels, as well as differences between the different cranial vessels need to be studied more comprehensively. One interesting aspect to be addressed could be the study

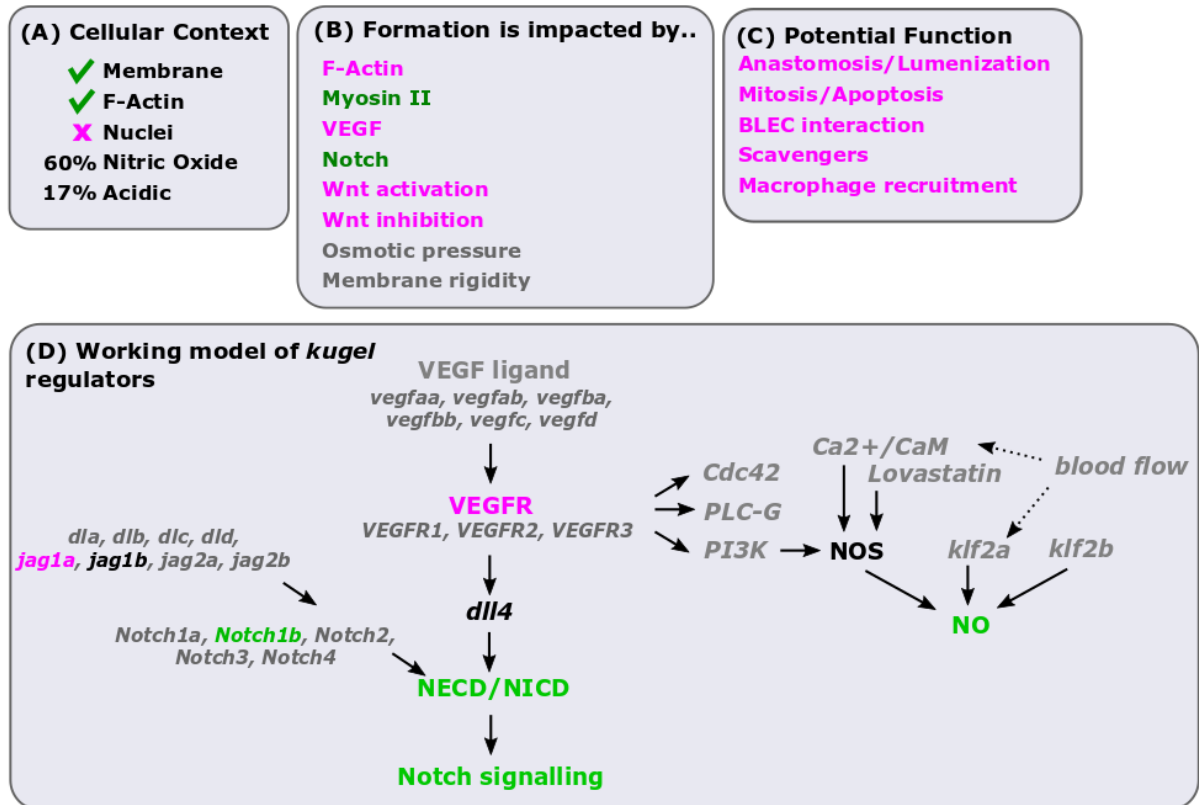


Figure 5.35: **Summary of *kugel* cellular context, examined regulators, potential function, and working model of regulation.** (A) Examination of *kugel* cellular context showed them to be formed by EC membrane with an underlying actin cortex and a subset of *kugel* to be positive for NO. (B) Several regulators of *kugel* formation were identified. (C) Several potential functions of *kugel* were examined. (D) Our findings suggest this working model of genetic regulation for *kugel* formation with VEGF being inhibitory, while Notch signalling is required for their formation and the role of NO needing future investigation (magenta - inhibits *kugel* formation, green - required for *kugel* formation), black - alteration does not alter *kugel*, grey - unknown function.

of microenvironmental mechanical pressure. This maybe could also elucidate mechanisms to artificially induce and/or rupture *kugeln*.

Role of blood flow in *kugel* formation and maintenance. In the scope of this project, a direct correlation between *kugel* formation and angiogenic remodelling, such as sprouting, constriction, or any other form of remodelling was observed. But more in-depth studies could examine whether quantitative correlations, or stochasticity, exist. Investigation of *kugeln* in *tnnt2a* morphants showed that blood flow during early embryonic development is required for *kugel* formation. Based on the fact that *kugeln* were not observed at 1dpf, the current working hypothesis is that *kugel* formation requires a certain vascular developmental time-point to be reached and that this may time-point may never be reached in *tnnt2* morphants, due to the lack of blood flow dependent EC changes.

Here, we suggest investigating mesenchymal-to-endothelial transition, endothelial cell differentiation, endothelial cell orientation, and the mechanical properties of endothelial cells. Also, it may be the case that a certain signalling context is not established by 1dpf, or by the loss of blood flow.

Moreover, further investigations into the diameter differences observed between uninjected controls and embryos which were injected with a standard control morpholino are suggested. Although this may just be a result of technical bias (eg concentration of injected control morpholino), it needs to be further investigated as to whether this finding is a true phenomenon.

The role of blood flow in *kugel* formation could also be studied more in-depth with the reduction of blood viscosity via *gata1* morpholino injection [431], and vice versa, the increase by erythropoietin [432].

Mechanical regulation. In the cellular context of mechanical regulation one may perform studies on endothelial mechanical changes occurring pre-, post- or during *kugel* formation. To study this, one could utilize conventional immunohistochemistry (eg. cellular junctions or polarity complexes) or *in vivo* examination via the endothelial tensor reporter line *Tg(Ve-Cadherin:gff;10xUAS:teal)^{uq13bh}* [433, 434, 435].

As shown above, *kugeln* do have an association with F-actin, and inhibition of actin polymerization lead to an overall increase in *kugel* number. Hence, it would be worth investigating the role of myosin II in *kugel* formation, maintenance, or retraction.

Also, the observed oscillatory shape changes of *kugeln* remain to be studied. Herein, an interesting aspect to be studied would be vasomotion or transcriptional bursts.

Membrane context. The membranous nature of *kugeln* suggests the need to perform further

experiments regarding membrane rigidity (preliminary results showed no difference; Fig. 5.34). Inducing membrane injuries via laser injury would allow to study whether *kugeln* are a result of membrane injury.

Another interesting possibility to be considered is that *kugeln* may act as extra-vascular-lumen lumina. It was shown that during embryonic development transient spatially-separated lumina are formed to either serve as a mechanical (eg. Kupffer's vesicle (KV) [436, 437]) or signalling (eg. posterior lateral line [438]) micro-environment.

Molecular foundation. Further descriptions of molecular-biological changes - as in gene expression or cellular protein localizations - would allow the study of causal relationships as well as feedback mechanisms.

Our data provided preliminary investigations on VEGF and Notch signalling; but it is unclear whether these act directly or via downstream factors. Moreover, studying other key signalling pathways (eg. BMP, HIF, etc.) in *kugel*-formation was beyond the scope of this study.

6 Overall Conclusion and Future Work

6.1 Summary of the conducted research and the contribution to knowledge

The aim of this study was to establish an image analysis pipeline to extract meaningful quantitative parameters describing the 3D architecture of the zebrafish vasculature to support the use of zebrafish as a pre-clinical model in cardiovascular research. The first step in this process was to gain an understanding of our data properties to allow for effective image enhancement as a foundation for image segmentation. To facilitate the study of inter-sample vascular similarity and variability, we developed inter-sample 3D registration. Based on this, we were able to extract quantitative shape descriptors such as vasculature branching points, segment length, and diameter. Together, we demonstrated that this objective image analysis approach allows novel insights into the 3D vascular architecture.

In the scope of the literature review and thesis introduction, we discussed zebrafish as a pre-clinical model in cardiovascular research and critically assessed the model limitations. Experimental advances towards transgenic lines (versus microangiography) and state-of-the-art microscopy were presented. In this scope, the current knowledge of the field was studied and gaps of knowledge relating to image analysis methods that provide an image quantification approach for the zebrafish cerebral vasculature in 3D in images acquired with LSFM identified. Particular challenges identified, included the following:

- transgenic zebrafish showed a cross-sectional double-peak intensity distribution, rather than a single-peak as is generally assumed previous application such as in the medical field,
- the vascular architecture in zebrafish is as highly complex enclosed circulatory network, while existing quantification approaches were optimized for individual vessels or vascular trees,
- quantification of the vasculature usually focused on 2D and/or single segment information, while our aim was to establish a 3D approach that encompassed the entire cranial vasculature.

6.1.1 Image understanding, pre-processing, and segmentation

The first step towards the development of a useful image analysis pipeline involved the understanding of the image acquisition setup as well as data properties, such as image quality

and noise patterns. Image quality was assessed using CNR measurements in different transgenic lines, during development, as well as different vessels, to gain a deeper understanding of data (section 2.3.1).

In the scope of this, motion artefacts were assessed and a method for motion-correction proposed to ensure that motion artefacts would not falsify subsequent quantification. Additionally, the proposed motion correction will allow the "rescue" of data in which motion would have made useful quantification impossible (section 2.3.2).

Based on the understanding of image properties and the correction of motion artefacts, methods of vascular enhancement, including general filtering and vessel specific enhancement were examined, using CNR as a quantitative image quality readout (section 2.3.3) [5]. Evaluating different segmentation approaches, subsequent to image pre-processing, revealed that intensity-based image binarization performed well, while more advanced segmentation methods performed disappointingly and likely require further bespoke optimisation if they are to be suitable (section 2.3.4). I found that vessel specific enhancement, considering a local tubular structure, prior to segmentation, resulted consistently in better segmentation outcomes than general image filters (section 2.3.4) [2]. In addition, enhancement and segmentation parameters were optimised and validated by comparison with manual measurements using vessel cross-sectional intensity profiles.

Vascular volume measurements after segmentation constituted the first meaningful vascular parameter to be extracted in this project, and was used to further examine segmentation robustness and sensitivity in section 2.3.5. As no gold standard or phantom model for image segmentation in zebrafish was available, we addressed the assessment of segmentation sensitivity and robustness using pragmatic experimental approaches. To test segmentation performance, different datasets were produced, vessels enhanced, segmented, and the cranial vascular volume quantified. The datasets consisted of the following:

- images with a controlled decrease in image quality (Fig. 2.22),
- images of different transgenic lines, which were found to have different image quality levels biologically (Fig. 2.4),
- images of double-transgenic fish, which are theoretically assumed to have the same cranial volume, but individual transgenics showing different CNR levels and fluorophore expression patterns (Fig. 2.23),
- embryos that had undergone exsanguination, which should lead to a decreased vascular volume due to loss of blood (Fig. 2.24),
- images of embryos at different stages of early vascular development (Fig. 2.25).

This was by far the most extensive segmentation evaluation and the first approach devised to overcome the lack of a segmentation gold-standard in zebrafish [4].

6.1.2 Intra-sample symmetry and inter-sample similarity

I developed the first approach to compare 3D zebrafish cerebrovascular left-right symmetry (section 3.3.1), finding no significant vascular asymmetry from 2-to-5dpf and that vessels formed by vasculogenesis (eg. BA, PHBC, and PMBC) are more left-right symmetric than vessels formed by angiogenesis (eg. CtAs and MMCTAs).

Next, inter-sample registration was studied to examine regions of vascular similarity and variability between fish (section 3.3.2), finding that both manual landmark-based and automatic 3D rigid registration were applicable to bring embryos into one spatial coordinate system, when applied to segmented data. Examining the impact of "target bias", inter-sample registration to an individual target outperformed registration to an averaged template (section 3.3.3). Comparing regions of similarity and variability between fish, the BA, PHBC, and PMBC showed a higher inter-sample similarity than CtAs and MMCTAs.

I applied the proposed inter-sample registration method to *dll4* MO, finding significant changes in vascular topology upon *dll4* loss (section 3.3.4). In addition, the inter-sample registration was used in the following chapter to map anatomical regions of *kugeln* (section 5.3.1).

6.1.3 Quantification of vascular topology

Based on the successful vascular segmentation, meaningful quantitative parameters of the 3D vasculature were extracted.

In 2D, ridge-based analysis was compared to skeleton-based analysis by examining developmental and *tnnt2a* MO data (section 4.3.3). I further examined 3D skeleton-based analysis by quantification of volume, network length, and branching points by using the "AnalyseSkeleton" Plugin after image segmentation and skeletonization (section 4.3.4). By applying our analysis to *tnnt2a* MO dataset, it was shown that all three of these quantitative parameters (volume, network length, and branching points) were statistically significantly reduced in zebrafish without blood flow.

By combining the extracted vascular skeleton with 3D EDMs, we were able to extract vascular diameters (section 4.3.7) showing that diameters are also statistically significantly reduced in zebrafish without blood flow. In addition to global diameter measurements and image outputs with voxel-wise diameter information, a raster-based analysis of vascular

subregions were developed, and the implemented code allowed for the analysis of sub-regional diameters based on user-defined ROI selection.

I next aimed to perform quantification on the level of individual vessels, discussing issues and limitations, and presented different potential methods to achieve this (section 4.3.8).

To analyse vascular complexity, Scholl analysis in 2D MIPs was used, which allowed for the examination of vascular complexity by measuring the number of intersections as well as the distance of these intersections from the centre (section 4.3.9), and applied it successfully to *tnnt2a* MO and early developmental data.

After testing and implementing all of the above analysis approaches, they were included into one GUI and workflow documentation was produced (Fig. 6.1).

Together, this allows for detailed analysis of zebrafish cerebrovascular data in 3D, which was the primary aim of this work (section 1.5).

6.1.4 Characterisation of a novel endothelial cell membrane behaviour

During the course of this work, previously undescribed endothelial membrane structures were discovered and we aimed to investigate the nature of these structures, called *kugel**n*. To achieve this, their morphology and patterns of occurrences were studied (diameter, number, 3D structure, vascular bed). This showed that these structures are transient 3D spheres protruding exclusively from central cranial vessels (section 5.3.1). Also, these structures were exceeding the size of any previously described membrane/vesicular structures.

Studying their cellular and sub-cellular context (cytoplasm, F-actin, nuclei) allowed us to understand that these structures were membranous, without individual nuclei, but had F-actin-rich necks (section 5.3.2).

Further examination focused on the specification/identity of *kugel*-parent vessels, vessel curvature, and *kugel*-lumen connection. We showed that *kugel**n* do not display a direct connection to the parent vessel lumen, which indicated that their inflation, maintenance, and retraction was independent of blood flow (section 5.3.3).

Investigating the role of key signalling pathways VEGF and Notch, by chemical inhibition, we showed that Notch had a positive effect on *kugel**n* (section 5.3.5), while VEGF inhibited them (section 5.3.4), suggesting a novel role for VEGF and Notch signalling in the regulation of endothelial cell behaviour.

Investigating the role of osmotic regulation and membrane rigidity in *kugel*-formation, no statistically significant impact was found (section 5.3.8).

The initial characterisation of *kugel**n* was published in EMBO Reports [1].

6.1.5 Publications in preparation

Building on the work presented in this thesis, the following publications are currently in preparation for publication (* corresponding author):

- submission April 2020 - Journal Article, **Kugler E.***, Rampun A., Chico T., and Armitage P., *Zebrafish Cranial Vasculature Segmentation using Vessel Enhancement and Machine Learning in Light Sheet Fluorescence Microscopy*. Target Journal - Medical Image Analysis (IF 8.79)

Following the validation of our proposed enhancement and segmentation pipeline we tested different deep learning network architectures for their ability to segment the zebrafish cerebral vasculature. We quantitatively compare the results obtained from conventional and deep learning based segmentation, finding that deep learning based segmentation is applicable to segment our data when trained on a robust segmentation method. Adding more convolutional layers, employing batch normalization, and applying dropout procedures to avoid overfitting to the original U-Net architecture, increased segmentation accuracy of our data. Together, we propose the first approach to validated zebrafish cerebral vascular segmentation, allowing objective extraction of true meaningful biological results as well as to provide the first deep learning study which allows segmentation of the zebrafish cerebral vasculature.

- submission April 2020 - Journal Article, **Kugler E.***, Snodgrass R., Bowley G., Plant K., Serbanovic- Canic J., Evans P., Chico T., and Armitage P., *Blood Flow Impact on the Cerebral and Trunk Vasculature in Developing Zebrafish Embryos*. Target Journal - EMBO Reports (IF 7.58)

Using tnnt2a morpholino oligonucleotides it is possible to prevent formation of heart contraction, thus study the impact of blood flow on vascular development. In this study we compare the role of blood flow in the cerebral and trunk vasculature by quantitatively assessing vascular topology as well as endothelial cell numbers. Our data show that the lack of blood flow impacts the cerebral vasculature more severely, but that endothelial cell numbers are reduced in both, the head and trunk vasculature. We show that blood flow significantly increases apoptosis and decreases proliferation to a lesser extent. Our data show that this happens without significant increases of tissue inflammation, as quantified by nitric oxide and cerebral immune cell numbers. Concluding, that blood flow is essential for cellular survival and to a lesser extent cellular proliferation, in both, the trunk and head vasculature.

- submission June 2020 - Invited Review, **Kugler E.*** and Chico T.*, *Diversity of Cranial*

Endothelial Cells. CMLS (IF 7.01)

The vasculature is an important organ system, permitting blood to circulate and transporting nutrients. It is increasingly apparent that endothelial cells that make up different vascular territories are heterogeneous in terms of their functional and molecular properties. Thus, it is important to understand what aspects of ECs are shared, and which are different, between different anatomic locations. Cerebrovascular ECs are of specific interest as vascular dysfunctions are associated with diseases such as stroke, cerebrovascular abnormalities, and vascular dementia. We here review the current knowledge about the impact of different signalling pathways on cerebral ECs. Next, we assemble the current literature about biomechanical properties such as blood flow, environment, and brain biomechanics as well as the importance of cilia in translating biomechanical cues in the cerebral vasculature. We examine how the surrounding tissue environment impacts cerebrovascular ECs, reviewing EC-neuron interaction, cranial lymphatics, and cells of the immune system and, lastly, briefly touch on future perspectives.

- submission July 2020 - Journal Article, **Kugler E.***, Plant K., Chico T., and Armitage P.*, *A 3D Cerebral Vasculature Atlas and Quantification Approach of Zebrafish Development*. Target journal - Nature Methods (IF 28.47)

Here, we describe an image analysis workflow to quantify vascular volume, surface, density, branching points, length and diameter. This is complemented by a workflow to examine intra-sample left-right similarity and variability as well as inter-sample similarity and variability, based on image registration. To investigate transferability, we applied our quantification approach to four different transgenic vascular reporter lines. Furthermore, we examined the impact of nine chemical components as well as six morpholinos on the vascular architecture.

6.2 Study limitations and future work

Probably the biggest limitation in the scope of this thesis was that no previous analysis approaches of any of the above were available to compare our workflows to. Therefore, in many ways, this project has provided a starting point from which future development can benchmark against. This thesis has covered a broad range of image analysis methodologies and implementations, so inevitably they can not have been studied in as much detail as a thesis that concentrated on one single aspect. However, we believe that we have developed a usable workflow for performing detailed quantification of zebrafish cranial vascular properties

from which future studies can build on, both in terms of methodological development and biological application. Some of the potential opportunities for further investigation are discussed below.

Our image analysis pipeline was mainly optimized for the cranial vasculature in *Tg(kdrl:HRAS-mCherry)^{sg16}*. Hence, applying the suggested image analysis pipeline to other transgenic lines, vascular beds, or ages is likely to require optimization to allow accurate vascular extraction and analysis.

Future work might examine intra-plane motion correction, which could be addressed by data interpolation from neighbouring slices, an aspect that was not investigated here due to time limitations.

In addition, we did not examine Frangi vessel enhancement or SRM, k-means clustering, and level-set segmentation methods further, which might show better performance if implemented differently.

Analytical limitations in the extraction of quantitative parameters may be encountered in structurally close, but distinctive vessels such as the caudal artery and caudal vein. Similarly, quantitative difficulties may emerge in less well-defined vascular regions such as the choroidal vascular plexus.

Using the "AnalyseSkeleton" Plugin in Fiji we encountered false-positive branching points to be extracted, future work might examine on improving this.

Additional information may be gained if the extracted vasculature quantification would be correlated to the overall embryonic physiology, such as body length or heart size.

Future work might examine vascular wall thickness further to study vascular inflammation and atherosclerosis. Similarly, blood flow analysis could be integrated in future studies.

Future translation of the presented quantification pipeline to broader applications may include data from similar models (eg Medaka transgenics) or different model aspects (eg zebrafish lymphatic system). We anticipate that these generalizations would require further investigations to ensure quantification accuracy. Broader generalizations, such as for mouse angiography data, are similarly likely to require optimization specific to this biological application. Especially due to the fact that the mouse circulatory system is typically visualized with other types of image acquisition modalities.

Inter-sample registration of zebrafish brains was previously shown to allow the establishment of component activity mapping [303] as well as the production of a co-localization atlas [302]. Based on our presented registration approach, similar atlases could now be established for the vasculature. This would be especially interesting to investigate vascular changes during early

development and whether these correlate with differential expression patterns of key signalling components, such as VEGF, Notch, or the *cxcr-cxcl* system.

In this thesis, we presented an initial characterisation of *kugel*, but appreciate that future work is needed to elucidate their function in vascular biology. These studies could address their conservation in other vertebrates, their restriction to the cerebral vasculature, and their developmental threshold, on the organism level. On the cellular level, *kugel* biomechanics in terms of actin-membrane coupling and impact on endothelial cells could be studied. On the molecular level, the factors regulating *kugel* formation and size, as well as their ultimate function could be studied.

6.3 Overall conclusion

Zebrafish are becoming an increasingly studied pre-clinical model (48.000 publications 2019; Google scholar 23.02.2020) in cardiovascular research (5.630 publications 2019; Google scholar 23.02.2020). Many of these studies rely on the vascular phenotype as an readout of the vascular status and health, but objective image quantification approaches are still lacking.

In the scope of this study, comprehensive image understanding and analysis for vascular images, acquired with state-of-the-art LSFM in transgenic zebrafish, was presented.

Performing image acquisition in transgenic lines overcame the necessity for laborious microangiography. This, provided the challenge of developing a method that worked effectively with the cross-vessel double-peak intensity distribution, which was successfully overcome during image pre-processing and segmentation.

Based on image understanding, pre-processing, segmentation, quantification, and registration, objective quantifications of the 3D vasculature in transgenic zebrafish is now possible. Inter-sample registration and the development of vascular growth templates allows direct visual and quantitative inter-sample assessments about regions of similarity and variability in the zebrafish vasculature, which were previously undescribed. The quantification established includes measurement of vascular volume, branching points, and diameter. Allowing direct comparability between embryos, ages, or pathological changes. Moreover, vascular complexity analysis was conducted to allow assessment of vascular topology on a more abstract level.

This method of objective quantification shall foster the investigation of normal vascular development and disease using zebrafish as a pre-clinical model in cardiovascular research.

Extending existing quantification approaches to the third dimension, allowed the vascular quantification to be more specific as well as accurate, as previous methods mainly considered

3D information collated into 2D.

In this study, we have shown that quantitative parameters can be successfully extracted and utilized to describe the vascular geometry in zebrafish. Herein, different biologically relevant examples, such as developmental changes, drug treatments, or the loss of blood, were presented to show the surplus provided by objective quantification over subjective visual assessment.

The workflows developed in this PhD project were implemented as Fiji Macros and are available as individual Macros as well as one complete workflow with a GUI (Fig. 6.1). The workflow implementation allows processing of whole datasets by simple selection of input and output folders. Additionally, workflow documentation is provided in the code, as well as an additional word document. All these being accessible on a shared team drive. See Appendix B for workflow overview, Appendix C for individual macros, and Appendix D for GUI.

We anticipate that the established analysis approach and pipeline will be useful to researchers wanting to examine vascular development and the impact of genetic or chemical manipulation on vascular architecture. This is exemplified by our study about the impact of F-actin polymerization inhibition (Fig. 5.12). Our approach can be applied to examine any data with similar properties, with the *caveat* that parameter optimisation was performed for *Tg(kdrl:HRAS-mCherry)* <5dpf. Importantly, by measuring multiple parameters (ie. volume, length, diameter, branching points, surface, complexity) these can be examined with respect to each other and new insights about vascular processes be gained. This is of special interest as data acquisition in embryonic zebrafish can be performed on the whole-brain level, *in vivo*, and 3D, while other models are limited to data acquisition in brain sub-regions, individual vessel segments, or *post mortem*. Hence, our analysis approach is the first of its kind to allow the study of the whole zebrafish brain vasculature in 3D *in vivo*. In addition to examining the brain vasculature globally, examinations of sub-regions can be performed by simple ROI selection, allowing for example to study mid- to hind-brain differences. Future application of our analysis to developmental data would be the first quantification and description of vascular parameters over time, providing the first study to describe the zebrafish brain vascular architecture with parameters other than volume or length. Similarly, our approach will provide novel insights into the impacts of drugs, which might have been previously overlooked. This is exemplified by our quantification of vascular volume upon VEGF inhibition with AV951, which showed a reduction in cerebrovascular volume which was inaccessible to the human observer (Fig. 2.28). As AV951 is an anti-cancer drug used in the medical field, we are confident that our analysis could aid the discovery of new anti-cancer drugs, as hyper-vascularization is a hallmark of

patient cancer progression. Similarly, we showed applicability of our analysis to knock-down experiments, such as loss of *dll4* or *tnnt2a*, showing that also genetic manipulations will be quantifiable with our analysis. Thus, our workflow will contribute to the understanding of genes, proteins, and genetic alterations, which are crucial for healthy vascular development and are often the underlying cause for the vascular status observed in patients. As mentioned above, generalization to other models (eg lymphatics, Medaka) or imaging modalities (eg confocal) are likely to require optimisation of parameters to meet data differences.

Together, as described in the introduction (Fig. 1.7), the aims of this project were to provide pre-processing, quantification, and registration steps to analyse zebrafish vascular topology, which were fulfilled and integrated into the above GUI (Fig. 6.2). Additionally, validation and testing was performed using biologically relevant datasets, to allow the extraction of meaningful vascular parameters.

Lastly, a novel endothelial membrane behaviour was described, which was previously undescribed and presented a novel role of Notch and VEGF signalling in angiogenesis.

With the increasing need for comprehensive and unbiased data analysis, we believe that the developed pipeline as well as the finding of *kugelIn*, contributed to the advancement of knowledge in the field of vascular research in zebrafish.

Having developed our image analysis pipeline in the open-source software Fiji, the analysis pipeline is available to the scientific community in the spirit of open-source, without the need for licensing. The computational foundation of Fiji and the developed image analysis pipeline was Java, as this allows for direct cross-operating-system applicability. By adding comprehensive documentation, future development by the community should be easily facilitated. Additionally, data can be made available upon request, which may benefit scientists, who do not have access to the particular transgenic lines and/or LSM data.

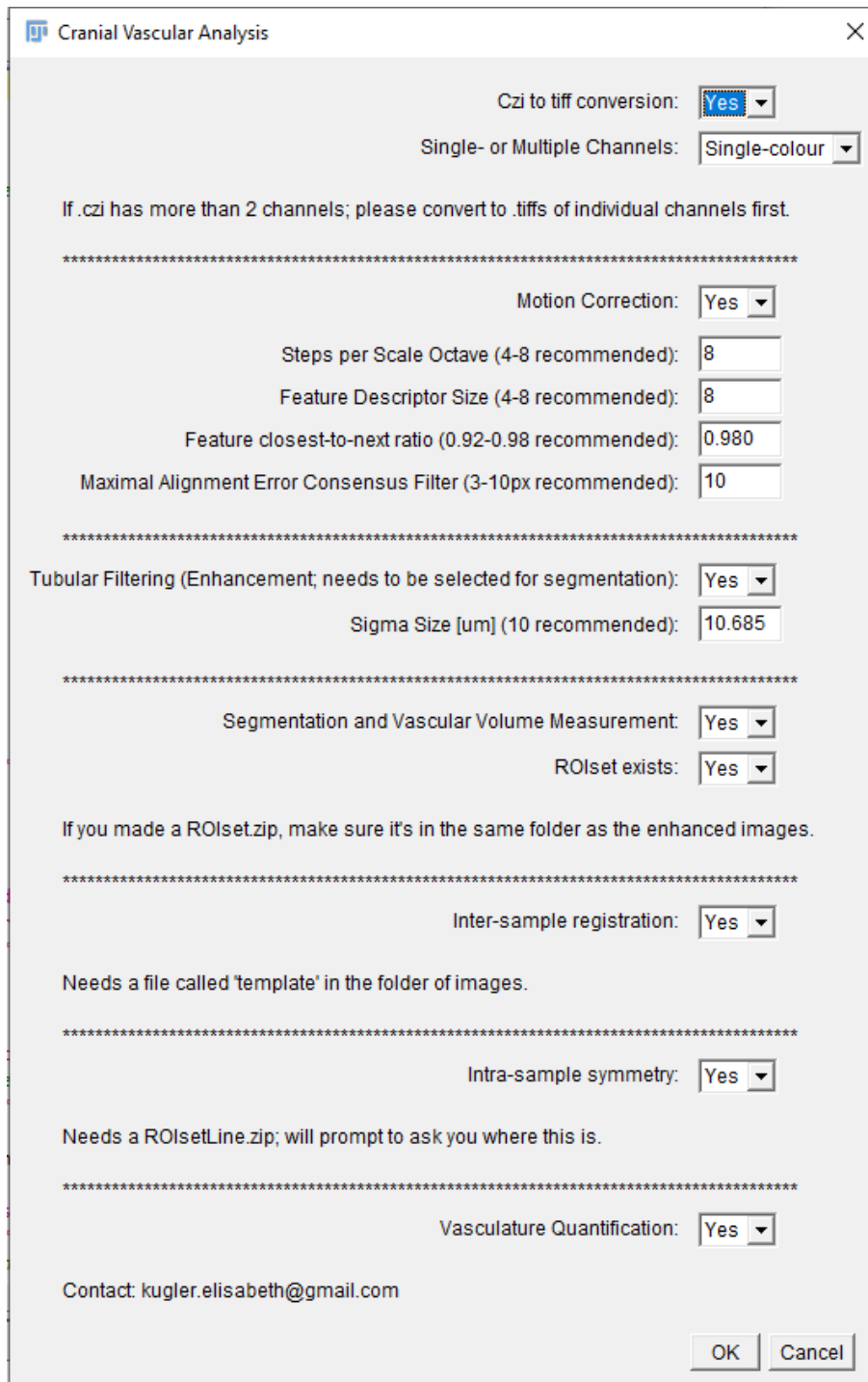


Figure 6.1: **Graphical User Interface (GUI)**. Graphical User Interface (GUI) for the image analysis workflows developed in this thesis.

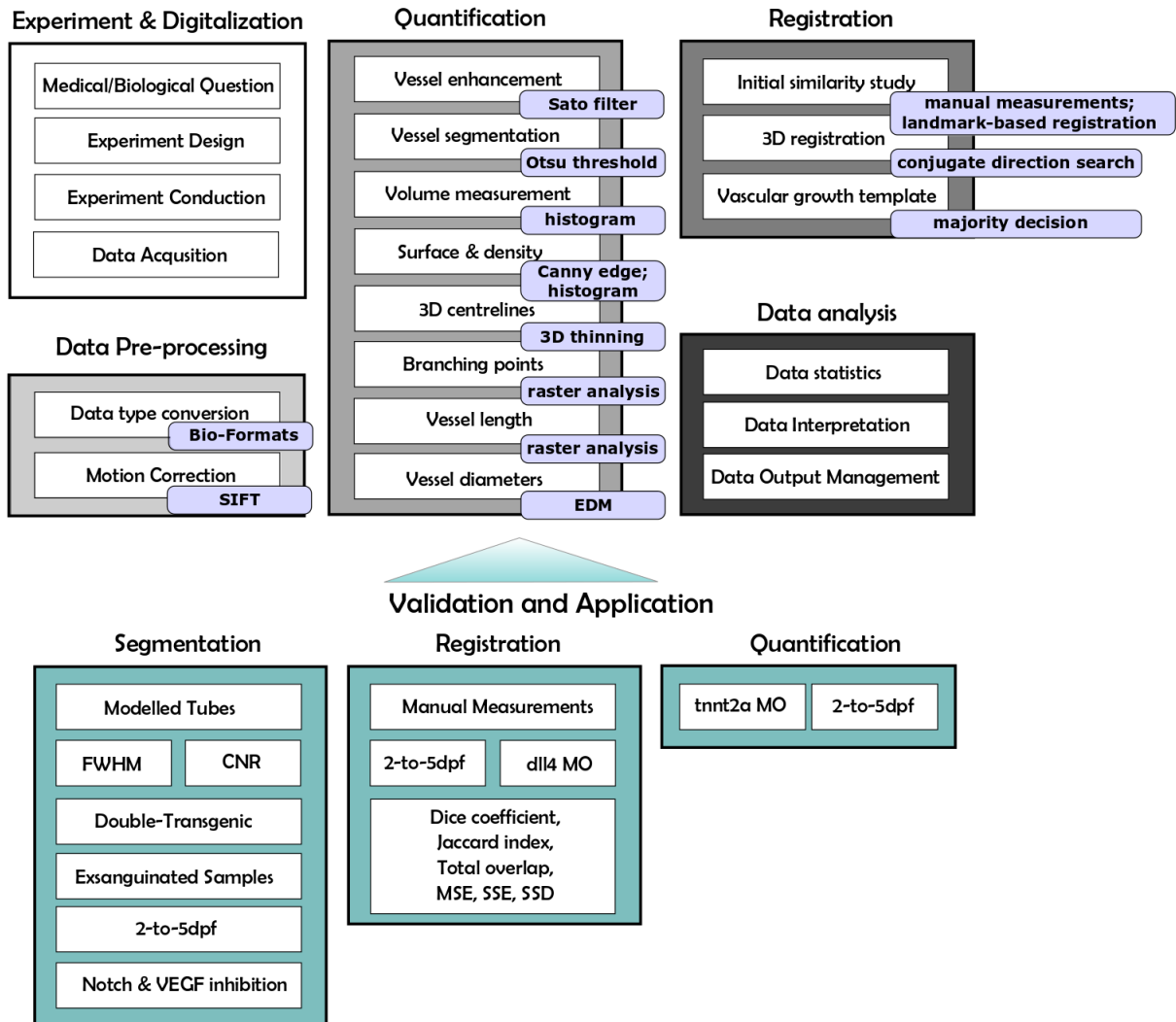


Figure 6.2: **Thesis Workflow Summary.** The developed image analysis workflow consists of pre-processing, quantification, and registration steps to analyse zebrafish vascular topology (aims - grey boxes, method - violet). Validation and cases for biological application were provided for segmentation, registration, and quantification (cyan).

Bibliography

- [1] Elisabeth C Kugler, Max van Lessen, Stephan Daetwyler, Karishma Chhabria, Aaron M Savage, Vishmi Silva, Karen Plant, Ryan B MacDonald, Jan Huisken, Robert N Wilkinson, Stefan Schulte-Merker, Paul Armitage, and Timothy JA Chico. Cerebrovascular endothelial cells form transient Notch-dependent cystic structures in zebrafish. *EMBO reports*, 20(8):e47047, August 2019. ISSN 1469-221X. doi: 10.15252/embr.201847047. URL <https://www.embopress.org/doi/10.15252/embr.201847047>.
- [2] Elisabeth Kugler, Karen Plant, Timothy Chico, and Paul Armitage. Enhancement and Segmentation Workflow for the Developing Zebrafish Vasculature. *Journal of Imaging*, 5(1):14, January 2019. doi: 10.3390/jimaging5010014. URL <https://www.mdpi.com/2313-433X/5/1/14>.
- [3] Karishma Chhabria, Karen Plant, Oliver Bandmann, Robert N. Wilkinson, Chris Martin, Elisabeth Kugler, Paul A. Armitage, Paola Lm Santoscoy, Vincent T. Cunliffe, Jan Huisken, Alexander McGown, Tennore Ramesh, Tim Ja Chico, and Clare Howarth. The effect of hyperglycemia on neurovascular coupling and cerebrovascular patterning in zebrafish. *Journal of Cerebral Blood Flow and Metabolism: Official Journal of the International Society of Cerebral Blood Flow and Metabolism*, page 271678X18810615, November 2018. ISSN 1559-7016. doi: 10.1177/0271678X18810615.
- [4] Elisabeth Kugler, Timothy Chico, and Paul A. Armitage. Validating Segmentation of the Zebrafish Vasculature. In Yalin Zheng, Bryan M. Williams, and Ke Chen, editors, *Medical Image Understanding and Analysis*, Communications in Computer and Information Science, pages 270–281, Cham, 2020. Springer International Publishing. ISBN 978-3-030-39343-4. doi: 10.1007/978-3-030-39343-4_23.
- [5] E. Kugler, T. Chico, and P. Armitage. Image Analysis in Light Sheet Fluorescence Microscopy Images of Transgenic Zebrafish Vascular Development. In Nixon M., Mahmoodi S., Zwiggelaar R. (eds) *Medical Image Understanding and Analysis. MIUA 2018.*, volume Communications in Computer and Information Science, vol 894, pages 343–353. Springer, Cham, 2018.
- [6] Ramazan Demir, Aylin Yaba, and Berthold Huppertz. Vasculogenesis and angiogenesis in the endometrium during menstrual cycle and implantation. *Acta Histochemica*, 112(3): 203–214, May 2010. ISSN 1618-0372. doi: 10.1016/j.acthis.2009.04.004.
- [7] Susanne Jung and Johannes Kleinheinz. Angiogenesis — The Key to Regeneration. 2013. doi: 10.5772/55542. URL <http://www.intechopen.com/books/regenerative-medicine-and-tissue-engineering/angiogenesis-the-key-to-regeneration>.
- [8] Adam J. Singer and Richard A.F. Clark. Cutaneous Wound Healing. *New England Journal of Medicine*, 341(10):738–746, September 1999. ISSN 0028-4793. doi: 10.1056/NEJM199909023411006. URL <http://dx.doi.org/10.1056/NEJM199909023411006>.
- [9] Peter Carmeliet. Angiogenesis in life, disease and medicine. *Nature*, 438(7070):932–936, December 2005. ISSN 1476-4687. doi: 10.1038/nature04478.
- [10] Codecà Carla, Ferrari Daris, Bertuzzi Cecilia, Broggio Francesca, Crepaldi Francesca, and Foa Paolo. Angiogenesis in Head and Neck Cancer: A Review of the Literature. *Journal of Oncology*, 2012, 2012. doi: 10.1155/2012/358472. URL [/pmcc/articles/PMC3216268/?report=abstract](http://pmcc/articles/PMC3216268/?report=abstract).
- [11] Marina Piccinelli, Alessandro Veneziani, David A. Steinman, Andrea Remuzzi, and Luca Antiga. A framework for geometric analysis of vascular structures: application to cerebral aneurysms. *IEEE transactions on medical imaging*, 28(8):1141–1155, August 2009. ISSN 1558-254X. doi: 10.1109/TMI.2009.2021652.
- [12] Michael J. Fowler. Microvascular and Macrovascular Complications of Diabetes. *Clinical Diabetes*, 26(2):77–82, April 2008. ISSN 0891-8929, 1945-4953. doi: 10.2337/diaclin.26.2.77. URL <http://clinical.diabetesjournals.org/content/26/2/77>.
- [13] Gregg L. Semenza. Vascular Responses to Hypoxia and Ischemia. *Arteriosclerosis, thrombosis, and vascular biology*, 30(4):648–652, April 2010. ISSN 1079-5642. doi: 10.1161/ATVBAHA.108.181644. URL <https://www.ncbi.nlm.nih.gov/pmc/articles/PMC2841694/>.
- [14] Philipp Gut, Sven Reischauer, Didier Y. R. Stainier, and Rima Arnaout. Little Fish, Big Data: Zebrafish as a Model for Cardiovascular and Metabolic Disease. *Physiological Reviews*, 97(3):889–938, July 2017. ISSN 0031-9333, 1522-1210. doi: 10.1152/physrev.00038.2016. URL <http://physrev.physiology.org/content/97/3/889>.

- [15] Oren Traub and Bradford C. Berk. Laminar Shear Stress: Mechanisms by Which Endothelial Cells Transduce an Atheroprotective Force. *Arteriosclerosis, Thrombosis, and Vascular Biology*, 18(5):677–685, May 1998. ISSN 1079-5642, 1524-4636. doi: 10.1161/01.ATV.18.5.677. URL <http://atvb.ahajournals.org/content/18/5/677>.
- [16] Juhyun Lee, René R. Sevag Packard, and Tzung K. Hsiai. Blood Flow Modulation of Vascular Dynamics. *Current opinion in lipidology*, 26(5):376–383, October 2015. ISSN 0957-9672. doi: 10.1097/MOL.000000000000218. URL <https://www.ncbi.nlm.nih.gov/pmc/articles/PMC4626080/>.
- [17] Filippo Arcadu, Fethallah Benmansour, Andreas Maunz, Jeff Willis, Zdenka Haskova, and Marco Prunotto. Deep learning algorithm predicts diabetic retinopathy progression in individual patients. *npj Digital Medicine*, 2(1):1–9, September 2019. ISSN 2398-6352. doi: 10.1038/s41746-019-0172-3. URL <https://www.nature.com/articles/s41746-019-0172-3>. Number: 1 Publisher: Nature Publishing Group.
- [18] Lily Peng. Deep Learning for Detection of Diabetic Eye Disease, 2016. URL <http://ai.googleblog.com/2016/11/deep-learning-for-detection-of-diabetic.html>. Library Catalog: ai.googleblog.com.
- [19] Bruce A. Barut and Leonard I. Zon. Realizing the potential of zebrafish as a model for human disease. *Physiological Genomics*, 2(2):49–51, March 2000. ISSN 1094-8341, 1531-2267. URL <http://physiolgenomics.physiology.org/content/2/2/49>.
- [20] JR Goldsmith and C Jobin. Think small: zebrafish as a model system of human pathology. *BioMed Research International*, 2012.
- [21] Graham J. Lieschke and Peter D. Currie. Animal models of human disease: zebrafish swim into view. *Nature Reviews Genetics*, 8(5):353–367, May 2007. ISSN 1471-0056. doi: 10.1038/nrg2091. URL <http://www.nature.com/nrg/journal/v8/n5/abs/nrg2091.html>.
- [22] Kimberly Dooley and Leonard I Zon. Zebrafish: a model system for the study of human disease. *Current Opinion in Genetics & Development.*, 10(3):252–256, 2000.
- [23] Timothy J. A. Chico, Philip W. Ingham, and David C. Crossman. Modeling Cardiovascular Disease in the Zebrafish. *Trends in Cardiovascular Medicine*, 18(4):150–155, May 2008. ISSN 1050-1738. doi: 10.1016/j.tcm.2008.04.002. URL <http://www.sciencedirect.com/science/article/pii/S1050173808000595>.
- [24] Nathan D. Lawson and Brant M. Weinstein. Arteries and veins: making a difference with zebrafish. *Nature Reviews Genetics*, 3(9):674–682, September 2002. ISSN 1471-0056. doi: 10.1038/nrg888. URL <http://www.nature.com/nrg/journal/v3/n9/full/nrg888.html>.
- [25] J. F. Amatruda and L. I. Zon. Dissecting hematopoiesis and disease using the zebrafish. *Developmental Biology*, 216(1):1–15, December 1999. ISSN 0012-1606. doi: 10.1006/dbio.1999.9462.
- [26] Mary C. McKinney and Brant M. Weinstein. Chapter 4. Using the zebrafish to study vessel formation. *Methods in Enzymology*, 444:65–97, 2008. ISSN 1557-7988. doi: 10.1016/S0076-6879(08)02804-8.
- [27] W. W. Burggren and A. W. Pinder. Ontogeny of cardiovascular and respiratory physiology in lower vertebrates. *Annual Review of Physiology*, 53:107–135, 1991. ISSN 0066-4278. doi: 10.1146/annurev.ph.53.030191.000543.
- [28] Didier Y. R. Stainier. Zebrafish genetics and vertebrate heart formation. *Nature Reviews Genetics*, 2(1):39–48, January 2001. ISSN 1471-0056. doi: 10.1038/35047564. URL http://www.nature.com/nrg/journal/v2/n1/execsumm/nrg0101_039a.html?foxtrotcallback=true.
- [29] M. C. Fishman and K. R. Chien. Fashioning the vertebrate heart: earliest embryonic decisions. *Development (Cambridge, England)*, 124(11):2099–2117, June 1997. ISSN 0950-1991.
- [30] Elin Ellertsdóttir, Anna Lenard, Yannick Blum, Alice Krudewig, Lukas Herwig, Markus Affolter, and Heinz-Georg Belting. Vascular morphogenesis in the zebrafish embryo. *Developmental Biology*, 341(1):56–65, May 2010. ISSN 0012-1606. doi: 10.1016/j.ydbio.2009.10.035. URL <http://www.sciencedirect.com/science/article/pii/S0012160609013116>.
- [31] S Isogai, M Horiguchi, and B M Weinstein. The vascular anatomy of the developing zebrafish: an atlas of embryonic and early larval development. *Developmental Biology*, 230(2):278–301, February 2001. ISSN 0012-1606. doi: 10.1006/dbio.2000.9995. URL <http://www.ncbi.nlm.nih.gov/pubmed/11161578>.

- [32] D. Y. Stainier and M. C. Fishman. Patterning the zebrafish heart tube: acquisition of anteroposterior polarity. *Developmental Biology*, 153(1):91–101, September 1992. ISSN 0012-1606.
- [33] N. Bahary and L. I. Zon. Use of the zebrafish (*Danio rerio*) to define hematopoiesis. *Stem Cells (Dayton, Ohio)*, 16(2):89–98, 1998. ISSN 1066-5099. doi: 10.1002/stem.160089.
- [34] Sumio Isogai, Nathan D. Lawson, Saioa Torrealday, Masaharu Horiguchi, and Brant M. Weinstein. Angiogenic network formation in the developing vertebrate trunk. *Development (Cambridge, England)*, 130(21):5281–5290, November 2003. ISSN 0950-1991. doi: 10.1242/dev.00733.
- [35] Amina A. Qutub, Feilim Mac Gabhann, Emmanouil D. Karagiannis, Prakash Vempati, and Aleksander S. Popel. Multiscale models of angiogenesis. *IEEE engineering in medicine and biology magazine: the quarterly magazine of the Engineering in Medicine & Biology Society*, 28(2):14–31, April 2009. ISSN 1937-4186. doi: 10.1109/MEMB.2009.931791.
- [36] Hossein Bazmara, Madjid Soltani, Mostafa Sefidgar, Majid Bazargan, Mojtaba Mousavi Naeenian, and Arman Rahmim. The Vital Role of Blood Flow-Induced Proliferation and Migration in Capillary Network Formation in a Multiscale Model of Angiogenesis. *PLoS One*, 10(6):e0128878, 2015. ISSN 1932-6203. doi: 10.1371/journal.pone.0128878.
- [37] Aniket V. Gore, Kathryn Monzo, Young R. Cha, Weijun Pan, and Brant M. Weinstein. Vascular Development in the Zebrafish. *Cold Spring Harbor Perspectives in Medicine*, 2(5), May 2012. ISSN 2157-1422. doi: 10.1101/cshperspect.a006684. URL <http://www.ncbi.nlm.nih.gov/pmc/articles/PMC3331685/>.
- [38] Sarah Childs, Jau-Nian Chen, Deborah M. Garrity, and Mark C. Fishman. Patterning of angiogenesis in the zebrafish embryo. *Development*, 129(4):973–982, February 2002. ISSN 0950-1991, 1477-9129. URL <http://dev.biologists.org/content/129/4/973>.
- [39] W. Risau and I. Flamme. Vasculogenesis. *Annual Review of Cell and Developmental Biology*, 11:73–91, 1995. ISSN 1081-0706. doi: 10.1146/annurev.cb.11.110195.000445.
- [40] T. J. Poole and J. D. Coffin. Vasculogenesis and angiogenesis: two distinct morphogenetic mechanisms establish embryonic vascular pattern. *The Journal of Experimental Zoology*, 251(2):224–231, August 1989. ISSN 0022-104X. doi: 10.1002/jez.1402510210.
- [41] Thomas H. Adair and Jean-Pierre Montani. *Angiogenesis. Integrated Systems Physiology: from Molecule to Function to Disease*. Morgan & Claypool Life Sciences, San Rafael (CA), 2010. URL <http://www.ncbi.nlm.nih.gov/books/NBK53242/>.
- [42] Benjamin M. Hogan and Stefan Schulte-Merker. How to Plumb a Pisces: Understanding Vascular Development and Disease Using Zebrafish Embryos. *Developmental Cell*, 42(6):567–583, September 2017. ISSN 1534-5807. doi: 10.1016/j.devcel.2017.08.015. URL [http://www.cell.com/developmental-cell/abstract/S1534-5807\(17\)30675-5](http://www.cell.com/developmental-cell/abstract/S1534-5807(17)30675-5).
- [43] Michael Potente and Taija Mäkinen. Vascular heterogeneity and specialization in development and disease. *Nature Reviews Molecular Cell Biology*, 18(8):477–494, August 2017. ISSN 1471-0072. doi: 10.1038/nrm.2017.36. URL <http://www.nature.com/nrm/journal/v18/n8/full/nrm.2017.36.html>.
- [44] Charles B. Kimmel, William W. Ballard, Seth R. Kimmel, Bonnie Ullmann, and Thomas F. Schilling. Stages of embryonic development of the zebrafish. *Developmental Dynamics*, 203(3):253–310, 1995. ISSN 1097-0177. doi: 10.1002/aja.1002030302. URL <http://onlinelibrary.wiley.com/doi/10.1002/aja.1002030302/abstract>.
- [45] Bernadette Fouquet, Brant M. Weinstein, Fabrizio C. Serluca, and Mark C. Fishman. Vessel Patterning in the Embryo of the Zebrafish: Guidance by Notochord. *Developmental Biology*, 183(1):37–48, March 1997. ISSN 0012-1606. doi: 10.1006/dbio.1996.8495. URL <http://www.sciencedirect.com/science/article/pii/S001216069698495X>.
- [46] Christian S. M. Helker, Annika Schuermann, Cathrin Pollmann, Serene C. Chng, Friedemann Kiefer, Bruno Reversade, and Wiebke Herzog. The hormonal peptide Elabela guides angioblasts to the midline during vasculogenesis. *eLife*, 4, May 2015. ISSN 2050-084X. doi: 10.7554/eLife.06726.
- [47] L. Sumoy, J. B. Keasey, T. D. Dittman, and D. Kimelman. A role for notochord in axial vascular development revealed by analysis of phenotype and the expression of VEGF-2 in zebrafish *flh* and *ntl* mutant embryos. *Mechanisms of Development*, 63(1):15–27, April 1997. ISSN 0925-4773.
- [48] Katarzyna Koltowska, Kelly L. Betterman, Natasha L. Harvey, and Benjamin M. Hogan. Getting out and about: the emergence and morphogenesis of the vertebrate lymphatic

- vasculature. *Development (Cambridge, England)*, 140(9):1857–1870, May 2013. ISSN 1477-9129. doi: 10.1242/dev.089565.
- [49] Wonshill Koh, Rachel D. Mahan, and George E. Davis. Cdc42- and Rac1-mediated endothelial lumen formation requires Pak2, Pak4 and Par3, and PKC-dependent signaling. *Journal of Cell Science*, 121(Pt 7):989–1001, April 2008. ISSN 0021-9533. doi: 10.1242/jcs.020693.
- [50] Wonshill Koh, Kamakshi Sachidanandam, Amber N. Stratman, Anastasia Sacharidou, Anne M. Mayo, Eric A. Murphy, David A. Cheresh, and George E. Davis. Formation of endothelial lumens requires a coordinated PKC-, Src-, Pak- and Raf-kinase-dependent signaling cascade downstream of Cdc42 activation. *Journal of Cell Science*, 122(11):1812–1822, June 2009. ISSN 0021-9533. doi: 10.1242/jcs.045799. URL <http://www.ncbi.nlm.nih.gov/pmc/articles/PMC2684834/>.
- [51] C Lee and V Bautch. Ups and Downs of Guided Vessel Sprouting: The role of Polarity. *Physiology*, 26:236–333, 2011. URL <http://physiologyonline.physiology.org/content/26/5/326>.
- [52] Kayla J. Bayless and Greg A. Johnson. Role of the Cytoskeleton in Formation and Maintenance of Angiogenic Sprouts. *Journal of Vascular Research*, 48(5):369–385, August 2011. ISSN 1018-1172. doi: 10.1159/000324751. URL <http://www.ncbi.nlm.nih.gov/pmc/articles/PMC3080587/>.
- [53] Kayla J. Bayless and George E. Davis. Microtubule depolymerization rapidly collapses capillary tube networks in vitro and angiogenic vessels in vivo through the small GTPase Rho. *The Journal of Biological Chemistry*, 279(12):11686–11695, March 2004. ISSN 0021-9258. doi: 10.1074/jbc.M308373200.
- [54] Kayla J. Bayless and George E. Davis. The Cdc42 and Rac GTPases are required for capillary lumen formation in three-dimensional extracellular matrices. *J Cell Sci*, 115:1123–1136, 2002.
- [55] Arndt F. Siekmann and Nathan D. Lawson. Notch signalling limits angiogenic cell behaviour in developing zebrafish arteries. *Nature*, 445(7129):781–784, February 2007. ISSN 1476-4687. doi: 10.1038/nature05577.
- [56] Tuomas Tammela, Georgia Zarkada, Elisabet Wallgard, Aino Murtomäki, Steven Suchting, Maria Wirzenius, Marika Waltari, Mats Hellström, Tibor Schomber, Reetta Peltonen, Catarina Freitas, Antonio Duarte, Helena Isoniemi, Pirjo Laakkonen, Gerhard Christofori, Seppo Ylä-Herttuala, Masabumi Shibuya, Bronislaw Pytowski, Anne Eichmann, Christer Betsholtz, and Kari Alitalo. Blocking VEGFR-3 suppresses angiogenic sprouting and vascular network formation. *Nature*, 454(7204):656–660, July 2008. ISSN 1476-4687. doi: 10.1038/nature07083.
- [57] Frederik De Smet, Inmaculada Segura, Katrien De Bock, Philipp J. Hohensinner, and Peter Carmeliet. Mechanisms of vessel branching: filopodia on endothelial tip cells lead the way. *Arteriosclerosis, Thrombosis, and Vascular Biology*, 29(5):639–649, May 2009. ISSN 1524-4636. doi: 10.1161/ATVBAHA.109.185165.
- [58] Holger Gerhardt, Matthew Golding, Marcus Fruttiger, Christiana Ruhrberg, Andrea Lundkvist, Alexandra Abramsson, Michael Jeltsch, Christopher Mitchell, Kari Alitalo, David Shima, and Christer Betsholtz. VEGF guides angiogenic sprouting utilizing endothelial tip cell filopodia. *The Journal of Cell Biology*, 161(6):1163–1177, June 2003. ISSN 0021-9525. doi: 10.1083/jcb.200302047. URL <http://www.ncbi.nlm.nih.gov/pmc/articles/PMC2172999/>.
- [59] Richard C. A. Sainson, Jason Aoto, Martin N. Nakatsu, Matthew Holderfield, Erin Conn, Erich Koller, and Christopher C. W. Hughes. Cell-autonomous notch signaling regulates endothelial cell branching and proliferation during vascular tubulogenesis. *FASEB journal: official publication of the Federation of American Societies for Experimental Biology*, 19(8):1027–1029, June 2005. ISSN 1530-6860. doi: 10.1096/fj.04-3172fje.
- [60] Arndt F. Siekmann, Markus Affolter, and Heinz-Georg Belting. The Tip Cell Concept Ten Years After : New Players Tune in for a Common Theme. *Experimental cell research*, Vol. 319, H. 9(HASH(0x9242d98)):S. 1255–1263, 2013. ISSN 0014-4827. URL <http://edoc.unibas.ch/dok/A6093986>.
- [61] Beth L. Roman, Van N. Pham, Nathan D. Lawson, Magdalena Kulik, Sarah Childs, Arne C. Lekven, Deborah M. Garrity, Randall T. Moon, Mark C. Fishman, Robert J. Lechleider, and Brant M. Weinstein. Disruption of *acvr11* increases endothelial cell number in zebrafish cranial vessels. *Development (Cambridge, England)*, 129(12):3009–3019, June 2002. ISSN 0950-1991.

- [62] Rachel M. Warga, Donald A. Kane, and Robert K. Ho. Fate-mapping embryonic blood in zebrafish: Multi- and uni-potential lineages are segregated at gastrulation. *Developmental cell*, 16(5):744–755, May 2009. ISSN 1534-5807. doi: 10.1016/j.devcel.2009.04.007. URL <http://www.ncbi.nlm.nih.gov/pmc/articles/PMC2764372/>.
- [63] Kira Proulx, Annie Lu, and Saulius Sumanas. Cranial vasculature in zebrafish forms by angioblast cluster-derived angiogenesis. *Developmental Biology*, 348(1):34–46, December 2010. ISSN 1095-564X. doi: 10.1016/j.ydbio.2010.08.036.
- [64] Eiji Kimura, Sumio Isogai, and Jiro Hitomi. Integration of vascular systems between the brain and spinal cord in zebrafish. *Developmental Biology*, 406(1):40–51, October 2015. ISSN 0012-1606. doi: 10.1016/j.ydbio.2015.07.015. URL <http://www.sciencedirect.com/science/article/pii/S0012160615300592>.
- [65] N. D. Lawson, N. Scheer, V. N. Pham, C. H. Kim, A. B. Chitnis, J. A. Campos-Ortega, and B. M. Weinstein. Notch signaling is required for arterial-venous differentiation during embryonic vascular development. *Development (Cambridge, England)*, 128(19):3675–3683, October 2001. ISSN 0950-1991.
- [66] JE Cannon, PD Upton, JC Smith, and NW Morrell. Intersegmental vessel formation in zebrafish: requirement for VEGF but not BMP signalling revealed by selective and non-selective BMP antagonists. *British Journal of Pharmacology*, 161(1):140–149, September 2010. ISSN 0007-1188. doi: 10.1111/j.1476-5381.2010.00871.x. URL <http://www.ncbi.nlm.nih.gov/pmc/articles/PMC2962823/>.
- [67] Jeroen Bussmann, Scot A. Wolfe, and Arndt F. Siekmann. Arterial-venous network formation during brain vascularization involves hemodynamic regulation of chemokine signaling. *Development (Cambridge, England)*, 138(9):1717–1726, May 2011. ISSN 0950-1991. doi: 10.1242/dev.059881. URL <http://www.ncbi.nlm.nih.gov/pmc/articles/PMC3074448/>.
- [68] Véronique Gebala, Russell Collins, Ilse Geudens, Li-Kun Phng, and Holger Gerhardt. Blood flow drives lumen formation by inverse membrane blebbing during angiogenesis in vivo. *Nature Cell Biology*, 18(4):ncb3320, February 2016. ISSN 1476-4679. doi: 10.1038/ncb3320. URL <https://www.nature.com/articles/ncb3320>.
- [69] Kerstin Howe, Matthew D. Clark, Carlos F. Torroja, James Torrance, Camille Berthelot, Matthieu Muffato, John E. Collins, Sean Humphray, Karen McLaren, Lucy Matthews, Stuart McLaren, Ian Sealy, Mario Caccamo, Carol Churcher, Carol Scott, Jeffrey C. Barrett, Romke Koch, Gerd-Jörg Rauch, Simon White, William Chow, Britt Kilian, Leonor T. Quintais, José A. Guerra-Assunção, Yi Zhou, Yong Gu, Jennifer Yen, Jan-Hinnerk Vogel, Tina Eyre, Seth Redmond, Ruby Banerjee, Jianxiang Chi, Beiyuan Fu, Elizabeth Langley, Sean F. Maguire, Gavin K. Laird, David Lloyd, Emma Kenyon, Sarah Donaldson, Harminder Sehra, Jeff Almeida-King, Jane Loveland, Stephen Trevanion, Matt Jones, Mike Quail, Dave Willey, Adrienne Hunt, John Burton, Sarah Sims, Kirsten McLay, Bob Plumb, Joy Davis, Chris Clee, Karen Oliver, Richard Clark, Clare Riddle, David Elliott, Glen Threadgold, Glenn Harden, Darren Ware, Beverly Mortimer, Giselle Kerry, Paul Heath, Benjamin Phillimore, Alan Tracey, Nicole Corby, Matthew Dunn, Christopher Johnson, Jonathan Wood, Susan Clark, Sarah Pelan, Guy Griffiths, Michelle Smith, Rebecca Glithero, Philip Howden, Nicholas Barker, Christopher Stevens, Joanna Harley, Karen Holt, Georgios Panagiotidis, Jamieson Lovell, Helen Beasley, Carl Henderson, Daria Gordon, Katherine Auger, Deborah Wright, Joanna Collins, Claire Raisen, Lauren Dyer, Kenric Leung, Lauren Robertson, Kirsty Ambridge, Daniel Leongamornlert, Sarah McGuire, Ruth Gilderthorp, Coline Griffiths, Deepa Manthravadi, Sarah Nichol, Gary Barker, Siobhan Whitehead, Michael Kay, Jacqueline Brown, Clare Murnane, Emma Gray, Matthew Humphries, Neil Sycamore, Darren Barker, David Saunders, Justene Wallis, Anne Babbage, Sian Hammond, Maryam Mashreghi-Mohammadi, Lucy Barr, Sancha Martin, Paul Wray, Andrew Ellington, Nicholas Matthews, Matthew Ellwood, Rebecca Woodmansey, Graham Clark, James Cooper, Anthony Tromans, Darren Grafham, Carl Skuce, Richard Pandian, Robert Andrews, Elliot Harrison, Andrew Kimberley, Jane Garnett, Nigel Fosker, Rebekah Hall, Patrick Garner, Daniel Kelly, Christine Bird, Sophie Palmer, Ines Gehring, Andrea Berger, Christopher M. Dooley, Zübeyde Ersan-Ürün, Cigdem Eser, Horst Geiger, Maria Geisler, Lena Karotki, Anette Kirn, Judith Konantz, Martina Konantz, Martina Oberländer, Silke Rudolph-Geiger, Mathias Teucke, Kazutoyo Osoegawa, Baoli Zhu, Amanda Rapp, Sara Widaa, Cordelia Langford, Fengtang Yang, Nigel P. Carter, Jennifer Harrow, Zemin Ning, Javier Herrero, Steve M. J. Searle, Anton Enright, Robert Geisler, Ronald H. A. Plasterk, Charles Lee, Monte Westerfield, Pieter J. de Jong, Leonard I. Zon, John H. Postlethwait,

- Christiane Nüsslein-Volhard, Tim J. P. Hubbard, Hugues Roest Crolius, Jane Rogers, and Derek L. Stemple. The zebrafish reference genome sequence and its relationship to the human genome. *Nature*, 496(7446):498–503, April 2013. ISSN 0028-0836. doi: 10.1038/nature12111. URL <https://www.ncbi.nlm.nih.gov/pmc/articles/PMC3703927/>.
- [70] A. Meyer and M. Schartl. Gene and genome duplications in vertebrates: the one-to-four (-to-eight in fish) rule and the evolution of novel gene functions. *Current Opinion in Cell Biology*, 11(6):699–704, December 1999. ISSN 0955-0674.
- [71] Halina Anton, Sebastien Harlepp, Caroline Ramspacher, Dave Wu, Fabien Monduc, Sandeep Bhat, Michael Liebling, Camille Paoletti, Gilles Charvin, Jonathan B. Freund, and Julien Vermot. Pulse propagation by a capacitive mechanism drives embryonic blood flow. *Development (Cambridge, England)*, 140(21):4426–4434, November 2013. ISSN 1477-9129. doi: 10.1242/dev.096768.
- [72] Francesco Boselli, Jonathan B. Freund, and Julien Vermot. Blood flow mechanics in cardiovascular development. *Cellular and molecular life sciences: CMLS*, 72(13):2545–2559, July 2015. ISSN 1420-9071. doi: 10.1007/s00018-015-1885-3.
- [73] B. M. Weinstein, D. L. Stemple, W. Driever, and M. C. Fishman. Gridlock, a localized heritable vascular patterning defect in the zebrafish. *Nature Medicine*, 1(11):1143–1147, November 1995. ISSN 1078-8956.
- [74] Nathan D. Lawson and Brant M. Weinstein. In Vivo Imaging of Embryonic Vascular Development Using Transgenic Zebrafish. *Developmental Biology*, 248(2):307–318, August 2002. ISSN 0012-1606. doi: 10.1006/dbio.2002.0711. URL <http://www.sciencedirect.com/science/article/pii/S0012160602907116>.
- [75] Jan Huisken, Jim Swoger, Filippo Del Bene, Joachim Wittbrodt, and Ernst H. K. Stelzer. Optical sectioning deep inside live embryos by selective plane illumination microscopy. *Science (New York, N.Y.)*, 305(5686):1007–1009, August 2004. ISSN 1095-9203. doi: 10.1126/science.1100035.
- [76] Michael Weber, Michaela Mickoleit, and Jan Huisken. Light sheet microscopy. *Methods in Cell Biology*, 123:193–215, 2014. ISSN 0091-679X. doi: 10.1016/B978-0-12-420138-5.00011-2.
- [77] Emmanuel G. Reynaud, Uroš Kržič, Klaus Greger, and Ernst H.K. Stelzer. Light sheet-based fluorescence microscopy: more dimensions, more photons, and less photodamage. *HFSP Journal*, 2(5):266–275, October 2008. ISSN 1955-2068. doi: 10.2976/1.2974980. URL <http://www.ncbi.nlm.nih.gov/pmc/articles/PMC2639947/>.
- [78] Peter A. Santi. Light sheet fluorescence microscopy: a review. *The Journal of Histochemistry and Cytochemistry: Official Journal of the Histochemistry Society*, 59(2):129–138, February 2011. ISSN 1551-5044. doi: 10.1369/0022155410394857.
- [79] Michael W. Adams, Andrew F. Loftus, Sarah E. Dunn, Matthew S. Joens, and James A.J. Fitzpatrick. Light Sheet Fluorescence Microscopy (LSFM). *Current protocols in cytometry / editorial board, J. Paul Robinson, managing editor ... [et al.]*, 71:12.37.1–12.37.15, January 2015. ISSN 1934-9297. doi: 10.1002/0471142956.cy1237s71. URL <http://www.ncbi.nlm.nih.gov/pmc/articles/PMC4294425/>.
- [80] Qi Chen, Luan Jiang, Chun Li, Dan Hu, Ji-wen Bu, David Cai, and Jiu-lin Du. Haemodynamics-Driven Developmental Pruning of Brain Vasculature in Zebrafish. *PLOS Biology*, 2012. URL https://www.researchgate.net/publication/230699539_Haemodynamics-Driven_Developmental_Pruning_of_Brain_Vasculature_in_Zebrafish.
- [81] Wade W. Sugden, Robert Meissner, Tinri Aegerter-Wilmsen, Roman Tsaryk, Elvin V. Leonard, Jeroen Bussmann, Mailin J. Hamm, Wiebke Herzog, Yi Jin, Lars Jakobsson, Cornelia Denz, and Arndt F. Siekmann. Endoglin controls blood vessel diameter through endothelial cell shape changes in response to haemodynamic cues. *Nature Cell Biology*, 19(6):653, June 2017. ISSN 1476-4679. doi: 10.1038/ncb3528. URL <https://www.nature.com/articles/ncb3528>.
- [82] Gerard Tortora and Mark Nielsen. *Principles of Human Anatomy, 13th Edition*. Wiley, December 2013. ISBN 978-1-118-34499-6. URL <https://www.wiley.com/en-gb/Principles+of+Human+Anatomy%2C+13th+Edition-p-9781118344996>.
- [83] Constantino Carlos Reyes-Aldasoro. *Biomedical Image Analysis Recipes in MATLAB: For Life Scientists and Engineers*. Wiley-Blackwell, Chichester, West Sussex Oxford Hoboken, NJ, 1 edition edition, June 2015. ISBN 978-1-118-65755-3.
- [84] Ralf Mikut, Thomas Dickmeis, Wolfgang Driever, Pierre Geurts, Fred A. Hamprecht, Bernhard X. Kausler, María J. Ledesma-Carbayo, Raphaël Marée, Karol Mikula, Periklis Pantazis, Olaf Ronneberger, Andres Santos, Rainer Stotzka, Uwe Strähle, and Nadine Peyriéras. Automated Processing of Zebrafish Imaging Data: A Survey. *Zebrafish*, 10

- (3):401–421, June 2013. ISSN 1545-8547. doi: 10.1089/zeb.2013.0886. URL <http://online.liebertpub.com/doi/abs/10.1089/zeb.2013.0886>.
- [85] Cemil Kirbas and Francis Quek. A Review of Vessel Extraction Techniques and Algorithms. *ACM Comput. Surv.*, 36(2):81–121, June 2004. ISSN 0360-0300. doi: 10.1145/1031120.1031121. URL <http://doi.acm.org/10.1145/1031120.1031121>.
- [86] David Lesage, Elsa D. Angelini, Isabelle Bloch, and Gareth Funka-Lea. A review of 3D vessel lumen segmentation techniques: Models, features and extraction schemes. *Medical Image Analysis*, 13(6):819–845, December 2009. ISSN 1361-8415. doi: 10.1016/j.media.2009.07.011. URL <http://www.sciencedirect.com/science/article/pii/S136184150900067X>.
- [87] Andrea Tagliasacchi, Thomas Delame, Michela Spagnuolo, Nina Amenta, and Alexandru Telea. 3D Skeletons: A State-of-the-Art Report. *Computer Graphics Forum*, 35(2):573–597, May 2016. ISSN 1467-8659. doi: 10.1111/cgf.12865. URL <http://onlinelibrary.wiley.com/doi/10.1111/cgf.12865/abstract>.
- [88] H Blum. A Transformation for Extracting New Descriptors of Shape. In *Models for the Perception of Speech and Visual Form*, pages 362–380. MIT Press, Cambridge, 1967.
- [89] H Blum and R Nagel. Shape description using weighted symmetric axes features. *Pattern Recognition*, 10:167–180, 1978.
- [90] Y. F Tsao and K. S Fu. A parallel thinning algorithm for 3-D pictures. *Computer Graphics and Image Processing*, 17(4):315–331, December 1981. ISSN 0146-664X. doi: 10.1016/0146-664X(81)90011-3. URL <http://www.sciencedirect.com/science/article/pii/0146664X81900113>.
- [91] T. C. Lee, R. L. Kashyap, and C. N. Chu. Building Skeleton Models via 3-D Medial Surface Axis Thinning Algorithms. *CVGIP: Graphical Models and Image Processing*, 56(6):462–478, November 1994. ISSN 1049-9652. doi: 10.1006/cgip.1994.1042. URL <http://www.sciencedirect.com/science/article/pii/S104996528471042X>.
- [92] Kálmán Palágyi and Attila Kuba. A 3D 6-subiteration thinning algorithm for extracting medial lines. *Pattern Recognition Letters*, 19(7):613–627, 1998. URL <http://www.sciencedirect.com/science/article/pii/S0167865598000312>.
- [93] Kálmán Palágyi. A Sequential 3D Curve-Thinning Algorithm Based on Isthmuses. In *Advances in Visual Computing*, Lecture Notes in Computer Science, pages 406–415. Springer, Cham, December 2014. ISBN 978-3-319-14363-7 978-3-319-14364-4. doi: 10.1007/978-3-319-14364-4_39. URL https://link.springer.com/chapter/10.1007/978-3-319-14364-4_39.
- [94] W Gong and G Bertrand. A simple parallel 3D thinning algorithm. *Proc. IEEE Pattern Recognition*, pages 188–190, 1990.
- [95] J Lim. Two-Dimensional Signal and Image Processing. *Englewood Cliffs, NJ, Prentice Hall*, pages 469–476, 1990.
- [96] T. M. Koller, G. Gerig, G. Szekely, and D. Dettwiler. Multiscale detection of curvilinear structures in 2-D and 3-D image data. In *Proceedings of IEEE International Conference on Computer Vision*, pages 864–869, June 1995. doi: 10.1109/ICCV.1995.466846.
- [97] C. Lorenz, I.-C. Carlsen, T. M. Buzug, C. Fassnacht, and J. Weese. Multi-scale line segmentation with automatic estimation of width, contrast and tangential direction in 2D and 3D medical images. In *CVRMed-MRCAS’97*, Lecture Notes in Computer Science, pages 233–242. Springer, Berlin, Heidelberg, 1997. ISBN 978-3-540-62734-0 978-3-540-68499-2. doi: 10.1007/BFb0029242. URL <https://link.springer.com/chapter/10.1007/BFb0029242>.
- [98] Yoshinobu Sato, Shin Nakajima, Hideki Atsumi, Thomas Koller, Guido Gerig, Shigeyuki Yoshida, and Ron Kikinis. 3D multi-scale line filter for segmentation and visualization of curvilinear structures in medical images. In *CVRMed-MRCAS’97*, Lecture Notes in Computer Science, pages 213–222. Springer, Berlin, Heidelberg, 1997. ISBN 978-3-540-62734-0 978-3-540-68499-2. doi: 10.1007/BFb0029240. URL <https://link.springer.com/chapter/10.1007/BFb0029240>.
- [99] Alejandro F. Frangi, Wiro J. Niessen, Koen L. Vincken, and Max A. Viergever. Multiscale vessel enhancement filtering. In *Medical Image Computing and Computer-Assisted Intervention — MICCAI’98*, pages 130–137. Springer, Berlin, Heidelberg, October 1998. doi: 10.1007/BFb0056195. URL <https://link.springer.com/chapter/10.1007/BFb0056195>.
- [100] K Krissian, G Malandain, and N Ayache. Model Based Multiscale Detection and Reconstruction of 3D Vessels. *INRIA*, (RR_3442), 1998.

- [101] Marius Erdt, Matthias Raspe, and Michael Suehling. Automatic Hepatic Vessel Segmentation Using Graphics Hardware. In *Medical Imaging and Augmented Reality*, Lecture Notes in Computer Science, pages 403–412. Springer, Berlin, Heidelberg, August 2008. ISBN 978-3-540-79981-8 978-3-540-79982-5. doi: 10.1007/978-3-540-79982-5_44. URL https://link.springer.com/chapter/10.1007/978-3-540-79982-5_44.
- [102] P. Sarder and A. Nehorai. Deconvolution methods for 3-D fluorescence microscopy images. *IEEE Signal Processing Magazine*, 23(3):32–45, May 2006. ISSN 1053-5888. doi: 10.1109/MSP.2006.1628876.
- [103] Michael H. F. Wilkinson and Michel A. Westenberg. Shape Preserving Filament Enhancement Filtering. In *Medical Image Computing and Computer-Assisted Intervention – MICCAI 2001*, Lecture Notes in Computer Science, pages 770–777. Springer, Berlin, Heidelberg, October 2001. ISBN 978-3-540-42697-4 978-3-540-45468-7. doi: 10.1007/3-540-45468-3_92. URL https://link.springer.com/chapter/10.1007/3-540-45468-3_92.
- [104] F. Zana and J. C. Klein. Segmentation of vessel-like patterns using mathematical morphology and curvature evaluation. *IEEE transactions on image processing: a publication of the IEEE Signal Processing Society*, 10(7):1010–1019, 2001. ISSN 1057-7149. doi: 10.1109/83.931095.
- [105] J. S. Lee. Digital Image Enhancement and Noise Filtering by Use of Local Statistics. *IEEE Transactions on Pattern Analysis and Machine Intelligence*, PAMI-2(2):165–168, March 1980. ISSN 0162-8828. doi: 10.1109/TPAMI.1980.4766994.
- [106] C. F. Westin, L. Wigström, T. Looock, L. Sjöqvist, R. Kikinis, and H. Knutsson. Three-dimensional adaptive filtering in magnetic resonance angiography. *Journal of magnetic resonance imaging: JMRI*, 14(1):63–71, July 2001. ISSN 1053-1807.
- [107] Karl Krissian, Grégoire Malandain, Nicholas Ayache, Régis Vaillant, and Yves Troussel. Model-Based Detection of Tubular Structures in 3D Images. *Computer Vision and Image Understanding*, 80(2):130–171, November 2000. ISSN 1077-3142. doi: 10.1006/cviu.2000.0866. URL <http://www.sciencedirect.com/science/article/pii/S107731420090866X>.
- [108] R. Manniesing, B. K. Velthuis, M. S. van Leeuwen, I. C. van der Schaaf, P. J. van Laar, and W. J. Niessen. Level set based cerebral vasculature segmentation and diameter quantification in CT angiography. *Medical Image Analysis*, 10(2):200–214, April 2006. ISSN 1361-8415. doi: 10.1016/j.media.2005.09.001.
- [109] Max Wai Kong Law. Three dimensional curvilinear structure detection using optimally oriented flux, 2008.
- [110] Gady Agam, Samuel G. Armato, and Changhua Wu. Vessel tree reconstruction in thoracic CT scans with application to nodule detection. *IEEE transactions on medical imaging*, 24(4):486–499, April 2005. ISSN 0278-0062.
- [111] G. Agam and C. Wu. Probabilistic modeling based vessel enhancement in thoracic CT scans. In *2005 IEEE Computer Society Conference on Computer Vision and Pattern Recognition (CVPR'05)*, volume 2, pages 649–654 vol. 2, June 2005. doi: 10.1109/CVPR.2005.280.
- [112] Muhammad Waseem Khan. A Survey: Image Segmentation Techniques. *International Journal of Future Computer and Communication; Singapore*, 3(2):89–93, April 2014. ISSN 20103751. doi: <http://dx.doi.org/10.7763/IJFCC.2014.V3.274>. URL <http://search.proquest.com/docview/1523995748/abstract/5F0EFD9381ED47FDPQ/1>.
- [113] Sara Moccia, Elena De Momi, Sara El Hadji, and Leonardo S. Mattos. Blood vessel segmentation algorithms — Review of methods, datasets and evaluation metrics. *Computer Methods and Programs in Biomedicine*, 158:71–91, May 2018. ISSN 0169-2607. doi: 10.1016/j.cmpb.2018.02.001. URL <http://www.sciencedirect.com/science/article/pii/S0169260717313421>.
- [114] Gehad Hassan and Aboul Ella Hassanien. A Review of Vessel Segmentation Methodologies and Algorithms: Comprehensive Review, 2017. URL www.igi-global.com/chapter/a-review-of-vessel-segmentation-methodologies-and-algorithms/180945.
- [115] T. Y. Kong. A digital fundamental group. *Computers & Graphics*, 13(2):159–166, January 1989. ISSN 0097-8493. doi: 10.1016/0097-8493(89)90058-7. URL <http://www.sciencedirect.com/science/article/pii/0097849389900587>.
- [116] DG Morgenthaler. *Three-dimensional simple points: serial erosion, parallel thinning, and skeletonization*. University of Maryland at College Park. Computer Science Center., 1981.

- [117] T Kong and Azriel Rosenfeld. Digital topology: Introduction and survey. *Computer Vision, Graphics, and Image Processing*, 48:357–393, September 1989. doi: 10.1016/0734-189X(89)90147-3.
- [118] T. Yung Kong. Problem of determining whether a parallel reduction operator for n-dimensional binary images always preserves topology. volume 2060, pages 69–78. International Society for Optics and Photonics, December 1993. doi: 10.1117/12.165013. URL <https://www.spiedigitallibrary.org/conference-proceedings-of-spie/2060/0000/Problem-of-determining-whether-a-parallel-reduction-operator-for-in/10.1117/12.165013.short>.
- [119] Sébastien Fourey and Rémy Malgouyres. A Concise Characterization of 3D Simple Points. In *Discrete Geometry for Computer Imagery*, Lecture Notes in Computer Science, pages 27–36. Springer, Berlin, Heidelberg, December 2000. ISBN 978-3-540-41396-7 978-3-540-44438-1. doi: 10.1007/3-540-44438-6_3. URL https://link.springer.com/chapter/10.1007/3-540-44438-6_3.
- [120] Kálmán Palágyi. A 3D fully parallel surface-thinning algorithm. *Theoretical Computer Science*, 406(1):119–135, October 2008. ISSN 0304-3975. doi: 10.1016/j.tcs.2008.06.041. URL <http://www.sciencedirect.com/science/article/pii/S0304397508004350>.
- [121] N Cornea, P Min, and D Silver. Curve-skeleton properties, applications, and algorithms. *IEEE Transactions on Visualization and Computer Graphics*, 13(3):530–548, 2007.
- [122] Kálmán Palágyi and Attila Kuba. A Parallel 3D 12-Subiteration Thinning Algorithm. *Graphical Models and Image Processing*, 61:199–221, 1999.
- [123] Gabriella Sanniti di Baja and Stina Svensson. A new shape descriptor for surfaces in 3D images. *Pattern Recognition Letters*, 23(6):703–711, April 2002. ISSN 0167-8655. doi: 10.1016/S0167-8655(01)00143-X. URL <http://www.sciencedirect.com/science/article/pii/S016786550100143X>.
- [124] S. Svensson, C. Arcelli, and G. Sanniti di Baja. Finding cavities and tunnels in 3D complex objects. In *12th International Conference on Image Analysis and Processing, 2003.Proceedings.*, pages 342–347, September 2003. doi: 10.1109/ICIAP.2003.1234073.
- [125] Peter C. Marks, Marilena Preda, Terry Henderson, Lucy Liaw, Volkhard Lindner, Robert E. Friesel, and Ilka M. Pinz. Interactive 3D Analysis of Blood Vessel Trees and Collateral Vessel Volumes in Magnetic Resonance Angiograms in the Mouse Ischemic Hindlimb Model. *The open medical imaging journal*, 7:19–27, October 2013. ISSN 1874-3471. doi: 10.2174/1874347101307010019. URL <http://www.ncbi.nlm.nih.gov/pmc/articles/PMC3929959/>.
- [126] Ignacio Arganda-Carreras, Rodrigo Fernández-González, Arrate Muñoz-Barrutia, and Carlos Ortiz-De-Solorzano. 3D reconstruction of histological sections: Application to mammary gland tissue. *Microscopy Research and Technique*, 73(11):1019–1029, October 2010. ISSN 1097-0029. doi: 10.1002/jemt.20829. URL <http://onlinelibrary.wiley.com/doi/10.1002/jemt.20829/abstract>.
- [127] Johannes Schindelin, Ignacio Arganda-Carreras, Erwin Frise, Verena Kaynig, Mark Longair, Tobias Pietzsch, Stephan Preibisch, Curtis Rueden, Stephan Saalfeld, Benjamin Schmid, Jean-Yves Tinevez, Daniel James White, Volker Hartenstein, Kevin Eliceiri, Pavel Tomancak, and Albert Cardona. Fiji - an Open Source platform for biological image analysis. *Nature methods*, 9(7), June 2012. ISSN 1548-7091. doi: 10.1038/nmeth.2019. URL <http://www.ncbi.nlm.nih.gov/pmc/articles/PMC3855844/>.
- [128] Inken D. Kelch, Gib Bogle, Gregory B. Sands, Anthony R. J. Phillips, Ian J. LeGrice, and P. Rod Dunbar. Organ-wide 3D-imaging and topological analysis of the continuous microvascular network in a murine lymph node. *Scientific Reports*, 5:srep16534, November 2015. ISSN 2045-2322. doi: 10.1038/srep16534. URL <https://www.nature.com/articles/srep16534>.
- [129] Gregory B. Sands, Dane A. Gerneke, Darren A. Hooks, Colin R. Green, Bruce H. Smail, and Ian J. LeGrice. Automated imaging of extended tissue volumes using confocal microscopy. *Microscopy Research and Technique*, 67(5):227–239, August 2005. ISSN 1059-910X. doi: 10.1002/jemt.20200.
- [130] Geert Peeters, Charlotte Debbaut, Wim Laleman, Diethard Monbaliu, Ingrid Vander Elst, Jan R. Detrez, Tim Vandecasteele, Thomas De Schryver, Luc Van Hoorebeke, Kasper Favere, Jonas Verbeke, Patrick Segers, Pieter Cornillie, and Winnok H. De Vos. A multilevel framework to reconstruct anatomical 3D models of the hepatic vasculature in rat livers. *Journal of Anatomy*, 230(3):471–483, March 2017. ISSN 1469-7580. doi: 10.1111/joa.12567.

- [131] H. Kirshner, F. Aguet, D. Sage, and M. Unser. 3-D PSF fitting for fluorescence microscopy: implementation and localization application. *Journal of Microscopy*, 249(1):13–25, January 2013. ISSN 1365-2818. doi: 10.1111/j.1365-2818.2012.03675.x.
- [132] Karel Zuiderveld. VIII.5. - Contrast Limited Adaptive Histogram Equalization. In Paul S. Heckbert, editor, *Graphics Gems*, pages 474–485. Academic Press, 1994. ISBN 978-0-12-336156-1. doi: 10.1016/B978-0-12-336156-1.50061-6. URL <http://www.sciencedirect.com/science/article/pii/B9780123361561500616>.
- [133] Arthur N. Strahler. Dynamic basis of geomorphology. *GSA Bulletin*, 63(9):923–938, September 1952. ISSN 0016-7606. doi: 10.1130/0016-7606(1952)63[923:DBOG]2.0.CO;2. URL <https://pubs.geoscienceworld.org/gsabulletin/article-abstract/63/9/923/4513/dynamic-basis-of-geomorphology>.
- [134] Z. L. Jiang, G. S. Kassab, and Y. C. Fung. Diameter-defined Strahler system and connectivity matrix of the pulmonary arterial tree. *Journal of Applied Physiology (Bethesda, Md.: 1985)*, 76(2):882–892, February 1994. ISSN 8750-7587. doi: 10.1152/jappl.1994.76.2.882.
- [135] Florian Milde, Stephanie Lauw, Petros Koumoutsakos, and M. Luisa Iruela-Arispe. The mouse retina in 3D: quantification of vascular growth and remodeling. *Integrative Biology: Quantitative Biosciences from Nano to Macro*, 5(12):1426–1438, December 2013. ISSN 1757-9708. doi: 10.1039/c3ib40085a.
- [136] K. F. L. Michielsen and H. A. de Raedt. Integral-geometry morphological image analysis. *Physics Reports-Review Section of Physics Letters*, 347(6):462–538, 2001. doi: 10.1016/S0370-1573(00)00106-X. URL [http://www.rug.nl/research/portal/publications/integralgeometry-morphological-image-analysis\(a315a089-4e96-4275-9ce5-0dd7e18ba818\).html](http://www.rug.nl/research/portal/publications/integralgeometry-morphological-image-analysis(a315a089-4e96-4275-9ce5-0dd7e18ba818).html).
- [137] H. Tan, D. Wang, R. Li, C. Sun, R. Lagerstrom, Y. He, Y. Xue, and T. Xiao. A robust method for high-precision quantification of the complex three-dimensional vasculatures acquired by X-ray microtomography. *Journal of Synchrotron Radiation*, 23(5):1216–1226, September 2016. ISSN 1600-5775. doi: 10.1107/S1600577516011498. URL <http://scripts.iucr.org/cgi-bin/paper?pp5087>.
- [138] Rongchang Chen, Ping Liu, Tiqiao Xiao, and Lisa X. Xu. X-ray Imaging for Non-Destructive Microstructure Analysis at SSRF. *Advanced Materials*, 26(46):7688–7691, December 2014. ISSN 1521-4095. doi: 10.1002/adma.201402956. URL <http://onlinelibrary.wiley.com/doi/10.1002/adma.201402956/abstract>.
- [139] S. Lobregt, P. W. Verbeek, and F. C. A. Groen. Three-Dimensional Skeletonization: Principle and Algorithm. *IEEE Transactions on Pattern Analysis and Machine Intelligence*, PAMI-2(1):75–77, January 1980. ISSN 0162-8828. doi: 10.1109/TPAMI.1980.4766974.
- [140] Dominique Attali, Jean-Daniel Boissonnat, and Herbert Edelsbrunner. Stability and Computation of Medial Axes - a State-of-the-Art Report. In *Mathematical Foundations of Scientific Visualization, Computer Graphics, and Massive Data Exploration*, Mathematics and Visualization, pages 109–125. Springer, Berlin, Heidelberg, 2009. ISBN 978-3-540-25076-0 978-3-540-49926-8. doi: 10.1007/b106657_6. URL https://link.springer.com/chapter/10.1007/b106657_6.
- [141] Dominique Attali, Gabriella Sanniti di Baja, and Edouard Thiel. Pruning discrete and semicontinuous skeletons. In *Image Analysis and Processing*, Lecture Notes in Computer Science, pages 488–493. Springer, Berlin, Heidelberg, September 1995. ISBN 978-3-540-60298-9 978-3-540-44787-0. doi: 10.1007/3-540-60298-4_303. URL https://link.springer.com/chapter/10.1007/3-540-60298-4_303.
- [142] R. Ogniewicz. Automatic medial axis pruning based on characteristics of the skeleton-space. In *Shape Structure and Pattern Recognition Proc.*, Nahariya, 1994.
- [143] Doron Shaked and Alfred M. Bruckstein. Pruning Medial Axes. *Comput. Vis. Image Underst.*, 69(2):156–169, February 1998. ISSN 1077-3142. doi: 10.1006/cviu.1997.0598. URL <http://dx.doi.org/10.1006/cviu.1997.0598>.
- [144] Stina Svensson and Gabriella Sanniti di Baja. Simplifying Curve Skeletons in Volume Images. *Comput. Vis. Image Underst.*, 90(3):242–257, June 2003. ISSN 1077-3142. doi: 10.1016/S1077-3142(03)00061-4. URL [http://dx.doi.org/10.1016/S1077-3142\(03\)00061-4](http://dx.doi.org/10.1016/S1077-3142(03)00061-4).
- [145] Allen Sanderson, Elaine Cohen, Thomas Henderson, and Dennis Parker. Vascular Models: From Raw Data to Geometric Models. *AAAI Technical Report*, SS-94-05, 1994.
- [146] M Petrou and C Petrou. *Image Processing: The Fundamentals*. Wiley, 2nd edition edition, 2010. ISBN 978-0-470-74586-1. URL <http://www.wiley.com/WileyCDA/WileyTitle/productCd-047074586X.html>.

- [147] Y Sato, C Westin, A Bhalerao, S Nakajima, N Shiraga, S Tamura, and R Kikinis. Tissue Classification Based on 3D Local Intensity Structure for Volume Rendering. *IEEE Trans on Visualization and Computer Graphics*, Volume 6(2):160–180, 2000.
- [148] Jan J. Koenderink. The structure of images. *Biological Cybernetics*, 50(5):363–370, August 1984. ISSN 0340-1200, 1432-0770. doi: 10.1007/BF00336961. URL <https://link.springer.com/article/10.1007/BF00336961>.
- [149] Tony Lindeberg. Scale-space theory: A basic tool for analyzing structures at different scales. *Journal of applied statistics*, 21(1-2):225–270, 1994.
- [150] Tony Lindeberg. Scale-space theory: A framework for handling image structures at multiple scales. In *CERN School of Computing, Egmond aan Zee, The Netherlands, Sep. 8–21, 1996*, pages 27–38, 1996.
- [151] A. F. Frangi, W. J. Niessen, R. M. Hoogeveen, T. van Walsum, and M. A. Viergever. Model-based quantitation of 3-D magnetic resonance angiographic images. *IEEE transactions on medical imaging*, 18(10):946–956, October 1999. ISSN 0278-0062. doi: 10.1109/42.811279.
- [152] Alejandro F. Frangi, Wiro J. Niessen, Paul J. Nederkoorn, Jeannette Bakker, Willem P.Th.M. Mali, and Max A. Viergever. Quantitative analysis of vascular morphology from 3D MR angiograms: In vitro and in vivo results. *Magnetic Resonance in Medicine*, 45(2):311–322, February 2001. ISSN 1522-2594. doi: 10.1002/1522-2594(200102)45:2<311::AID-MRM1040>3.0.CO;2-7. URL [http://onlinelibrary.wiley.com/doi/10.1002/1522-2594\(200102\)45:2<311::AID-MRM1040>3.0.CO;2-7/abstract](http://onlinelibrary.wiley.com/doi/10.1002/1522-2594(200102)45:2<311::AID-MRM1040>3.0.CO;2-7/abstract).
- [153] Carl de Boor. *A Practical Guide to Spline - Revised Edition*. Springer, 1978. ISBN 978-0-387-95366-3. doi: <http://dx.doi.org/10.2307/2006241>. URL https://www.researchgate.net/publication/200744645_A_Practical_Guide_to_Spline.
- [154] M Unser. Splines: a perfect fit for signal and image processing. *IEEE Signal Processing Magazine*, 1999. URL <http://ieeexplore.ieee.org/document/799930/>.
- [155] Demetri Terzopoulos, John Platt, Alan Barr, and Kurt Fleischer. Elastically Deformable Models. In *Proceedings of the 14th Annual Conference on Computer Graphics and Interactive Techniques, SIGGRAPH '87*, pages 205–214, New York, NY, USA, 1987. ACM. ISBN 978-0-89791-227-3. doi: 10.1145/37401.37427. URL <http://doi.acm.org/10.1145/37401.37427>.
- [156] M Kass, A Witkin, and D Terzopoulos. Snakes: Active Contour Models. *International Journal of Computer Vision*, pages 321–331, 1988.
- [157] Kok Fung Lai. *Deformable Contours: Modeling, Extraction, Detection And Classification*. 1994.
- [158] Julie A. Rytlewski, Laura R. Geuss, Chinedu I. Anyaeji, Evan W. Lewis, and Laura J. Suggs. Three-dimensional image quantification as a new morphometry method for tissue engineering. *Tissue Engineering. Part C, Methods*, 18(7):507–516, July 2012. ISSN 1937-3392. doi: 10.1089/ten.TEC.2011.0417.
- [159] A Enquobahrie, L Ibanez, E Bullit, and Stephen R. Aylward. Vessel enhancement diffusion filter. *Insight Journal*, pages 1–7, 2007. URL https://www.researchgate.net/profile/Luis_Ibanez/publication/28358999_Vessel_Enhancing_Diffusion_Filter/links/00b7d524300b74d1eb000000.pdf.
- [160] Luca Antiga, Marina Piccinelli, Lorenzo Botti, Bogdan Ene-lordache, Andrea Remuzzi, and David A. Steinman. An image-based modeling framework for patient-specific computational hemodynamics. *Medical & Biological Engineering & Computing*, 46(11):1097–1112, November 2008. ISSN 1741-0444. doi: 10.1007/s11517-008-0420-1.
- [161] Luca Antiga, Bogdan Ene-lordache, and Andrea Remuzzi. Computational geometry for patient-specific reconstruction and meshing of blood vessels from MR and CT angiography. *IEEE transactions on medical imaging*, 22(5):674–684, May 2003. ISSN 0278-0062. doi: 10.1109/TMI.2003.812261.
- [162] Laurent D. Cohen and Thomas Deschamps. Segmentation of 3D tubular objects with adaptive front propagation and minimal tree extraction for 3D medical imaging. *Computer Methods in Biomechanics and Biomedical Engineering*, 10(4):289–305, August 2007. ISSN 1025-5842. doi: 10.1080/10255840701328239.
- [163] R. Ogniewicz and M. Ilg. Voronoi skeletons: theory and applications. In *Proceedings 1992 IEEE Computer Society Conference on Computer Vision and Pattern Recognition*, pages 63–69, June 1992. doi: 10.1109/CVPR.1992.223226.
- [164] Marcela Hernández-Hoyos, Alfred Anwander, Maciej Orkisz, Jean-Pierre Roux, Philippe Douek, and Isabelle E. Magnin. A Deformable Vessel Model with Single Point Initialization for Segmentation, Quantification, and Visualization of Blood Vessels in 3D MRA. In

- Medical Image Computing and Computer-Assisted Intervention – MICCAI 2000*, Lecture Notes in Computer Science, pages 735–745. Springer, Berlin, Heidelberg, October 2000. ISBN 978-3-540-41189-5 978-3-540-40899-4. doi: 10.1007/978-3-540-40899-4_76. URL https://link.springer.com/chapter/10.1007/978-3-540-40899-4_76.
- [165] M Hernandez-Hoyos, M Orkisz, P Puech, C Mansard-Desbleds, P Douek, and I Magnin. Computer-assisted Analysis of Three-Dimensional MR Angiograms. *RadioGraphics*, (22):421–436, 2002.
- [166] L Cohen. On active contour models and balloons. *CVGIP: Image Understanding*, (53): 211–218, 1991.
- [167] R. Adams and L. Bischof. Seeded region growing. *IEEE Transactions on Pattern Analysis and Machine Intelligence*, 16(6):641–647, June 1994. ISSN 0162-8828. doi: 10.1109/34.295913.
- [168] Jianping Fan, Guihua Zeng, Mathurin Body, and Mohand-Said Hacid. Seeded region growing: an extensive and comparative study. *Pattern Recognition Letters*, 26(8):1139–1156, June 2005. ISSN 0167-8655. doi: 10.1016/j.patrec.2004.10.010. URL <http://www.sciencedirect.com/science/article/pii/S0167865504003150>.
- [169] David Adalsteinsson and James A. Sethian. A Fast Level Set Method for Propagating Interfaces. *Journal of Computational Physics*, 118(2):269–277, May 1995. ISSN 0021-9991. doi: 10.1006/jcph.1995.1098. URL <http://www.sciencedirect.com/science/article/pii/S0021999185710984>.
- [170] J Sethian. *Level Set Methods: Evolving Interfaces in Geometry, Fluid Mechanics, Computer Vision, and Materials Science*. Cambridge University Press, 1996.
- [171] Sila Kurugol, Carolyn E. Come, Alejandro A. Diaz, James C. Ross, Greg L. Kinney, Jennifer L. Black-Shinn, John E. Hokanson, Matthew J. Budoff, George R. Washko, and Raul San Jose Estepar. Automated quantitative 3D analysis of aorta size, morphology, and mural calcification distributions. *Medical Physics*, 42(9):5467–5478, September 2015. ISSN 2473-4209. doi: 10.1118/1.4924500.
- [172] P. V. C. Hough. Method and Means for Recognizing Complex Patterns. Technical Report US 3069654, Originating Research Org. not identified, December 1962. URL <https://www.osti.gov/scitech/biblio/4746348>.
- [173] J. A. Sethian. A fast marching level set method for monotonically advancing fronts. *Proceedings of the National Academy of Sciences*, 93(4):1591–1595, February 1996. ISSN 0027-8424, 1091-6490. doi: 10.1073/pnas.93.4.1591. URL <http://www.pnas.org/content/93/4/1591>.
- [174] N Gagvani and D Silver. Parameter controlled skeletonization of three dimensional objects. *Rutgers University Technical Report CAIPTR216*, 1997.
- [175] Tamás Kovács, Philippe Cattin, Hatem Alkadhi, Simon Wildermuth, and Gábor Székely. Automatic Segmentation of the Vessel Lumen from 3D CTA Images of Aortic Dissection. In *Bildverarbeitung für die Medizin 2006*, Informatik aktuell, pages 161–165. Springer, Berlin, Heidelberg, 2006. ISBN 978-3-540-32136-1 978-3-540-32137-8. doi: 10.1007/3-540-32137-3_33. URL https://link.springer.com/chapter/10.1007/3-540-32137-3_33.
- [176] C. McIntosh and G. Hamarneh. Vessel Crawlers: 3D Physically-based Deformable Organisms for Vasculature Segmentation and Analysis. In *2006 IEEE Computer Society Conference on Computer Vision and Pattern Recognition (CVPR'06)*, volume 1, pages 1084–1091, June 2006. doi: 10.1109/CVPR.2006.329.
- [177] Rahul Shingrani, Gary Krenz, and Robert Molthen. Automation process for morphometric analysis of volumetric CT data from pulmonary vasculature in rats. *Computer methods and programs in biomedicine*, 97(1):62, January 2010. ISSN 0169-2607. doi: 10.1016/j.cmpb.2009.07.009. URL <http://www.ncbi.nlm.nih.gov/pmc/articles/PMC2815231/>.
- [178] K. L. Karau, R. C. Molthen, A. Dhyani, S. T. Haworth, C. C. Hanger, D. L. Roerig, R. H. Johnson, and C. A. Dawson. Pulmonary arterial morphometry from microfocal X-ray computed tomography. *American Journal of Physiology. Heart and Circulatory Physiology*, 281(6):H2747–2756, December 2001. ISSN 0363-6135.
- [179] M Lourakis. A Brief Description of the Levenberg-Marquardt Algorithm Implemented by levmar. *Foundation of Research and Technology*, 4(1), 2005.
- [180] Erlen Lugo-Hernandez, Anthony Squire, Nina Hagemann, Alexandra Brenzel, Maryam Sardari, Jana Schlechter, Eduardo H Sanchez-Mendoza, Matthias Gunzer, Andreas Faissner, and Dirk M Hermann. 3D visualization and quantification of microvessels in the whole ischemic mouse brain using solvent-based clearing and light sheet microscopy. *Journal of Cerebral Blood Flow & Metabolism*, page 0271678X17698970, March 2017.

- ISSN 0271-678X. doi: 10.1177/0271678X17698970. URL <http://dx.doi.org/10.1177/0271678X17698970>.
- [181] Ali Erturk, Daniel Lafkas, and Cecile Chalouni. Imaging Cleared Intact Biological Systems at a Cellular Level by 3DISCO. *Journal of Visualized Experiments : JoVE*, (89), July 2014. ISSN 1940-087X. doi: 10.3791/51382. URL <http://www.ncbi.nlm.nih.gov/pmc/articles/PMC4212806/>.
- [182] P Barber, S Ameer-Beg, B Vojnovic, R Hodgkiss, G Tozer, J Wilson, and V Prise. 3D Imaging and Quantification of Complex Vascular Networks. *SPIE*, 5139:67–78, 2003.
- [183] H. A. Lehr, M. Leunig, M. D. Menger, D. Nolte, and K. Messmer. Dorsal skinfold chamber technique for intravital microscopy in nude mice. *The American Journal of Pathology*, 143(4):1055–1062, October 1993. ISSN 0002-9440.
- [184] I Sobel and G Feldman. A 3x3 Isotropic Gradient Operator for Image Processing, 1968.
- [185] Laurent Risser, Franck Plouraboué, Peter Cloetens, and Caroline Fonta. A 3D-investigation shows that angiogenesis in primate cerebral cortex mainly occurs at capillary level. *International Journal of Developmental Neuroscience: The Official Journal of the International Society for Developmental Neuroscience*, 27(2):185–196, April 2009. ISSN 1873-474X. doi: 10.1016/j.ijdevneu.2008.10.006.
- [186] Nicu D. Cornea, Deborah Silver, Xiaosong Yuan, and Raman Balasubramanian. Computing hierarchical curve-skeletons of 3D objects. *The Visual Computer*, 21(11):945–955, October 2005. ISSN 0178-2789, 1432-2315. doi: 10.1007/s00371-005-0308-0. URL <https://link.springer.com/article/10.1007/s00371-005-0308-0>.
- [187] S. Roychowdhury, D. D. Koozekanani, and K. K. Parhi. DREAM: Diabetic Retinopathy Analysis Using Machine Learning. *IEEE Journal of Biomedical and Health Informatics*, 18(5):1717–1728, September 2014. doi: 10.1109/JBHI.2013.2294635.
- [188] Javier Mazzaferri, Bruno Larrivé, Bertan Cakir, Przemyslaw Sapieha, and Santiago Costantino. A machine learning approach for automated assessment of retinal vasculature in the oxygen induced retinopathy model. *Scientific Reports*, 8(1):1–11, March 2018. ISSN 2045-2322. doi: 10.1038/s41598-018-22251-7. URL <https://www.nature.com/articles/s41598-018-22251-7>.
- [189] Deo Rahul C. Machine Learning in Medicine. *Circulation*, 132(20):1920–1930, November 2015. doi: 10.1161/CIRCULATIONAHA.115.001593. URL <https://www.ahajournals.org/doi/full/10.1161/circulationaha.115.001593>.
- [190] Mohammad Haft-Javaherian, Linjing Fang, Victorine Muse, Chris B. Schaffer, Nozomi Nishimura, and Mert R. Sabuncu. Deep convolutional neural networks for segmenting 3D in vivo multiphoton images of vasculature in Alzheimer disease mouse models. *PLoS ONE*, 14(3), March 2019. ISSN 1932-6203. doi: 10.1371/journal.pone.0213539. URL <https://www.ncbi.nlm.nih.gov/pmc/articles/PMC6415838/>.
- [191] Mihail Ivilinov Todorov, Johannes Christian Paetzold, Oliver Schoppe, Giles Tetteh, Suprosanna Shit, Velizar Efremov, Katalin Todorov-Völgyi, Marco Düring, Martin Dichgans, Marie Piraud, Bjoern Menze, and Ali Ertürk. Machine learning analysis of whole mouse brain vasculature. *Nature Methods*, 17(4):442–449, April 2020. ISSN 1548-7105. doi: 10.1038/s41592-020-0792-1. URL <https://www.nature.com/articles/s41592-020-0792-1>. Number: 4 Publisher: Nature Publishing Group.
- [192] Jun Feng, Horace H. S. Ip, Shuk H. Cheng, and Po K. Chan. A relational-tubular (ReTu) deformable model for vasculature quantification of zebrafish embryo from microangiography image series. *Computerized Medical Imaging and Graphics: The Official Journal of the Computerized Medical Imaging Society*, 28(6):333–344, September 2004. ISSN 0895-6111. doi: 10.1016/j.compmedimag.2004.03.005.
- [193] Jun Feng, Shuk Han Cheng, Po K. Chan, and Horace H. S. Ip. Reconstruction and representation of caudal vasculature of zebrafish embryo from confocal scanning laser fluorescence microscopic images. *Computers in Biology and Medicine*, 35(10):915–931, December 2005. ISSN 0010-4825. doi: 10.1016/j.compbiomed.2004.05.003.
- [194] Jun Feng and Horace H. S. Ip. A statistical assembled deformable model (SAMTUS) for vasculature reconstruction. *Computers in Biology and Medicine*, 39(6):489–500, June 2009. ISSN 0010-4825. doi: 10.1016/j.compbiomed.2009.03.002. URL <http://www.sciencedirect.com/science/article/pii/S0010482509000444>.
- [195] H Ip, J Feng, and H Cheng. Automatic Segmentation and Tracking of Vasculature From Confocal Scanning Laser Fluorescence Microscope Images sequences using Multi-Orientation Dissection Sections. In *Proceedings of IEEE*, pages 249–252, 2002.
- [196] L. Rong and A. K. C. Wong. Attributed hypergraph representations for dynamic vision. In *1996 IEEE International Conference on Systems, Man and Cybernetics*.

- Information Intelligence and Systems (Cat. No.96CH35929)*, volume 1, pages 498–503 vol.1, October 1996. doi: 10.1109/ICSMC.1996.569842.
- [197] A. K. C. Wong, S. W. Lu, and M. Rioux. Recognition and shape synthesis of 3-D objects based on attributed hypergraphs. *IEEE Transactions on Pattern Analysis and Machine Intelligence*, 11(3):279–290, March 1989. ISSN 0162-8828. doi: 10.1109/34.21797.
- [198] Stephen J. Tam, David L. Richmond, Joshua S. Kaminker, Zora Modrusan, Baby Martin-McNulty, Tim C. Cao, Robby M. Weimer, Richard A. D. Carano, Nick van Bruggen, and Ryan J. Watts. Death Receptors DR6 and TROY Regulate Brain Vascular Development. *Developmental Cell*, 22(2):403–417, February 2012. ISSN 1534-5807. doi: 10.1016/j.devcel.2011.11.018. URL <http://www.sciencedirect.com/science/article/pii/S1534580711005284>.
- [199] Kun Zhang, Hongbin Zhang, Huiyu Zhou, Danny Crookes, Ling Li, Yeqin Shao, and Dong Liu. Zebrafish Embryo Vessel Segmentation Using a Novel Dual ResUNet Model. *Computational Intelligence and Neuroscience*, 2019:8214975, 2019. ISSN 1687-5273. doi: 10.1155/2019/8214975.
- [200] Stephan Daetwyler, Ulrik Günther, Carl D. Modes, Kyle Harrington, and Jan Huisken. Multi-sample SPIM image acquisition, processing and analysis of vascular growth in zebrafish. *Development*, page dev.173757, January 2019. ISSN 0950-1991, 1477-9129. doi: 10.1242/dev.173757. URL <http://dev.biologists.org/content/early/2019/02/28/dev.173757>.
- [201] Jan Huisken and Didier Y. R. Stainier. Selective plane illumination microscopy techniques in developmental biology. *Development*, 136(12):1963–1975, June 2009. doi: 10.1242/dev.022426. URL <http://dev.biologists.org/content/136/12/1963.abstract>.
- [202] Ernst H. K. Stelzer. Light-sheet fluorescence microscopy for quantitative biology. *Nature Methods*, 12(1):23–26, January 2015. ISSN 1548-7105. doi: 10.1038/nmeth.3219.
- [203] G. N. Serbedzija, E. Flynn, and C. E. Willett. Zebrafish angiogenesis: a new model for drug screening. *Angiogenesis*, 3(4):353–359, 1999. ISSN 0969-6970.
- [204] J. S. Duncan and N. Ayache. Medical image analysis: progress over two decades and the challenges ahead. *IEEE Transactions on Pattern Analysis and Machine Intelligence*, 22(1):85–106, January 2000. ISSN 0162-8828. doi: 10.1109/34.824822.
- [205] Sara Jonmarker, Alexander Valdman, Anna Lindberg, Magnus Hellström, and Lars Egevad. Tissue shrinkage after fixation with formalin injection of prostatectomy specimens. *Virchows Archiv*, 449(3):297–301, September 2006. ISSN 0945-6317, 1432-2307. doi: 10.1007/s00428-006-0259-5. URL <https://link.springer.com/article/10.1007/s00428-006-0259-5>.
- [206] Varun Rastogi, Naveen Puri, Swati Arora, Geetpriya Kaur, Lalita Yadav, and Rachna Sharma. Artefacts: A Diagnostic Dilemma – A Review. *Journal of Clinical and Diagnostic Research : JCDR*, 7(10):2408–2413, October 2013. ISSN 2249-782X. doi: 10.7860/JCDR/2013/6170.3541. URL <https://www.ncbi.nlm.nih.gov/pmc/articles/PMC3843421/>.
- [207] Shailja Chatterjee. Artefacts in histopathology. *Journal of Oral and Maxillofacial Pathology : JOMFP*, 18(Suppl 1):S111–S116, September 2014. ISSN 0973-029X. doi: 10.4103/0973-029X.141346. URL <https://www.ncbi.nlm.nih.gov/pmc/articles/PMC4211218/>.
- [208] Claudio Vinegoni, Sungon Lee, Aaron D. Aguirre, and Ralph Weissleder. New techniques for motion-artifact-free in vivo cardiac microscopy. *Frontiers in Physiology*, 6, 2015. ISSN 1664-042X. doi: 10.3389/fphys.2015.00147. URL <https://www.frontiersin.org/articles/10.3389/fphys.2015.00147/full>.
- [209] Maxim Zaitsev, Julian. Maclaren, and Michael Herbst. Motion Artefacts in MRI: a Complex Problem with Many Partial Solutions. *Journal of magnetic resonance imaging : JMRI*, 42(4):887–901, October 2015. ISSN 1053-1807. doi: 10.1002/jmri.24850. URL <https://www.ncbi.nlm.nih.gov/pmc/articles/PMC4517972/>.
- [210] William C. Aird. Phenotypic heterogeneity of the endothelium: II. Representative vascular beds. *Circulation Research*, 100(2):174–190, February 2007. ISSN 1524-4571. doi: 10.1161/01.RES.0000255690.03436.ae.
- [211] Axel R. Pries, Annemiek J. M. Cornelissen, Anoek A. Sloot, Marlene Hinkeldey, Matthew R. Dreher, Michael Höpfner, Mark W. Dewhirst, and Timothy W. Secomb. Structural Adaptation and Heterogeneity of Normal and Tumor Microvascular Networks. *PLOS Computational Biology*, 5(5):e1000394, May 2009. ISSN 1553-7358. doi: 10.1371/journal.pcbi.1000394. URL <http://journals.plos.org/ploscompbiol/article?id=10.1371/journal.pcbi.1000394>.

- [212] Kenneth R Castleman. *Digital image processing*. Englewood Cliffs, N.J. : Prentice-Hall, 1979. ISBN 978-0-13-212365-5. URL <https://trove.nla.gov.au/version/45431912>.
- [213] T.F. Watson. Fact and Artefact in Confocal Microscopy. *Advances in Dental Research*, 11(4):433–441, November 1997. ISSN 0895-9374, 1544-0737. doi: 10.1177/08959374970110040901. URL <http://journals.sagepub.com/doi/10.1177/08959374970110040901>.
- [214] Stelzer. Contrast, resolution, pixelation, dynamic range and signal-to-noise ratio: fundamental limits to resolution in fluorescence light microscopy. *Journal of Microscopy*, 189(1):15–24, January 1998. ISSN 1365-2818. doi: 10.1046/j.1365-2818.1998.00290.x. URL <http://onlinelibrary.wiley.com/doi/10.1046/j.1365-2818.1998.00290.x/abstract>.
- [215] M. P. Wiedeman. Dimensions of blood vessels from distributing artery to collecting vein. *Circulation Research*, 12:375–378, April 1963. ISSN 0009-7330.
- [216] J. D. Humphrey. Vascular adaptation and mechanical homeostasis at tissue, cellular, and sub-cellular levels. *Cell Biochemistry and Biophysics*, 50(2):53–78, 2008. ISSN 1085-9195. doi: 10.1007/s12013-007-9002-3.
- [217] Claudia Korn and Hellmut G. Augustin. Mechanisms of Vessel Pruning and Regression. *Developmental Cell*, 34(1):5–17, July 2015. ISSN 1878-1551. doi: 10.1016/j.devcel.2015.06.004.
- [218] Stephanie Paone, Amy A. Baxter, Mark D. Hulett, and Ivan K. H. Poon. Endothelial cell apoptosis and the role of endothelial cell-derived extracellular vesicles in the progression of atherosclerosis. *Cellular and Molecular Life Sciences*, December 2018. ISSN 1420-9071. doi: 10.1007/s00018-018-2983-9. URL <https://doi.org/10.1007/s00018-018-2983-9>.
- [219] L. P. Cramer, T. J. Mitchison, and J. A. Theriot. Actin-dependent motile forces and cell motility. *Current Opinion in Cell Biology*, 6(1):82–86, February 1994. ISSN 0955-0674.
- [220] Laurent Blanchoin, Rajaa Boujemaa-Paterski, Cécile Sykes, and Julie Plastino. Actin Dynamics, Architecture, and Mechanics in Cell Motility. *Physiological Reviews*, 94(1): 235–263, January 2014. ISSN 0031-9333. doi: 10.1152/physrev.00018.2013. URL <https://www.physiology.org/doi/10.1152/physrev.00018.2013>.
- [221] Marina Colombo, Graça Raposo, and Clotilde Théry. Biogenesis, secretion, and intercellular interactions of exosomes and other extracellular vesicles. *Annual Review of Cell and Developmental Biology*, 30:255–289, 2014. ISSN 1530-8995. doi: 10.1146/annurev-cellbio-101512-122326.
- [222] Dilyana Todorova, Stéphanie Simoncini, Romaric Lacroix, Florence Sabatier, and Françoise Dignat-George. Extracellular Vesicles in Angiogenesis. *Circulation Research*, 120(10):1658–1673, May 2017. ISSN 0009-7330, 1524-4571. doi: 10.1161/CIRCRESAHA.117.309681. URL <http://circres.ahajournals.org/content/120/10/1658>.
- [223] Vesa M. Loitto, Thommie Karlsson, and Karl-Eric Magnusson. Water flux in cell motility: expanding the mechanisms of membrane protrusion. *Cell Motility and the Cytoskeleton*, 66(5):237–247, May 2009. ISSN 1097-0169. doi: 10.1002/cm.20357.
- [224] Florian Lang, Gillian L. Busch, Markus Ritter, Harald Vökl, Siegfried Waldegger, Erich Gulbins, and Dieter Häussinger. Functional Significance of Cell Volume Regulatory Mechanisms. *Physiological Reviews*, 78(1):247–306, January 1998. ISSN 0031-9333. doi: 10.1152/physrev.1998.78.1.247. URL <https://www.physiology.org/doi/abs/10.1152/physrev.1998.78.1.247>.
- [225] Ewa K Paluch and Erez Raz. The role and regulation of blebs in cell migration. *Current Opinion in Cell Biology*, 25(5):582–590, October 2013. ISSN 0955-0674. doi: 10.1016/j.ceb.2013.05.005. URL <https://www.ncbi.nlm.nih.gov/pmc/articles/PMC3989058/>.
- [226] G. T. Charras. A short history of blebbing. *Journal of Microscopy*, 231(3):466–478, 2008. ISSN 1365-2818. doi: 10.1111/j.1365-2818.2008.02059.x. URL <https://onlinelibrary.wiley.com/doi/abs/10.1111/j.1365-2818.2008.02059.x>.
- [227] Parvin Zamani, Narges Fereydouni, Alexandra E. Butler, Jamshid Gholizadeh Navashenaq, and Amirhossein Sahebkar. The therapeutic and diagnostic role of exosomes in cardiovascular diseases. *Trends in Cardiovascular Medicine*, October 2018. ISSN 1873-2615. doi: 10.1016/j.tcm.2018.10.010.
- [228] Leon Bernal-Mizrachi, Wenche Jy, Joaquin J. Jimenez, Juan Pastor, Lucia M. Mauro, Lawrence L. Horstman, Eduardo de Marchena, and Yeon S. Ahn. High levels of circulating endothelial microparticles in patients with acute coronary syndromes. *American Heart Journal*, 145(6):962–970, June 2003. ISSN 1097-6744. doi: 10.1016/S0002-8703(03)00103-0.

- [229] Thomas E. Woolley, Eamonn A. Gaffney, James M. Oliver, Ruth E. Baker, Sarah L. Waters, and Alain Goriely. Cellular blebs: pressure-driven, axisymmetric, membrane protrusions. *Biomechanics and Modeling in Mechanobiology*, 13(2):463–476, April 2014. ISSN 1617-7940. doi: 10.1007/s10237-013-0509-9.
- [230] Thomas E. Woolley, Eamonn A. Gaffney, James M. Oliver, Sarah L. Waters, Ruth E. Baker, and Alain Goriely. Global contraction or local growth, bleb shape depends on more than just cell structure. *Journal of Theoretical Biology*, 380:83–97, September 2015. ISSN 1095-8541. doi: 10.1016/j.jtbi.2015.04.023.
- [231] Thomas E. Woolley, Eamonn A. Gaffney, and Alain Goriely. Membrane shrinkage and cortex remodelling are predicted to work in harmony to retract blebs. *Royal Society Open Science*, 2(7):150184, July 2015. ISSN 2054-5703. doi: 10.1098/rsos.150184.
- [232] Hiroshi Y. Kubota. Creeping locomotion of the endodermal cells dissociated from gastrulae of the Japanese newt, *Cynops pyrrhogaster*. *Experimental Cell Research*, 133(1):137–148, May 1981. ISSN 0014-4827. doi: 10.1016/0014-4827(81)90364-5. URL <http://www.sciencedirect.com/science/article/pii/0014482781903645>.
- [233] Guillaume T. Charras, Chi-Kuo Hu, Margaret Coughlin, and Timothy J. Mitchison. Reassembly of contractile actin cortex in cell blebs. *The Journal of Cell Biology*, 175(3):477–490, November 2006. ISSN 0021-9525. doi: 10.1083/jcb.200602085. URL <https://www.ncbi.nlm.nih.gov/pmc/articles/PMC2064524/>.
- [234] Guillaume T. Charras, Margaret Coughlin, Timothy J. Mitchison, and L. Mahadevan. Life and Times of a Cellular Bleb. *Biophysical Journal*, 94(5):1836–1853, March 2008. ISSN 0006-3495. doi: 10.1529/biophysj.107.113605. URL <https://www.ncbi.nlm.nih.gov/pmc/articles/PMC2242777/>.
- [235] Maryna Kapustina, Denis Tsygankov, Jia Zhao, Timothy Wessler, Xiaofeng Yang, Alex Chen, Nathan Roach, Timothy C. Elston, Qi Wang, Ken Jacobson, and M. Gregory Forest. Modeling the Excess Cell Surface Stored in a Complex Morphology of Bleb-Like Protrusions. *PLOS Computational Biology*, 12(3):e1004841, March 2016. ISSN 1553-7358. doi: 10.1371/journal.pcbi.1004841. URL <https://journals.plos.org/ploscompbiol/article?id=10.1371/journal.pcbi.1004841>.
- [236] Maryna Kapustina, Timothy C. Elston, and Ken Jacobson. Compression and dilation of the membrane-cortex layer generates rapid changes in cell shape. *The Journal of Cell Biology*, 200(1):95–108, January 2013. ISSN 0021-9525, 1540-8140. doi: 10.1083/jcb.201204157. URL <http://jcb.rupress.org/content/200/1/95>.
- [237] Jonathan L. Brisman, Joon K. Song, and David W. Newell. Cerebral Aneurysms. *New England Journal of Medicine*, 355(9):928–939, August 2006. ISSN 0028-4793. doi: 10.1056/NEJMra052760. URL <https://doi.org/10.1056/NEJMra052760>.
- [238] Fuyu Wang, Bainan Xu, Zhenghui Sun, Chen Wu, and Xiaojun Zhang. Wall shear stress in intracranial aneurysms and adjacent arteries. *Neural Regeneration Research*, 8(11):1007–1015, April 2013. ISSN 1673-5374. doi: 10.3969/j.issn.1673-5374.2013.11.006. URL <https://www.ncbi.nlm.nih.gov/pmc/articles/PMC4145888/>.
- [239] Pablo M. Munarriz, Pedro A. Gómez, Igor Paredes, Ana M. Castaño-Leon, Santiago Cepeda, and Alfonso Lagares. Basic Principles of Hemodynamics and Cerebral Aneurysms. *World Neurosurgery*, 88:311–319, April 2016. ISSN 1878-8750. doi: 10.1016/j.wneu.2016.01.031. URL [http://www.worldneurosurgery.org/article/S1878-8750\(16\)00117-0/fulltext](http://www.worldneurosurgery.org/article/S1878-8750(16)00117-0/fulltext).
- [240] K. S. Fu and J. K. Mui. A survey on image segmentation. *Pattern Recognition*, 13(1):3–16, January 1981. ISSN 0031-3203. doi: 10.1016/0031-3203(81)90028-5. URL <http://www.sciencedirect.com/science/article/pii/0031320381900285>.
- [241] Kemal Polat, Hariharan Muthusamy, Rajendra Acharya, and Yanhui Guo. Guest editorial: New trends in data pre-processing methods for signal and image classification. *Neural Computing and Applications*, 28(10):2839–2841, October 2017. ISSN 0941-0643, 1433-3058. doi: 10.1007/s00521-017-3202-6. URL <https://link.springer.com/article/10.1007/s00521-017-3202-6>.
- [242] Wilfried Maï, Cristian T. Badea, Charles T. Wheeler, Laurence W. Hedlund, and G. Allan Johnson. Effects of breathing and cardiac motion on spatial resolution in the microscopic imaging of rodents. *Magnetic Resonance in Medicine*, 53(4):858–865, April 2005. ISSN 0740-3194. doi: 10.1002/mrm.20400.
- [243] Neil C. Chi, Robin M. Shaw, Sarah De Val, Guson Kang, Lily Y. Jan, Brian L. Black, and Didier Y.R. Stainier. Foxn4 directly regulates tbx2b expression and atrioventricular canal formation. *Genes & Development*, 22(6):734–739, March 2008. ISSN 0890-

9369. doi: 10.1101/gad.1629408. URL <https://www.ncbi.nlm.nih.gov/pmc/articles/PMC2275426/>.
- [244] Benjamin M. Hogan, Frank L. Bos, Jeroen Bussmann, Merlijn Witte, Neil C. Chi, Henricus J. Duckers, and Stefan Schulte-Merker. Ccbe1 is required for embryonic lymphangiogenesis and venous sprouting. *Nature Genetics*, 41(4):396–398, April 2009. ISSN 1546-1718. doi: 10.1038/ng.321.
- [245] A. M. Savage, C. Mayo, H. R. Kim, E. Markham, F. J. M. van Eeden, T. J. A. Chico, and R. N. Wilkinson. Generation and characterisation of novel transgenic zebrafish allowing in vivo imaging of endothelial cell biology. *Atherosclerosis*, 244:e10, January 2016. ISSN 0021-9150, 1879-1484. doi: 10.1016/j.atherosclerosis.2015.10.080. URL [http://www.atherosclerosis-journal.com/article/S0021-9150\(15\)01502-6/fulltext](http://www.atherosclerosis-journal.com/article/S0021-9150(15)01502-6/fulltext).
- [246] Rafael Gonzalez and Richard Woods. *Digital Image Processing*. Pearson Prentice Hall, 2007. ISBN 0-13-168728-X.
- [247] S Sternberg. Biomedical Image Processing. *Computer*, 16:22–34, 1983. doi: 10.1109/MC.1983.1654163. URL <https://www.computer.org/csdl/mags/co/1983/01/01654163-abs.html>.
- [248] Tony Lindeberg. *Scale-space theory in computer vision*, volume 256. Springer Science & Business Media, 2013.
- [249] K. Drechsler and C. Oyarzun Laura. Comparison of vesselness functions for multiscale analysis of the liver vasculature. In *Proceedings of the 10th IEEE International Conference on Information Technology and Applications in Biomedicine*, pages 1–5, November 2010. doi: 10.1109/ITAB.2010.5687627.
- [250] Katie Bentley, Giovanni Mariggi, Holger Gerhardt, and Paul A. Bates. Tipping the balance: robustness of tip cell selection, migration and fusion in angiogenesis. *PLoS computational biology*, 5(10):e1000549, October 2009. ISSN 1553-7358. doi: 10.1371/journal.pcbi.1000549.
- [251] Monte Westerfield. *The Zebrafish Book: A Guide for Laboratory use of Zebrafish (Brachydanio rerio)*. University of Oregon Press, 2nd edition edition, 1993.
- [252] Rory M. Power and Jan Huisken. A guide to light-sheet fluorescence microscopy for multiscale imaging. *Nature Methods*, 14(4):360–373, March 2017. ISSN 1548-7105. doi: 10.1038/nmeth.4224.
- [253] Anna Kaufmann, Michaela Mickoleit, Michael Weber, and Jan Huisken. Multilayer mounting enables long-term imaging of zebrafish development in a light sheet microscope. *Development (Cambridge, England)*, 139(17):3242–3247, September 2012. ISSN 1477-9129. doi: 10.1242/dev.082586.
- [254] Lambert M. Surhone, Miriam T. Timpledon, and Susan F. Marseken. *Signal to Noise Ratio (Image Processing)*. VDM Publishing, June 2010. ISBN 978-613-0-48303-6. Google-Books-ID: zpuucQAACAAJ.
- [255] David G. Lowe. Distinctive Image Features from Scale-Invariant Keypoints. *International Journal of Computer Vision*, 60(2):91–110, November 2004. ISSN 0920-5691, 1573-1405. doi: 10.1023/B:VISI.0000029664.99615.94. URL <https://link.springer.com/article/10.1023/B:VISI.0000029664.99615.94>.
- [256] Frank Y. Shih. *Introduction in Image Processing and Pattern Recognition*. John Wiley & Sons, Inc., Hoboken, N.J, USA, August 2010. ISBN 978-0-470-59041-6. URL <https://vpn.uibk.ac.at/+CSC0+00756767633A2F2F62617976617279766F656E656C2E6A7679726C2E70627A++/doi/10.1002/9780470590416.ch1/summary>.
- [257] Lindsey MacDonald. *Digital Heritage*. Butter-Heinemann, 2006. ISBN 0-7506-6183-6.
- [258] Pawan Patidar and Sumit Srivastava. Image De-noising by Various Filters for Different Noise. *International Journal of Computer Applications*, 9(4):45–50, 2010. URL https://www.researchgate.net/publication/49586888_Image_De-noising_by_Various_Filters_for_Different_Noise.
- [259] Anil K. Jain and Richard C. Dubes. *Algorithms for Clustering Data*. Prentice-Hall, Inc., Upper Saddle River, NJ, USA, 1988. ISBN 978-0-13-022278-7.
- [260] David Arthur and Sergei Vassilvitskii. K-means++: The Advantages of Careful Seeding. In *Proceedings of the Eighteenth Annual ACM-SIAM Symposium on Discrete Algorithms, SODA '07*, pages 1027–1035, Philadelphia, PA, USA, 2007. Society for Industrial and Applied Mathematics. ISBN 978-0-89871-624-5. URL <http://dl.acm.org/citation.cfm?id=1283383.1283494>.
- [261] M. Emre Celebi and Hassan A. Kingravi. Deterministic Initialization of the K-Means Algorithm Using Hierarchical Clustering. *International Journal of Pattern Recognition*

- and *Artificial Intelligence*, 26(07):1250018, November 2012. ISSN 0218-0014, 1793-6381. doi: 10.1142/S0218001412500188. URL <http://arxiv.org/abs/1304.7465>. arXiv: 1304.7465.
- [262] Richard Nock and Frank Nielsen. Statistical region merging. *IEEE transactions on pattern analysis and machine intelligence*, 26(11):1452–1458, November 2004. ISSN 0162-8828. doi: 10.1109/TPAMI.2004.110.
- [263] F. Nielsen and R. Nock. On region merging: the statistical soundness of fast sorting, with applications. In *2003 IEEE Computer Society Conference on Computer Vision and Pattern Recognition, 2003. Proceedings.*, volume 2, pages II–19–26 vol.2, June 2003. doi: 10.1109/CVPR.2003.1211447.
- [264] Eric Schechter. *Handbook of Analysis and Its Foundations*. Academic Press, October 1996. ISBN 978-0-08-053299-8. Google-Books-ID: eqUv3Bcd56EC.
- [265] Andrea Geling, Harald Steiner, Michael Willem, Laure Bally-Cuif, and Christian Haass. A gamma-secretase inhibitor blocks Notch signaling in vivo and causes a severe neurogenic phenotype in zebrafish. *EMBO Reports*, 3(7):688–694, July 2002. ISSN 1469-221X. doi: 10.1093/embo-reports/kvf124. URL <http://www.ncbi.nlm.nih.gov/pmc/articles/PMC1084181/>.
- [266] Kazuhide Nakamura, Eri Taguchi, Toru Miura, Atsushi Yamamoto, Kazumi Takahashi, Francis Bichat, Nicolas Guilbaud, Kazumasa Hasegawa, Kazuo Kubo, Yasunari Fujiwara, Rika Suzuki, Kinya Kubo, Masabumi Shibuya, and Toshiyuki Ise. KRN951, a highly potent inhibitor of vascular endothelial growth factor receptor tyrosine kinases, has antitumor activities and affects functional vascular properties. *Cancer Research*, 66(18): 9134–9142, September 2006. ISSN 0008-5472. doi: 10.1158/0008-5472.CAN-05-4290.
- [267] Ralph B. D’Agostino and Albert Belanger. A Suggestion for Using Powerful and Informative Tests of Normality. *The American Statistician*, 44(4):316–321, 1990. ISSN 0003-1305. doi: 10.2307/2684359. URL <http://www.jstor.org/stable/2684359>.
- [268] N Otsu. A threshold selection method from gray-level histograms. *Trans. Sys.Man.*, 9(1): 62–66, 1979.
- [269] C. H. Li and C. K. Lee. Minimum cross entropy thresholding. *Pattern Recognition*, 26(4):617–625, April 1993. ISSN 0031-3203. doi: 10.1016/0031-3203(93)90115-D. URL <http://www.sciencedirect.com/science/article/pii/003132039390115D>.
- [270] C. H. Li and P. K. S. Tam. An iterative algorithm for minimum cross entropy thresholding. *Pattern Recognition Letters*, 19(8):771–776, June 1998. ISSN 0167-8655. doi: 10.1016/S0167-8655(98)00057-9. URL <http://www.sciencedirect.com/science/article/pii/S0167865598000579>.
- [271] G. W. Zack, W. E. Rogers, and S. A. Latt. Automatic measurement of sister chromatid exchange frequency. *The Journal of Histochemistry and Cytochemistry: Official Journal of the Histochemistry Society*, 25(7):741–753, July 1977. ISSN 0022-1554. doi: 10.1177/25.7.70454.
- [272] Lee M. Ellis and Daniel J. Hicklin. VEGF-targeted therapy: mechanisms of anti-tumour activity. *Nature Reviews Cancer*, 8(8):579–591, August 2008. ISSN 1474-1768. doi: 10.1038/nrc2403. URL <https://www.nature.com/articles/nrc2403>.
- [273] Adela R. Cardones and Lionel L. Banez. VEGF inhibitors in cancer therapy. *Current Pharmaceutical Design*, 12(3):387–394, 2006. ISSN 1381-6128.
- [274] David Lowe. Object Recognition from Local Scale-Invariant Features. In *Proc. of the International Conference on Computer Vision*, Corfu, 1999.
- [275] Holló Gábor. A new paradigm for animal symmetry. *Interface Focus*, 5(6):20150032, December 2015. doi: 10.1098/rsfs.2015.0032. URL <https://royalsocietypublishing.org/doi/full/10.1098/rsfs.2015.0032>.
- [276] Martin Blum, Kerstin Feistel, Thomas Thumberger, and Axel Schweickert. The evolution and conservation of left-right patterning mechanisms. *Development*, 141(8):1603–1613, April 2014. ISSN 0950-1991, 1477-9129. doi: 10.1242/dev.100560. URL <http://dev.biologists.org/content/141/8/1603>.
- [277] Jeffrey J. Essner, Kyle J. Vogan, Molly K. Wagner, Clifford J. Tabin, H. Joseph Yost, and Martina Brueckner. Left–right development: Conserved function for embryonic nodal cilia. *Nature*, 418(6893):37–38, July 2002. ISSN 1476-4687. doi: 10.1038/418037a. URL <https://www.nature.com/articles/418037a>.
- [278] Angela E. Lin, Sergey Krikov, Tiffany Riehle-Colarusso, Jaime L. Frías, John Belmont, Marlene Anderka, Tal Geva, Kelly D. Getz, and Lorenzo D. Botto. Laterality defects in the national birth defects prevention study (1998–2007): Birth prevalence and descriptive epidemiology. *American Journal of Medical Genetics Part A*, 164(10):2581–2591, 2014.

- ISSN 1552-4833. doi: 10.1002/ajmg.a.36695. URL <https://onlinelibrary.wiley.com/doi/abs/10.1002/ajmg.a.36695>.
- [279] Irene D. Lytrivi and Wyman W. Lai. Cardiac Malpositions and Heterotaxy Syndrome. In *Echocardiography in Pediatric and Congenital Heart Disease*, pages 558–583. John Wiley & Sons, Ltd, 2016. ISBN 978-1-118-74244-0. doi: 10.1002/9781118742440.ch29. URL <https://onlinelibrary.wiley.com/doi/abs/10.1002/9781118742440.ch29>.
- [280] K. Anukampa Barth, Adam Miklosi, Jenny Watkins, Isaac H. Bianco, Stephen W. Wilson, and Richard J. Andrew. fsi Zebrafish Show Concordant Reversal of Laterality of Viscera, Neuroanatomy, and a Subset of Behavioral Responses. *Current Biology*, 15(9):844–850, May 2005. ISSN 0960-9822. doi: 10.1016/j.cub.2005.03.047. URL <http://www.sciencedirect.com/science/article/pii/S0960982205003416>.
- [281] Kenneth Hugdahl. Symmetry and asymmetry in the human brain. *European Review*, 13(2):119–133, 2005.
- [282] Myriam Roussigné, Patrick Blader, and Stephen W. Wilson. Breaking symmetry: The zebrafish as a model for understanding left-right asymmetry in the developing brain. *Developmental Neurobiology*, 72(3):269–281, 2012. ISSN 1932-846X. doi: 10.1002/dneu.20885. URL <https://onlinelibrary.wiley.com/doi/abs/10.1002/dneu.20885>.
- [283] Nobutaka Hirokawa, Yosuke Tanaka, Yasushi Okada, and Sen Takeda. Nodal flow and the generation of left-right asymmetry. *Cell*, 125(1):33–45, April 2006. ISSN 0092-8674. doi: 10.1016/j.cell.2006.03.002.
- [284] Mark Mercola. Left-right asymmetry: Nodal points. *Journal of Cell Science*, 116(16):3251–3257, August 2003. ISSN 0021-9533, 1477-9137. doi: 10.1242/jcs.00668. URL <http://jcs.biologists.org/content/116/16/3251>.
- [285] Tetsuya Nakamura and Hiroshi Hamada. Left-right patterning: conserved and divergent mechanisms. *Development*, 139(18):3257–3262, September 2012. ISSN 0950-1991, 1477-9129. doi: 10.1242/dev.061606. URL <http://dev.biologists.org/content/139/18/3257>.
- [286] Hidenori Aizawa, Isaac H. Bianco, Takanori Hamaoka, Toshio Miyashita, Osamu Uemura, Miguel L. Concha, Claire Russell, Stephen W. Wilson, and Hitoshi Okamoto. Laterotopic Representation of Left-Right Information onto the Dorso-Ventral Axis of a Zebrafish Midbrain Target Nucleus. *Current Biology*, 15(3):238–243, February 2005. ISSN 0960-9822. doi: 10.1016/j.cub.2005.01.014. URL <http://www.sciencedirect.com/science/article/pii/S0960982205000400>.
- [287] Vincent Bertrand, Paul Bisso, Richard J. Poole, and Oliver Hobert. Notch-Dependent Induction of Left/Right Asymmetry in *C. elegans* Interneurons and Motoneurons. *Current Biology*, 21(14):1225–1231, July 2011. ISSN 0960-9822. doi: 10.1016/j.cub.2011.06.016. URL <http://www.sciencedirect.com/science/article/pii/S0960982211006610>.
- [288] Alexander Jones, Clive Osmond, Keith M. Godfrey, and David I. W. Phillips. Evidence for Developmental Programming of Cerebral Laterality in Humans. *PLOS ONE*, 6(2):e17071, February 2011. ISSN 1932-6203. doi: 10.1371/journal.pone.0017071. URL <https://journals.plos.org/plosone/article?id=10.1371/journal.pone.0017071>.
- [289] Margriet A Groen, Andrew J O Whitehouse, Nicholas A Badcock, and Dorothy V M Bishop. Does cerebral lateralization develop? A study using functional transcranial Doppler ultrasound assessing lateralization for language production and visuospatial memory. *Brain and Behavior*, 2(3):256–269, May 2012. ISSN 2162-3279. doi: 10.1002/brb3.56. URL <https://www.ncbi.nlm.nih.gov/pmc/articles/PMC3381631/>.
- [290] Soo Hyun Kwon, Dustin Scheinost, Cheryl Lacadie, Gordon Sze, Karen C. Schneider, Feng Dai, R. Todd Constable, and Laura R. Ment. Adaptive Mechanisms of Developing Brain: Cerebral Lateralization in the Prematurely-Born. *NeuroImage*, 108:144–150, March 2015. ISSN 1053-8119. doi: 10.1016/j.neuroimage.2014.12.032. URL <https://www.ncbi.nlm.nih.gov/pmc/articles/PMC4324328/>.
- [291] Susan N. Wright, Peter Kochunov, Fernando Mut, Maurizio Bergamino, Kerry M. Brown, John C. Mazziotta, Arthur W. Toga, Juan R. Cebral, and Giorgio A. Ascoli. Digital reconstruction and morphometric analysis of human brain arterial vasculature from magnetic resonance angiography. *NeuroImage*, 82:170–181, November 2013. ISSN 1053-8119. doi: 10.1016/j.neuroimage.2013.05.089. URL <http://www.sciencedirect.com/science/article/pii/S1053811913005910>.
- [292] Raquel E. Gur, Susan M. Resnick, and Ruben C. Gur. Laterality and frontality of cerebral blood flow and metabolism in schizophrenia: Relationship to symptom specificity. *Psychiatry Research*, 27(3):325–334, March 1989. ISSN 0165-1781. doi: 10.1016/

- 0165-1781(89)90147-9. URL <http://www.sciencedirect.com/science/article/pii/S0165178189901479>.
- [293] G. Vingerhoets and N. Stroobant. Lateralization of cerebral blood flow velocity changes during cognitive tasks. A simultaneous bilateral transcranial Doppler study. *Stroke*, 30(10):2152–2158, October 1999. ISSN 0039-2499.
- [294] Miho Ota, Noriko Sato, Koji Sakai, Mitsutoshi Okazaki, Norihide Maikusa, Kotaro Hattori, Hiroaki Hori, Toshiya Teraishi, Keigo Shimoji, Kei Yamada, and Hiroshi Kunugi. Altered coupling of regional cerebral blood flow and brain temperature in schizophrenia compared with bipolar disorder and healthy subjects. *Journal of Cerebral Blood Flow and Metabolism: Official Journal of the International Society of Cerebral Blood Flow and Metabolism*, 34(12):1868–1872, December 2014. ISSN 1559-7016. doi: 10.1038/jcbfm.2014.151.
- [295] Morton H Friedman and Zhaohua Ding. Variability of the planarity of the human aortic bifurcation. *Medical Engineering & Physics*, 20(6):469–472, September 1998. ISSN 1350-4533. doi: 10.1016/S1350-4533(98)00039-3. URL <http://www.sciencedirect.com/science/article/pii/S1350453398000393>.
- [296] Morton H. Friedman. Variability of 3D arterial geometry and dynamics, and its pathologic implications. *Biorheology*, 39(3,4):513–517, January 2002. ISSN 0006-355X. URL <https://content.iospress.com/articles/biorheology/bir249>.
- [297] Jan L Bruse, Giuliano Giusti, Catriona Baker, Elena Cervi, Tain-Yen Hsia, Andrew M Taylor, and Silvia Schievano. Statistical Shape Modeling for Cavopulmonary Assist Device Development: Variability of Vascular Graft Geometry and Implications for Hemodynamics. *Journal of medical devices*, 11(2), June 2017. ISSN 1932-6181. doi: 10.1115/1.4035865. URL <https://www.ncbi.nlm.nih.gov/pmc/articles/PMC5417365/>.
- [298] Lisa Gottesfeld Brown. A Survey of Image Registration Techniques. *ACM Comput. Surv.*, 24(4):325–376, December 1992. ISSN 0360-0300. doi: 10.1145/146370.146374. URL <http://doi.acm.org/10.1145/146370.146374>.
- [299] A Goshtasby. 2-D and 3-D Image Registration: for Medical, Remote Sensing, and Industrial Applications. *Wiley*, pages 1–284, 2005. URL <http://www.wiley.com/WileyCDA/WileyTitle/productCd-0471649546.html>.
- [300] B Khajone, R Kokate, and V Shandilya. A Survey of Image Registration Techniques. *International Journal of Research in Information Technology*, 2(4):554–560, 2014.
- [301] J Modersitzki. *Numerical Methods for Image Registration*. Oxford University Press, 2003. ISBN 978-0-19-852841-8.
- [302] Olaf Ronneberger, Kun Liu, Meta Rath, Dominik Ruess, Thomas Mueller, Henrik Skibbe, Benjamin Drayer, Thorsten Schmidt, Alida Filippi, Roland Nitschke, Thomas Brox, Hans Burkhardt, and Wolfgang Driever. ViBE-Z: a framework for 3D virtual colocalization analysis in zebrafish larval brains. *Nature Methods*, 9(7):735–742, June 2012. ISSN 1548-7105. doi: 10.1038/nmeth.2076.
- [303] Owen Randlett, Caroline L. Wee, Eva A. Naumann, Onyeka Nnaemeka, David Schoppik, James E. Fitzgerald, Ruben Portugues, Alix M. B. Lacoste, Clemens Riegler, Florian Engert, and Alexander F. Schier. Whole-brain activity mapping onto a zebrafish brain atlas. *Nature Methods*, 12(11):1039–1046, November 2015. ISSN 1548-7105. doi: 10.1038/nmeth.3581.
- [304] Gregory D. Marquart, Kathryn M. Tabor, Eric J. Horstick, Mary Brown, Alexandra K. Geoca, Nicholas F. Polys, Damian Dalle Nogare, and Harold A. Burgess. High-precision registration between zebrafish brain atlases using symmetric diffeomorphic normalization. *GigaScience*, 6(8):1–15, August 2017. doi: 10.1093/gigascience/gix056. URL <https://academic.oup.com/gigascience/article/6/8/1/4085311>.
- [305] Ilse Geudens, Robert Herpers, Karlien Hermans, Inmaculada Segura, Carmen Ruiz de Almodovar, Jeroen Bussmann, Frederik De Smet, Wouter Vandevelde, Benjamin M. Hogan, Arndt Siekmann, Filip Claes, John C. Moore, Anna Silvia Pistocchi, Sonja Loges, Massimiliano Mazzone, Giovanni Mariggi, Françoise Bruyère, Franco Cotelli, Dontscho Kerjaschki, Agnes Noël, Jean-Michel Foidart, Holger Gerhardt, Anneli Ny, Tobias Langenberg, Nathan D. Lawson, Henricus J. Duckers, Stefan Schulte-Merker, Peter Carmeliet, and Mieke Dewerchin. Role of delta-like-4/Notch in the formation and wiring of the lymphatic network in zebrafish. *Arteriosclerosis, Thrombosis, and Vascular Biology*, 30(9):1695–1702, September 2010. ISSN 1524-4636. doi: 10.1161/ATVBAHA.110.203034.
- [306] Aurelie Quillien, John C. Moore, Masahiro Shin, Arndt F. Siekmann, Tom Smith, Luyuan Pan, Cecilia B. Moens, Michael J. Parsons, and Nathan D. Lawson. Distinct Notch signaling outputs pattern the developing arterial system. *Development (Cambridge*,

- England*), 141(7):1544–1552, April 2014. ISSN 0950-1991. doi: 10.1242/dev.099986. URL <https://www.ncbi.nlm.nih.gov/pmc/articles/PMC4074308/>.
- [307] David R. Corey and John M. Abrams. Morpholino antisense oligonucleotides: tools for investigating vertebrate development. *Genome Biology*, 2(5):reviews1015.1, April 2001. ISSN 1474-760X. doi: 10.1186/gb-2001-2-5-reviews1015. URL <https://doi.org/10.1186/gb-2001-2-5-reviews1015>.
- [308] David Legland, Ignacio Arganda-Carreras, and Philippe Andrey. MorphoLibJ: integrated library and plugins for mathematical morphology with ImageJ. *Bioinformatics*, 32(22):3532–3534, November 2016. ISSN 1367-4803. doi: 10.1093/bioinformatics/btw413. URL <https://academic.oup.com/bioinformatics/article/32/22/3532/2525592>.
- [309] Abdel Aziz Taha and Allan Hanbury. Metrics for evaluating 3D medical image segmentation: analysis, selection, and tool. *BMC Medical Imaging*, 15, August 2015. ISSN 1471-2342. doi: 10.1186/s12880-015-0068-x. URL <https://www.ncbi.nlm.nih.gov/pmc/articles/PMC4533825/>.
- [310] S Preibisch, S Saalfeld, J Schindelin, and P Tomancak. Software for bead-based registration of selective plane illumination microscopy data. *Nature Methods*, 7(6):418, June 2010. ISSN 1548-7105. doi: 10.1038/nmeth0610-418. URL <https://www.nature.com/articles/nmeth0610-418>.
- [311] Matthew Brown, D. Lowe, and web support@bath.ac.uk. Invariant Features from Interest Point Groups. In *BMVC 2002: 13th British Machine Vision Conference*, pages 253–262. University of Bath, September 2002. URL <http://www.bmva.org/bmvc/2002/index.html>.
- [312] Martin A. Fischler and Robert C. Bolles. Random Sample Consensus: A Paradigm for Model Fitting with Applications to Image Analysis and Automated Cartography. *Commun. ACM*, 24(6):381–395, June 1981. ISSN 0001-0782. doi: 10.1145/358669.358692. URL <http://doi.acm.org/10.1145/358669.358692>.
- [313] Arnim Jenett, Johannes E. Schindelin, and Martin Heisenberg. The Virtual Insect Brain protocol: creating and comparing standardized neuroanatomy. *BMC Bioinformatics*, 7(1):544, December 2006. ISSN 1471-2105. doi: 10.1186/1471-2105-7-544. URL <https://doi.org/10.1186/1471-2105-7-544>.
- [314] Benjamin Schmid. *Computational tools for the segmentation and registration of confocal brain images of Drosophila melanogaster*. PhD Thesis, Bayerischen Julius-Maximilians-Universitaet Wuerzburg, Wuerzburg, Germany, 2010. URL https://opus.bibliothek.uni-wuerzburg.de/opus4-wuerzburg/frontdoor/deliver/index/docId/4275/file/thesis_schmid2010.pdf.
- [315] RP Brent. *Algorithms for finding zeros and extrema of functions without calculating derivatives*. PhD thesis, Stanford University, 1971. URL <https://apps.dtic.mil/dtic/tr/fulltext/u2/726170.pdf>.
- [316] R Duda and P Hart. *Pattern Classification and Scene Analysis*. Wiley, New York, 1973.
- [317] Irwin Sobel. An Isotropic 3 3 Image Gradient Operator. *Presentation at Stanford A.I. Project 1968*, February 2014.
- [318] A Lieutier. Any open bounded subset of \mathbb{R}^n has the same homotopy type than its medial axis. *Proc. ACM SMI*, 2003.
- [319] Sunil Kumar, Nicola Lockwood, Marie-Christine Ramel, Teresa Correia, Matthew Ellis, Yuriy Alexandrov, Natalie Andrews, Rachel Patel, Laurence Bugeon, Margaret J. Dallman, Sebastian Brandner, Simon Arridge, Matilda Katan, James McGinty, Paul Frankel, and Paul M.W. French. Quantitative in vivo optical tomography of cancer progression & vasculature development in adult zebrafish. *Oncotarget*, 7(28):43939–43948, June 2016. ISSN 1949-2553. doi: 10.18632/oncotarget.9756. URL <http://www.ncbi.nlm.nih.gov/pmc/articles/PMC5190069/>.
- [320] Stephen R. Aylward and Elizabeth Bullitt. Initialization, noise, singularities, and scale in height ridge traversal for tubular object centerline extraction. *IEEE transactions on medical imaging*, 21(2):61–75, February 2002. ISSN 0278-0062. doi: 10.1109/42.993126.
- [321] Tamal K. Dey and Wulue Zhao. Approximate medial axis as a Voronoi subcomplex. *Computer-Aided Design*, 36(2):195–202, February 2004. ISSN 0010-4485. doi: 10.1016/S0010-4485(03)00061-7. URL <http://www.sciencedirect.com/science/article/pii/S0010448503000617>.
- [322] Tamal K. Dey and Wulue Zhao. Approximating the Medial Axis from the Voronoi Diagram with a Convergence Guarantee. *Algorithmica*, 38(1):179–200, January 2004. ISSN 0178-4617, 1432-0541. doi: 10.1007/s00453-003-1049-y. URL <https://link.springer.com/article/10.1007/s00453-003-1049-y>.

- [323] E. W. Dijkstra. A note on two problems in connexion with graphs. *Numerische Mathematik*, 1(1):269–271, December 1959. ISSN 0029-599X, 0945-3245. doi: 10.1007/BF01386390. URL <https://link.springer.com/article/10.1007/BF01386390>.
- [324] Ingmar Bitter, Mie Sato, Michael Bender, Kevin T. McDonnell, Arie Kaufman, and Ming Wan. CEASAR: A Smooth, Accurate and Robust Centerline Extraction Algorithm. In *Proceedings of the Conference on Visualization '00, VIS '00*, pages 45–52, Los Alamitos, CA, USA, 2000. IEEE Computer Society Press. ISBN 978-1-58113-309-7. URL <http://dl.acm.org/citation.cfm?id=375213.375217>.
- [325] M Sato, I Bitter, M Bender, and A Kaufmann. TEASAR: Tree-structure Extraction Algorithm for Accurate and Robust Skeletons. *IEEE Pacific Con. Comput. Graph. Appl.*, pages 281–289, 2000.
- [326] Julien Touati, Marco Bologna, Adeline Schwein, Francesco Migliavacca, and Marc Garbey. A robust construction algorithm of the centerline skeleton for complex aortic vascular structure using computational fluid dynamics. *Computers in Biology and Medicine*, 86(Supplement C):6–17, July 2017. ISSN 0010-4825. doi: 10.1016/j.compbio.2017.04.017. URL <http://www.sciencedirect.com/science/article/pii/S0010482517301142>.
- [327] Gunilla Borgefors. Distance transforms in digital images. *Computer Vision, Graphics, and Image Processing*, 34:344–371, 1986.
- [328] Kaleem Siddiqi, Sylvain Bouix, Allen Tannenbaum, and Steven W. Zucker. Hamilton-Jacobi Skeletons. *International Journal of Computer Vision*, 48(3):215–231, July 2002. ISSN 0920-5691, 1573-1405. doi: 10.1023/A:1016376116653. URL <https://link.springer.com/article/10.1023/A:1016376116653>.
- [329] Ming Wan, Zhengrong Liang, Qi Ke, Lichan Hong, I. Bitter, and A. Kaufman. Automatic centerline extraction for virtual colonoscopy. *IEEE Transactions on Medical Imaging*, 21(12):1450–1460, December 2002. ISSN 0278-0062. doi: 10.1109/TMI.2002.806409.
- [330] Azriel Rosenfeld. Connectivity in Digital Pictures. *J. ACM*, 17(1):146–160, January 1970. ISSN 0004-5411. doi: 10.1145/321556.321570. URL <http://doi.acm.org/10.1145/321556.321570>.
- [331] Daniel S. Fritsch, Stephen M. Pizer, Bryan S. Morse, David H. Eberly, and Alan Liu. The multiscale medial axis and its applications in image registration. *Pattern Recognition Letters*, 15(5):445–452, 1994. ISSN 0167-8655. doi: 10.1016/0167-8655(94)90135-X. URL <https://uncch.pure.elsevier.com/en/publications/the-multiscale-medial-axis-and-its-applications-in-image-registra>.
- [332] Lei Qu and Hanchuan Peng. A principal skeleton algorithm for standardizing confocal images of fruit fly nervous systems. *Bioinformatics*, 26(8):1091–1097, April 2010. ISSN 1367-4803. doi: 10.1093/bioinformatics/btq072. URL <https://academic.oup.com/bioinformatics/article/26/8/1091/205560>.
- [333] Stephen R. Aylward, Julien Jomier, Sue Weeks, and Elizabeth Bullitt. Registration and Analysis of Vascular Images. *International Journal of Computer Vision*, 55(2-3):123–138, November 2003. ISSN 0920-5691, 1573-1405. doi: 10.1023/A:1026126900358. URL <https://link.springer.com/article/10.1023/A:1026126900358>.
- [334] Q. Zheng, A. Sharf, A. Tagliasacchi, B. Chen, H. Zhang, A. Sheffer, and D. Cohen-Or. Consensus Skeleton for Non-rigid Space-time Registration. *Computer Graphics Forum*, 29(2):635–644, May 2010. ISSN 1467-8659. doi: 10.1111/j.1467-8659.2009.01633.x. URL <http://onlinelibrary.wiley.com/doi/10.1111/j.1467-8659.2009.01633.x/abstract>.
- [335] CW Niblack, PB Gibbson, and DW Capson. Generating Skeletons and Centrelines from the Distance Transform. *Graphical Models and Image Processing*, 54(5):420–437, 1992.
- [336] Eric Ferley, Marie-Paule Cani-Gascuel, and Dominique Attali. Skeletal Reconstruction of Branching Shapes. *Computer Graphics Forum*, 16(5):283–293, December 1997. ISSN 1467-8659. doi: 10.1111/1467-8659.00195. URL <http://onlinelibrary.wiley.com/doi/10.1111/1467-8659.00195/abstract>.
- [337] B. Durix, G. Morin, S. Chambon, C. Roudet, and L. Garnier. Towards Skeleton Based Reconstruction: From Projective Skeletonization to Canal Surface Estimation. In *2015 International Conference on 3D Vision*, pages 545–553, October 2015. doi: 10.1109/3DV.2015.67.
- [338] Dong-Goo Kang and Jong Beom Ra. A new path planning algorithm for maximizing visibility in computed tomography colonography. *IEEE Transactions on Medical Imaging*, 24(8):957–968, August 2005. ISSN 0278-0062. doi: 10.1109/TMI.2005.850551.

- [339] Y. Shinagawa, T. L. Kunii, and Y. L. Kergosien. Surface coding based on Morse theory. *IEEE Computer Graphics and Applications*, 11(5):66–78, September 1991. ISSN 0272-1716. doi: 10.1109/38.90568.
- [340] Jayaram K Udupa and Venkatramana G Ajjanagadde. Boundary and object labelling in three-dimensional images. *Computer Vision, Graphics, and Image Processing*, 51(3):355–369, September 1990. ISSN 0734-189X. doi: 10.1016/0734-189X(90)90008-J. URL <http://www.sciencedirect.com/science/article/pii/0734189X9090008J>.
- [341] Gisela Klette. Branch Voxels and Junctions in 3D Skeletons. In *Combinatorial Image Analysis*, Lecture Notes in Computer Science, pages 34–44. Springer, Berlin, Heidelberg, June 2006. ISBN 978-3-540-35153-5 978-3-540-35154-2. doi: 10.1007/11774938_4. URL https://link.springer.com/chapter/10.1007/11774938_4.
- [342] Carsten Steger. An Unbiased Detector of Curvilinear Structures. 20(2):113–125, 1998.
- [343] D. A. Sholl. Dendritic organization in the neurons of the visual and motor cortices of the cat. *Journal of Anatomy*, 87(4):387–406, October 1953. ISSN 0021-8782.
- [344] Gunilla Borgefors. On Digital Distance Transforms in Three Dimensions. *Computer Vision and Image Understanding*, 64(3):368–376, November 1996. ISSN 1077-3142. doi: 10.1006/cviu.1996.0065. URL <http://www.sciencedirect.com/science/article/pii/S107731429690065X>.
- [345] Amy J. Sehnert, Anja Huq, Brant M. Weinstein, Charline Walker, Mark Fishman, and Didier Y. R. Stainier. Cardiac troponin T is essential in sarcomere assembly and cardiac contractility. *Nature Genetics*, 31(1):106–110, May 2002. ISSN 1061-4036. doi: 10.1038/ng875.
- [346] M. Coué, S. L. Brenner, I. Spector, and E. D. Korn. Inhibition of actin polymerization by latrunculin A. *FEBS letters*, 213(2):316–318, March 1987. ISSN 0014-5793.
- [347] Mark H. Longair, Dean A. Baker, and J. Douglas Armstrong. Simple Neurite Tracer: open source software for reconstruction, visualization and analysis of neuronal processes. *Bioinformatics*, 27(17):2453–2454, September 2011. ISSN 1367-4803. doi: 10.1093/bioinformatics/btr390. URL <https://academic.oup.com/bioinformatics/article/27/17/2453/223685>. Publisher: Oxford Academic.
- [348] Tiago A. Ferreira, Arne V. Blackman, Julia Oyrer, Sriram Jayabal, Andrew J. Chung, Alanna J. Watt, P. Jesper Sjöström, and Donald J. van Meyel. Neuronal morphometry directly from bitmap images. *Nature Methods*, 11(10):982–984, October 2014. ISSN 1548-7105. doi: 10.1038/nmeth.3125. URL <https://www.nature.com/articles/nmeth.3125>.
- [349] Xing Ming, Anan Li, Jingpeng Wu, Cheng Yan, Wenxiang Ding, Hui Gong, Shaoqun Zeng, and Qian Liu. Rapid Reconstruction of 3D Neuronal Morphology from Light Microscopy Images with Augmented Rayburst Sampling. *PLoS ONE*, 8(12), December 2013. ISSN 1932-6203. doi: 10.1371/journal.pone.0084557. URL <https://www.ncbi.nlm.nih.gov/pmc/articles/PMC3877282/>.
- [350] Maysa M. G. Macedo, Miguel A. Galarreta-Valverde, Choukri Mekkaoui, and Marcel P. Jackowski. A centerline-based estimator of vessel bifurcations in angiography images. In *Medical Imaging 2013: Computer-Aided Diagnosis*, volume 8670, page 86703K. International Society for Optics and Photonics, March 2013. doi: 10.1117/12.2007812. URL <https://www.spiedigitallibrary.org/conference-proceedings-of-spie/8670/86703K/A-centerline-based-estimator-of-vessel-bifurcations-in-angiography-images/10.1117/12.2007812.short>.
- [351] Juan F. Carrillo, Maciej Orkisz, and Marcela Hernández Hoyos. Extraction of 3D Vascular Tree Skeletons Based on the Analysis of Connected Components Evolution. In André Galgawicz and Wilfried Philips, editors, *Computer Analysis of Images and Patterns*, Lecture Notes in Computer Science, pages 604–611, Berlin, Heidelberg, 2005. Springer. ISBN 978-3-540-32011-1. doi: 10.1007/11556121_74.
- [352] Jozef Šamaj, František Baluška, Boris Voigt, Markus Schlicht, Dieter Volkmann, and Diedrik Menzel. Endocytosis, Actin Cytoskeleton, and Signaling. *Plant Physiology*, 135(3):1150–1161, July 2004. ISSN 0032-0889, 1532-2548. doi: 10.1104/pp.104.040683. URL <http://www.plantphysiol.org/content/135/3/1150>.
- [353] Li-Kun Phng, Fabio Stanchi, and Holger Gerhardt. Filopodia are dispensable for endothelial tip cell guidance. *Development*, 140(19):4031–4040, October 2013. ISSN 0950-1991, 1477-9129. doi: 10.1242/dev.097352. URL <http://dev.biologists.org/content/140/19/4031>.

- [354] Jonathan D. Leslie, Linda Ariza-McNaughton, Adam L. Bermange, Ryan McAdow, Stephen L. Johnson, and Julian Lewis. Endothelial signalling by the Notch ligand Delta-like 4 restricts angiogenesis. *Development (Cambridge, England)*, 134(5):839–844, March 2007. ISSN 0950-1991. doi: 10.1242/dev.003244.
- [355] Nathan D. Lawson, Joshua W. Mugford, Brigid A. Diamond, and Brant M. Weinstein. phospholipase C gamma-1 is required downstream of vascular endothelial growth factor during arterial development. *Genes & Development*, 17(11):1346–1351, June 2003. ISSN 0890-9369. doi: 10.1101/gad.1072203. URL <http://www.ncbi.nlm.nih.gov/pmc/articles/PMC196067/>.
- [356] Nathalie Lambeng, Yann Wallez, Christine Rampon, Francine Cand, Georges Christé, Danielle Gulino-Debrac, Isabelle Vilgrain, and Philippe Huber. Vascular endothelial-cadherin tyrosine phosphorylation in angiogenic and quiescent adult tissues. *Circulation Research*, 96(3):384–391, February 2005. ISSN 0009-7330. doi: 10.1161/01.RES.0000156652.99586.9f. URL <https://www.ncbi.nlm.nih.gov/pmc/articles/PMC2798002/>.
- [357] Monica Giannotta, Marianna Trani, and Elisabetta Dejana. VE-Cadherin and Endothelial Adherens Junctions: Active Guardians of Vascular Integrity. *Developmental Cell*, 26(5):441–454, September 2013. ISSN 15345807. doi: 10.1016/j.devcel.2013.08.020. URL <http://linkinghub.elsevier.com/retrieve/pii/S1534580713005078>.
- [358] S. Esser, M. G. Lampugnani, M. Corada, E. Dejana, and W. Risau. Vascular endothelial growth factor induces VE-cadherin tyrosine phosphorylation in endothelial cells. *Journal of Cell Science*, 111 (Pt 13):1853–1865, July 1998. ISSN 0021-9533.
- [359] Sabu Abraham, Margaret Yeo, Mercedes Montero-Balaguer, Hugh Paterson, Elisabetta Dejana, Christopher J. Marshall, and Georgia Mavria. VE-Cadherin-Mediated Cell-Cell Interaction Suppresses Sprouting via Signaling to MLC2 Phosphorylation. *Current Biology*, 19(8):668–674, April 2009. ISSN 0960-9822. doi: 10.1016/j.cub.2009.02.057. URL <http://www.sciencedirect.com/science/article/pii/S0960982209008100>.
- [360] Sara M. Weis and David A. Cheresh. Pathophysiological consequences of VEGF-induced vascular permeability. *Nature*, 437(7058):497, September 2005. ISSN 1476-4687. doi: 10.1038/nature03987. URL <https://www.nature.com/articles/nature03987>.
- [361] Xavier F. Figueroa, Mauricio A. Lillo, Pablo S. Gaete, Manuel A. Riquelme, and Juan C. Sáez. Diffusion of nitric oxide across cell membranes of the vascular wall requires specific connexin-based channels. *Neuropharmacology*, 75:471–478, December 2013. ISSN 1873-7064. doi: 10.1016/j.neuropharm.2013.02.022.
- [362] L. J. Ignarro. Nitric oxide as a unique signaling molecule in the vascular system: a historical overview. *Journal of Physiology and Pharmacology: An Official Journal of the Polish Physiological Society*, 53(4 Pt 1):503–514, December 2002. ISSN 0867-5910.
- [363] J. N. Sharma, A. Al-Omran, and S. S. Parvathy. Role of nitric oxide in inflammatory diseases. *Inflammopharmacology*, 15(6):252–259, December 2007. ISSN 0925-4692. doi: 10.1007/s10787-007-0013-x.
- [364] Vittorio Calabrese, Cesare Mancuso, Menotti Calvani, Enrico Rizzarelli, D. Allan Butterfield, and Anna Maria Giuffrida Stella. Nitric oxide in the central nervous system: neuroprotection versus neurotoxicity. *Nature Reviews. Neuroscience*, 8(10):766–775, October 2007. ISSN 1471-0048. doi: 10.1038/nrn2214.
- [365] S. Moncada and E. A. Higgs. Nitric oxide and the vascular endothelium. *Handbook of Experimental Pharmacology*, (176 Pt 1):213–254, 2006. ISSN 0171-2004.
- [366] Ulrich Förstermann. Nitric oxide and oxidative stress in vascular disease. *Pflugers Archiv: European Journal of Physiology*, 459(6):923–939, May 2010. ISSN 1432-2013. doi: 10.1007/s00424-010-0808-2.
- [367] T. M. Millar, C. R. Stevens, N. Benjamin, R. Eienthal, R. Harrison, and D. R. Blake. Xanthine oxidoreductase catalyses the reduction of nitrates and nitrite to nitric oxide under hypoxic conditions. *FEBS letters*, 427(2):225–228, May 1998. ISSN 0014-5793.
- [368] Kenyatta Cosby, Kristine S. Partovi, Jack H. Crawford, Rakesh P. Patel, Christopher D. Reiter, Sabrina Martyr, Benjamin K. Yang, Myron A. Waclawiw, Gloria Zalos, Xiuli Xu, Kris T. Huang, Howard Shields, Daniel B. Kim-Shapiro, Alan N. Schechter, Richard O. Cannon, and Mark T. Gladwin. Nitrite reduction to nitric oxide by deoxyhemoglobin vasodilates the human circulation. *Nature Medicine*, 9(12):1498–1505, December 2003. ISSN 1078-8956. doi: 10.1038/nm954.

- [369] J. L. Zweier, A. Samouilov, and P. Kuppusamy. Non-enzymatic nitric oxide synthesis in biological systems. *Biochimica Et Biophysica Acta*, 1411(2-3):250–262, May 1999. ISSN 0006-3002.
- [370] Fahima Syeda, David Hauton, Steven Young, and Stuart Egginton. How ubiquitous is endothelial NOS? *Comparative Biochemistry and Physiology Part A: Molecular & Integrative Physiology*, 166(1):207–214, September 2013. ISSN 1095-6433. doi: 10.1016/j.cbpa.2013.05.027. URL <http://www.sciencedirect.com/science/article/pii/S1095643313001578>.
- [371] R. Fritsche, T. Schwerte, and B. Pelster. Nitric oxide and vascular reactivity in developing zebrafish, *Danio rerio*. *American Journal of Physiology. Regulatory, Integrative and Comparative Physiology*, 279(6):R2200–2207, December 2000. ISSN 0363-6119. doi: 10.1152/ajpregu.2000.279.6.R2200.
- [372] Bo Holmqvist, Lars Ebbesson, and Per Alm. Nitric oxide and the zebrafish (*Danio rerio*): Developmental neurobiology and brain neurogenesis. In Bruno Tota and Barry Trimmer, editors, *Advances in Experimental Biology*, volume 1 of *Nitric Oxide*, pages 229–465. Elsevier, January 2007. doi: 10.1016/S1872-2423(07)01011-3. URL <http://www.sciencedirect.com/science/article/pii/S1872242307010113>.
- [373] J. R. Shutter, S. Scully, W. Fan, W. G. Richards, J. Kitajewski, G. A. Deblandre, C. R. Kintner, and K. L. Stark. Dll4, a novel Notch ligand expressed in arterial endothelium. *Genes & Development*, 14(11):1313–1318, June 2000. ISSN 0890-9369.
- [374] Natalia Sacilotto, Rui Monteiro, Martin Fritzsche, Philipp W. Becker, Luis Sanchez-del Campo, Ke Liu, Philip Pinheiro, Indrika Ratnayaka, Benjamin Davies, Colin R. Goding, Roger Patient, George Bou-Gharios, and Sarah De Val. Analysis of Dll4 regulation reveals a combinatorial role for Sox and Notch in arterial development. *Proceedings of the National Academy of Sciences of the United States of America*, 110(29), July 2013. ISSN 0027-8424. doi: 10.1073/pnas.1300805110. URL <http://www.ncbi.nlm.nih.gov/pmc/articles/PMC3718163/>.
- [375] Tsutomu Kume. Specification of arterial, venous, and lymphatic endothelial cells during embryonic development. *Histology and Histopathology*, 25(5):637–646, 2010. ISSN 1699-5848. doi: 10.14670/HH-25.637.
- [376] Nancy L. Parmalee and Jan Kitajewski. Wnt Signaling in Angiogenesis. *Current drug targets*, 9(7):558–564, July 2008. ISSN 1389-4501. URL <https://www.ncbi.nlm.nih.gov/pmc/articles/PMC4052372/>.
- [377] Benoit Vanhollebeke, Oliver A. Stone, Naguissa Bostaille, Chris Cho, Yulian Zhou, Emilie Maquet, Anne Gauquier, Pauline Cabochette, Shigetomo Fukuhara, Naoki Mochizuki, Jeremy Nathans, and Didier Yr Stainier. Tip cell-specific requirement for an atypical Gpr124- and Reck-dependent Wnt/beta-catenin pathway during brain angiogenesis. *eLife*, 4, June 2015. ISSN 2050-084X. doi: 10.7554/eLife.06489.
- [378] Jan M. Stenman, Jay Rajagopal, Thomas J. Carroll, Makoto Ishibashi, Jill McMahon, and Andrew P. McMahon. Canonical Wnt Signaling Regulates Organ-Specific Assembly and Differentiation of CNS Vasculature. *Science*, 322(5905):1247–1250, November 2008. ISSN 0036-8075, 1095-9203. doi: 10.1126/science.1164594. URL <http://science.sciencemag.org/content/322/5905/1247>.
- [379] Kathleen Hübner, Pauline Cabochette, Rodrigo Diéguez-Hurtado, Cora Wiesner, Yuki Wakayama, Kathrin S. Grassme, Marvin Hubert, Stefan Guenther, Heinz-Georg Belting, Markus Affolter, Ralf H. Adams, Benoit Vanhollebeke, and Wiebke Herzog. Wnt/beta-catenin signaling regulates VE-cadherin-mediated anastomosis of brain capillaries by counteracting S1pr1 signaling. *Nature Communications*, 9(1):4860, November 2018. ISSN 2041-1723. doi: 10.1038/s41467-018-07302-x. URL <https://www.nature.com/articles/s41467-018-07302-x>.
- [380] Kathleen Hübner, Kathrin S. Grassme, Jyoti Rao, Nina K. Wenke, Cordula L. Zimmer, Laura Korte, Katja Müller, Saulius Sumanas, Boris Greber, and Wiebke Herzog. Wnt signaling positively regulates endothelial cell fate specification in the Fli1a-positive progenitor population via Lef1. *Developmental Biology*, 430(1):142–155, October 2017. ISSN 00121606. doi: 10.1016/j.ydbio.2017.08.004. URL <https://linkinghub.elsevier.com/retrieve/pii/S0012160617301240>.
- [381] Max van Lessen, Shannon Shibata-Germanos, Andreas van Impel, Thomas A Hawkins, Jason Rihel, and Stefan Schulte-Merker. Intracellular uptake of macromolecules by brain lymphatic endothelial cells during zebrafish embryonic development. *eLife*, 6:e25932, May 2017. ISSN 2050-084X. doi: 10.7554/eLife.25932. URL <https://doi.org/10.7554/eLife.25932>.

- [382] Alessandro Fantin, Joaquim M. Vieira, Gaia Gestri, Laura Denti, Quenten Schwarz, Sergey Prykhodzhiy, Francesca Peri, Stephen W. Wilson, and Christiana Ruhrberg. Tissue macrophages act as cellular chaperones for vascular anastomosis downstream of VEGF-mediated endothelial tip cell induction. *Blood*, 116(5):829–840, August 2010. ISSN 1528-0020. doi: 10.1182/blood-2009-12-257832.
- [383] Chi Liu, Chuan Wu, Qifen Yang, Jing Gao, Li Li, Deqin Yang, and Lingfei Luo. Macrophages Mediate the Repair of Brain Vascular Rupture through Direct Physical Adhesion and Mechanical Traction. *Immunity*, 44(5):1162–1176, 2016. ISSN 1097-4180. doi: 10.1016/j.immuni.2016.03.008.
- [384] Richard Mark White, Anna Sessa, Christopher Burke, Teresa Bowman, Jocelyn LeBlanc, Craig Ceol, Caitlin Bourque, Michael Dovey, Wolfram Goessling, Caroline Erter Burns, and Leonard I. Zon. Transparent adult zebrafish as a tool for in vivo transplantation analysis. *Cell stem cell*, 2(2):183–189, February 2008. ISSN 1934-5909. doi: 10.1016/j.stem.2007.11.002. URL <http://www.ncbi.nlm.nih.gov/pmc/articles/PMC2292119/>.
- [385] David Traver, Barry H. Paw, Kenneth D. Poss, W. Todd Penberthy, Shuo Lin, and Leonard I. Zon. Transplantation and in vivo imaging of multilineage engraftment in zebrafish bloodless mutants. *Nature Immunology*, 4(12):1238, December 2003. ISSN 1529-2916. doi: 10.1038/ni1007. URL <https://www.nature.com/articles/ni1007>.
- [386] Yannick Blum, Heinz-Georg Belting, Elin Ellertsdottir, Lukas Herwig, Florian Lüders, and Markus Affolter. Complex cell rearrangements during intersegmental vessel sprouting and vessel fusion in the zebrafish embryo. *Developmental Biology*, 316(2):312–322, April 2008. ISSN 0012-1606. doi: 10.1016/j.ydbio.2008.01.038. URL <http://www.sciencedirect.com/science/article/pii/S0012160608000791>.
- [387] Katharina Bergmann, Paola Meza Santoscoy, Konstantinos Lygdas, Yulia Nikolaeva, Ryan B. MacDonald, Vincent T. Cunliffe, and Anton Nikolaev. Imaging Neuronal Activity in the Optic Tectum of Late Stage Larval Zebrafish. *Journal of Developmental Biology*, 6(1): 6, March 2018. doi: 10.3390/jdb6010006. URL <http://www.mdpi.com/2221-3759/6/1/6>.
- [388] Nikolay Ninov, Maxim Borius, and Didier Y. R. Stainier. Different levels of Notch signaling regulate quiescence, renewal and differentiation in pancreatic endocrine progenitors. *Development (Cambridge, England)*, 139(9):1557–1567, May 2012. ISSN 0950-1991. doi: 10.1242/dev.076000. URL <https://www.ncbi.nlm.nih.gov/pmc/articles/PMC3317964/>.
- [389] C. Gray, C. A. Loynes, M. K. B. Whyte, D. C. Crossman, S. A. Renshaw, and T. J. A. Chico. Simultaneous intravital imaging of macrophage and neutrophil behaviour during inflammation using a novel transgenic zebrafish. *Thrombosis and Haemostasis*, 105(5): 811–819, May 2011. ISSN 2567-689X. doi: 10.1160/TH10-08-0525.
- [390] Hyouk-Bum Kwon, Shigetomo Fukuhara, Kazuhide Asakawa, Koji Ando, Takeru Kashiwada, Koichi Kawakami, Masahiko Hibi, Young-Guen Kwon, Kyu-Won Kim, Kari Alitalo, and Naoki Mochizuki. The parallel growth of motoneuron axons with the dorsal aorta depends on Vegfc/Vegfr3 signaling in zebrafish. *Development*, 140(19):4081–4090, October 2013. ISSN 0950-1991, 1477-9129. doi: 10.1242/dev.091702. URL <http://dev.biologists.org/content/140/19/4081>.
- [391] Takeru Kashiwada, Shigetomo Fukuhara, Kenta Terai, Toru Tanaka, Yuki Wakayama, Koji Ando, Hiroyuki Nakajima, Hajime Fukui, Shinya Yuge, Yoshinobu Saito, Akihiko Gemma, and Naoki Mochizuki. beta-catenin-dependent transcription is central to Bmp-mediated formation of venous vessels. *Development*, page dev.115576, January 2015. ISSN 0950-1991, 1477-9129. doi: 10.1242/dev.115576. URL <http://dev.biologists.org/content/early/2015/01/06/dev.115576>.
- [392] Christopher E. Schmitt, Melinda B. Holland, and Suk-Won Jin. Visualizing vascular networks in zebrafish: an introduction to microangiography. *Methods in Molecular Biology (Clifton, N.J.)*, 843:59–67, 2012. ISSN 1940-6029. doi: 10.1007/978-1-61779-523-7_6.
- [393] Jan Huisken and Didier Y. R. Stainier. Even fluorescence excitation by multidirectional selective plane illumination microscopy (mSPIM). *Optics Letters*, 32(17):2608–2610, September 2007. ISSN 0146-9592.
- [394] Stephan Preibisch, Stephan Saalfeld, and Pavel Tomancak. Globally optimal stitching of tiled 3D microscopic image acquisitions. *Bioinformatics*, 25(11):1463–1465, June 2009. ISSN 1367-4803. doi: 10.1093/bioinformatics/btp184. URL <http://www.ncbi.nlm.nih.gov/pmc/articles/PMC2682522/>.
- [395] Jaroslav Icha, Christopher Schmied, Jaydeep Sidhaye, Pavel Tomancak, Stephan Preibisch, and Caren Norden. Using Light Sheet Fluorescence Microscopy to Image Zebrafish Eye Development. *Journal of Visualized Experiments : JoVE*, (110), April

2016. ISSN 1940-087X. doi: 10.3791/53966. URL <https://www.ncbi.nlm.nih.gov/pmc/articles/PMC4941907/>.
- [396] S Preibisch, F Amat, E Stamatakis, M Sarov, R Singer, E Myers, and P Tomancak. Efficient Bayesian-based multiview deconvolution. *Nature Methods*, 11(6):645, April 2014. ISSN 1548-7105. doi: 10.1038/nmeth.2929. URL <https://www.nature.com/articles/nmeth.2929>.
- [397] Tiziana de Filippis, Federica Marelli, Gabriella Nebbia, Patrizia Porazzi, Sabrina Corbetta, Laura Fugazzola, Roberto Gastaldi, Maria Cristina Vigone, Roberta Biffanti, Daniela Frizziero, Luana Mandarà, Paolo Prontera, Mariacarina Salerno, Mohamad Maghnie, Natascia Tiso, Giorgio Radetti, Giovanna Weber, and Luca Persani. JAG1 Loss-Of-Function Variations as a Novel Predisposing Event in the Pathogenesis of Congenital Thyroid Defects. *The Journal of Clinical Endocrinology & Metabolism*, 101(3):861–870, March 2016. ISSN 0021-972X. doi: 10.1210/jc.2015-3403. URL <https://academic.oup.com/jcem/article/101/3/861/2804765>.
- [398] Ludovic Le Guen, Terhi Karpanen, Dörte Schulte, Nicole C. Harris, Katarzyna Koltowska, Guy Roukens, Neil I. Bower, Andreas van Impel, Steven A. Stacker, Marc G. Achen, Stefan Schulte-Merker, and Benjamin M. Hogan. Ccbe1 regulates Vegfc-mediated induction of Vegfr3 signaling during embryonic lymphangiogenesis. *Development*, 141(6):1239–1249, March 2014. ISSN 0950-1991, 1477-9129. doi: 10.1242/dev.100495. URL <http://dev.biologists.org/content/141/6/1239>.
- [399] Stefania Nicoli, Clive Standley, Paul Walker, Adam Hurlstone, Kevin E. Fogarty, and Nathan D. Lawson. MicroRNA-mediated integration of haemodynamics and Vegf signalling during angiogenesis. *Nature*, 464(7292):1196–1200, July 2012. ISSN 1476-4687. doi: 10.1038/nature08889. URL <https://www.nature.com/articles/nature08889>.
- [400] H. Kojima, N. Nakatsubo, K. Kikuchi, S. Kawahara, Y. Kirino, H. Nagoshi, Y. Hirata, and T. Nagano. Detection and imaging of nitric oxide with novel fluorescent indicators: diaminofluoresceins. *Analytical Chemistry*, 70(13):2446–2453, July 1998. ISSN 0003-2700.
- [401] null Kojima, null Urano, null Kikuchi, null Higuchi, null Hirata, and null Nagano. Fluorescent Indicators for Imaging Nitric Oxide Production. *Angewandte Chemie (International Ed. in English)*, 38(21):3209–3212, November 1999. ISSN 1521-3773.
- [402] Congcong He and Daniel J. Klionsky. Analyzing autophagy in zebrafish. *Autophagy*, 6(5):642–644, July 2010. ISSN 1554-8627. doi: 10.4161/auto.6.5.12092. URL <https://www.ncbi.nlm.nih.gov/pmc/articles/PMC3654832/>.
- [403] Walter M. Morton, Kathryn R. Ayscough, and Paul J. McLaughlin. Latrunculin alters the actin-monomer subunit interface to prevent polymerization. *Nature Cell Biology*, 2(6):376–378, June 2000. ISSN 1476-4679. doi: 10.1038/35014075. URL https://www.nature.com/articles/ncb0600_376.
- [404] Chung-Der Hsiao, Wei-Yuan Tsai, Long-Shyan Horng, and Huai-Jen Tsai. Molecular structure and developmental expression of three muscle-type troponin T genes in zebrafish. *Developmental Dynamics: An Official Publication of the American Association of Anatomists*, 227(2):266–279, June 2003. ISSN 1058-8388. doi: 10.1002/dvdy.10305.
- [405] A. Nasevicius and S. C. Ekker. Effective targeted gene 'knockdown' in zebrafish. *Nature Genetics*, 26(2):216–220, October 2000. ISSN 1061-4036. doi: 10.1038/79951.
- [406] Wei Huang, Ruilin Zhang, and Xiaolei Xu. Myofibrillogenesis in the developing zebrafish heart: A functional study of tnnt2. *Developmental biology*, 331(2):237–249, July 2009. ISSN 0012-1606. doi: 10.1016/j.ydbio.2009.04.039. URL <https://www.ncbi.nlm.nih.gov/pmc/articles/PMC2857981/>.
- [407] Jay R. Hove, Reinhard W. Koster, Arian S. Forouhar, Gabriel Acevedo-Bolton, and et al. Intracardiac fluid forces are an essential epigenetic factor for embryonic cardiogenesis. *Nature; London*, 421(6919):172–7, January 2003. ISSN 00280836. URL <https://search.proquest.com/docview/204559484/abstract/4B2D307C7459459DPQ/1>.
- [408] Jan-Renier A. J. Moonen, Ee Soo Lee, Marc Schmidt, Monika Maleszewska, Jasper A. Koerts, Linda A. Brouwer, Theo G. van Kooten, Marja J. A. van Luyn, Clark J. Zeebregts, Guido Krenning, and Martin C. Harmsen. Endothelial-to-mesenchymal transition contributes to fibro-proliferative vascular disease and is modulated by fluid shear stress. *Cardiovascular Research*, 108(3):377–386, December 2015. ISSN 1755-3245. doi: 10.1093/cvr/cvv175.
- [409] Stefan Schulte-Merker and Didier Y. R. Stainier. Out with the old, in with the new: reassessing morpholino knockdowns in light of genome editing technology. *Development*

- (Cambridge, England), 141(16):3103–3104, August 2014. ISSN 1477-9129. doi: 10.1242/dev.112003.
- [410] F. O. Kok, M. Shin, C-W. Ni, A. Gupta, A. S. Grosse, A. van Impel, B. C. Kirchmaier, J. Peterson-Maduro, G. Kourkoulis, I. Male, D.F. DeSantis, S. Sheppard-Tindell, L. Ebarasi, C. Betsholtz, S. Schulte-Merker, S. A. Wolfe, and N. D. Lawson. Reverse genetic screening reveals poor correlation between Morpholino-induced and mutant phenotypes in zebrafish. *Developmental cell*, 32(1):97–108, January 2015. ISSN 1534-5807. doi: 10.1016/j.devcel.2014.11.018. URL <https://www.ncbi.nlm.nih.gov/pmc/articles/PMC4487878/>.
- [411] Eva Kochhan, Anna Lenard, Elin Ellertsdottir, Lukas Herwig, Markus Affolter, Heinz-Georg Belting, and Arndt F. Siekmann. Blood flow changes coincide with cellular rearrangements during blood vessel pruning in zebrafish embryos. *PLoS One*, 8(10): e75060, 2013. ISSN 1932-6203. doi: 10.1371/journal.pone.0075060.
- [412] Anna Lenard, Stephan Daetwyler, Charles Betz, Elin Ellertsdottir, Heinz-Georg Belting, Jan Huisken, and Markus Affolter. Endothelial Cell Self-fusion during Vascular Pruning. *PLOS Biology*, 13(4):e1002126, April 2015. ISSN 1545-7885. doi: 10.1371/journal.pbio.1002126. URL <http://journals.plos.org/plosbiology/article?id=10.1371/journal.pbio.1002126>.
- [413] Nicolas Ricard and Michael Simons. When It Is Better to Regress: Dynamics of Vascular Pruning. *PLoS Biology*, 13(5), May 2015. ISSN 1544-9173. doi: 10.1371/journal.pbio.1002148. URL <https://www.ncbi.nlm.nih.gov/pmc/articles/PMC4433099/>.
- [414] Deshun Lu and Ghassan S. Kassab. Role of shear stress and stretch in vascular mechanobiology. *Journal of the Royal Society Interface*, 8(63):1379–1385, October 2011. ISSN 1742-5689. doi: 10.1098/rsif.2011.0177. URL <https://www.ncbi.nlm.nih.gov/pmc/articles/PMC3163429/>.
- [415] T. Haller, P. Dietl, P. Deetjen, and H. Vökl. The lysosomal compartment as intracellular calcium store in MDCK cells: a possible involvement in InsP3-mediated Ca²⁺ release. *Cell Calcium*, 19(2):157–165, February 1996. ISSN 0143-4160.
- [416] R. M. Zucker, S. Hunter, and J. M. Rogers. Confocal laser scanning microscopy of apoptosis in organogenesis-stage mouse embryos. *Cytometry*, 33(3):348–354, November 1998. ISSN 0196-4763.
- [417] R. A. Gottlieb. Cell acidification in apoptosis. *Apoptosis*, 1(1):40–48, August 1996. ISSN 1360-8185, 1573-675X. doi: 10.1007/BF00142077. URL <https://link.springer.com/article/10.1007/BF00142077>.
- [418] D. Lagadic-Gossmann, L. Huc, and V. Lecureur. Alterations of intracellular pH homeostasis in apoptosis: origins and roles. *Cell Death and Differentiation*, 11(9): 953–961, September 2004. ISSN 1476-5403. doi: 10.1038/sj.cdd.4401466. URL <https://www.nature.com/articles/4401466>.
- [419] Daniel A. Goodenough and David L. Paul. Beyond the gap: functions of unpaired connexon channels. *Nature Reviews Molecular Cell Biology*, 4(4):285–295, April 2003. ISSN 1471-0080. doi: 10.1038/nrm1072. URL <https://www.nature.com/articles/nrm1072>.
- [420] W. Howard Evans, Elke De Vuyst, and Luc Leybaert. The gap junction cellular internet: connexin hemichannels enter the signalling limelight. *Biochemical Journal*, 397(1):1–14, July 2006. ISSN 0264-6021, 1470-8728. doi: 10.1042/BJ20060175. URL <http://www.biochemj.org/content/397/1/1>.
- [421] H. F. Dovey, V. John, J. P. Anderson, L. Z. Chen, P. de Saint Andrieu, L. Y. Fang, S. B. Freedman, B. Folmer, E. Goldbach, E. J. Holsztynska, K. L. Hu, K. L. Johnson-Wood, S. L. Kennedy, D. Kholodenko, J. E. Knops, L. H. Latimer, M. Lee, Z. Liao, I. M. Lieberburg, R. N. Motter, L. C. Mutter, J. Nietz, K. P. Quinn, K. L. Sacchi, P. A. Seubert, G. M. Shopp, E. D. Thorsett, J. S. Tung, J. Wu, S. Yang, C. T. Yin, D. B. Schenk, P. C. May, L. D. Altstiel, M. H. Bender, L. N. Boggs, T. C. Britton, J. C. Clemens, D. L. Czilli, D. K. Dieckman-McGinty, J. J. Droste, K. S. Fuson, B. D. Gitter, P. A. Hyslop, E. M. Johnstone, W. Y. Li, S. P. Little, T. E. Mabry, F. D. Miller, and J. E. Audia. Functional gamma-secretase inhibitors reduce beta-amyloid peptide levels in brain. *Journal of Neurochemistry*, 76(1): 173–181, January 2001. ISSN 0022-3042.
- [422] Shih-Min A. Huang, Yuji M. Mishina, Shanming Liu, Atwood Cheung, Frank Stegmeier, Gregory A. Michaud, Olga Charlat, Elizabeth Wiellelte, Yue Zhang, Stephanie Wiessner, Marc Hild, Xiaoying Shi, Christopher J. Wilson, Craig Mickanin, Vic Myer, Aleem Fazal, Ronald Tomlinson, Fabrizio Serluca, Wenlin Shao, Hong Cheng, Michael Shultz, Christina Rau, Markus Schirle, Judith Schlegl, Sonja Ghidelli, Stephen Fawell, Chris Lu, Daniel Curtis, Marc W. Kirschner, Christoph Lengauer, Peter M. Finan, John A. Tallarico,

- Tewis Bouwmeester, Jeffery A. Porter, Andreas Bauer, and Feng Cong. Tankyrase inhibition stabilizes axin and antagonizes Wnt signalling. *Nature*, 461(7264):614–620, October 2009. ISSN 1476-4687. doi: 10.1038/nature08356.
- [423] Jing Du, Yanling Wei, Lidong Liu, Yun Wang, Rushaniya Khairova, Rayah Blumenthal, Tyson Tragon, Joshua G. Hunsberger, Rodrigo Machado-Vieira, Wayne Drevets, Yu Tian Wang, and Hussein K. Manji. A kinesin signaling complex mediates the ability of GSK-3beta to affect mood-associated behaviors. *Proceedings of the National Academy of Sciences of the United States of America*, 107(25):11573–11578, June 2010. ISSN 0027-8424. doi: 10.1073/pnas.0913138107. URL <https://www.ncbi.nlm.nih.gov/pmc/articles/PMC2895136/>.
- [424] Rebecca Notman, Massimo Noro, Brendan O'Malley, and Jamshed Anwar. Molecular basis for dimethylsulfoxide (DMSO) action on lipid membranes. *Journal of the American Chemical Society*, 128(43):13982–13983, November 2006. ISSN 0002-7863. doi: 10.1021/ja063363t.
- [425] Kotaro Oyama, Tomomi Arai, Akira Isaka, Taku Sekiguchi, Hideki Itoh, Yusuke Seto, Makito Miyazaki, Takeshi Itabashi, Takashi Ohki, Madoka Suzuki, and Shin'ichi Ishiwata. Directional Bleb Formation in Spherical Cells under Temperature Gradient. *Biophysical Journal*, 109(2):355–364, July 2015. ISSN 0006-3495. doi: 10.1016/j.bpj.2015.06.016. URL <https://www.ncbi.nlm.nih.gov/pmc/articles/PMC4621819/>.
- [426] Guillaume T. Charras, Justin C Yarrow, Mike A. Horton, L. Mahadevan, and T.J. Mitchison. Non-equilibration of hydrostatic pressure in blebbing cells. *Nature*, 435(7040):365–369, May 2005. ISSN 0028-0836. doi: 10.1038/nature03550. URL <https://www.ncbi.nlm.nih.gov/pmc/articles/PMC1564437/>.
- [427] Hyun Min Jung, Daniel Castranova, Matthew R. Swift, Van N. Pham, Marina Venero Galanternik, Sumio Isogai, Matthew G. Butler, Timothy S. Mulligan, and Brant M. Weinstein. Development of the larval lymphatic system in zebrafish. *Development*, 144(11):2070–2081, June 2017. ISSN 0950-1991, 1477-9129. doi: 10.1242/dev.145755. URL <http://dev.biologists.org/content/144/11/2070>.
- [428] Teymuraz V Kurzchalia and Robert G Partan. Membrane microdomains and caveolae. *Current Opinion in Cell Biology*, 11(4):424–431, August 1999. ISSN 0955-0674. doi: 10.1016/S0955-0674(99)80061-1. URL <http://www.sciencedirect.com/science/article/pii/S0955067499800611>.
- [429] Ejaife O. Agbani, Marion T. J. van den Bosch, Ed Brown, Christopher M. Williams, Nadine J. A. Mattheij, Judith M. E. M. Cosemans, Peter W. Collins, Johan W. M. Heemskerk, Ingeborg Hers, and Alastair W. Poole. Coordinated Membrane Ballooning and Procoagulant Spreading in Human Platelets Clinical Perspective. *Circulation*, 132(15):1414–1424, October 2015. ISSN 0009-7322, 1524-4539. doi: 10.1161/CIRCULATIONAHA.114.015036. URL <http://circ.ahajournals.org/content/132/15/1414>.
- [430] Ejaife O. Agbani, Christopher M. Williams, Yong Li, Marion T. J. van den Bosch, Samantha F. Moore, Adele Mauroux, Lorna Hodgson, Alan S. Verkman, Ingeborg Hers, and Alastair W. Poole. Aquaporin-1 regulates platelet procoagulant membrane dynamics and in vivo thrombosis. *JCI Insight*, 3(10), May 2018. ISSN 0021-9738. doi: 10.1172/jci.insight.99062. URL <https://insight.jci.org/articles/view/99062>.
- [431] Julien Vermot, Arian S. Forouhar, Michael Liebling, David Wu, Diane Plummer, Morteza Gharib, and Scott E. Fraser. Reversing Blood Flows Act through klf2a to Ensure Normal Valvulogenesis in the Developing Heart. *PLOS Biology*, 7(11):e1000246, November 2009. ISSN 1545-7885. doi: 10.1371/journal.pbio.1000246. URL <http://journals.plos.org/plosbiology/article?id=10.1371/journal.pbio.1000246>.
- [432] Noëlle Paffett-Lugassy, Nelson Hsia, Paula G. Fraenkel, Barry Paw, Irene Leshinsky, Bruce Barut, Nathan Bahary, Jaime Caro, Robert Handin, and Leonard I. Zon. Functional conservation of erythropoietin signaling in zebrafish. *Blood*, 110(7):2718–2726, October 2007. ISSN 0006-4971. doi: 10.1182/blood-2006-04-016535. URL <https://www.ncbi.nlm.nih.gov/pmc/articles/PMC1988930/>.
- [433] Jon D. Larson, Shannon A. Wadman, Eleanor Chen, Lesa Kerley, Karl J. Clark, Mark Eide, Sarah Lippert, Aidas Nasevicius, Stephen C. Ekker, Perry B. Hackett, and Jeffrey J. Essner. Expression of VE-cadherin in zebrafish embryos: A new tool to evaluate vascular development. *Developmental Dynamics*, 231(1):204–213, September 2004. ISSN 1097-0177. doi: 10.1002/dvdy.20102. URL <http://onlinelibrary.wiley.com/doi/10.1002/dvdy.20102/abstract>.

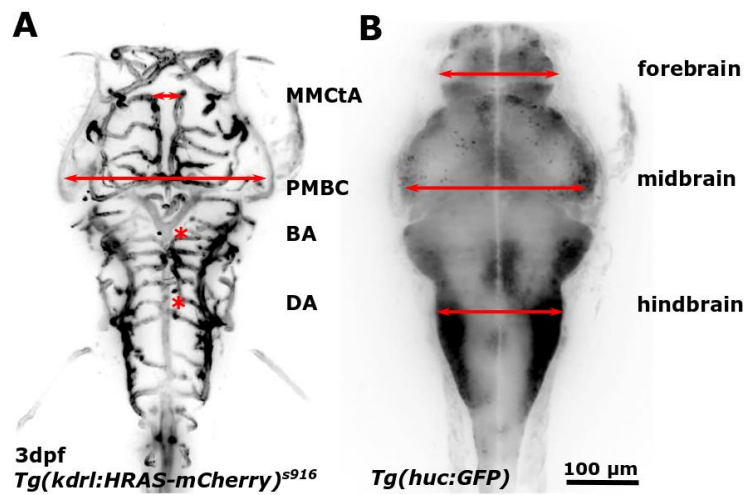
- [434] Dietmar Vestweber. VE-Cadherin: The Major Endothelial Adhesion Molecule Controlling Cellular Junctions and Blood Vessel Formation. *Arteriosclerosis, Thrombosis, and Vascular Biology*, 28(2):223–232, February 2008. ISSN 1079-5642, 1524-4636. doi: 10.1161/ATVBAHA.107.158014. URL <http://atvb.ahajournals.org/content/28/2/223>.
- [435] Anne Karine Lagendijk, Guillermo A. Gomez, Sungmin Baek, Daniel Hesselton, William E. Hughes, Scott Paterson, Daniel E. Conway, Heinz-Georg Belting, Markus Affolter, Kelly A. Smith, Martin A. Schwartz, Alpha S. Yap, and Benjamin M. Hogan. Live imaging molecular changes in junctional tension upon VE-cadherin in zebrafish. *Nature Communications*, 8(1):1402, November 2017. ISSN 2041-1723. doi: 10.1038/s41467-017-01325-6. URL <https://www.nature.com/articles/s41467-017-01325-6>.
- [436] Yvette W. Kunz. Kupffer’s vesicle. In *Developmental Biology of Teleost Fishes*, Fish & Fisheries Series, pages 259–266. Springer, Dordrecht, 2004. ISBN 978-1-4020-2996-7 978-1-4020-2997-4. doi: 10.1007/978-1-4020-2997-4_14. URL https://link.springer.com/chapter/10.1007/978-1-4020-2997-4_14.
- [437] Jeffrey J. Essner, Jeffrey D. Amack, Molly K. Nyholm, Erin B. Harris, and H. Joseph Yost. Kupffer’s vesicle is a ciliated organ of asymmetry in the zebrafish embryo that initiates left-right development of the brain, heart and gut. *Development*, 132(6):1247–1260, March 2005. ISSN 0950-1991, 1477-9129. doi: 10.1242/dev.01663. URL <http://dev.biologists.org/content/132/6/1247>.
- [438] Sevi Durdu, Murat Iskar, Céline Revenu, Nicole Schieber, Andreas Kunze, Peer Bork, Yannick Schwab, and Darren Gilmour. Luminal signalling links cell communication to tissue architecture during organogenesis. *Nature*, (515):120–124, November 2014. doi: 10.1038.

Appendix A: Manual Measurements

Growth measurements

Open 3D stack in Fiji. Use line ROI.

- **Primordial midbrain channel (PMBC)** width: measure distance posterior to eye (Fig. A).
- **Basal artery (BA)** diameter: measure diameter about 50um before splitting into PCS (Fig. A).
- Measurements of **brain growth** (Fig. B):
 - Forebrain
 - Midbrain
 - Hindbrain
- **ISV diameter**: diameter of 3 ISVs at cloaca; consider if you want to measure aISV and vISV differences
- **DA diameter**



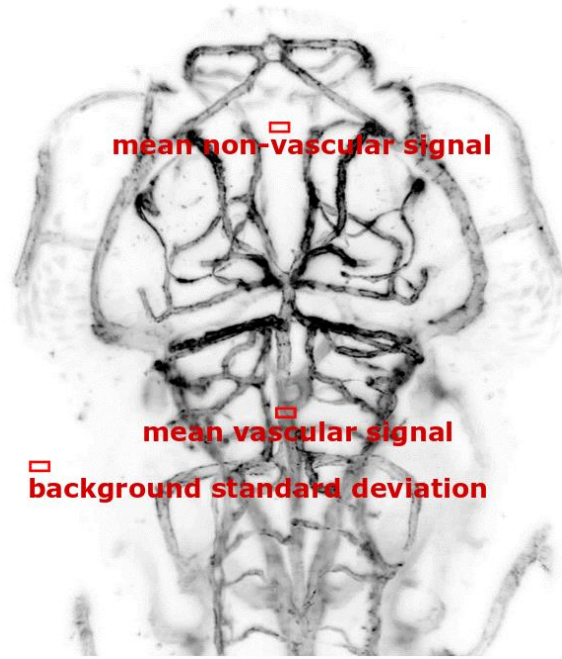
Contrast-to-Noise Ratio (CNR)

- Select rectangle ROI (in 3D stack; position as indicated in image; 5um long; crossing basal artery width)
- Analyse > Histogram [h] > *Mean vascular value*
- Live > move to non-vascular region (same plane but without vessels) > *mean non-vascular signal*
- Move to background region (same plane but outside embryo) > *background standard deviation*

Formulas

(1) **SNR (signal-to-noise ratio)** = mean vascular signal / standard deviation of background

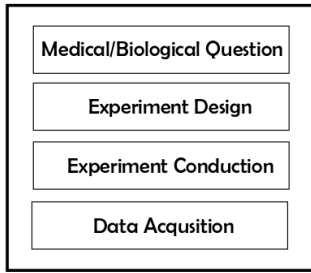
(2) **CNR (contrast-to-noise ratio)** = (mean vascular signal - mean non-vascular signal) / standard deviation of background



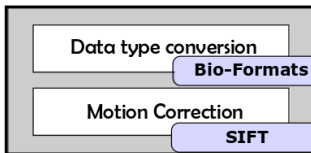
Appendix B: Workflow overview

- Steps can be done individually or all at once; see below for requirements, input, and output details.
- All steps are developed for the image-analysis software Fiji (<https://imagej.net/Fiji>).
- The MorphoLibJ plugin needs to be downloaded and installed separately (<https://imagej.net/MorphoLibJ>)
- **Important** - do not have more than 10 images in one folder for quantification steps, as this can cause issues with selection of correct ROIs.
- Before initializing code close all other windows (ROI manager, results, other open images).
- Once you start a processing step, do not interfere (do not click anything). Once the respective step(s) are done, the window "Macro finished" will appear.
- **For all steps:** select correct input folder (data need to be in a folder); output folder will be created automatically.
- **Computer specification:** LSFM data are large, RAM higher than 8GB recommended.
- **Time:** Computation time depends on computer specifications. For 64Gb RAM HP Z820 workstation:
 - *czi to tiff conversion:* <5min per image
 - *Intra-stack Motion Correction:* ~15min per image
 - *Vascular Enhancement:* ~45min per image
 - *Segmentation and Volume Quantification:* ~5min per image
 - *Intra-sample Symmetry:* ~15min per image
 - *Inter-sample Registration:* ~20min per image
 - *Quantification of Parameters:* ~5min

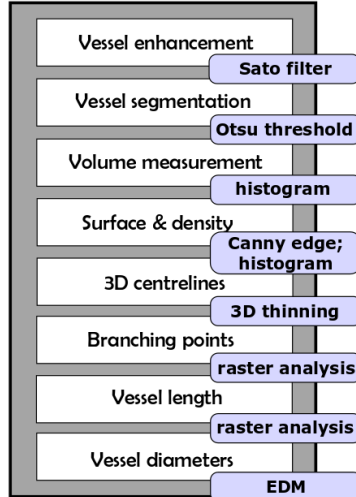
Experiment & Digitalization



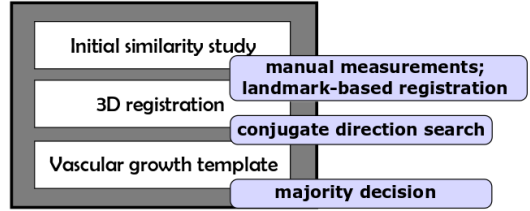
Data Pre-processing



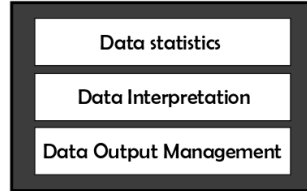
Quantification



Registration

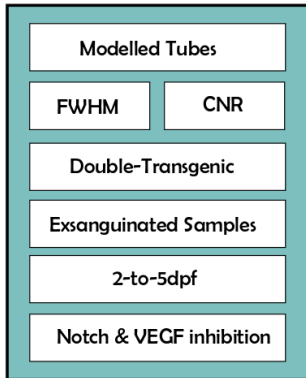


Data analysis

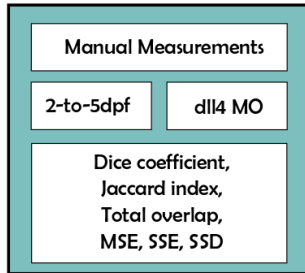


Validation and Application

Segmentation



Registration



Quantification



Appendix C: Individual Macros

Single-channel .czi to .tiff conversion and automatic MIP creation

- Create folder for .tiff files in the folder with .czi files
- “Plugins” > “Macros” > “Run”
 - single-colour: **EKugler_cziToTiffConversion.ijm**
- “Run”
- Select input folder

```
/* EKugler 2019
 * Macro for .czi to .tiff conversion and automatic MIP creation
 * USE:
 *
 *      hit run
 *      select input folder (path to .czi files)
 *      select output folder (path for .tiff and MIPs)
 *      when Macro is done - popup window will say "Macro is finished."
 *      contact: kugler.elisabeth@gmail.com
 */

// input and output path
path = getDirectory("Input Folder");
filelist = getFileList(path);
VascDir = path + "/VascTiff/";
File.makeDirectory(VascDir);

for (i=0; i< filelist.length; i++) {
    if (endsWith(filelist[i], ".czi")) {
        // Import czi with Bioformater
        run("Bio-Formats Importer", "open=" + path + filelist[i] + " autoscale
        color_mode=Default view=Hyperstack stack_order=XYCZT");
        // MIP with Contrast Enhancement
        run("Z Project...", "projection=[Max Intensity]");
        run("Color Balance...");
        run("Enhance Contrast", "saturated=0.35");
        saveAs("Jpeg", VascDir + "MAX_" + filelist[i]);
        run("Close");
        // Save as Tiff Stack
        selectWindow(filelist[i]);
        saveAs("Tiff", VascDir + filelist[i]);
        run("Close");
    }
}
close();

showMessage("Macro is finished.");
```

Multi-channel .czi to .tiff conversion and automatic MIP creation

- Create folder for .tiff files in the folder with .czi files
- “Plugins” > “Macros” > “Run”
 - multi-colour: **EKugler_MultiColourcziToTiffConversion.ijm**
- “Run”
- Select input folder

```

/* EKugler 2019
 * Macro for multi-colour .czi to .tiff conversion and automatic MIP creation
 * USE:
 *
 *         hit run
 *         select input folder (path to .czi files)
 *         select output folder (path for .tiff and MIPs)
 *         when Macro is done - popup window will say "Macro is finished."
 *         contact: kugler.elisabeth@gmail.com
 */

// input and output path
path = getDirectory("Input Folder");
//outputFolder = getDirectory("Output Folder");
filelist = getFileList(path);

NonVascDir = path + "/NonVascTiff/";
File.makeDirectory(NonVascDir);

VascDir = path + "/VascTiff/";
File.makeDirectory(VascDir);

for (i=0; i< filelist.length; i++) {
    if (endsWith(filelist[i], ".czi")) {
        // czi import using Bioformats
        run("Bio-Formats Importer", "open=" + path + filelist[i] + " autoscale
        color_mode=Default split_channels view=Hyperstack stack_order=XYCZT");

// Save as tiff stack
        selectWindow(filelist[i] + " - C=0"); // green
        saveAs("Tiff", NonVascDir + filelist[i]);
        run("Z Project...", "projection=[Max Intensity]");
        saveAs("Jpeg", path + "MAX_" + filelist[i]);
        close();
        selectWindow(filelist[i] + " - C=1"); // red
        saveAs("Tiff", VascDir + filelist[i]);
        run("Z Project...", "projection=[Max Intensity]");
        saveAs("Jpeg", path + "MAX_" + filelist[i]);
        close();
        close();
    }
}
close();
showMessage("Macro is finished");

```

Intra-Stack Motion Correction

- Create folder for motion corrected files in the folder with original files
- “Plugins” > “Macros” > “Run”
 - ***EKugler_MotionCorrectionSIFT.ijm***
- “Run”
- Select input folder
- Select output folder

/* EKugler 2019

* Macro for motion correction using Scale Invariant Feature Transform (SIFT)
 * USE:
 * hit run
 * select input folder (path to .czi files)
 * select output folder (path for .tiff and MIPs)
 * when Macro is done - popup window will say "Macro is finished."
 * contact: kugler.elisabeth@gmail.com
 *
 * paper SIFT: Lowe, David G. (2004) Distinctive Image Features from Scale-Invariant
 Keypoints, International Journal of Computer Vision. 60 (2): 91–110. CiteSeerX
 10.1.1.73.2924.
 *
 * papers motion correction zebrafish vasculature:
 * (1) Kugler, Chico, Armitage, (2018) Image Analysis in Light Sheet Fluorescence
 Microscopy Images of Transgenic Zebrafish Vascular Development. In Nixon M., Mahmoodi
 S., Zwiggelaar R. (eds) Medical Image Understanding and Analysis. MIUA 2018.; Springer,
 Cham, 2018; Vol. Communications in Computer and Information Science, vol 894, pp. 343–
 353.
 * (2) Kugler, Plant, Chico and Armitage (2019), Enhancement and Segmentation
 Workflow for the Developing Zebrafish Vasculature, J. Imaging 2019, 5(1), 14;
<https://doi.org/10.3390/jimaging5010014>
 */

```
// input and output path
path = getDirectory("Input Folder");
outputFolder = getDirectory("Output Folder");
filelist = getFileList(path);

for (i=0; i< filelist.length; i++) {
    if (endsWith(filelist[i], ".tif")) {
        open(path + filelist[i]);
        selectWindow(filelist[i]);

//get image properties
        getDimensions(width, height, channels, slices, frames);
        preChannels = channels;
        preSlices = slices;
        preFrames = frames;

        getPixelSize(unit,pixelWidth,pixelHeight,voxelDepth);
        prePixelWidth =pixelWidth;
        prePixelHeight = pixelHeight;
        preVoxelDepth = voxelDepth;

// Intrastack Linear Stack Alignment using SIFT algorithm
        run("Linear Stack Alignment with SIFT", "initial_gaussian_blur=1.60
steps_per_scale_octave=5      minimum_image_size=64      maximum_image_size=1920
feature_descriptor_size=8      feature_descriptor_orientation_bins=8
closest/next_closest_ratio=0.95      maximal_alignment_error=5      inlier_ratio=0.05
expected_transformation=Rigid interpolate");

// re-set original image values
```

```

        run("Properties...", "channels=" + preChannels + " slices=" + preSlices + "
frames=" + preFrames + " unit= $\mu$ m pixel_width=" + prePixelWidth + " pixel_height=" +
prePixelHeight + " voxel_depth=" + preVoxelDepth);

// get MIP of SIFT-aligned stack
        run("Z Project...", "projection=[Max Intensity]");
        saveAs("PNG", outputFolder + "SIFTAligned_" + filelist[i]);
        run("Close");

// Save SIFT-aligned stack as tiff stack
        saveAs("Tiff", outputFolder + "SIFTAligned_" + filelist[i]);
        run("Close");
    }
}
close();

showMessage("Macro is finished.");

```

Vascular Enhancement

- Create folder for enhanced files in the folder with original files
- “*Plugins*” > “*Macros*” > “*Run*”
 - **EKugler_VascularEnhancement.ijm**
- “*Run*”
- Select input folder
- Select output folder

```

/* EKugler 2019
 * Macro for vascular enhancement using Tubeness Filter
 * USE:
 *     hit run
 *     select input folder (path to .czi files)
 *     select output folder (path for .tiff and MIPs)
 *     when Macro is done - popup window will say "Macro is finished."
 *     contact: kugler.elisabeth@gmail.com
 *
 *     paper tubeness filter: Sato, Nakajima, Atsumi, Koller, Gerig, Yoshida and Kikinis
(1997) 3D multi-scale line filter for segmentation and visualization of curvilinear structures in
medical images, International Conference on Computer Vision, Virtual Reality, and Robotics
in Medicine, CVRMed 1997, MRCAS 1997: CVRMed-MRCAS'97 pp 213-222.
 */

```

```

// input and output path

path = getDirectory("Input Folder");
outputFolder = getDirectory("Output Folder");
filelist = getFileList(path);

for (i=0; i< filelist.length; i++) {
    if (endsWith(filelist[i], ".tif")) {
        open(path + filelist[i]);

        selectWindow(filelist[i]);
    }
}

```

```

//get image properties
    getDimensions(width, height, channels, slices, frames);
    preChannels = channels;
    preSlices = slices;
    preFrames = frames;

    getPixelSize(unit,pixelWidth,pixelHeight,voxelDepth);
    prePixelWidth =pixelWidth;
    prePixelHeight = pixelHeight;
    preVoxelDepth = voxelDepth;

// Run Plugins > Analyze > Tubeness Filter (Frangi Vessel Enhancement Implementation)

    run("Tubeness", "sigma=10.6848"); // scale size to be changed
// re-set original image values
    run("Properties...", "channels=" + preChannels + " slices=" + preSlices + "
frames=" + preFrames + " unit=µm pixel_width=" + prePixelWidth + " pixel_height=" +
prePixelHeight + " voxel_depth=" + preVoxelDepth);
// get MIP of vessel enhanced stack and save it
    run("Z Project...", "projection=[Max Intensity]");
    saveAs("PNG", outputFolder + "TF_" + filelist[i]);
    run("Close");
// Save enhanced stack as tiff stack
    saveAs("Tiff", outputFolder + "TF_" + filelist[i]);
    run("Close");

    selectWindow(filelist[i]);
    close();
}
}
close();

showMessage("Macro is finished");

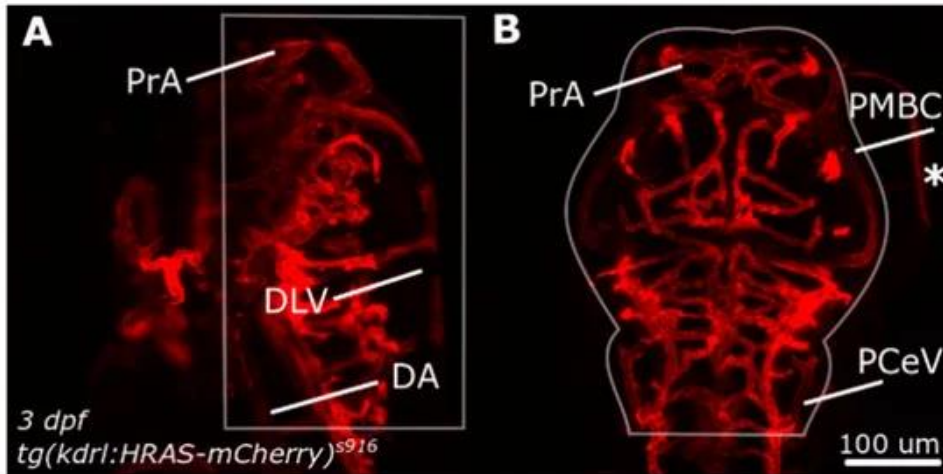
```

Segmentation and Volume Quantification

- a. Create folder for enhanced files in the folder with original files
- b. Create ROIs:
 - Open MIP
 - Draw ROI with Freehand Selection tool
 - Edit > Selection > Add to Manager > Save > ROI_imageTitle
 - Open next MIP > draw next ROI > Add [t] > Save > ROI_imageTitle
 - Select all ROIs (click individually and hold "ctrl" > Save > save as "RoiSet" in folder with enhanced images)
- c. **"Plugins" > "Macros" > "Run" *make sure ROI manager etc is closed***
- d. **"Run"**
- d. Select input folder
- e. Select output folder
- f. will create a folder **"TH"** inside the input folder containing **.tiffs** and **MIPs** of segmented images
- g. will create folder **"Edges"** inside the input folder containing **.tiffs** and **MIPs** of vascular edges

h. will create a file “**VascVolResults**” inside the input folder containing results of vascular volume, vascular density and vascular surface

Definition of cranial vascular volume ROI: <https://www.mdpi.com/2313-433X/5/1/14>



/* EKugler 2019

* Macro for vascular segmentation and volume quantification

* USE:

* hit run

* select input folder (path to .czi files)

* select output folder (path for .tiff and MIPs)

* when Macro is done - popup window will say "Macro is finished."

* contact: kugler.elisabeth@gmail.com

*

* paper Otsu thresholding: N Otsu. A threshold selection method from gray-level histograms. Trans. Sys.Man., 9(1):62–66, 1979.

*

* papers segmentation: (1) Kugler, Plant, Chico and Armitage (2019), Enhancement and Segmentation Workflow for the Developing Zebrafish Vasculature, J. Imaging 2019, 5(1), 14; <https://doi.org/10.3390/jimaging5010014>

*/

// input and output path

path = getDirectory("Input Folder");

outputFolder = getDirectory("Output Folder");

filelist = getFileList(path);

// create file to write volume measurements

f = File.open(path + "VascVolResults.txt");

EdgeDir = path + "/Edges/";

// output folder

File.makeDirectory(EdgeDir);

//open ROI set

roiManager("Open", path + "RoiSet.zip");

n = roiManager("count");

r=0; // counter for ROIset

// colourSetting needed for clearing outside for vascular volume quantification

```

setForegroundColor(255, 255, 255);
setBackgroundcolor(255, 255, 255);

// start processing of files
for (i=0; i< filelist.length; i++) {
    if (endsWith(filelist[i], ".tif")) {
        open(path + filelist[i]);
// segmentation
        selectWindow(filelist[i]);

//get image properties
        getDimensions(width, height, channels, slices, frames);
        preChannels = channels;
        preSlices = slices;
        preFrames = frames;

        getPixelSize(unit,pixelWidth,pixelHeight,voxelDepth);
        prePixelWidth =pixelWidth;
        prePixelHeight = pixelHeight;
        preVoxelDepth = voxelDepth;

        voxelVol= (prePixelWidth * prePixelHeight * preVoxelDepth);

        run("8-bit");
        setAutoThreshold("Default dark");
        run("Threshold...");
        setThreshold(4, 255); // threshold to be changed if other image acquisition
settings
        setOption("BlackBackground", false);
        run("Convert to Mask", "method=Default background=Dark");

        // re-set original image values
        run("Properties...", "channels=" + preChannels + " slices=" + preSlices + "
frames=" + preFrames + " unit= $\mu\text{m}$  pixel_width=" + prePixelWidth + " pixel_height=" +
prePixelHeight + " voxel_depth=" + preVoxelDepth);
        // Save segmented stack as tiff stack
        saveAs("Tiff", outputFolder + "TH_" + filelist[i]);
        // create MIP
        run("Z Project...", "projection=[Max Intensity]");
        saveAs("Jpeg", outputFolder + filelist[i]);
run("Close");

//vascular volume [vx] quantification - ROI from MIPs
selectWindow("TH_" + filelist[i]);
//iterate through ROI set
roiManager("Select", r);
run("Measure"); // for density
AeaUm = getResult("Area");
r++; // counter for ROI in ROIset
// clear outside
run("Clear Outside", "stack");
// histogram count black
run("Histogram", "stack");
// [255] is VascVox
Plot.getValues(values, counts);

```

```

VascVox=counts[255];
VascVol = voxelVol * VascVox;// vascular density
selectWindow("TH_" + fileListTH[i]);
AreaVx = AreaUm / voxelVol; // change um to vx
FullVox = AreaVx * slices;
density = AreaVx / FullVox; // min 0, max 1

// vascular surface
selectWindow("TH_" + fileListTH[i]);
run("Find Edges", "stack");
saveAs("Tiff", EdgeDir + "Edges_" + fileListTH[i]);
run("Z Project...", "projection=[Max Intensity]");
saveAs("Jpeg", EdgeDir + "MAX_Edges_" + fileListTH[i]);
run("Close");
selectWindow("Edges_" + fileListTH[i]);
// histogram count black
run("Histogram", "stack");
// [255] is VascVox
Plot.getValues(values, counts);
EdgeVox=counts[255];

EdgeVol = voxelVol * EdgeVox;
print(f, fileListTH[i] + " \t" + "VascVox" + "\t" + VascVox + "\t" + "VascVol"
+ "\t" + VascVol + "\t" + "EdgeVox" + "\t" + EdgeVox + "\t" + "EdgeVol" + "\t" + EdgeVol + "\t"
+ "density" + "\t" + density);
close();
}
}
close();

showMessage("Macro is finished.");

```

Intra-sample Symmetry

To compare left and right vascular symmetry. To be applied to pre-processed and segmented images.

important MorphoLibJ plugin needed (<https://imagej.net/MorphoLibJ>)

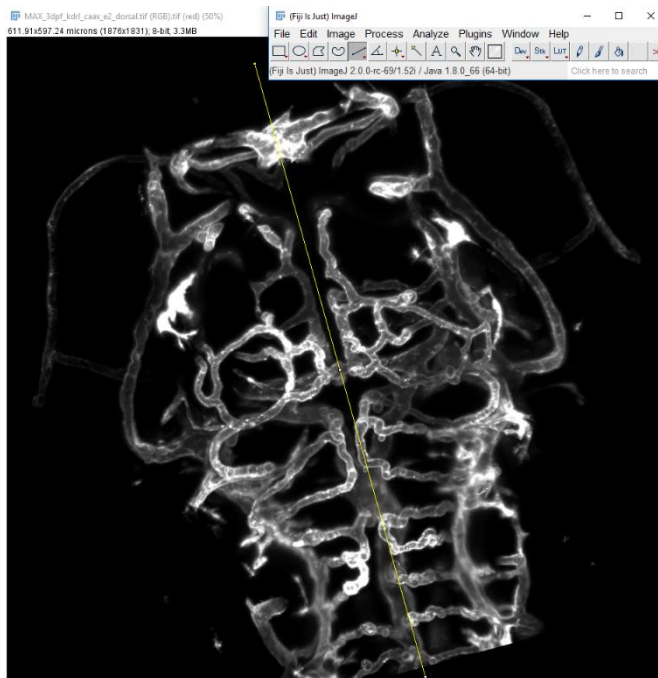
important

- During image acquisition - make sure embryos are not left-right tilted (z-axis). If they are - register to non-tilted sample before quantifying L-R symmetry.
- Create “*OutputFolder*” before starting. (in this folder all your output will be saved; logic could for example be “*../tiff/TF/TH/outputfolder*”)
- Create “*RoiSetLine.zip*” before starting in the folder with images. This is needed to rotate the image and bring the fish anterior-posterior axis into alignment with the image y-axis.

This is done as follows

important: have to be in order (ie 1,2,3)

- “*Drag and drop*” MIP (original, pre-processed or segmented) into Fiji
- Select Line ROI tool
- Draw along anterior posterior



- “Add” to ROI manager
- Repeat for all images
- When all ROIs are drawn - select all ROIs and “save” as “RoiSetLine” in the folder where the images which will be processed are saved (logic could for example be “../tiff/TF/TH”)
- “Plugins” > “Macros” > “Run”
 - *make sure ROI manager and results table are closed*
- “Run”
- Select input folder
- Select output folder
- Macro will prompt you to draw another line ROI after images were rotated. This line ROI will be used to split L and R vol.
 - *****important: have to be in order (ie 1,2,3)*****
 - Draw line ROI and “add” to ROI manager
 - Close images
 - Click “ok”
- **IntraSampleSymmetryResults.csv** with left and right vascular volume and skeleton voxels will be created in input folder (VascVox = number of black voxels; VascVol = vascular volume in um³)
- Individual files for LR similarity quantification (Jaccard Index, Dice Coefficient and Total Overlap; see <https://imagej.net/MorphoLibJ>) will be created in **LRVol** folder

Inter-sample Registration

- Create folder for enhanced files in the folder with original files
- ***** important ***** one file needs to be called "template"
- “Plugins” > “Macros” > “Run”
 - **EKugler_AutomaticRigidInterSampleRegistration.ijm**
- “Run”
- Select input folder
- Select output folder

```

/* EKugler 2019
* Macro for automatic rigid inter-sample registration
* USE:
*   *** important *** one file needs to be called "template"
*   hit run
*   select input folder (path to .czi files)
*   when Macro is done - popup window will say "Macro is finished."
*   contact: kugler.elisabeth@gmail.com
*/

// input and output path
path = getDirectory("Input Folder");
// user prompt to select template image
// template = XXX;

filelistReg = getFileList(path);

open(path + "template.tif");
template=getTitle();
print("Running Inter-Sample Registration.");

RegDir = path + "/Reg/"; // output folder
File.makeDirectory(RegDir); // make output folder

// inter-sample registration

// get image/voxel properties
getDimensions(width, height, channels, slices, frames);
preChannels = channels;
preSlices = slices;
preFrames = frames;
getPixelSize(unit,pixelWidth,pixelHeight,voxelDepth);
preUnit=unit;
prePixelWidth =pixelWidth;
prePixelHeight = pixelHeight;
preVoxelDepth = voxelDepth;

for (i=0; i< filelistReg.length; i++) {
    if (endsWith(filelistReg[i], ".tif")){
        open(path + filelistReg[i]);
        // segmentation
        selectWindow(filelistReg[i]);
        run("Rigid Registration", "initialtransform=[] n=1 tolerance=20
level=7 stoplevel=4 materialcenterandbbox=[] showtransformed template=" + template + "
measure=Euclidean");
        run("Invert", "stack");
        //setThreshold(0, 132);
        setOption("BlackBackground", false);
        run("Make Binary", "method=Default background=Default");
        // set image/voxel properties
        run("Properties...", "channels=" + preChannels + " slices=" +
preSlices + " frames=" + preFrames + " unit=" + preUnit + " pixel_width=" + prePixelWidth + "
pixel_height=" + prePixelHeight + " voxel_depth=" + preVoxelDepth);
    }
}

```

```

        saveAs("Tiff", RegDir + "InterSReg_" + filelistReg[i]);
        // create MIP
        run("Z Project...", "projection=[Max Intensity]");
        saveAs("Jpeg", RegDir + "MAX_InterSReg_" + filelistReg[i]);
        close();
        close();
    }
}
close();
close();
showMessage("Macro is finished");

```

Intra-sample Symmetry using Anatomical Landmarks

To be applied to pre-processed and segmented images.

Based on https://imagej.net/Name_Landmarks_and_Register

important first image/template and following images (moving images) have to be the same age. (ie select one template for each age!)

important if you want to measure sample similarities (before and after registration) - MorphoLibJ plugin needed (<https://imagej.net/MorphoLibJ>)

First Image // template (which will be template - make sure this one is aligned in x,y, and z):

Open segmented images and select “*Plugins > Landmarks > Name Landmarks and Register*”

- select landmarks (see figure) using single point tool 
- **Named Point (0)** after selecting first point
- **Rename** to rename point eg right ACeV
- **Add New Point** and repeat this for all points from the figure (left PrA, right PrA, left ACeV to PrA, right ACeV to PrA, left PCS to MtA, right PCS to MtA, left ACeV, right ACeV, left PCeV to PHBC, right PCeV to PHBC, MCeV to DLV)
- **Save** to save these landmarks
- **Choose** this file in it's file location AND **Set As Default** (so the computer knows this is your template)

Images to register // moving images (these will be registered to the first/template image):

- Landmark names and template should be saved from the above (if there is nothing, something went wrong)
- Make sure the **correct template** is chosen; otherwise **Choose**
- “*Plugins > Landmarks > Name Landmarks and Register*”
- select landmarks (see figure) using single point tool and select respective anatomical landmark; eg **right ACeV**
- **Save** to save these landmarks

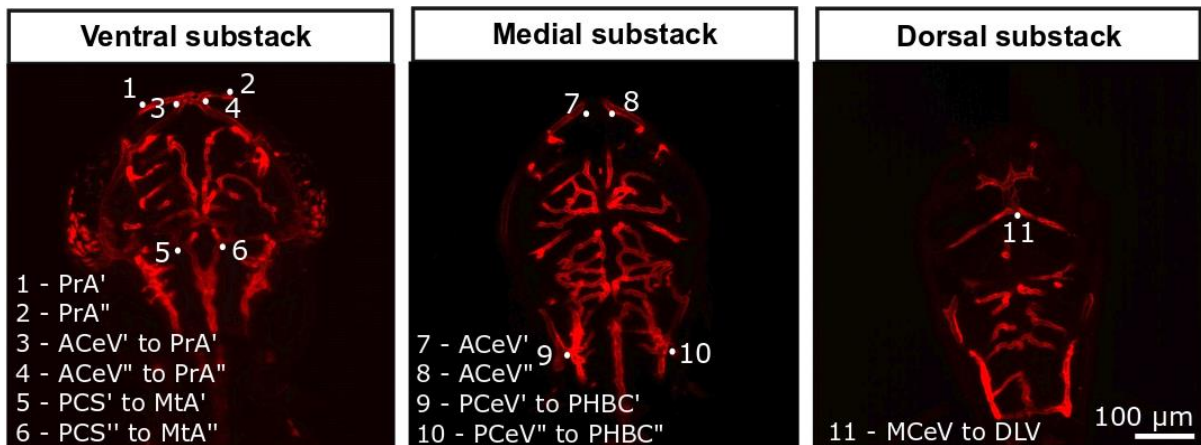
Registration:

- make sure you select **Overlay result** (and have the right template selected)
- **Best Rigid Registration**

Save file:

- Image > colour > split channels
- Select green channel > Edit > invert (yes, whole stack)
- File > Save as ...

Anatomical landmarks:



Downscaling to 512x512 with ROI selection

- Create folder for enhanced files in the folder with original files
- ***** important ***** need to open ROIs in ROI Manager
- “Plugins” > “Macros” > “Run”
 - **EKugler_512Conversion.ijm**
- “Run”
- Select input folder
- Select output folder

```
path = getDirectory("Input Folder");
filelist = getFileList(path);
```

```
n = roiManager("count");
r=0;
```

```
for (i=0; i< filelist.length; i++) {
    if (endsWith(filelist[i], ".tif")) {
        open(filelist[i]);
        run("Invert", "stack");
        roiManager("Select", r);
        setBackgroundColor(0, 0, 0);
        run("Clear Outside", "stack");
        setTool("point");
        makePoint(508, 4, "small yellow hybrid");
    }
}
```

```

run("Invert", "stack");
r++; // counter for ROI in ROIset

run("Scale...", "x=- y=- z=1.0 width=512 height=512 depth=425
interpolation=Bilinear average process create");
saveAs("Tiff", path + "/512x512/" + filelist[i]);
setThreshold(123, 255);
setOption("BlackBackground", false);
run("Make Binary", "method=Default background=Default");
run("Z Project...", "projection=[Max Intensity]");
saveAs("Jpeg", path + "/512x512/" + "MAX_" + filelist[i]);
run("Close");
// run("Skeletonize (2D/3D)");
// saveAs("Tiff",
"E:/15122018_3dpf_dll4MO_Rep3/enhanced/TH/512x512/skel/" + filelist[i]);
close();
close();
}
}
showMessage("Macro is finished");

```

Quantification of Parameters

- Create folder for enhanced files in the folder with original files
- “*Plugins*” > “*Macros*” > “*Run*”
 - **EKugler_Quantification.ijm**
- “*Run*”
- Select input folder
- Select output folder

```

// vascular diameters, BPs, endpoints, and vessel lengths
// 04022020_EKugler

```

```

// needs binarized or thresholded images as input
// use 2D MIP of 3D skeleton and 2D Distance map for diameter (dia) estimation
// branching points (BPs), endpoints (EPs), and average vessel length (avgLength) are
calculated in 3D, displayed in 2D

```

```

// meep to be replaced with filelist

```

```

// check whether ROIs for input needed (aka clear outside)

```

```

path = getDirectory("Input Folder");
outputFolder = getDirectory("Output Folder");
SeletonList = getFileList(path);
filelist = getFileList(path);

```

```

ROImanual = getBoolean("Do you want to select a region manually?");

```

```

for (i=0; i< filelist.length; i++) {
    if (endsWith(filelist[i], ".tif")) {

```

```

open(path + filelist[i]);

```

```

selectWindow(filelist[i]); // later to be changed to iterate through all and embed into code
GUI.ijm
meep = getTitle();
short = replace(meep, ".tif", "");

skeletonFile = File.open(path + short + ".txt"); // txt file for results
print(skeletonFile, "\t" + "NetworkVoxel" + "\t" + "BPVoxel" + "\t" + "EPVoxel" + "\t" +
"averageDia [whole]");

getDimensions(width, height, channels, slices, frames);
getPixelSize(unit, pixelWidth, pixelHeight, voxelDepth);

BoxROIWidth = 0;
BoxROIHeight = 0;

///// create MIP and Distance Map for diameters /////
selectWindow(meep); // select original thresholded image
run("Duplicate...", "title=ForSkel duplicate"); // for skeletonization later
run("Duplicate...", "title=For3DEDM duplicate");
selectWindow(meep);
// need to run it on 2D to get exact values
run("Z Project...", "projection=[Max Intensity]");
run("Geometry to Distance Map", "threshold=1");
saveAs("Tiff", outputFolder + "MAX_" + short + "_EDT"); // save 2D distance map

///// skeletonize original tresholded image in 3D /////
selectWindow("ForSkel"); // duplicate from original thresholded image; to skeletonize in 3D
run("Skeletonize (2D/3D)");
rename("Skel_");
run("Duplicate...", "title=ForEDMSkel duplicate");

///// save skeletonized image /////
saveAs("Tiff", outputFolder + "Skel_" + short); // stack
run("Z Project...", "projection=[Max Intensity]");
run("Skeletonize (2D/3D)"); // remove spurious branches in 2D
saveAs("Tiff", outputFolder + "MAX_Skel_" + short); // MIP

///// merge 2D skel and 2D distance map for diameter measurements /////
imageCalculator("AND create", "MAX_" + short + "_EDT.tif", "MAX_Skel_" + meep);
run("Fire");
saveAs("Tiff", outputFolder + "MAX_LUTFire_EDM_Skel_" + short); // stack
rename("LUTFire_EDM");

///// quantify diameters /////
///// NUMBER 1 - average diameter for whole 2D image - iterate through whole image in (x,y)
counter = 0;0
value = 0;
total = 0;
avgLength = 0;

selectWindow("LUTFire_EDM");

```

```

// .. use image properties and brightness/intensity to quantify width at the respective vx in
microns
    for (y = 0; y < height; y++) {
        for (x = 0; x < width; x++) {
            properties = getPixel(x, y);
            if (properties != 0){
                // skip if intensity
                value under 30-ish?
                counter++;
                total += properties;
                //value = properties * 1.15;
                //setPixel(x, y, value);
            }
        }
    }

    average = (total/counter); // multiply with conversionFactor!!!!!!!!!!!!!!!!!!!! // don't
think a conversion factor is needed -- will need to double-check
    saveAs("Tiff", outputFolder + "MAX_Dia_" + short); // stack
    // print(counter);
    // debug

// duplicate for dia quantifications in ROIs
run("Duplicate...", "title=ForROIRaster duplicate");
run("Duplicate...", "title=ForManualROI duplicate");

//////// NUMBER 2 - Quantify avg Diameter of predetermined bounding box ROIs (10x10 ROIs)
// get box size from image size (width and height)
BoxROIWidth = width/10;
BoxROIHeight = height/10;

selectWindow("ForROIRaster");
// initialize ROI rectangle positions
setForegroundColor(255, 255, 255);
setTool("rectangle");

// iterate through image to create 10 x 10 ROI boxes
    for (b=0; b < width; b=b+BoxROIWidth) { // b = breite
        for (l=0; l < height; l=l+BoxROIHeight) { // l = laenge
            // initial box
            makeRectangle(b, l, BoxROIWidth, BoxROIHeight); // x,y,w,h

            var    counterBox = 0; totalBox = 0; propertiesBox = 0; averageBox =
0;

            // quantify avg dia for THIS ROI box
            for (yB = 0; yB < BoxROIHeight; yB++) {
                for (xB = 0; xB < BoxROIWidth; xB++) {
                    propertiesBox = getPixel(xB, yB);
                    if (propertiesBox != 0){
                        counterBox++;
                        totalBox += propertiesBox;
                    }
                }
            }
        }
    }

```

```

        print(averageBox);

        averageBox = (totalBox/counterBox);
        setSelectionName(averageBox);

        run("Add Selection...");
        run("Labels...", "color=white font=10 show use bold");

        // write into excel file ID 1, 2, etc...

    }
}
saveAs("Jpeg", outputFolder + "ROIBoxes" + short);

///// NUMBER 3 - Quantify avg Diameter in manually selected ROI /////
selectWindow("ForManualROI");
if(ROImanual == true){

    do {
        do {
            // Prompt user to select region (default to rectangle selection tool)
            setTool(0);
            waitForUser("Select ROI", "Select a vessel segment, then click OK.");
        } while(selectionType() != 0);

        getSelectionCoordinates(x, y);
        startX = x[0];
        startY = y[0];
        endX = x[2];
        endY = y[2];

        var dist=0, count=0, total=0, average=0;

        // Loop through pixels in ROI
        for (v = startY; v <= endY; v++) {
            for (h = startX; h <= endX; h++) {
                dist = getPixel(h,v);

                // Account for non-black pixels only
                if (dist != 0) {
                    count++;
                    total += dist;
                }
            }
        }

        // Print average diameter
        average = (total/count);
        setSelectionName(average);

        // Overlay label for selected ROI
        run("Add Selection...");
        run("Labels...", "color=white font=10 show use bold");
    }
}

```

```

region?");
    cont = getBoolean("Would you like to calculate the average diameter of another
region?");

    } while(cont)

    run("Save");
    flatten = getBoolean("Would you like to save a copy of the flattened image?");
    if (flatten) {
        setBatchMode(true);
        run("Flatten");
        name = getTitle();
        save(outputFolder + "ManualROIs" + short);
        setBatchMode(false);
    }
}

///// NUMBER 4 - Quantify avg Diameter of vessels from 3D BPs
// quantify diameters for individual vessels by using 3D BPs (x,y) coordinates as start and end
point

///// quantify whole 3D network length in voxel /////
selectWindow("Skel_" + meep);
run("Histogram", "stack");
Plot.getValues(values, counts);
NetworkVoxel=counts[255];
close(); // histogram

///// quantify avgLength from 3D Skel /////
selectWindow("For3DEDM");
run("Make Binary", "method=Default background=Light");
// run("Invert", "stack");
run("Distance Map", "stack");
run("Color Balance...");
run("Enhance Contrast", "saturated=0.35");

imageCalculator("AND create stack", "Skel_", "For3DEDM");

saveAs("Tiff", outputFolder + "3DEDM_" + short); // stack
run("Analyze Skeleton (2D/3D)", "prune=[shortest branch] show display");
saveAs("Results", outputFolder + "BranchInformation_" + short + ".csv"); // window 1
saveAs("Results", outputFolder + "Results_" + short + ".csv"); // window 2
close();

///// VISUAL BPs and endpoints from 3D skel /////
///// EPs - endpoints
selectWindow("Tagged skeleton");
run("Duplicate...", "title=ForEPs duplicate"); // for skeletonization later
run("Z Project...", "projection=[Max Intensity]");
setAutoThreshold("Default");
run("Threshold...");
setThreshold(2, 33);
setOption("BlackBackground", false);
run("Convert to Mask");

```

```

run("Histogram", "stack");
Plot.getValues(values, counts);
EPVoxel=counts[255];
close(); // histogram

///// BPs - branching points
selectWindow("Tagged skeleton");
run("Duplicate...", "title=ForBPs duplicate"); // for skeletonization later
run("Z Project...", "projection=[Max Intensity]");

// clean up BPs -- aka testing BPs 3D and 2D (x,y) against each other
// only the ones which are true for BOTH are considered true BPs here (no 100% accurate,
but the best to achieve here at that time)

// extract BPs via Thresholding
setAutoThreshold("Default");
run("Threshold...");
setThreshold(64, 70);
setOption("BlackBackground", false);
run("Convert to Mask");

imageCalculator("AND create", "MAX_Skel_" + meep, "MAX_ForBPs");
selectWindow("Result of MAX_Skel_" + meep);
rename("BPsClean");

run("Histogram", "stack");
Plot.getValues(values, counts);
BPVoxel=counts[255];
close(); // histogram

selectWindow("Tagged skeleton");
run("Z Project...", "projection=[Max Intensity]");
run("8-bit");

run("Merge Channels...", "c2=[MAX_ForEPs] c6=[MAX_Tagged skeleton] create
keep"); // EPs
saveAs("Jpeg", outputFolder + "MAX_EPs_" + short);
close();
run("Merge Channels...", "c2=[BPsClean] c6=[MAX_Tagged skeleton] create keep");
// BPs
saveAs("Jpeg", outputFolder + "MAX_BPs_" + short);
close();
selectWindow("MAX_Tagged skeleton");
close();
selectWindow("Tagged skeleton");
close();

// write BP and EP numbers into it...
print(skeletonFile, short + "\t" + NetworkVoxel + "\t" + BPVoxel + "\t" + EPVoxel
+ "\t" + average)

///// need to close everything
run("Close All");

```

```
        }  
    }  
    showMessage("Macro is finished");
```

Appendix D: Graphical User Interface Use

 Cranial Vascular Analysis ✕

Czi to tiff conversion:

Single- or Multiple Channels:

If .czi has more than 2 channels; please convert to .tiffs of individual channels first.

Motion Correction:

Steps per Scale Octave (4-8 recommended):

Feature Descriptor Size (4-8 recommended):

Feature closest-to-next ratio (0.92-0.98 recommended):

Maximal Alignment Error Consensus Filter (3-10px recommended):

Tubular Filtering (Enhancement; needs to be selected for segmentation):

Sigma Size [um] (10 recommended):

Segmentation and Vascular Volume Measurement:

ROIset exists:

If you made a ROIset.zip, make sure it's in the same folder as the enhanced images.

Inter-sample registration:

Needs a file called 'template' in the folder of images.

Intra-sample symmetry:

Needs a ROIsetLine.zip, make sure it's in the same folder as the segmented images.

Vasculature Quantification:

Contact: kugler.elisabeth@gmail.com

Step 1: .czi to .tiff conversion.

Cranial Vascular Analysis ×

Czi to tiff conversion:

Single- or Multiple Channels:

If .czi has more than 2 channels; please convert to .tiffs of individual channels first.

- to be done to convert .czi files to .tiff format (not to be done if your data are .tiff)
- select if single-colour or dual-colour (if more than 2 channels, convert your .czi to .tiffs using Bioformater and save channels individually)
- will create a folder “**VascTiff**” inside the input folder containing **.tiffs** and **MIPs**

Step 2: Motion Correction.

Motion Correction:

Steps per Scale Octave (4-8 recommended):

Feature Descriptor Size (4-8 recommended):

Feature closest-to-next ratio (0.92-0.98 recommended):

Maximal Alignment Error Consensus Filter (3-10px recommended):

- to correct for motions occurred during image acquisition (ie heart beat, gravity and muscle twitches)
- parameters were optimized for transgenic zebrafish data acquired with lightsheet microscopy (see papers above for details)
- will create a folder “**SIFT**” inside the input folder containing **.tiffs** and **MIPs**

Step 3: Tubular filtering, ie vessel enhancement.

Tubular Filtering (Enhancement; needs to be selected for segmentation):

Sigma Size [um] (10 recommended):

- to be done **before** segmentation
- scale size optimized for the cranial vasculature in zebrafish (see papers above for details)
- will create a folder “**TF**” inside the input folder containing **.tiffs** and **MIPs**

Step 4: Segmentation and vascular volume measurements.

(Note: if error comes up - just rerun, sometimes it has a little hiccup)

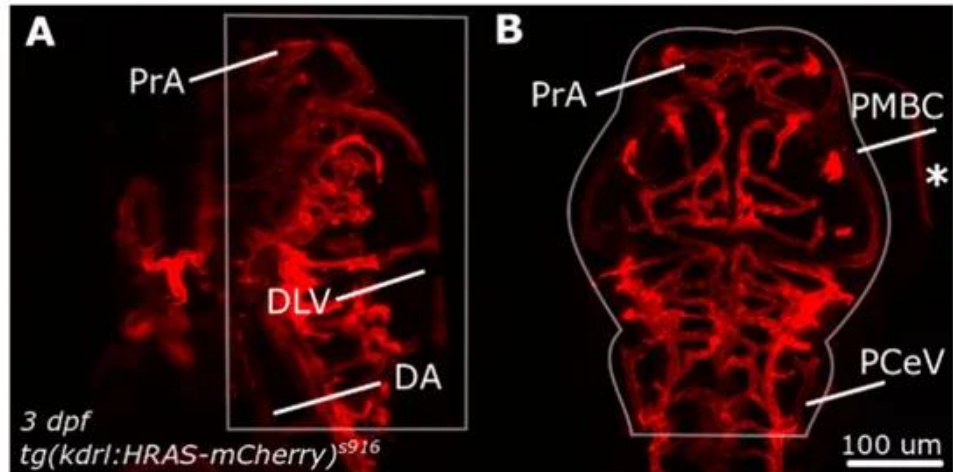
Segmentation and Vascular Volume Measurement:

ROIset exists:

If you made a ROIset.zip, make sure it's in the same folder as the enhanced images.

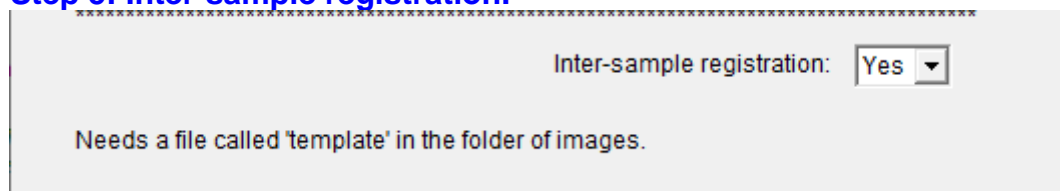
- **Enhanced** images as input required.

- Vascular volume quantification can be done as follows.
 - **Create ROIset before (recommended)**
 - Open MIP
 - Draw ROI with Freehand Selection tool
 - Edit > Selection > Add to Manager > Save > ROI_imageTitle
 - Open next MIP > draw next ROI > Add [t] > Save > ROI_imageTitle
 - Select all ROIs (click individually and hold “ctrl” > Save > save as “RoiSet” in folder with enhanced images)
 - Definition of cranial vascular volume ROI: <https://www.mdpi.com/2313-433X/5/1/14>



- **Create ROIs as segmentation proceeds**
 - ***important*** Select images in the order they are in the folder
 - Draw ROI with Freehand Selection tool
 - Edit > Selection > Add to Manager (can be saved as ROIset)
 - Once all ROIs are drawn click “ok” in the pop-up window
- **Stop after segmentation (not recommended)**
- will create a folder “**TH**” inside the input folder containing **.tiffs** and **MIPs** of segmented images
- will create folder “**Edges**” inside the input folder containing **.tiffs** and **MIPs** of vascular edges
- will create a file “**VascVolResults**” inside the input folder containing results of vascular volume, vascular density and vascular surface

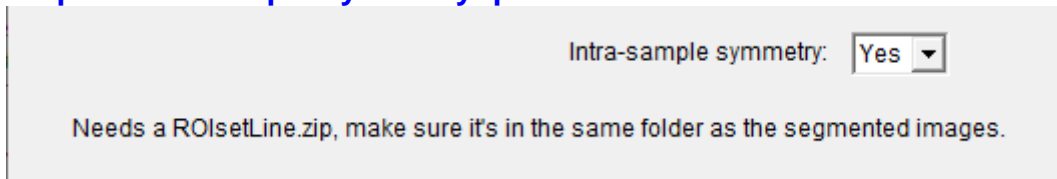
Step 5: Inter-sample registration.



- Needs **segmented** data as input.
- Needs one file called “**template**” in the input folder.
- Automatic registration is an iterative optimization algorithm (conjugate direction search) using scale space down-sampling to align stacks rigidly.
- will create a folder “**Reg**” inside the input folder containing **.tiffs** and **MIPs**

- will create files of similarity quantification (Dice, Jaccard and Total Overlap) before and after registration (respective to the template)

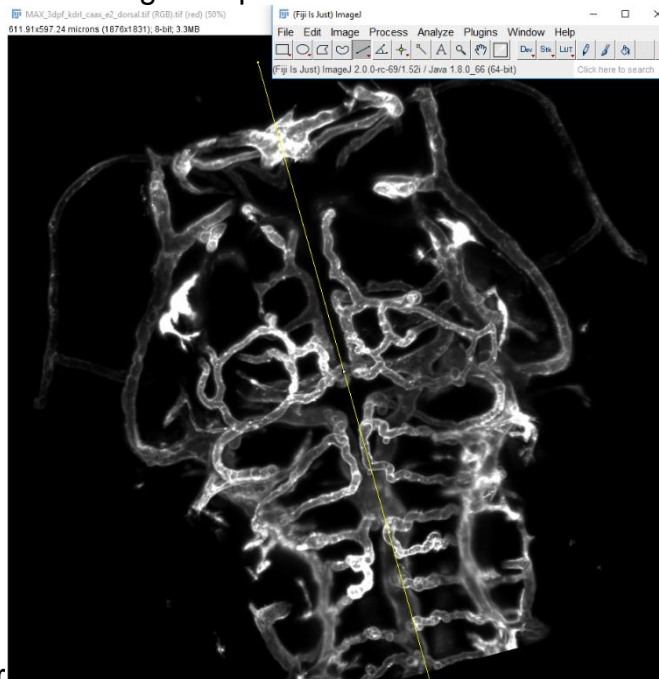
Step 6: Intra-sample symmetry quantification.



- Needs **segmented** data as input.
- Create "**RoiSetLine.zip**" before starting in the folder with images. This is needed to rotate the image and bring the fish anterior-posterior axis into alignment with the image y-axis. This is done as follows

*****important: have to be in order (ie 1,2,3)*****

- "Drag and drop" MIP (original, pre-processed or segmented) into Fiji
- Select Line ROI tool
- Draw along from posterior to anterior!



- "Add" to ROI manager
- Repeat for all images
- When all ROIs are drawn - select all ROIs and "save" as "**RoiSetLine**"
- will create a folder "**Sym**" inside the input folder containing **.tiffs** and **MIPs** of rotated images
- will create a folder "**LRVol**" inside the input folder containing **.tiffs** and **MIPs** of the left and right vasculature
- will create a file "**IntraSampleSymmetryResults**" in the input folder containing L and R vascular voxel, vascular volume and skeleton voxel
- will create files of similarity quantification (Dice, Jaccard and Total Overlap) between L and R in folder "**LRVol**"

Step 7: Quantification of vascular properties.

Vasculature Quantification:

Contact: kugler.elisabeth@gmail.com